Higgs sector characterization and aspects of the flavor puzzle

Jeremy Bernon

▶ To cite this version:

Jeremy Bernon. Higgs sector characterization and aspects of the flavor puzzle. High Energy Physics - Theory [hep-th]. Université Grenoble Alpes, 2016. English. NNT : 2016GREAY020 . tel-01491339

HAL Id: tel-01491339
https://tel.archives-ouvertes.fr/tel-01491339

Submitted on 16 Mar 2017

Communauté
UNIVERSITÉ Grenoble Alpes

THÈSE

Pour obtenir le grade de

DOCTEUR DE LA COMMUNAUTÉ UNIVERSITÉ GRENOBLE ALPES

Spécialité : **Physique Théorique**

Arrêté ministériel : 7 Août 2006

Présentée par

Jérémy BERNON

Thèse dirigée par **Dr. Sabine KRAML et Dr. Christopher SMITH**

préparée au sein du
Laboratoire de Physique Subatomique et Cosmologie
et de **l'École Doctorale de Physique de Grenoble**

Caractérisation du secteur de Higgs et aspects du problème de la saveur

Thèse soutenue publiquement le **Vendredi 16 Septembre 2016**, devant le jury composé de :

Pr. Aldo DEANDREA
Professeur, Université Claude Bernard, Président

Pr. Bohdan GRZADKOWSKI
Professeur, Université de Varsovie, Rapporteur

Dr. Felix BRÜMMER
Maître de Conférence, Université de Montpellier, Examinateur

Dr. Marie-Hélène GENEST
Chargé de recherche, LPSC Grenoble, Examinatrice

Pr. Jean ORLOFF
Professeur, Université Blaise Pascal, Examinateur

Dr. Sabine KRAML
Directeur de Recherche, LPSC Grenoble, Directeur de thèse

Dr. Christopher SMITH
Chargé de recherche, LPSC Grenoble, Co-Directeur de thèse

Pr. Ulrich ELLWANGER
Professeur, Université Paris-Sud, Rapporteur (non membre du jury)

CONTENTS

1

INTRODUCTION

Version française

Les symétries sont omniprésentes dans la nature, et en conséquence elles ont un rôle unique en physique. En particulier, le théorème découvert par Emmy Noether liant symétries et quantités conservées [1] est extrêmement profond. Non seulement les symétries d'un système peuvent être utilisées pour en faciliter sa description, elles sont également aux racines de notre compréhension des lois fondamentales de la physique; de la mécanique classique à la mécanique relativiste et quantique, et plus tard, en théorie quantique des champs, les symétries ont toujours eu ce rôle central. Les espace-temps peuvent être définis par le biais de leurs isométries et d'autres symétries (discrètes), *e.g.* le groupe de Galilée et le groupe de Poincaré. En mécanique quantique, les symétries d'un système contraignent fortement le spectre de son Hamiltonien. En théorie quantique des champs, la description des interactions fondamentales est basée sur les symétries de jauge. Non seulement elles prédisent l'existence de particules de spin-1, les bosons de jauge, elles contraignent également les interactions possibles entre particules élémentaires.

Depuis la découverte de la première particule élémentaire, l'électron en 1895, la construction expérimentale du Modèle Standard (MS) de la physique des particules et sa confirmation se sont étendues sur plus d'un siècle. Avec la découverte des atomes, noyaux et ensuite des protons et neutrons, les idées atomistiques grecques se sont avérées être réalisées dans la nature. D'autant plus avec la découverte dans les années 40 et 50 d'une large variété de particules hadroniques qui a résulté en la formulation du modèle des quarks et finalement, à la ChromoDynamique Quantique (CDQ). Au coeur de la CDQ se trouve le phénomène de liberté asymptotique découvert en 1973 par Gross [2], Wilczek et Politzer [3]: l'intensité de la force forte augmente avec la distance entre deux objets colorés. En particulier, la CDQ devient perturbative à faible distance, ou de manière équivalente, à grande énergie. L'unification de l'électromagnétisme et de la force faible a commencé en 1957 avec une proposition de Schwinger [4], qui ne pouvait cependant pas expliquer pourquoi les interactions électromagnétiques conservent la symétrie de parité alors que ce n'est pas le cas de la force faible. Quatre années plus tard, Glashow propose un modèle électro-faible basé sur la symétrie de jauge $SU(2) \times U(1)$ qui introduit pour la première fois un mélange entre le boson de jauge lié à $U(1)$ et l'un de ceux liés à $SU(2)$ [5]. De manière indépendante, Salam et Ward propose un modèle similaire en 1964 [6]. Des développements supplémentaires dans l'étude des symétries de jauge spontanément brisées étaient par la suite nécessaires afin d'expliquer la masse des bosons de jauge sans devoir briser

explicitement la symétrie de jauge, et afin d'éviter les bosons de Nambu-Goldstone [7, 8] non observés. Cela a été accompli indépendamment par trois groupes en 1964: Englert et Brout [9], Higgs [10], et Guralnik, Hagen et Kibble [11]. La théorie électro-faible, telle que présente dans le MS, a été formalisée par Weinberg [12] et Salam [13] en 1967 et 1968 respectivement. La découverte des bosons W et Z et les mesures de précision établies par la suite au grand collisionneur électron-positron (LEP) ont définitivement confirmé la validité du modèle. Malgré ses succès formidables, le MS souffre cependant de nombreux problèmes à la fois observationnels et théoriques, tels que son incapacité à décrire la matière noire, l'instabilité quantique de l'échelle électro-faible (le problème de la hiérarchie) et l'origine inconnue du secteur de saveur. Une théorie fondamentale de la physique des particules devrait clairement adresser ces problèmes.

De grands collisionneurs de particules sont utilisés afin de sonder la matière aux échelles les plus faibles et pour produire des particules lourdes en laboratoire. Aujourd'hui, le grand collisionneur de hadrons (LHC) fonctionne à une énergie de centre de masse de 13 TeV, ce qui permet une caractérisation précise de l'échelle du TeV, où des effets de nouvelle physique sont attendus s'il existe une solution naturelle au problème de la hiérarchie. Le point d'orgue des efforts expérimentaux et théoriques des siècles précédents se trouve assurément dans la découverte d'une particule scalaire, aux propriétés très proches de celles du boson de Higgs du MS, au LHC le 4 Juillet 2012 par les deux expériences généralistes ATLAS et CMS [14, 15]. Avec une masse de 125.09 GeV [16], elle est également compatible avec les contraintes directes du LEP [17] et du Tevatron [18], ainsi que les contraintes indirectes dérivées des mesures de précision électro-faible du LEP [19]. Suite à ce premier triomphe, des mesures de précision des propriétés de ce boson de Higgs ont été conduites jusqu'à la fin de la première période d'exploitation du LHC. Aucune déviation significative des prédictions du MS n'a été observée. Les taux de production et de désintégration de cette particule sont des informations essentielles afin d'identifier sa vraie nature. Ils permettent de déterminer ses couplages aux autres particules, et d'identifier de possibles nouveaux modes de désintégration non présents dans le MS. Ces résultats permettent de contraindre sévèrement des scénarios avec un secteur de Higgs étendu. Cela constitue la première partie de ce manuscrit de thèse, composée des Chapitres 2 et 3. Dans le **Chapitre 2**, nous détaillons en premier lieu la construction du MS. Après avoir rappelé son mécanisme de brisure de la symétrie électro-faible, nous discutons plusieurs aspects du secteur de Higgs; la présence de la symétrie custodiale et les contraintes théoriques d'unitarité et stabilité en particulier. Nous présentons ensuite les modes de désintégration du boson de Higgs du MS afin de poser les bases des études phénoménologiques qui suivent. Le secteur de Yukawa est ensuite décrit. Finalement les problèmes du MS sont discutés plus en détail. Dans le **Chapitre 3**, nous présentons les contraintes actuelles sur le secteur de Higgs. Nous commençons par introduire les contraintes issues du LEP et du Tevatron, puis celles obtenues au LHC. La détermination des nombres quantiques du boson de Higgs est discutée, ainsi que celle de ses couplages. Nous présentons ensuite `Lilith`, un outil public développé durant cette thèse afin de dériver des contraintes sur des scénarios de nouvelle physique grâce aux mesures des taux de production et désintégration du boson de Higgs. Une étude globale de ses couplages est ensuite réalisée en utilisant les résultats finaux de la première période d'exploitation du LHC.

Phénoménologiquement, il est possible d'étudier des modèles effectifs limités à une gamme d'énergie assez restreinte, afin de raffiner notre compréhension du secteur électrofaible à basse énergie. De ce point de vue, les modèles à deux doublets de Higgs (M2DH) sont particulièrement intéressants et leur présence pourrait contraindre fortement la théorie fondamentale sous-jacente. Dans la seconde partie de ce manuscrit, composée des Chapitres 4 et 5, nous étudions en détail la phénoménologie de ces modèles. Dans la première partie du **Chapitre 4**, nous donnons une présentation générale des M2DH. Étant donné que le boson de Higgs observé est compatible avec celui du MS, nous décrivons ensuite la limite d'alignement, dans laquelle l'un des deux états propres de masse (pair sous CP) est aligné dans la direction des valeurs moyennes dans le vide des deux doublets, ce qui lui confère des propriétés proches de celles prédites par le MS. Dans le **Chapitre 5**, nous explorons les conséquences de cette limite pour le LHC. En particulier, les mesures de précision des propriétés de l'état à 125 GeV permettent de la contraindre. De plus, étant donné que certains des états scalaires du M2DH peuvent être légers dans la limite d'alignement, nous discutons des perspectives de les observer lors de la seconde période d'exploitation du LHC et identifions des canaux de grand intérêt. Finalement, nous étudions la possible présence de bosons de Higgs légers, en deçà d'environ 60 GeV, dans les M2DH.

La supersymétrie est une extension de la symétrie de Poincaré qui offre naturellement une vue unifiée des fermions et bosons. Les modèles supersymétriques peuvent grandement améliorer, voire résoudre, certains des problèmes du MS. En particulier, ils peuvent offrir une solution naturelle au problème de la hiérarchie. Cependant, dans un modèle phénoménologiquement viable, la supersymétrie doit être brisée spontanément et cela introduit de nombreux nouveaux paramètres. En particulier, le secteur de la saveur d'un tel modèle peut être complètement générique et cela peut mener à de graves contradictions avec les observables de saveur, qui sont toutes en excellent accord avec les prédictions du MS. L'hypothèse de Violation Minimale de la Saveur (VMS) tente précisément de résoudre ce problème en permettant un alignement dans l'espace de la saveur entre les nouvelles structures de saveur et celles du MS, au travers d'un principe de symétrie bien défini. Cela sera le sujet de la dernière partie de ce manuscrit, composée du Chapitre 6. Dans ce **Chapitre 6**, l'hypothèse VMS est introduite comme un moyen systématique de résoudre les problèmes de la saveur au-delà du MS. Nous vérifions en particulier si un tel alignement de la saveur peut être généré à haute énergie et être conservé à basse énergie sous le groupe de renormalisation. Cette étude est effectuée pour les couplages violant la parité R et le nombre baryonique dans le Modèle Standard Supersymétrique Minimal.

Nos conclusions sont finalement données dans le **Chapitre 7**.

Dans le reste de ce chapitre d'introduction, nous introduisons certaines notions à propos des symétries en physique des particules. Nous décrivons d'abord les symétries d'espace-temps, puis les symétries de jauge et globales en théorie quantique des champs. En particulier, une construction des théories de Yang-Mills au niveau classique est présentée. Les effets quantiques sont brièvement discutés. Cette partie n'a pas pour but d'être exhaustive mais nous permet de commenter des notions importantes de nos constructions théoriques.

Symmetries are omnipresent in nature, and as a consequence, they have a unique role in physics. In particular, Emmy Noether discovered the beautiful result that they are associated with conserved quantities [1]. Not only can symmetries of a given system be used to facilitate its description, they are also at the roots of our current understanding of the fundamental laws of physics; from classical to relativistic and quantum mechanics, and later on, in relativistic quantum field theories (QFTs), symmetries always had this central role. Space-time frameworks may be defined through their isometries and additional (discrete) symmetries, *e.g.* the Galilean group and the Poincaré group. In a quantum theory, symmetries lead to strong constraints on the spectrum of the Hamiltonian. In QFT, our modern understanding of the fundamental interactions is based on local gauge symmetries. Not only they predict the existence of spin-1 particles, the gauge bosons, they also tightly constrain the possible interactions between elementary particles.

From the discovery of the first elementary particle, the electron in 1895, the experimental development and establishment of the Standard Model (SM) of particle physics has extended over more than a century. With the discovery of atoms, nuclei, and subsequently of protons and neutrons, nature seemed to realize the ancient atomistic ideas of matter being composed of elementary bricks. This certainly culminated with the discovery of a large variety of hadronic resonances in the late 1940s and early 1950s that eventually lead to the formulation of the quark model and later on, of Quantum ChromoDynamics (QCD). At the heart of QCD lies the phenomenon of asymptotic freedom discovered in 1973 by Gross [2], and Wilczek and Politzer [3]: the strength of the strong interaction increases with the distance between two colored objects. In particular, QCD therefore becomes perturbative at small distances, or at high energies. The unification of electromagnetism and weak forces started in 1957 with Schwinger's proposal [4], which could however not describe why electromagnetic interactions are parity-conserving while weak interactions are not. Four years later, Glashow introduced an electroweak SU(2)× U(1) gauge theory, introducing for the first time a mixing between the U(1) gauge boson and the neutral component of the SU(2) ones [5]. Salam and Ward independently proposed a similar model in 1964 [6]. Developments in the study of spontaneously broken gauge symmetries were however needed in order to explain the gauge boson masses without explicitly breaking the gauge symmetry, and to escape Nambu-Goldstone's massless bosons [7, 8]. This was achieved by three independent groups in 1964; Englert and Brout [9], Higgs [10], and Guralnik, Hagen and Kibble [11]. The electroweak model, as present in the SM, was finally formalized by Weinberg [12] and Salam [13] in 1967 and 1968 respectively. The discovery of the W and Z bosons at CERN and the subsequent precision measurements of the electroweak sector at the Large Electron Position (LEP) collider provided the full-fledged confirmation of the model. Despite its tremendous success, the SM suffers from several shortcomings of both observational and esthetical nature, such as the lack of a dark matter candidate, the quantum instability of the electroweak scale (the hierarchy problem) and the unknown origin of flavor in particular. A fundamental theory of particle physics should clearly provide a solution to these problems.

Large colliders are used in order to directly probe matter at the shortest possible scales and produce heavy particles in laboratories. Today, the Large Hadron Collider (LHC) runs at a center of mass energy of 13 TeV, allowing precise characterization of physics at the TeV scale, where new physics effects are expected if there exists a natural stabilization of

the electroweak scale. All the experimental and theoretical efforts aimed at describing and understanding the fundamental interactions surely culminated on July 4th, 2012 with the discovery of a scalar particle, with properties very close to that of the SM Higgs boson, at the LHC by the two multi-purposes experiments ATLAS and CMS [14, 15]. With a mass of 125.09 GeV [16], it is also compatible with the bounds derived at LEP through precise electroweak measurements [19] and direct searches from LEP [17] and the Tevatron [18]. Following this first triumph of the LHC, precision measurements of the Higgs boson were conducted during the first LHC run, with no large deviation from the SM properties observed. Measurements of the production and decay rates of the observed Higgs boson are crucial to reconstruct its couplings to other SM particles and possibly identify the presence of channels not present in the SM. Such results can then be used to derive important constraints on extended Higgs sectors beyond the SM. This will constitute the subject of the first part of this thesis manuscript, composed of Chapters 2 and 3. In **Chapter 2**, we detail the construction of the Standard Model. After recalling its mechanism for spontaneous electroweak symmetry breaking, we discuss various aspects of the Higgs sector; custodial symmetry and theoretical constraints from unitarity and stability in particular. We then present the SM Higgs boson decays as a basis for the phenomenological aspects dealt with in subsequent parts of the manuscript. The Yukawa sector is then described. Shortcomings of the SM are finally discussed. In **Chapter 3**, we present how the Higgs sector has so far been constrained experimentally. We start by reviewing constraints from LEP and Tevatron and go on with the searches performed at the LHC. The characterization of the Higgs boson quantum numbers is discussed, as well as of its couplings. We then present `Lilith`, a public tool developed during this Ph.D. thesis to derive constraints on new physics scenarios from the measurements of the Higgs boson production and decay rates. A global fit using all final run 1 results from then LHC is finally performed.

From a phenomenological point of view, it is possible to study effective models, suitable for a limited range of energies, in order to refine our views of the electroweak sector at low energy. Well-motivated effective models include simple extensions of the SM Higgs sector such as the two-Higgs-doublet models (2HDMs). If present in nature, this Higgs structure would shine a new light on the electroweak sector and its symmetry breaking mechanism, it could also strongly constrain the underlying fundamental theory. In the second part of this manuscript, composed of Chapters 4 and 5, we will study the phenomenology of such models under the light of the results from the first run of the LHC. In the first part of **Chapter 4**, we give a general presentation of the 2HDMs. As the observed Higgs boson has properties close to the SM one, we then describe the alignment limit of the 2HDM, in which one of the two CP-even mass eigenstate aligns with the direction of the vacuum expectation values, thereby automatically acquiring SM-like properties. In **Chapter 5**, we explore the phenomenological consequences of the alignment limit of the 2HDM. We show and quantify how the precise measurements of the properties of the 125 GeV state are an important probe of this limit. Moreover, since alignment does not necessarily involve the decoupling of the extra Higgs states, we discuss the prospects to observe these additional scalars at the second run of the LHC and pin-down channels with high potential. Finally, we also explore the parameter region of the 2HDM in which light Higgs states, with masses below ~ 60 GeV, are present and explore its phenomenology at the LHC.

Supersymmetry is an extension of the space-time Poincaré symmetry that naturally links fermions and bosons together. Supersymmetric models can soften or even solve some of the SM problems. In particular, it can provide a natural solution to the hierarchy problem. However, in realistic models, supersymmetry should be spontaneously broken and this introduces a plethora of new parameters. In particular, the flavor sector of such models can be totally generic and this leads to severe problems with flavor observables, all in very good agreement with the SM predictions. The Minimal Flavor Violation (MFV) hypothesis precisely tackles this problem, by effectively aligning the new flavor structures with the SM ones, through a well-defined symmetry principle. This will be the focus of the last part of the manuscript, composed of Chapter 6. In **Chapter 6**, we present the MFV hypothesis, a systematic way to ensure a flavor alignment through a symmetry principle and a naturalness criterion, as a possible solution to the flavor puzzles beyond the SM. In particular, we analyze whether such an alignment, if generated at a very high scale, can hold down to low scales under the renormalization group evolution. This study is performed for the baryonic R-parity violating couplings of the Minimal Supersymmetric Standard Model.

Our conclusions are finally presented in **Chapter 7**.

In the rest of this introductory chapter, we introduce notions about symmetries in particle physics. We first describe space-time symmetries and then go on with gauge and global symmetries in QFTs. In particular, a short construction of Yang-Mills theories at the classical level is performed. Quantum effects are briefly discussed. This section is not meant to be exhaustive or even be a self-contained introduction to the subject but allows us to comment upon important notions of our theoretical constructions.

Lie groups and algebras

Let us recall a few basic facts about Lie algebras and their representations (a very clear and complete discussion can be found in, *e.g.*, [20]). A Lie group G is both a group and a smooth differentiable manifold. As such, its elements depend continuously and differentially on a set of parameters $\theta = \{\theta_a\}$, where a ranges from 1 to n_G, the dimension of the group. In the following, we henceforth denote a general group element as $g = g(\theta) \in G$. Focusing on the region connected to the identity, the parametrization θ_a can be defined such that $g(\mathbf{0}) \equiv e$, where e is the group identity element, without loss of generality.

A representation ρ of the group G on a vector space V is a group homomorphism

$$\rho : g \in G \to D_\rho(g) \in \text{End}(V)\,, \tag{1.1}$$

where $\text{End}(V)$ is the set of endomorphisms on V, satisfying $D(e) = \mathbb{1}_V$ and $D(g_1)D(g_2) = D(g_1 g_2)$. The dimension of V is called the dimension of the representation. Given a basis of V, the group elements can be represented as matrix transformations on the vectors v of V, $v \to D_\rho(g)v$, or in components,

$$v^i \to \left(D_\rho(g)\right)^i{}_j\, v^j\,, \tag{1.2}$$

where a sum over repeated indices is implied. While the group elements are only defined through abstract relations among each other, representations allow to define concrete trans-

formations on physical quantities through the matrices $D_\rho(g)$. Close to the identity, $D_\rho(g)$ may be written as

$$D_\rho(g) = \mathbb{1}_V - i\theta_a T_\rho^a \,, \tag{1.3}$$

where $\{T_\rho^a\}$ are the matrix representation of the so-called *group generators*. Away from the identity, a general group element g connected to the identity can be represented in full generality as

$$D_\rho(g) = e^{-i\theta_a T_\rho^a}. \tag{1.4}$$

If the matrix representations of the group generators are hermitian, $D_\rho(g)$ are then unitary matrices for every element g, and such a representation is dubbed unitary,

$$D_\rho(g)D_\rho^\dagger(g) = D_\rho(g)D_\rho(g^{-1}) = D_\rho(e) = \mathbb{1}_V. \tag{1.5}$$

For a given Lie group, there exists a natural representation called the adjoint representation. This is the representation of the group on its own Lie algebra, $V = \mathcal{G}$,

$$\text{ad}: \mathcal{G} \quad \to \quad \mathcal{G} \tag{1.6}$$
$$t \quad \to \quad [t, .] \,, \tag{1.7}$$

where the explicit matrix representation of the generators is given by the structure constants of $\mathcal{G}$, $(T_{\text{adj}}^a)^{ij} = f^{aij}$.

Though the explicit form of the $\{T_\rho^a\}$ depends on the specific representation, there exists a local information about the group that does not depend on it. It is the Lie algebra $\mathcal{G}$, characterized by

$$[T^a, T^b] = if^{abc}T^c, \tag{1.8}$$

where $f^{abc} = -f^{bac}$ are the structure constants of the Lie algebra, $[. , .]$ is a bilinear skew-symmetric internal product satisfying the Jacobi identity and the $\{T^a\}$ form a basis of the Lie algebra.[1] The structure constants are defined at the algebra level and therefore do not depend on a specific group representation. On a given representation, the matrix form of the $\{T^a\}$ are fixed, and Eq. (1.8) is realized with the usual matrix commutator. For abelian Lie groups, all group generators commute and all structure constants therefore vanish, $f^{abc} = 0$. Geometrically, the Lie algebra is defined on the tangent plane at the origin of G, as such, it encodes a local property of the group. The group generators $\{T^a\}$ are seen here to form a basis of $\mathcal{G}$ and a generic vector of the Lie algebra can therefore be written as $\theta_a T^a$. In the case of simply connected algebras, a Lie group can be constructed out of the exponential map. However, this construction is not unique, two Lie groups can share the same Lie algebra, *i.e.*, have the same local properties near the identity, but differ globally.

Lie algebras with no proper ideal are called simple, *i.e.*, there does not exist a subset $I \supset \mathcal{G}$ such that for any element i of I and x of $\mathcal{G}$, $[i, x] \in I$ with $I \neq \mathcal{G}, \{0\}$. All simple

---

1 An algebra is a vector space over a field, *e.g.* the field of real or complex numbers, with an internal bilinear product. As such, the $\{T^a\}$ can indeed be interpreted as a set of vectors forming a basis of the algebra.

Lie algebras are known and were classified by Cartan [21]. Semi-simple Lie algebras are algebras with no abelian proper ideal, they can also be constructed as a direct sum of commuting simple Lie algebras. Compact semi-simple Lie algebras [possibly including some U(1) factors] are at the basis of gauge theories, the reason is that a necessary condition for the unitarity of the theory is the existence of a non-degenerate positive-definite bilinear form on the gauge Lie algebra $\mathcal{G} \times \mathcal{G} \to \mathbb{R}$, see Section 15.2 of [22]. For semi-simple Lie algebra, such a form is automatically given by the Killing form. It guarantees the existence of a positive-definite gauge kinetic term.

Space-time symmetries

Einstein's principle of relativity states that the laws of physics have the same form in any inertial frames and that there exists a maximal finite velocity for the propagation of interactions. Physics in the Minkowski space-time can naturally account for this principle. The components of the metric are given by

$$\eta^{\mu\nu} = \text{Diag}(+1, -1, -1, -1) \tag{1.9}$$

where, for our purposes, a flat 3+1 dimensional space-time is considered. While Einstein's principle can be accounted for in a curved space-time, we stick to the flat Minkowski space here as we will only be interested in the interaction of particles over very small distances where geometrical effects play no role beyond those of special relativity. This then naturally leads us to the study of the isometries of the 3+1 Minkowski space-time. These are the linear transformations that leave the space-time interval invariant,

$$\eta_{\mu\nu} dx'^\mu dx'^\nu = \eta_{\mu\nu} dx^\mu dx^\nu \ , \tag{1.10}$$

where $\mu, \nu = 0, 1, 2, 3$ and,

$$x'^\mu = \Lambda^\mu{}_\nu x^\nu + a^\mu. \tag{1.11}$$

Combining Eqs. (1.10) and (1.11), the matrix Λ should then satisfy

$$\eta_{\mu\nu} = \eta_{\rho\sigma} \Lambda^\rho{}_\mu \Lambda^\sigma{}_\nu. \tag{1.12}$$

Following Weinberg's notation [23], if $T(\Lambda, a)$ denotes such a transformation, it is easy to show that the composition of two of them is given by

$$T(\Lambda', a')T(\Lambda, a) = T(\Lambda'\Lambda, \Lambda'a + a'), \tag{1.13}$$

The set of such transformations forms the inhomogeneous Lorentz group or the *Poincaré group*. The elements are referred to as either inhomogeneous Lorentz transformations or *Poincaré transformations*. The group structure is indeed justified as the identity transformation is given by $T(\mathbf{1}, 0)$, the inverse element is given by

$$T^{-1}(\Lambda, a) = T(\Lambda^{-1}, -\Lambda^{-1}a), \tag{1.14}$$

and the composition of two Poincaré transformations is a Poincaré transformation as shown in Eq. (1.13). From Eq. (1.12), it is clear that $(\det\Lambda) = \pm 1$. The $+1$ (-1) solution is (not) connected to the identity and define *proper* (*improper*) transformations. Moreover,

it is easy to see that $\Lambda^0{}_0$ is either larger than $+1$ or smaller than -1. A transformation with $\Lambda^0{}_0 \geq 1$ is called *orthochronous* as it leaves the direction of the time untouched. The subgroup of transformations without translation, $T(\Lambda, 0)$, is called the *homogeneous Lorentz group*. In the following, we will refer as the *Lorentz group*, the set of homogeneous proper-orthochronous Lorentz transformations, generically called *Lorentz transformations* for short.

Considering an infinitesimal Lorentz transformation

$$\Lambda^\mu{}_\nu = \delta^\mu{}_\nu + \omega^\mu{}_\nu, \tag{1.15}$$

it easy to see that ω is anti-symmetric, $\omega_{\mu\nu} = -\omega_{\nu\mu}$ from Eq. (1.12). The Lorentz group is thus 6-dimensional. Three parameters parametrize space rotations (3 Euler angles), while the three remaining ones parametrize boosts (3 rapidities for instance). The Poincaré group has therefore dimension 6+4=10, where 6 is the dimension of the Lorentz group and 4 is the number of independent space-time translations.

The Lie algebra of the Poincaré group can be derived from the infinitesimal form of $T(\Lambda, a)$. Considering transformations connected to the identity, $\Lambda = \mathbb{1} + \omega$ and $a = \epsilon$, we can generically parametrize them as

$$T(\mathbb{1} + \omega, \epsilon) = 1 - \frac{i}{2}\omega_{\mu\nu}J^{\mu\nu} - i\epsilon_\mu P^\mu, \tag{1.16}$$

where $J^{\mu\nu} = -J^{\nu\mu}$ are the Lorentz generators while P^μ are the space-time translation generators. Examining the product $T(\Lambda, a)T(\mathbb{1} + \omega, \epsilon)T^{-1}(\Lambda, a)$, one can obtain the transformation laws of J and P under a general Poincaré transformation. The algebra of the Poincaré group is then obtained by identifying all terms of the same order in ω and ϵ,

$$[J^{\mu\nu}, J^{\rho\sigma}] = i\left(\eta^{\nu\rho}J^{\mu\sigma} + \eta^{\sigma\mu}J^{\nu\rho} - \eta^{\mu\rho}J^{\nu\sigma} - \eta^{\sigma\nu}J^{\mu\rho}\right), \tag{1.17}$$

$$[P^\mu, J^{\rho\sigma}] = i\left(\eta^{\mu\rho}P^\sigma - \eta^{\mu\sigma}P^\rho\right), \tag{1.18}$$

$$[P^\mu, P^\nu] = 0. \tag{1.19}$$

The vectors $\mathbf{J} = \{(1/2)\epsilon_{ijk}J^{jk}\}$, $\mathbf{K} = \{J^{i0}\}$ and $\mathbf{P} = \{P^i\}$ can be identified with the angular-momentum, boost and momentum vectors respectively, using the previous commutation relations. The 0-*th* component of P^μ is identified with the energy operator, the Hamiltonian H. One can show that the Hamiltonian commutes with the angular-momentum and momentum three-vectors but not with the boost vector. States can thus be labeled according to their angular-momentum j and momentum $\mathbf{p}$.

The (complexified) Lorentz algebra, Eq. (1.17), is equivalent to two independent, *i.e.*, commuting, SU(2) algebras, the *left* and *right* ones. Indeed, defining,

$$\mathbf{J}_{R,L} = \frac{\mathbf{J} \pm i\mathbf{K}}{2}, \tag{1.20}$$

Eq. (1.17) can be written as,

$$[J_L^i, J_L^j] = i\epsilon^{ikj}J_L^k, \tag{1.21}$$

$$[J_R^i, J_R^j] = i\epsilon^{ikj}J_R^k, \tag{1.22}$$

$$[J_L^i, J_R^j] = 0. \tag{1.23}$$

The quantities $\mathbf{J}_{R,L}$ are therefore generators of SU(2) algebras. Spinorial representations of the Lorentz group can thus be represented by two half-integers (j_L, j_R) and have dimension $(2j_L + 1)(2j_R + 1)$. The simplest non-trivial representations are 2-dimensional, $(1/2, 0)$ and $(0, 1/2)$ and are called the left-handed and right-handed Weyl spinors, respectively. In the following, we will denote a generic left-handed Weyl spinor by ψ_L and a right-handed one by ψ_R. On such representations, the generators take the form of the Pauli matrices σ^i. Considering the transformations of ψ_L and ψ_R under the Lorentz group, one can show that

$$\psi_L^c \equiv i\sigma^2 \psi_L^* \in \left(0, \frac{1}{2}\right) , \quad \psi_R^c \equiv -i\sigma^2 \psi_R^* \in \left(\frac{1}{2}, 0\right). \tag{1.24}$$

This defines the charge conjugation operation on Weyl spinors, an operation that transforms a left-handed Weyl spinor to a right-handed one and vice-versa. Experimentally, we know that for scales above $\mathcal{O}(100\,\text{GeV})$ fermions need to be described by Weyl spinors, as weak interactions maximally break parity. Indeed, under a parity transformation, an object in the representation (j_L, j_R) is transformed to an object of (j_R, j_L), see Eq. (1.20) where $\mathbf{J}$ transforms as a pseudo-vector while $\mathbf{K}$ as a true vector under a parity transformation. Below the weak scale, however, electromagnetic interactions conserve parity and a more appropriate basis for spinor representations should be considered: the Dirac representation whose elements are the Dirac spinors,

$$\Psi = \left(\begin{array}{c} \psi_L \\ \psi_R \end{array}\right) \in \left(\frac{1}{2}, 0\right) \otimes \left(0, \frac{1}{2}\right) , \tag{1.25}$$

Bosonic representations of the Lorentz group are easy to construct. Equation (1.11) with $a^\mu = 0$ defines a contravariant vector. Covariant vectors can be defined as

$$x'_\mu = \Lambda_\mu^{\ \nu} x_\nu, \tag{1.26}$$

with $\Lambda_\mu^{\ \nu} = \eta_{\mu\rho}\eta^{\nu\sigma}\Lambda^\rho_{\ \sigma}$, while general tensors are defined as

$$T'^{\ \mu_1\mu_2\cdots}_{\ \nu_1\nu_2\cdots} = \Lambda^{\mu_1}_{\ \rho_1}\Lambda^{\mu_2}_{\ \rho_2}\cdots \Lambda_{\nu_1}^{\ \sigma_1}\Lambda_{\nu_2}^{\ \sigma_2}\cdots T^{\rho_1\rho_2\cdots}_{\sigma_1\sigma_2\cdots} . \tag{1.27}$$

One can then define various types of field representations of the Lorentz group, $i.e.$, infinite-dimensional representations. In particular, the scalar, Weyl spinor, Dirac spinor and vector fields representations are instrumental in the construction of QFTs. With them, Lorentz-invariant field theories describing interactions between particles can then be constructed. For that, explicit representations of the generators $J^{\mu\nu}$ and P^μ are found,

$$J^{\mu\nu} = L^{\mu\nu} + S^{\mu\nu} , \quad L^{\mu\nu} = i(x^\mu\partial^\nu - x^\nu\partial^\mu) \tag{1.28}$$

$$P^\mu = i\partial^\mu , \tag{1.29}$$

where $L^{\mu\nu}$ is the orbital angular-momentum while $S^{\mu\nu}$ is the internal spin part whose explicit form depends on the Lorentz representation.

No matter the Lorentz representation, particle states are asked to be invariant under space-time translations and can thus be labeled by the eigenvalues of the Poincaré Casimir operators, see $e.g.$ [23, 24] for explicit details. There are two of them, the mass operator $P_\mu P^\mu$ which has value m^2 on a representation of mass m, and the Pauli-Lubanski operator

$W^\mu W_\mu$, where $W^\mu = -(1/2)\epsilon^{\mu\nu\rho\sigma}J_{\nu\rho}P_\sigma$, whose value depends on whether the representation is massive ($m^2 \neq 0$) or not ($m^2 = 0$). In the massive case, $W^\mu W_\mu = -m^2 j(j+1)$ where j is an half-integer, the spin. Such a representation has $2j+1$ degrees of freedom, labeled by $j_z = -j, -j+1, \ldots, j-1, j$. In the massless case, representations only have one degree of freedom, the projection of their angular-momentum on their direction of motion, the so-called helicity h. This quantity is quantized and takes half-integer values, both positive and negative. Of course, under a parity transformation, the helicity of a representation changes sign. In a parity invariant theory, such as electromagnetism, it is thus natural to group together the two helicity states with opposite h into a single particle with two degrees of freedom $\pm h$. The photon is precisely defined with two degrees of freedom, called polarization, ± 1. The graviton, on the other hand, is defined with the two polarizations ± 2. As weak interactions are not invariant under parity, the neutrino state with $h = -1/2$ and the one with $h = +1/2$ actually represent two different particles, respectively called the neutrino and the anti-neutrino.

Guided by symmetry principles, one is naturally lead to the question of identifying the most general symmetry of the S-matrix of a quantum field theory. A famous theorem was proved in 1965 by Coleman and Mandula [25] who showed that the symmetry group of quantum field theories can only consist of a direct product of the space-time Poincaré group and the possible internal symmetry groups. This means in particular that the action of the internal group generators on the space-time part can only be trivial. However, this result only holds for space-time generators that are bosonic. Ten years later, Haag, Lopuszanski and Sohnius [26] proved that the space-time symmetry can be extended to the supersymmetry, the largest space-time symmetry compatible with quantum field theories. Supersymmetric generators are fermionic (anti-commuting) objects and therefore can transform a bosonic state into a fermionic one and vice-versa. Supersymmetry offers a unified view of fermions and bosons.

Gauge symmetries

Our present formulation of fundamental interactions is based on gauge theories: quantum field theories invariant under a local gauge group. Without knowing it, Maxwell was the first to introduce such a theory in 1861–1862 (which moreover satisfied Eintein's principle of relativity). The first non-abelian gauge theory was proposed by Yang and Mills [27] in order to provide a local description of the approximate isospin symmetry observed in strong interactions. Following Yang and Mills' construction, let us build a local gauge theory, with gauge group G (generically non-abelian), for a single Dirac fermion species ψ, in a unitary representation ρ of G,

$$\psi(x) \xrightarrow{G} \psi'(x) = \left(e^{-i\theta_a(x)T_\rho^a}\right)\psi(x) \equiv R(x)\psi(x) . \tag{1.30}$$

The free Dirac Lagrangian density is

$$\mathscr{L}_{\text{Dirac}}(x) = \overline{\psi}(x)(i\slashed{\partial} - m)\psi(x), \tag{1.31}$$

where for notation simplicity, the explicit references to the space-time point x will be omitted from now on. While the mass term is clearly gauge invariant, the kinetic terms

transforms non-trivially under G because the gauge parameters θ_a depend on the space-time point,

$$\overline{\psi}' i\partial_\mu \psi' = \overline{\psi}(i\partial_\mu \mathbb{1}_\rho + \partial_\mu \theta_a T^a_\rho)\psi. \tag{1.32}$$

Inspired by the classical electrodynamics minimal-coupling procedure, the covariant derivative is introduced,

$$D_\mu \equiv \partial_\mu \mathbb{1}_\rho - ig T^a_\rho A^a_\mu = \partial_\mu \mathbb{1}_\rho - ig\mathbb{A}_\mu , \tag{1.33}$$

where g is the gauge coupling, A^a_μ the gauge field and $\mathbb{A}_\mu \equiv T^a_\rho A^a_\mu$ is the Lie algebra-valued gauge field. Under the replacement $\partial_\mu \rightarrow D_\mu$ in Eq. (1.31), the Dirac Lagrangian will be locally gauge invariant if $D'_\mu \psi' = R D_\mu \psi$, which fixes the gauge field transformation,

$$\mathbb{A}'^a_\mu = R\, \mathbb{A}_\mu R^\dagger - \frac{i}{g}(\partial_\mu R)R^\dagger . \tag{1.34}$$

This replacement also completely fixes the interaction term between the fermion ψ and the gauge fields. Under an infinitesimal gauge transformation,

$$\delta A^a_\mu \equiv A'^a_\mu - A^a_\mu = -\frac{1}{g}\partial_\mu \theta_a T^a_\rho + f^{abc}\theta_b A^c_\mu . \tag{1.35}$$

Defining the Lie algebra-valued field strength tensor $\mathbb{F}_{\mu\nu}$ as $[D_\mu, D_\nu]\psi \equiv -ig\mathbb{F}_{\mu\nu}\psi$,

$$\mathbb{F}_{\mu\nu} = \partial_\mu \mathbb{A}_\nu - \partial_\nu \mathbb{A}_\mu - ig[\mathbb{A}_\mu, \mathbb{A}_\nu], \tag{1.36}$$

which fixes the gauge transformation,

$$\mathbb{F}'_{\mu\nu} = R\, \mathbb{F}_{\mu\nu} R^\dagger , \tag{1.37}$$

$$\delta F^a_{\mu\nu} \equiv F'^a_{\mu\nu} - F^a_{\mu\nu} = f^{abc}\theta^b F^c_{\mu\nu} . \tag{1.38}$$

From Eq. (1.37), it is clear that a gauge invariant kinetic term for $\mathbb{F}$ can be written as

$$\mathscr{L}_{\text{gauge}} = -\frac{1}{2}\text{Tr}\left(\mathbb{F}_{\mu\nu}\mathbb{F}^{\mu\nu}\right) = -\frac{1}{4}F^a_{\mu\nu}F^{a,\mu\nu} , \tag{1.39}$$

where the normalization factor is such as to reproduce Maxwell's equations for an abelian gauge field and the group generators are normalized as $\text{Tr}(T^a T^b) = (1/2)\delta^{ab}$. In the abelian case, i.e., $G = $U(1), $f^{abc} = 0$ and $T^a = \mathbb{1}_\rho$, and all results known from quantum electrodynamics are recovered. In particular, $F_{\mu\nu}$ is gauge invariant on its own, allowing for kinetic mixing of various U(1) groups. The generalization of this gauge theory to several fermion species or to a direct product of gauge groups is straightforward. Scalar and vector particles may be added to the particle content by the exact same reasoning.

The construction of non-abelian gauge theories certainly does not stop there. Even at the classical level, an additional term is needed to regularize the partition function of the theory that would otherwise be infinite as a result of the gauge redundancy: the gauge fixing term. Very tightly connected to this matter is the presence of Faddeev-Popov ghosts [28], which can alternatively be seen as a way to eliminate gauge degrees of freedom in a pure gauge theory. While gauge fixing obviously breaks the gauge symmetry of a theory, there

is an underlying symmetry under which the full theory is invariant, the Becchi-Rouet-Stora-Tyutin (BRST) symmetry [29, 30], which is deeply linked to the renormalizability of the theory and to possible gauge anomalies. While our approach was essentially algebraic, Yang-Mills theories are geometrical by nature and have a very elegant picture in the context of differential geometry, see *e.g.* [31, 32] for details.

Global symmetries

The complete Lagrangian of a gauge theory is invariant under its gauge group G, but may also be invariant under additional global symmetries that were not explicitly asked for, the *accidental symmetries*. Naturally, a Lorentz-invariant theory is invariant under the discrete CPT symmetry [33, 34], but there might be additional continuous symmetries.

Global symmetries and conservation laws have profound connections in field theory. Noether's theorem [1] states that a theory invariant under a global symmetry group, G of dimension n_G, has n_G conserved currents on-shell. Let us consider a theory describing a collection of fields ϕ_i, invariant under a global symmetry G. Under an infinitesimal G transformation, the fields transforms as

$$\phi(x) \to \phi_i(x) + \epsilon^a f_{i,a}(\phi, \partial\phi), \tag{1.40}$$

where $a = 1, ..., n_G$ is a group index. The currents

$$j_\mu^a = -\frac{\partial\mathscr{L}}{\partial(\partial_\mu \phi_i)} f_{i,a}, \tag{1.41}$$

are then conserved for fields satisfying the classical equation of motions, *i.e.*, on-shell fields. This theorem is indeed proven by splitting the total action variation under an infinitesimal G transformation into a surface term and local terms, the latter leading to the Euler-Lagrange equations.

The free Dirac Lagrangian, Eq. (1.31), happens to be invariant under two global accidental symmetries,

$$\psi \;\to\; e^{i\alpha}\psi, \tag{1.42}$$
$$\psi \;\to\; e^{i\gamma_5\beta}\psi \text{ (if } m = 0), \tag{1.43}$$

respectively called vector (V) and axial (A) U(1) symmetries. The naming becomes transparent when the two associated currents are obtained,

$$j_V^\mu = \overline{\psi}\gamma^\mu\psi \;\;\Rightarrow\; \partial_\mu j_V^\mu = 0\,, \tag{1.44}$$
$$j_A^\mu = \overline{\psi}\gamma^\mu\gamma_5\psi \;\;\Rightarrow\; \partial_\mu j_A^\mu = 2im\overline{\psi}\gamma_5\psi\,. \tag{1.45}$$

where the axial current is conserved only for $m = 0$ as expected. More generally, for ψ in a unitary representation ρ of a global symmetry group G, under an infinitesimal transformation ψ transforms as

$$\psi^i \to \psi^i - i\theta_a(T_\rho^a)^i_j\psi^j, \tag{1.46}$$

where i, j are representation indices and the n_G conserved currents are then given by

$$j_\mu^a = \overline{\psi}_i\gamma_\mu(T_\rho^a)^i_j\psi^j. \tag{1.47}$$

An important theorem about global symmetries is Nambu and Goldstone's one [7, 8]. Although initially stated in the context of a theory of superconductivity, its reach is universal. For any global symmetry of dimension n spontaneously broken, the spectrum of the theory necessarily involves n massless scalar particles, now called Nambu-Goldstone bosons, that have the quantum numbers of the previously conserved current. If however, the symmetry is slightly explicitly broken before spontaneous breaking, the scalar fields acquire a relatively low mass and are called pseudo-Nambu-Goldstone bosons.

Another very important concept of quantum field theories is that of anomalies. So far our discussion was limited to conserved currents at the classical level. However at the quantum level, classical currents need not be conserved. Essentially, the failure of the classical picture may come from the regularization of the theory needed at the quantum level in the presence of gauge fields. The axial current, Eq. (1.45), is actually anomalous in the presence of a gauged background. In Quantum Electrodynamics for instance,

$$\partial_\mu j_A^\mu = 2im\overline{\psi}\gamma_5\psi + \frac{e^2}{16\pi^2}\epsilon_{\mu\nu\rho\sigma}F^{\mu\nu}F^{\rho\sigma}. \tag{1.48}$$

An important physical consequence of this result is that it explains the decay of the neutral pion in two photons, which would otherwise have a very small width in the absence of the anomalous term and be in strong disagreement with the experimental observation [35, 36]. This mismatch between the experimental observation and the theoretical prediction led Adler, Bell and Jackiw to discover anomalies in the late 1960's [37, 38]. Another important consequence is that, in the SM, baryon $\mathcal{B}$ and lepton $\mathcal{L}$ numbers are anomalous. 't Hooft computed the rate at which $\Delta_{\mathcal{B}+\mathcal{L}} \neq 0$ processes (sphaleron transitions) take place [39], it turns out to be proportional to $\exp(-8\pi^2/g_{\text{weak}}^2)$, an extremely small number at our energy scales. (See however [40] for a recent reappraisal of the possibility to observe these processes at colliders and [41, 42] for phenomenological studies.) However, in the early universe, at high temperature, the rate of such transitions might have been non-negligible. This paved the way to the construction of consistent scenarios of baryogenesis, *e.g.* electroweak baryogenesis [43] or leptogenesis [44]. Anomalies of gauged symmetries are more critical, they indicate an inconsistency of the theory at the quantum level and interfere with the renormalization procedure. There are thus consistency conditions on the particle content and on the gauge group of the theory in order to avoid them. It is quite intriguing that the SM fulfills these relations while it was, in no way, constructed to avoid such anomalies.

Part I

SETTING THE STAGE

In this part, we first construct the Standard Model of particle physics, with a strong emphasis on the Higgs sector and the various theoretical constraints that it is subjected to. The Yukawa sector is also described in detail. We then discuss how the Higgs sector has been experimentally constrained so far at LEP, the Tevatron and the LHC. Making use of the precise measurements of the production and decay rates of the observed Higgs states, one can infer severe constraints on the parameter space of new physics models. This is the purpose of the public tool `Lilith` that we then introduce. Finally, to end this part, we perform a global fit to the Higgs couplings using the final Run 1 LHC results.

Dans cette première partie, nous construisons en premier lieu le Modèle Standard de la physique des particules, avec une attention particulière portée au secteur de Higgs et aux diverses contraintes théoriques qui s'y appliquent. Le secteur de Yukawa est également décrit en détail. Nous discutons ensuite des caractérisations expérimentales du secteur de Higgs effectuées au sein des collisionneurs de particules LEP, Tevatron et LHC. En utilisant les mesures précises des taux de production et désintégration du boson de Higgs observé, il est possible de dériver des contraintes sévères sur l'espace de paramètres de scénarios de nouvelle physique. C'est précisément l'objet du code public `Lilith` que nous introduisons dans la suite. Finalement, pour clôturer cette première partie, nous effectuons un ajustement global des couplages du Higgs en utilisant les résultats finaux de la première période d'exploitation du LHC.

2

THE STANDARD MODEL OF PARTICLE PHYSICS

After decades of investigation, the Standard Model of particle physics [2, 3, 5, 9–13] still remains unshaken and stands as our best description of the microscopic dynamics of nature so far. It is quite exceptional that the most complex phenomena we have observed can be described by such a compact theory. Though it will only take us a few pages to write down the SM at the classical level, one should certainly not mistake this *apparent* simplicity for triviality. Indeed, in addition to the important aspects linked to the quantization and renormalization of the theory, profound phenomena lie in the core of the SM: confinement, anomalies, instantons etc. or in general, non-perturbative and topological effects. Though these subjects will not be described in this manuscript, they should be kept in mind in order to fully appreciate the SM.

In order to build the SM, four ingredients are needed. The first one is a description of a space-time and its associated symmetries. In our case, we are only interested in describing the (local and unitary) interactions between particles over short spatial distances, thus, a flat Minkowskian space-time associated to the Lorentz invariance are what we need. The question of supersymmetry will partially be addressed in Section 6. The second ingredient is obviously a list of the objects that we want to study, *i.e.*, the particle content of the theory. Today, for the SM, this list is an established experimental input. The third ingredient is a description of how these particles interact which is given by the gauge group as discussed in the Introduction. The SM gauge group, G_{SM}, is given by $G_{\mathrm{SM}} = \mathrm{SU}(3)_c \times \mathrm{SU}(2)_L \times \mathrm{U}(1)_Y$ and is also an experimental input.[2] The gauge couplings of these three groups are denoted respectively g_3, g and g' in the following. A particular focus will be given on the $\mathrm{SU}(2)_L \times \mathrm{U}(1)_Y$ part in the following, the electroweak (EW) sector, which will spontaneously be broken to $\mathrm{U}(1)_{em}$. Finally, the last ingredient, though not strictly mandatory, is the renormalizability criterion which allows us to focus on operators of dimension 4 at maximum. Operators of dimension larger than 4 may be considered in the framework of effective field theories (EFTs), they are parametrically suppressed by powers of a scale Λ at which the transition between the SM and a more fundamental theory occurs.[3] The SM itself should be viewed as a low-energy approximation of a more fundamental theory, which is no surprise in light of the various open questions that it leaves unanswered and

---

2 Regarding the electroweak part, as S. Weinberg expressed it, "*Leptons interact only with photons, and with the intermediate bosons that presumably mediate weak interactions. What could be more natural than to unite these spin-one bosons into a multiplet of gauge fields ?*" [12].

3 More specifically, it is the scale at which the heavy states of the fundamental theory are integrated out. If the mass splittings between these states are large, several scales may be introduced.

its intrinsic problems. These questions and issues will be discussed in Section 2.5. Let us now start our technical description of the SM.

2.1 THE PARTICLE CONTENT

In practice, in the context of QFTs, we associate a field to all particles that are described. Two criteria enter this association. First, the Poincaré representation of the particle determines the nature of the field, *i.e.* massive or massless spin-0, 1/2, 1, 3/2 or 2 particles, while higher-spin are theoretically disfavored (for elementary particles). Second, the quantum numbers of the particle determines the field's behavior under a group transformation. The SM particle content and the associated notation used throughout the manuscript is given in Table 1.

Fields	SU(2)$_L$ notation	Spin	SU(3)$_c$	SU(2)$_L$	U(1)$_Y$	$\mathcal{L}$	$\mathcal{B}$
Q	$(u_L, d_L)^T$	1/2	**3**	**2**	$+1/3$	0	1/3
U	$(u_R)^c$	1/2	$\bar{\mathbf{3}}$	**1**	$-4/3$	0	-1/3
D	$(d_R)^c$	1/2	$\bar{\mathbf{3}}$	**1**	$+2/3$	0	-1/3
L	$(\nu_L, e_L)^T$	1/2	**1**	**2**	-1	1	0
E	$(e_R)^c$	1/2	**1**	**1**	$+2$	-1	0
G	G	1	**8**	**1**	0	0	0
W	$(W^1, W^2, W^3)^T$	1	**1**	**3**	0	0	0
B	B	1	**1**	**1**	0	0	0
H	$(H^+, H^0)^T$	0	**1**	**2**	$+1$	0	0

×3 families { (bracket spanning Q, U, D, L, E)

Table 1: Particle content of the SM and conventions for the field notations. All Lorentz, gauge and flavor indices have been omitted for simplicity. The first two columns introduce the notation for the particle fields. The L and R subscripts indicate the left and right chiralities respectively. Note that U, D and E refer to the charge conjugate of right-handed fields and are thus left-handed. The fourth column gives the fields quantum numbers under the SM gauge group G_{SM}. The hypercharge normalization is such that the $U(1)_{em}$ charge reads $Q = T_3 + \frac{Y}{2}$. The last column gives the usual lepton and baryon number assignments. Three families of fermions need to be considered.

The hypercharge Y is normalized such that the electric charge will read $Q = T_3 + Y/2$ after electroweak symmetry breaking (EWSB), with T_3 being (the third component of) the weak isospin. The lepton ($\mathcal{L}$) and baryon ($\mathcal{B}$) number assignments, defined more explicitly later, are also given. From this table, one clearly sees an asymmetry between the quark and lepton sectors: the absence of a right-handed neutrino. As no such particle was observed experimentally and neutrinos were considered to be massless for a long time, the SM was originally built in this fashion.[4] It is certainly trivial to add a right-handed neutrino,

---

4 This also rises the question of the nature of the neutrinos; they could either be Dirac or Majorana fermions, see [45] for a review.

however we refrain from doing so as the neutrino sector will not play any role in what follows. Similarly, one can easily extend this particle content with new hypothetical fields. Examples are singlet extensions of the SM, multi-doublet Higgs sectors, triplet Higgs extensions and vector-like fermions. Care should however be taken when introducing new (non vector-like) fermions, as they can contribute to gauge anomalies. Anomaly-free sets of fermions should be constructed in order to maintain the consistency of the quantized theory.

A central point of the SM is that it is a chiral theory, this means that the left and right-handed particles behave differently under the gauge group. As can be seen in Table 1, only left-handed particles (right-handed antiparticles) feel the weak $SU(2)_L$ interaction while their right-handed counterparts do not: parity is maximally violated [46]. This fact ultimately calls for a Higgs sector in order to generate mass terms for the fermions.

2.2 FREE GAUGE BOSONS

The gauge bosons kinetic terms are written as

$$\mathscr{L}_{\text{gauge}} = -\frac{1}{4}G^{a,\mu\nu}G^a_{\mu\nu} - \frac{1}{4}W^{b,\mu\nu}W^b_{\mu\nu} - \frac{1}{4}B^{\mu\nu}B_{\mu\nu}, \tag{2.1}$$

where $a = 1$–8 and $b = 1$–3 are $SU(3)_c$ and $SU(2)_L$ gauge indices respectively. For non-abelian gauge fields, this term thus induces 3- and 4-point interactions among gauge bosons, see Eq. (1.36).

Similar (CP-violating) terms built upon the dual field strength tensors could also be written in principle,

$$\mathscr{L}_{\text{gauge}} = \theta^{tot}_c \frac{g_3^2}{32\pi^2}G^{a,\mu\nu}\widetilde{G}^a_{\mu\nu} + \theta_L \frac{g^2}{32\pi^2}W^{b,\mu\nu}\widetilde{W}^b_{\mu\nu} + \theta_Y \frac{g'^2}{32\pi^2}B^{\mu\nu}\widetilde{B}_{\mu\nu}, \tag{2.2}$$

where $\widetilde{X}^{\mu\nu} = (1/2)\epsilon^{\mu\nu\rho\sigma}X_{\rho\sigma}$ and $\epsilon^{\mu\nu\rho\sigma}$ is the totally anti-symmetric Levi-Civita tensor with $\epsilon^{0123} = +1$. Such terms are actually total derivative and thus, by Gauss' law, do not lead to any physical effect if the gauge fields approach zero at infinity sufficiently fast enough. For non-abelian groups, there exists on the contrary a special configuration of the fields with non-vanishing surface terms, which can then lead to physical effects. It turns out that the $SU(2)_L$ term has actually no physical consequence and only the QCD term has a possible role in nature.[5] This new operator induces a contribution to the neutron electric dipole moment [49, 50]. Experimental measurements force θ^{tot}_c to be less than about 10^{-10} [51]. There is however a priori no reason why this parameter should be that small. This is the strong CP-problem. The leading solution to this puzzle comes from Peccei and Quinn [52, 53] and involves a new pseudoscalar particle, the axion [54, 55]. Despite decades of direct and indirect searches for such a particle, no sign of it was found so far [56].

Mass terms such as

$$\mathscr{L}_{\text{mass}} = m_g^2 G^{a,\mu}G^a_\mu + m_W^2 W^{b,\mu}W^b_\mu + m_B^2 B^\mu B_\mu \tag{2.3}$$

---

5 An explanation of this mechanism and of the underlying physics is beyond the scope of this section, which is intended to introduce the Higgs and Yukawa sectors of the SM. Essentially, it relies on the fact that the Adler-Bell-Jackiw anomaly, see *e.g.* Eq. (1.48) in the context of Quantum Electrodynamics, has the same form as the θ-operators. An anomalous symmetry transformation can then be performed in order to cancel some CP-violating terms, see [31, 47, 48] for proper introductions.

are not gauge invariant. At this level, pure gauge theories thus imply massless gauge bosons. There exists a way to render the U(1) gauge boson massive while keeping the consistency and renormalizability of the theory. For this, a scalar field coupling to B_μ is introduced with a local transformation under U(1) such that the gauge invariance is actually present (but not manifest). This is the Stuckelberg mechanism [57]. While this works perfectly well for abelian gauge fields, extensions of this mechanism to non-abelian theories may lead to non-renormalizable and non-unitary theories [58]. In the SM, another mechanism is needed to describe the electroweak gauge bosons masses.

2.3 THE HIGGS SECTOR

In order to break the electroweak gauge group and provide mass terms to the electroweak gauge bosons (and subsequently unitarize the longitudinal scattering of the latter, see Section 2.3.3), a complex $\mathrm{SU}(2)_L$ doublet of scalar fields H, with non-vanishing hypercharge, acquiring a vacuum expectation value (vev) is introduced. The doublet can be parametrized in terms of four real or two complex scalar fields,

$$H = \frac{1}{\sqrt{2}} \begin{pmatrix} \phi_3 + i\phi_4 \\ \phi_1 + i\phi_2 \end{pmatrix} = \frac{1}{\sqrt{2}} \begin{pmatrix} \phi^+ \\ \phi^0 \end{pmatrix}. \tag{2.4}$$

where the second equality is an a posteriori result, in which the charges under $\mathrm{U}(1)_{em}$ are supposed to be known.

2.3.1 *Spontaneous electroweak symmetry breaking*

The most general renormalizable, Lorentz and gauge invariant Higgs potential for this weak doublet is

$$\mathcal{V}_{\mathrm{SM}} = -\mu^2 H^\dagger H + \lambda (H^\dagger H)^2 \mathrel{\widehat{=}} \lambda \left(H^\dagger H - \frac{\mu^2}{2\lambda} \right)^2, \tag{2.5}$$

where $\widehat{=}$ denotes the equivalence of the two potentials up to a constant term. Vacuum stability demands λ to be positive while the existence of an electroweak breaking vacuum requires $\mu^2 > 0$. The SM provides a description of the potential instability, but not an explanation as why a wrong-sign mass term is needed. An important mass scale appears, the Higgs vacuum expectation value,

$$v \equiv \frac{\mu^2}{\lambda}, \tag{2.6}$$

it is the field value which minimizes the above potential. By Poincaré invariance, v has to be constant over all space-time. Writing H as a collection of four real scalar fields, as in Eq. (2.4), v may in principle be distributed among all the four components. Physical arguments however lead us to seek for a solution in which only the neutral CP-even component of the doublet, ϕ_1 acquires a vev. Indeed, the charged component should not acquire a vev as we live in a vacuum in which the electric charge is a good quantum number. Further-

more, since our vacuum is CP-conserving, the CP-odd component of the doublet cannot acquire a vev. It is then particularly useful to rewrite H as

$$H = \exp\left[-i\Pi^a \frac{\sigma^a}{2}\right] \frac{1}{\sqrt{2}} \begin{pmatrix} 0 \\ v+h \end{pmatrix} \equiv R \frac{1}{\sqrt{2}} \begin{pmatrix} 0 \\ v+h \end{pmatrix}, \tag{2.7}$$

where R is an SU(2) matrix, and h is the field that will lead to the physical massive Higgs boson. The matrix R can be constructed explicitly in terms of the original four ϕ_i components. The number of degrees of freedom is then conserved: 3 Goldstone bosons parametrized in Π^a and h, versus the four real scalar fields ϕ_i. Having expressed H as such, the Goldstone bosons can be gauged away through an SU(2)$_L$ transformation with matrix R^{-1}, this is the unitary gauge. In this process, the SU(2)$_L$ gauge fields are redefined according to Eq. (1.34), acquiring a longitudinal component.

The electroweak gauge boson masses can be found from the Higgs kinetic term, $(D_\mu H)^\dagger (D^\mu H)$, where in the unitary gauge,

$$D_\mu H = \left[\partial_\mu \mathbb{1}_{2\times 2} - ig \frac{\sigma_a}{2} W_\mu^a - ig' \frac{Y}{2} B_\mu\right] \frac{1}{\sqrt{2}} \begin{pmatrix} 0 \\ v+h \end{pmatrix}. \tag{2.8}$$

Developing, we have,

$$(D_\mu H)^\dagger (D^\mu H) \supset \frac{(v+h)^2}{4} \left[\frac{g^2}{2}\left(2W_\mu^+ W^{-\mu} + W_\mu^3 W^{3\mu}\right) + \frac{g'^2}{2} B_\mu B^\mu - gg' W_\mu^3 B^\mu\right], \tag{2.9}$$

where the $W_\mu^\pm$ fields have been defined as

$$W_\mu^\pm = \frac{W_\mu^1 \mp iW_\mu^2}{\sqrt{2}}. \tag{2.10}$$

It is indeed possible to show that the above combinations have indeed well defined electrical charges under U(1)$_{em}$. The $W^\pm$ mass and the neutral mass matrix in the (W^3, B) basis are

$$m_{W^\pm}^2 = \frac{g^2 v^2}{4}, \tag{2.11}$$

$$\mathcal{M}_{W^3-B}^2 = \frac{v^2}{4} \begin{pmatrix} g^2 & -gg' \\ -gg' & g'^2 \end{pmatrix}. \tag{2.12}$$

Note that since W^3 is part of the SU(2)$_L$ triplet containing W^1 and W^2, the (1,1) matrix element also corresponds to $m_{W^\pm}^2$. The vanishing determinant of the mass matrix reveals a massless gauge boson, the photon, associated to a surviving U(1) symmetry under which the vacuum is invariant. The remaining massive state, the Z boson, has a mass,

$$m_Z^2 = \text{Tr}(\mathcal{M}_{W^3-B}^2) = \frac{g^2 + g'^2}{4} v^2. \tag{2.13}$$

The three generators of SU(2)$_L$ map the vacuum to three independent directions, one of which happens to be the same as the U(1)$_Y$ direction. This is a sign of an underlying symmetry. Indeed, under a hypercharge transformation, $Y = y\mathbb{1}$,

$$H_0 \to \exp\left[-ig\theta_Y Y\right] H_0 \simeq H_0 + \frac{1}{\sqrt{2}} \begin{pmatrix} 0 \\ -i\theta_Y yv \end{pmatrix}. \tag{2.14}$$

While under an $SU(2)_L$ transformation in the third $SU(2)_L$ direction,

$$H_0 \to \exp\left[-i\theta_3\frac{\sigma_3}{2}\right]H_0 \simeq H_0 + \frac{1}{\sqrt{2}}\begin{pmatrix} 0 \\ i\frac{\theta_3}{2}v \end{pmatrix}. \tag{2.15}$$

The two transformations thus map the vacuum to the ϕ_2 direction, see Eq. (2.4). A combination of these two transformations can therefore leave H_0 invariant if $\theta_Y = \theta_3/(2y)$. The generator of this symmetry is the electric charge Q_{em}

$$\exp\left[-i\theta_3\frac{\sigma_3}{2}\right] \times \exp\left[-i\theta_Y Y\right] = \exp\left[-i\theta_3\left(\frac{\sigma_3}{2} + \frac{Y}{2y}\right)\right] \equiv \exp\left[-i\theta_{em}Q_{em}\right]. \tag{2.16}$$

Generalizing this result for any representation,

$$Q_{em} = T^3 + \frac{Y}{2}. \tag{2.17}$$

The electroweak gauge group $SU(2)_Y \times U(1)_Y$ is broken to $U(1)_{em}$. The photon and Z fields are obtained in the process of diagonalization as

$$Z_\mu = \cos\theta_W W_\mu^3 - \sin\theta_W B_\mu \tag{2.18}$$
$$A_\mu = \sin\theta_W W_\mu^3 + \cos\theta_W B_\mu, \tag{2.19}$$

where $\cos\theta_W = g/\sqrt{g^2 + g'^2}$ is the cosine of the electroweak Weinberg mixing angle. The electromagnetic gauge coupling e can easily be found by considering the gauge transformations of W_μ^3 and B_μ, see Eq. (1.35),

$$W_\mu^3 \to W_3^\mu - \frac{1}{g}\partial_\mu\theta_{em}, \tag{2.20}$$

$$B_\mu \to B_\mu - \frac{1}{g'}\partial_\mu\theta_{em}. \tag{2.21}$$

First, the invariance of Z_μ under $U(1)_{em}$, yields to

$$\frac{\cos\theta_W}{g} - \frac{\sin\theta_W}{g'} = 0 \Rightarrow \tan\theta_W = \frac{g'}{g}. \tag{2.22}$$

Defining e through the gauge photon field transformation,

$$A_\mu \to A_\mu - \frac{1}{e}\partial_\mu\theta_{em}, \tag{2.23}$$

then yields to,

$$\frac{1}{e} = \frac{\sin\theta_W}{g} + \frac{\cos\theta_W}{g'} = \frac{g'}{g\sqrt{g^2 + g'^2}} + \frac{g}{g'\sqrt{g^2 + g'^2}} = \sqrt{\frac{1}{g^2} + \frac{1}{g'^2}}. \tag{2.24}$$

This relation can also be easily found by rewriting the covariant derivative in terms of the A_μ field.

Defining the ρ parameter [59] as

$$\rho \equiv \frac{m_W^2}{\cos^2\theta_W m_Z^2}, \tag{2.25}$$

we have $\rho^{\text{SM}} = 1$ at tree-level in the SM, in very close agreement with the experimental result $\rho = 1.00040 \pm 0.00024$ [60]. In general, for a model with n Higgs multiplets in the representations $2T_i + 1$ of $\text{SU}(2)_L$, with hypercharges Y_i and vevs v_i,

$$\rho = \frac{\sum_i \left[T_i(T_i + 1) - \frac{1}{4}Y_i^2\right] v_i^2}{\sum_i \frac{1}{2}Y_i^2 v_i^2}. \tag{2.26}$$

Considering a single Higgs representation, $\rho = 1$ is thus achieved if $T(T+1) = 3Y^2/4$, under the condition that $T + Y/2$ is an integer (the larger electric charge in this representation). The first few pairs that satisfy the two conditions are $(T, Y) = (0, 0)$, $(1/2, 1)$, $(3, 4)$, $(25/2, 15)$, $(48, 56)$ and $(361/2, 209)$. The SM Higgs, with the $(1/2, 1)$ representation, is thus the minimal non-trivial realization of $\rho = 1$ in the $\text{SU}(2)_L \times \text{U}(1)_Y$ electroweak model. Note however that Higgs representations above it cannot actually couple to the SM fermions and are thus irrelevant phenomenologically. Though this success of the SM might seem a simple coincidence, it is in fact the consequence of an underlying symmetry, the custodial symmetry [61, 62].

2.3.2 *Custodial symmetry*

Following Eq. (2.4), we can write,

$$H^\dagger H = \frac{1}{2} \sum_{i=1}^{4} \phi_i^2 \equiv \frac{1}{2}\varphi^2, \tag{2.27}$$

where φ^2 can be seen as the squared norm of a 4-dimensional vector of $\mathbb{R}^4$. As such, the Higgs scalar potential is invariant under $\text{SO}(4)$ transformations, under which all four real scalar fields ϕ_i rotate into one another. The $\text{SO}(4)$ algebra is isomorphic to that of a product of two $\text{SU}(2)$ factors, which we denote here as $\text{SU}(2)_L \times \text{SU}(2)_R$ (left and right transformations). Using the self-conjugacy property of $\mathbf{2}$: $i\sigma_2 H^* \sim H \sim \mathbf{2}$, one can combine $\widetilde{H} \equiv i\sigma_2 H^*$ and H into a single 2×2 matrix Φ defined as

$$\Phi = (i\sigma_2 H^* \ \ H) = \begin{pmatrix} \phi^{0*} & \phi^+ \\ -\phi^{+*} & \phi^0 \end{pmatrix}, \quad \Phi^\dagger\Phi = \begin{pmatrix} \varphi^2 & 0 \\ 0 & \varphi^2 \end{pmatrix}, \tag{2.28}$$

which transforms as $\Phi \to U_L \Phi U_R^\dagger$ under a $\text{SU}(2)_L \times \text{SU}(2)_R$ transformation. In particular, $\text{Tr}\left[\Phi^\dagger\Phi\right]$ is invariant under both left and right transformations. The invariance under $\text{SU}(2)_L \times \text{SU}(2)_R$ can most easily be seen by expressing the scalar potential as,

$$\mathcal{V}_{\text{SM}} = \frac{\lambda}{4}\left(\frac{1}{2}\,\text{Tr}\left[\Phi^\dagger\Phi\right] - \frac{\mu^2}{\lambda}\right)^2. \tag{2.29}$$

In the vacuum, $\langle\Phi\rangle = v\mathbb{1}_{2\times2}$, and $\text{SU}(2)_L \times \text{SU}(2)_R$ is broken to the diagonal subgroup $\text{SU}(2)_V$ which is isomorphic to $\text{SO}(3)$, the custodial symmetry group.

Assuming the existence of such a symmetry in the vacuum (no matter its origin and the realization of the electroweak breaking), (W^1, W^2, W^3) should be a triplet of $\text{SU}(2)_V$,

hence all three components should be mass-degenerate. Based on this, the mass matrix in the (W^3, B) basis has the generic form

$$\mathcal{M}_V^2 = \begin{pmatrix} m_{W^\pm}^2 & Y \\ Y & Z \end{pmatrix}, \tag{2.30}$$

where Y and $Z \geq 0$ are unknown real parameters. To reproduce $m_\gamma^2 = 0$, the determinant of $\mathcal{M}_V^2$ should vanish, i.e., $Z m_W^2 - Y^2 = 0$. Using the definition Eqs. (2.18) and (2.19) of $\cos\theta_W$, the photon mass can be expressed as

$$m_\gamma^2 = c_W^2 Z + s_W^2 m_{W^\pm}^2 - 2 s_W c_W Y = 0, \tag{2.31}$$

where the shorthand notation $c_W \equiv \cos\theta_W$, $s_W \equiv \sin\theta_W$ is used. This leads to

$$c_W^2 Z = s_W^2 m_{W^\pm}^2, \tag{2.32}$$

using the determinant condition. Finally, using $\mathrm{Tr}(\mathcal{M}_V^2) = m_Z^2 = m_{W^\pm}^2 + Z$ we get

$$m_Z^2 c_W^2 = m_{W^\pm}^2, \tag{2.33}$$

and thus $\rho = 1$. The conclusion holds irrespective of the explicit realization of electroweak symmetry breaking and is thus a sole consequence of the custodial symmetry of the vacuum.

Let us now discuss the two explicit violation of custodial symmetry in the SM. So far we did not consider the Higgs kinetic term, which takes the form $\frac{1}{2}\,\mathrm{Tr}\left[(D_\mu\Phi)^\dagger(D^\mu\Phi)\right]$, where $(D^\mu\Phi) \supset +ig'\frac{\sigma_3}{2}B_\mu\Phi$. We see that because of the explicit σ_3 matrix, the kinetic term is $\mathrm{SU}(2)_L \times \mathrm{SU}(2)_R$ invariant only if $g' = 0$, i.e., custodial symmetry is explicitly broken in the SM due to hypercharge interactions. Note also that Eq. (2.28) implicitly asked for H to be neutral under $\mathrm{U}(1)_Y$. The W^a dependent terms of the kinetic term are custodial symmetric if the weak gauge bosons form a custodial triplet. Another source of custodial breaking comes from the Yukawa sector. Exact custodial invariance would otherwise require mass-degenerate up- and down-fermions in each family.

Since custodial symmetry is explicitly broken in the SM, radiative corrections to the ρ parameter proportional to the breaking of $\mathrm{SU}(2)_V$ are expected. Though $g' \neq 0$ in the SM, corrections proportional to g' only arise at the two-loop level [63]. Corrections due to the mass splitting between quark doublets arise at one-loop and are proportional to the loop-function F [63],

$$\delta\rho = \frac{1}{(4\pi m_{W^\pm})^2} F(m_u, m_d), \tag{2.34}$$

where,

$$F(m_u, m_d) = m_u^2 + m_d^2 - \frac{2 m_u^2 m_d^2}{m_u^2 - m_d^2} \ln\left(\frac{m_u^2}{m_d^2}\right), \tag{2.35}$$

which indeed vanishes in the custodial limit $m_u = m_d$. The most important contribution thus comes from the third quark family, $m_t \gg m_b$, for which $F(m_t, m_b) \simeq m_t^2$.
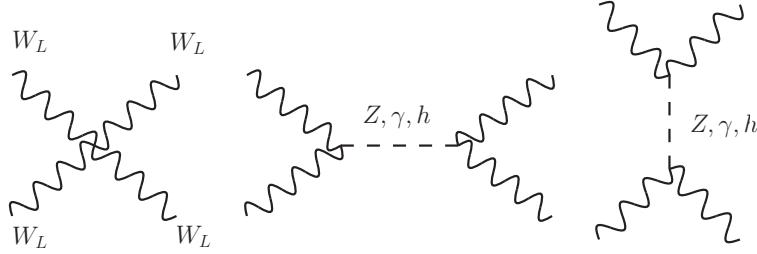
Figure 2.1: Tree-level contributions to $W_L W_L \to W_L W_L$ in the SM.

2.3.3 *Theoretical constraints*

Unitarity

While massless gauge bosons only have two transverse degrees of freedom, massive ones have a supplementary longitudinal component. In the SM, the latter comes from the Nambu-Goldstone bosons absorbed by the gauge fields after spontaneous EWSB. The scattering processes of such modes in the high-energy limit are to be considered with attention as they may lead to a violation of unitarity, as *e.g.* in $\nu_e \bar{\nu}_e \to W_L^+ W_L^-$, $Z_L W_L^\pm \to Z_L W_L^\pm$ and $W_L^+ W_L^- \to W_L^+ W_L^-$. Indeed, according to the equivalence theorem [64], the high-energy limit of an amplitude involving longitudinal gauge bosons can be obtained by replacing the latter by their corresponding Nambu-Goldstone bosons, *i.e.*,

$$\mathcal{M}(W_L^+, W_L^-, Z_L, ...) = \mathcal{M}(w^+, w^-, z^-, ...) + \mathcal{O}\left(\frac{E}{m_{W,Z}}\right) \tag{2.36}$$

where $w^\pm$ and z denote the Nambu-Goldstone bosons associated to $W^\pm$ and Z respectively, and E the typical momentum exchange. Here Nambu-Goldstone bosons actually refer to any scalar x that couples derivatively to a gauge boson X, *i.e.*, $\mathcal{L} \supset m_X X_\mu^- \partial^\mu x^+ +$ h.c. Considering for definiteness the 4-point contribution to the $W_L W_L \to W_L W_L$ scattering, leftmost diagram in Fig. 2.1, we therefore observe that $\mathcal{M}_{4W} \simeq E^4/v^4$ where v is the characteristic scale associated to the Nambu-Goldstone bosons. The amplitude has a very large quartic divergence, leading to violation of unitarity at large enough energies.

Let us consider the previous example, $W_L W_L \to W_L W_L$, in more details. At tree-level, seven diagrams need to be considered: the 4-point interaction and the Z, γ, h-mediated ones in the s and t channels as shown in Fig. 2.1. The longitudinal polarization vector of a massive $W^\pm$ propagating along the z-axis, with 4-momentum $k^\mu = (E, 0, 0, k_z)$, can be written $\epsilon_L^\mu(k) = (k_z, 0, 0, E)/m_{W^\pm}$ which, for $E \gg m_{W^\pm}$, takes the form $\epsilon_L^\mu \simeq k^\mu/m_{W^\pm}$. Considering the first diagram, the Feynman rule for the 4-W vertex can be read off the gauge kinetic term

$$-\frac{1}{4} W_{\mu\nu}^a W^{\mu\nu a} \supset \left(\frac{1}{4i}\right) ig^2 W^{-\mu} W^{-\nu} W^{+\rho} W^{+\sigma} \left[2\eta_{\mu\nu}\eta_{\rho\sigma} - \eta_{\mu\rho}\eta_{\nu\sigma} - \eta_{\mu\sigma}\eta_{\nu\rho}\right]. \tag{2.37}$$

It is then clear that the amplitude for this diagram increases as first and second powers of Mandelstam variables [65] at high-energy, indeed, in this limit,

$$\mathcal{M}_{4W} \simeq g^2 \frac{k_1^\mu}{m_{W^\pm}} \frac{k_2^\nu}{m_{W^\pm}} \frac{k_3^\rho}{m_{W^\pm}} \frac{k_4^\sigma}{m_{W^\pm}} \left[2\eta_{\mu\nu}\eta_{\rho\sigma} - \eta_{\mu\rho}\eta_{\nu\sigma} - \eta_{\mu\sigma}\eta_{\nu\rho}\right]. \tag{2.38}$$

For $E \gg m_{W^\pm}$, one can write $\mathcal{M}_i = A_i x^2 + B_i x + C_i + \mathcal{O}(1/x)$ where $x = s/(4m_{W^\pm}^2) \simeq E^2/(4m_{W^\pm}^2)$ and i labels the seven contributions to the process (see *e.g.* [66] for a recent and comprehensive discussion). One should however sum up all relevant contributions before concluding. Ignoring the Higgs contributions so far (which actually do not contribute to the A term), and summing over the five other diagrams leads to an exact cancellation among the various A_i. The high-energy behavior is therefore dominated by the term proportional to x, with $\sum_{4W,Z,\gamma} B_i = g^2$ for the forward scattering. Unitarity would then be violated for

$$\mathcal{M} \simeq \frac{g^2 E^2}{4m_{W^\pm}^2} \gtrsim 16\pi^2 \Rightarrow E \gtrsim \frac{8\pi m_{W^\pm}}{g} \simeq 3 \text{ TeV}. \tag{2.39}$$

This argument provides the scale at which tree and loop diagrams have approximatively the same size, *i.e.*, the scale at which perturbation theory breaks down and the theory becomes strongly coupled. A stronger bound may be derived considering the various scattering channels involving the longitudinal components of the gauge bosons. One can as well use a partial wave decomposition and the optical theorem to formally derive such bounds. Assuming that the unitarity-violating behavior should be regularized by an extra sector provided a no-go theorem to the LHC, something had to be found beyond the electroweak gauge sector [67]. In Higgs-less models, a typical E^2-growth of the longitudinal vector boson amplitudes is expected. Finally, summing up all gauge boson and Higgs contributions, an exact cancellation among the terms proportional to x occur, leaving only the constant term and terms with negative powers of E. The SM Higgs sector is therefore seen to unitarize the scattering of longitudinal gauge bosons. Using the partial wave decomposition, Lee, Quigg and Thacker derived an upper bound on the Higgs mass by requiring tree-level unitarity: $m_h^2 < 8\pi\sqrt{2}/(3G_F) \simeq (1 \text{ TeV})^2$ [68, 69]. Today, it remains to be checked experimentally whether such a unitarization mechanism is at work in nature or not.

Triviality and Stability

Important constraints on the Higgs parameters and the scale of applicability of the EW model can be derived considering the renormalization group evolution of the Higgs self-coupling $\lambda(Q^2)$ [70]. At one-loop, considering the Higgs, gauge bosons and the dominant top fermionic contribution, one finds [71]

$$\frac{d\lambda}{d\log Q^2} = \frac{1}{16\pi^2}\left[12\lambda^2 + 6\lambda y_t^2 - 3y_t^4 - \frac{3}{2}\lambda(3g^2 + g'^2) + \frac{3}{16}\left(2g^4 + (g'^2 + g^2)^2\right)\right], \tag{2.40}$$

where y_t is the top Yukawa coupling. Representative examples of the diagrams leading to these terms can be found in Fig. 2.2.

In the strong λ regime, the evolution equation can be approximated as

$$\frac{d\lambda}{d\log Q^2} \simeq \frac{3}{4\pi^2}\lambda^2, \tag{2.41}$$

which leads to the solution

$$\lambda(Q^2) = \frac{\lambda(v^2)}{1 - \frac{3}{4\pi^2}\lambda(v^2)\log\left(\frac{Q^2}{v^2}\right)}, \tag{2.42}$$
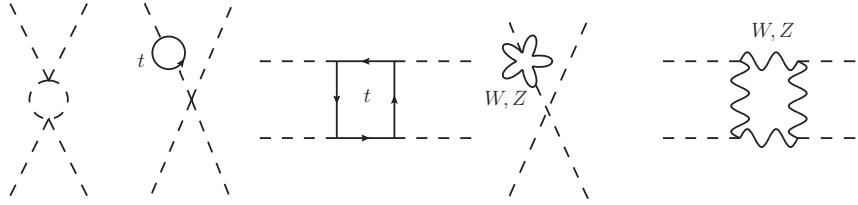
Figure 2.2: Representatives diagrams contributing to the Higgs self-coupling beta function at the one-loop level.
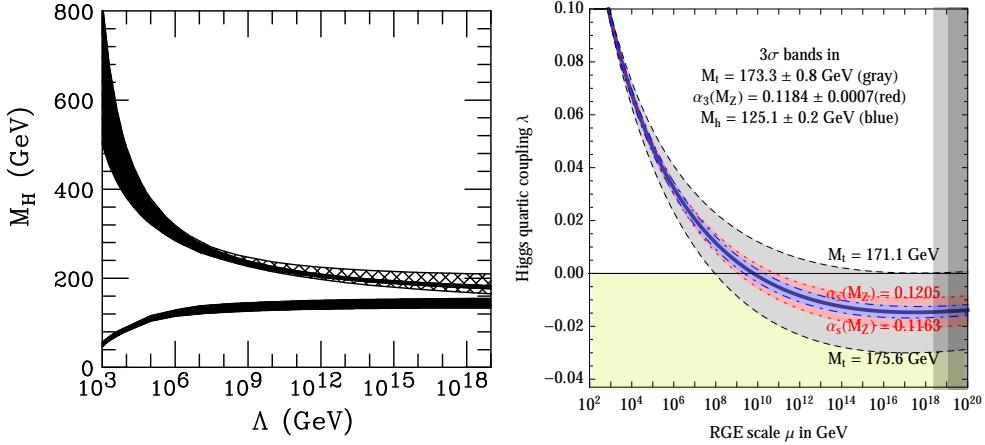
Figure 2.3: <u>Left panel</u>: Triviality (upper band) and stability (lower band) bound on the Higgs mass as a function of the renormalization scale Q from [72]. Only the region in between the two bands is allowed. <u>Right panel</u>: Running of λ in the SM at the 2/3-loop level for $m_h = 125.1$ GeV and $m_t = 173.3$ GeV from [73]. Around 10^{10} GeV, the central value of λ turns negative.

where $\lambda(v^2) = m_h^2/(2v^2)$. For a given Higgs mass m_h, the λ evolution will thus hit a Landau pole at the scale Q_L for which the denominator vanishes,

$$Q_L = v \exp\left[\frac{4\pi^2 v^2}{m_h^2}\right]. \tag{2.43}$$

Conversely, if we require our model to be perturbative until the Planck scale $\sim 10^{19}$ GeV, we obtain an upper bound on the Higgs mass $m_h \lesssim 144$ GeV. This is called the *triviality* bound, as only a trivial theory, $\lambda(Q^2) = 0 \; \forall Q^2$, is free from a Landau pole.

As the Higgs potential should be bounded from below, *i.e.*, $\lambda(Q^2) > 0$, it is also primordial to look at the behavior of λ around 0. The evolution then reads

$$\frac{d\lambda}{d\log Q^2} \simeq \frac{1}{16\pi^2}\left[-3y_t^4 + \frac{3}{16}\left(2g^4 + (g'^2 + g^2)^2\right)\right], \tag{2.44}$$

and is mostly dominated by the negative top contribution which tends to destabilize the Higgs potential, on the contrary to the gauge contributions that slightly stabilize it. As y_t, g and g' are also subject to RG running, a coupled system of differential equations should actually be solved. For simplicity, let us assume that these quantities are actually constant. We can then solve for λ,

$$\lambda(Q^2) = \frac{m_h^2}{2v^2} + \frac{1}{16\pi^2}\left[-3y_t^4 + \frac{3}{16}\left(2g^4 + (g'^2 + g^2)^2\right)\right]\log\left(\frac{Q^2}{v^2}\right). \tag{2.45}$$

27
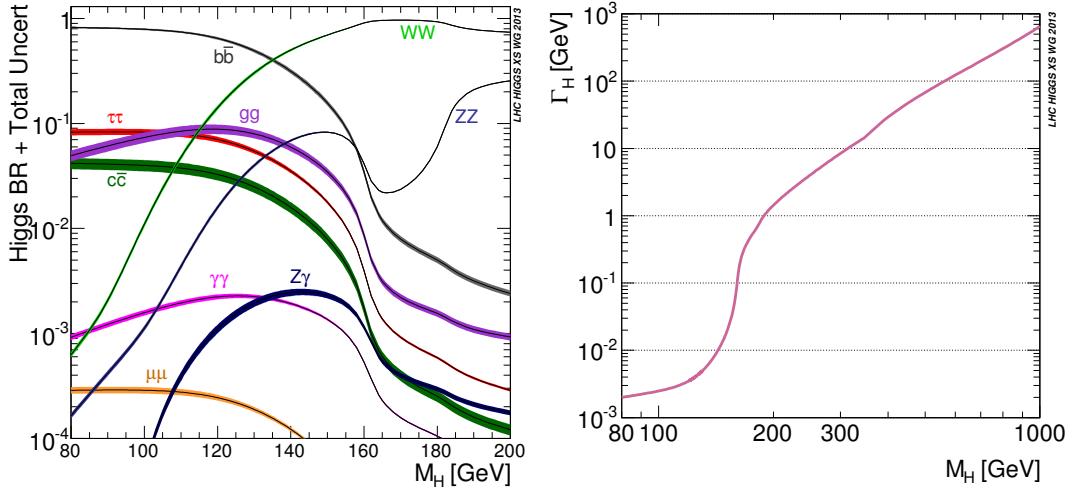
Figure 2.4: <u>Left panel</u>: Branching ratios of the SM Higgs as a function of m_h. <u>Right panel</u>: Higgs total width in the SM as a function of m_h. Both results are from the LHC Higgs Cross Section Working Group (LHC-HXSWG) [75–77].

Requiring stability of the potential down to a given scale Q thus imposes a lower bound on m_h, the *stability* bound.

A detailed and fully consistent computation of these bounds were performed in Ref. [72] and lead to the result shown in the left panel of Fig. 2.3. The Higgs potential can only be stable up to the Planck scale $\sim 10^{19}$ GeV if the Higgs mass is the 130-180 GeV range. With an observed Higgs mass of 125.1 GeV, the stability bound is violated around 10^{10} GeV [73], see right panel of Fig. 2.3. This does not however bring our universe in an unstable state, but rather, due to the measured top mass, to a metastable state for which the decay lifetime is several orders of magnitude larger than the age of our universe.

These arguments however suppose that the SM is the correct description of fundamental interactions up to the scale Q considered. If instead a more fundamental theory kicks in at a lower scale, the corresponding new contributions to the λ running should be evaluated. It has been shown that even Planck-suppressed operators can sizably influence these conclusions [74]. Care is thus needed when interpreting such results.

2.3.4 *Higgs decays*

The SM Higgs boson couples to all fermions and massive gauge bosons in a precise and well-defined way. Indeed, the Higgs couplings to SM particles depend solely on their masses, see next subsection. This is very good news as this allows to compute all the various branching ratios as a function of a unique parameter, the Higgs mass which is itself not predicted by the theory and was only recently measured precisely [16]. All other relevant parameters, *i.e.* the gauge boson and fermion masses, the Higgs vev and the gauge couplings can indeed be considered as fixed [60]. The branching ratio of the SM Higgs as a function of its mass are shown in the left-panel of Fig. 2.4.

At tree-level, the Higgs partial width for the decay into two fermions is simply given by,

$$\Gamma(h \to f\bar{f}) = N_c^f \frac{m_h}{8\pi v^2} m_f^2 \beta_f^3, \tag{2.46}$$

where $N_c^f = 1(3)$ for leptons (quarks) and $\beta_f = (1-4x_f)^{-1/2}$ where $x_f = m_f^2/m_h^2$. While the width is proportional to β_f^3 for a scalar Higgs, it would be linear on β_f in the case of a pseudo-scalar, this dependence can be used to discriminate between various parity hypotheses. The partial width grows linearly with the Higgs mass, while it grows quadratically with the fermion mass. For fixed m_h, there is therefore a strong hierarchy in branching ratios between the various fermionic final states. Figure 2.4 indeed illustrates this behavior, $\text{BR}(h \to b\bar{b}) > \text{BR}(h \to \tau\tau) > \text{BR}(h \to c\bar{c})$ for any m_h. The decays into the first and second generation of fermions are extremely suppressed and alternative ways to probe the corresponding couplings should be considered to experimentally probe them, see *e.g.* [78] for an attempt to access *hee* coupling in atomic transitions and [79] for the $hc\bar{c}$ coupling in $h \to J/\psi\gamma$. Naturally, the above expression should be corrected with radiative corrections. The largest effect comes from QCD corrections for the Higgs decay into light quarks, leading to an approximative 40% suppression with respect to the Born level result [80, 81].

Turning to the massive electroweak gauge bosons $V = W^\pm, Z$, for a Higgs boson below 160 GeV the two gauge bosons cannot be both on-shell, and the only open channels are $h \to V^{(*)}V^*$. Although suppressed by the virtuality of the gauge boson, such decay channels may actually be very important because of the large hVV coupling, Fig. 2.4 shows that for $m_h \gtrsim 130$ GeV WW^* is the primary Higgs decay channel. Though $m_{W^\pm} < m_Z$, the Higgs decay in W^+W^- dominates over ZZ on the full mass range since the two Z's are identical particles. Above the kinematic threshold, the partial width takes the form

$$\Gamma(h \to VV) = N_V \frac{m_h^3}{16\pi v^2}\sqrt{1 - 4x_V}\left(1 - 4x_V + 12x_V^2\right) \tag{2.47}$$

where $N_{W^\pm(Z)} = 2(1)$ and $x_v = m_V^2/m_h^2$. The partial width grows as the third power of the Higgs mass, and the total Higgs width is thus completely dominated by the VV decays for $m_h \gtrsim 160$ GeV as can be seen in the right-panel of Fig. 2.4. For $m_h \gg m_Z$, *i.e.*, $x_V \simeq 0$, the partial width for $h \to W^+W^-$ is two times larger than for $h \to ZZ$ as expected from a simple counting of the degrees of freedom.

Finally, the $h \to gg$, $h \to \gamma\gamma$ and $h \to Z\gamma$ decays necessarily occur through loop-processes as the Higgs does not couple directly to massless particles. The $h \to gg$ decay goes through loops of colored-particles, the top quark (and the bottom quark to a less extent) providing the dominant contribution in the SM because of its large mass. At leading-order, the partial width takes the form [82],

$$\Gamma(h \to gg) = \frac{\alpha_3^2 m_H^3}{72v^2\pi^3}\left|\frac{3}{4}\sum_q A_{1/2}^h(\tau_q)\right|^2, \tag{2.48}$$

where $\tau_q = m_h^2/(4m_q^2)$,

$$A_{1/2}^h(\tau) = 2\left[\tau + (\tau - 1)f(\tau)\right]\tau^{-2}, \tag{2.49}$$

and

$$f(\tau) = \begin{cases} \arcsin^2\sqrt{\tau} & \text{if } \tau \leq 1 \\ -\frac{1}{4}\left[\log\frac{1+\sqrt{1-\tau^{-1}}}{1-\sqrt{1-\tau^{-1}}} - i\pi\right]^2 & \text{if } \tau > 1 \end{cases}. \tag{2.50}$$

The function $A^h_{1/2}$ approaches 4/3 (0) in the large (vanishing) quark mass limit. In particular, $A^h_{1/2}(\tau_t) \simeq 1.4$, $A^h_{1/2}(\tau_b) \simeq (1.2 + 4.1i) \times 10^{-2}$, $A^h_{1/2}(\tau_c) \simeq (0.4 + 5.3i) \times 10^{-3}$, showing that the dominant contributions are indeed from the top quark and the bottom quark to a lesser extent. Next-to-leading order QCD corrections lead to a 70% (40%) increase of the partial width for $m_h \lesssim 2m_{W^\pm}$ ($m_h \simeq 1$ TeV) [83].

The partial width $h \to \gamma\gamma$ is given by,

$$\Gamma(h \to \gamma\gamma) = \frac{\alpha^2 m_h^3}{256 v^2 \pi^3} \left| \sum_f N_c^f Q_f^2 A^h_{1/2}(\tau_f) + A^h_1(\tau_W) \right|^2, \tag{2.51}$$

where

$$A^h_1(\tau) = -[2\tau^2 + 3\tau + 3(2\tau - 1)f(\tau)]\tau^{-2}. \tag{2.52}$$

The $W^\pm$ and fermion amplitudes have a different sign by virtue of Wick's theorem and this leads to a destructive interference between the two. In models of new physics (NP), the top and $W^\pm$ amplitudes might be rescaled independently and this can have interesting phenomenological consequences. It is clear that these loop-induced processes form a window to NP. Heavy new charged particles may not be directly produced in colliders but can contribute to the loop-induced Higgs decays. Precision measurements of the Higgs properties are of primary importance in that respect. We extend and quantify these considerations in the next chapter.

The total Higgs width is then defined through,

$$\Gamma^h_{\text{tot, SM}} = \sum_f \Gamma(h \to f\bar{f}) + \sum_V \Gamma(h \to V^{(*)}V^{(*)}) + \Gamma(h \to gg, \gamma\gamma, Z\gamma), \tag{2.53}$$

and the various branching ratios are given by,

$$\text{BR}(h \to Y)_{\text{SM}} = \frac{\Gamma(h \to Y)}{\Gamma^h_{\text{tot, SM}}}. \tag{2.54}$$

Beyond the SM (BSM), the Higgs boson may have new decay channels accessible. Collectively noting the additional width contributions as Γ_{BSM}, the Higgs total width and branching ratios would be modified as

$$\Gamma^h_{\text{tot, BSM}} \equiv \Gamma^h_{\text{tot, SM}} + \Gamma^h_{\text{BSM}}, \tag{2.55}$$

$$\text{BR}(h \to Y)_{\text{BSM}} = \text{BR}(h \to Y)_{\text{SM}} \left[1 - \frac{\Gamma^h_{\text{BSM}}}{\Gamma^h_{\text{tot, BSM}}} \right], \tag{2.56}$$

where $\Gamma^h_{\text{BSM}}/\Gamma^h_{\text{tot, BSM}} \equiv \text{BR}(h \to \text{BSM})_{\text{BSM}}$. The existence of such new decay channels would modify the branching ratios to SM particles.

As can be seen from Eq. (2.5), the Higgs boson also interacts with itself through triple and quartic self-couplings. The $h^* \to hh$ and $h^* \to hhh$ decays are however very suppressed. These are nonetheless the only experimental direct probes of λ, the parameter that determines the shape and stability of the Higgs potential. As such, the experimental determination of the Higgs self-couplings is crucial to fully confirm the SM EWSB mechanism. Although the quartic interaction is not expected to be observable at the LHC [84], unless immensely enlarged by new physics effects, the triple Higgs coupling is the subject of many phenomenological studies and the prospects to measure it in the second run of the LHC are interesting [85, 86].

2.4 THE YUKAWA SECTOR

2.4.1 *A flavor mismatch*

Since the gauge boson interactions to fermions are flavor blind, *i.e.*, the covariant derivative does not carry any flavor index, the fermion kinetic term is invariant under independent unitary transformations of the five SM fermion representations in flavor space,

$$\mathscr{L}_K = \sum_{k,I} \bar{\psi}_k^I (i\slashed{D}_k)\psi_k^I \xrightarrow{\psi_k^I \to g_k^{IJ}\psi_k^J} \mathcal{L}_K \tag{2.57}$$

where $g_k \in \mathrm{U}(3)_k$, $k = Q, U, D, L, E$ and $I = 1, 2, 3$ is a flavor index. This large symmetry group is noted $G_F \equiv \mathrm{U}(3)_Q \times \mathrm{U}(3)_U \times \mathrm{U}(3)_D \times \mathrm{U}(3)_L \times \mathrm{U}(3)_E$, the flavor symmetry group [87], under which,

$$Q \to g_Q Q, \quad L \to g_L L, \quad U \to U g_U^\dagger, \quad D \to D g_D^\dagger, \quad E \to E g_E^\dagger . \tag{2.58}$$

Using the isomorphism $\mathrm{U}(3) \simeq \mathrm{SU}(3) \times \mathrm{U}(1)$, G_F is usually written as $G_F = \mathrm{SU}(3)^5 \times \mathrm{U}(1)^5$. This symmetry and its consequences will be discussed in more details in Chapter 6, where the idea of Minimal Flavor Violation is introduced.

The SM Yukawa Lagrangian is given by,

$$-\mathscr{L}_{\text{Yukawa}} = U^I \mathbf{Y}_U^{IJ} Q^J H + D^I \mathbf{Y}_D^{IJ} Q^J \widetilde{H} + E^I \mathbf{Y}_E^{IJ} L^J \widetilde{H} + \text{h.c.}, \tag{2.59}$$

where $I, J = 1, 2, 3$ are flavor indices, $\widetilde{H} = i\sigma_2 H^*$ and $\mathbf{Y}_{U,D,E}$ are 3×3 matrices in flavor space. The Yukawa sector is the only source of (explicit) breaking of the flavor symmetry in the SM. Note that there still remains some phase freedom, in particular the global subgroups $g_Q = g_U = g_D = e^{i\mathcal{B}}$ and $g_L = g_E = e^{i\mathcal{L}}$ are conserved, this is nothing less than the baryon and lepton number conservations $\mathrm{U}(1)_{\mathcal{B},\mathcal{L}}$. As can be seen, their conservation is purely accidental in the SM. After EWSB, in the unitary gauge,

$$-\mathscr{L}_{\text{Yukawa}} \supset \frac{v}{\sqrt{2}} \left(\bar{u}_R^I \mathbf{Y}_U^{IJ} u_L^J + \bar{d}_R^I \mathbf{Y}_D^{IJ} d_L^J + \bar{e}_R^I \mathbf{Y}_E^{IJ} e_L^J + \text{h.c.} \right), \tag{2.60}$$

this will eventually lead to fermions-Higgs interactions and fermion mass terms. The Yukawa couplings can be brought to a diagonal form through singular value decompositions,

$$\frac{v}{\sqrt{2}} V_R^{u\dagger} \mathbf{Y}_u V_L^u = \mathbf{m}_u, \quad \frac{v}{\sqrt{2}} V_R^{d\dagger} \mathbf{Y}_d V_L^d = \mathbf{m}_d, \quad \frac{v}{\sqrt{2}} V_R^{e\dagger} \mathbf{Y}_e V_L^e = \mathbf{m}_e, \tag{2.61}$$

where $\mathbf{m}_{u,d,e}$ are diagonal matrices with real positive entries. Because of the $\mathrm{SU}(2)_L$ gauge symmetry, both up and down left-handed quarks should be rotated with the same matrix under a G_F transformation. Since V_L^u is generically different from V_L^d, both the up- and down-type quarks cannot be brought to their mass-eigenstates simultaneously at this level. Performing the following G_F rotation, and thereby fixing the G_F freedom,

$$g_Q = V_L^d, \quad g_U^\dagger = V_R^{u\dagger}, \quad g_D^\dagger = V_R^{d\dagger}, \quad g_L = V_L^e, \quad g_E^\dagger = V_R^{e\dagger}, \tag{2.62}$$

the Lagrangian is brought to the form,

$$-\mathscr{L}_{\text{Yukawa}} \supset \frac{v}{\sqrt{2}} \left(\bar{u}_R^I (\mathbf{m}_u V_L^{u\dagger} V_L^d)^{IJ} u_L^J + \bar{d}_R^I \mathbf{m}_d^{IJ} d_L^J + \bar{e}_R^I \mathbf{m}_e^{IJ} e_L^J + \text{h.c.} \right). \tag{2.63}$$

Defining the Cabibbo-Kobayashi-Maskawa (CKM) matrix [88, 89] as $V_{CKM} \equiv V_L^{u\dagger} V_L^d$, *i.e.*, parametrizing the flavor mismatch between left up- and down-type quarks, the Yukawa couplings can be written as

$$\frac{v}{\sqrt{2}} \mathbf{Y}_u = \mathbf{m}_u . V_{CKM}, \quad \frac{v}{\sqrt{2}} \mathbf{Y}_d = \mathbf{m}_d, \quad \frac{v}{\sqrt{2}} \mathbf{Y}_e = \mathbf{m}_e. \tag{2.64}$$

With this choice, the gauge and mass eigenstates for the d-type quarks and for the leptons coincide. Including a right-handed neutrino representation $N \sim (\mathbf{1}, \mathbf{1})_0$, a similar reasoning could be applied in the lepton sector, leading to the Pontecorvo-Maki-Nakagawa-Sakata (PMNS) matrix [90, 91].

The number of parameters of the quark sector with $N_f > 0$ flavors can be obtained as follows. The total number of real degrees of freedom is equal to the real dimension of the flavor group $U(N_f)_Q \times U(N_f)_U \times U(N_f)_D$, that is $3N_f^2$. Among them, $3N_f^2 - 1$ freedoms can be fixed to arbitrary values as the flavor group breaks down to $U(1)_\mathcal{B}$ once Yukawa couplings are introduced. The two Yukawa matrices contain $2 \times 2N_f^2$ real parameters, with $3N_f^2 - 1$ of them that can be fixed using the flavor freedom. There therefore remains $4N_f^2 - (3N_f^2 - 1) = N_f^2 + 1$ physical parameters, among which $2N_f$ are quark masses. The $N_{\mathrm{CKM}} \equiv (N_f - 1)^2$ remaining ones are thus the CKM parameters. In N_f dimensions, there are $C_{N_f}^2 = N_f(N_f - 1)/2$ Euler angles, *i.e.*, CKM mixing angles here. The remaining $N_{\mathrm{CKM}} - C_{N_f}^2 = (N_f - 1)(N_f - 2)/2$ parameters are phases, *i.e.*, explicit sources of CP-violation in the quark sector. Therefore, as well-known, the number of phases is non-zero only for $N_f \geq 3$ flavors.

In the SM, the CKM matrix is a 3×3 unitary matrix hence parametrized by 3 angles and a CP-violating phase,

$$\begin{aligned} V_{CKM} &\equiv \begin{pmatrix} V_{ud} & V_{us} & V_{ub} \\ V_{cd} & V_{cs} & V_{cb} \\ V_{td} & V_{ts} & V_{tb} \end{pmatrix} \\ &= \begin{pmatrix} c_{12}c_{13} & s_{12}c_{13} & s_{13}e^{-i\delta} \\ -s_{12}c_{23} - c_{12}s_{23}s_{13}e^{i\delta} & c_{12}c_{23} - s_{12}s_{23}s_{13}e^{i\delta} & s_{23}c_{13} \\ s_{12}s_{23} - c_{12}c_{23}s_{13}e^{i\delta} & -c_{12}s_{23} - s_{12}c_{23}s_{13}e^{i\delta} & c_{23}c_{13} \end{pmatrix}, \end{aligned} \tag{2.65}$$

where $s_{ij} = \sin\theta_{ij}$ and $c_{ij} = \cos\theta_{ij}$. In the Wolfenstein's parametrization [92]:

$$s_{12} = \lambda, \qquad s_{23} = A\lambda^2, \qquad s_{13}e^{i\delta} = \frac{A\lambda^3(\bar\rho + i\bar\eta)\sqrt{1 - A^2\lambda^4}}{\sqrt{1 - \lambda^2}[1 - A^2\lambda^4(\bar\rho + i\bar\eta)]} \tag{2.66}$$

where the best-fit central values are $A = 0.8227$, $\lambda = 0.22543$, $\bar\rho = 0.1504$ and $\bar\eta = 0.3540$ [93, 94]. The expansion of V_{CKM} at the order λ^2 is worth writing explicitly,

$$V_{CKM} = \begin{pmatrix} 1 - \frac{\lambda^2}{2} & \lambda & \mathcal{O}(\lambda^3) \\ -\lambda & 1 - \frac{\lambda^2}{2} & A\lambda^2 \\ \mathcal{O}(\lambda^3) & -A\lambda^2 & 1 \end{pmatrix} + \mathcal{O}(\lambda^4), \tag{2.67}$$

where the upper-left 2×2 block is recognized as an approximation to the Cabibbo matrix. While we experimentally observed that the CKM matrix is close to the unit matrix, *i.e.*, that λ is a good expansion parameter, we lack a fundamental explanation of the CKM parameters.
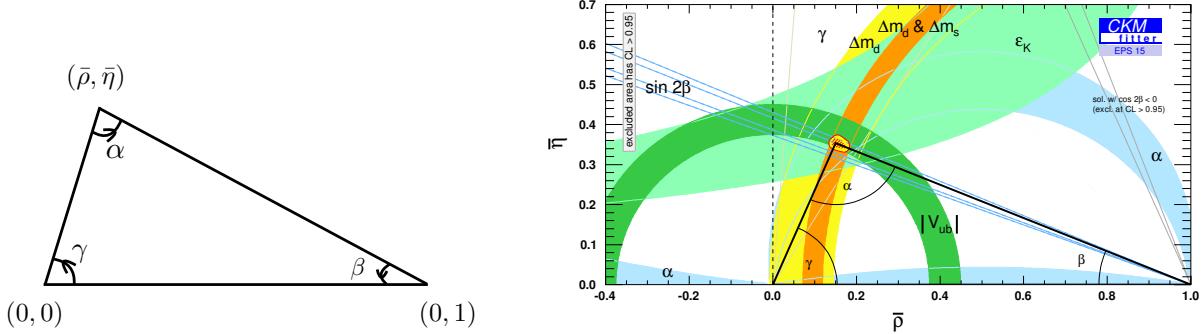
Figure 2.5: Left panel: Definition of the α, β, γ (also referred to as ϕ_1, ϕ_2, ϕ_3) angles and $(\bar{\rho}, \bar{\eta})$, adapted from [95]. Right panel: Experimental constraints in the $(\bar{\rho}, \bar{\eta})$ plane by the CKMfitter Collaboration [93].

2.4.2 A delicate system

Unitarity of the CKM matrix implies in particular, among five other such relations,

$$V_{ud}^* V_{ub} + V_{cd}^* V_{cb} + V_{td}^* V_{td} = 0. \tag{2.68}$$

In the complex plane, this relation can be represented as a closed triangle whose opening angles characterize the strength of CP-violation in the quark sector, all angles would indeed vanish for $\delta = 0$. It is conventional to normalize to unity one side of the triangle and define the three opening angles as

$$\alpha = \arg\left(-\frac{V_{td}V_{tb}^*}{V_{ud}V_{ub}^*}\right), \ \beta = \arg\left(-\frac{V_{cd}V_{cb}^*}{V_{td}V_{tb}^*}\right), \ \gamma = \arg\left(-\frac{V_{ud}V_{ub}^*}{V_{cd}V_{cb}^*}\right), \tag{2.69}$$

see left panel of Fig. 2.5. Large efforts have been dedicated to measure these triangles experimentally as they provide a unique handle on the flavor sector of the SM and its consistency. No deviation from the expected unitary behavior was ever observed, and the large number of experimental results used to constrain these parameters are all compatible and build together a perfectly consistent picture, see right panel of Fig. 2.5.

The areas of the 6 unitarity triangles are all identical and are equal to $|J|/2$ where J is the Jarlskog invariant [96],

$$J \sum_{m,n} \epsilon_{ikm} \epsilon_{jln} = \text{Im}\left[V_{ij}V_{kl}V_{il}^*V_{kj}^*\right] = c_{12}c_{23}c_{13}^2 s_{12}s_{23}s_{13}\sin\delta = A^2\lambda^6\bar{\eta}, \tag{2.70}$$

where no sum other than that on m, n is implied and i, k (j, l) label the three up-type (down-type) quark flavors. J controls the size of all CP-violating effects in the SM and is invariant under the phase redefinition $V_{CKM} \to D_\phi V_{CKM} D_\beta$ where $D_X \equiv \text{Diag}\left(e^{iX_1}, e^{iX_2}, e^{iX_3}\right)$ and $X_{1,2,3} \in [0, 2\pi]$. In the Wolfenstein's parametrization J is proportional to λ^6, this illustrates the smallness of CP-violating effects in the SM and attributes them mainly to the smallness of the 3 mixing angles rather than to the smallness of δ. CP-violation in the SM is thus deeply connected to flavor physics. In general, however, this does not have to be the case, this link is an accidental property of the SM. More precisely, the SM is CP-conserving if and only if $M_U M_D J = 0$, where,

$$M_U = (m_u^2 - m_c^2)(m_c^2 - m_t^2)(m_t^2 - m_u^2), \ M_D = (m_d^2 - m_s^2)(m_s^2 - m_b^2)(m_b^2 - m_d^2). \tag{2.71}$$
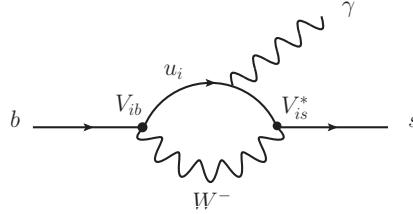
Figure 2.6: Contribution to $b \to s\gamma$ in the SM.

Indeed, were two quarks mass-degenerate, an extra-phase freedom would be present and the CP-violating phase δ could be rotated away from the CKM matrix.

The only observable effects of the CKM matrix reside in the charged $W^\pm$ currents, while the neutral Z, γ and g currents are flavor diagonal. Indeed, acting on a general quark representation (neglecting QCD interaction), the covariant derivative takes the form

$$D_\mu = \partial_\mu \mathbb{1} - i\frac{g}{\sqrt{2}} \left(\sigma^+ W_\mu^+ + \sigma^- W_\mu^-\right) - i\frac{g}{c_W}\left(\sigma^3 - Qs_W^2\right)Z_\mu - ieQA_\mu, \qquad (2.72)$$

where $\sigma^\pm = (\sigma^1 \pm i\sigma^2)/2$ and only the first and last term remain for the U and D $SU(2)_L$ singlet quark representations. Once $SU(2)_L$ is broken, a G_F transformation diagonalizing both quark mass matrices can actually be performed and terms mixing up- and down-type quarks acquire a CKM factor. The only term sensitive to the CKM matrix is thus

$$\overline{Q}i\slashed{D}Q \supset \frac{g}{\sqrt{2}}\left(\overline{u}_L\gamma^\mu d_L W_\mu^+ + \text{h.c.}\right) \xrightarrow{G_F} \frac{g}{\sqrt{2}}\left(\overline{u}_L V_{CKM}\gamma^\mu d_L W_\mu^+ + \text{h.c.}\right). \qquad (2.73)$$

Flavor-changing neutral currents are thus absent at tree-level in the SM. The g and γ mediated currents are flavor-conserving because of gauge symmetry, while the Z current is only accidentally flavor-conserving: quarks that have the same electric charge also happened to have the same $SU(2)_L$ charge before EWSB.

What about flavor changing neutral currents (FCNCs) at the one-loop level ? Such processes are certainly possible and they should involve two $\bar{u}_i d_j W^+$ vertices with $i \neq j$. Let us focus on $b \to s$ transitions for concreteness, see a diagram contributing to $b \to s\gamma$ in Fig. 2.6 for instance. Focusing on the W loop structure, the amplitude for this diagram is seen to be proportional to

$$\mathcal{M} \propto \sum_{i=u,c,t} V_{is}^* V_{ib} f(m_i/m_{W^\pm}), \qquad (2.74)$$

where $f(m_i/m_{W^\pm})$ is a Inami-Lim function [97]. At the first order in m_i, this function can be well approximated as

$$f(m_i/m_{W^\pm}) \simeq C_0 + C_1\frac{m_i^2}{m_{W^\pm}^2} + \dots \, . \qquad (2.75)$$

The constant term vanishes in the amplitude by virtue of the unitarity of the CKM matrix, while the first non-vanishing term is proportional to the fermion in the loop. The top quark is thus expected to dominate this diagram. While this function has an intuitive behavior in the heavy $m_{W^\pm} \to \infty$ limit, $i.e.$, the W boson decouples as expected, this is

not the case for the quarks. This is because for very large loop momentum, the equivalence theorem states that W behaves as its corresponding Goldstone boson, which couples to quarks proportionally to their mass, leading thus to a non-decoupling of heavy quarks. One also observes that if all quarks were mass-degenerate, the one-loop amplitude would vanish. This is the essence of the Glashow-Iliopoulos-Maiani (GIM) mechanism [98] which reflects the unitarity of the CKM matrix. Even though allowed, the SM one-loop FCNC are extremely suppressed due to their loop nature, the smallness of the off-diagonal CKM entries and the GIM mechanism. Chirality suppression, *i.e.*, Dirac mass insertion forced by angular-momentum conservation, may as well contribute to this suppression.

Processes with FCNCs therefore constitute a leading probe of physics beyond the SM. Indeed, new physics contributions may easily be several orders of magnitudes larger than the SM expectation. The $B_s \to \mu^+\mu^-$ process is particularly interesting in this respect, the SM prediction for the branching ratio is $\mathrm{BR}(B_s \to \mu^+\mu^-) = 3.65 \pm 0.23 \times 10^{-9}$ [99] making it a very rare decay subject to, *e.g.*, large SUSY corrections [100–102]. In 2014, the LHCb and CMS collaborations at CERN announced a joint analysis, describing their observation of $B_s \to \mu^+\mu^-$ with a significance of 6.2σ, with a branching ratio of $2.8^{+0.7}_{-0.6} \times 10^{-9}$ [103], in perfect agreement with the SM prediction. The flavor sector of the SM describes astonishingly well all experimental observations so far and successfully passed all precision tests ever designed.

Interpreting all these flavor measurements in an EFT approach, the new heavy degrees of freedom are integrated out at a scale Λ and the effects of new physics are parametrized through Wilson coefficients scaling operators of dimension 5 or more. Considering the contribution of an operator to a given flavor observable, fixing its Wilson coefficient to 1 and comparing with the actual measurement, generically gives a very strong constraint on the scale Λ, forced to lie several orders of magnitudes above the TeV scale in order to sufficiently suppress this new contribution [104–106]. This behavior is observed globally in the flavor sector and this leads to the so-called *flavor puzzle*. Alternatively, fixing Λ around the TeV scale requires very suppressed coefficients. In Section 6, we will introduce the idea of Minimal Flavor Violation that generically reconciles these flavor observations with TeV scale new physics.

2.5 SHORTCOMINGS OF THE STANDARD MODEL

Though incredibly successful, the SM has numerous shortcomings of esthetical, theoretical and observational nature. We already encountered several of them in our discussions so far.

The main esthetical issue is certainly the total arbitrariness of the particle content and gauge group of the theory. Although all known particles and their quantum numbers manage to explain with unrivaled precision the vast majority of all experimental observations ever performed, their origins are completely unknown. Could there be any reason why the low-energy theory describing nature is described by the field representations given in Table 1, with 3 flavor families ? These representations can appear automatically when considering representations of larger gauge groups such as SU(5) and SO(10). In particular, the **16** representation of SO(10) contains precisely a full generation of fermions as described in Table 1 with an additional right-handed neutrino. Whether such groups have anything to do with the real world can only be determined experimentally, but this striking

coincidence is certainly something to keep in mind. The question of the gauge group then comes, why does $SU(3)_c \times SU(2)_L \times U(1)_Y$ provide a good description of the microscopic interactions below the TeV scale ? As the SM should be seen as an EFT, a larger gauge group may be responsible for the fundamental interactions at larger energies. This leads to the question of grand-unified theories (GUTs), see *e.g.* [107] for a comprehensive introduction. There are, at least, two other reasons to be interested in GUTs at this level. The first one has to do with gauge anomalies cancellation. In the SM, they vanish for quite a troubling reason; the fermion electric charges are multiple of $1/(N_c = 3)$. Representations of larger gauge groups may naturally explain this cancellation; in $SU(5)$, the gauge anomalies vanish automatically when fermions in $\bar{\mathbf{5}}$ and $\mathbf{10}$ representations are present while in $SO(10)$ the $\mathbf{16}$ representation is non-anomalous on its own. The second reason has to do with the unification of gauge couplings at high energy. It is well known that evolving the SM gauge couplings towards high scales does not lead to the unification of the three couplings but still show a weak sign of convergence around 10^{13}–10^{16} GeV. A quasi-perfect meeting of the three gauge couplings at some scale would be a strong hint for the unification of the three SM forces above this scale.

A second source of problem is the apparent arbitrariness of the SM parameters. The SM cannot indeed predict the values of its parameters (9 fermion masses, 3 gauge couplings, 4 CKM parameters, 2 Higgs potential parameters + θ_{QCD} + possible neutrino masses and mixings). Naive naturalness arguments moreover do not hold, though one could expect all fermion masses to be of the order v, there is a strong hierarchy between the various Yukawa couplings. In this respect, only the top mass can be seen as natural, as $m_t \simeq v/\sqrt{2}$. As discussed previously, the CKM matrix elements and the CP-violating phase are as well not explained in the SM and have such a structure that they make it very challenging to extend the flavor sector beyond the SM without facing contradiction with the experimental measurements.

The accidental $\mathcal{B}$ and $\mathcal{L}$ conservations in the SM at tree-level are also interesting as they are actually broken because of electroweak non-perturbative effects [39]. Despite the existence of $\mathcal{B}$ and $\mathcal{L}$ violation in theories beyond the SM at the renormalizable level, no such process was ever observed experimentally (proton decay, neutrino-less double beta decay as a probe of the Majorana nature of the neutrino etc.). Strong constraints then arise on extended flavor sectors. Either the NP scale should be very high, which then leads to quantum instability of the electroweak scale as discussed below, or the NP flavor structure should have a very fine-tuned structure as in the SM. The latter possibility will be discussed in Section 6. The strong CP-problem, based on the non-observation of a neutron electric dipole moment is also of this nature.

Finally, if the SM is considered as an EFT, the electroweak scale should generically be of the order of the SM cut-off scale due to radiative corrections in the scalar sector not being protected by any symmetry. In the absence of new physics, the existence of gravitational interactions should still bring the electroweak scale towards the Planck scale $\sim 10^{18}$ GeV, while in nature it lies around 10^2 GeV. Naturalness here would predict new physics around the TeV scale in order to avoid a too large fine-tuning of the electroweak scale. The LHC is precisely probing this region at the moment. One of the leading contender for the TeV-scale new physics is certainly supersymmetry which, in the minimal viable realization,

solves the hierarchy problem assuming extra degrees-of-freedom at the TeV scale. Technically, the Higgs mass gets protected from a chiral symmetry. Null-results in the searches for supersymmetric phenomena at the LHC so far however increases this tension. Another class of models that generically solves this problem relies on well-known mechanisms of QCD. A new global strong sector is introduced that is spontaneously broken to a smaller group (that can be partially gauged to recover the SM gauge group), under which the observed Higgs would be a pseudo-Nambu-Goldstone boson (similar to the pions in QCD). A natural cut-off scale is then given by the (inverse) size of the composite states (similar to Λ_{QCD}) and the Higgs mass gets protected by an approximate shift-symmetry. Extra-dimension models with specific configurations can also solve the hierarchy problem. As of today, in April 2016, no discovery of TeV-scale new physics was made by the LHC or any other experiment.

So far, only esthetic imperfections have been considered. The SM has however also more "down-to-earth" problems of experimental nature, some observations can simply not be addressed within its framework. The first obvious one is the presence of gravity, neglected in the SM. A unified description of all fundamental forces, if such a theory actually exists, should unify both the QCD and electroweak with the gravitational interactions. Developments in this direction are conducted and the leading contender is certainly string theory (historically, its discovery had actually nothing to do with the unification of gravity and the SM, string theory originates from a lucky incident in the study of strong interactions). Neutrino oscillations are as well not explained in the SM as we constructed it. One could certainly just add right-handed neutrinos and construct a Dirac mass term for the neutrinos, but such particles have not been observed so far and the corresponding Yukawa couplings would be extremely small. The see-saw mechanisms could be a way to explain both of these problems [108].
Cosmological observations allow us to identify the various energy components present in our Universe [109]; $\sim 5\%$ of baryonic matter, $\sim 68\%$ of a substance acting as a repulsive gravitational force, the dark energy, and $\sim 27\%$ of dark matter. The last component may actually be given a massive particle interpretation. As such, it might be described within the context of a particle physics theory and since it has not been directly observed, it must be neutral under $U(1)_{em}$ and $SU(3)_c$. Though neutrinos can be dark matter candidates in the SM, their very small masses automatically make them a "hot dark matter" candidate, *i.e.*, in the early universe their kinetic energy was much larger than their mass. However, the growth of small-scale formations (such as galaxies) requires a large "cold dark matter" component, *i.e.*, a slow moving component that does not run away from the gravitational wells. As such, the SM neutrinos can only form a small fraction of the observed dark matter and new particles are needed to explain the observations (if dark matter really has a particle nature). Finally, an important aspect not explained by the SM is the observation of the baryon-antibaryon asymmetry in the Universe. Sakharov identified three conditions that should be fulfilled at the time of baryogenesis in order to generate such an asymmetry [110]. The first one is naturally that the baryon number $\mathcal{B}$ should not be conserved, *i.e.*, there must exist reactions of the type $X \rightarrow Y + B$ where X and Y do not carry baryon number while B does. In the SM, such transitions occur as briefly discussed in Section 1, they are non-perturbative solutions called sphalerons. Beyond the SM, explicit $\mathcal{B}$ violation

may be present at the renormalizable level, as is the case in GUTs because of gauge bosons coupling to quarks and leptons simultaneously or in supersymmetric theories. The second one is that the C and CP should not be exact symmetries. If C were an exact symmetry then $\overline{X} \to \overline{Y} + \overline{B}$ would happen at the same rate as the previous reaction and thus baryon number would globally be conserved. This is however still not enough since the $\mathcal{B}$-charged particles can be either left- or right-handed fermions for instance, CP needs to be violated as well. In the SM, CP is explicitly violated in the Yukawa sector, however the Jarlskog invariant that tunes all CP violating phenomena is too small to account for this asymmetry and new sources of CP-violation are needed. Finally, these transitions should happen out of the statistical equilibrium, as otherwise, both $X \to Y + B$ and $Y + B \to X$ would happen at the same rate, effectively washing away any baryon asymmetry. In the SM, during the electroweak phase transition such an out-of-equilibrium state could have been realized had the Higgs mass been smaller than 80 GeV [111].

While it is clear that any fundamental theory of particle physics should tackle these problems to their roots, in the majority of this manuscript we do not attempt to do so. In the next chapter we detail how to experimentally characterize the Higgs sector, while in the next part of this manuscript, we make detailed phenomenological studies of the 2HDMs. There, the 2HDMs are taken as an effective theory well suited to describe physics at the LHC and not as a new fundamental picture. All in all, most of this manuscript is part of a bottom-top strategy to refine our views of the EW sector.

CONSTRAINING THE HIGGS SECTOR EXPERIMENTALLY

The first phenomenological studies of the Higgs boson appeared in the mid-1970's, with [112] opening the way. The experimental challenge to find this particle seemed immense as the Higgs mass is not predicted by the theory, and thus, experiments could not know where and what to look for precisely. Most of the phenomenological analyses focused on the sub-GeV region at that time. Theoretical constraints on the mass, from triviality and stability bounds and unitarity arguments as discussed in the previous section, appeared a couple of years later but still only provided a wide range of possibilities. Experimentally, the strongest lower bound on the Higgs mass obtained during this period came from an angular analysis of the neutron-nucleus scattering, which led to $m_h \gtrsim 13$ MeV [113]. It is only in the late 1980's that the LEP collaborations considered Higgs searches as a major part of their physics objectives. Later completed with searches performed at the Tevatron experiments, they opened the way towards the full-fledged confirmation of the SM.

In the following, we discuss the observed properties of the Higgs boson, in both the pre- and post-LHC eras. An important characterization of the Higgs nature is provided by determining its couplings to itself (Higgs self-couplings) and to other particles. As the latter are uniquely predicted in the SM, all particles masses are indeed known, any observed deviation from these predictions would be a tell-tale sign of new physics. We present a formalism to describe these deviations and introduce the public code Lilith, a tool to constrain new physics from Higgs measurements. A global fit to the LHC measurements is then performed.

This chapter is partly based on the publications "*Lilith: a tool for constraining new physics from Higgs measurements*" [114] in collaboration with Béranger Dumont and published in European Journal of Physics C, and "*Status of Higgs couplings after run 1 of the LHC*" [115] in collaboration with Béranger Dumont and Sabine Kraml and published in Physical Review D. In the latter paper, we performed a global fit to the latest Higgs measurements as per Summer 2014, for the purpose of this manuscript, all results have been updated with the final Run 1 results (data from September 2015).

3.1 PRE-LHC CONSTRAINTS

3.1.1 *Higgs searches at LEP*

The first decisive searches for Higgs bosons are due to LEP, a e^+e^- collider operating at CERN from 1989 to 2000. The three main production modes of the Higgs boson at LEP are shown in Fig. 3.1. The direct $e^-e^+ \to h$ production mode is expected to have

a very low cross-section as the *hee* coupling is extremely suppressed in the SM. The left-most diagram, on-shell Z decay into $hf\bar{f}$, is the dominant production mode for a light Higgs boson, $m_h \lesssim m_Z$. The first run of LEP, at a center-of-mass-energy of $\sqrt{s} = m_Z$, allowed all four L3, ALEPH, DELPHI and OPAL collaborations to collect a data sample of around 1 million Z hadronic decays [116–119]. Due to the non-observation of a Higgs boson originating from $Z \to hf\bar{f}$ decays, lower bounds on the Higgs mass were derived, the stronger one being from DELPHI, with a 95% confidence level (CL) lower bound of 58.4 GeV [117] in 1993.
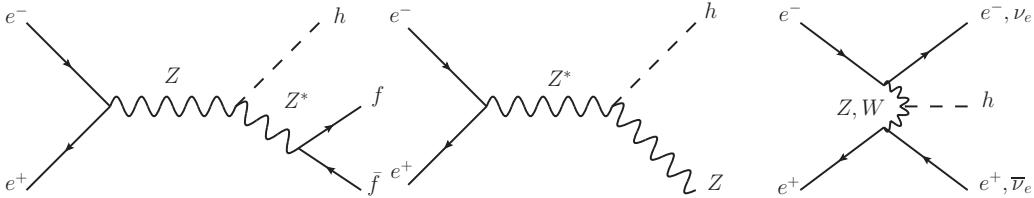
Figure 3.1: Higgs boson production at LEP.

Progressively, the LEP center-of-mass-energy was increased up to 207 GeV in 2000. For $m_h > m_Z$, the direct decay of a Z in h is kinematically forbidden and the Higgs-strahlung process, middle diagram of Fig. 3.1, dominates up to $m_h = \sqrt{s} - m_Z$. Above, the right-most diagram, production through weak boson fusion, should take over. Despite some tantalizing hints for a Higgs boson at a mass of around 114 GeV [120, 121], LEP collaborations could not confirm this result in their joint analysis [17] and the lack of evidence translated into a lower bound on the Higgs mass of 114.4 GeV at the 95% CL.

In parallel to the direct searches for the Higgs boson, the precise characterization of electroweak observables allowed to derive indirect constraints on the Higgs mass (and top mass). Radiative corrections to the $W^\pm$ and Z masses depend logarithmically on the Higgs mass [122] and quadratically on the top mass. Before the top discovery [123], m_t was inferred from such a fit. With the experimental determination of m_t, the Higgs mass indirect inference naturally became more accurate. Several low-energy and $Z, W^\pm$-pole observables are taken into account in the full fit; corrections to the Z decay widths, Z hadronic cross-section and various asymmetries $[\Gamma(Z \to f_L \bar{f}_L) - \Gamma(Z \to f_R \bar{f}_R)]/\Gamma(Z \to f\bar{f})$ in particular. Figure 3.2 shows the result of such a combined fit by the four LEP collaborations [19]. Precision electroweak observables clearly favor a light Higgs, very close to the lower bound coming from direct searches. See [124] for an update or [125, 126] for fits by the Gfitter collaboration before and after the Higgs discovery.

Although a new scalar particle could not be discovered, the LEP legacy is of great importance as it provides, in particular, strong direct constraints on the properties of light Higgs states; direct production of a light scalar state from a Z on/off-shell decay, possible $\phi_+ \phi_- Z$ coupling where $\phi_{+(-)}$ is a generic light CP-even (odd) state, $b\bar{b}\phi_{+,-}$ associated production, double and triple production of the light states, constraints on charged Higgs states and so on. They form a very rich set of constraints for the studies of extended Higgs sectors. In particular, we will use them in our phenomenological studies of the two-Higgs-doublet models presented in the second part of this manuscript.
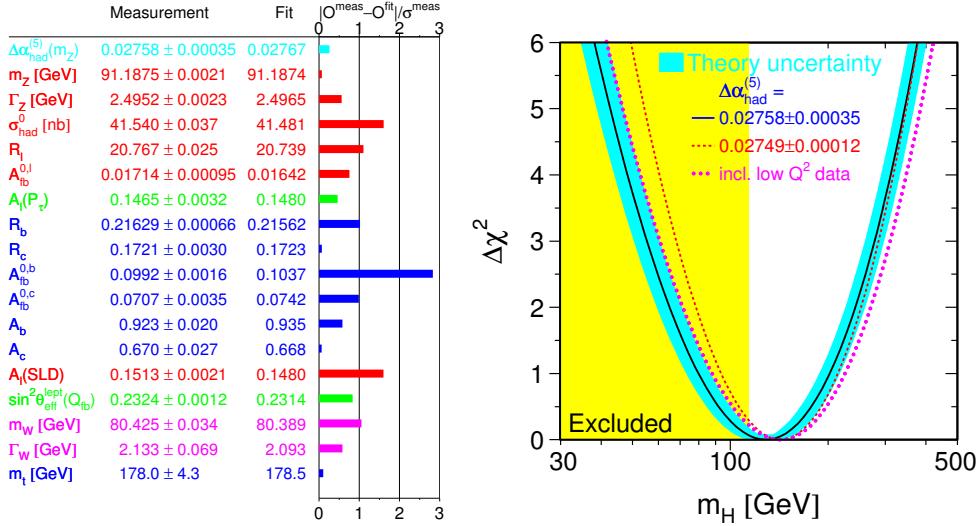
Figure 3.2: Left panel: Pulls from a global electroweak fit. For each observable, the corresponding bar quantifies the agreement between the experimental and the best-fit values. Right panel: Indirect contraint on the Higgs mass from the fit (solid black line + blue band) and the direct LEP searches (yellow region). From the LEP Electroweak Working Group [19].
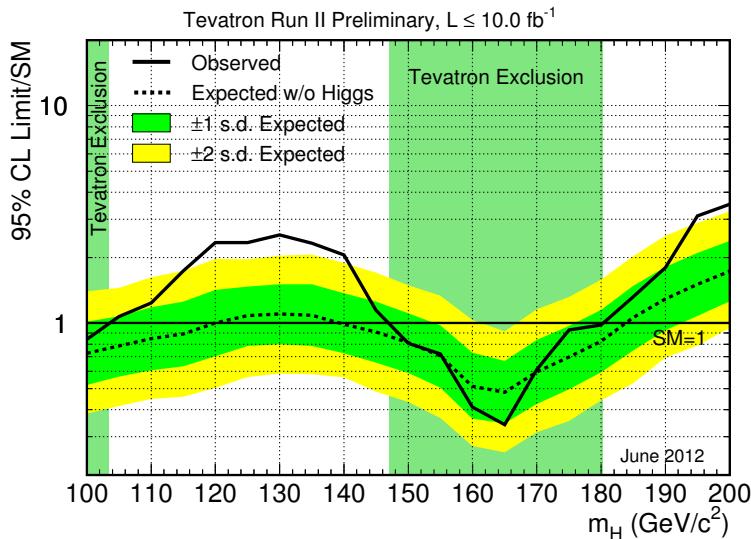
Figure 3.3: Higgs mass exclusion from the combined CDF and DØ analysis of July 2012 [18].

3.1.2 *Higgs searches at the Tevatron*

As discussed previously, the discovery of the top quark at the Tevatron was directly used to infer information on the Higgs boson mass from the electroweak fit. With a center-of-mass-energy of 1.96 TeV, the $p\bar{p}$ collider also actively searched for direct signs of a Higgs boson. Higgs production modes at the Tevatron are identical as at the LHC, the relative contributions of the different production modes are however different in $p\bar{p}$ and pp collisions, and we refrain from expliciting them from now and refer to the next section for more details. In July 2012, a joint analysis of the CDF and DØ results was performed

with different channels combined together to increase the sensitivity to a possible scalar state; $h \rightarrow b\bar{b}, W^+W^-, ZZ, \tau\tau$ and $\gamma\gamma$ [18]. A representative result of this analysis is presented in Fig. 3.3. A SM Higgs boson with a mass within the intervals $[100, 103]$ GeV and $[147, 180]$ GeV is excluded at the 95% CL. A broad excess of events is observed between 115 and 140 GeV, with the most significant local excess reaching locally 3σ (2.5σ globally) for $m_h = 120$ GeV, in agreement with the indirect LEP constraints. Disentangling the various contributions of this signal, it was found that $b\bar{b}$ is the dominant sub-contribution to this excess, however the statistical significance of the signal was not enough to claim a discovery.

3.2 CONSTRAINTS FROM THE LHC

Despite several decades of intense experimental efforts at LEP and Tevatron, the Higgs boson escaped detection up to 2012. While it probably would have taken large modifications of the LEP infrastructures to increase the center-of-mass-energy and discover the 125 GeV state, only time was lacking to the Tevatron. After some delay due to technical incidents, the LHC started colliding protons on November 2009 at a center-of-mass-energy of 0.9 TeV, the energy of each beam was then increasingly improved and reached 3.5 TeV per beam in March 2010. Both ATLAS and CMS collected approximatively 5 fb^{-1} of luminosity at $\sqrt{s} = 7$ TeV. In December 2011, the analysis of the full 7 TeV dataset by ATLAS [127] and CMS [128] showed a $\sim 3\sigma$ hint for a Higgs boson with a mass $m_h \approx 124$–126 GeV. Beginning of 2012, the LHC started colliding protons at $\sqrt{s} = 8$ TeV until the end of the year. The LHC collaborations could finally announce the discovery of a Higgs boson in July 2012 at a mass of 125–126 GeV [14, 15] and the precise characterization of its properties constituted the major efforts of the rest of the first run as we discuss in the following.

3.2.1 *Higgs production at the LHC*

In a hadronic collider, the SM Higgs boson has several production modes, depicted in the left-panel of Fig. 3.4. The corresponding cross sections are shown in the right-panel of Fig. 3.4 as a function of the center-of-mass-energy. Let us discuss them individually.

Gluon fusion (ggH)

Gluon fusion, $gg \rightarrow h$, was quite early identified as the leading production mode in hadronic colliders [129]. (Direct production from $q\bar{q} \rightarrow h$ is extremely suppressed as the heavy quark content of protons is very small and the coupling to light u, d quarks is somehow negligible for collider phenomenology.) Despite being a loop-induced process, and thus naively suppressed, this is the dominant Higgs production mode because of the large gg density in hadrons (which depends on the collision center-of-mass energy) and the large coupling of the Higgs to the top quark as discussed in Section 2.3.4. At the LHC, the gluon production accounts for $\sim 86\%$ of the total Higgs cross section (for $\sqrt{s} = 8, 13$ TeV).

As the dominant mode, it is crucial to know the SM prediction as accurately and precisely as possible in order to conduct precision measurements of the Higgs boson properties. In particular, loops of new colored particles may contribute to the ggH cross section or the
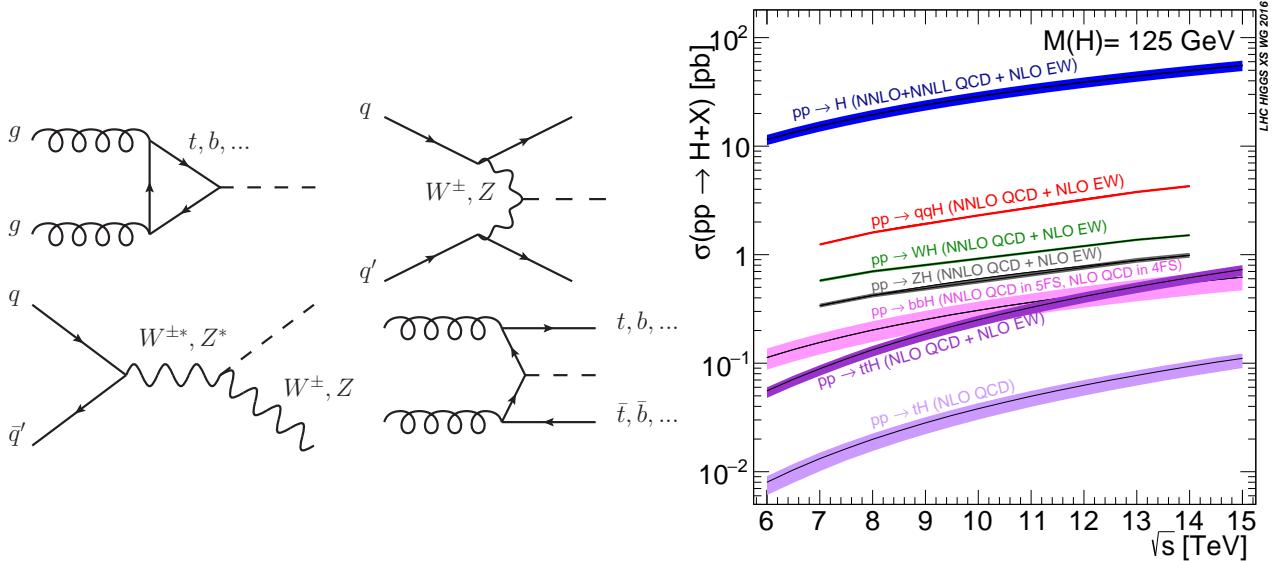
Figure 3.4: <u>Left panel:</u> SM Higgs boson production modes in a hadronic collider; from left to right and top to bottom: gluon-fusion (ggH), vector-boson-fusion (VBF), associated-production with a vector boson (WH, ZH collectively denoted as VH) and associated production with a pair of top or bottom quarks (ttH, bbH). <u>Right panel:</u> Corresponding cross-sections for $m_h = 125$ GeV as a function of the LHC center-of-mass-energy, from the LHC-HXSWG [75–77]. The bands represent the theoretical uncertainties coming from the QCD scale variation and parton distribution function + α_3 uncertainties.

couplings of the Higgs to heavy quarks may not be as predicted in the SM. The gluon fusion cross section is subject to very large QCD corrections, the next-to-leading-order (NLO) result enhances the born result by approximatively 70% but is subject to very large scale uncertainties [130, 131]. Next-to-NLO (NNLO) results were then obtained in the infinite [132, 133] and finite [134] top mass limits, they showed a good convergence of the perturbative series (enhancement of $\sim 15\%$ in cross section as compared to the NLO result) and reduced scale dependence. Regarding EW effects, NLO-EW corrections were obtained in Ref. [135] and showed a $\sim 5\%$ enhancement as compared to the QCD NNLO result. Three-loop mixed QCD-EW corrections were obtained in Ref. [136]. Finally, a large part of the last decade's efforts was focused on the QCD next-to-NNLO calculation which recently culminated with [137] in the infinite top mass limit and showed a quasi-flat variation with the renormalization scale; there remains a small ~ 2–3% residual scale uncertainty.

As contrary to the other production modes, in gluon fusion, the Higgs boson is produced alone and for $m_h = 125$ GeV it predominantly decays to $b\bar{b}$. Such a fully hadronic signal cannot be singled out of the very rich hadronic environment of the LHC. Considering initial state radiation or real QCD corrections to $gg \to h$ only worsens the situation. Therefore, only final states with photons or leptons can be observed if h is produced through gluon fusion. For the same reason, the large QCD background will make it difficult to observe $h \to c\bar{c}$, while lighter quarks are expected to be produced with an insufficient rate to be observed.

Vector boson fusion (VBF)

Vector boson fusion, $pp \to qq'h$, is the second production mode for a SM Higgs boson above ~ 85 GeV. For $m_h = 125$ GeV, the VBF mode amounts to $\sim 7\%$ of the total cross section. The VBF cross section is known up to the NNLO in QCD and NLO in EW corrections [138–141]. The scalar state is produced in association with two light forward quarks, *i.e.*, the two quarks propagate quite close to the beam lines, which upon hadronization form two forward jets. As such, a central jet veto is imposed in the experimental analyses in order to isolate the VBF mode from other production modes. Nevertheless, there exists a contamination from $gg \to h + 2j$ that cannot be entirely removed. The VBF production mode provides, together with the VH mode, a direct way to measure the Higgs coupling to massive electroweak gauge bosons. As discussed in Section 2.3, these couplings are an essential piece of the SM EWSB mechanism and are linked to custodial symmetry. Many BSM models predict modifications of these couplings, for instance in extended Higgs sectors the couplings might be shared among the several states contributing to EWSB, or custodial-violating models can change the ratio between the hW^+W^- and hZZ couplings.

Associated production with a massive vector boson or higgs-strahlung (WH+ZH=VH)

Associated production with a $W^\pm$ or Z [142] is an important mode to characterize the Higgs properties as discussed for VBF previously. The cross section is known up to NNLO in QCD and NLO in EW corrections [143–145]. The WH mode amounts to $\sim 60\%$ of the total VH cross section and thus dominates over the ZH mode because of the larger phase-space and the additional degrees of freedom.

Associated production with a pair of top or bottom quarks (ttH, bbH)

Associated production with a pair of top quarks [146–150] or bottom quarks [151–154] is a crucial production mode to characterize the Higgs boson as it provides a direct access to the $ht\bar{t}$ and $hb\bar{b}$ couplings (though the latter may also be probed in the $h \to b\bar{b}$ decay). As discussed in Section 2.3, the top Yukawa coupling plays a very special role in the stability of the Higgs potential and may be generically modified in BSM scenarios. The latter assertion is particularly true in the case of the bottom Yukawa coupling in supersymmetric models for instance, or more generally in Type II 2HDMs as will be discussed in Section 4.1, where it can be sizably increased as compared to the SM prediction. We note that for $m_h \approx 125$ GeV, the $h \to b\bar{b}$ partial width is the dominant one in the SM, BR($h \to b\bar{b}$) $\simeq 57\%$, a large modification of the $hb\bar{b}$ coupling could therefore have important consequences on all branching ratios to SM states. The ttH and bbH production modes are well differentiated from the VBF mode which only involves light quarks originating from the colliding hadrons. Also, for ttH, as the top quark decays before hadronization, there cannot be any confusion with the VBF topology.

To finish this discussion, we show in Table 2 the increase in cross section of the various production modes at the LHC 13 TeV as compared to 8 TeV. All σ_{13}/σ_8 ratios are quite close to 2, with the notable exception of the ttH production mode due to a lucky kinematical

Production mode	ggH	VBF	WZ	ZH	ttH	bbH	total cross section
σ_{13}/σ_8	2.27	2.36	1.96	2.10	3.82	2.41	2.27

Table 2: Ratio of the (central values of the) main SM Higgs production cross sections at the LHC 13 TeV as compared to the LHC 8 TeV for $m_h = 125.09$ GeV, from the LHC-HXSWG [75–77].
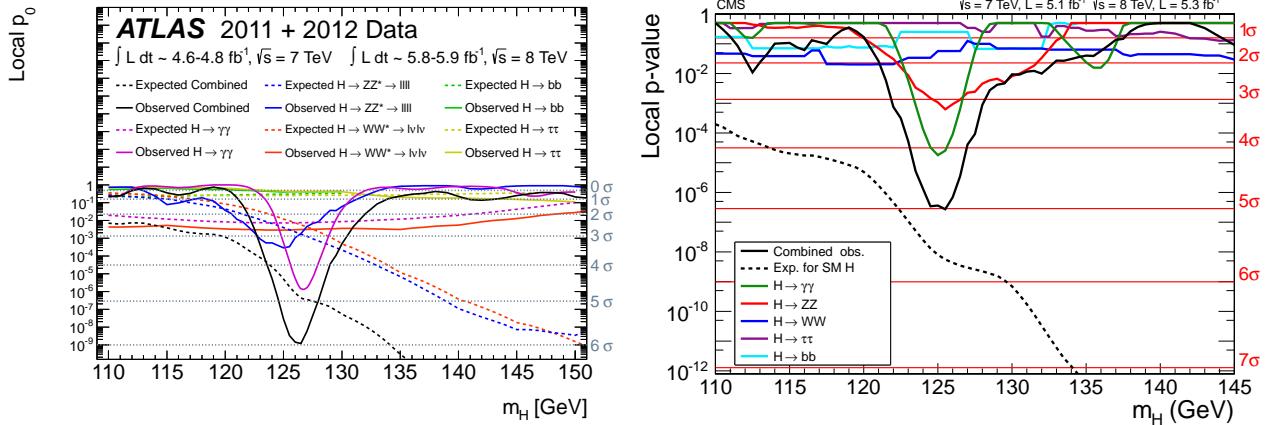
Figure 3.5: <u>Left panel:</u> Local p-value in the Higgs search of the ATLAS collaboration [14]. The individual contributions from the different channels $h \to \gamma\gamma, ZZ^*, WW^*, b\bar{b}, \tau\tau$ (color lines) and their combination (solid black line) are shown. <u>Right panel:</u> Same for the CMS collaboration [15].

effect which will allow the second run of the LHC to probe the top Yukawa coupling more precisely.

3.2.2 *A Higgs discovery*

The ATLAS collaboration, with 4.8 fb^{-1} of luminosity collected in 2011 at $\sqrt{s} = 7$ TeV and 5.8 fb^{-1} at $\sqrt{s} = 8$ TeV in 2012, and the CMS collaboration, with 5.1 fb^{-1} at $\sqrt{s} = 7$ TeV and 5.3 fb^{-1} at $\sqrt{s} = 8$ TeV, announced the discovery of a new scalar state in the search for a Higgs boson on July 4th, 2012 [14, 15]. The local significance of this discovery as a function of the Higgs mass is shown in Fig. 3.5. Both collaborations reported at least a 5σ excess at a similar mass around 125.5 GeV when combining all channels. Looking at the various contributions of the different channels included in these analyses, the $h \to \gamma\gamma$, and to a lesser extent $h \to ZZ^* \to 2\ell + 2\ell$ with $\ell = e, \mu$, are seen to drive this discovery. Though for a SM Higgs the corresponding branching ratios are quite small, 2.27×10^{-3} and $(2.74 \times 10^{-2}) \times (6.73 \times 10^{-2})^2 \simeq 1.24 \times 10^{-4}$ respectively, the corresponding signatures are very clean as they clearly stand out of the QCD background. The $h \to ZZ^* \to 4\ell$ signature is in particular referred to as the "golden-channel" due to the excellent reconstruction of the leptons properties in the ATLAS and CMS detectors. For this reason, these two channels also provide the most precise determination of the Higgs mass, as the decay products can be very well reconstructed. A combination of the 7 and 8 TeV datasets from the
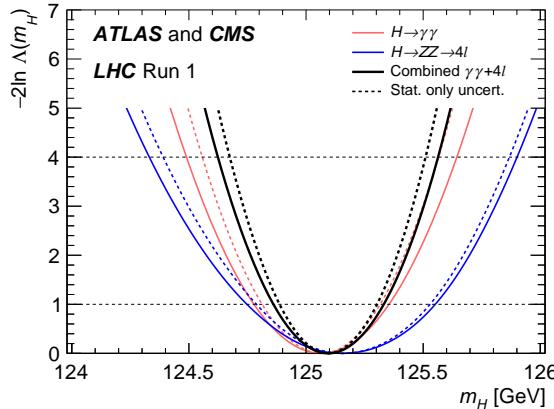
Figure 3.6: Higgs mass determination from a combination of the $h \to \gamma\gamma$ and $h \to ZZ^* \to 4\ell$ searches of ATLAS and CMS using the full Run 1 datasets [16]. The intersection of the solid black line and the dashed horizontal line at $-2\log\Lambda(m_h) = 1$ defines the 68% CL interval for the Higgs mass.

ATLAS and CMS collaboration lead to an impressive sub-percent determination of the Higgs mass, $m_h = 125.09 \pm 0.21\,(\text{stat}) \pm 0.11\,(\text{syst})$ GeV [16], see Fig. 3.6. Turning to the other channels, $h \to WW^* \to \ell\nu\ell\nu$ suffers from the neutrino missing energy that does not allow for a precise reconstruction of the Higgs mass, $h \to b\bar{b}$ is plagued by very large QCD backgrounds and $h \to \tau\tau$ suffers from both problems depending on the hadronic or leptonic nature of the τ decays.

3.2.3 Quantum numbers

Following the discovery, a precise exploration and determination of the Higgs quantum numbers were engaged. First, due to the Landau-Yang theorem [155, 156], the observed state cannot be a spin-1 particle as it decays to two photons. The spin-2 hypothesis is tested against the $J^P = 0^+$ by considering a general graviton-like resonance model. If CP is conserved, the goal is to determine the CP-eigenvalue of the observed state, if it is not, there could be a mixing between some CP-even and odd components that should be quantified [157, 158]. Experimental discrimination between various spin and parity hypotheses can be performed using angular distributions and correlations of the Higgs decay products and/or of the particles produced in association with the Higgs. The main handles being the Higgs decays into gauge bosons, $h \to WW^* \to \ell\nu\ell\nu$, $h \to ZZ^* \to 4\ell$ and $h \to \gamma\gamma$.

In order to discriminate the 0^- hypothesis from the 0^+, one can for instance use the various angles of the $ZZ^* \to 4\ell$ topology in the Higgs rest frame which are strongly sensitive to the parity composition of h and provide a direct constraint on the hVV vertex tensor structure. The invariant masses of the two lepton-pairs are also discriminating quantities. Moreover, the angular correlations between the two VBF and $gg + 2j$ jets provide a probe to the parity of the Higgs. Discrimination between 0^+ from 0^- may also be possible in the $h \to f\bar{f}$ decays, where CP-odd contributions to the $hf\bar{f}$ vertex can be generated at tree-level, while they necessarily are loop-suppressed in hZZ, hWW. Even if the 0^+ hypothesis is confirmed, a detailed study of the different hVV Higgs vertices is necessary in order to
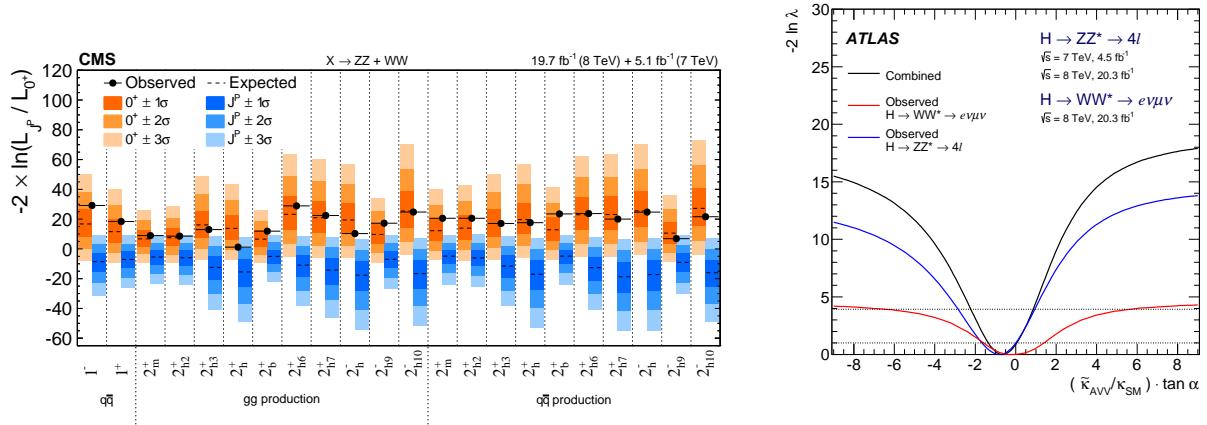
Figure 3.7: <u>Left panel:</u> Various spin-1 and spin-2 hypotheses tested against the SM 0^+ one, from a combination of the $h \to ZZ^*$ and $h \to WW^*$ channels in CMS [161]. <u>Right panel:</u> Constraint on a possible CP-mixing from a combination of the $h \to ZZ^*$ and $h \to WW^*$ channels in ATLAS [160].

test the SM tensor structure, 0^+ terms such as $hV_{\mu\nu}V^{\mu\nu}$ are indeed not present in the SM but might be in BSM scenarios. In $h \to \gamma\gamma$, the θ^* angle in the Collins-Soper frame [159] can be used to discriminate between various J^P hypotheses.

The ATLAS and CMS collaborations tested various spin and parity hypotheses using the full Run 1 dataset in Refs. [160] and [161] respectively, see Fig. 3.7. The left panel shows the CMS test-statistic $q_{J^P} = -2\ln(L_{J^P}/L_{0^+})$ for various J^P hypotheses. For each J^P, the orange (blue) bar shows the expected q_{J^P} distribution under the hypothesis that the observed particle is a 0^+ (J^P) state. The observed q_{J^P} is represented by the black dot for each J^P hypotheses and is seen to fall rather close to the central values of the orange bars. From that, the CMS collaboration is able to exclude any tested $J^P \neq 0^+$ hypothesis with more than a 99% CL. The right panel of Fig. 3.7 shows a constraint from the AT-LAS collaboration [160] on the mixing parameter $(\widetilde{\kappa}_{\mathrm{AVV}}/\kappa_{\mathrm{SM}})\tan\alpha$ that characterizes the mixing between a CP-even and odd component, defined through

$$
\begin{aligned}
\mathcal{L} \supset{} & \kappa_{\mathrm{SM}}\cos\alpha\left[\frac{1}{2}g_{hZZ}Z^\mu Z_\mu + g_{hWW}W^{+\mu}W^-_\mu\right]h \\
& -\frac{2\sin\alpha}{v}\left[\frac{1}{2}\widetilde{\kappa}_{AZZ}Z_{\mu\nu}\widetilde{Z}^{\mu\nu} + \widetilde{\kappa}_{AWW}W_{\mu\nu}\widetilde{W}^{\mu\nu}\right]h \, ,
\end{aligned}
\tag{3.1}
$$

where the SM case is recovered for $\alpha = 0$ or $\widetilde{\kappa}_{AVV} = 0$. The obtained 95% CL interval is $(\widetilde{\kappa}_{\mathrm{AVV}}/\kappa_{\mathrm{SM}})\tan\alpha \in [-2.18, 0.83]$ and is perfectly compatible with the vanishing SM value. As there is now little doubt that h is mostly a 0^+ state, these constraints on the CP admixture are becoming very relevant and may indirectly signal the presence of an additional state if a deviation from 0 is observed in the future.

3.2.4 *Production and decay rates*

The results of the Higgs searches at the LHC are given in terms of signal strengths, μ, which scale the number of signal events expected for the SM Higgs, n_s. For a given set of selection criteria, the expected number of events is therefore $\mu \cdot n_s + n_b$, where n_b is the

expected number of background events, so that $\mu = 0$ corresponds to the no-Higgs scenario and $\mu = 1$ to a SM-like Higgs. Equivalently, signal strengths can be expressed as

$$\mu = \frac{\sigma \times A \times \varepsilon}{[\sigma \times A \times \varepsilon]^{\text{SM}}}, \tag{3.2}$$

where $A \times \varepsilon$ is the product acceptance times efficiency of the selection criteria. Two assumptions can subsequently be made: first, the signal is a sum of processes that exist for a 125 GeV SM Higgs boson, *i.e.*, $\sigma = \sum_{X,Y} \sigma(X) \mathcal{B}(H \to Y)$ for the various production modes $X \in (\text{ggH}, \text{VBF}, \text{VH}, \text{ttH})$ and decay modes $Y \in (\gamma\gamma, ZZ^*, WW^*, b\bar{b}, \tau\tau, \ldots)$. Second, the acceptance times efficiency is identical to the SM one for all processes, that is $(A \times \varepsilon)_{X,Y} = [(A \times \varepsilon)_{X,Y}]^{\text{SM}}$ for every X and Y. These conditions require in particular that no new production mechanism (such as $pp \to A \to Zh$, where A is a CP-odd Higgs boson) exist and that the tensor structure of the couplings of the Higgs boson to SM particles is as in the SM.[6] Assuming moreover that the narrow-width-approximation holds, signal strengths read

$$\mu = \frac{\sum_{X,Y} (A \times \varepsilon)_{X,Y} \, \sigma(X) \mathcal{B}(h \to Y)}{\sum_{X,Y} (A \times \varepsilon)_{X,Y} \, \sigma^{\text{SM}}(X) \mathcal{B}^{\text{SM}}(h \to Y)} = \sum_{X,Y} \text{eff}_{X,Y} \frac{\sigma(X) \mathcal{B}(h \to Y)}{\sigma^{\text{SM}}(X) \mathcal{B}^{\text{SM}}(h \to Y)}, \tag{3.3}$$

where the $\text{eff}_{X,Y}$ are "reduced efficiencies", corresponding to the relative contribution of each combination for the production and decay of a Higgs boson to the signal. These can be estimated from the $A \times \varepsilon$ obtained in a Monte Carlo simulation of individual processes. In the case of an inclusive search targeting a given decay mode Y [*i.e.*, $\forall X, (A \times \varepsilon)_{X,Y} = (A \times \varepsilon)_Y$], eff_Y is equal to the ratio of SM cross sections, $\sigma_X^{\text{SM}}/(\sum_X \sigma_X^{\text{SM}})$.

Both the ATLAS and CMS collaborations have measured such quantities throughout the first run of the LHC [171, 172] in a wide variety of production and decay modes. Table 3 shows the various decay modes accessible to the LHC and their statistical significance if already observed. As the $\mu\mu$ and $Z\gamma$ have not been observed so far, the upper limit at the 95% CL on the corresponding rate is given.

Figure 3.8 shows a signal strength determination from a combination of the ATLAS and CMS run 1 datasets [188]. On the left-panel is shown the determination of the μ_X assuming that the partial widths of the observed state are as in the SM. All measurements are in perfect agreement with the SM predictions with the exception of the ttH production mode which shows a $\sim 2\sigma$ excess driven by the CMS measurement. Also shown is the total signal strength, defined assuming that all cross sections and partial widths are scaled universally by a factor μ. The combination results in $\mu = 1.09^{+0.11}_{-0.10}$ in agreement with the SM prediction. Note that assuming that the SM production and decay modes of the observed state are fixed to their SM values, this measurement puts a direct constraint on additional production and/or decay modes. On the right-panel are shown the signal strengths obtained assuming that all production cross sections of the observed state are as in the SM. No deviation from the SM expectations is observed, with all measurements in agreement at the $\sim 1\sigma$ level.

---

6 More general constraints on the Higgs properties can be obtained through the use of EFTs [162, 163], pseudo-observables [164, 165] or, truly model-independently, through fiducial cross section measurements [166–170].

| Channel | Statistical significance [σ] | |
	ATLAS	CMS
$\gamma\gamma$	5.0 [173]	5.6 [174]
$ZZ^* \to 4\ell$	6.6 [175]	7.0 [176]
WW	6.8 [177, 178]	4.8 [179]
$\tau\tau$	4.4 [180]	3.4 [181]
$b\bar{b}$	1.7 [182]	2.0 [183]
$\mu\mu$	$\sigma(h \to \mu\mu) < 7.0\times$SM [184]	$\sigma(h \to \mu\mu) < 7.4\times$SM [185]
$Z\gamma$	$\sigma(h \to Z\gamma) < 11\times$SM [186]	$\sigma(h \to Z\gamma) < 9.5\times$SM [187]

Table 3: Higgs observed decay modes and their statistical significance. The $\mu\mu$ and $Z\gamma$ modes have not been observed so far, the upper limit at the 95% CL on the corresponding rate is given instead. Adapted from [188].

The quantities presented in Fig. 3.8 are obtained by making a strong hypothesis on either the production or decay of the observed state. As such, they are not completely useful to derive significant constraints on the Higgs properties. As will be discussed in details in the next section, signal strengths for given production times decay modes are also measured. They provide very valuable information on the Higgs properties as the allow to lift the degeneracies that the simple production or decay signal strengths lead to if used in a global fit.

3.3 LILITH: CONSTRAINING NEW PHYSICS FROM HIGGS MEASUREMENTS

Precision measurements of the properties of the observed Higgs state are of utmost importance to assess its role in the breaking of the electroweak symmetry. They could reveal a more complicated Higgs sector, indicating the presence of more elementary scalars or compositeness of the observed particle, and could also shed light on a large variety of new particles that couple to the Higgs boson. Conversely, precision measurements can be used to rule out new physics scenarios affecting the properties of the Higgs boson.

That the mass of the observed Higgs boson is about 125 GeV is a very fortunate coincidence as many decay modes of the SM Higgs boson are accessible with a modest integrated luminosity at the LHC [77], see also Fig. 2.4. Hence, complementary information on the properties of the Higgs boson was already obtained from the measurements performed during Run 1 of the LHC at 7–8 TeV center-of-mass energy [171, 172]. A large variety of models of new physics (both effective and explicit ones) can be constrained from the measurements presented in terms of signal strengths. These results were used in a large number of phenomenological studies in the past three years (see Refs. [115, 189–214] for a sample of studies based on the full data collected at Run 1 up to January 2015).

It is however not straightforward to put constraints on new physics from the measured signal strengths. Indeed, a large number of analyses have already been performed by the ATLAS and CMS collaborations and they usually include several event categories, and
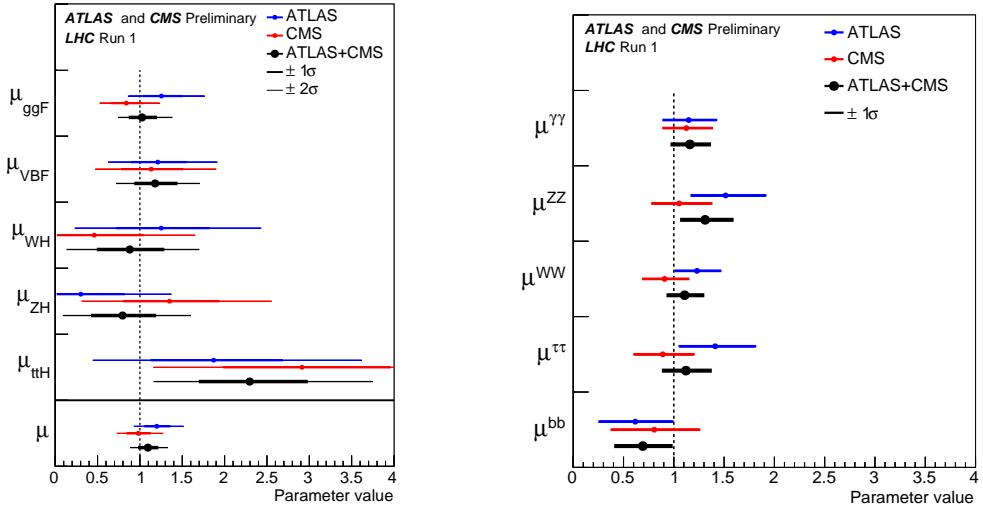
Figure 3.8: Signal strengths from a combination of the ATLAS and CMS datasets [188]. Left panel: Signal strengths for the different production modes assuming that all Higgs decays are as in the SM. Also shown is the total signal strength μ determined assuming that all production modes and decay modes are altered by a single scaling factor. Right panel: Signal strengths for the different decay modes assuming that all production cross sections are as in the SM.

present signal strength results in different ways. Extracting all necessary information from the figures of the various publications is a quite tedious and lengthy task. Moreover, as the full statistical models used by the experimental collaborations are not public, a number of assumptions need to be made for constructing a likelihood. The validity of these approximations should be assessed from a comparison with the results provided by ATLAS and CMS.

In order to put constraints on new physics from the LHC Higgs results, many groups have been developing private codes, and a public tool, `HiggsSignals` [215], became available in May 2013. `HiggsSignals` is a `FORTRAN` code that uses the signal strengths for individual measurements, taking into account the associated efficiencies. In this section, we present the public tool `Lilith`.[7] It follows a different approach than `HiggsSignals` in that it uses as primary input results in which the fundamental production and decay modes are unfolded from experimental categories. This method was first introduced and used in Refs. [216, 217]. `Lilith` is a library written in `Python`, that can easily be used in any `Python` script as well as in `C` and `C++`/`ROOT` codes, and for which a command-line interface is also provided. The experimental results are stored in `XML` files, forming a database, which are easy to modify and extend. The user input can be given in terms of reduced couplings or signal strengths for one or multiple Higgs states, and is also specified in an `XML` format. Given the experimental database, a global likelihood is constructed and then evaluated at the user input. Using this quantity, constraints on the Higgs sector of various scenarios can be obtained.

---

7 Lilith not only refers to a mythological female demon, it incidentally also stands for "light likelihood fit for the Higgs".

In Section 3.3.1, we present the signal strength framework used to encode deviations from the SM at the LHC, as well as the experimental results that we use as input in `Lilith`. The parametrization of new physics effects on the observed Higgs boson, as well as the derivation of signal strengths, are presented in Section 3.3.2. Some practical details on how to use `Lilith` and the various `XML` formats defined are then given in Section 3.3.3. Constraints derived from `Lilith` are validated in Section 3.3.4, and two concrete examples of its capabilities are given in Section 3.3.5. Finally, prospects for Run 2 of the LHC are discussed in Section 3.3.6.

3.3.1 *From experimental results to likelihood functions*

3.3.1.1 *Signal strength measurements*

Thanks to the excellent operation of the LHC and to the wealth of accessible final states for a 125 GeV SM-like Higgs boson, the properties of the observed Higgs boson have been measured with unforeseeable precision by the ATLAS and CMS collaborations already during the Run 1 of the LHC at 7–8 TeV center-of-mass energy [171, 172]. LHC searches are targeting the different combinations of production and decay modes of a Higgs boson. The SM Higgs boson has several production mechanisms at a hadron collider, see Section 3.2.1: gluon fusion, vector-boson fusion, associated production with an electroweak gauge boson ($W^{\pm}$ or Z) and associated production with a pair of top quarks.[8] Observation of these production modes constrains the couplings of the Higgs to vector bosons and to third-generation quarks (ggH, ttH). The main decay modes accessible at the LHC are $h \to \gamma\gamma$, $h \to ZZ^* \to 4\ell$, $h \to WW^* \to 2\ell2\nu$, $h \to b\bar{b}$ and $h \to \tau\tau$ (with $\ell \equiv e, \mu$). They can provide complementary information on the couplings of the Higgs to vector bosons (from the decay into ZZ^*, WW^*, and $\gamma\gamma$) and to third-generation fermions (from the decay into $b\bar{b}$, $\tau\tau$, and $\gamma\gamma$). Being loop-induced processes, $gg \to h$ and $h \to \gamma\gamma$ also have sensitivity to BSM colored particles and BSM electrically-charged particles, respectively.

The signal strength framework used by the ATLAS and CMS collaborations is based on the general form of Eq. (3.3), hence on the assumption that new physics only results in a modification of the production and decay rates of the observed state as compared to the SM Higgs. This makes it possible to combine the information from various Higgs searches and assess the compatibility of given scalings of SM production and/or decay processes from a global fit to the Higgs data. This framework is very powerful as it can be used to constrain a wide variety of new physics models (some examples can be found in Ref. [218]). This is the approach that we will follow with `Lilith`. However, in order to derive constraints on new physics, one first needs to construct a likelihood function from the signal strength information given in the experimental publications. In particular, combining the results from several Higgs searches is non-trivial and deserves scrutiny.

3.3.1.2 *Event categories versus unfolded production and decay modes*

The searches for the Higgs boson performed by the ATLAS and CMS collaborations are divided into individual analyses usually focusing on a single decay mode. Within each

---

8 Current searches do not constrain the associated production with a pair of bottom quarks, whose SM cross section is small and which is plagued with the very large QCD background.
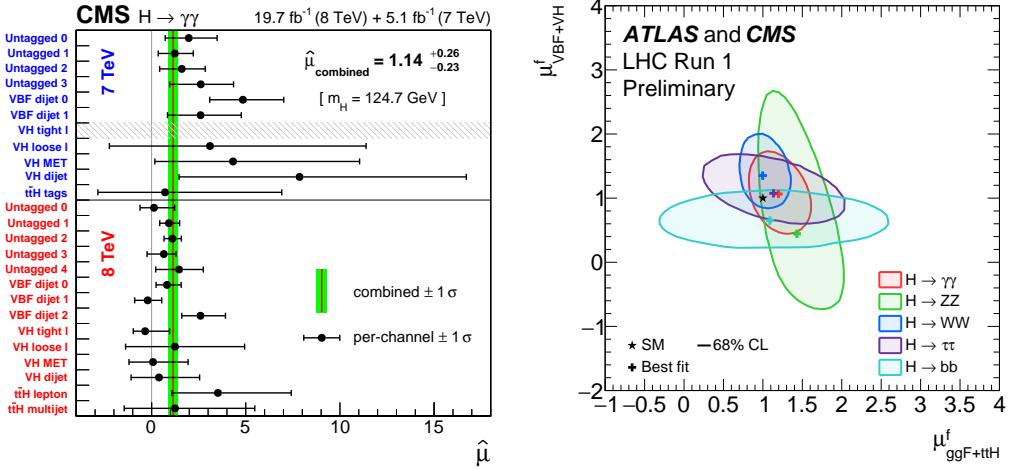
Figure 3.9: Signal strength measurements by the ATLAS and CMS collaborations. Left panel: results of the CMS search $h \to \gamma\gamma$ [174] category per category. Right panel: 2-dimensional ATLAS and CMS results in which the fundamental production modes are unfolded from experimental categories, in the plane $(\mu(\text{ggH} + \text{ttH}, Y), \mu(\text{VBF} + \text{VH}, Y))$ for $Y \in (\gamma\gamma, ZZ^*, WW^*, \tau\tau, b\bar{b})$ [188].

analysis several event categories are then considered. They are in particular designed to optimize the sensitivity to the different production mechanisms of the SM Higgs boson (hence, they are characterized with different reduced efficiencies $\text{eff}_{X,Y}$). In order to put constraints on new physics from the results in a given event category, one needs to extract the measurement of the signal strength and the relevant $\text{eff}_{X,Y}$ information from the experimental publication. For example, results of the CMS $h \to \gamma\gamma$ analysis [174], in terms of signal strengths for all categories, are shown in the left panel of Fig. 3.9. With the addition of the reduced efficiencies $\text{eff}_{X,\gamma\gamma}$, also given in Ref. [174], combinations of $\sigma(X)\mathcal{B}(h \to \gamma\gamma)$ can be constrained.

However, several problems arise when constructing a likelihood. First of all, as can be seen on the left panel of Fig. 3.9, only two pieces of information are given: the best fit to the data, that will be denoted as $\hat{\mu}$ in the following, and the 68% CL interval or 1σ interval. The full likelihood function category per category is never provided by the experimental collaborations. Assuming that the measurements are approximately Gaussian, it is however possible to reconstruct a simple likelihood, $L(\mu)$, from this information. In that case, $-2\log L(\mu)$ follows a χ^2 law. From the boundaries of the 68% CL interval, left and right uncertainties at 68% CL, $\Delta\mu^-$ and $\Delta\mu^+$, with respect to the best fit point can be derived. The likelihood can then be defined as

$$
-2\log L(\mu) = \begin{cases} \left(\frac{\mu-\hat{\mu}}{\Delta\mu^-}\right)^2 & \text{if } \mu < \hat{\mu}\,, \\[2em] \left(\frac{\mu-\hat{\mu}}{\Delta\mu^+}\right)^2 & \text{if } \mu > \hat{\mu}\,, \end{cases} \tag{3.4}
$$

with $\Delta\mu^- = \Delta\mu^+$ in the Gaussian regime. While this is often a valid approximation to the likelihood, it should be pointed out that signal strength measurements are not necessarily Gaussian, depending in particular on the size of the event sample. For $h \to ZZ^* \to 4\ell$ in

particular, the small cross section and the split in different categories may lead to important distortions from the Gaussian regime.

Barring this limitation, Eq. (3.4) can be used to constrain new physics. However, it requires that at least the 68% CL interval and the relevant reduced efficiencies $\text{eff}_{X,Y}$ are provided by the experimental collaboration for every individual category. This is very often, but not always, the case. Categories are sometimes defined without giving the corresponding signal efficiencies (as in, *e.g.*, the CMS ttH analysis [219]), and/or the result is given for a (set of) combined signal strength(s) but not in terms of signal strengths category per category (as in the ATLAS ZZ^* and $\tau\tau$ analyses [175, 180]). Such combined μ should in general not be used because they have been obtained under the assumption of SM-like production or decay of the Higgs boson as discussed earlier for the results shown in Fig. 3.8. Whenever the $\text{eff}_{X,Y}$ are not given in the experimental publications it is in principle possible to obtain estimates from a reproduction of the selection criteria applied on signal samples generated by Monte Carlo simulation. However, this turns out to be a very difficult or impossible task. Indeed, searches for the Higgs boson typically rely on complex search strategies, such as multivariate analysis techniques that are impossible to reproduce in practice with the information publicly available. Whenever the information on reduced efficiencies is not available, we are left to a guesswork, with a natural default choice being that eff_X is equal to the ratio of SM cross sections, $\sigma_X^{\text{SM}}/(\sum_X \sigma_X^{\text{SM}})$, which would correspond to a fully inclusive search.

Constraining new physics from a single search category can already be a non-trivial task and come with some uncertainty. However, more severe complications typically arise when using several categories/searches at the same time, as is needed for a global fit to the Higgs data. The simplest solution is to define the full likelihood as the product of individual likelihoods,

$$L(\boldsymbol{\mu}) = \prod_{i=1}^{n} L(\mu_i) \quad \Rightarrow \quad -2\log L(\boldsymbol{\mu}) = \sum_{i=1}^{n} -2\log L(\mu_i) = \sum_{i=1}^{n} \left(\frac{\mu_i - \hat{\mu}_i}{\Delta\mu_i}\right)^2 , \quad (3.5)$$

which assumes that all measurements are completely independent. We know that this is not the case as the various individual measurements may share common systematic uncertainties. They are two sorts of them: the shared experimental uncertainties, coming from the presence of the same final state objects and from the estimation of the luminosity, and the shared theoretical uncertainties, dominated by the contributions from identical production and/or decay modes to the expected Higgs signal in different categories [220]. The estimation of the experimental uncertainties in ATLAS should be largely independent of the one in CMS, hence these correlations can be treated separately for measurements performed by one collaboration or the other. Conversely, theoretical uncertainties are estimated in the same way in ATLAS and CMS and should be correlated between all measurements.

In the case where all measurements are well within the Gaussian regime, it is possible to take these correlations into account in a simple way, defining the likelihood as

$$-2\log L(\boldsymbol{\mu}) = \chi^2(\boldsymbol{\mu}) = (\boldsymbol{\mu} - \hat{\boldsymbol{\mu}})^T C^{-1} (\boldsymbol{\mu} - \hat{\boldsymbol{\mu}}) , \quad (3.6)$$

where C^{-1} is the inverse of the $n \times n$ covariance matrix, with $C_{ij} = \text{cov}[\hat{\mu}_i, \hat{\mu}_j]$ (leading to $C_{ii} = \sigma_i^2$). However, the off-diagonal elements of this matrix are not given by the experimental collaborations and are very difficult to estimate from outside the collaboration. This

simple and compact expression for the likelihood is naturally only valid under the Gaussian approximation; beyond that, the expression and the communication of the likelihood by the experimental collaborations become more complicated.

An alternative way of constraining new physics from the experimental results is to consider results in which the fundamental production and decay modes are unfolded from experimental categories. These so-called "signal strengths in the theory plane" are defined as

$$\mu(X, Y) \equiv \frac{\sigma(X)\,\mathcal{B}(h \to Y)}{\sigma^{\mathrm{SM}}(X)\,\mathcal{B}^{\mathrm{SM}}(h \to Y)}\,, \tag{3.7}$$

where as before X labels the production mode and Y the decay mode of the Higgs boson. These quantities can be estimated from a fit to the results in several event categories; as the $\mathrm{eff}_{X,Y}$ will differ from measurement to measurement, complementary information on various (X, Y) couples can be obtained and break possible degeneracies. The resulting signal strengths are then directly comparable to the predictions of a given new physics model.

It has become a common practice of the ATLAS and CMS collaborations to present such results in 2-dimensional likelihood planes for every decay mode. In that case, the five production modes of the SM Higgs boson are usually combined to form just two effective X modes, VBF + VH and ggH + ttH. The likelihood is then shown in the $(\mu(\mathrm{ggH + ttH}, Y), \mu(\mathrm{VBF + VH}, Y))$ plane. The combined ATLAS and CMS results in this 2-dimensional plane for $Y \in (\gamma\gamma,\, ZZ^*,\, WW^*,\, \tau\tau)$, as given in Ref. [188], are shown in the right panel of Fig. 3.9. The solid contours delineate the 68% CL allowed regions. As the unfolding of the individual measurements is done by the experimental collaborations themselves, all correlations between systematic uncertainties (both experimental and theoretical) are taken into account for a given decay mode Y, and are encompassed in the correlation between $\mu(\mathrm{ggH + ttH}, Y)$ and $\mu(\mathrm{VBF + VH}, Y)$. (Other 2-dimensional planes can be relevant, depending on the sensitivity of the searches, for instance $(\mu(\mathrm{WH}, Y), \mu(\mathrm{ZH}, Y))$ for $Y = b\bar{b}$.) This is a very significant improvement over the naive combination of categories of Eq. (3.5), in which all measurements are assumed to be independent. Moreover, in this approach, no approximation needs to be made because of missing information on the signal efficiencies or signal strengths category per category. This is why we chose to use the results in terms of signal strengths in the theory plane as the primary experimental inputs of Lilith.

A remark is in order regarding the grouping of the five production modes into just two. First of all, grouping together VBF, WH and ZH is unproblematic for testing the vast majority of the new physics models because custodial symmetry requires that the couplings of the Higgs to W and Z bosons scale in the same way. Probing models that violate custodial symmetry based on this input and on the inclusive breaking into the individual production modes VBF, WH, and ZH, may lead to results that deviate significantly from the ones using the full likelihood. This will be discussed and illustrated in Eq. (3.19) and Section 3.3.4.2. The combination of the ggH and ttH production modes is more problematic at first sight. While gluon fusion is dominated by the top-quark contribution in the SM, this can be modified drastically if BSM colored particles are present. However, for all decay modes except $h \to b\bar{b}$ (where gluon fusion-initiated production of the Higgs is not accessible), the ttH production mode is currently constrained with much poorer precision

than ggH because of its small cross section (being 150 times smaller than ggH at $\sqrt{s} = 8$ TeV [77]). Therefore, with the current data it is justified to take $\mu(\text{ggH} + \text{ttH}, Y) = \mu(\text{ggH}, Y)$ for all channels except $h \to b\bar{b}$, and $\mu(\text{ggH} + \text{ttH}, b\bar{b}) = \mu(\text{ttH}, b\bar{b})$ as discussed previously.[9]

Finally, note that all results given in terms of signal strengths are derived assuming the current theoretical uncertainties in the SM predictions. Hence, constraining a scenario with different (usually larger) uncertainties from a fit to the signal strength measurements is a delicate task. This issue will also be discussed, alongside with a possible solution, in Section 3.3.6.

3.3.1.3 *Statistical procedure*

We use signal strengths for pure production and decay modes as basic ingredients for the construction of the Higgs likelihood in `Lilith`. However, the full likelihood in the $\mu(X, Y)$ basis is not accessible as only 1- and 2-dimensional (1D and 2D) results are provided by the experimental collaborations; therefore some of the correlations are necessarily missing. In the currently available 1D and 2D results, the full likelihood is provided in some cases in addition to contours of constant likelihood. This is extremely helpful since the communication of the results between the collaboration and the readers does not cause any loss of information. Two examples from the CMS collaboration are given in Fig. 3.10. The 1D likelihood as a function of $\mu(\text{VH}, b\bar{b})$ [221] is shown in the left panel.[10] On the right panel, the full likelihood in the 2D plane $(\mu(\text{ggH} + \text{ttH}, \gamma\gamma), \mu(\text{VBF} + \text{VH}, \gamma\gamma))$ [174] is shown as a "temperature plot". Moreover, we note that likelihood grids have been provided by ATLAS in a numerical format on the 2D plane $(\mu(\text{ggH} + \text{ttH}, Y), \mu(\text{VBF} + \text{VH}, Y))$ for $Y \in (\gamma\gamma, ZZ^*, WW^*)$ [222–224].

Any result given in terms of signal strengths can be used in `Lilith`. Whenever available, we take into account the full likelihood information. The provision of numerical grids for the di-boson final states by the ATLAS collaboration was an important step forward in the communication of the likelihood. Unfortunately, they were derived with previous versions of the analyses, and the same information has not been systematically given for the corresponding final Run 1 results [173, 175, 177]. Moreover, in the CMS $h \to \gamma\gamma$ result shown in the right panel of Fig. 3.10, the Higgs boson mass has been profiled over instead of being fixed to a given value, making the interpretation of the result very difficult. Limitations of the current way of presenting signal strength results, as well as possible improvements, will be discussed in Section 3.3.6, see also [225].

If only contours of constant likelihood (the 68% CL interval in 1D, 68% and 95% CL contours in 2D) are present, assumptions about the shape of the likelihood have to be made in order to reconstruct it in the full plane. The 1D case was already discussed above and resulted in the likelihood of Eq. (3.4). In the 2D case, a natural choice is to use a

---

9 Constraints on the ttH production mode for decay modes other than $b\bar{b}$ are taken into account independently in `Lilith`, see Table 4.

10 Note that 2D results in the plane $(\mu(\text{WH}, b\bar{b}), \mu(\text{ZH}, b\bar{b}))$ also exist for this analysis [183]. Both results are present in the database of `Lilith`.
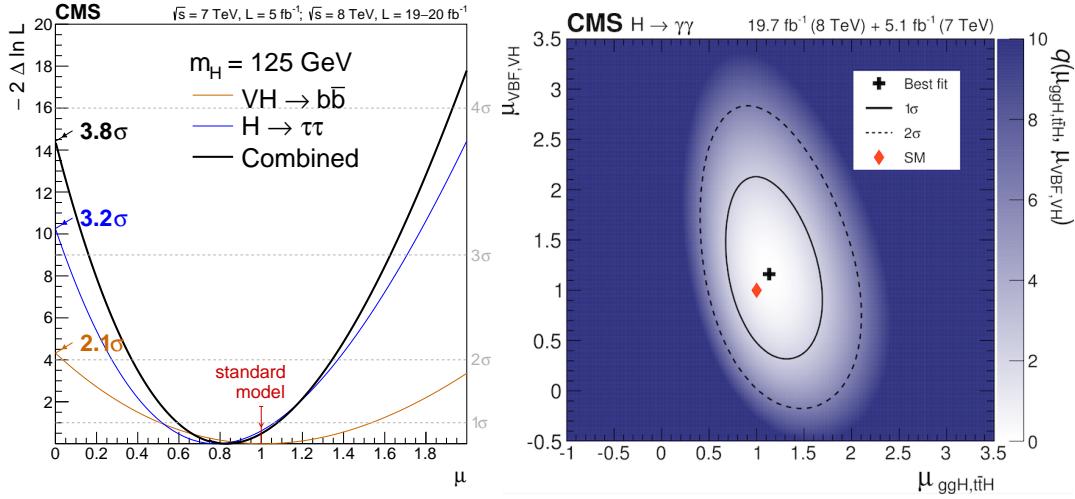
Figure 3.10: Signal strength results from the CMS collaboration. Left panel: 1D likelihood for the $X = \mathrm{VH}$, $Y = b\bar{b}$ channel (red curve) [221]. Right panel: 2D temperature plot in the $(\mu(\mathrm{ggH} + \mathrm{ttH}, \gamma\gamma), \mu(\mathrm{VBF} + \mathrm{VH}, \gamma\gamma))$ [174] plane.

bivariate normal (Gaussian) distribution. For two (combination of) production and decay processes (X, Y) and (X', Y'), we obtain the following likelihood:

$$- 2 \log L(\boldsymbol{\mu}) = (\boldsymbol{\mu} - \hat{\boldsymbol{\mu}})^T C^{-1} (\boldsymbol{\mu} - \hat{\boldsymbol{\mu}}),\qquad(3.8)$$

where $\boldsymbol{\mu} = \begin{pmatrix} \mu(X, Y) \\ \mu(X', Y') \end{pmatrix}$, and $C^{-1} = \begin{pmatrix} a & b \\ b & c \end{pmatrix}$ is the inverse of the covariance matrix. Under the bivariate normal approximation, the 68% and 95% CL contours (which are iso-contours of $-2 \log L$) are then ellipses and the information on a single contour suffices to reconstruct the likelihood in the full plane: the parameters a, b and c, as well as $\hat{\mu}(X, Y)$ and $\hat{\mu}(X', Y')$, can be fitted from points sitting on the 68% CL or 95% CL contours as they have known values of $-2 \log L$ (2.30 and 5.99, respectively). In the following, unless stated otherwise, we choose to reconstruct the full likelihood from a fit to the 68% CL contour provided by the experimental collaboration. Then, having more than one contour of constant likelihood is very useful as it allows to check the validity of Gaussian approximation. This will be presented in Section 3.3.4 for the experimental results included in the original database of Lilith. Finally, the generalization of the previous equations would be trivial should higher-dimensional likelihoods be published by the experimental collaborations.

A database of up-to-date experimental results is shipped with Lilith, along with recommended sets of results to use to build the likelihood. The default dataset of results includes the latest measurements from the ATLAS and CMS collaborations. Its content as of February 2015 (database 15.02) is displayed in Table 4. All considered 2D results are in the plane $(\mu(\mathrm{ggH}, Y), \mu(\mathrm{VBF} + \mathrm{VH}, Y))$ except for $Y = \gamma\gamma$ in ATLAS, where only VBF is considered instead of VBF+VH, and for $Y = b\bar{b}$ in CMS, which is given in the plane $(\mu(\mathrm{ttH}, b\bar{b}), \mu(\mathrm{VH}, b\bar{b}))$. The CMS 2D results are taken from the combination of Ref. [171], and correspond to the individual results from Refs. [174, 176, 179, 181, 219]. We also take into account all available searches on production in association with a top-quark pair, as well as searches for invisible decays of the Higgs boson from both ATLAS and CMS. Note

Collaboration	Analysis	Type	Reference
ATLAS	$h \to \gamma\gamma, ZZ^*, WW^*, \tau\tau$	2D contour	[173, 175, 177, 180]
	VH, $h \to b\bar{b}$	2D contour	[182]
	ttH, $h \to b\bar{b}$	1D interval	[226]
	ttH, $h \to \gamma\gamma$	1D interval	[173]
	ZH, $h \to$ invisible	full 1D	[227]
CMS	$h \to \gamma\gamma, ZZ^*, WW^*, \tau\tau$	2D contours	[174, 176, 179, 181]
	$h \to b\bar{b}$	2D interval	[171]
	ttH, $h \to \gamma\gamma, \tau\tau$	1D interval	[171]
	ttH, $h \to$ leptons	1D interval	[219]
	ZH + VBF, $h \to$ invisible	full 1D	[228]
CDF & DØ	VH, $h \to b\bar{b}$	1D interval	[229]

Table 4: Recommended set of experimental results in the `Lilith` database version `15.02`. This set is used by default by `Lilith` to construct the experimental likelihood.

the presence of the CDF and DØ combined result for VH, $h \to b\bar{b}$ [229]; only in this channel the precision of the Tevatron result is comparable with the one of the LHC at Run 1.

All considered experimental results are given at a fixed Higgs mass in the [125, 125.6] GeV range. Variations of the experimental results within this narrow interval are expected to be small, hence limiting the inconsistencies when combining the results. However, it would be desirable to take into account the variation of the results with mass. The final Higgs likelihood is the product of the individual (1- or 2-dimensional) likelihoods. Validation of the Higgs likelihood used in `Lilith` against official LHC results will be presented in Section 3.3.4.

3.3.2 *Parametrization of new physics*

In order to assess the compatibility of a new physics hypothesis with the LHC measurements presented in the previous section, one needs to compute the expected signal strengths $\mu(X, Y)$ [see Eq. (3.7)] for the relevant production mechanisms X and decay modes Y. This can be achieved in a direct way from $\sigma(X)$, $\sigma^{\text{SM}}(X)$, $\mathcal{B}(h \to Y)$, and $\mathcal{B}^{\text{SM}}(h \to Y)$, but is often found to be impracticable. Indeed, in order to have well-defined signal strengths (for which $\mu = 1$ corresponds to the SM prediction) one should take the same prescription for computing cross sections and branching fractions in the SM and in the considered new physics scenario [77].

In most new physics scenarios only leading order (LO) computations are available. Thus, all available NLO corrections to the SM predictions should be ignored. While this leads to properly defined signal strengths, $\sigma_{\text{NLO}}(X)/\sigma_{\text{NLO}}^{\text{SM}}(X)$ will typically differ from $\sigma_{\text{LO}}(X)/\sigma_{\text{LO}}^{\text{SM}}(X)$ (and similarly for branching ratios) as soon as one deviates from the SM prediction. This is because the relative contributions of SM particles to the process will be affected by the NLO corrections. For instance, higher-order corrections to the gluon fusion

process will change the relative contribution of the top and bottom quark loops. Therefore, considering LO or NLO cross sections will yield different $\mu(\text{ggH}, Y)$ if new physics affects the couplings of the Higgs to top and bottom quarks in a different way.

These two problems come from the parametrization of new physics effects from cross sections and branching ratios but can be alleviated if new physics is instead parametrized using reduced couplings. In `Lilith`, the user has the choice of parametrizing the new physics effects directly in terms of physical quantities, *i.e.*, cross sections and branching ratios, or reduced couplings.

3.3.2.1 *Scaling factors and reduced couplings*

Introducing *scaling factors* C_X^2 (C_Y^2) as multiplicative factors to the cross section (partial width) for each process X (Y) as compared to the SM predictions[11], the general signal strength expression given in Eq. (3.3) can be rewritten as

$$\mu = \sum_{X,Y} \text{eff}_{X,Y} \times \frac{\sigma(X)\,\mathcal{B}(h \to Y)}{\sigma^{\text{SM}}(X)\,\mathcal{B}^{\text{SM}}(h \to Y)} = \sum_{X,Y} \text{eff}_{X,Y} \times \frac{C_X^2 \sigma^{\text{SM}}(X)}{\sigma^{\text{SM}}(X)} \times \frac{C_Y^2 \Gamma_Y^{\text{SM}}}{\Gamma_Y^{\text{SM}}} \times \frac{\Gamma_h^{\text{SM}}}{\sum_Y C_Y^2 \Gamma_Y^{\text{SM}}}$$

$$= \frac{1}{\sum_Y C_Y^2\,\mathcal{B}^{\text{SM}}(h \to Y)} \sum_{X,Y} \text{eff}_{X,Y} C_X^2 C_Y^2 \,, \qquad (3.9)$$

where Γ_h^{SM} is the total decay width of the SM Higgs boson. The term $\sum_Y C_Y^2\,\mathcal{B}^{\text{SM}}(h \to Y)$ accounts for the scaling of the total width of the Higgs boson.

Furthermore, we introduce *reduced couplings* through the following Lagrangian,

$$\mathcal{L} = g \left[C_W m_W W^\mu W_\mu + C_Z \frac{m_Z}{\cos\theta_W} Z^\mu Z_\mu \right] h$$
$$+ g \left[-C_t \frac{m_t}{2m_W} \bar{t}t - C_b \frac{m_b}{2m_W} \bar{b}b - C_c \frac{m_c}{2m_W} \bar{c}c - C_\tau \frac{m_\tau}{2m_W} \bar{\tau}\tau - C_\mu \frac{m_\mu}{2m_W} \bar{\mu}\mu \right] h \,, \qquad (3.10)$$

where $C_{W,Z}$ and $C_{t,b,c,\tau,\mu}$ are bosonic and fermionic reduced couplings, respectively. In the limit where they all go to 1, the SM prediction is recovered. Lighter fermions are not taken into account here as their phenomenological impact on the SM Higgs sector is negligible. At leading order in perturbation theory, the scaling factors C_X and C_Y from Eq. (3.9) can be directly identified with the reduced couplings C_i from Eq. (3.10) for production or decay modes involving just one coupling to the Higgs boson. We obtain

$$C_{\text{WH}}^2 = C_W^2 \,, \quad C_{\text{ZH}}^2 = C_Z^2 \,, \quad C_{\text{ttH}}^2 = C_t^2 \,, \quad C_{f\bar{f}}^2 = C_f^2 \,, \quad C_{VV}^2 = C_V^2 \,, \qquad (3.11)$$

where $f = b, c, \tau, \mu$ and $V = W, Z$. The last two scaling factors, $C_{f\bar{f}}$ and C_{VV}, rescale the Higgs partial widths $\Gamma(h \to f\bar{f}, VV^*)$, respectively.

For the remaining main processes (ggH and VBF production, decay into gg, $\gamma\gamma$ and $Z\gamma$), there is no direct identification unless the Higgs couplings to all involved SM particles scale in the same way. In the general case, the C_X and C_Y for these processes will be given by a

---

11 The scaling factors C_i are also commonly denoted as κ_i [230].

combination of reduced couplings C_i, weighted according to the contribution of the particle i to the process. For the production mechanisms, we have

$$C_{\text{ggH}}^2 = \frac{\sum\limits_{i,j=t,b,c} C_i C_j \, \sigma_{ij}^{\text{SM}}(\text{ggH})}{\sum\limits_{i,j=t,b,c} \sigma_{ij}^{\text{SM}}(\text{ggH})} \, , \quad C_{\text{VBF}}^2 = \frac{\sum\limits_{i,j=W,Z} C_i C_j \, \sigma_{ij}^{\text{SM}}(\text{VBF})}{\sum\limits_{i,j=W,Z} \sigma_{ij}^{\text{SM}}(\text{VBF})} \, , \tag{3.12}$$

where the σ_{ij}^{SM} are the different contributions to the cross section in the SM. For $i = j$ it corresponds to the cross section contribution from the particle i alone, while $i \neq j$ comes from the interference between the particles i and j (in order to avoid double-counting, these terms need to be counted only once in the previous sums). Similarly, the reduced couplings for the gg, $\gamma\gamma$, and $Z\gamma$ loop-induced decay modes are computed as

$$C_{gg}^2 = \frac{\sum\limits_{i,j=t,b,c} C_i C_j \, \Gamma_{ij}^{\text{SM}}(h \to gg)}{\sum\limits_{i,j=t,b,c} \Gamma_{ij}^{\text{SM}}(h \to gg)} \, , \quad C_{\gamma\gamma,Z\gamma}^2 = \frac{\sum\limits_{i,j=W,t,b,c,\tau} C_i C_j \, \Gamma_{ij}^{\text{SM}}(h \to \gamma\gamma, Z\gamma)}{\sum\limits_{i,j=W,t,b,c,\tau} \Gamma_{ij}^{\text{SM}}(h \to \gamma\gamma, Z\gamma)} \, , \tag{3.13}$$

where the Γ_{ij}^{SM} are the SM partial widths of the process under consideration. In all cases, all relevant SM contributions have been taken into account. As expected, the relative sign of the reduced couplings will affect the interference terms. Moreover, the contributions $\Gamma_{i \neq j}^{\text{SM}}$ may be negative on their own, this is the case for $\Gamma_{tW}^{\text{SM}}(h \to \gamma\gamma)$ for instance due to the bosonic (fermionic) nature of the $W^\pm$ (t).

At LO, the various σ_{ij}^{SM} and Γ_{ij}^{SM} can be obtained from tree-level amplitudes (for VBF) or from the 1-loop amplitudes (for $gg \to h$ and $h \to gg, \gamma\gamma, Z\gamma$).[12] It would naturally be desirable to take into account the NLO corrections to the Higgs cross sections and partial widths as they modify the relations $C_{X,Y}(C_i)$. This can be achieved in a simple way as long as higher-order corrections only rescale the σ_{ij}^{SM} and Γ_{ij}^{SM} that are already existing in Eqs. (3.12)–(3.13), and do not induce new couplings to the Higgs boson. This is the case for the QCD corrections, but not for the electroweak corrections (as the Higgs doublet is charged under SU(2)$_L$ but not SU(3)$_c$). Thus, as will be explained in Section 3.3.3.5, the QCD corrections for all five processes of Eqs. (3.12)–(3.13) will be included in `Lilith`.

One last remark is in order. The signal strength framework requires that the signal in all searches be a sum of processes that exist for the SM Higgs boson. However, new production or decay modes may exist without spoiling the signal strength interpretation as long as they do not yield sizable contribution in the current Higgs searches. Two particularly interesting cases are Higgs boson decays into undetected particles, or into invisible particles. In the first case, this new decay is simply missed by current searches (as would, *e.g.*, be the case for the decay of the Higgs into light quarks or gluons), while in the second case this new decay mode gives rise to missing energy in the detector. As was discussed in Section 3.3.1.3, invisible decays of the Higgs boson are constrained by current searches which are taken into account in `Lilith`. In the presence of undetected or invisible decays, the width of the Higgs boson becomes larger and modifies the signal strength predictions of Eq. (3.9) as shown in Eq. (2.56),

$$\mu(C_X, C_Y) \longrightarrow (1 - \mathcal{B}_{\text{invisible}} - \mathcal{B}_{\text{undetected}})\mu(C_X, C_Y) \, . \tag{3.14}$$

---

12 At LO, one obtains the same scaling for gluon fusion and for the decay into two gluons, $C_{\text{ggH}} = C_{gg}$.

In `Lilith`, arbitrary invisible and/or undetected decays can be specified, as will be discussed in Section 3.3.3.5.

3.3.2.2   *CP-violating admixtures*

`Lilith` can also consider the case where the observed Higgs boson is a mixture of CP-even and CP-odd states [157, 158]. The SM Higgs coupling to vector bosons has the form

$$VVh: \quad C_V \frac{gM_V^2}{m_W} g^{\mu\nu}, \tag{3.15}$$

where as above C_V measures the departure from the SM: $C_V = 1$ for a pure scalar 0^+ (CP-even) state with SM-like couplings and $C_V = 0$ for a pure pseudoscalar 0^- (CP-odd) state. In the fermion sector, we find the general scalar and axial structure of the Higgs coupling to fermions. Concretely, we have

$$f\bar{f}h: \quad -\bar{f}\left[\mathrm{Re}(C_f) + i\,\mathrm{Im}(C_f)\gamma_5\right] f \frac{gm_f}{2m_W}, \tag{3.16}$$

where in the SM one has $\mathrm{Re}(C_f) = 1$ and $\mathrm{Im}(C_f) = 0$, while a purely CP-odd Higgs would have $\mathrm{Re}(C_f) = 0$ and $\mathrm{Im}(C_f) = 1$. Since $m_f^2 \ll m_h^2$ for $f = b, c, \tau$, the partial decay widths scale as $\Gamma(h \to f\bar{f}) \propto \mathrm{Re}(C_f)^2 + \mathrm{Im}(C_f)^2 = |C_f|^2$ to a very good approximation [82]. This is what is implemented in `Lilith`. Modifications of the production and decay rates due to some CP-mixing mainly arise in loop-induced processes, in particular in the $gg \to h$ and $h \to \gamma\gamma$ rates. A test of the CP properties of the observed Higgs from a global fit to the signal strengths was presented in [192, 231]. Following Ref. [192], at leading order the Higgs rates normalized to the SM expectations can be written as

$$\frac{\Gamma(h \to \gamma\gamma)}{\Gamma^{\mathrm{SM}}(h \to \gamma\gamma)} \simeq \frac{\left|\frac{1}{4}C_W A_1^+[m_W] + \left(\frac{2}{3}\right)^2 \mathrm{Re}(C_t)\right|^2 + \left|\left(\frac{2}{3}\right)^2 \frac{3}{2}\mathrm{Im}(C_t)\right|^2}{\left|\frac{1}{4}A_1^+[m_W] + \left(\frac{2}{3}\right)^2\right|^2},$$

$$\frac{\sigma(gg \to h)}{\sigma^{\mathrm{SM}}(gg \to h)} = \frac{\Gamma(h \to gg)}{\Gamma^{\mathrm{SM}}(h \to gg)} \simeq |\mathrm{Re}(C_t)|^2 + \left|\frac{3}{2}\mathrm{Im}(C_t)\right|^2, \tag{3.17}$$

with $A_1^+[m_W] \simeq -8.32$ for $m_h = 125$ GeV is the loop form factor for the $W^\pm$ contribution. For convenience, the contributions from lighter quarks have been omitted in the above equations but are fully taken into account in `Lilith`.

In the case of ttH production, the approximation used above for the other fermions does not hold since $m_t > m_h$. Instead, the cross section scales as

$$\sigma(\mathrm{ttH}_{0+/-}) \propto \mathrm{Re}(C_f)^2 + \mathrm{Im}(C_f)^2 \times \frac{\sigma(\mathrm{ttH}_{0-})}{\sigma^{\mathrm{SM}}(\mathrm{ttH}_{0+})}. \tag{3.18}$$

Following Ref. [232], $\sigma(\mathrm{ttH}_{0-})/\sigma^{\mathrm{SM}}(\mathrm{ttH}_{0+}) \approx 1/3$, this is what is considered in `Lilith`. However, a significant coupling of the CP-odd component of the Higgs boson to top quarks may modify the acceptance times efficiency compared to the SM value in searches for the Higgs boson in association with a pair of top quarks [232, 233], *i.e.*, $(A \times \varepsilon)_{\mathrm{ttH},Y} \neq [(A \times \varepsilon)_{\mathrm{ttH},Y}]^{\mathrm{SM}}$. As this cannot be taken into account in `Lilith`, such cases should be

interpreted with care. Moreover, only after the end of Run 2 will the LHC have enough sensitivity to probe CP violating effects in the $h \to \tau\tau$ decays [234], and the product $(A \times \varepsilon)_{X,\tau\tau}$ can thus be approximated by the SM one for now. Precise measurements at Run 2 of the LHC could ultimately call for an implementation of CP-admixture effects at NLO in `Lilith`.

3.3.3 *Running Lilith*

We give here an overview of how to use `Lilith` at a practical level. Full details can be found in Section 4 of [114].

3.3.3.1 *Getting started*

`Lilith` is a library written in `Python` for constraining model of new physics against the LHC results. The `Lilith` versions and databases of experimental results as well as all necessary information can be found at

<div align="center">

http://lpsc.in2p3.fr/projects-th/lilith.

</div>

The archive of `Lilith` can be unpacked in any directory. It contains a root directory called `Lilith-1.x/` where the following directories can be found:

- `lilith/`: the `Python` package itself. The `Lilith` application programming interface (API) will be presented in Section 3.3.3.2.

- `data/`: contains the database of experimental results in `XML` format, as well as text files for the recommended sets of results. Details are given in Section 3.3.3.4.

- `userinput/`: where parametrizations of new physics models, in the `XML` format described in Section 3.3.3.5 can be stored. Some basic user input files that include extensive comments are provided with the `Lilith` distribution.

- `examples/`: concrete examples on how to use `Lilith` for constraining new physics. Two of them will be presented in detail in Section 3.3.5.

- `results/`: empty folder where results from `Lilith` can be stored.

The folder `Lilith-1.x/` moreover contains `run_lilith.py`, the command-line interface (CLI) of `Lilith` which will be presented in Section 3.3.3.3.

`Lilith` requires `Python 2.6` [235] or more recent and has not been tested with the `3.X` series. The standard `Python` scientific libraries, `SciPy` and `NumPy` [236], should furthermore be installed. The easiest way to check if all dependencies of `Lilith` are correctly installed is to try to compute the likelihood from an example file. This can be achieved by typing to the shell, within the directory `Lilith-1.x/`, the command

```
python run_lilith.py userinput/example_couplings.xml
```

Everything is correctly installed if basic information as well as the value of the likelihood are printed on the screen.

3.3.3.2 *The Lilith application programming interface*

`Lilith` provides an API from which all tasks (reading the user and the experimental input, compute the likelihood, print the results in a file, etc.) can be performed, using the methods described below. This is the recommended way of using `Lilith`. In order to be used in any `Python` code (or in an interactive session of `Python`), the `Lilith` library, called `lilith`, first needs to be imported. Once this is done, objects of the class **Lilith** can be created, we present here the main methods and attributes of the API.

class lilith.**lilith**(*verbose=false*, *timer=false*)

> Instantiate the **Lilith** class. The following public attributes are initialized:
>
> EXP_MU
> > list of experimental results read from the database,
>
> COUPLINGS
> > list of reduced couplings for each Higgs particle contributing to the signal as read from the user input,
>
> USER_MU
> > list of signal strengths for each Higgs particle contributing to the signal as read (or derived from) the user input,
>
> RESULTS
> > list of results after computation of the likelihood for each individual measurement,
>
> L
> > value of $-2\log L$.

lilith.**readuserinput**(*userinput*)

> Read the string in XML format given as argument and fill the attribute **couplings** (if the user input is given in terms of reduced couplings) or **user_mu** (if the user input is given in terms of signal strengths).

lilith.**readuserinputfile**(*filepath*)

> Read the user input located at *filepath* and call **readuserinput**().

lilith.**readexpinput**(*filepath=default_exp_list*)

> Read the experimental input specified in a list file and store the results in **exp_mu**. By default, the list file is `data/latest.list`, which gathers the recommended set of experimental results.

lilith.**computelikelihood**(*userinput=none*, *exp_filepath=none*, *userfilepath=none*)

> Evaluate the likelihood function from signal strengths derived from the user input and the experimental results and store the results in the attribute **results**.

lilith.**writeresults**(*filepath*, *slha=false*)

> Write the content of the attribute **results** at the location *filepath* in the XML format (if *slha=False*) or the SUSY Les Houches Accord (SLHA)-like format [237].

A minimal example of use of the API is as follows:

```
import lilith
lcal = lilith.Lilith()
lcal.readexpinput()
lcal.readuserinputfile('userinput/example_mu.xml')
lcal.computelikelihood()
print '-2log(likelihood) =', lcal.l
```

The first two lines import the `Lilith` library into the global namespace and initialize the computations. The three following lines successively read the default experimental input, read the user input from the file `userinput/example_mu.xml`, and compute the likelihood. Alternatively, they could be replaced with a single line,

```
lcal.computelikelihood(userfilepath='userinput/example_mu.xml')
```

Finally, the value of $-2 \log L$ is printed on the screen on the last line.

3.3.3.3 *Command-line interface*

A command-line interface (CLI) is also shipped with `Lilith` for a more basic usage of the tool. It corresponds to the file `run_lilith.py` located in the directory `Lilith-1.x/`. The CLI can be called by typing to the shell (with current directory `Lilith-1.x/`) the command

```
python run_lilith.py user_input_file (experimental_input_file) (options)
```

where arguments in parentheses are optional.

The first argument, `user_input_file`, is the path to the user input file in the `XML` format described in Section 3.3.3.5. New physics can be parametrized in terms of reduced couplings or directly in terms of signal strengths. Examples are shipped with `Lilith` in the directory `userinput/`. The second argument, `experimental_input_file`, is the path to the list of experimental results to be used for the construction of the likelihood. If not given, the latest LHC results (plus a Tevatron result) will be used (`data/latest.list`; its content is given in Table 4). It is the recommended list of experimental results to be used for performing a global fit.

If no option is given, basic information as well as the value of the likelihood and the number of measurements are printed on the screen. A number of options are provided to control the information printed on the screen and the output format, see [114] for details.

3.3.3.4 *Experimental input*

We have seen that the evaluation of the likelihood in `Lilith` requires the input of a list of experimental results to be considered. It corresponds to a simple text file with a `.list` extension listing the paths to experimental result files in `XML` format (each containing a single 1D or 2D signal strength result). `Lilith` is shipped with the latest LHC Higgs results (plus a Tevatron result), see Table 4 for the status in February 2015, in the form of `XML` files present in subdirectories of `data/`. Moreover, several lists of experimental results are provided in `data/`, with `latest.list` being the default list file. This is the one recommended for a global fit to the LHC+Tevatron Higgs data. Every single experimental

Attribute	1D interval	full 1D	2D contour	full 2D
`dim`	`"1"`	`"1"`	`"2"`	`"2"`
`type`	`"n"`	`"f"`	`"n"`	`"f"`
(`prod`)	`"ggH"`, `"ttH"`, `"VBF"`, `"WH"`, `"ZH"`, `"VH"`, `"VVH"`			
(`decay`)	`"gammagamma"`, `"ZZ"`, `"WW"`, `"Zgamma"`, `"tautau"`, `"mumu"`, `"bb"`, `"cc"`, `"invisible"`			

Table 5: Allowed values for the attributes of the `<expmu>` tag, in experimental files in XML format. The four different formats of experimental data are defined by the mandatory `dim` and `type` attributes.

result (1D or 2D) is stored in a different XML file. In this way, modifying and updating the database is an easy process.

Before showing an explicit example, let us discuss the structure of the files. The root tag of each experimental file is `<expmu>`. It has two mandatory attributes, `dim` and `type`, that specify the type of signal strength result (1D interval, full 1D, 2D contour, or full 2D). The possible values for the attributes are given in Table 5. In addition, the `<expmu>` tag has two optional attributes: `prod` and `decay`. They can be given a value listed in Table 5 if the analysis under consideration is only sensitive to one production mode (*e.g.* ttH) or to one decay mode (*e.g.* $\gamma\gamma$) of the Higgs boson. Note that, if `prod="VH"` or `prod="VVH"` is given as attribute to the `<expmu>` tag or to an `<eff>` tag, the relative contributions of WH and ZH (for VH) and of WH, ZH and VBF (for VVH) will be computed internally assuming an inclusive search, *i.e.*, for VVH,

$$\text{eff}(X, Y) = \frac{\sigma^{\text{SM}}(X)}{\sigma^{\text{SM}}(\text{VBF}) + \sigma^{\text{SM}}(\text{ZH}) + \sigma^{\text{SM}}(\text{WH})} \quad \text{for } X \in (\text{VBF}, \text{WH}, \text{ZH}), \quad (3.19)$$

where the cross sections are evaluated at the Higgs mass given in the `<mass>` tag using the LHC-HXSWG results for the 8 TeV LHC [77].

In the general case, the `prod` and `decay` attributes can be omitted. Indeed, all relevant efficiencies $\text{eff}_{X,Y}$ can be specified in `<eff>` tags. For instance, one could specify efficiencies in the following way

```
<eff prod="ggH" decay="WW">0.5</eff>
<eff prod="VBF" decay="WW">0.5</eff>
<eff prod="ggH" decay="tautau">0.5</eff>
<eff prod="VBF" decay="tautau">0.5</eff>
```

where all efficiencies for a given decay mode should sum up to 1. In the case of 2D signal strengths (*i.e.* if `dim="2"` in `<expmu>`) the efficiencies should be given for both dimensions (and separately add up to 1).

An explicit example of well-formed experimental input, for the results of the ATLAS $h \to ZZ^*$ analysis [175], is given by

```
<expmu dim="2" type="n" decay="ZZ">
```

```
    <experiment>ATLAS</experiment>
    <source type="published">HIGG-2013-21</source>
    <sqrts>7+8</sqrts>
    <mass>125.36</mass>
    <CL>68%</CL>


    <eff axis="x" prod="ggH">1.0</eff>
    <eff axis="y" prod="VVH">1.0</eff>


    <!-- (likelihood specification) -->
  </expmu>
```

where the tags `experiment`, `source`, `sqrts`, `CL` provide optional information. If `mass` is not given, a Higgs mass of 125 GeV will be assumed by default. The comment `<!- (...) ->` indicates where the likelihood information should be placed. The four likelihood types (interval or full, 1 or 2D) have a different format. For the 1D interval, the central value and the left and right 1σ uncertainties should be provided as described in Eq. (3.4), while for the 2D interval, the central value and the (a, b, c) parametrization of the (inverse of the) covariance matrix should be specified as in Eq. (3.8). For the full likelihoods, an explicit table of the form $x = \mu(X, Y)$, $(y = \mu(X', Y))$, $z = -2\log(L)$ should be provided for 1D (2D) results. This allows the specification of a likelihood with an arbitrary form as desired.

3.3.3.5 *User model input*

The user model input, parametrizing the new physics model under consideration, can be given either in terms of signal strengths $\mu(X, Y)$ directly [defined as in Eq. (3.7)], or in terms of reduced couplings and scale factors. In the latter case, scale factors involving more than one coupling to the Higgs boson that would be missing from the input are computed automatically by `Lilith` assuming the presence of SM particles only, and signal strengths are derived from the scale factors.

XML *format for signal strengths*

In the signal strengths mode, the basic inputs are the signal strengths defined as in Eq. (3.7). An example of an (arbitrary) XML input file for the signal strengths mode is now presented.

```
  <lilithinput>
    <signalstrengths>
      <mass>125.1</mass>
      <mu prod="ggH" decay="gammagamma">1.1</mu>
      <mu prod="ggH" decay="VV">1.3</mu>
      <mu prod="ggH" decay="tautau">0.9</mu>

      <mu prod="VVH" decay="gammagamma">1.2</mu>
      <mu prod="VVH" decay="VV">1.1</mu>
      <mu prod="VVH" decay="tautau">1.1</mu>
```

```
    <mu prod="ttH" decay="VV">1.0</mu>
    <mu prod="ttH" decay="bb">1.0</mu>
    <mu prod="ttH" decay="tautau">0.8</mu>

    <redxsBR prod="ZH" decay="invisible">0.1</redxsBR>
    <redxsBR prod="VBF" decay="invisible">0.0</redxsBR>
        </signalstrengths>
 </lilithinput>
```

- `<lilithinput>` is the root tag of the XML file, it defines a Lilith input file.

- The `<signalstrengths>` tag indicates that the user input is given in terms of signal strengths.

- The `<mass>` tag defines the Higgs boson mass at which the likelihood should be computed. It should be in the $[123, 128]$ GeV range. This information is not used in the calculations with the current experimental input, where results are only given for a fixed Higgs mass.

- The signal strengths themselves are defined in `<mu>` tags. Two mandatory arguments should be given:
  - The `prod` attribute can be `ggH`, `WH`, `ZH`, `VBF`, `ttH`. For convenience, multi-particle attributes have been defined. They are listed in Table 6.
  - The `decay` attribute can be `gammagamma`, `Zgamma`, `WW`, `ZZ`, `bb`, `cc`, `tautau`, `mumu`. Multi-particle labels can be found in Table 6.

  Note that every `<mu>` tag can be omitted and in such case the SM unity value is assumed.

- Finally, there is the possibility to specify an invisible or undetected branching ratio in the `<redxsBR>` tag. This is defined as

$$\text{redxsBR}(X, \text{inv./und.}) = \frac{\sigma(X)}{\sigma^{\text{SM}}(X)} \mathcal{B}_{\text{inv./und.}} \,. \tag{3.20}$$

  If not given, the SM value will be assumed by default, *i.e.*, 0.

Note that the signal strengths for several Higgs states contributing to the signal can be defined by specifying an arbitrary number of `<signalstrengths> ... </signalstrenths>` tags in the input. The signal strengths from each individual state contributing to the signal will be stored and summed together. We neglect possible interferences between the different states. An identifier for each particle can be given through the `part` attribute of the `<signalstrengths>` tag.

XML *format for reduced couplings*

New physics can be parametrized in terms of scaling factors that can be identified as (or derived from) reduced couplings, as was presented in Section 3.3.2. In this section we

Attribute		shortcut for...
prod	`"VVH"`	`"VBF"`, `"WH"`, `"ZH"`
	`"VH"`	`"WH"`, `"ZH"`
decay	`"VV"`	`"ZZ"`, `"WW"`
	`"ff"`	`"cc"`, `"bb"`, `"tautau"`, `"mumu"`
	`"ll"`	`"tautau"`, `"mumu"`
	`"uu"`	`"cc"`
	`"dd"`	`"bb"`, `"tautau"`, `"mumu"`

Table 6: Possible multi-particle attributes for the tag `<mu>` in the signal strengths mode.

present the user input in terms of reduced couplings. Before turning to the format of the user input, we comment on the computation of couplings and of signal strengths. First of all, as we have seen in Section 3.3.2.1, predictions for the Higgs boson can be obtained from the reduced couplings C_W, C_Z, C_t, C_b, C_c, C_μ and C_τ appearing in Eq. (3.10). Scaling factors for VBF production and loop-induced processes are functions of the C_i and can be expressed in as Eqs. (3.12)–(3.13). In the following, we will consider two possible cases: that these scaling factors are obtained from leading-order calculations (*i.e.* tree-level results for VBF and one-loop analytical expressions for other processes), or including NLO QCD corrections. The former case will be denoted as `LO`, the latter one as `BEST-QCD`. We comment on the computations currently implemented in `Lilith`:

VBF

The contribution from the W boson, the one from the Z boson, and the interference between them have been obtained from `VBFNLO-2.6.3` [238] for Higgs masses in the $[123, 128]$ GeV range with (for `BEST-QCD` mode) and without (for `LO` mode) NLO QCD corrections at the LHC 8 TeV, using the MSTW2008 parton distribution functions [239]. The results for $\sigma_{WW}^{\mathrm{SM}}(\mathrm{VBF})$, $\sigma_{ZZ}^{\mathrm{SM}}(\mathrm{VBF})$ and $\sigma_{WZ}^{\mathrm{SM}}(\mathrm{VBF})$ as a function of the Higgs mass are stored in text files shipped with `Lilith`.

ggH

The contributions from the three heaviest quarks (t, b, c) to the SM cross section are taken into account. In the `LO` mode, we use analytical expressions [82]. In the `BEST-QCD` mode, those have been generated in the $[123, 128]$ GeV range with `HIGLU` [240] at the LHC 8 TeV with the MSTW2008 parton distribution functions [239].

$h \to gg, \gamma\gamma, Z\gamma$

The relevant SM partial widths of these processes (taking into account particles listed in Eq. (3.13)) are obtained from analytical expressions [82] in the `LO` mode. In the `BEST-QCD` mode, those have been generated in the $[123, 128]$ GeV range with `HDECAY` [241] including the available QCD corrections.

However, the Lagrangian defined in Eq. (3.10) does not exhaust the possibilities for new physics affecting the properties of the Higgs processes. One particularly interesting case is

that BSM particles enter the loop-induced processes, such as $gg \rightarrow h$ and $h \rightarrow \gamma\gamma$. To account for these cases, we allow for a direct definition of the scaling factors of the four main loop-induced processes ($gg \rightarrow h$ and $h \rightarrow gg, \gamma\gamma, Z\gamma$), *i.e.*, for a direct definition of C_{ggH} and $C_{gg,\gamma\gamma,Z\gamma}$. If some or all of the scaling factors are missing from the input, they will be computed internally using Eq. (3.12)–(3.13), *i.e.*, assuming that only SM particles are involved. Finally, note that we use the SM branching ratios provided by the LHC HXSWG [77], at the Higgs mass given in the user input, when computing the signal strengths [see Eq. (3.9)].

The user input file for the `Lilith` reduced couplings mode has the following structure.

```
<lilithinput>
  <reducedcouplings>
    <mass>125</mass>

    <C to="ZZ">1.0</C>
    <C to="WW">1.0</C>
    <C to="tt">1.0</C>
    <C to="cc">1.0</C>
    <C to="bb">1.0</C>
    <C to="tautau">1.0</C>

    <C to="gammagamma">1.0</C>
    <C to="Zgamma">1.0</C>
    <C to="gg">1.0</C>
    <C to="VBF">1.0</C>

    <precision>BEST-QCD</precision>

    <extraBR>
      <BR to="invisible">0.0</BR>
      <BR to="undetected">0.0</BR>
    </extraBR>
  </reducedcouplings>
</lilithinput>
```

- `<lilithinput>` is the root tag of the `XML` file, it defines a `Lilith` input file.

- The `<reducedcouplings>` tag is specific to the reduced couplings mode. This is where the reduced couplings are specified. The correspondence between the `XML` notation and Eq. (3.10) is given in Table 7. Note the possibility to define common couplings for the up-type fermions, down-type fermions, all fermions, and electroweak gauge bosons.

- The tag `<mass>` defines the Higgs boson mass at which the likelihood should be computed. The allowed range is $[123, 128]$ GeV. This affects the computation of the SM branching ratios and partial cross sections and widths as explained above. If it is not given, a Higgs mass of 125 GeV is assumed.

to attribute	"tt"	"bb"	"cc"	"tautau"	"mumu"	"WW"	"ZZ"
corresponds to	C_t	C_b	C_c	C_τ	C_μ	C_W	C_Z

to attribute	"gammagamma"	"Zgamma"	"gg" for="prod"	"gg" for="decay"	"VBF"
corresponds to	$C_{\gamma\gamma}$	$C_{Z\gamma}$	C_{ggH}	C_{gg}	C_{VBF}

to attribute	shortcut for...
"VV"	"WW", "ZZ"
"ff"	"tt", "cc", "bb", "tautau", "mumu"
"ll"	"tautau", "mumu"
"uu"	"tt", "cc"
"dd"	"bb", "tautau", "mumu"

Table 7: Upper and middle tables: correspondence between the XML notation and that of Eq. (3.10). Bottom table: common reduced couplings definitions.

- Regarding the effective coupling to a pair of gluons, NLO corrections affect gluon fusion (ggH) and the decay into two gluons ($h \rightarrow gg$) in a different way. Therefore, scaling factors C_{ggH} and C_{gg} can be specified separately as

```
<C to="gg" for="prod">1.0</C>
<C to="gg" for="decay">1.05</C>
```

  If for="all" is specified, the same coupling is assigned to the production and decay modes. This is the default behavior if the for attribute is missing. Note however that the effects of a modified C_{gg} coupling are very mild, it will only change the total Higgs width by a small amount while it is not directly constrained experimentally.

- CP violation was presented in Section 3.3.2.2. In the LO mode, the fermionic couplings C_t, C_b, C_c, C_τ can be given a real and an imaginary component. For the top quark for instance, this can be specified as

```
<C to="tt" part="re">0.9</C>
<C to="tt" part="im">0.2</C>
```

  If part="re|im" is not specified, the coupling is assumed to be purely real. In the BEST-QCD mode, only the real part of the coupling is taken into account.

- The <precision> tag contains either BEST-QCD or LO. If not specified, or wrongly spelled, the BEST-QCD mode is the default mode.

- The <extraBR> tag contains the declaration of the invisible or undetected branching ratios (see Section 3.3.2).

As in the case of input in terms of signal strengths, several tags `<reducedcouplings> ...
</reducedcouplings>` can be defined, corresponding to the case where several Higgs states contribute to the observed signal around 125 GeV. These particles can also be given a name with a `part` attribute to the `<reducedcouplings>` tag. An example of user input in terms of reduced couplings is stored in `userinput/example_couplings.xml` for the case of a single Higgs boson contributing to the signal, and in `userinput/example_couplings_multiH.xml` for the case of two or more Higgs states.

3.3.4 *Validation*

Having explained how to use `Lilith` in the previous section, we now turn to the validation of the likelihood derived from the experimental input shipped with the code. We begin by discussing the validity of the bivariate normal distribution as an approximation to the 2D likelihood functions in the signal strength planes $(\mu(X, Y), \mu(X', Y'))$. The use of this approximation is necessary whenever only contours of constant likelihood are provided instead of the full information. Several coupling fits from the ATLAS and CMS collaboration are then reproduced. The results from `Lilith` are compared to the official ones in order to assess the validity of the likelihood used in `Lilith`.

3.3.4.1 *Reconstruction of the experimental likelihoods*

In the signal strength plane $(\mu(X, Y), \mu(X', Y'))$, an approximation to the likelihood function can be obtained assuming that the measurements follow a bivariate normal distribution, as explained in Section 3.3.1.3. Using the 68% CL contour provided by the experimental collaboration, we reconstruct the shape of the likelihood and compare the location of the best-fit point as well as the 68% and 95% CL contours with what is provided by ATLAS or CMS.

Two examples are shown in Fig. 3.11: the reconstruction of the likelihood for the ATLAS WW^* [177] and the CMS $\gamma\gamma$ [174] final states. In both cases, we observe an excellent agreement between the reconstructed likelihood and the official result. The 68% CL regions are perfectly reproduced and the reconstructed best-fit points are very close to the experimental ones. The extrapolation towards the 95% CL regions also shows very good agreement. We find equally good agreements with all other decay modes (with the exception of $h \to ZZ^*$), and we conclude that the Gaussian distribution is a very good approximation to the true distribution.

The largest deviations from the normal approximation are expected to occur for final states with low statistics since the counting of the events, that follows the Poisson distribution, has not yet entered the Gaussian regime. In particular, this is the case for the ZZ^* channel. In Fig. 3.12, we show the comparison between the `Lilith` reconstructed likelihood in the ZZ^* final state and the corresponding ATLAS and CMS ones. As can be seen, the deviation of the ATLAS likelihood from the bivariate normal approximation can be substantial. In particular, for negative $\mu(\text{VBF} + \text{VH})$ the experimental likelihood is cut, this is because the measured quantity is $n_{exp} = \mu(\text{VBF} + \text{VH}).n_s + n_b$ and cannot be negative, only the presence of a non-vanishing n_b allows negative μ to be tested. In the positive region of the plane (the one that is relevant), the approximation holds well
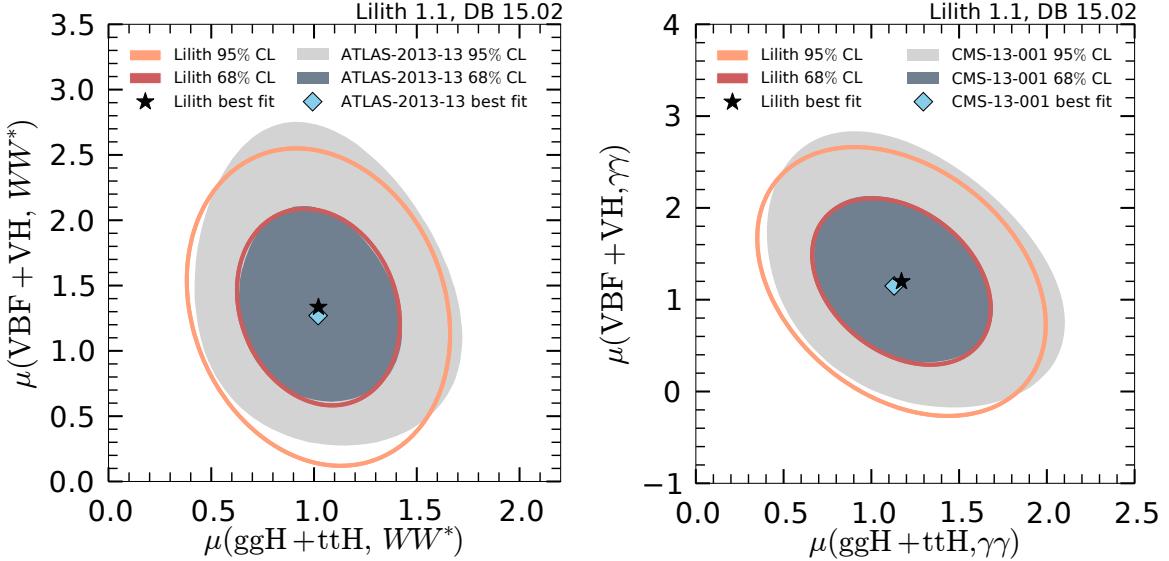
Figure 3.11: Reconstruction of the experimental likelihood from a bivariate normal approximation for the ATLAS WW^* search [177] (left) CMS $\gamma\gamma$ search [174] (right). The filled dark and light gray contours show the 68% and 95% CL experimental contours while the red and orange solid lines show the reconstructed likelihood contours. The blue diamond and the black star indicates the experimental and reconstructed best-fit points, respectively.
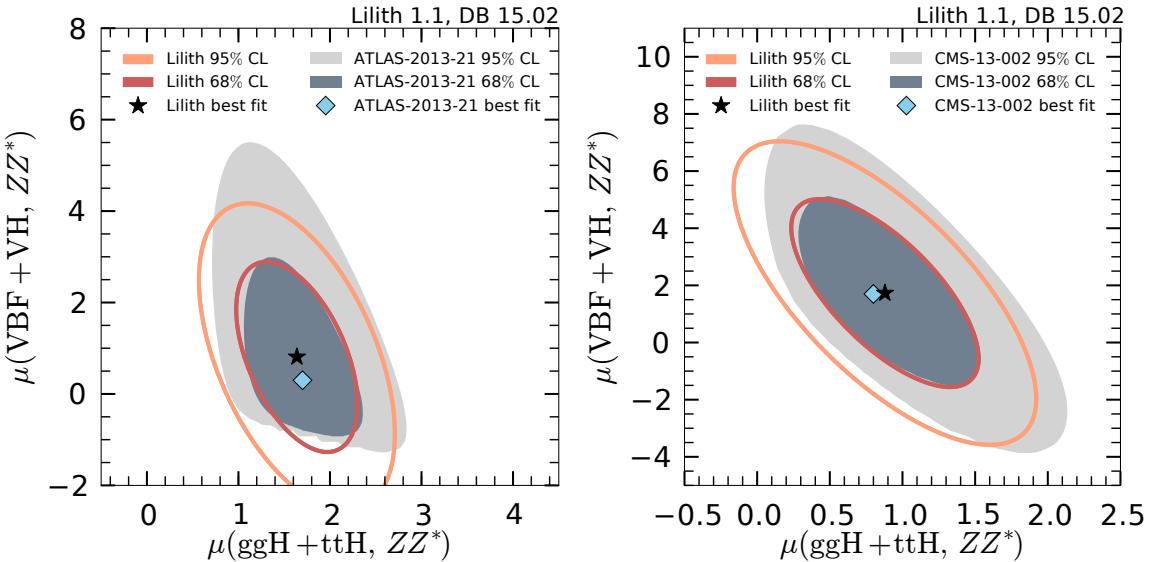
Figure 3.12: Reconstruction of the experimental likelihood from a bivariate normal approximation for the ATLAS [175] (left) and CMS [176] (right) $h \to ZZ^*$ searches. The filled dark and light gray contours show the 68% and 95% CL experimental contours while the red and orange solid lines show the reconstructed likelihood contours. The blue diamond and the black star indicates the experimental and reconstructed best-fit points, respectively.
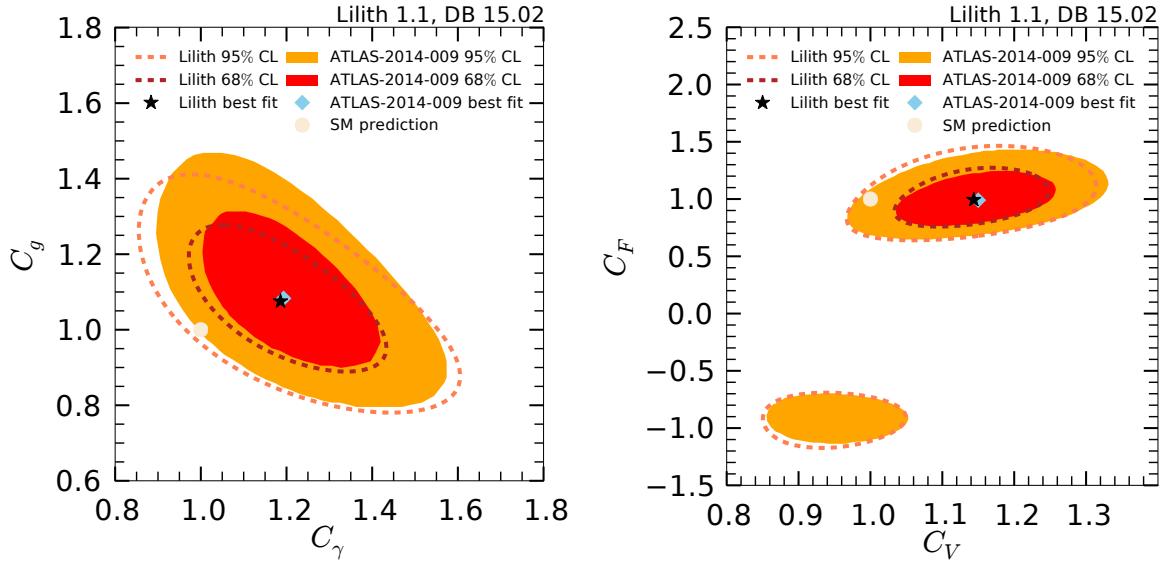
Figure 3.13: (C_γ, C_g) (left) and (C_V, C_F) (right) fits using data from the ATLAS combination [242]. The red and orange filled surfaces correspond to the 68% and 95% CL regions obtained by the ATLAS collaboration while the corresponding dashed lines show the `Lilith` results. The black star indicates the position of the `Lilith` best-fit point, the blue diamond is the ATLAS best-fit point and the white circle shows the SM prediction.

near the best-fit point. However, going away from it, the reconstructed shape fails to reproduce the ATLAS 95% CL contour at large $\mu(\text{VBF} + \text{VH}, ZZ^*)$. Due to non-Gaussian effects, the reconstructed best-fit point is quite distant to the experimental one. For the CMS case, the approximation holds to a better approximation. The reconstructed best-fit point is very close to the experimental one and the shape of the 95% CL contour is very well reproduced although a small shift in the $\mu(\text{ggH} + \text{ttH}, ZZ^*)$ direction is observed. As argued in Section 3.3.6, provision of the full likelihood information would yield a significant improvement over the normal approximation in such cases.

3.3.4.2 *Comparison to Higgs coupling fits from ATLAS and CMS*

In order to validate the approximate Higgs likelihood used in `Lilith`, we attempt to reproduce coupling fit results from combination notes of ATLAS [242] and CMS [171]. Note that while the CMS combination [171] makes use of the final Run 1 results, a number of analyses considered in the combination of the ATLAS results given in Ref. [242] have been updated since then.

First, results for two benchmark scenarios proposed by the LHC-HXSWG in Ref. [230] are presented. In the first scenario, SM-like tree-level couplings are assumed [*i.e.*, all $C_i = 1$ in Eq. (3.10)] but two scaling factors are introduced: $C_\gamma \equiv C_{\gamma\gamma}$ (scaling $h \to \gamma\gamma$), and $C_g \equiv C_{\text{ggH}} = C_{gg}$ (scaling ggH production and $h \to gg$). In the second benchmark scenario, two reduced couplings are introduced: $C_V \equiv C_W = C_Z$, for the coupling of the Higgs boson to a pair massive vector bosons, and $C_F \equiv C_t = C_b = C_c = C_\tau$, a universal coupling to fermions. In this case, the effective coupling to gluons is simply C_F, while $C_{\gamma\gamma}$ is a function

of both C_V and C_F that can be obtained taking into account QCD corrections as discussed in Section 3.3.3.5.

Let us first discuss the comparison with the ATLAS results, Fig. 3.13. In both scenarios, very good agreement is observed between the results from ATLAS and the ones obtained with `Lilith`. Both the reconstructed best-fit point and contours reproduce very well the ATLAS results. The most significant deviation is a slight deformation of the 95% CL region in the (C_γ, C_g) plane. The corresponding results for CMS are shown in Fig. 3.14. CMS results are well reproduced with `Lilith`, even for the contour at 99.7% CL. Slight shifts of the best-fit points and minor deformations of the contours are observed. The overall agreement is nevertheless very good.
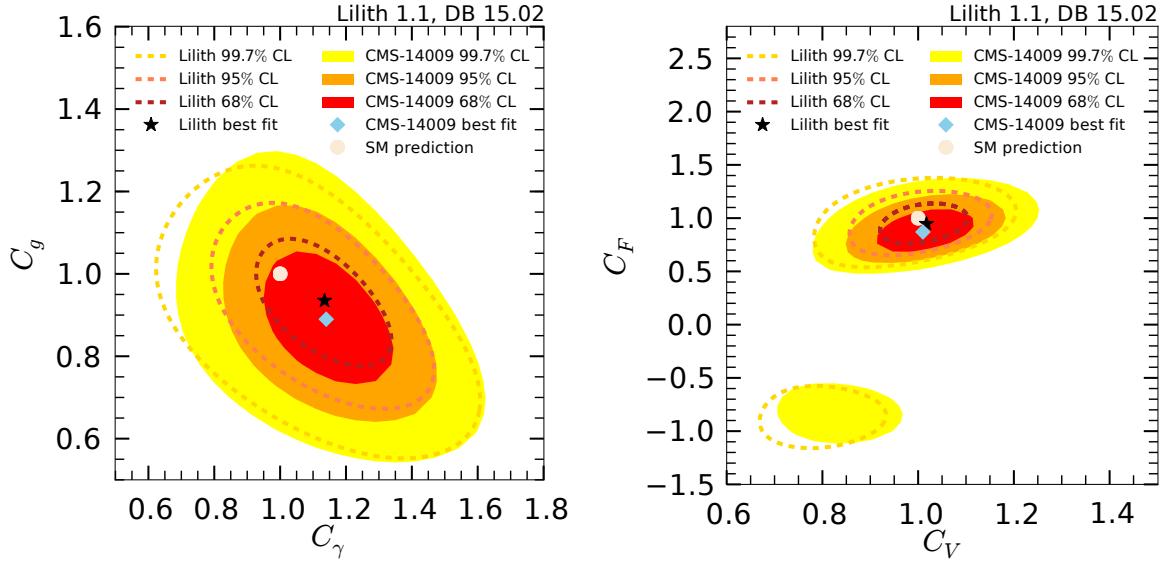

Figure 3.14: (C_γ, C_g) (left) and (C_V, C_F) (right) fits using data from the CMS combination [171]. The red, orange and yellow filled surfaces correspond to the 68%, 95% and 99.7% CL regions obtained by the CMS collaboration while the corresponding dashed lines show the `Lilith` results. The black star indicates the position of the `Lilith` best-fit point, the blue diamond is the CMS best-fit point and the white circle shows the SM prediction.

Let us move on to the 3-parameter fit (C_W, C_Z, C_F). As in the (C_V, C_F) benchmark scenario discussed above, a universal coupling to fermions is introduced, but instead of a single coupling to vector boson we define separately the reduced coupling to W bosons, C_W, and to Z bosons, C_Z. Defining $C_{WZ} \equiv C_W/C_Z$, a direct test of custodial symmetry can be performed using the Higgs measurements alone. The 1-dimensional likelihood profile for C_{WZ} is shown in Fig. 3.15 for both the ATLAS and CMS combination.[13]

Although the ATLAS result is almost perfectly reproduced, a significant discrepancy is observed in the case of CMS for $C_{WZ} > 1$. This does not come as a surprise: several experimental results were considered in the $(\mu(\text{ggH} + \text{ttH}, Y), \mu(\text{VBF} + \text{VH}, Y))$ plane and the breaking of VBF + VH into the individual production modes VBF, WH and ZH [assumed to be inclusive, see Eq. (3.19)] becomes relevant whenever $C_W \neq C_Z$. Moreover, ATLAS

---

13 In general for a function $-2\log L(\{C_i\}, \{C_j\})$, where $\{C_i\}, \{C_j\}$ can be sets of parameters, the profile likelihood $-2\log L(\{C_i\})$ is obtained by minimizing the full function with respect to $\{C_j\}$ for each $\{C_i\}$.
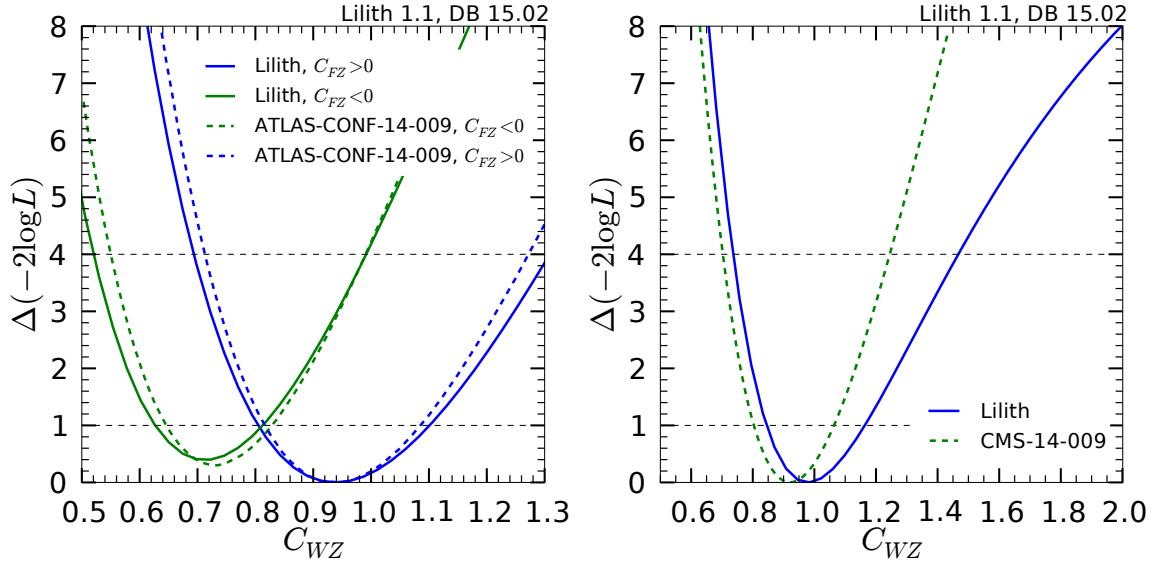
Figure 3.15: 1D likelihood profiles of $C_{WZ} \equiv C_W/C_Z$ from a (C_W, C_Z, C_F) fit to the ATLAS [242] (left) and CMS [171] (right) data and comparison to the official results. The ATLAS fit considers both signs for the Higgs–fermion–fermion coupling and furthermore defines $C_{FZ} \equiv C_F/C_Z$. The results are given for both signs of C_{FZ}.
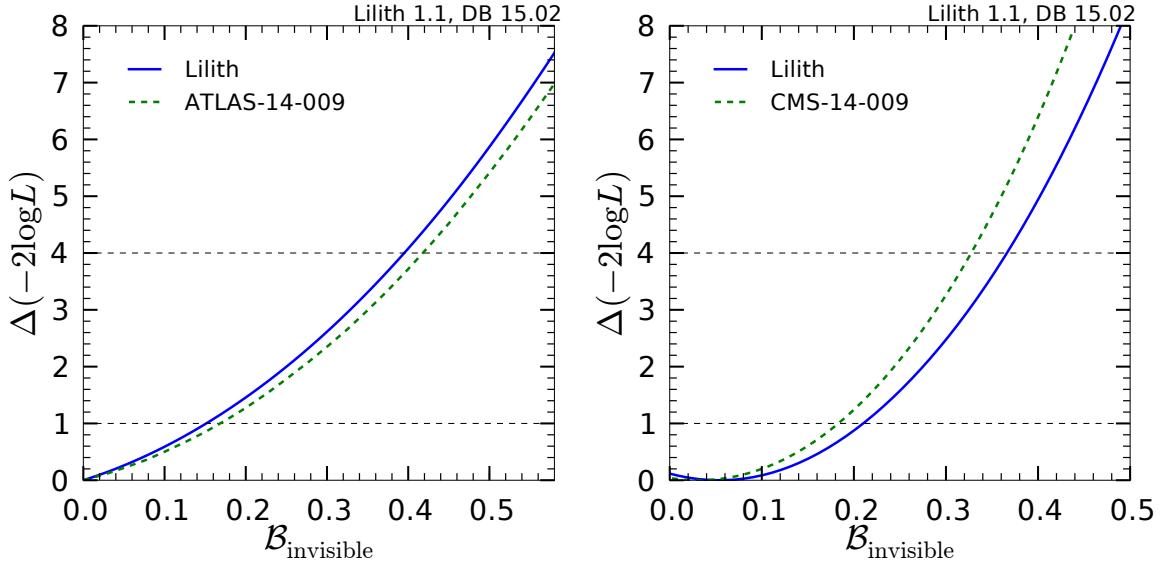
Figure 3.16: 1D likelihood profiles of $\mathcal{B}_{\text{invisible}}$ from a $(C_\gamma, C_g, \mathcal{B}_{\text{invisible}})$ fit and comparison to the ATLAS [242] (left) and CMS [171] (right) results.

results make use of the full numerical likelihood grids that were provided in Refs. [222–224] while the bivariate normal approximation is used in the case of CMS. Thus, constraints on models in which $C_W \neq C_Z$ should be interpreted with care given the experimental information being used as input to Lilith.

Finally, we present the result of a 3-parameter fit $(C_\gamma, C_g, \mathcal{B}_{\text{invisible}})$ in terms of the 1D profile likelihood of $\mathcal{B}_{\text{invisible}}$ in Fig. 3.16. A very good agreement is observed in ATLAS, and in CMS for moderate values of $\mathcal{B}_{\text{invisible}}$. As explained in Section 3.3.2.1, the presence

of a branching ratio into invisible particles is constrained by direct searches for invisible decays of the Higgs boson, and also by every Higgs search since it modifies the total Higgs width and therefore scales all signal strengths collectively.

3.3.5 *Examples of applications*

Having validated the Higgs likelihood of `Lilith` from results obtained by the ATLAS and CMS collaborations, we now turn to deriving constraints on specific new physics scenarios using the latest LHC results as of February 2015. We leave a study of the latest LHC results for the next section. The `Python` routines used to obtain these results are available in the folder `examples/python` and will be described shortly.

3.3.5.1 *Reduced coupling determination*

As a first illustration of the use of `Lilith`, constraints on the benchmark scenario (C_V, C_F) introduced previously. While the right panels of Figs. 3.13 and 3.14 showed results on this scenario in the 2D plane (C_V, C_F) using only ATLAS or CMS results, here we combine the ATLAS and CMS results and derive 1D profile likelihood constraints on C_V and C_F. Results are shown in Fig. 3.17.
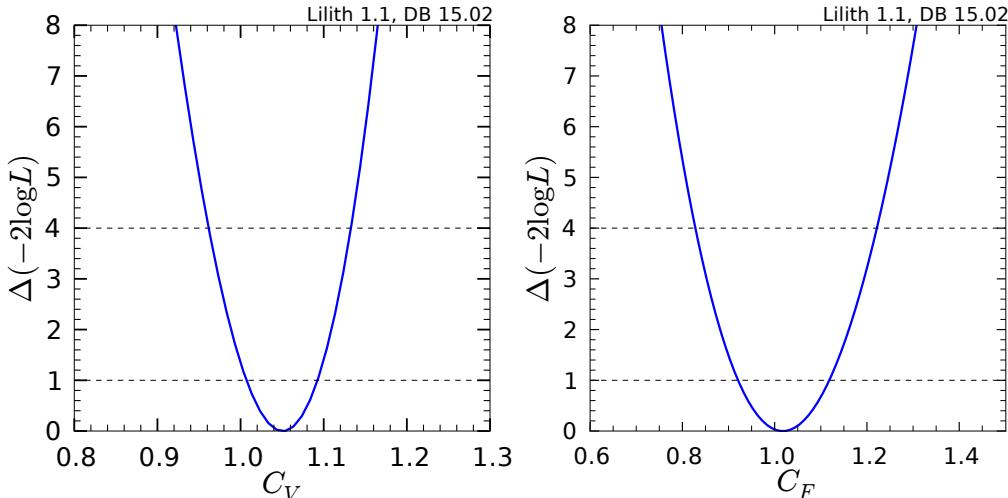
Figure 3.17: 1-dimensional likelihood profiles of C_V (left) and C_F (right) from a global fit of the benchmark scenario (C_V, C_F).

The `Python` routine used to obtain this result is `CVCF_1dprofile.py` and is provided with `Lilith`. It can be executed from the `Lilith-1.x/` folder with the command line

```
python examples/python/CVCF_1dprofile.py
```

This example uses the class `Minuit` of the library `iminuit` [243], a `Python` implementation of the `MINUIT` [244] minimization library, in order to minimize $-2 \log L$ and derive the 1D profile around the minimum. After having instantiated the `Lilith` class and read the experimental data with,

```
lilithcalc = lilith.Lilith(verbose, timer)
```
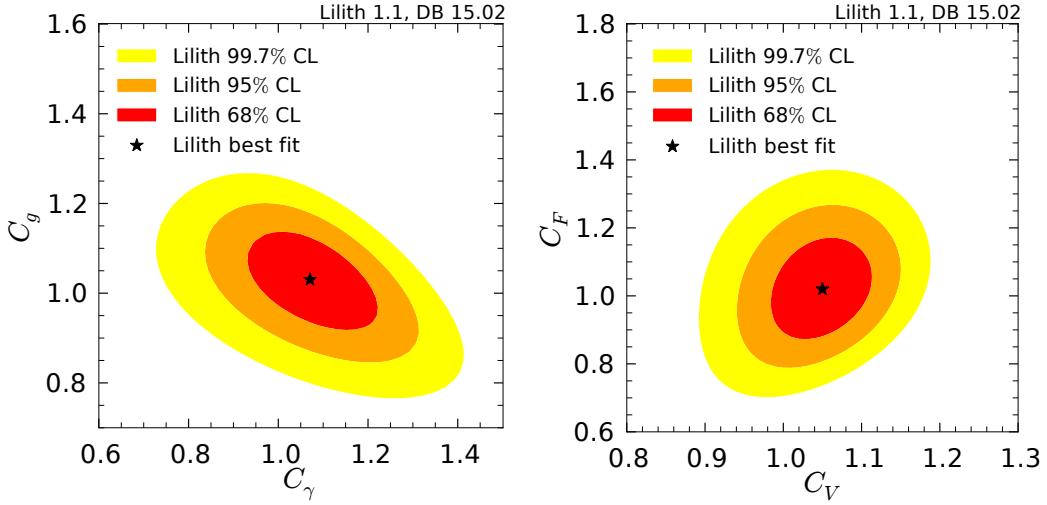
Figure 3.18: Contraints on (C_γ, C_g) (left) and (C_V, C_F) (right) from a global fit to the Higgs data. The red, orange and yellow filled surfaces correspond to the 68%, 95% and 99.7% CL regions. The black star shows the position of the best-fit point.

```
lilithcalc.readexpinput(myexpinput)
```

a function `getL` returning $-2 \log L(C_V, C_F)$ is defined,

```
def getL(CV, CF):
    myXML_user_input = usrXMLinput(mh=mh, CV=CV, CF=CF, precision=precision)
    lilithcalc.computelikelihood(userinput=myXML_user_input)
    return lilithcalc.l
```

where the function `usrXMLinput` creates a `XML` user input string from C_V and C_F, for a given precision mode `precision`. An object `m` of the class `Minuit` is then created,

```
m = Minuit(getL, CV=1, limit_CV=(0,3), CF=1, limit_CF=(0,3))
```

where the initial point of the minimization and the range of parameters are defined. The function `m.mnprofile` is then called

```
xV, yV, rV = m.mnprofile("CV", bins=300, bound=(0., 2), subtract_min=True)
```

and returns the 1D likelihood profile $\Delta(-2 \log L(C_V)) \equiv -2 \log(L(C_V)/L(\text{best fit}))$ on a given range of C_V. Without the option `substract_min=True`, the "absolute" likelihood $-2 \log L(C_V)$ would be returned instead. The parameter range in which $\Delta(-2 \log L(C_V)) < 1$ (4) defines the 68% (95%) CL intervals of C_V. The constraints on C_F are derived in the exact same way. In this scenario, the best-fit point is obtained for $C_V = 1.05$ and $C_F = 1.02$. In 1D, *i.e.* profiling over the other parameter, the 68% (95%) CL intervals read $C_V = [1.00, 1.09]$ $([0.96, 1.13])$ and $C_F = [0.92, 1.12]$ $([0.83, 1.22])$.

We also provide an example on how to derive constraints and produce figures for a 2D parameter space. The left panel of Fig. 3.18 presents the 2D constraints obtained from a global fit of the (C_γ, C_g) model presented above. The corresponding `Python` routine is `CgammaCg_2d.py`. It can be executed from the `Lilith-1.x/` folder with the command line

```
python examples/python/CgammaCg_2d.py
```

A scan of the (C_γ, C_g) parameter space is performed, and results are stored in the form

```
0.04040     0.00000     119.05462
0.04040     0.02020     119.00658
0.04040     0.04040     118.86261
0.04040     0.06061     118.62314

......      ......      ......
```

where the first, second and third columns contain the values of C_γ, C_g and $-2 \log L(C_\gamma, C_g)$, respectively. For completeness, the 2D constraints on the (C_V, C_F) benchmark scenario, using the latest LHC measurements, are also presented in the right panel of Fig. 3.18. They have been derived in the same way.

3.3.5.2 *Higgs constraints on superpartners of the tau lepton*

Supersymmetric scalar partners of the tau leptons, known as staus, can have a substantial contribution to the $h \to \gamma\gamma$ decay rate if they are light and have a large mixing [245, 246]. Constraints on the parameters controlling this new contribution can therefore be obtained from the Higgs precision measurements. Here, we consider a very simplified scenario based on the Minimal Supersymmetric Standard Model and assume that the only deviation from the SM Higgs properties comes from the contribution of staus to the loop-induced process $h \to \gamma\gamma$. More precisely, it is assumed that the supersymmetric partners of the Higgs boson and of the remaining fermions are decoupled, that the second Higgs doublet is phenomenologically irrelevant and that a Higgs mass of 125 GeV can be obtained for any point of the analysis. In this case, the contribution from staus to the $h \to \gamma\gamma$ decay width is parametrized by the two physical masses $m_{\tilde{\tau}_1}$ and $m_{\tilde{\tau}_2}$ (with $m_{\tilde{\tau}_1} < m_{\tilde{\tau}_2}$), the mixing angle $\theta_{\tilde{\tau}}$ and the ratio of vacuum expectation values for the two Higgs doublets, $\tan\beta$. The corresponding amplitude at leading order reads [82, 247]

$$\mathcal{M}_{h\gamma\gamma}^{\tilde{\tau}} = \sum_{i=1,2} \frac{g_{h\tilde{\tau}_i\tilde{\tau}_i}(m_{\tilde{\tau}_1}, m_{\tilde{\tau}_2}, \theta_{\tilde{\tau}}, \tan\beta)}{m_{\tilde{\tau}_i}^2} A_0^H\left((m_h/(2m_{\tilde{\tau}_i}))^2\right) \tag{3.21}$$

where the sum runs over the two stau mass-eigenstates, A_0^H is a loop form factor and $g_{H\tilde{\tau}_i\tilde{\tau}_i}$ is the Higgs–stau–stau coupling.

The effective Higgs–γ–γ reduced coupling can therefore be expressed as

$$C_\gamma(m_{\tilde{\tau}_1}, m_{\tilde{\tau}_2}, \theta_{\tilde{\tau}}, \tan\beta) = \frac{\left|\mathcal{M}_{h\gamma\gamma}^{\mathrm{SM}} + \mathcal{M}_{h\gamma\gamma}^{\tilde{\tau}}(m_{\tilde{\tau}_1}, m_{\tilde{\tau}_2}, \theta_{\tilde{\tau}}, \tan\beta)\right|}{\left|\mathcal{M}_{h\gamma\gamma}^{\mathrm{SM}}\right|} \tag{3.22}$$

Note that the SM amplitude $\mathcal{M}_{h\gamma\gamma}^{\mathrm{SM}}$ appears both in the numerator and denominator of Eq. (3.22) since SM tree-level couplings are assumed.

Fixing $\tan\beta = 10$ and the mass of the lightest stau $m_{\tilde{\tau}_1} = 85, 100$ GeV, we show constraints in the plane $(m_{\tilde{\tau}_2}, \theta_{\tilde{\tau}})$ in Fig. 3.19. For $\theta_{\tilde{\tau}} = \pi/4$, the 2-dimensional 95% CL upper limit on $m_{\tilde{\tau}_2}$ reads $m_{\tilde{\tau}_2} < 360$ (460) GeV for $m_{\tilde{\tau}_1} = 85$ (100) GeV. More generally, the upper limit on $m_{\tilde{\tau}_2}$ becomes weaker as $m_{\tilde{\tau}_1}$ is increased.

The corresponding `Python` code is `stau_gammagamma.py`. It can be executed by typing the following command line to the shell from the `Lilith-1.x/` folder:
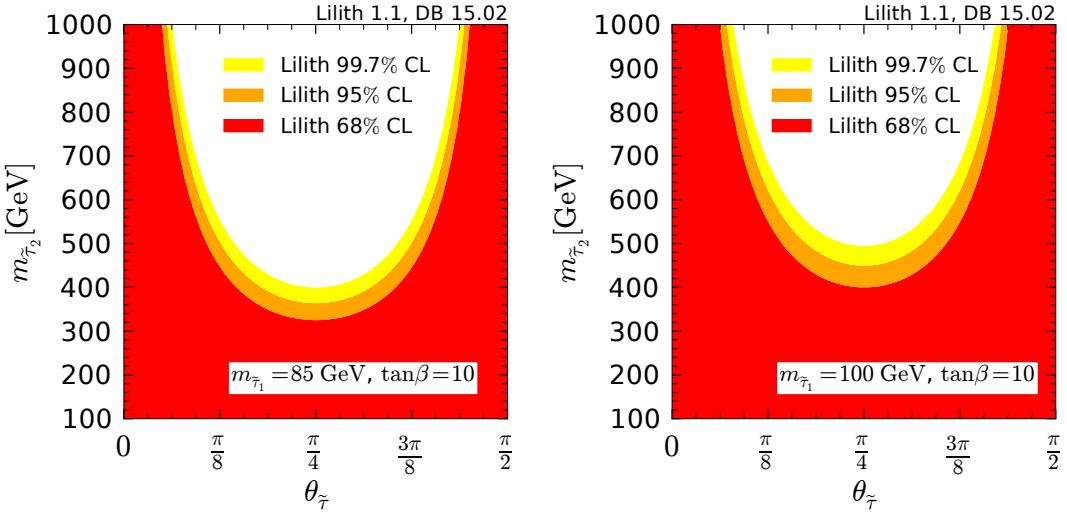
Figure 3.19: Constraints on the staus masses and mixing angle in the $(m_{\tilde{\tau}_2}, \theta_{\tilde{\tau}})$ plane for $m_{\tilde{\tau}_1} = 85$ GeV (left) and $m_{\tilde{\tau}_1} = 100$ GeV (right) and $\tan\beta = 10$. The red, orange and yellow filled surfaces correspond to the allowed 68%, 95% and 99.7% CL regions, respectively.

```
python examples/python/stau_gammagamma.py
```

The routine works as follows. Functions returning C_γ according to Eq. (3.22) and $-2\log L(C_\gamma)$ are defined. Since $\tan\beta$ and $m_{\tilde{\tau}_1}$ are fixed, a 2-dimensional grid scan is then performed over the two remaining parameters: for each couple $(m_{\tilde{\tau}_2}, \theta_{\tilde{\tau}})$, the corresponding $\Delta(-2\log L)$ is obtained. The 2-dimensional 68%, 95%, 99.7% CL regions in the plane $(m_{\tilde{\tau}_2}, \theta_{\tilde{\tau}})$ are obtained with $\Delta(-2\log L) < 2.3, 5.99, 11.83$, respectively.

Note that direct searches from LEP [248] and vacuum metastability condition [249] impose further constraints on this scenario. Moreover, this simplified SUSY scenario could easily be generalized, *e.g.* by taking into account $h \to \tilde{\chi}_1^0 \tilde{\chi}_1^0$. Light staus are especially relevant in the case where $\tilde{\chi}_1^0$ is light in order to have a viable neutralino dark matter candidate in the MSSM (see, *e.g.*, Ref. [250] and references therein).

3.3.6   *Prospects for Run 2 of the LHC*

As discussed in Section 3.3.1, approximations necessarily need to be made when combining signal strength results from several categories or several searches, making it necessary to validate the approach. In Section 3.3.4, we have shown that we reproduce well the results of coupling fits from ATLAS and CMS (separately). However, it is clear that the situation will change as more statistics will be collected at Run 2 of the LHC.

Indeed, systematic uncertainties will then dominate over statistical uncertainties in the majority of the channels. Missing correlations between systematic uncertainties (both theoretical and experimental) will thus become a more pressing issue. Moreover, more combinations for production and decay of the Higgs boson, (X, Y), will be determined with a good precision. This will spoil the simple interpretation we have for a number of the results we currently use, in particular for results given in the plane $(\mu(\text{ggH} + \text{ttH}, Y), \mu(\text{VBF} + \text{VH}, Y))$.

In the following, we recall the main limitations when using the information currently provided by the ATLAS and CMS collaborations for constructing a likelihood. We also discuss new ways of presenting the LHC Higgs results in order to be able to construct a good approximation to the Higgs likelihood at Run 2 of the LHC. This paragraph partly collects arguments put forward in "*On the presentation of the LHC Higgs Results*" [225] by a collaboration of theorists and experimentalists with the aim to maximize the impact of the LHC Higgs results and their utility to the whole high-energy physics community.

First of all, in most cases only contours of constant likelihood (at least the 68% CL interval or contour, sometimes contours at 95% CL) are provided by ATLAS and CMS. This makes it necessary to extrapolate the likelihood assuming, most naturally, a Gaussian shape. When using a given contour to extrapolate the likelihood, the validity of this approximation can be tested from a comparison of the position of the best-fit point and from contours provided by the experimental collaboration. This was done in Section 3.3.4.1, where we concluded that the reconstruction is generally very good, although in some cases asymmetrical effects are washed out (see, *e.g.*, Fig. 3.12). However, in all cases, it induces an unnecessary approximation. The ATLAS and CMS collaborations initiated some efforts during Run 1 to provide the full likelihood information in 1D and 2D planes (see the right panel of Fig. 3.10 and Refs. [222–224]).

Another issue is the dependence of the results on the assumed Higgs boson mass m_h. Currently, we use results given at a fixed Higgs mass. As not all results are provided at the same m_h, a slight inconsistency is introduced in the combination of the different results (the assumed Higgs mass varies within a few hundreds of MeV). Official combination notes allow us to get rid of this inconsistency, as all results are therein given at the same Higgs mass. However, the dependence of the experimental results on the Higgs mass can be very important for the high-resolution channels, that target decays of the Higgs boson into charged leptons and photons (such as $h \to ZZ^* \to 4\ell$ and $h \to \gamma\gamma$). Therefore, it would be highly desirable to have access to mass-dependent likelihood results.

Current results are presented in 1- or 2-dimensional projections, often corresponding to the combination of production modes (in 2D, typically ggH + ttH and VBF + VH). As we discussed earlier, this becomes a limitation as measurements get more precise, in which case we would like to investigate deviations in all of the five production modes separately. For such reasons, a total breakdown of the signal strength measurements in terms of the five Higgs production modes (ggH, VBF, WH, ZH, ttH) would be a considerable step forward regarding the interpretation of the LHC Higgs results. We would therefore like to advocate the experimental collaborations to provide the likelihood as a function of the Higgs mass and a full set of production modes, that is to say, in the

$$(m_h, \mu(\text{ggH}, Y), \mu(\text{ttH}, Y), \mu(\text{VBF}, Y), \mu(\text{ZH}, Y), \mu(\text{WH}, Y)) \qquad (3.23)$$

parameter space for each final state Y. For some final states, all five production modes are certainly not constrained by the experimental searches and only lower dimensional projections of this space would be relevant. Naturally this raises the question on the transmission of this function from the experimental collaborations to the community. A simple grid would be too cumbersome. If the full function cannot be provided numerically, a smarter discretization should be developed (through Markov Chain Monte Carlo or a scan along the eigenvectors of the covariance matrix for instance).

Though this would solve most of the limitations currently faced, the notable issue of correlations between the measurements of different decay modes would still remain. For instance, theoretical uncertainties on gluon fusion production affect both the $\gamma\gamma$ and ZZ^* final states, and simply multiplying the currently available likelihood functions to combine them lead to a double counting of these uncertainties. Moreover, the profiling of the nuisance parameters describing systematic uncertainties may not be consistent as different channels may pull them in different directions. Recently, an interesting proposal was made in this direction in Ref. [251]. Provided experimental collaborations publish likelihoods that are not profiled over a set of theoretical nuisance parameters of interest, but instead given for a fixed scenario, it is then possible to build a "recoupled" likelihood incorporating these uncertainties at the later stage. This has the advantage of not being restricted to the Gaussian approximation. It would certainly be of great interest if the information in the 2D plane $(\mu(\text{ggH} + \text{ttH}, Y), \mu(\text{VBF} + \text{VH}, Y))$, or even better in the possibly 6D plane discussed above, could be given without profiling over the theoretical uncertainties on the Higgs signal. With the method presented in Ref. [251], one could then fully correlate the theoretical uncertainties between the different channels and experiments, and modify these uncertainties compared to what is done in ATLAS and CMS if desired.

The Higgs likelihood of `Lilith` obtained from the latest measurements at the LHC has been thoroughly validated against ATLAS and CMS results and can be used to constrain new physics. Future measurements at Run 2 of the LHC will, however, call for new ways of presenting results in order to derive a good approximation to the Higgs likelihood. In particular, further disentanglement of the different production and decay modes will become necessary. Moreover, correlations between systematic uncertainties, and in particular the treatment of theoretical uncertainties, will become a more pressing issue. The structure of the code is such that `Lilith` can easily be adapted to handle extended signal strength information.

3.4 GLOBAL FIT OF THE HIGGS COUPLINGS AFTER THE RUN 1 OF THE LHC

We now provide an update of the global fits of the couplings of the 125 GeV Higgs boson using the final results from the first run of the LHC using `Lilith`. The global likelihood L is constructed using the database `DB 15.09`. We present a selection of results given in terms of signal strengths, reduced couplings, and for the Two-Higgs-Doublet Models of Type I and II assuming that the lighter CP-even state is the observed one.

Fits to various combinations of reduced Higgs couplings, *i.e.*, Higgs couplings to fermions and gauge bosons relative to their SM values, have been performed by the experimental collaborations themselves, *e.g.* in Refs. [171, 172, 188]. Moreover, theorists combine the results from ATLAS and CMS in global fits, see *e.g.* [194, 202] and references therein, in order to test consistency with SM expectations and to constrain models with modified Higgs couplings. In particular, the couplings of the observed Higgs boson could deviate from the SM predictions due to the presence of other Higgs states mixing with the observed one and/or due to new particles contributing to the loop-induced couplings.

In Ref. [194], a comprehensive analysis of the Higgs signal strengths and couplings and implications for extended Higgs sectors was performed based on the experimental results

as per Spring 2013. Since then, the final results from the first LHC run have been published and a number of new measurements or updates of existing ones became available. In this global fit, we use the final Run 1 results of both ATLAS and CMS. The complete list can be found in Table 8.

Collaboration	Analysis	Reference
ATLAS	$h \to \gamma\gamma$	[173]
	$h \to ZZ^*$	[175]
	$h \to WW^*$	[178]
	$h \to \tau\tau$	[180]
	VH, $h \to b\bar{b}$	[182]
	ZH, $h \to$ invisible	[227]
	VBF, $h \to$ invisible	[252]
	ttH, $h \to$ multi-leptons	[253]
	ttH, $h \to b\bar{b}$	[254]
	ttH, $h \to \gamma\gamma$	[173]
	$h \to \mu\mu$	[184]
	$h \to Z\gamma$	[186]
CMS	$h \to \gamma\gamma$	[174]
	$h \to ZZ^*$	[176]
	$h \to WW^*$	[179]
	$h \to \tau\tau$	[181]
	VH, $h \to b\bar{b}$	[183]
	VBF, $h \to b\bar{b}$	[255]
	ttH, $h \to \gamma\gamma$, multi-leptons	[219]
	ttH, $h \to b\bar{b}$	[256]
	ZH + VBF, $h \to$ invisible	[228]
CDF & DØ	VH, $h \to b\bar{b}$	[229]

Table 8: Experimental results used in the global fit. This list corresponds to the default set of experimental results of the `Lilith` database `15.09`. We note that this database contains slightly more results than used in the official ATLAS+CMS combination [188], which does take into account the Higgs to invisible measurements and the CMS VBF, $h \to b\bar{b}$ result in particular.

In the following, we provide an updated fit for *i)* the combined signal strengths, *ii)* the most important reduced coupling fits, and *iii)* Two Higgs Doublet Models of Type I and Type II, using the final LHC run 1 results.
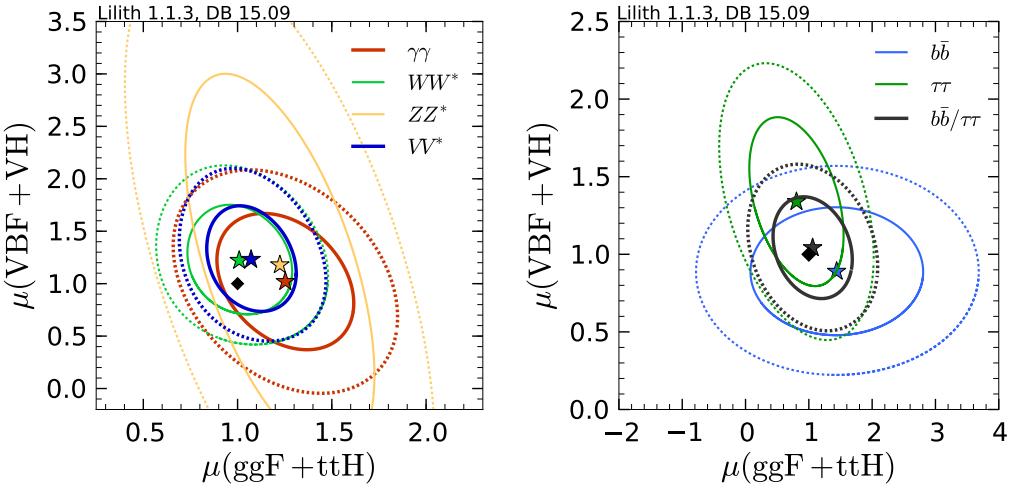
Figure 3.20: Combined signal strengths in the plane of (ggF + ttH) versus (VBF + VH) produc-
tion, on the left for the $\gamma\gamma$, ZZ^*, WW^* and VV^* decay modes (the latter assuming
$ZZ^* = WW^*$), on the right for the $b\bar{b}$ and $\tau\tau$ decay modes and their combination
$b\bar{b} = \tau\tau$. The full (dashed) contours denote the 68.3% (95.4%) CL regions, derived
by combining the ATLAS, CMS and Tevatron results. The best-fit points are marked
as stars and the SM case by a black diamond.

3.4.1 Combined Signal Strengths

We begin by showing in Fig. 3.20 contours of constant confidence level for the combined
signal strengths in the $\mu(\text{ggF} + \text{ttH})$ versus $\mu(\text{VBF} + \text{VH})$ plane for different Higgs decay
modes.[14] The left panel shows the bosonic channels $H \to \gamma\gamma$, WW^*, ZZ^* as well as VV^*,
where $VV^* \equiv ZZ^* + WW^*$, and the right panel shows the fermionic channels $b\bar{b}$, $\tau\tau$ as well
as $b\bar{b} = \tau\tau$. The combination of the ZZ^* and WW^* decay modes is justified by custodial
symmetry, which implies that the HZZ and HWW couplings are rescaled by the same
factor with respect to the SM. The combination of the $b\bar{b}$ and $\tau\tau$ decay modes is justified,
in principle, in models where one specific Higgs doublet has the same couplings, with
respect to the SM, to down-type quarks and leptons, although QCD corrections can lead
to deviations of the reduced Hbb and $H\tau\tau$ couplings from a common value.

All results show an excellent agreement with the SM. Compared to [194], uncertainties
have been significantly reduced for the fermionic channels, particularly for $H \to b\bar{b}$ in
ttH production. As for $H \to \gamma\gamma$, while previously small excesses were observed in ggF
by ATLAS and in VBF + VH by both ATLAS and (to a lesser extent) CMS, updated
results point to a SM-like behavior. Overall, this leads to a central value only slightly
larger than unity.

In the Gaussian approximation, we can derive a simple expression for $-2\log(L)$ for each
decay mode j in the form of ellipses [194], see also Eq. (3.6),

$$\chi_j^2 = a_j(\mu_j^{\text{ggF}} - \widehat{\mu}_j^{\text{ggF}})^2 + c_j(\mu_j^{\text{VBF}} - \widehat{\mu}_j^{\text{VBF}})^2 + 2b_j(\mu_j^{\text{ggF}} - \widehat{\mu}_j^{\text{ggF}})(\mu_j^{\text{VBF}} - \widehat{\mu}_j^{\text{VBF}}), \quad (3.24)$$

where the upper indices ggF and VBF stand for (ggF + ttH) and (VBF + VH), respec-
tively, and $\widehat{\mu}_j^{\text{ggF}}$ and $\widehat{\mu}_j^{\text{VBF}}$ denote the best-fit points obtained from the measurements. The

---

14 Here the gluon fusion process is abbreviated as ggF.

	$\widehat{\mu}^{\text{ggF}}$	$\widehat{\mu}^{\text{VBF}}$	ρ	a	b	c
$\gamma\gamma$	1.25 ± 0.24	1.02 ± 0.43	-0.32	19.42	3.44	6.05
VV^*	1.07 ± 0.16	1.23 ± 0.33	-0.24	43.29	4.91	9.61
ZZ^*	1.22 ± 0.33	1.18 ± 1.20	-0.58	13.70	2.17	1.04
WW^*	1.00 ± 0.18	1.22 ± 0.34	-0.17	30.63	2.80	8.70
$b\bar{b}$	1.44 ± 0.90	0.89 ± 0.27	0	1.24	0	13.52
$\tau\tau$	0.80 ± 0.49	1.34 ± 0.36	-0.40	4.93	2.68	9.23
$b\bar{b}/\tau\tau$	1.06 ± 0.41	1.04 ± 0.22	-0.23	6.19	2.68	22.53

Table 9: Combined best-fit signal strengths $\widehat{\mu}^{\text{ggF}}$, $\widehat{\mu}^{\text{VBF}}$ and correlation coefficient ρ for various Higgs decay modes (with $VV^* \equiv WW^*, ZZ^*$), as well as the coefficients a, b and c for the approximate χ^2 in Eq. (3.24).

parameters $\widehat{\mu}^{\text{ggF}}$, $\widehat{\mu}^{\text{VBF}}$, a, b and c for Eq. (3.24) (and, for completeness, the correlation coefficient ρ) resulting from the Gaussian approximation of the experimental results are listed in Table 9. Approximating $-2\ln(L)$ in this form can be useful for applications that aim at a quick assessment of the compatibility with the experimental data without invoking the complete likelihood calculation. In the fits presented below, we will apply the full machinery of `Lilith`, *i.e.*, we do not restrict ourselves to the Gaussian approximation whenever we can go beyond.

3.4.2 *Fits to reduced Higgs couplings*

Let us now turn to the fits of reduced couplings. To this end, as was already done in Eq. (3.10), we define scaling factors through the following Lagrangian,

$$
\mathscr{L} = g \left[C_W m_W W^\mu W_\mu + C_Z \frac{m_Z}{\cos\theta_W} Z^\mu Z_\mu \right.
$$
$$
\left. - C_U \frac{m_t}{2m_W} \bar{t}t - C_D \frac{m_b}{2m_W} \bar{b}b - C_D \frac{m_\tau}{2m_W} \bar{\tau}\tau \right] h \,, \tag{3.25}
$$

where the C_I are scaling factors for the couplings relative to their SM values, introduced to test possible deviations in the data from SM expectations. We set $C_W, C_Z > 0$ by convention while custodial symmetry implies $C_V \equiv C_W = C_Z$.

In addition to these tree-level couplings, we define the loop-induced couplings C_g and C_γ of the H to gg and $\gamma\gamma$, respectively. The contributions of SM particles to C_g and C_γ (as well as the corrections to VBF production) are computed at NLO QCD from the given values for C_U, C_D, C_W and C_Z following the procedure recommended by the LHC Higgs Cross Section Working Group [230] (using grids generated from `HIGLU` [240], `HDECAY` [241], and `VBFNLO` [257]). Alternatively, C_g and C_γ can be taken as free parameters. Finally, invisible or undetected branching ratios can also be included in the fit.

Deviations from SM expectations can be divided into two categories: 1. modifications of the tree-level couplings, as in extended Higgs sectors or Higgs portal models, and 2. vertex

loop effects from new particles beyond the SM, modifying in particular C_g and/or C_γ. We first discuss the former.
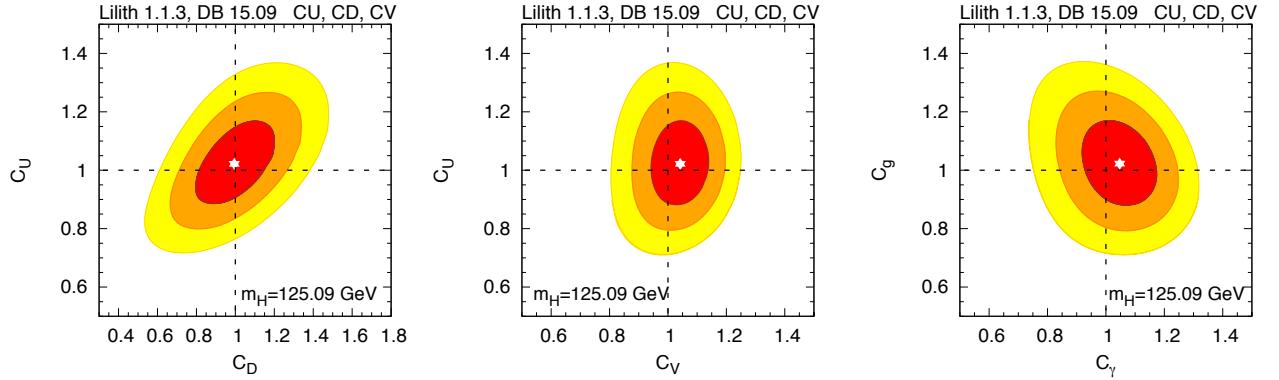

Figure 3.21: Fits of C_U, C_D and C_V (left and middle panels) and resulting C_g versus C_γ (right panel). The red, orange and yellow areas are the 68.3%, 95.4% and 99.7% CL regions, respectively. The best-fit points are marked as white stars. Invisible or undetected decays are assumed to be absent.

Figure 3.21 shows results for a 3-parameter fit of C_U, C_D, C_V, assuming custodial symmetry and taking C_U, $C_D > 0$. We note that at the 95.4% CL in 2D, C_U and C_V are constrained within roughly $\pm 20\%$; the uncertainty on C_D is about twice as large. The fact that $\hat{\mu}_{\gamma\gamma}^{\text{ggF}}$ and $\hat{\mu}_{VV}^{\text{VBF}}$ lie somewhat above one (cf. Fig. 3.20 and Table 9) leads to a slight preference for $C_V > 1$. The best fit is obtained for $C_U = 1.02$, $C_D = 0.99$ and $C_V = 1.04$, resulting in $C_g = 1.02$ and $C_\gamma = 1.05$. All these reduced couplings are however consistent with unity at the 1σ level. In 1D, i.e., profiling over the other parameters, we find $C_U = [0.93, 1.12]$ $([0.83, 1.22])$, $C_D = [0.86, 1.13]$ $([0.72, 1.27])$, and $C_V = [0.98, 1.11]$ $([0.91, 1.17])$ at the 68.3% (95.4%) CL. Correspondingly, for the loop-induced couplings, $C_g = [0.92, 1.12]$ $([0.83, 1.23])$ and $C_\gamma = [0.96, 1.13]$ $([0.87, 1.21])$.

To test possible deviations from custodial symmetry, we next define $C_{WZ} \equiv C_W/C_Z$ and perform a 4-parameter fit of C_U, C_D, C_Z, C_{WZ}. In 1D, we find $C_{WZ} = [0.87, 1.08]$ $([0.79, 1.24])$ and $C_Z = [0.96, 1.18]$ $([0.85, 1.28])$ at the 68.3% (95.4%) CL, see Fig. 3.22. The corresponding 68.3% and 95.4% CL intervals for C_W are $[0.96, 1.10]$ and $[0.89, 1.17]$.
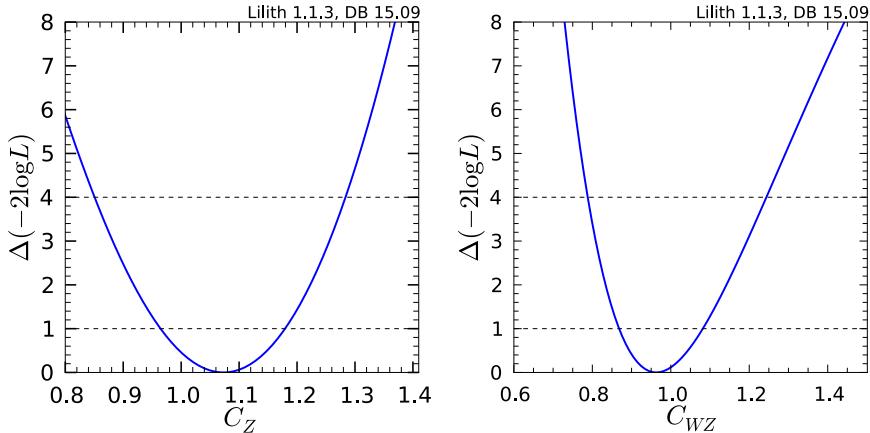

Figure 3.22: 1-dimensional profiles of C_Z and C_{WZ} from the 4-parameter fit of C_U, C_D, C_Z, C_{WZ}.

Direct Higgs measurements hence provide a significant constraint on deviations from custodial symmetry. Since values of C_W and C_Z greater than 1 cannot be excluded at the moment, the direct Higgs measurements still allow for the possibility that the observed state contains a component coming from Higgs representations higher than doublets or singlets. Indeed, for singlets or doublets, the reduced couplings $C_{W,Z}$ are necessarily smaller or equal to the SM unity value.

So far, we considered deviations of the tree-level reduced couplings from unity, but no extra loop contributions to the effective couplings to gluons and/or photons. If instead we fix $C_{U,D,V}$ but allow C_g and C_γ to vary freely, corresponding to loop contributions ΔC_g, ΔC_γ from new physics, we obtain the result shown in Fig. 3.23. (In this case, $C_{g,\gamma} \equiv \overline{C}_{g,\gamma} + \Delta C_{g,\gamma}$, with $\overline{C}_{g,\gamma}$ the contribution from SM particles.)
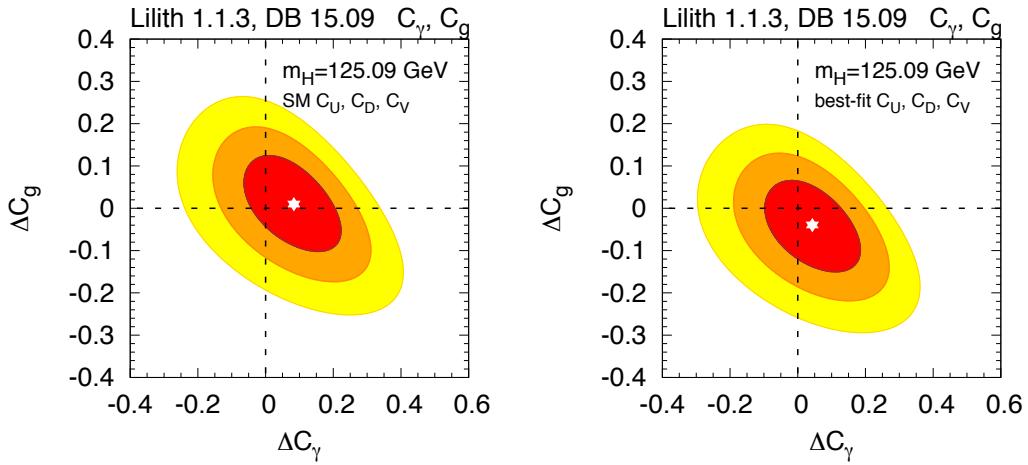
Figure 3.23: As Fig. 3.21 but for a 2-parameter fit of C_g and C_γ; in the left panel $\Delta C_g = C_g - 1$, $\Delta C_\gamma = C_\gamma - 1$ (SM values of C_U, C_D, C_V), while in the right panel C_U, C_D, C_V are fixed to their best-fit values and hence $\Delta C_g = C_g - 1.02$, $\Delta C_\gamma = C_\gamma - 1.05$.

The left panel corresponds to the case where $C_U = C_D = C_V = 1$; here the best-fit point has $\Delta C_g = 0.01$ and $\Delta C_\gamma = 0.08$. The right panel shows the situation when C_U, C_D, C_V are fixed to the best-fit values previously obtained: $C_U = 1.02$, $C_D = 0.99$, $C_V = 1.04$; in this case the best-fit point has $\Delta C_g = -0.04$ and $\Delta C_\gamma = 0.04$. In both cases, the SM solution $\Delta C_g = \Delta C_\gamma = 0$ lies perfectly well within the 1σ contour.

The current status of invisible (unseen) decays is as follows: (all limits are at the 95.4% CL)

- for SM-like couplings, $BR_{inv} < 0.09$ ($BR_{new} < 0.10$);

- for $C_{U,D,V} = 1$ but C_g, C_γ free, we find $BR_{inv} < 0.15$ ($BR_{new} < 0.17$);

- for free C_U, C_D, C_V but $C_V < 1$, we find $BR_{inv} < 0.16$ ($BR_{new} < 0.19$); this increases to $BR_{inv} < 0.22$ when C_V is unconstrained (in this case no limit on BR_{new} can be obtained [194]).

- for free $C_\gamma, C_g, C_W, C_Z, C_t, C_b, C_\tau$ with $C_W, C_Z \leq 1$, we find $BR_{inv} < 0.22$ ($BR_{new} < 0.32$).
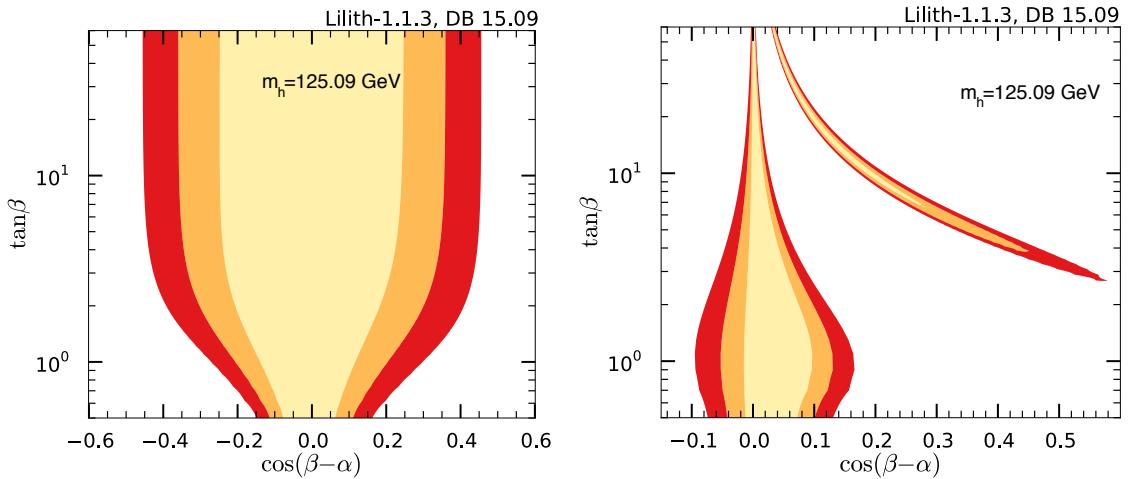
Figure 3.24: Fits of $\cos(\beta - \alpha)$ versus $\tan\beta$ for the 2HDM of Type I (left) and of Type II (right) for $m_h = 125.09$ GeV. The yellow, orange and red areas are the 68.3%, 95.4% and 99.7% CL regions, respectively. Effects of the extra Higgs states (such as $h \to AA$ or the charged Higgs contribution to $h \to \gamma\gamma$) are assumed to be absent.

3.4.3 *Two-Higgs-doublet models*

In view of the discussion above it is clear that models with an extended Higgs sector will be significantly constrained by the data. In particular, it is interesting to consider one of the simplest of such extensions of the SM, namely the two-Higgs-doublet models of Type I and Type II. The basic parameters describing the couplings of the neutral Higgs states to SM particles are only two at tree-level: the CP-even Higgs mixing angle α and the ratio of the vacuum expectation values, $\tan\beta = v_u/v_d$. The couplings, normalized to their SM values, of the light CP-even state h to vector bosons (C_V) and to up- and down-type fermions (C_U and C_D) are functions of α and β as given in Table 10; see *e.g.* [258] for details. The Type I and Type II models are distinguished only by the pattern of their fermionic couplings.

	Type I and II	Type I		Type II	
Higgs	C_V	C_U	C_D	C_U	C_D
h	$\sin(\beta - \alpha)$	$\cos\alpha/\sin\beta$	$\cos\alpha/\sin\beta$	$\cos\alpha/\sin\beta$	$-\sin\alpha/\cos\beta$

Table 10: Tree-level couplings C_V, C_U, C_D of the lighter CP-even state h in Type I and Type II 2HDMs.

To investigate the impact of the current Higgs data on 2HDMs, we vary α in $[-\pi/2, \pi/2]$ and β in $]0, \pi/2[$. We implicitly assume that there are no contributions from non-SM particles to the loop diagrams for C_γ and C_g. In particular, this means our results correspond to the case where the charged Higgs boson, whose loop might contribute to C_γ, is decoupled.

The results of the 2HDM fits are shown in Fig. 3.24 in the case that the observed state at 125.09 GeV is the lighter CP-even state h. In the case of the Type I model, we note a broad valley along the SM limit of $\cos(\beta - \alpha) = 0$, which is rather flat in $\tan\beta$. For $\tan\beta \gtrsim 2$, at 95.4% CL $|\cos(\beta - \alpha)|$ can be as large as ~ 0.35; only for $\tan\beta \ll 1$, one is forced to $|\cos(\beta - \alpha)| \approx 0$. The situation is quite different for the Type II model. Here we

observe two narrow valleys in the $\tan\beta$ versus $\cos(\beta-\alpha)$ plane. The first one lies along the SM solution $\cos(\beta-\alpha) = 0$; the largest deviation here occurs around $\tan\beta \approx 1$, where $\cos(\beta-\alpha) \approx 0.13$ is allowed at 95.4% CL; for both $\tan\beta \gg 1$ and $\tan\beta \ll 1$ one is forced into $|\cos(\beta-\alpha)| \approx 0$. The second minimum is a banana-shaped valley with $\tan\beta \gtrsim 4$ (7) and $\cos(\beta-\alpha) \lesssim 0.28$ (0.45) at 68.3% (95.4%) CL. This corresponds to a solution with $C_D \approx -1$, while $C_U \approx 1$, the so-called wrong-sign Yukawa coupling region [259].

In both Types, the SM limit $|\cos(\beta-\alpha)| \approx 0$ cannot be excluded since the measurements are all in agreement with the SM predictions. This so-called alignment limit is a major topic of the next part of this manuscript.

3.4.4 *Summary of the main results*

We presented an update of the global fits of the 125 GeV Higgs boson using all publicly available experimental results at the end of the first run of the LHC. The fits were performed using `Lilith-1.1.3` with the database `DB 15.09`. Our results can be summarized as follows:

1. The final ATLAS and CMS results for the different decay channels do not exhibit any deviation from the SM expectations, in particular for $h \to \gamma\gamma$ we get $\widehat{\mu}_{\gamma\gamma}^{\mathrm{ggF+ttH}} = 1.25 \pm 0.24$ and $\widehat{\mu}_{\gamma\gamma}^{\mathrm{VBF+VH}} = 1.02 \pm 0.43$ with a correlation of $\rho = -0.32$. This can be compared to the official ATLAS+CMS combination [188] which obtains $\widehat{\mu}_{\gamma\gamma}^{\mathrm{ggF+ttH}} = 1.19_{-0.25}^{+0.28}$ and $\widehat{\mu}_{\gamma\gamma}^{\mathrm{VBF+VH}} = 1.05_{-0.41}^{+0.44}$. While, as explained in Section 3.3, the official results cannot be exactly reproduced due to the lack of experimental information, the agreement is nevertheless very good.

2. In the C_U, C_D, C_V reduced coupling fit, we found $C_U = 1.02 \pm 0.10$, $C_D = 0.99 \pm 0.14$ and $C_V = 1.04 \pm 0.07$; in terms of the loop-induced couplings this corresponds to $C_g = 1.02 \pm 0.10$ and $C_\gamma = 1.05 \pm 0.08$ (in 1D), in perfect agreement with the SM predictions.

3. Custodial symmetry can also be tested. We found $C_{WZ} = 0.96_{-0.09}^{+0.12}$ in the C_U, C_D, C_Z, C_{WZ} fit, hence compatibility with custodial symmetry at the 1σ level.

4. Assuming SM-like couplings, the limit for invisible decays is $\mathrm{BR_{inv}} < 0.09$ at 95.4% CL. This changes to $\mathrm{BR_{inv}} < 0.22$ when C_U, C_D, C_V are allowed to vary.

5. In the general $C_\gamma, C_g, C_W, C_Z, C_t, C_b, C_\tau, \mathrm{BR_{new}}$ fit, we find $\mathrm{BR_{new}} < 0.32$ at 95.4% CL. The upper limit from the official ATLAS+CMS combination is $\mathrm{BR_{new}} < 0.34$ [188].

6. In the context of 2HDMs, barring loop contributions from the charged Higgs, the 95.4% CL limits in 1D are $\sin(\beta-\alpha) > 0.95$ in Type I and $\sin(\beta-\alpha) > 0.92$ (0.99) in Type II (requiring $C_D > 0$).

The results presented in the points 2, 3, 4 and 6 cannot be compared to the ATLAS+CMS official combination as the corresponding fits have not been performed in Ref. [188]. To provide an additional comparison with Ref. [188], we perform a 2-parameter fit of C_F and C_V. The comparison of the `Lilith` and official ATLAS+CMS fits can be found in Fig. 3.25. Though slightly more constraining for low values of C_F, the `Lilith` fit reproduces
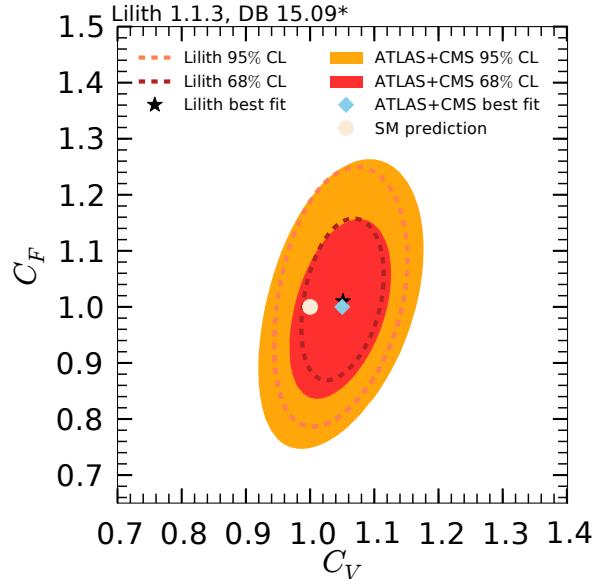
Figure 3.25: Fit of C_V and C_F and comparison to the official ATLAS+CMS combination [188].

with a good agreement the ATLAS+CMS result. For this specific plot, since the results contained in the database `DB 15.09` do not match exactly those used in the ATLAS+CMS combination (see caption of Table 8), the CMS VBF, $h \to b\bar{b}$ result [255] was not used in our fit (the $h \to$ invisible results have no impact on the current fit). This leads to a small improvement in the agreement with the official result.

With this slightly modified `Lilith` database, `DB 15.09`*, the determination of the BSM branching ratio $\mathrm{BR}_{\mathrm{new}}$ in the general fit ($C_\gamma, C_g, C_W, C_Z, C_t, C_b, C_\tau, \mathrm{BR}_{\mathrm{new}}$), summarized in point 5, is affected and the 95% CL limit becomes $\mathrm{BR}_{\mathrm{new}} < 0.35$ which improves the agreement with the ATLAS+CMS result.

While the direct measurements of the Higgs properties constrain sizably parts of the 2HDMs parameter space, this is just one of the numerous constraints that should be evaluated in order to fully assess the viability of these models. In the next chapter, we discuss in detail the phenomenology of the 2HDMs.

Part II

TWO-HIGGS-DOUBLET MODEL PHENOMENOLOGY

In this second part of the manuscript, we study the phenomenology of the CP-conserving two-Higgs-doublet models focusing on two aspects: the alignment limit and the presence of light Higgs states. Since the properties of the observed Higgs state are close to the Standard Model ones, we study the limit in which one of the two CP-even mass-eigenstates is aligned with the direction of the vacuum expectation values, hence automatically providing it Standard Model-like properties. Interestingly, this limit can be achieved with non-decoupled scalar states. After a general presentation of the theoretical framework, we study in detail the phenomenology of the alignment without decoupling limit and discuss the future prospects for observation of the extra scalar states at the Run 2 of the LHC. A focus on the regions with light Higgs bosons, below 60 GeV, is then given. Since both CP-even mass-eigenstates can be identified with the observed state, these two cases are systematically investigated and lead to a vast phenomenology.

Dans cette seconde partie du manuscrit, nous étudions la phénoménologie des modèles à deux doublets de Higgs conservant CP, en nous concentrant sur deux aspects : la limite d'alignement et la possible présence de bosons de Higgs légers. Étant donné que les propriétés du boson de Higgs observé sont similaires à celles prédites par le Modèle Standard, nous étudions la limite dans laquelle l'un des deux états propres de masse pair sous CP, est aligné dans la direction des valeurs moyennes dans le vide des deux doublets de Higgs, ce qui lui confère automatiquement des propriétés proches de celles du Modèle Standard. De manière intéressante, cette limite peut être achevée sans découplage des autres états scalaires. Après une présentation générale du cadre théorique, nous étudions en détail la phénoménologie de cette limite d'alignement sans découplage et présentons les perspectives d'observation des états scalaires supplémentaires pour la seconde période d'exploitation du LHC. Nous nous concentrons dans la suite à l'étude des bosons de Higgs légers, au-deçà de 60 GeV. Puisque les deux états propres de masse pairs sous CP peuvent être identifiés avec le boson observé au LHC, nous étudions systématiquement ces deux possibilités dans nos analyses, ce qui mène à une vaste phénoménologie.

TWO-HIGGS-DOUBLET MODELS: THEORETICAL FRAMEWORK

Though the observed Higgs properties show no significant deviation from the SM predictions, there is no conceptual reason for why the Higgs sector should be as minimal as in the SM. Theoretically, an extended Higgs sector is very attractive and, if experimentally confirmed, would deepen our comprehension of the EWSB mechanism at work in nature.

One of the simplest extension of the SM Higgs sector is that of the 2HDM. The idea of adding a second Higgs doublet to the SM was first introduced by T.D. Lee [260], as an attempt to find new sources of T/CP violation, either explicit or spontaneous. As mentioned earlier, new sources of CP violation are needed to achieve a viable scenario of baryogenesis, making the 2HDMs particularly attractive. The development of supersymmetry and of the Peccei-Quinn mechanism as a possible solution to the strong CP problem, then lead to a large literature on the study of multi-doublet Higgs sectors in general.

Here, we consider the non-supersymmetric CP-conserving 2HDM as an effective model relevant for LHC phenomenology. Though it may seem surprising not to consider CP-violation in a model originally constructed for this purpose, we do not aim at solving the baryogenesis problem here or any other problem of the SM, neither do we consider the 2HDM as a fundamental theory. We thus take an agnostic point of view and make no assumption on the origin of the model.

As shown in the previous chapter, the observed Higgs state has properties very similar to the SM one. In multi-doublet Higgs sectors, the alignment limit is a particular parameter space region in which one of the Higgs mass eigenstates aligns in field space with the direction of the scalar field vacuum expectation values, and its couplings automatically approach those of the SM Higgs boson. Naturally, this state can then be identified as the observed Higgs boson. A large part of the next chapter will be dedicated to a phenomenological study of this limit. Here, after a general presentation of the 2HDM, the theoretical structure of the alignment limit is discussed in details.

Parts of the following discussions are based on the publications "*Scrutinizing the alignment limit in two-Higgs-doublet models: $m_h = 125$ GeV*" [261] and "*Scrutinizing the alignment limit in two-Higgs-doublet models. II. $m_H = 125$ GeV*" [262] both in collaboration with John F. Gunion, Howard E. Haber, Yun Jiang and Sabine Kraml, and published in Physical Review D.

4.1 THE TWO-HIGGS-DOUBLET MODELS

In this section, we review the theoretical structure of the 2HDM. Comprehensive reviews of the model can be found in, *e.g.*, [258, 263–265]. In order to avoid tree-level Higgs-mediated

FCNCs, we will impose a Type-I or II structure on the Higgs-fermion interactions. This structure can be naturally implemented [266, 267] by imposing a softly-broken discrete $\mathbb{Z}_2$ symmetry on the dimension-four terms of the Higgs Lagrangian. Nevertheless, the absence of tree-level Higgs-mediated FCNCs is maintained, and FCNC effects generated at one loop are all small enough to be consistent with phenomenological constraints over a significant fraction of the 2HDM parameter space [268–271].

Even with the softly-broken discrete $\mathbb{Z}_2$ symmetry, new CP-violating phenomena in the Higgs sector are still possible, either explicitly due to a physical complex phase that cannot be removed from the scalar potential parameters or spontaneously due to a CP-violating vacuum state. Here, we shall assume that these CP-violating effects are absent, in which case one can choose a basis of scalar doublet Higgs fields such that all scalar potential parameters and the two neutral Higgs field vacuum expectation values are simultaneously real. Moreover, we will assume that only the neutral Higgs fields acquire non-zero vacuum expectation values, *i.e.*, the scalar potential does not admit the possibility of stable charge-breaking minima [272, 273].

4.1.1 The $\mathbb{Z}_2$-basis

The general 2HDM is obtained by adding a second $Y = +1$ weak doublet of complex scalar fields to the SM, we note Φ_1 and Φ_2 the two doublets,

$$\Phi_i = \frac{1}{\sqrt{2}} \begin{pmatrix} \sqrt{2}\phi_i^+ \\ v_i e^{i\xi_i} + \phi_i + i\eta_i \end{pmatrix} , \tag{4.1}$$

where ϕ_i^+ are complex scalar fields, and ϕ_i and η_i are the CP-even and -odd components of the doublets, respectively. In principle, both doublets can acquire a complex vev,

$$\langle \Phi_i^0 \rangle = v_i e^{i\xi_i}/\sqrt{2} , \tag{4.2}$$

where $i = 1, 2$, Φ_i^0 denotes the neutral component of the i-th doublet, $v_i \in \mathbb{R}$ and $0 \leq \xi_i \leq \pi$. Note that we explicitly require that the vacuum is invariant under $\mathrm{U}(1)_{em}$; the charged components do not acquire a vev. By a suitable $\mathrm{U}(1)_Y$ gauge transformation, the phase of one of the two doublets can always be chosen to be real and positive, say $v_1 \geq 0$ and $\xi_1 = 0$. In the following, we will furthermore assume that $v_2 \geq 0$ and $\xi_2 = 0$, *i.e.*, both vev are simultaneously real and positive, this is possible if the model does not exhibit spontaneous CP-violation. Conditions for the lack of explicit and spontaneous CP-violation will be discussed in Section 4.1.2, but for the moment, we assume that a fully CP-conserving model can be constructed.

The two doublets have kinetic terms $\sum_{i=1,2}(D_\mu \Phi_i)^\dagger (D^\mu \Phi_i)$ where the covariant derivative is defined exactly as in the SM. Therefore, the masses of the Z and $W^\pm$ bosons are expressed in terms of v_1 and v_2 as

$$m_{W^\pm}^2 = \frac{g^2(v_1^2 + v_2^2)}{4}, \; m_Z^2 = \frac{(g^2 + g'^2)(v_1^2 + v_2^2)}{4} , \tag{4.3}$$

and a comparison with Eqs. (2.11) and (2.13) shows that $v_1^2 + v_2^2 = v^2$. A convenient way to parametrize this relation is obtained by introducing the angle β as

$$v_1 = v \cos\beta , \; v_2 = v \sin\beta , \tag{4.4}$$

where $\beta \in [0, \pi/2]$ since $v_{1,2} \geq 0$. Note that $\tan \beta = v_2/v_1$ has in general no physical meaning since one is free to perform a redefinition of the two doublets: $(\Phi_1, \Phi_2)^T \to U(\Phi_1, \Phi_2)^T$ where U is a 2×2 unitary matrix. Basis-independent methods for the 2HDM were developed [274–276], leading in particular to Feynman rules free of $\tan \beta$. It is only when considering a specific model that a preferred basis may be singled out, in which case $\tan \beta$ is promoted to a physical parameter. In particular, asking for certain Higgs-fermion interactions to vanish in a preferred basis makes $\tan \beta$ physical [275]. In the following, we will not employ basis-independent methods but will only work in models where a physical distinction between the two doublets is present.

The most general renormalizable, Lorentz and gauge invariant scalar potential with these two Higgs doublets can be written as

$$
\begin{aligned}
\mathcal{V}_{2\text{HDM}} \;=\; & m_{11}^2 \Phi_1^\dagger \Phi_1 + m_{22}^2 \Phi_2^\dagger \Phi_2 - [m_{12}^2 \Phi_1^\dagger \Phi_2 + \text{h.c.}] + \tfrac{1}{2}\lambda_1 (\Phi_1^\dagger \Phi_1)^2 + \tfrac{1}{2}\lambda_2 (\Phi_2^\dagger \Phi_2)^2 \\
& + \lambda_3 (\Phi_1^\dagger \Phi_1)(\Phi_2^\dagger \Phi_2) + \lambda_4 (\Phi_1^\dagger \Phi_2)(\Phi_2^\dagger \Phi_1) \\
& + \left\{ \tfrac{1}{2}\lambda_5 (\Phi_1^\dagger \Phi_2)^2 + \left[\lambda_6 (\Phi_1^\dagger \Phi_1) + \lambda_7 (\Phi_2^\dagger \Phi_2) \right] \Phi_1^\dagger \Phi_2 + \text{h.c.} \right\}, \quad (4.5)
\end{aligned}
$$

where $m_{12}^2, \lambda_{5,6,7}$ are in principle complex parameters. As announced previously however, we will assume that all the parameters are real in order to avoid explicit CP-violation. Moreover, the softly-broken $\mathbb{Z}_2$ symmetry that we will impose in order to forbid Higgs-mediated tree-level FCNCs, $\Phi_i \to (-1)^{i-1} \Phi_i$, leads to $\lambda_6 = \lambda_7 = 0$. The softly-breaking term is the dimension-2 operator parametrized by m_{12}^2. This basis of scalar doublets, (Φ_1, Φ_2), is called the $\mathbb{Z}_2$-basis. Under these restrictions, minimizing the potential with respect to v_1 and v_2 leads to the conditions

$$
m_{11}^2 \;=\; m_{12}^2 t_\beta - \tfrac{1}{2}v^2 \left(\lambda_1 c_\beta^2 + \lambda_{345} s_\beta^2 \right), \tag{4.6}
$$

$$
m_{22}^2 \;=\; m_{12}^2 t_\beta^{-1} - \tfrac{1}{2}v^2 \left(\lambda_2 s_\beta^2 + \lambda_{345} c_\beta^2 \right), \tag{4.7}
$$

where the shorthand notations $s_x \equiv \sin x$, $c_x \equiv \cos x$ and $t_x \equiv \tan x$ are used and $\lambda_{345} \equiv \lambda_3 + \lambda_4 + \lambda_5$.

Since the EWSB mechanism is the same as in the SM, only with two doublets sharing the breaking, we expect $8 - 3 = 5$ physical scalar states. From Eq. (4.5) it is straightforward to derive the tree-level masses of the physical states of the model. For the pseudoscalar A and charged $H^\pm$ states,

$$
m_A^2 \;=\; \overline{m}^2 - \lambda_5 v^2, \tag{4.8}
$$

$$
m_{H^\pm}^2 \;=\; m_A^2 + \frac{1}{2}v^2(\lambda_5 - \lambda_4), \tag{4.9}
$$

where,

$$
\overline{m}^2 \equiv \frac{m_{12}^2}{s_\beta c_\beta}. \tag{4.10}
$$

In the CP-even sector, the components from the two doublets generically mix according to the squared-mass matrix

$$
\mathcal{M}^2 \equiv \begin{pmatrix} \lambda_1 v^2 c_\beta^2 + (m_A^2 + \lambda_5 v^2)s_\beta^2 & \left[\lambda_{345} v^2 - (m_A^2 + \lambda_5 v^2) \right] s_\beta c_\beta \\ \left[\lambda_{345} v^2 - (m_A^2 + \lambda_5 v^2) \right] s_\beta c_\beta & \lambda_2 v^2 s_\beta^2 + (m_A^2 + \lambda_5 v^2) c_\beta^2 \end{pmatrix}. \tag{4.11}
$$

The two CP-even mass-eigenstates h and H are found by diagonalizing this matrix, introducing the mixing angle α,

$$
\begin{pmatrix} \sqrt{2}\ \mathrm{Re}\ \Phi_1^0 - v_1 \\ \sqrt{2}\ \mathrm{Re}\ \Phi_2^0 - v_2 \end{pmatrix} = \begin{pmatrix} \phi_1 \\ \phi_2 \end{pmatrix} = \begin{pmatrix} c_\alpha & -s_\alpha \\ s_\alpha & c_\alpha \end{pmatrix} \begin{pmatrix} H \\ h \end{pmatrix} = R_\alpha \begin{pmatrix} H \\ h \end{pmatrix}, \tag{4.12}
$$

where,

$$
R_\alpha \equiv \begin{pmatrix} c_\alpha & -s_\alpha \\ s_\alpha & c_\alpha \end{pmatrix}. \tag{4.13}
$$

This then leads to

$$
m_{H,h}^2 = \tfrac{1}{2}\left[\mathcal{M}_{11}^2 + \mathcal{M}_{22}^2 \pm \Delta\right], \tag{4.14}
$$

where $m_H \geq m_h$ by definition and the non-negative quantity Δ is defined by

$$
\Delta \equiv \sqrt{(\mathcal{M}_{11}^2 - \mathcal{M}_{22}^2)^2 + 4(\mathcal{M}_{12}^2)^2}. \tag{4.15}
$$

The mixing angle α, which is defined modulo π, can easily be evaluated from Eqs. (4.11) and (4.12). It is often convenient to restrict the range of this mixing angle to $|\alpha| \leq \pi/2$. In this case, c_α is non-negative and is given by

$$
c_\alpha = \sqrt{\frac{\Delta + \mathcal{M}_{11}^2 - \mathcal{M}_{22}^2}{2\Delta}} = \sqrt{\frac{\mathcal{M}_{11}^2 - m_h^2}{m_H^2 - m_h^2}}, \tag{4.16}
$$

and the sign of s_α is given by the sign of $\mathcal{M}_{12}^2$. Explicitly,

$$
s_\alpha = \frac{\sqrt{2}\,\mathcal{M}_{12}^2}{\sqrt{\Delta(\Delta + \mathcal{M}_{11}^2 - \mathcal{M}_{22}^2)}} = \mathrm{sgn}(\mathcal{M}_{12}^2)\sqrt{\frac{m_H^2 - \mathcal{M}_{11}^2}{m_H^2 - m_h^2}}. \tag{4.17}
$$

In deriving Eqs. (4.16) and (4.17), we have implicitly assumed that $m_h \neq m_H$. The mass-degenerate case is singular; in this situation, the angle α is undefined since any two linearly independent combinations of h and H can serve as the physical states. In the rest of this manuscript, we will not consider this case further.

4.1.2 *CP-violation in the 2HDM scalar sector*

We go back to the general scalar potential Eq. (4.5) and analyze conditions for CP-violation. Let us first discuss the conditions for the lack of explicit CP-violation in the general 2HDM. Such an analysis should in principle be carried in a basis-independent way, since going into a different basis for the doublets through a U(2) transformation generically introduces new phases. They have first been carried through with such methods in Refs. [274, 277–281]. More general or recent discussions of CP-violation in the 2HDMs can be found *e.g.* in Refs. [158, 273, 282–287]. Here, conditions for CP-conservation in the 2HDM are derived in a basis dependent way [264], they turn out to be sufficient but not necessary conditions [281].

CP is explicitly conserved whenever there exists a basis in which all the parameters are simultaneously real. The scalar potential is given by Eq. (4.5), and performing the rephasing $\Phi_2 \to e^{-i\xi}$ leads to the following ξ-dependent terms,

$$\mathcal{V} \supset -e^{-i\xi}m_{12}^2\Phi_1^\dagger\Phi_2 + \frac{1}{2}e^{-2i\xi}\lambda_5(\Phi_1^\dagger\Phi_2)^2 + e^{-i\xi}\left[\lambda_6(\Phi_1^\dagger\Phi_1) + \lambda_7(\Phi_2^\dagger\Phi_2)\right]\Phi_1^\dagger\Phi_2 + \text{h.c.} \quad (4.18)$$

The parameters in front of each operator can thus be complex and be written as $m_{12}^2 = |m_{12}^2|e^{i\alpha_m}$ and $\lambda_{5,6,7} = |\lambda_{5,6,7}|e^{i\alpha_{5,6,7}}$. The potential will then be explicitly CP-conserving if there exists a rephasing of all the terms such that the dependence on ξ completely disappears, i.e.,

$$\xi = \alpha_m + n_m\pi, \quad (4.19)$$

$$2\xi = \alpha_5 + n_5\pi, \quad (4.20)$$

$$\xi = \alpha_{6,7} + n_{6,7}\pi, \quad (4.21)$$

where $n_{m,5,6,7}$ are integers. Fixing ξ as in the first equation, such as to make m_{12}^2 real, yield

$$(2\alpha_m - \alpha_5) = (n_5 - 2n_m)\pi \implies \text{Im}\left[(m_{12}^2)^2\lambda_5^*\right] = 0, \quad (4.22)$$

$$(\alpha_m - \alpha_{6,7}) = (n_{6,7} - n_m)\pi \implies \text{Im}\left[m_{12}^2\lambda_{6,7}^*\right] = 0, \quad (4.23)$$

which are all satisfied if $\alpha_{5,6,7} = 0$, i.e., if all parameters of the general 2HDM scalar potential are real.

Spontaneous CP-violation occurs whenever a CP-symmetry of the Lagrangian is not conserved by the vacuum. Technically, writing $\langle\Phi_1^0\rangle = v_1/\sqrt{2}$ (always possible because of U(1) gauge symmetry) and $\langle\Phi_2^0\rangle = v_2e^{i\xi_2}/\sqrt{2}$, this would mean that in the vacuum $\xi_2 \neq 0, \pi$. In the vacuum, assuming explicit CP-conservation, the ξ_2 dependent terms of the scalar potential takes the form

$$\langle\mathcal{V}\rangle \supset -m_{12}^2v_1v_2\cos\xi_2 + \frac{1}{4}\lambda_5(v_1v_2)^2\cos(2\xi_2) + \frac{1}{2}(\lambda_6v_1 + \lambda_7v_2)v_1v_2\cos\xi_2. \quad (4.24)$$

The first and second derivatives of $\langle\mathcal{V}\rangle$ with respect to $\cos\xi_2$ are

$$\frac{\partial\langle\mathcal{V}\rangle}{\partial\cos\xi_2} = -m_{12}^2v_1v_2 + \lambda_5(v_1v_2)^2\cos\xi_2 + \frac{1}{2}(\lambda_6v_1 + \lambda_7v_2)v_1v_2, \quad (4.25)$$

$$\frac{\partial^2\langle\mathcal{V}\rangle}{\partial(\cos\xi_2)^2} = \lambda_5(v_1v_2)^2. \quad (4.26)$$

While the curvature of the potential at the minimum imposes $\lambda_5 > 0$, the first derivative imposes

$$\left|m_{12}^2 - \frac{1}{2}(\lambda_6v_1^2 + \lambda_7v_2^2)\right| < \lambda_5v_1v_2, \quad (4.27)$$

as the condition for the presence of spontaneous CP-violation in the 2HDM. For $\lambda_6 = \lambda_7 = 0$, the region of the 2HDM that we will consider as a consequence of the $\mathbb{Z}_2$ symmetry, using Eq. (4.8) for determining the mass of A in the spontaneous CP-violating case leads to $m_A^2 < 0$ as may have been expected. This existence of such a tachyonic direction indeed leads to an instability of the scalar potential which then develop a CP-violating vacuum. For all analyses performed in this section, we enforce CP-conservation, i.e., we require that all parameters of the scalar potential are real and that $m_A^2 > 0$ (we will indeed only consider the case $\lambda_6 = \lambda_7 = 0$ in the following).

4.1.3 *The Higgs basis*

Though we chose $\tan\beta$ to be a physical parameter, it is still possible to redefine the two scalar doublets and go a basis in which the full vev resides entirely in one doublet [274, 279]. This is the Higgs-basis (H_1, H_2), for which the doublets vevs are thus

$$\langle H_1^0 \rangle = v/\sqrt{2} > 0 \ , \quad \langle H_2^0 \rangle = 0. \tag{4.28}$$

Looking back at Eq. (4.4), (H_1, H_2) can are therefore defined as

$$\begin{pmatrix} \Phi_1 \\ \Phi_2 \end{pmatrix} \equiv \begin{pmatrix} c_\beta & -s_\beta \\ s_\beta & c_\beta \end{pmatrix} \begin{pmatrix} H_1 \\ H_2 \end{pmatrix} = R_\beta \begin{pmatrix} H_1 \\ H_2 \end{pmatrix} . \tag{4.29}$$

As H_1 carries the full vev, it must contain the Goldstone bosons that will form the longitudinal component of the Z and $W^\pm$ bosons. It can thus be parametrized as

$$H_1 = \frac{1}{\sqrt{2}} \begin{pmatrix} \sqrt{2}G^+ \\ v + h_1 + iG^0 \end{pmatrix} , \tag{4.30}$$

where G^+ and G^0 are the SM Goldstone fields. The field h_1 is not a mass-eigenstate, it will actually mix with the neutral CP-even component of H_2, the later being parametrized as

$$H_2 = \frac{1}{\sqrt{2}} \begin{pmatrix} \sqrt{2}H^+ \\ h_2 + iA \end{pmatrix} , \tag{4.31}$$

where H^+ is the charged Higgs field and A the CP-odd scalar field.

Comparing Eqs. (4.12) and (4.29), we see that

$$\begin{pmatrix} H \\ h \end{pmatrix} = R_\alpha^{-1} \begin{pmatrix} \phi_1 \\ \phi_2 \end{pmatrix} = R_\alpha^{-1} R_\beta \begin{pmatrix} h_1 \\ h_2 \end{pmatrix} = R_{\beta-\alpha} \begin{pmatrix} h_1 \\ h_2 \end{pmatrix} , \tag{4.32}$$

or more explicitly,

$$\begin{align} H &= (\sqrt{2}\,\mathrm{Re}\,H_1^0 - v)c_{\beta-\alpha} - \sqrt{2}\,\mathrm{Re}\,H_2^0\, s_{\beta-\alpha} , \tag{4.33} \\ h &= (\sqrt{2}\,\mathrm{Re}\,H_1^0 - v)\, s_{\beta-\alpha} + \sqrt{2}\,\mathrm{Re}\,H_2^0\, c_{\beta-\alpha} , \tag{4.34} \end{align}$$

and $\beta - \alpha$ can thus be interpreted as the CP-even mixing angle in the Higgs basis. As such it will play a crucial role in the phenomenology of the CP-even sector. In particular, the couplings of H and h to electroweak gauge bosons will be driven by $c_{\beta-\alpha}$ and $s_{\beta-\alpha}$ respectively, since these are the factors that respectively project the H_1 component, *e.g.* the doublet with the full vev, out of H and h.

The scalar potential in the Higgs basis can be written as

$$\begin{align} \mathcal{V} &= Y_1 H_1^\dagger H_1 + Y_2 H_2^\dagger H_2 + Y_3[H_1^\dagger H_2 + \text{h.c.}] + \tfrac{1}{2}Z_1(H_1^\dagger H_1)^2 + \tfrac{1}{2}Z_2(H_2^\dagger H_2)^2 + Z_3(H_1^\dagger H_1)(H_2^\dagger H_2) \\ &+ Z_4(H_1^\dagger H_2)(H_2^\dagger H_1) + \left\{ \tfrac{1}{2}Z_5(H_1^\dagger H_2)^2 + \left[Z_6(H_1^\dagger H_1) + Z_7(H_2^\dagger H_2)\right]H_1^\dagger H_2 + \text{h.c.} \right\} . \tag{4.35} \end{align}$$

As performed explicitly previously for the $\mathbb{Z}_2$-basis, it is possible to find a rephasing of H_2 such that all potential parameters are real, in which case the scalar potential and Higgs

vacuum are CP-conserving. Henceforth, we will always adopt such a real basis. Note that no rephasing of H_1 is permitted since by assumption the vev v is real and positive. The relation between the $\mathbb{Z}_2$-basis parameters and the Higgs basis parameters are obtained as follows for $\lambda_6 = \lambda_7 = 0$,

$$
\begin{align}
Z_1 &\equiv \lambda_1 c_\beta^4 + \lambda_2 s_\beta^4 + \tfrac{1}{2}\lambda_{345} s_{2\beta}^2 \,, \tag{4.36}\\
Z_2 &\equiv \lambda_1 s_\beta^4 + \lambda_2 c_\beta^4 + \tfrac{1}{2}\lambda_{345} s_{2\beta}^2 \,, \tag{4.37}\\
Z_i &\equiv \tfrac{1}{4} s_{2\beta}^2 \left[\lambda_1 + \lambda_2 - 2\lambda_{345}\right] + \lambda_i \,, \quad \text{(for } i = 3, 4 \text{ or } 5) \,, \tag{4.38}\\
Z_6 &\equiv -\tfrac{1}{2} s_{2\beta} \left[\lambda_1 c_\beta^2 - \lambda_2 s_\beta^2 - \lambda_{345} c_{2\beta}\right] \,, \tag{4.39}\\
Z_7 &\equiv -\tfrac{1}{2} s_{2\beta} \left[\lambda_1 s_\beta^2 - \lambda_2 c_\beta^2 + \lambda_{345} c_{2\beta}\right] \,, \tag{4.40}
\end{align}
$$

and,

$$
\begin{align}
Y_1 &= m_{11}^2 c_\beta^2 + m_{22}^2 s_\beta^2 - m_{12}^2 s_{2\beta} \,, \tag{4.41}\\
Y_2 &= m_{11}^2 s_\beta^2 + m_{22}^2 c_\beta^2 + m_{12}^2 s_{2\beta} \,, \tag{4.42}\\
Y_3 &= \tfrac{1}{2}(m_{22}^2 - m_{11}^2)s_{2\beta} - m_{12}^2 c_{2\beta} \,. \tag{4.43}
\end{align}
$$

Since there are five non-vanishing λ_i and seven non-vanishing Z_i, there should be some relations between the Z_i, specifically, the following two identities are satisfied if $\beta \neq 0, \tfrac{1}{4}\pi, \tfrac{1}{2}\pi$ [288]:[15]

$$
\begin{align}
Z_2 &= Z_1 + 2(Z_6 + Z_7)\cot 2\beta \,, \tag{4.44}\\
Z_{345} &= Z_1 + 2Z_6 \cot 2\beta - (Z_6 - Z_7)\tan 2\beta \,, \tag{4.45}
\end{align}
$$

where $Z_{345} \equiv Z_3 + Z_4 + Z_5$. Furthermore, at the scalar potential minimum, Y_1 and Y_2 can be expressed in terms of the Z_1 and Z_6 as

$$
Y_1 = -\tfrac{1}{2}Z_1 v^2 \,, \quad Y_3 = -\tfrac{1}{2}Z_6 v^2 \,. \tag{4.46}
$$

The masses of the physical scalar states can easily be obtained from the scalar potential Eq. (4.35),

$$
\begin{align}
m_{H^\pm}^2 &= Y_2 + \tfrac{1}{2}Z_3 v^2 \,, \tag{4.47}\\
m_A^2 &= m_{H^\pm}^2 + \tfrac{1}{2}(Z_4 - Z_5)v^2 \,, \tag{4.48}
\end{align}
$$

and the two CP-even physical masses are obtained from the squared-mass matrix

$$
\mathcal{M}_H^2 = \begin{pmatrix} Z_1 v^2 & Z_6 v^2 \\ Z_6 v^2 & m_A^2 + Z_5 v^2 \end{pmatrix} \,. \tag{4.49}
$$

Upon diagonalization, the CP-even scalar masses are expressed as

$$
m_{H,h}^2 = \tfrac{1}{2}\left[m_A^2 + (Z_1 + Z_5)v^2 \pm \Delta_H\right] \,, \tag{4.50}
$$

---

[15] For $\beta = 0, \tfrac{1}{2}\pi$, the $\mathbb{Z}_2$-basis and the Higgs basis coincide, in which case $Z_6 = Z_7 = 0$ and Z_1, Z_2, Z_{345} are independent quantities. For $\beta = \tfrac{1}{4}\pi$, the two relations are $Z_1 = Z_2$ and $Z_6 = Z_7$, and Z_{345} is an independent quantity.

where

$$\Delta_H \equiv \sqrt{\left[m_A^2 + (Z_5 - Z_1)v^2\right]^2 + 4Z_6^2 v^4}\,. \tag{4.51}$$

The off-diagonal term may be expressed as

$$|Z_6|v^2 = \sqrt{(m_H^2 - Z_1 v^2)(Z_1 v^2 - m_h^2)}\,. \tag{4.52}$$

The three squared-mass matrix elements can be expressed in terms of the physical CP-even masses and the mixing angle $\beta - \alpha$,

$$
\begin{aligned}
Z_1 v^2 &= m_h^2 s_{\beta-\alpha}^2 + m_H^2 c_{\beta-\alpha}^2\,, & (4.53)\\
Z_5 v^2 &= m_H^2 s_{\beta-\alpha}^2 + m_h^2 c_{\beta-\alpha}^2 - m_A^2\,, & (4.54)\\
Z_6 v^2 &= (m_h^2 - m_H^2) s_{\beta-\alpha} c_{\beta-\alpha}\,, & (4.55)
\end{aligned}
$$

which then lead to

$$m_h^2 = m_A^2 + \left(Z_5 + Z_6 \frac{s_{\beta-\alpha}}{c_{\beta-\alpha}}\right)v^2 = \left(Z_1 + Z_6 \frac{c_{\beta-\alpha}}{s_{\beta-\alpha}}\right)v^2\,, \tag{4.56}$$

$$m_H^2 = m_A^2 + \left(Z_5 - Z_6 \frac{c_{\beta-\alpha}}{s_{\beta-\alpha}}\right)v^2 = \left(Z_1 - Z_6 \frac{s_{\beta-\alpha}}{c_{\beta-\alpha}}\right)v^2\,. \tag{4.57}$$

The two above equations are not singular in the $c_{\beta-\alpha}, s_{\beta-\alpha} \to 0$ limits because Z_6 is proportional to $s_{\beta-\alpha} c_{\beta-\alpha}$, see Eq. (4.55). Note also that Eq. (4.55) implies that

$$Z_6 s_{\beta-\alpha} c_{\beta-\alpha} \leq 0\,, \tag{4.58}$$

because of the definite mass hierarchy between H and h. Having established a convention where $0 \leq \beta \leq \frac{1}{2}\pi$, we are no longer free to redefine the Higgs basis field $H_2 \to -H_2$. Consequently, the sign of Z_6 is meaningful in this convention.

To complete the set of Eqs. (4.53)–(4.55), we give the expressions of the rest of the Z_i in terms of the physical masses and the mixing angles,

$$
\begin{aligned}
Z_2 v^2 &= m_h^2 (s_{\beta-\alpha} + 2c_{\beta-\alpha}\cot 2\beta)^2 + m_H^2 (c_{\beta-\alpha} - 2s_{\beta-\alpha}\cot 2\beta)^2 - 4\overline{m}^2 \cot^2 2\beta\,, & (4.59)\\
Z_3 v^2 &= m_h^2 s_{\beta-\alpha}^2 + m_H^2 c_{\beta-\alpha}^2 + 2(m_h^2 - m_H^2)c_{\beta-\alpha}s_{\beta-\alpha}\cot 2\beta + 2(m_{H^\pm}^2 - \overline{m}^2)\,, & (4.60)\\
Z_4 v^2 &= m_H^2 s_{\beta-\alpha}^2 + m_h^2 c_{\beta-\alpha}^2 + m_A^2 - 2m_{H^\pm}^2\,. & (4.61)\\
Z_7 v^2 &= 2\left(m_h^2 c_{\beta-\alpha}^2 + m_H^2 s_{\beta-\alpha}^2 - \overline{m}^2\right)\cot 2\beta + (m_h^2 - m_H^2)s_{\beta-\alpha}c_{\beta-\alpha}\,. & (4.62)
\end{aligned}
$$

4.1.4 Yukawa interactions

In the $\mathbb{Z}_2$-basis, the more general Yukawa Lagrangian reads

$$
\begin{aligned}
-\mathscr{L}_Y &= \sum_{i=1,2} \overline{Q}_L \mathbf{Y}_{U,i} \widetilde{\Phi}_i u_R + \overline{Q}_L \mathbf{Y}_{D,i}\Phi_i d_R + \overline{L}_L \mathbf{Y}_{E,i}\Phi_i e_R + \text{h.c.}\\
&= \sum_{i=1,2} \overline{Q}_L \left(\frac{\sqrt{2}\mathbf{m}_{U,i}}{v_i}\right)\widetilde{\Phi}_i u_R + \overline{Q}_L \left(\frac{\sqrt{2}\mathbf{m}_{D,i}}{v_i}\right)\Phi_i d_R + \overline{L}_L \left(\frac{\sqrt{2}\mathbf{m}_{E,i}}{v_i}\right)\Phi_i e_R + \text{h.c.},
\end{aligned}
$$

$$\tag{4.63}$$

where the sum is over the two Higgs doublets, all gauge, flavor and Lorentz indices are omitted for clarity, and the fermion mass matrices are introduced as

$$\mathbf{m}_{f,i} = \frac{v_i \mathbf{Y}_{f,i}}{\sqrt{2}} \ . \tag{4.64}$$

Since the two scalar doublets $\Phi_{i=1,2}$ have the same quantum numbers, they can both couple to the fermion bilinears $\overline{Q}_L d_R$, $\overline{Q}_L u_R$ and $\overline{L}_L e_R$ with different Yukawa couplings. This is quite problematic as this generically induces tree-level FCNCs through neutral Higgs exchange. This can most easily be observed in the Higgs basis, where the Yukawa Lagrangian reads

$$-\mathscr{L}_Y = \overline{Q}_L \left(\widetilde{\mathbf{Y}}_U \widetilde{H_1} + \boldsymbol{\rho}_U \widetilde{H_2} \right) u_R + \overline{Q}_L \left(\widetilde{\mathbf{Y}}_U H_1 + \boldsymbol{\rho}_U H_2 \right) d_R + \overline{L}_L \left(\widetilde{Y}_E H_1 + \boldsymbol{\rho}_E H_2 \right) e_R + \text{h.c.}, \tag{4.65}$$

where

$$\begin{aligned} \widetilde{\mathbf{Y}}_f &= \ c_\beta \mathbf{Y}_{f,1} + s_\beta \mathbf{Y}_{f,2}, \\ \boldsymbol{\rho}_f &= -s_\beta \mathbf{Y}_{f,1} + c_\beta \mathbf{Y}_{f,2}, \end{aligned} \tag{4.66}$$

and $f = U, D, E$. Since H_1 is the SM-like doublet, *i.e.*, it has the full vev, the matrices $\widetilde{\mathbf{Y}}_f$ can be identified with the SM Yukawa couplings. The $\boldsymbol{\rho}_f$ matrices hence only contribute to the Higgs-fermion interactions and not to the fermion masses. Now, since $\widetilde{\mathbf{Y}}_f$ and $\boldsymbol{\rho}_f$ are linearly independent, diagonalizing the former by going to the fermion mass eigenstate basis will not simultaneously diagonalize the latter, hence non-diagonal Higgs-fermion interactions are a generic feature of the general 2HDM. This completely general Yukawa sector is sometimes referred to as the Type III 2HDM in the literature. With arbitrary parameters, the tree-level contributions to flavor observables are generally very large and in conflict with flavor experimental observations. A popular ansatz proposed by Cheng and Sher [289] to overcome this problem consists in expressing the $\boldsymbol{\rho}_f$ matrices in the fermion mass eigenstate basis in terms of geometric means of the fermion masses, $\boldsymbol{\rho}_f^{ij} = \lambda^{ij} \sqrt{m_f^i m_f^j}/v$ where no sum on i, j is understood. This naturally suppress undesirable FCNCs effects upon a possible tuning of the λ^{ij}. We won't pursue the analysis of this model further here.

Natural flavor conservation [266, 267] is a solution to the problem of tree-level FCNCs. A $\mathbb{Z}_2$ symmetry is imposed on the dimension-four terms of the Higgs scalar potential in the $\mathbb{Z}_2$-basis under which the two doublets transform as $(\Phi_1, \Phi_2) \rightarrow (\Phi_1, -\Phi_2)$ and the quark fields have non trivial transformations as well. This then forbids both Φ_i to couple simultaneously to a given fermion bilinear [see Eq. (4.63)] and as a result, either $\mathbf{Y}_f^1$ or $\mathbf{Y}_f^2$ should vanish for each f. The $\widetilde{\mathbf{Y}}_f$ and $\boldsymbol{\rho}_f$ matrices become then proportional to each other and can be diagonalized simultaneously. Higgs mediated tree-level FCNCs are thus absent. There are only four independent choices of the fermion charges under the $\mathbb{Z}_2$ symmetry, they lead to the so-called Type I, II, X and Y models as exhibited in Table 11.

From these charge assignments, the Higgs-fermion couplings can be computed in terms of α and β. We show this explicitly in the Type I and II models for the neutral states. A summary of these results can be found in Table 12. The Type X, Y and the charged Higgs couplings are not considered in the rest of this document but can be obtained in the exact same fashion.

	Φ_1	Φ_2	Q_L, L_L	u_R	d_R	e_R	Conditions
Type I	+	−	+	−	−	−	$\mathbf{Y}_{(U,D,E),2} = 0$
Type II	+	−	+	−	+	+	$\mathbf{Y}_{U,2} = 0,\ \mathbf{Y}_{(D,E),2} = 0$
Type X (lepton specific)	+	−	+	−	−	+	$\mathbf{Y}_{(U,D),1} = 0,\ \mathbf{Y}_{E,2} = 0$
Type Y (flipped)	+	−	+	−	+	−	$\mathbf{Y}_{(U,E),1} = 0,\ \mathbf{Y}_{D,2} = 0$

Table 11: Four possible $\mathbb{Z}_2$ charge assignments that forbid tree-level Higgs-mediated FCNC effects in the 2HDM [290].

From Table 11, the Yukawa Lagrangian in Type I reads

$$
\begin{aligned}
-\mathscr{L}_Y^{\mathrm{I}} = \ & \overline{Q}_L \mathbf{Y}_{U,2} \left[s_\beta \widetilde{H_1} + c_\beta \widetilde{H_2} \right] u_R + \overline{Q}_L \mathbf{Y}_{D,2} \left[s_\beta H_1 + c_\beta H_2 \right] d_R \\
& + \overline{L}_L \mathbf{Y}_{E,2} \left[s_\beta H_1 + c_\beta H_2 \right] e_R + \text{h.c.}
\end{aligned}
\tag{4.67}
$$

Developing the $\mathrm{SU}(2)_L$ products and keeping only terms involving the CP-even states yields

$$
-\mathscr{L}_Y^{\mathrm{I}} \supset \sum_{f=u,d,e} \overline{f}_L \mathbf{Y}_{f,2} \left[s_\beta (h_1 + v) + c_\beta h_2 \right] f_R + \text{h.c.}
\tag{4.68}
$$

Projecting on the Higgs mass eigenstates, see Eq. (4.32),

$$
\begin{aligned}
-\mathscr{L}_Y^{\mathrm{I}} \supset\ & \sum_f \overline{f}_L \left(\frac{\mathbf{Y}_{f,2}}{\sqrt{2}} \right) \left[(s_\beta c_{\beta-\alpha} - c_\beta s_{\beta-\alpha}) H + (s_\beta s_{\beta-\alpha} + c_\beta c_{\beta-\alpha}) h + v_2 \right] f_R + \text{h.c.} \\
=\ & \sum_f \overline{f}_L \left(\frac{\mathbf{Y}_{f,2}}{\sqrt{2}} s_\alpha \right) \left[\frac{s_\alpha}{s_\beta} H + \frac{c_\alpha}{s_\alpha} h + v \right] f_R + \text{h.c.} \\
=\ & \sum_f \overline{f}_L \left(\frac{\mathbf{m}_{f,2}}{v} \right) \left[\frac{s_\alpha}{s_\beta} H + \frac{c_\alpha}{s_\alpha} h + v \right] f_R + \text{h.c.}
\end{aligned}
\tag{4.69}
$$

Finally, going in the fermion mass eigenstate basis, the matrices $\mathbf{m}_f \equiv \mathbf{m}_{f,2}$ can be identified to their SM counterparts and Eq. (4.69) thus describes the mass generation of all SM fermions and their interactions with the physical h, H Higgs states. The reduced couplings $C_f^{H,h}$ in Type I can be straightforwardly read as

$$
\begin{aligned}
C_F^H &\equiv C_U^H = C_D^H = C_E^H = \frac{\sin \alpha}{\sin \beta}, \\
C_F^h &\equiv C_U^h = C_D^h = C_E^h = \frac{\cos \alpha}{\sin \beta},
\end{aligned}
\tag{4.70}
$$

and are seen to be universal for all fermions. Similarly, for the couplings to A, developing Eq. (4.67) and keeping only the terms proportional to A,

$$
\begin{aligned}
\mathscr{L}_Y^{\mathrm{I}} \supset\ & \overline{u}_L \left(\frac{\mathbf{m}_{U,2}}{v} \right) (-\cot \beta)(iA) u_R + \overline{d}_L \left(\frac{\mathbf{m}_{D,2}}{v} \right) (\cot \beta)(iA) d_R \\
& + \overline{e}_L \left(\frac{\mathbf{m}_{E,2}}{v} \right) (\cot \beta)(iA) e_R + \text{h.c.}
\end{aligned}
\tag{4.71}
$$

The reduced couplings C_f^A can be therefore defined as

$$
\begin{aligned}
C_U^A &= -\cot\beta \,, \\
C_D^A &= C_E^A = \cot\beta \,.
\end{aligned}
\tag{4.72}
$$

We now consider the Type II case. A look at Table 11 shows that the Type II up-type quarks have the same behavior as in Type I, we therefore only consider the down-type quarks and leptons in the following. The Yukawa Lagrangian reads

$$
-\mathscr{L}_Y^{\text{II}} \supset \ \overline{Q}_L \mathbf{Y}_{D,1} \left[c_\beta H_1 - s_\beta H_2\right] d_R + \overline{L}_L \mathbf{Y}_{E,1} \left[c_\beta H_1 - s_\beta H_2\right] e_R + \text{h.c.}
\tag{4.73}
$$

Developing the $\text{SU}(2)_L$ products and keeping only terms proportional to h_1 and h_2,

$$
\begin{aligned}
-\mathscr{L}_Y^{\text{II}} \supset \ &\sum_{f=d,e} \overline{f}_L \mathbf{Y}_{f,1} \left[c_\beta (h_1 + v) - s_\beta h_2\right] f_R + \text{h.c.} \\
=\ &\sum_{f=d,e} \overline{f}_L \left(\frac{\mathbf{Y}_{f,1}}{\sqrt{2}}\right) \left[(c_\beta c_{\beta-\alpha} + s_\beta s_{\beta-\alpha})H + (c_\beta s_{\beta-\alpha} - s_\beta c_{\beta-\alpha})h\right] f_R + \text{h.c.} \\
=\ &\sum_{f=d,e} \overline{f}_L \left(\frac{\mathbf{m}_{f,1}}{v}\right) \left[\frac{c_\alpha}{c_\beta}H - \frac{s_\alpha}{c_\beta}h\right] f_R + \text{h.c.}
\end{aligned}
\tag{4.74}
$$

The reduced couplings therefore read,

$$
\begin{aligned}
C_D^H &= C_E^H = \frac{\cos\alpha}{\cos\beta} \,, \\
C_D^h &= C_E^h = -\frac{\sin\alpha}{\cos\beta} \,.
\end{aligned}
\tag{4.75}
$$

To determine the A couplings, we isolate the terms proportional to A in Eq. (4.73),

$$
\begin{aligned}
\mathscr{L}_Y^{\text{II}} \supset \ &-\overline{d}_L \mathbf{Y}_{D,1}(-s_\beta)(iA)d_R - \overline{e}_L \mathbf{Y}_{E,1}(-s_\beta)(iA)e_R + \text{h.c.} \\
=\ &\overline{d}_L \left(\frac{\mathbf{m}_{D,1}}{v}\right)(\tan\beta)(iA)d_R + \overline{e}_L \left(\frac{\mathbf{m}_{E,1}}{v}\right)(\tan\beta)(iA)e_R + \text{h.c.}
\end{aligned}
\tag{4.76}
$$

Therefore,

$$
C_D^A = C_E^A = \tan\beta \,.
\tag{4.77}
$$

Note that since $C_D^{H,h,A} = C_E^{H,h,A}$ in both Types I and II, we will commonly refer to both couplings as $C_D^{H,h,A}$ from now on. The subscript D thus now refers to the down-type fermions rather than down-type quarks.

To finish, we obtain the couplings of the neutral Higgs states to the massive gauge bosons. For H and h, we already discussed them in the paragraph following Eq. (4.32),

$$
C_V^H = \cos(\beta - \alpha), \ C_V^h = \sin(\beta - \alpha) \,.
\tag{4.78}
$$

The sum of these squared couplings equals to 1. This is a generic property of general multi-doublet and -singlet Higgs sectors and is valid when the sum is taken over all Higgs states that couple to VV [258]. For Higgs bosons originating from a higher dimensional representation of $\text{SU}(2)_L$, the reduced coupling to VV can exceed 1. Finally, $C_V^A = 0$ because A belongs to H_2 which does not couple to the Z or $W^\pm$ since $\langle H_2 \rangle = 0$.

Table 12: Tree-level vector boson couplings C_V ($V = W, Z$) and fermionic couplings C_U and C_D to up-type and down-type fermions respectively, normalized to their SM values for the two scalars h, H and the pseudoscalar A in Type I and Type II 2HDMs.

Higgs	Types I, II VV	Type I up-type	down-type	Type II up-type	down-type
h	$\sin(\beta - \alpha)$	$\cos\alpha/\sin\beta$	$\cos\alpha/\sin\beta$	$\cos\alpha/\sin\beta$	$-\sin\alpha/\cos\beta$
H	$\cos(\beta - \alpha)$	$\sin\alpha/\sin\beta$	$\sin\alpha/\sin\beta$	$\sin\alpha/\sin\beta$	$\cos\alpha/\cos\beta$
A	0	$\cot\beta$	$-\cot\beta$	$\cot\beta$	$\tan\beta$

All of the above results are summarized in Table 12. Important insights can be gained by re-expressing the various trigonometric functions appearing in the reduced couplings as

$$C_F^{h,\mathrm{I}} = C_U^{h,\mathrm{II}} = \cos\alpha/\sin\beta = \sin(\beta - \alpha) + \cos(\beta - \alpha)\cot\beta, \quad (4.79)$$

$$C_D^{h,\mathrm{II}} = -\sin\alpha/\cos\beta = \sin(\beta - \alpha) - \cos(\beta - \alpha)\tan\beta, \quad (4.80)$$

$$C_F^{H,\mathrm{I}} = C_U^{H,\mathrm{II}} = \sin\alpha/\sin\beta = \cos(\beta - \alpha) - \sin(\beta - \alpha)\cot\beta, \quad (4.81)$$

$$C_D^{H,\mathrm{II}} = \cos\alpha/\cos\beta = \cos(\beta - \alpha) + \sin(\beta - \alpha)\tan\beta. \quad (4.82)$$

The precise role of $s_{\beta-\alpha}$ and $c_{\beta-\alpha}$ and the connection with the so-called alignment limit will be discussed in details in Section 4.2. In Type II, the coupling of the CP-even states to down-type fermions can be $\tan\beta$ enhanced. This is particularly relevant phenomenologically. Indeed, identifying either h or H as the observed state, the partial width $\Gamma(h/H \to b\bar{b})$ accounts for the major part of the corresponding total width, hence a $\tan\beta$ dependence may sizably affect all production and decay rates.

Moreover in Type II, as previously observed in Fig. 3.24, there exists a parameter regime in which C_D has an opposite sign relative to C_U and C_V; the wrong-sign Yukawa regime. For the h couplings, this happens for $\sin(\beta + \alpha) \approx 1$, and in the exact limit: $C_D^h = -1$, $C_U^h = 1$ and $C_V^h = (t_\beta^2 - 1)/(t_\beta^2 + 1)$. Consistency with the Higgs measurements requires C_V^h close enough to unity and hence sufficiently large t_β ($C_V^h \gtrsim 0.95$ for $t_\beta > 6$). For the H couplings, this happens for $\cos(\beta + \alpha) \approx 1$. This interesting possibility might be probed by the precision measurements of the signal strengths. Indeed, this would lead to a change of sign of the interference between the top and bottom loops in the gluon-fusion production process or in the decay into two photons for instance, and hence modify the SM predicted rates [259]. As we will see in the next chapter, direct production of the pseudoscalar A followed by the decay into $\tau\tau$ also probes this possibility.

In principle, there also exists a situation in which the coupling to up-type fermions in Type II has an opposite sign with respect to C_D and C_V. However, such a possibility is excluded at more than the 5σ level by the $h \to \gamma\gamma$ signal rate measurements. Indeed, considering that all reduced couplings are equal to 1 as in the SM with the exception of C_U which is set to -1, leads to $C_g \approx 1.06$ and $C_\gamma \approx 1.53$. Such a large enhancement of the $\gamma\gamma$ coupling is completely excluded by LHC measurements as can be seen in Fig. 3.21 for instance.

4.1.5 *Theoretical constraints*

Before delving into the details of the alignment limit, let us discuss theoretical constraints on the 2HDMs. First, the positivity condition requires the scalar potential to be bounded from below in any directions of the scalar field space. Conditions on the 2HDM parameters in the $\lambda_6 = \lambda_7 = 0$ case are given by [291],

$$\lambda_1 > 0, \quad \lambda_2 > 0, \quad \min(\lambda_3, \ \lambda_3 + \lambda_4 - \lambda_5) > -\sqrt{\lambda_1 \lambda_2} \,. \tag{4.83}$$

Alternatively, in terms of the Higgs basis parameters,

$$Z_1 > 0, \quad Z_2 > 0, \quad Z_3 > -\sqrt{Z_1 Z_2} \,, \tag{4.84}$$

are necessary conditions for the positivity of the potential.

Another question is that of the vacuum stability. In the beginning of this section, we explicitly chose to work in a $U(1)_{em}$-conserving vacuum. However, there might in principle exist solutions in which vacua of different nature co-exist. References [272, 292, 293] showed that such a case was actually impossible in the 2HDM. It was also shown that two electric charge conserving vacua may however co-exist, quantum tunneling may then happen towards the deeper vacuum if we lived in such a false vacuum. There exists a simple relation to check whether a given minimum is the global one [293]. Defining $k = (\lambda_1/\lambda_2)^{1/4}$, if $D > 0$, where

$$D = m_{12}^2 (m_{11}^2 - k^2 m_{22}^2)(\tan\beta - k) \,, \tag{4.85}$$

then our vacuum is necessarily the global one. Though it is then trivial to check the absolute stability of a given vacuum, in the phenomenological studies presented in the next chapter, we chose not to discard parameter space points with $D < 0$. Such vacua may indeed be metastable, with a lifetime longer than the Universe age. More fundamentally, as previously discussed, we do not make any assumption about the high-energy origin of the 2HDM as an effective theory. For this reason, we do not know the full scalar potential at all energies and new physics effects may stabilize a $D < 0$ vacuum with a small lifetime.

In order to preserve perturbativity and tree-level unitarity [294–299], the dimensionless couplings Z_i cannot be taken arbitrarily large. Specifically, in our analyses, we demand perturbativity of the quartic Higgs couplings by requiring them to be smaller than 4π. Tree-level unitarity depends, as discussed in Section 2.3.3 for the SM Higgs boson, on the high-energy scattering of scalar and longitudinal gauge boson states. Reference [298] provided the necessary and sufficient conditions in the 2HDM for tree-level unitarity under the form of upper bounds on eigenvalues of scattering-matrices. These matrices solely depend on combinations of the λ_i parameters and this is what we impose in our subsequent analyses. Imposing unitarity at the tree-level is enough in weakly coupled models, as contrary to strongly interacting models where the contributions of higher-orders to the scattering-matrices become larger and larger. All in all, the combination of the perturbativity and tree-level unitarity naturally induces upper bounds on the $|\lambda_i|$ and $|Z_i|$. Though they are generically $\mathcal{O}(1)$ constants, it is possible for some of them to be as large as ~ 10 without violating any low-energy constraints. Taking the λ_i, or alternatively the Z_i, significantly larger than $\mathcal{O}(1)$ will lead to Landau poles at an energy scale below the Planck scale [300–303]. However, as mentioned previously, we shall take an agnostic view by treating the

2HDM as an effective low-energy theory with no assumption on its behavior at higher energies and thus ignore the possible presence of such Landau poles.

4.2 THE ALIGNMENT LIMIT

As noted in a previous subsection, the Higgs basis doublet H_1 behaves precisely as the SM one. Thus, if one of the neutral CP-even Higgs mass eigenstates is approximately aligned with $\sqrt{2}\,\mathrm{Re}\,H_1^0 - v$, then its properties will approximately coincide with those of the SM Higgs boson. The alignment limit is then defined as the limit in which one of the two neutral CP-even Higgs mass eigenstates aligns with the direction of the scalar field vacuum expectation values. Defined in this way, it is clear that the alignment limit is independent of the choice of basis for the two Higgs doublet fields. Nevertheless, the alignment limit is most clearly exhibited in the Higgs basis. In light of Eqs. (4.33) and (4.34), the alignment limit corresponds either to the limit of $c_{\beta-\alpha} \to 0$ if h is identified as the observed SM-like Higgs boson (hereinafter referred to as the h–125 scenario), or to the limit of $s_{\beta-\alpha} \to 0$ if H is identified as the SM-like Higgs boson (H–125 scenario). In this case, the $W^\pm$ and Z gauge bosons dominantly acquire their masses from this state, and its coupling to W^+W^- (and ZZ) tends toward its SM value, $C_V \to 1$, see Table 12. As we will see, the alignment limit is most easily attained in the decoupling limit [264], where all the other non-SM-like Higgs scalars of the model are heavy. However, the alignment limit of the 2HDM can also be achieved in a parameter regime in which one or more of the non-SM-like Higgs scalars are light (and in some cases very light). This region of *alignment without decoupling* is a primary focus of this part of the manuscript.

Very important insights about the alignment limit might be gained from the explicit expressions of $c_{\beta-\alpha}$ and $s_{\beta-\alpha}$. This can be done either directly from Eqs. (4.53) and (4.55) or by using Eqs. (4.16) and (4.17) with α replaced by $\alpha - \beta$. Since $Z_6 s_{\beta-\alpha} c_{\beta-\alpha} \le 0$ [see Eq.(4.58)], the sign of the product $s_{\beta-\alpha} c_{\beta-\alpha}$ is fixed by the sign of Z_6. However, since $\beta - \alpha$ is only defined modulo π, we are free to choose a convention where either $c_{\beta-\alpha}$ or $s_{\beta-\alpha}$ is always non-negative.[16] A convenient choice of convention is dictated by the form of the couplings of the neutral CP-even Higgs bosons to VV (where $VV = W^+W^-$ or ZZ). When identifying h as the observed state, we will always use the convention in which $s_{\beta-\alpha}$ is non-negative since $C_V^h = s_{\beta-\alpha}$. In this case,

$$c_{\beta-\alpha} = -\,\mathrm{sgn}(Z_6)\sqrt{\frac{Z_1 v^2 - m_h^2}{m_H^2 - m_h^2}} = \frac{-Z_6 v^2}{\sqrt{(m_H^2 - m_h^2)(m_H^2 - Z_1 v^2)}}\,, \tag{4.86}$$

where we have used Eq. (4.52) to obtain the second form for $c_{\beta-\alpha}$ in Eq. (4.86). Alternatively, when identifying H as the SM-like state, we use a convention where $c_{\beta-\alpha}$ is non-negative and in that case,

$$s_{\beta-\alpha} = -\,\mathrm{sgn}(Z_6)\sqrt{\frac{m_H^2 - Z_1 v^2}{m_H^2 - m_h^2}} = \frac{-Z_6 v^2}{\sqrt{(m_H^2 - m_h^2)(Z_1 v^2 - m_h^2)}}\,. \tag{4.87}$$

Moreover, from Eq. (4.49), we can derive equivalent conditions that yield a SM-like Higgs boson. Since $\sqrt{2}\,\mathrm{Re}\,H_1^0 - v$ should be an approximate mass eigenstate, the mixing of H_1^0

---

16 Such a convention, if adopted, would replace the convention employed in Eq. (4.16) in which c_α is taken to be non-negative.

and H_2^0 should be subdominant, which implies that either $|Z_6| \ll 1$ and/or $m_A^2 + Z_5 v^2 \gg Z_1 v^2$, $Z_6 v^2$. Moreover, if in addition $m_A^2 + Z_5 v^2 > Z_1 v^2$, then h is SM-like, whereas if $m_A^2 + Z_5 v^2 < Z_1 v^2$, then H is SM-like. In both cases, the squared-mass of the SM-like Higgs boson is approximately equal to $Z_1 v^2$.

4.2.1 A Standard Model-like Higgs

Consider first the h–125 scenario. It follows from Eq. (4.86) that the alignment limit can be achieved in two ways: (i) $Z_6 \to 0$ or (ii) $m_H \gg v$. The case of $m_H \gg v$ (or equivalently $Y_2 \gg v$) is called the *decoupling limit* in the literature. More precisely, we are assuming that $m_H^2 \gg |Z_6| v^2$. Since Z_6 is a dimensionless coefficient in the Higgs basis scalar potential, we are implicitly assuming that Z_6 cannot get too large without spoiling perturbativity and/or unitarity as we discussed previously. One might roughly expect $|Z_6| \lesssim 4\pi$, in which case $m_H \gg v$ provides a reasonable indication of the domain of the decoupling limit. In this limit, $m_H \simeq m_A \simeq m_{H^\pm}$, so the heavy scalar states can integrated out below the scale of m_H. The effective Higgs theory below the scale m_H is a theory with one Higgs doublet and corresponds to the SM Higgs sector. Thus not surprisingly, h is a SM-like Higgs boson. However, it is possible to achieve the alignment limit even if the masses of all scalar states are similar in magnitude, this happens the limit of $Z_6 \to 0$ with $m_H = \mathcal{O}(v)$. This is the very attracting case of *alignment without decoupling* that will be analyzed in the next chapter. This possibility was first noted in [264] and further clarified in [263, 304]. Finally, if both $|Z_6| \ll 1$ and $m_H \gg m_h$ are satisfied, the alignment is even more pronounced and such a limit might be referred to as the *double alignment limit*.

In the H–125 scenario, we have $m_A^2 + Z_5 v^2 < Z_1 v^2$, $|s_{\beta-\alpha}| \ll 1$ and $m_H^2 \simeq Z_1 v^2$. Looking back at Eq. (4.87), there is only one way to achieve $|s_{\beta-\alpha}| \ll 1$, that is $Z_6 \to 0$. Indeed, the denominator of Eq. (4.87) cannot be arbitrarily large since $m_H > m_h$ by definition and Z_1 cannot be larger than roughly 4π. This scenario hence does not have a decoupling limit. This is intuitively clear since the low-energy effective Higgs theory necessarily contains at least one additional scalar state, h. The masses of A and $H^\pm$ are then typically of the order v since $m_A^2 + Z_5 v^2 < Z_1 v^2$ and $m_{H^\pm}^2 = m_A^2 - \frac{1}{2}(Z_4 - Z_5)v^2$ [see Eq. (4.47)]. Nevertheless, a parameter regime exists in which A and/or $H^\pm$ can be considerably heavier than H. To see how this can arise, we rewrite the A and $H^\pm$ masses as follows,

$$m_A^2 \;=\; m_H^2 s_{\beta-\alpha}^2 + m_h^2 c_{\beta-\alpha}^2 - Z_5 v^2 \,, \tag{4.88}$$

$$m_{H^\pm}^2 \;=\; m_H^2 s_{\beta-\alpha}^2 + m_h^2 c_{\beta-\alpha}^2 - \tfrac{1}{2}(Z_4 + Z_5)v^2 \,. \tag{4.89}$$

Consequently,

$$m_A \gg m_H \,, \; m_{H^\pm} \,, \quad \text{if } Z_5 \text{ is large and negative and } |Z_4 + Z_5| \lesssim \mathcal{O}(1) \,, \tag{4.90}$$

$$m_{H^\pm} \gg m_H \,, \; m_A \,, \quad \text{if } Z_4 + Z_5 \text{ is large and negative and } |Z_5| \lesssim \mathcal{O}(1) \,, \tag{4.91}$$

$$m_A \,, \; m_{H^\pm} \gg m_H \,, \quad \text{if both } Z_5 \text{ and } Z_4 + Z_5 \text{ are large and negative} \,, \tag{4.92}$$

under the condition that the magnitudes of Z_4 and Z_5 are consistent with tree-level unitarity bounds and that $m_A^2 + Z_5 v^2 < Z_1 v^2$ is satisfied. None of these three cases above however corresponds to a decoupling limit, since in each case the light scalar state h is still present. Note that in the parameter regime where Eqs. (4.90) or (4.91) is satisfied, a

second scalar state beyond h may be present whose mass lies below $m_H = 125$ GeV. If the conditions of Eq. (4.90) are satisfied, then $m_{H^\pm} < m_H$ if $(Z_4 + Z_5)v^2 > -2(m_H^2 - m_h^2)c_{\beta-\alpha}^2$ [see Eq. (4.89)]. Similarly, if the conditions of Eq. (4.91) are satisfied, then $m_A < m_H$ if $Z_5 v^2 > -(m_H^2 - m_h^2)c_{\beta-\alpha}^2$ [see Eq. (4.88)].

4.2.2 *Couplings in the alignment limit*

By definition, in the alignment limit the coupling of the SM-like Higgs to ZZ and W^+W^- tends to 1 while the other CP-even state becomes partially gauge-phobic (though the XVV interactions are suppressed, $XXVV$ couplings may be non-vanishing, where X is the 125 GeV state).

Looking back at the fermionic reduced couplings Eqs. (4.79)–(4.81), we see that, as expected, in the exact alignment limit, the reduced couplings of the SM-like state go to their SM values. However, if $\tan\beta \gg 1$, then the alignment limit is realized for the Type-II Yukawa couplings to down-type fermions only if $|c_{\beta-\alpha}|\tan\beta \ll 1$ ($|s_{\beta-\alpha}|\tan\beta \ll 1$) if h (H) is the SM-like state. That is, if $|c_{\beta-\alpha}| \ll 1$ ($|s_{\beta-\alpha}| \ll 1$) but $|c_{\beta-\alpha}|\tan\beta \sim \mathcal{O}(1)$ ($|s_{\beta-\alpha}|\tan\beta \sim \mathcal{O}(1)$), then the hVV (HVV) couplings and the $ht\bar{t}$ ($Ht\bar{t}$) couplings are SM-like whereas the $hb\bar{b}$ ($Hb\bar{b}$) and $h\tau^+\tau^-$ ($H\tau^+\tau^-$) couplings deviate from their SM values. The approach to the alignment limit is said to be *delayed* when $\tan\beta \gg 1$. We denote this phenomenon as the *delayed alignment limit* [259, 264, 305, 306]. This phenomenon has very important phenomenological consequences as will be shown in the next chapter. Similar considerations can also apply if $\cot\beta \gg 1$; however, this region of parameter space is disfavored as the corresponding $ht\bar{t}$ ($Ht\bar{t}$) coupling quickly becomes non-perturbative if $\cot\beta$ is too large. For this reason, we won't pursue further the exploration of the small $\tan\beta$ region and restrict ourselves to $\tan\beta > 0.5$ in the subsequent analyses.

Finally, we examine some trilinear Higgs self-couplings. Using the results of Ref. [264] (see also Ref. [275]), the three-Higgs vertex Feynman rules (including the corresponding symmetry factor for identical particles but excluding an overall factor of i) are given by:

$$g_{hhh} = -3v\big[Z_1 s_{\beta-\alpha}^3 + Z_{345} s_{\beta-\alpha} c_{\beta-\alpha}^2 + 3Z_6 c_{\beta-\alpha} s_{\beta-\alpha}^2 + Z_7 c_{\beta-\alpha}^3\big], \tag{4.93}$$

$$g_{HHH} = -3v\big[Z_1 c_{\beta-\alpha}^3 + Z_{345} c_{\beta-\alpha} s_{\beta-\alpha}^2 - 3Z_6 s_{\beta-\alpha} c_{\beta-\alpha}^2 - Z_7 s_{\beta-\alpha}^3\big], \tag{4.94}$$

$$g_{hH^+H^-} = -v\big[Z_3 s_{\beta-\alpha} + Z_7 c_{\beta-\alpha}\big], \tag{4.95}$$

$$g_{HH^+H^-} = -v\big[Z_3 c_{\beta-\alpha} - Z_7 s_{\beta-\alpha}\big]. \tag{4.96}$$

The trilinear Higgs couplings expressed in terms of the physical Higgs masses can be found in Appendix B of [261]. Let us first consider the Higgs self-coupling in the approach to the alignment limit in the h–125 scenario. Equations (4.56) and (4.93) yield,

$$g_{hhh} = g_{hhh}^{\text{SM}}\left[1 + \frac{2Z_6}{Z_1}c_{\beta-\alpha} + \left(\frac{Z_{345}}{Z_1} - \frac{2Z_6^2}{Z_1^2} - \frac{3}{2}\right)c_{\beta-\alpha}^2 + \mathcal{O}(c_{\beta-\alpha}^3)\right], \tag{4.97}$$

where the self-coupling of the SM Higgs boson is given by

$$g_{hhh}^{\text{SM}} = -\frac{3m_h^2}{v}. \tag{4.98}$$

Note that this is a tree-level result and possibly large radiative corrections can be present in the alignment limit [307, 308]. Remember that in the alignment limit, $m_h^2 \simeq Z_1 v^2$, which implies that $Z_1 \simeq 0.26$. It is convenient to make use of Eq. (4.86) to write $c_{\beta-\alpha} = -\eta Z_6$ where

$$\eta \equiv \frac{v^2}{\sqrt{(m_H^2 - m_h^2)(m_H^2 - Z_1 v^2)}} = \begin{cases} \mathcal{O}(1), & \text{for } m_H^2 \sim \mathcal{O}(v^2), \\ \mathcal{O}\left(\dfrac{v^2}{m_H^2}\right) \ll 1, & \text{in the decoupling limit.} \end{cases} \tag{4.99}$$

Equation (4.97) then yields

$$g_{hhh} = g_{hhh}^{\mathrm{SM}}\left\{1 + \left[\left(Z_{345} - \tfrac{3}{2}Z_1\right)\eta^2 - 2\eta\right]\frac{Z_6^2}{Z_1} + \mathcal{O}(\eta^3 Z_6^3) + \mathcal{O}(\eta^2 Z_6^4)\right\}. \tag{4.100}$$

In the decoupling limit (where $\eta \ll 1$),

$$g_{hhh} = g_{hhh}^{\mathrm{SM}}\left\{1 - \frac{2\eta Z_6^2}{Z_1} + \mathcal{O}(\eta^2 Z_6^2)\right\}. \tag{4.101}$$

It follows that g_{hhh} is always suppressed with respect to the SM in the decoupling limit, indeed $Z_1 > 0$ by positivity of the potential [see Eq. (4.84)]. In the double decoupling limit where $\eta \ll 1$ *and* $|Z_6| \ll 1$, Eq. (4.101) shows that the deviation of g_{hhh} from the corresponding SM value is highly suppressed.

In contrast, in the alignment limit without decoupling, $|Z_6|$ is significantly smaller than 1 and $\eta \sim \mathcal{O}(1)$. It is now convenient to use Eq. (4.45) to eliminate Z_{345},

$$g_{hhh} = g_{hhh}^{\mathrm{SM}}\left\{1 + \left[\left(Z_7 \tan 2\beta - \tfrac{1}{2}Z_1\right)\eta^2 - 2\eta\right]\frac{Z_6^2}{Z_1} + (2\cot 2\beta - \tan 2\beta)\eta^2\frac{Z_6^3}{Z_1} + \mathcal{O}(Z_6^3)\right\}, \tag{4.102}$$

where the term above designated by $\mathcal{O}(Z_6^3)$ contains no potential enhancements in the limit of $s_{2\beta} \to 0$ or $c_{2\beta} \to 0$. Given that $\eta \sim \mathcal{O}(1)$ in the alignment limit without decoupling, the form of Eq. (4.102) suggests two ways in which g_{hhh} can be enhanced with respect to the SM. For example if $\tan \beta \sim 1$, then one must satisfy $(Z_7 - Z_6)\eta \tan 2\beta \gtrsim 2 + \tfrac{1}{2}Z_1\eta$. Alternatively, if $\tan \beta \gg 1$, then one must satisfy $Z_6 \eta \cot 2\beta \gtrsim 1 + \tfrac{1}{4}Z_1\eta$ (the latter inequality requires $Z_6 < 0$, since $\cot 2\beta < 0$ when $\tfrac{1}{4}\pi < \beta < \tfrac{1}{2}\pi$). In both cases, $g_{hhh} > g_{hhh}^{\mathrm{SM}}$ is possible even when $|Z_6|$ and $|Z_7|$ are significantly smaller than 1. Indeed, both of the above alternatives correspond to $Z_{345} \gg Z_1$ and $\eta Z_{345} \gg 1$ in Eq. (4.100).

Similarly, if H is the SM-like state, Eqs. (4.57) and (4.94) yield

$$g_{HHH} = g_{HHH}^{\mathrm{SM}}\left[1 - \frac{2Z_6}{Z_1}s_{\beta-\alpha} + \left(\frac{Z_{345}}{Z_1} - \frac{2Z_6^2}{Z_1^2} - \frac{3}{2}\right)s_{\beta-\alpha}^2 + \mathcal{O}(s_{\beta-\alpha}^3)\right], \tag{4.103}$$

where the self-coupling of the SM Higgs boson is given by

$$g_{HHH}^{\mathrm{SM}} = -\frac{3m_H^2}{v} = -3v\left(Z_1 - Z_6\frac{s_{\beta-\alpha}}{c_{\beta-\alpha}}\right). \tag{4.104}$$

We first define $s_{\beta-\alpha} = -\eta Z_6$ where

$$\eta \equiv \frac{v^2}{\sqrt{(m_H^2 - m_h^2)(Z_1 v^2 - m_h^2)}} \tag{4.105}$$

is a positive $\mathcal{O}(1)$ parameter. In the approach of the alignment limit,

$$\eta = \frac{v^2}{|m_A^2 + (Z_5 - Z_1)v^2|} + \mathcal{O}(Z_6^2)\,, \tag{4.106}$$

and therefore, after re-expressing Z_{345} in terms of Z_6,

$$g_{HHH} = g_{HHH}^{\rm SM}\left\{1 + \left[(Z_7\tan 2\beta - \tfrac{1}{2}Z_1)\eta^2 + 2\eta\right]\frac{Z_6^2}{Z_1} + (2\cot 2\beta - \tan 2\beta)\eta^2\frac{Z_6^3}{Z_1} + \mathcal{O}(Z_6^3)\right\}, \tag{4.107}$$

where the term designated by $\mathcal{O}(Z_6^3)$ contains no potential enhancements in the limit of $s_{2\beta} \to 0$ or $c_{2\beta} \to 0$. The HHH coupling can thus be either suppressed or enhanced with respect to the SM. For example $g_{HHH} > g_{HHH}^{\rm SM}$ is possible in two cases. If $\tan\beta \sim 1$, then one must satisfy $(Z_7 - Z_6)\eta\tan 2\beta \gtrsim \tfrac{1}{2}Z_1\eta - 2$. Alternatively, if $\tan\beta \gg 1$, then one must satisfy $Z_6\eta\cot 2\beta \gtrsim \tfrac{1}{4}Z_1\eta - 1$. In both cases, the HHH coupling is enhanced even when $|Z_6|$ is significantly smaller than 1.

Of great phenomenological importance is the hH^+H^- coupling when h is the SM-like state. In the alignment limit,

$$g_{hH^+H^-} = -v\big[Z_3 + \mathcal{O}(c_{\beta-\alpha})\big]\,, \tag{4.108}$$

approaches a finite nonzero value, with or without decoupling. This is relevant for the analysis of the one-loop process $h \to \gamma\gamma$, which has a contribution that is mediated by a $H^\pm$ loop. In the decoupling limit, the charged Higgs loop amplitude is suppressed by a factor of $\mathcal{O}(v^2/m_{H^\pm}^2)$ relative to the $W^\pm$ and the top quark loop contributions. However, in the alignment limit without decoupling, the charged Higgs loop is parametrically of the same order as the corresponding SM loop contributions, thereby leading to a shift of the $h \to \gamma\gamma$ decay rate from its SM value. This is in stark contrast to the behavior of tree-level Higgs couplings, which approach their SM values in the alignment limit with or without decoupling.

Similarly, and extending the discussion, if H is the SM-like state,

$$g_{HH^+H^-} = -v\big[Z_3 + \mathcal{O}(s_{\beta-\alpha})\big]\,. \tag{4.109}$$

Although we expect $m_{H^\pm} \lesssim \mathcal{O}(v)$ over most of the 2HDM parameter space when H is a SM-like Higgs boson, there exists a parameter regime [cf. Eqs. (4.91) and (4.92)] in which $m_{H^\pm} \gg m_H$. Moreover, a heavy charged Higgs mass is required in Type II to avoid conflict with the observed rate for $b \to s\gamma$ [309]. In light of Eqs. (4.47) and (4.48), let us suppose that $Y_2 \ll Z_3 v^2$ where Z_3 is large [say, of $\mathcal{O}(10)$] but still consistent with the unitarity bounds. Then, in order to satisfy the inequality $m_A^2 + Z_5 v^2 < Z_1 v^2$ required for H to be the SM-like state, $Z_4 + Z_5$ must be negative and its magnitude must be large (but not too large in order to satisfy the unitarity bounds). It then follows that $m_{H^\pm}^2 \simeq \tfrac{1}{2}Z_3 v^2$, in which case Eq. (4.96) yields

$$g_{HH^+H^-} \simeq -\frac{2m_{H^\pm}^2}{v} + \mathcal{O}(s_{\beta-\alpha})\,, \tag{4.110}$$

in the approach to the alignment limit. One can also obtain Eq. (4.110) by expressing $g_{HH^+H^-}$ in terms of the Higgs masses and the squared-mass parameter $\overline{m}^2 = m_{12}^2/(s_\beta c_\beta)$ defined in Eq. (4.10). Inserting Eqs. (4.60) and (4.62) into Eq. (4.96) yields

$$g_{HH^+H^-} = -\frac{1}{v}\left\{\big[m_H^2 + 2(m_{H^\pm}^2 - \overline{m}^2)\big]c_{\beta-\alpha} - 2\cot 2\beta(m_H^2 - \overline{m}^2)s_{\beta-\alpha}\right\}. \tag{4.111}$$

In the alignment limit where $c_{\beta-\alpha} \to 1$ (or equivalently, $Z_6 \to 0$),

$$g_{HH^+H^-} = -\frac{1}{v}(m_H^2 + 2m_{H^\pm}^2 - 2\overline{m}^2) + \mathcal{O}(s_{\beta-\alpha}) \, , \tag{4.112}$$

where $m_H \simeq 125$ GeV. In the parameter regime where $m_{H^\pm}$ is large [such that $Y_2 \ll Z_3 v^2$ as discussed above Eq. (4.110)], it follows that $\overline{m}^2 \sim \mathcal{O}(v^2)$. Thus, in the alignment limit with $m_{H^\pm}$ large compared to v, one again obtains the asymptotic result of Eq. (4.110).

Denoting the one-loop $H \to \gamma\gamma$ amplitude normalized to the corresponding SM value by C_γ^H, the coupling given in Eq. (4.110) matches precisely the HH^+H^- interaction term of

$$\mathscr{L}_{\text{int}} = -\frac{gm_t}{2m_W}\bar{t}tH + gm_W W_\mu^+ W^{\mu-}H - \frac{gm_{H^\pm}^2}{m_W}H^+H^-H \, , \tag{4.113}$$

given in Eq. (2.15) of [258]. Hence, we can immediately obtain an estimate for C_γ^H in the alignment limit by employing the asymptotic forms for the contributions to the $H \to \gamma\gamma$ amplitude, A_i^H (corresponding to a particle in the loop with spin $i = 0, \frac{1}{2}, 1$) given in Eq. (2.21) of [258] and discussed in Section 2.3.4,

$$C_\gamma^H = \frac{A_0^H + A_1^H + 3e_t^2 A_{1/2}^H}{A_1^H + 3e_t^2 A_{1/2}^H} \approx 0.94 \, , \tag{4.114}$$

where $e_t = \frac{2}{3}$ is the charge of the top quark in units of e, $A_0^H = \frac{1}{3}$, $A_{1/2}^H = \frac{4}{3}$ and $A_1^H = -7$.[17] A more complete calculation taking into account finite-mass effects yields a very similar result, $C_\gamma^H \simeq 0.95$. That is, the contribution of the charged Higgs loop asymptotically yields a 5% reduction in C_γ^H. In contrast, in the case of lighter charged Higgs boson masses (which are allowed in Type I), the approximate form for the HH^+H^- coupling given in Eq. (4.110) and the asymptotic form for A_0^H employed in Eq. (4.114) are no longer valid. In particular, in the approach to the alignment limit, $g_{HH^+H^-} \simeq -vZ_3$. When $Z_3 > 0$ [as in Eq. (4.110) where $Z_3 \sim 2m_{H^\pm}^2/v^2$], the charged Higgs loop interferes destructively with the W boson loop. However, for small values of $m_{H^\pm}$ there exist regions of the 2HDM parameter space where $Z_3 < 0$, which then yields an HH^+H^- coupling of the opposite sign. In this case, the charged Higgs boson loop interferes constructively with the W boson loop, thereby generating a value of $C_\gamma^H > 1$. Using Eq. (4.112), it follows that the sign flip of $g_{HH^+H^-}$ occurs roughly when $2\overline{m}^2 > 2m_{H^\pm}^2 + m_H^2$. In practice, as we shall see in the next chapter, positive values of $\overline{m}^2$ do not exceed about $(150 \text{ GeV})^2$, which implies that a light charged Higgs boson with a mass of about $m_{H^\pm} < 160$ GeV is required for $C_\gamma^H > 1$. The non-decoupling of the charged Higgs contribution and the possible sign flip in $g_{HH^+H^-}$ was also addressed in Appendix B of [207].

Finally, as will be shown in the next chapter, the Higgs-gauge boson vertices AZh and AZH are very interesting phenomenologically. Their expressions are given by

$$g_{AZh} = \frac{gc_{\beta-\alpha}}{2\cos\theta_W}, \quad g_{AZH} = \frac{-gs_{\beta-\alpha}}{2\cos\theta_W} \, , \tag{4.115}$$

and their behavior in the alignment limit is trivial.

---

17 These asymptotic forms are valid when $4m_i^2/m_H^2 \gg 1$, where m_i is the mass of the particle in the loop. Nevertheless, these approximations work quite well even for the t-quark and the W boson.

4.2.3 *Can alignment be natural ?*

Before concluding these theoretical developments, we examine another theoretical distinction between the decoupling limit and alignment limit without decoupling. The SM Higgs sector is famously unnatural [310, 311], in particular, a fine tuning of the Higgs sector squared-mass parameter is required in order to explain the observed value of the vev. The 2HDM generically requires two separate and independent fine tunings. In addition to identifying $v \approx 246$ GeV, which fixes the values of Y_1 and Y_3 through the potential minimization conditions Eq. (4.46), one must also perform a second fine-tuning to fix the squared-mass parameter Y_2 to be of $\mathcal{O}(v^2)$. Thus, in the h–125 scenario, the regime of the decoupling limit (where $Y_2 \gg v^2$) is less fine-tuned than the general 2HDM, since the natural value for Y_2 is the ultraviolet cutoff of the theory beyond which new physics presumably enters. As long as the extra Higgs scalars (whose squared masses are of order Y_2) are sufficiently massive, then h will be a SM-like state. As discussed previously, such a limit does not exist in the H–125 scenario.

In contrast, in the case of alignment without decoupling (or in the double decoupling limit), we have $|Z_6| \ll 1$, which is a finely-tuned region of the 2HDM parameter space (beyond the two tunings discussed above) unless we can demonstrate that $Z_6 = 0$ is a consequence of an enhanced symmetry of the theory. The possibility of a natural implementation of alignment has been previously treated in Ref. [312]. In the absence of Higgs–fermion Yukawa couplings, it is sufficient to consider the symmetry properties of the scalar potential. Note that we have already imposed a softly-broken $\mathbb{Z}_2$ symmetry, which yields $\lambda_6 = \lambda_7 = 0$ in the original basis. In addition, we observe that $Z_6 = Z_7 = 0$ [which also implies that $Y_3 = 0$ in light of minimization conditions Eq. (4.46)] corresponds to an exact $\mathbb{Z}_2$ symmetry in the Higgs basis, $H_i \to (-1)^{i-1} H_i$.

The conditions $Z_6 = Z_7 = 0$ can be implemented in three ways. If $s_{2\beta} = 0$, then only one of the two Higgs fields acquires a non-zero vev. This means that the $\mathbb{Z}_2$-basis and the Higgs basis coincide, in which case the original $\mathbb{Z}_2$ symmetry is unbroken and transmitted to the Higgs basis. If $\lambda_6 = \lambda_7 = 0$ and $s_{2\beta} c_{2\beta} \neq 0$, then setting $Z_6 = Z_7 = 0$ in Eqs. (4.39) and (4.40) yields $\lambda_1 = \lambda_2 = \lambda_{345}$. Such a scalar potential exhibits a softly-broken CP3 symmetry, one of the three possible generalized CP symmetries that can be imposed on the 2HDM [313].[18] Finally, if the scalar potential exhibits an exact CP2 symmetry, defined in Ref. [313], or equivalently there is a basis in which the $\mathbb{Z}_2$ discrete symmetry ($\Phi_1 \to +\Phi_1$, $\Phi_2 \to -\Phi_2$) and a second $\mathbb{Z}_2$ interchange symmetry ($\Phi_1 \longleftrightarrow \Phi_2$) coexist [274, 313], then it follows that $\lambda_6 = \lambda_7 = 0$, $\lambda_1 = \lambda_2$ (with λ_5 real), $m_{11}^2 = m_{22}^2$ and $m_{12}^2 = 0$. In this case, Eqs. (4.6) and (4.7) yield $\tan\beta = 1$.[19] The latter can be maintained when the CP2 symmetry is softly broken such that $m_{12}^2 \neq 0$. Using Eqs. (4.39) and (4.40) then yields $Z_6 = Z_7 = 0$. Thus, in the absence of the Higgs-fermion Yukawa couplings, $Z_6 = 0$ is a consequence of an enhanced symmetry of the scalar potential, in which case the regime of

---

18 If $m_{12}^2 = 0$ in Eq. (4.5) in addition to $\lambda_6 = \lambda_7 = 0$, then the $\mathbb{Z}_2$ discrete symmetry ($\Phi_1 \to +\Phi_1$, $\Phi_2 \to -\Phi_2$) is exact. In this case, $Z_6 = Z_7 = 0$ implies that $\lambda_1 = \lambda_2 = \lambda_{345}$ *and* $m_{11}^2 = m_{22}^2$ [the latter via Eq. (4.43)], and corresponds to an *exact* CP3 symmetry of the scalar potential. This restriction of scalar potential parameters has also been obtained in Ref. [312].

19 Here we assume that $\lambda_1 \neq \lambda_{345}$, otherwise the CP2 symmetry is promoted to the CP3 symmetry previously considered.

alignment without decoupling and the double decoupling regime are both natural in the sense of 't Hooft [314].

If we now include the Higgs-fermion Yukawa coupling, we can still maintain the symmetry of the scalar potential in special cases. If the $\mathbb{Z}_2$ symmetry transformation is defined in the Higgs basis such that H_2 is odd (*i.e.*, $H_2 \to -H_2$) and H_1 and all fermion and vector fields are even, then the resulting model corresponds a Type I 2HDM with $s_{2\beta} = 0$, which we recognize as the inert 2HDM (IDM) [291, 315, 316]. In light of the above discussion, we see that the alignment limit is exact in the IDM and $\sqrt{2}H_1^0 - v$ is identified as the SM Higgs boson, which can either be the lighter or the heavier of the two CP-even Higgs bosons. If we perturb the IDM by taking Z_6 and Z_7 small, then either h or H will be approximately SM-like. The phenomenology of the IDM has been treated in detail in [317–319] and won't be pursued further here. In the case of $s_{2\beta} \neq 0$, we would need to extend the (softly-broken) CP3 or CP2 symmetry of the scalar potential to the Higgs-fermion Yukawa sector. As shown in [320], no phenomenologically acceptable CP2-symmetric model exists. A unique softly-broken CP3-symmetric 2HDM does exist with an acceptable fermion mass spectrum; however this model does not appear to be phenomenologically viable due to insufficient CP-violation and potentially large FCNC effects [320]. Hence, for generic choices of the 2HDM parameters, the regime of alignment without decoupling and the double decoupling regime must be regarded as more finely tuned than the generic 2HDM. Note that Refs. [312, 321] discuss the existence of various symmetries of the 2HDM that lead to a natural alignment without decoupling limit, the simplest one being a custodial SO(5) broken by the m_{12}^2 term, hypercharge and Yukawa effects. It however puts important restrictions on the 2HDM spectrum that we do not want to introduce in our subsequent studies.

<div style="text-align: right; font-size: 3em; color: #8B0000;">5</div>

ALIGNMENT LIMIT AND LIGHT HIGGSES AT THE LHC

After the theoretical presentation of the 2HDM and its alignment limit in the previous chapter, we perform here detailed phenomenological analyses of this limit in the context of the Type I and Type II models and in both the h–125 and H–125 scenarios. Taking into account all relevant flavor and collider constraints, we contrast the phenomenological consequences of the alignment limit with and without decoupling. Contrary to naive expectations, the properties of the SM-like state may be sizably affected in this limit and patterns of Higgs couplings deviations may hint at an extended Higgs sector. Naturally, the most direct way to experimentally verify the 2HDM structure would be an observation the extra-states.

The first section of this chapter gives a description of the general setup of the analyses; the strategy, the constraints considered and the tools that have been used. The two next sections respectively describe the results obtained in the study of the alignment limit in the h–125 and H–125 scenarios. Finally, following the non-decoupling idea, we study the possible existence of light Higgs states with masses below about 60 GeV in the last section.

This chapter constitutes an updated version of the analysis performed in "*Scrutinizing the alignment limit in two-Higgs-doublet models: $m_h = 125$ GeV*" [261] that takes into account more recent searches for heavy Higgs bosons from the ATLAS and CMS collaborations and corrects a numerical bug and "*Scrutinizing the alignment limit in two-Higgs-doublet models. II. $m_H = 125$ GeV*" [262] both in collaboration with John F. Gunion, Howard E. Haber, Yun Jiang and Sabine Kraml, and published in Physical Review D. The last section is based on "*Light Higgs bosons in Two-Higgs-Doublet Models*" [322] in collaboration with John F. Gunion, Yun Jiang and Sabine Kraml and published in Physical Review D.

5.1 SETUP OF THE ANALYSES

First, let us note that an extensive review of the status of 2HDMs of Type I and Type II was given in [207, 208] and interpretations of the recently discovered Higgs boson at 125 GeV in the context of the 2HDMs were also studied in Refs. [199, 303, 323–327]. Previous studies of alignment without decoupling scenarios in the light of the LHC Higgs results were conducted in [328–330]. The specific case of additional light Higgs states in 2HDMs with mass below 125/2 GeV will be discussed in a subsequent section.

Considering experimental as well as theoretical uncertainties, the expected precision for coupling measurements at the 13 TeV LHC after collecting 300 fb^{-1} of data is about 4–6% for the coupling to gauge bosons, and of the level of 6–13% for the couplings to

<div style="text-align: center;">113</div>

fermions [331]. The precision improves by roughly a factor of 2 at the high-luminosity run of the LHC with 3 ab^{-1} of luminosity. At a future e^+e^- international linear collider (ILC) with $\sqrt{s} = 250$ GeV to 1 TeV, one may measure the couplings to fermions at the percent level, and the coupling to gauge bosons at the sub-percent level [331].

We take this envisaged $\sim 1\%$ accuracy on C_V as the starting point for the numerical analysis of the alignment limit. Concretely, we will investigate the parameter spaces of the 2HDMs of Type I and Type II assuming that the observed 125 GeV state is h (H), the lighter (heavier) of the two CP-even Higgs bosons in these models, and imposing that $C_V^h = s_{\beta-\alpha} > 0.99$ which corresponds to $|c_{\beta-\alpha}| \lesssim 0.14$ ($C_V^H = c_{\beta-\alpha} > 0.99$ which corresponds to $|s_{\beta-\alpha}| \lesssim 0.14$) using the non-negative $s_{\beta-\alpha}$ ($c_{\beta-\alpha}$) convention.

Imposing a softly-broken $\mathbb{Z}_2$ symmetry ($\Phi_1 \to +\Phi_1$, $\Phi_2 \to -\Phi_2$) on the scalar potential given in Eq. (4.5) which sets $\lambda_6 = \lambda_7 = 0$, the free parameters of the 2HDM scalar potential can be chosen to be the four physical Higgs masses $m_h, m_H, m_{H^\pm}, m_A$, the mass term m_{12}^2, the ratio of the two Higgs vacuum expectation values $\tan\beta$ and the mixing angle α of the CP-even Higgs squared-mass matrix. The vev modulus $\sqrt{v_1^2 + v_2^2}$ is naturally fixed by the $W^\pm$ and Z masses and identified as the SM vev $v \approx 246$ GeV. In the subsequent analyses, we choose the following ranges for the scan,

$$\alpha \in [-\pi/2, \pi/2], \quad \tan\beta \in [0.5, 60], \quad m_{12}^2 \in [-(2000 \text{ GeV})^2, (2000 \text{ GeV})^2],$$

$$m_{H^\pm} \in [m^*, 2000 \text{ GeV}], \quad m_A \in [5 \text{ GeV}, 2000 \text{ GeV}], \tag{5.1}$$

where m^* is a lower bound on the charged Higgs mass originating either from the LEP direct searches [332] or constraints from B-physics; mainly from the $Z \to b\bar{b}$ (R_b), $\epsilon_K, \Delta m_{B_s}$, $B \to X_s\gamma$ and $B \to \tau\nu$ constraints [268–271, 309]. In particular, the latest bound on the charged Higgs mass in Type II is $m_{H^\pm} > 480$ GeV at 95% CL [309], based on the observed rates for radiative B-meson decay, $B \to X_s\gamma$. Both h and H can have the same properties as the SM Higgs and thus serve as possible candidates for the observed SM-like Higgs state. In the h–125 scenario, we will consider $m_h \equiv 125.5$ GeV[20], taking

$$m_H \in [129.5 \text{ GeV}, 2000 \text{ GeV}]. \tag{5.2}$$

As mentioned in Section 4.1.1, the degenerate case $m_h \simeq m_H$ is not considered in this manuscript. Instead, we require a 4 GeV mass splitting between h and H in order to avoid H contamination of the h signal. Similarly, in the H–125 scenario, $m_H = 125.5$ GeV, and

$$m_h \in [10 \text{ GeV}, 121.5 \text{ GeV}]. \tag{5.3}$$

Regarding the definition of the mixing angle, the α range chosen in Eq. (5.1) covers the full 2HDM, subject to the restrictions made on the other parameters. In order to be in the alignment limit, we only generate points that have $C_V \geq 0.99$ for the SM-like state. However, there exist values of t_β such that $c_{\beta-\alpha}$ and/or $s_{\beta-\alpha}$ can take on either sign. It is a simple matter to translate to the non-negative $s_{\beta-\alpha}$ or $c_{\beta-\alpha}$ conventions that we want to impose in the h–125 and H–125 scenarii respectively. For example, given any 2HDM

---

20 Having performed the analyses before the publication of the ATLAS and CMS combination of the Higgs mass which reports a central value of 125.09 GeV [16], we use 125.5 GeV as the observed Higgs mass in the following.

parameter point (α, β) with $-\frac{1}{2}\pi \leq \alpha \leq \frac{1}{2}\pi$ and $0 < \beta < \frac{1}{2}\pi$ (actually the β range is a bit smaller in our analyses since we only consider values of t_β between 0.5 and 60), one can compute the values of $s_{\beta-\alpha}$ and $c_{\beta-\alpha}$. Then, to convert to the convention of non-negative $c_{\beta-\alpha}$ for instance, one would simply replace

$$(s_{\beta-\alpha}, c_{\beta-\alpha}) \rightarrow (-s_{\beta-\alpha}, -c_{\beta-\alpha}) \tag{5.4}$$

if $c_{\beta-\alpha}$ is initially negative. This can be achieved by shifting $\alpha \rightarrow \alpha + \pi$. Only the relative sign of $s_{\beta-\alpha}$ and $c_{\beta-\alpha}$ is indeed physical.

We perform a flat random scan over this parameter space using the public code 2HDMC [333] for a precise state-of-the-art computation of the couplings and decay widths of the various Higgs states. Only points satisfying positivity of the scalar potential, coupling perturbativity and tree-level unitarity are retained. We also require the S, T, and U Peskin-Takeuchi parameters [334] to be compatible with their corresponding values derived from electroweak precision observables [335]. These constraints are also checked by means of 2HDMC.

Next, we impose constraints from the non-observation of Higgs states other than the one at 125 GeV. From the LEP direct searches for light Higgs states, we consider the cross-section upper limits on $e^+e^- \rightarrow Z + h/H$ and $e^+e^- \rightarrow A + h/H$ from [17] and [336] respectively. For very light A below 9.5 GeV, the limits from Upsilon decays [337] are important, for which we follow the implementation in NMSSMTools 4.6.0 [338]. Moreover, we consider the limits from CMS on light pseudo scalars decaying into $\mu^+\mu^-$ [339] in the mass range $m_A = 5.5$–9 GeV and 11.5–14 GeV, which are relevant in particular in Type II models. The recent CMS constraint [340] on neutral Higgs bosons with masses between 25 GeV and 80 GeV, produced in association with a pair of b quarks, followed by the decay into $\tau\tau$, is also applied in our analysis. We find that this constraint eliminates a substantial part of the Type II parameter space at large $\tan\beta$.

When applicable, limits from LHC searches for additional heavy Higgs states are also taken into account. These include the model-independent limits from the searches for $H \rightarrow ZZ^{(*)} \rightarrow 4\ell$ from ATLAS [341] and CMS [176] and for $H \rightarrow ZZ^{(*)} \rightarrow 2\ell2\nu$ from CMS [342] for the h–125 scenario. These limits are however easily evaded since $C_V^h = s_{\beta-\alpha} > 0.99$, while the HVV coupling is suppressed, $|c_{\beta-\alpha}| \lesssim 0.14$. More important are the limits from the $A \rightarrow \tau\tau$ and $h/H \rightarrow \tau\tau$ searches in gluon-fusion or associated production with a pair of b quarks from ATLAS [343] and CMS [344]. These are particularly relevant in the large $\tan\beta$ region of the Type II models where a significant enhancement of the down-type fermion coupling to the neutral Higgs states occurs. The $h/H \rightarrow b\bar{b}$ search from CMS [345] is also imposed. Finally, we take into account the recent CMS result [346] on the search for a new heavy resonance decaying to a Z boson and a light resonance, followed by $Z \rightarrow \ell^+\ell^-$ and the light resonance decaying to $b\bar{b}$ or $\tau\tau$. A very important feature of this analysis is that the masses of the two resonances are left as free parameters. This analysis is sensitive to light resonances with masses down to ~ 35 GeV. The cross section upper limit for the $\ell\ell b\bar{b}$ final state in the plane of the masses of the two resonances then puts a very severe constraint on sizable regions of our analyses. In the context of the 2HDM, this search can indeed be interpreted as $A \rightarrow Z + h/H$ or $H \rightarrow Z + A$ (since in both scenarii h is below or at 125.5 GeV, $h \rightarrow Z + A$ is only opened when $m_A \lesssim 35$ GeV, a region that the analysis is not sensitive to yet). The corresponding ATLAS search for $A \rightarrow Z + h/H$ with $Z \rightarrow \ell\ell$ and $h/H \rightarrow b\bar{b}$ or $\tau\tau$ [347] assumes a SM-like h/H with a fixed mass of

125 GeV and does not provide a constraint as strong as the CMS search. To evaluate all these constraints, production of the h/H and A via gluon-gluon fusion and via associated production with a pair of bottom quarks are computed at NNLO QCD[21] accuracy using `SusHi-1.3.0` [348], while the vector-boson fusion mode for the h/H is computed at NLO with `VBFNLO-2.6.3` [238].

Signal strength constraints coming from the precise measurements of the properties of the 125 GeV state are taken into account by means of `Lilith 1.1.2`. We require each point of the analysis to be allowed at the 95% CL from a global fit to the Higgs measurements as performed in Section 3.4. The CL is derived from the log-likelihood ratio

$$\Delta(-2\ln L)(\mathcal{P}) = -2\ln L(\mathcal{P}/\widehat{2\text{HDM}}), \tag{5.5}$$

where L is the likelihood constructed by `Lilith` using up-to-date signal strength measurements, $\mathcal{P}$ represents the set of parameters of the tested point and $\widehat{2\text{HDM}}$ the best-fit point of the model. The `Lilith` database 15.04 is used for this analysis. It contains all the latest Higgs signal strengths measurements from ATLAS [173, 175, 180, 182, 184, 186, 227, 254, 349, 350] and CMS [171, 174, 176, 179, 181, 183, 219, 228, 256] as of April 2015 and a combined DØ and CDF result [351]. Unless stated otherwise, all parameter space points shown in the following satisfy all of the latest constraints.

5.2 THE $h-125$ SCENARIO IN THE ALIGNMENT LIMIT

5.2.1 *Parameter space*

Let us start by reviewing the allowed parameter space under all constraints discussed previously. Figure 5.1 shows the crucial relation between $|Z_6|$, $|c_{\beta-\alpha}|$ and m_H, illustrating the different ways alignment can occur with and without decoupling. Since $|Z_6| = |(m_H^2 - m_h^2)s_{\beta-\alpha}c_{\beta-\alpha}|/v^2$, it exhibits a clear dependence on the $H-h$ mass difference, and steeply drops towards zero in the limit $|c_{\beta-\alpha}| \to 0$. When m_H is of the order of 1 TeV, one needs to be extremely close to $s_{\beta-\alpha} = 1$ to have small $|Z_6|$—for instance $|Z_6| \approx 10^{-3}$ requires $|c_{\beta-\alpha}| \approx 6 \times 10^{-5}$ for $m_H = 1$ TeV. In contrast, for a lighter H, the departure of $s_{\beta-\alpha}$ from 1 can be more important. It is in principle always possible to obtain arbitrarily small values of $|Z_6|$ if one pushes $s_{\beta-\alpha}$ arbitrarily close to 1. For the purpose of the numerical analysis, we limit ourselves to $|c_{\beta-\alpha}| \geq 10^{-5}$ and have checked that this captures all the phenomenology of the $|c_{\beta-\alpha}| \to 0$ limit. Interestingly, as m_H becomes large, we observe that the decoupling limit sets a stronger upper limit on $|c_{\beta-\alpha}|$ than the one set in the numerical scan ($|c_{\beta-\alpha}| \lesssim 0.14$). Observing a heavy $m_H \gtrsim 850$ GeV at the LHC would thus provide a better-than-1% indirect determination of the h-coupling to electroweak gauge bosons in the framework of these scenarios.

The range of m_A is also interesting. In principle m_A can be above or below $m_{h,H}$ and even $m_A < m_h/2$ is possible and consistent with all the constraints as will be detailed in Section 5.4. However, once m_H is fixed, the allowed range of m_A is limited (and vice versa) as illustrated in Fig. 5.2. We see that in both Type I and Type II, if the scalar H is

---

21 The NNLO corrections for ggF are only computed for the top quark loop, as those for the bottom quark loop are very small.
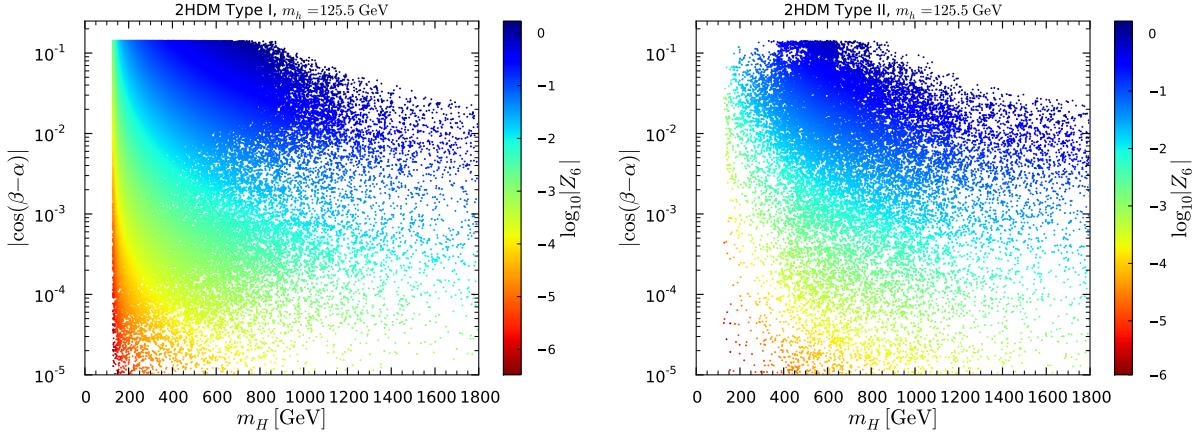
Figure 5.1: $|c_{\beta-\alpha}|$ versus m_H in Type I (left) and Type II (right) with $\log_{10}|Z_6|$ color code. Points are ordered from high to low $\log_{10}|Z_6|$ values.[22]

heavy and decoupled, the same is true for the pseudoscalar A. Conversely, if H is light, say below 600 GeV, then A must be below about 800 GeV. Furthermore, it appears that for $|c_{\beta-\alpha}| \lesssim 10^{-3}$ (or, equivalently, small $|Z_6|$) $m_H < m_A$ is favored. This can be understood from Eq. (4.54), since the $m_h^2 c_{\beta-\alpha}^2$ term therein is always quite small, the mass ordering between m_H and m_A is largely determined by the sign of Z_5. The value of Z_5, in turn, is driven by λ_5, which according to our analysis tends to be negative for small $c_{\beta-\alpha}$. The absence of points over a large region of low $m_{H,A}$ in Type II is in part due to the $H, A \to \tau\tau$ limits [343, 344], which eliminate a large swath of parameter space with $C_h^D \approx -1$ and $m_A \simeq 150$–350 GeV, and to the CMS $H \to ZA$ search [346] which eliminates points down to $m_A \approx 60$ GeV (with a mild dependence on m_H). We note that the surviving points with $m_A \lesssim 60$ GeV have $\tan\beta < 2$. In addition, the charged Higgs mass limit, $m_{H^\pm} > 480$ GeV, in Type II [309], results in the elimination of the remaining quadrant with $m_{H,A} \lesssim 400$ GeV (actually up to $m_H \approx 430$ GeV for very light m_A). In general, the non-trivial correlation between the extra states masses comes from the T parameter contraint which limits the maximum amount of mass splitting between these states. Perturbativity and unitarity, which result in upper bounds on the various λ_i or Z_i, can also play a role.

The interrelation between m_A, m_H and $m_{H^\pm}$ is illustrated in Fig. 5.3. The two panels show m_H versus m_A with color-coding according to $m_{H^\pm}$, with the ordering going from high (blue) to low (red) $m_{H^\pm}$ values. While the correlation of $m_{H^\pm}$ with m_H and m_A is somewhat different in Type I and Type II, in both models a light charged Higgs below 500–600 GeV requires that the H and A also be not too heavy, with masses below about 800 GeV. We also find that for any given $m_{H^\pm}$ there is a lower limit on m_H and m_A: for $m_{H^\pm} \sim 1$ TeV, also $m_{H,A}$ are of that order. In turn, when m_H and m_A are in the non-decoupling regime, $m_{H^\pm}$ cannot be much heavier. The absence of points in the light mass

---

22 In this and subsequent figures, we give 3d information on a 2d plot by means of a color code in the third dimension. To this end, we must choose a definite plotting order. Ordering the points from high to low values in the third dimension, as done for $\log_{10}|Z_6|$ in Fig. 5.1, means that the highest values are plotted first and lower and lower values are plotted on top of them. As a consequence, regions with low values may (partly) cover regions with high values. The opposite of course hold when ordering from low to high values.
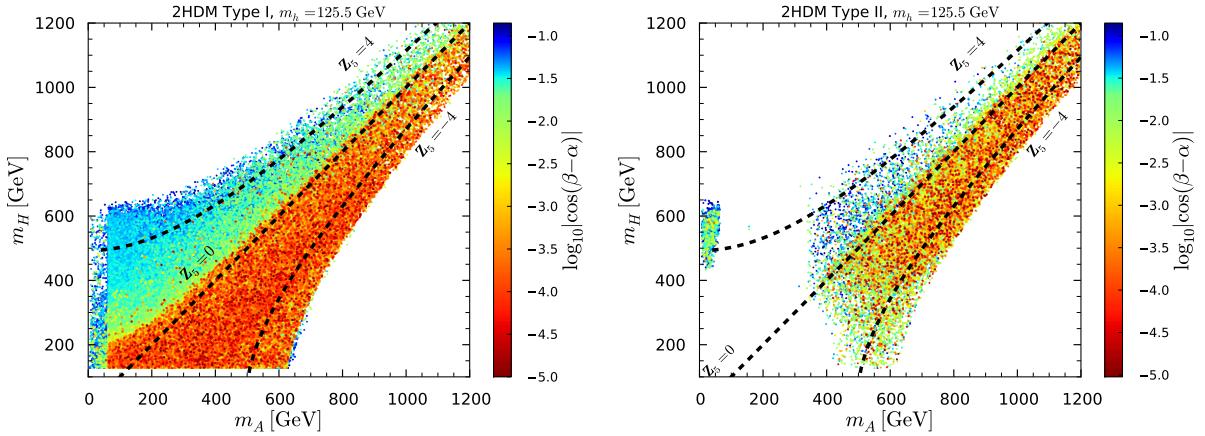
Figure 5.2: m_H versus m_A in Type I (left) and Type II (right) with the color code indicating the value of $\log_{10}|c_{\beta-\alpha}|$. Points are ordered from high to low $\log_{10}|c_{\beta-\alpha}|$. The dashed lines are isolines of $Z_5=4$ (upper line), 0 (middle line) and -4 (lower line) for $|c_{\beta-\alpha}| = 0.015$ (varying $|c_{\beta-\alpha}|$ from 0 to 0.14 has no visible effect on them).
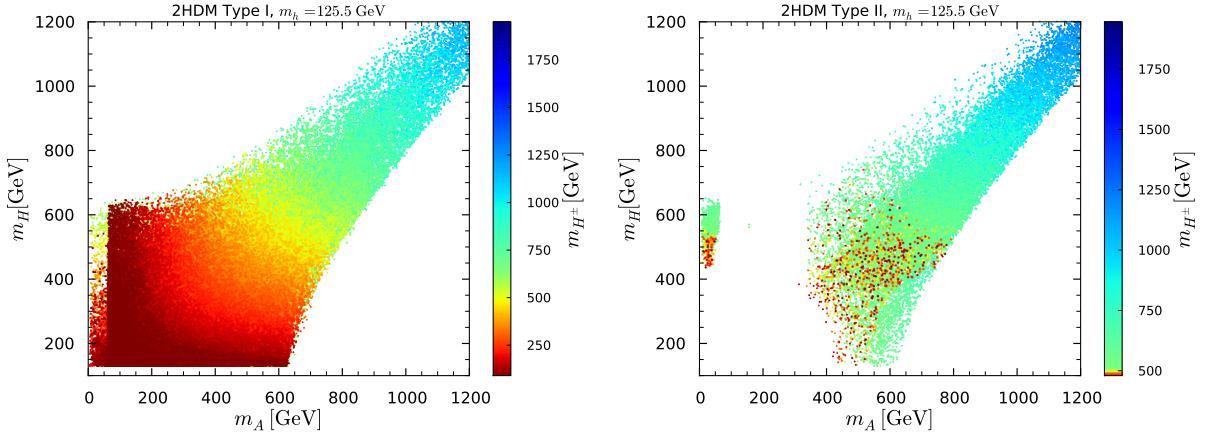

Figure 5.3: m_H versus m_A in Type I (left) and Type II (right) with the color code indicating the value of $m_{H^\pm}$. Points are ordered from high to low $m_{H^\pm}$.

region $m_{H,A} \lesssim 400$ GeV in Type II (but not for Type I), already noted in the previous paragraph, is due to the fact that in the Type II model B-physics requires $m_{H^\pm} \gtrsim 480$ GeV and at low m_A the precision electroweak T parameter constraint would be violated if m_H differs very much from $m_{H^\pm}$. As also mentioned above, an additional band with $m_A \approx 150$–350 GeV is cut out by the $H, A \to \tau\tau$ limits. We will see that this corresponds to a large extent to the wrong-sign C_D^h solution with large $\tan\beta$ in Type II.

5.2.2 Couplings of the SM-like state h

The next question to address is to quantify the range of variations allowed for the couplings of the 125.5 GeV state in the approximate alignment limit where $C_V^h \approx 1$. In particular, recall that in this analysis we impose $s_{\beta-\alpha} > 0.99$ with $m_h = 125.5$ GeV, without requiring however that the other couplings of h are SM-like. To answer this question, we first show
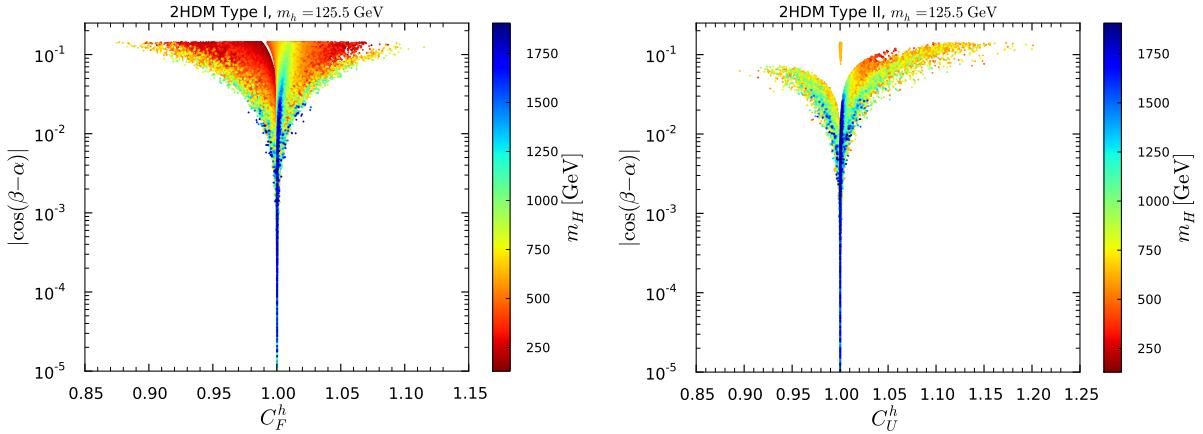
Figure 5.4: $|c_{\beta-\alpha}|$ versus C_F^h in Type I (left) and $|c_{\beta-\alpha}|$ versus C_U^h in Type II (right) with m_H color code. Points are ordered from low to high m_H. The points with $C_U^h \approx 1$ and $|c_{\beta-\alpha}| > 0.03$ are the points for which $C_D^h \approx -1$.
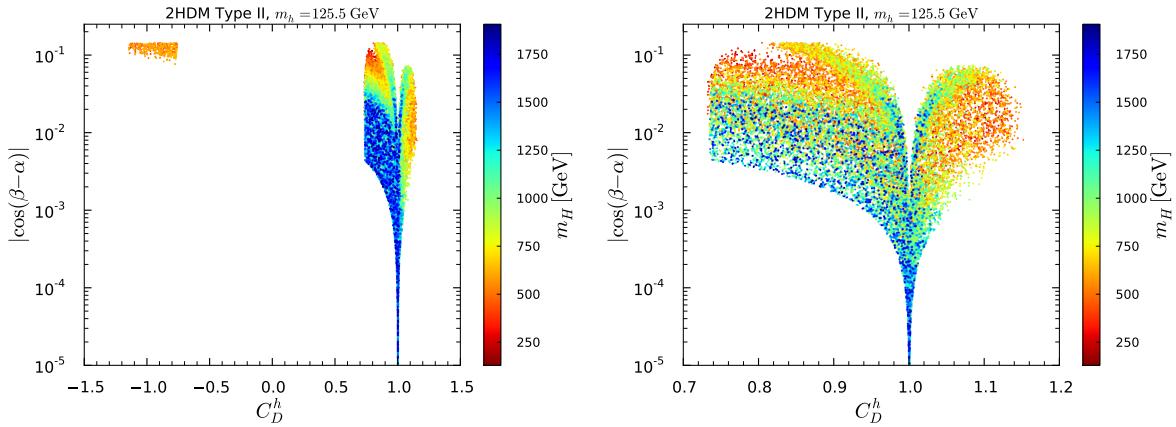

Figure 5.5: $|c_{\beta-\alpha}|$ versus C_D^h in Type II with m_H color code for the full C_D^h range (left) and zooming on the $C_D^h > 0$ region (right). Points are ordered from low to high m_H.

in Fig. 5.4 the dependence of the reduced couplings to (up-type) fermions, $C_F^h \equiv C_U^h = C_D^h$ in Type I (C_U^h in Type II) on $|c_{\beta-\alpha}|$. The mass of the heavier scalar H is shown as a color code. We see that when m_H is light, for only 1% deviation from unity in C_V^h, C_U^h can deviate as much as about 10% (20%) from unity in Type I (Type II). Inverting the plotting order of m_H (not shown), it is interesting to note that these deviations are largest for $m_H \approx 700\text{–}800$ GeV while slightly more constrained for lighter m_H. On the other hand, in the decoupling limit the deviations in C_U^h are more constrained, with a maximum of 5% for $m_H \gtrsim 1.2$ TeV in both Type I and Type II. It is also interesting to observe how quickly alignment leads to SM-like couplings: for $|c_{\beta-\alpha}| \lesssim 10^{-2}$ the deviations in C_U^h are limited to just a few percent no matter the value of m_H.

The situation is quite different for the coupling to down-type fermions, C_D^h, in Type II, see Fig. 5.5. First of all, the possible deviations are larger than for C_U^h, with C_D^h ranging from about 0.70 to 1.15 even for $|c_{\beta-\alpha}| \sim 10^{-2}$. This is an illustration of the delayed approach to the alignment limit at large t_β as discussed below Eq. (4.82). Let us recall indeed that $C_D^h = s_{\beta-\alpha} - c_{\beta-\alpha} t_\beta$. This will drive the whole phenomenology of the scenario;

sizable deviations of C_D^h from 1 lead to possible large deviations in the signal strengths even for quite small $|c_{\beta-\alpha}|$ since the $h \to b\bar{b}$ partial width accounts for the majority of the total decay width. We note that $C_D^h = 1$ is not possible unless $|c_{\beta-\alpha}|$ is very small (again a few times 10^{-3} or smaller) as a consequence of the lower bound imposed on t_β of 0.5. For the larger positive deviation of C_D^h possible (up to ~ 1.12), only points with $m_H \lesssim 750$ GeV are observed. On the contrary, C_D^h values which are substantially smaller than 1 can be achieved in both the decoupling and non-decoupling regimes except for a small island of points located around $C_D^h \approx 0.8$ and $|c_{\beta-\alpha}| \approx 0.1$ that is achieved only for $m_H \lesssim 400$ GeV. Thus, for instance, a discovery of a light H state in association with a measured value of $C_D^h \sim 0.8$ would give an indirect way to probe sub-percent deviation of C_V^h in this Type II scenario. On the contrary, this also illustrates how, in a given framework, the precise measurements of the Higgs properties may provide indirect hints on the presence of new states.

Finally, for light m_H the sign of C_D^h relative to C_V^h and C_U^h can be opposite to the corresponding SM value. This is realized for not so small values of $|c_{\beta-\alpha}| \geq 0.07$, i.e. at the boundary of what we consider as the alignment limit, for 330 GeV $\leq m_H \leq$ 660 GeV, 350 GeV $\leq m_A \leq$ 660 GeV and $0.22 \leq |Z_6| \leq 0.90$. For the points in this region, the up-type coupling is very close to 1, corresponding to the few isolated points observed in the right panel of Fig. 5.4. As discussed in [259], the eventual precision reached in LHC Run 2 will allow one to either confirm or eliminate the wrong-sign coupling possibility using precise signal rate measurements of h in a few channels. Should the wrong-sign coupling be confirmed, one would expect to also see A signals (plus perhaps H signals) in the above mass range, thereby providing a confirmation of this scenario. (The cross sections for A and H signals will be discussed in Section 5.3.5.) Since the wrong-sign solution occurs at large $\tan\beta$, it should be noted that this region is already much affected by the $A \to \tau\tau$ searches when A is produced in association with a pair of bottom quarks.

The $\tan\beta$ dependence of the fermion couplings of h is shown in Fig. 5.6. We see that large $\tan\beta$ leads to C_F^h very close to 1 in Type I and C_U^h very close to 1 in Type II. However in Type II, at large $\tan\beta$, small $c_{\beta-\alpha}$ is not enough to drive $C_D^h \to 1$: the approach to SM-like coupling is delayed. Note also that the wrong-sign C_D^h solution in Type II requires $\tan\beta \gtrsim 10$ and $C_V^h \approx 0.9994$ (which is experimentally indistinguishable from exact alignment).

The loop-induced coupling to photons, C_γ^h, is presented in Fig. 5.7. Even at very small $c_{\beta-\alpha}$, C_γ^h can deviate substantially from 1. This is due to the charged-Higgs contribution to the $h\gamma\gamma$ coupling. This contribution can be large with either sign, positive or negative, in Type I, while in Type II *large* contributions are always negative and suppress C_γ^h [259]. Note in particular the Type II points with $C_\gamma^h \approx 0.95$ associated with the wrong-sign C_D^h cases for which the charged Higgs loop contribution does not decouple and always leads to a suppression. Regarding the loop-induced coupling to gluons, in the Type I model, C_g^h, is equal to C_F^h, the dependence of which on $|c_{\beta-\alpha}|$ was presented in Fig. 5.4. In the case of Type II, C_g^h and C_U^h are very similar despite the difference between up- and down-type couplings, due to the fact that the b-loop contribution to C_g^h is rather small. The one exception in the case of Type II arises for the wrong-sign scenarios for which the b-loop contribution changes sign and interferes constructively with the t-loop contribution. In this case, C_g^h is always enhanced and $C_g^h \sim 1.06$, this was also first discussed in Ref. [259].
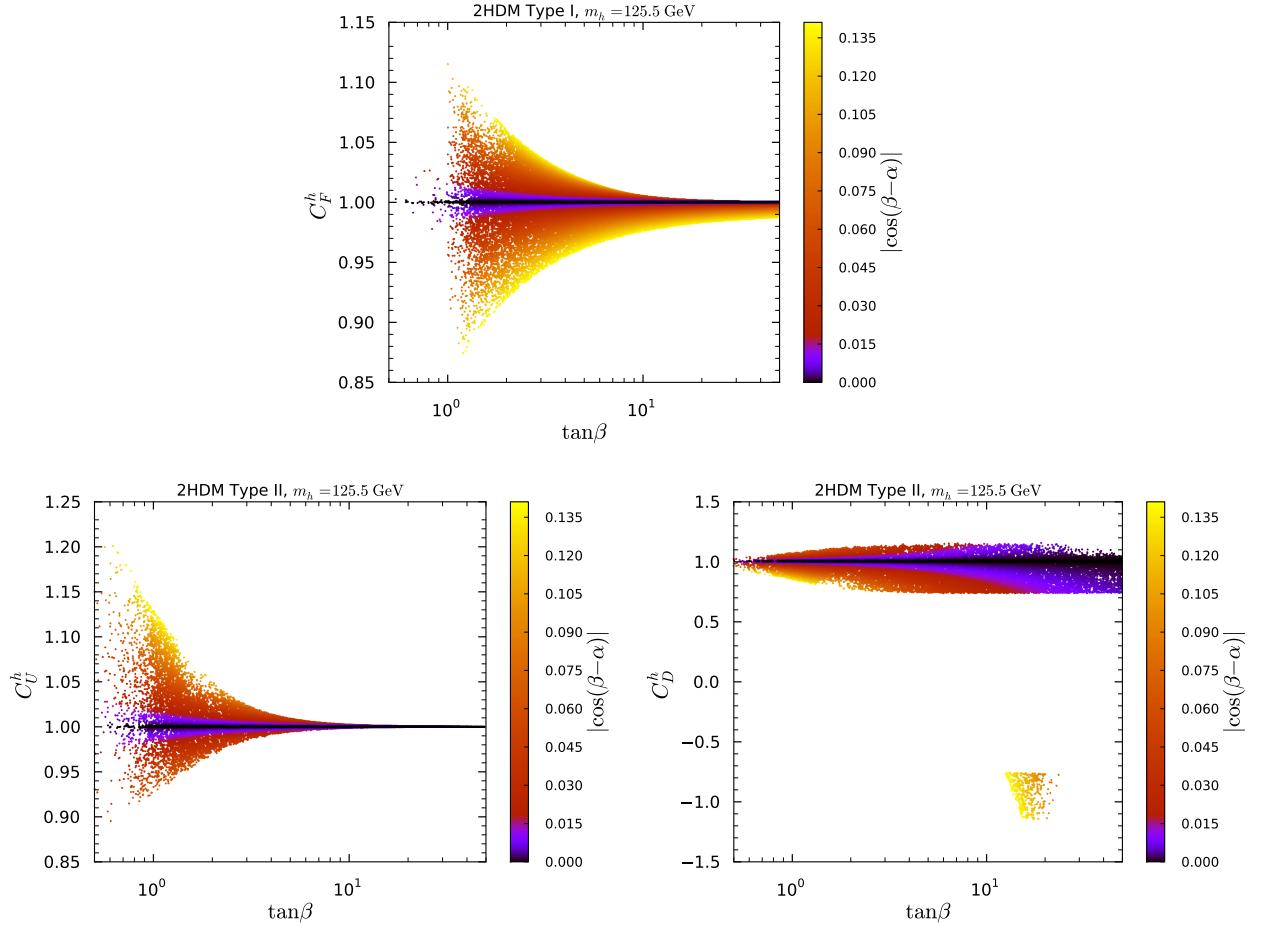
Figure 5.6: Fermionic couplings versus $\tan\beta$ in Type I (upper panel) and Type II (lower panels) with $|c_{\beta-\alpha}|$ color code. Points are ordered from high to low $|c_{\beta-\alpha}|$.
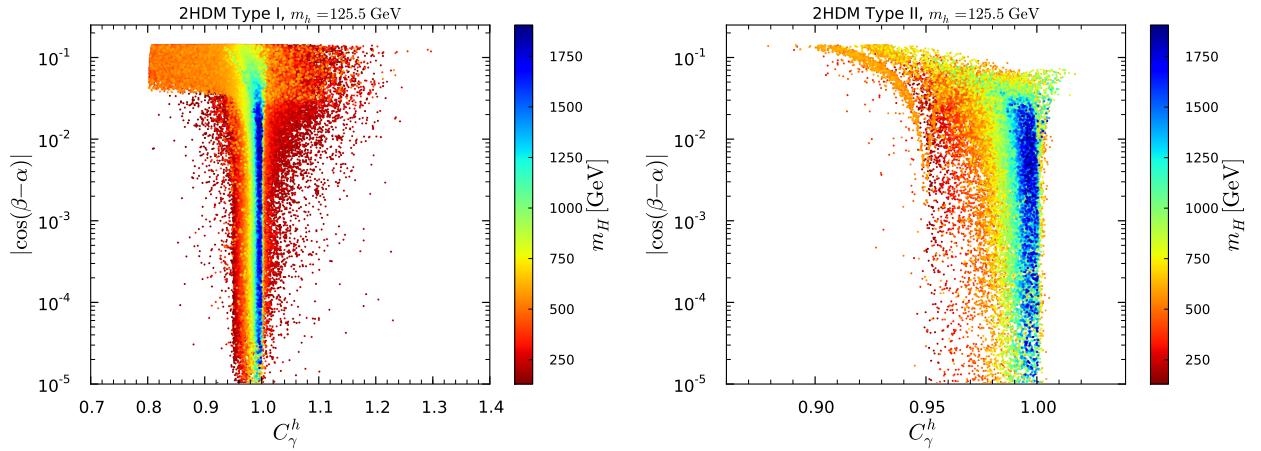

Figure 5.7: $|c_{\beta-\alpha}|$ versus C_γ^h in Type I (left) and Type II (right) with m_H color code. Points are ordered from low to high m_H.

While the exceedingly small deviations in C_V^h that we consider here will not be directly accessible at the LHC, precision measurements of the other couplings together with a
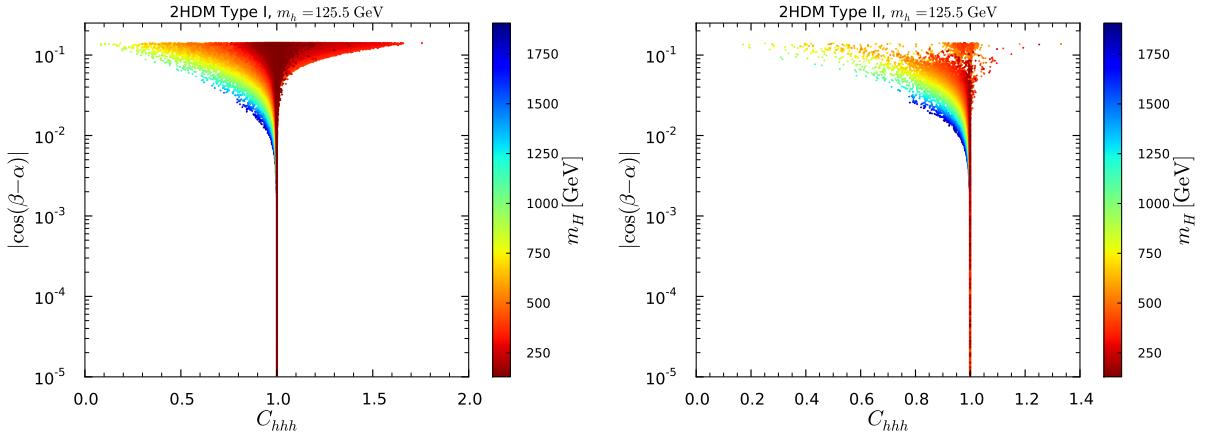
Figure 5.8: $|c_{\beta-\alpha}|$ versus the reduced triple Higgs coupling C_{hhh} in Type I (left) and Type II (right) with m_H color code. Points are ordered from high to low m_H values.

measurement of, or a limit on, $m_{H,A}$ can be used for consistency checks and for eventually pinning down the model realized in nature. Of special interest in this context is also the triple Higgs coupling. The dependence of $C_{hhh} \equiv g_{hhh}/g_{hhh}^{SM}$ on $c_{\beta-\alpha}$ and m_H is shown in Fig. 5.8. It is quite striking that large values of $C_{hhh} > 1$ (up to $C_{hhh} \approx 1.7$ in Type I and up to $C_{hhh} \approx 1.35$ in Type II) can be achieved in the non-decoupling regime, roughly $m_H \lesssim 600$ GeV, for $|c_{\beta-\alpha}|$ values of the order of 0.1, whereas for heavier m_H, C_{hhh} is always suppressed as compared to its SM prediction. These features were explained in the discussion below Eq. (4.97). This cannot be seen directly in Fig. 5.8, but we verified that points with $m_H > 630$ GeV never have $C_{hhh} > 1$ as expected in the decoupling limit. Note also that for $m_H \approx 1$ TeV, C_{hhh} approaches the SM limit of 1 as $|c_{\beta-\alpha}|$ decreases more slowly than is the case for lighter m_H; substantial deviations $C_{hhh} < 1$ are possible as long as $|c_{\beta-\alpha}|$ is roughly greater than a few times 10^{-2}. This comes from the $(2Z_6/Z_1)c_{\beta-\alpha}$ term in Eq. (4.97): since $Z_6 c_{\beta-\alpha}$ is always negative (in our non-negative $s_{\beta-\alpha}$ convention), Z_1 is positive by positivity of the potential, and since Z_6 can be sizable when $m_H \approx 1$ TeV, see Fig. 5.1, this can lead to a suppression as extreme as $C_{hhh} \approx 0.1$. (For $m_H \gtrsim 1$ TeV the deviations are smaller in part because the possible range of $c_{\beta-\alpha}$ is limited as seen in Fig. 5.1.) For very light m_H, on the other hand, Z_6 is much smaller and hence the deviations with $C_{hhh} < 1$ are more limited. For $m_H \lesssim 250$ GeV we find $C_{hhh} \simeq 0.80$–1.40 in Type I and $C_{hhh} \simeq 0.95$–1.13 in Type II. This is at the limit of what can be measured, as the expected precision is about 50% at the high-luminosity options of the LHC and the ILC with 500 GeV, and about 10–20% at a 1–3 TeV e^+e^- linear collider with polarized beams [331].

The relation between the triple Higgs coupling g_{Hhh}, $|c_{\beta-\alpha}|$ and m_H is presented in Fig. 5.9. In Type I, large values of g_{Hhh} can be achieved in the non-decoupling regime for $|c_{\beta-\alpha}|$ of the order 10^{-1}. This is also true in Type II, though the range of g_{Hhh} is somewhat smaller. We observe moreover that for given $|c_{\beta-\alpha}| \lesssim 10^{-1}$, the achievable Hhh coupling grows with m_H. Nonetheless, as will be shown in Section 5.3.5, the $H \to hh$ decay is only relevant below the $t\bar{t}$ threshold. Moreover, in the exact alignment limit, the Hhh coupling vanishes.
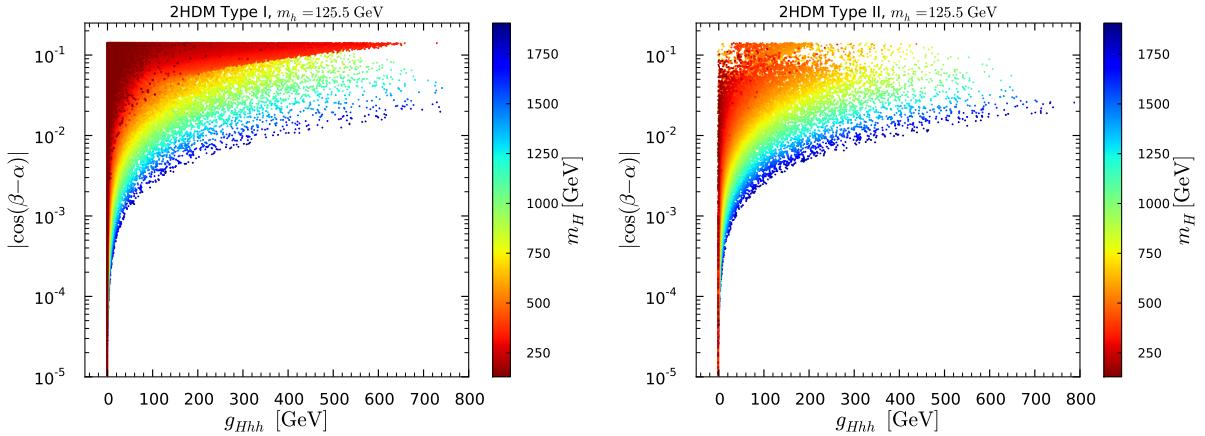
Figure 5.9: $|c_{\beta-\alpha}|$ versus the triple Higgs coupling g_{Hhh} in Type I (left) and Type II (right) with m_H color code. Points are ordered from high to low m_H values.

5.2.3 *Signal strengths of the SM-like state h*

The variations in the couplings to fermions discussed above have direct consequences for the signal strengths of the SM-like Higgs boson. Since the results depend a lot on the fermion coupling structure, we examine this separately for Type I and Type II.

Let us start with Type I. Figure 5.10 shows the signal strengths for gluon-gluon fusion and decay into $\gamma\gamma$ ($\mu_{gg}^h(\gamma\gamma)$[23], left panel), and decay into ZZ^* ($\mu_{gg}^h(ZZ^*)$, right panel). Recalling that C_F^h varies between 0.87 and 1.11 in Type I and comparing with Fig. 5.7, it is clear that the variation in $\mu_{gg}^h(\gamma\gamma)$ comes to a large extent from the charged Higgs contribution to the $\gamma\gamma$ loop. Even for $|c_{\beta-\alpha}| \to 0$, large deviations from 1 can occur due to a sizable charged Higgs contribution or the presence of a light pseudoscalar $m_A < m_h/2$ that increases the SM-like Higgs total width. On the other hand, in the decoupling limit, the charged Higgs loop is small and C_γ^h is largely determined by the relative size of the top and bottom loops compared to the W loop (which enters with opposite sign). On the contrary, C_g^h is solely determined by the size of the t and b loop contributions. One finds numerically that the $h\gamma\gamma$ coupling is slightly more suppressed than the hgg coupling is enhanced, so that $\mu_{gg}^h(\gamma\gamma) \lesssim 1$ in the decoupling regime.

In contrast, $\mu_{gg}^h(ZZ^*)$ shows less variation, $\mu_{gg}^h(ZZ^*) = [0.92, 1.04]$ if the $h \to AA$ decay channel is closed, with small excursions around 1 allowed in the decoupling limit. It also exhibits a less distinct dependence on m_H compared to $\mu_{gg}^h(\gamma\gamma)$. The reason is that $\mu_{gg}^h(ZZ^*)$ is driven by C_F^h and $\tan\beta$, as illustrated in Fig. 5.11. The dependence on C_F^h is clear as larger (smaller) C_F^h leads to larger (smaller) cross section for $gg \to h$. The dependence on $\tan\beta$ results from an interplay between the top (which drives the $gg \to h$ cross section) and bottom (which drives the total h width) Yukawa couplings both given by $C_F^h = s_{\beta-\alpha} + c_{\beta-\alpha}/t_\beta$. The scattered points with suppressed $\mu_{gg}^h(ZZ^*)$ are those where the $h \to AA$ decay mode is open and increases the total width. An analogous picture emerges for the VBF-induced $h\tau\tau$ signal strengths, since $\mu_{\mathrm{VBF}}^h(\tau\tau) = \mu_{gg}^h(ZZ^*)$ in Type I.

In Type II, we find that the situation is quite different. Here, the signal strengths are driven by both the top quark coupling, which impacts C_g^h, and by the bottom Yukawa

---

23 We switch from the notation $\mu(X, Y)$ of Eq. (3.7) to $\mu_X(Y)$ to denote the signal strengths.
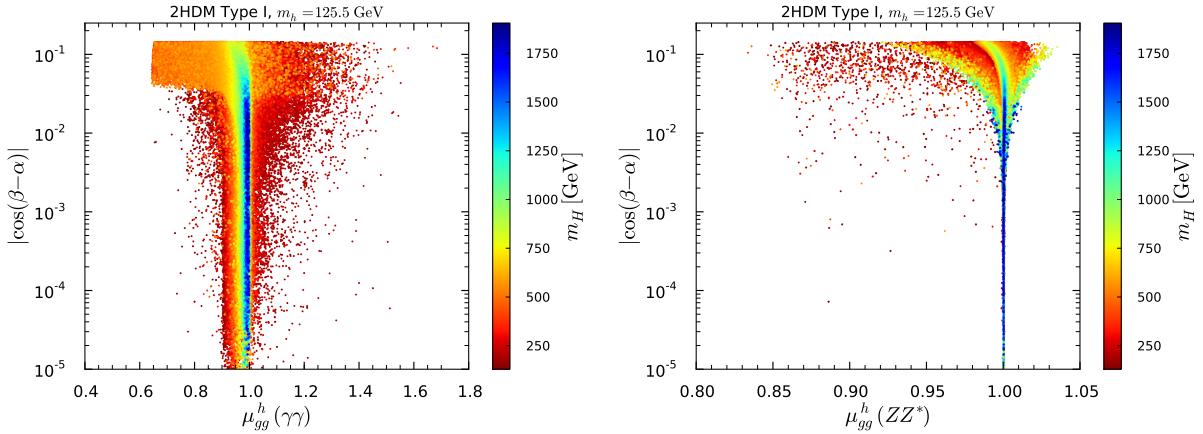
Figure 5.10: Signal strengths in Type I for the 125.5 GeV state, for $gg \to h \to \gamma\gamma$ (left) and $gg \to h \to ZZ^*$ (right) with m_H color code. Points are ordered from low to high m_H values. Points with $\mu^h_{gg}(ZZ^*) < 0.92$ are ones for which $h \to AA$ decays are present, so that the total h width is increased, which suppresses this particular channel's rate.
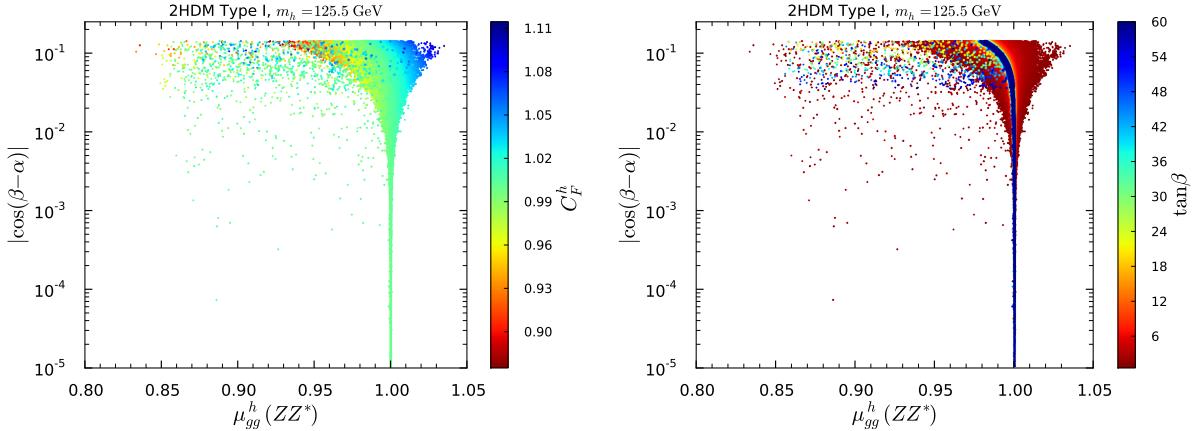

Figure 5.11: Signal strength for $gg \to h \to ZZ^*$ in Type I for the 125.5 GeV state with C^h_F (left) and $\tan\beta$ (right) color code. Points are ordered from low to high C^h_F and $\tan\beta$ values.

coupling C^h_D, which also enters C^h_g and, often of greatest importance, determines the $h \to b\bar{b}$ decay width. In Fig. 5.12 we show the signal strengths $\mu^h_{gg}(\gamma\gamma)$, $\mu^h_{gg}(ZZ^*)$ and $\mu^h_{\text{VBF}}(\tau\tau)$ in Type II comparing the dependence on m_H (left panels) to the dependence on $|C^h_D|$ (right panels). Note that the m_H dependence of the signal strengths reflects the m_H dependence of C^h_D in Fig. 5.5. As a consequence, $\mu^h_{gg}(\gamma\gamma)$ and $\mu^h_{gg}(ZZ^*)$ can be enhanced in the decoupling regime, with values going as high as 1.4–1.5 (mainly due to suppression of the total h width), to be compared to the current model-independent 95% CL limits of $\mu^h_{gg}(\gamma\gamma) \in [0.76, 1.69]$ and $\mu^h_{gg}(ZZ^*) \in [0.71, 1.80]$. Suppression is also possible, reaching a level of $\mu^h_{gg}(\gamma\gamma) = 0.74$–0.76 for low m_H if $|c_{\beta-\alpha}| > 0.01$ but limited to 0.9 for large $m_H \gtrsim 1250$ GeV. For all m_H, the amount of possible suppression decreases systematically with decreasing $|c_{\beta-\alpha}|$. For $\mu^h_{\text{VBF}}(\tau\tau)$ the behaviour is exactly opposite. For completeness we note that the horizontal bar at $|c_{\beta-\alpha}| \sim 10^{-1}$ is the $C^h_D < 0$ region, and the scattered points are those where the $h \to AA$ decay is open. Finally note that as $|c_{\beta-\alpha}|$ decreases, the signal strengths in
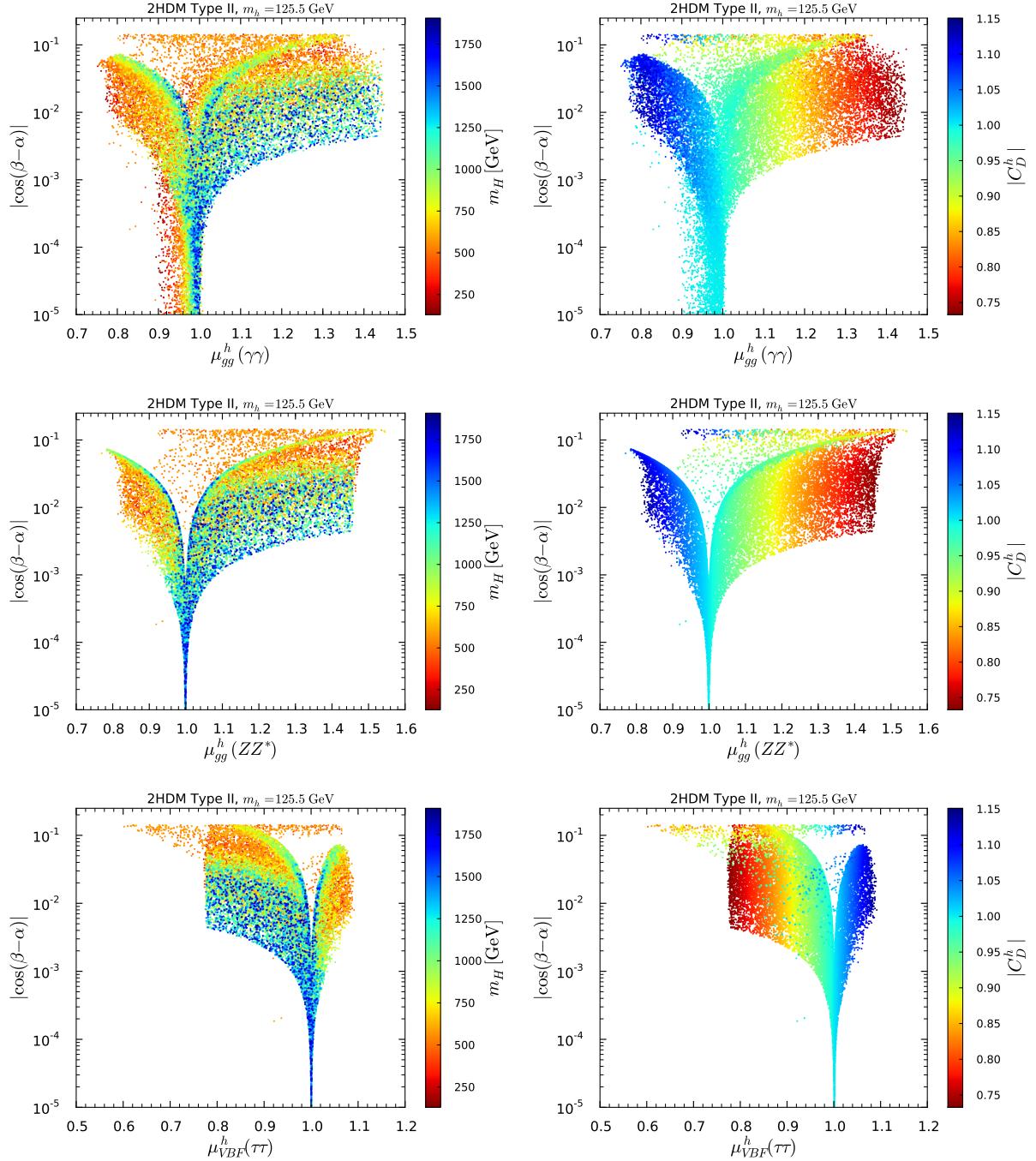
Figure 5.12: Signal strengths in Type II for the 125.5 GeV state with m_H (left) and $|C_D^h|$ color code. Points are ordered from low to high m_H and $|C_D^h|$ values.

Type II converge to 1 much more slowly than in Type I. This is a consequence of the delayed alignment of C_D^h to 1 in Type II when $\tan\beta$ is large. An additional effect arises in $\mu_{gg}^h(\gamma\gamma)$ due to the charged Higgs loop contribution to the $h \to \gamma\gamma$ amplitude. In particular, there exists an intermediate range of charged Higgs masses for which $g_{hH^+H^-} \simeq -2m_{H^\pm}^2/v$ [cf. Eq. (4.110)], which yields a constant non-decoupling contribution that suppresses the
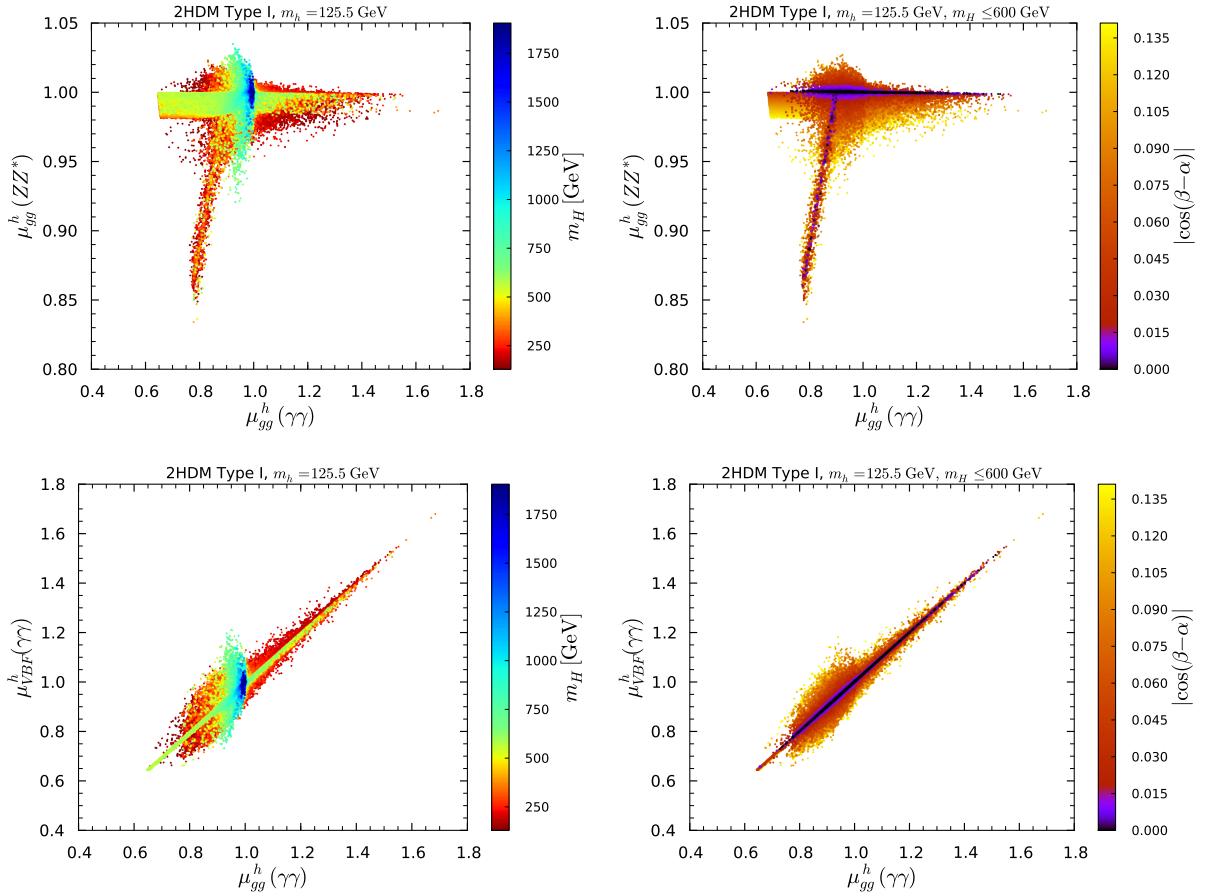
Figure 5.13: Correlations of signal strengths in Type I, on the left illustrating the dependence on m_H, on the right illustrating the dependence in $|c_{\beta-\alpha}|$. Points are ordered from low to high m_H values (left) and high to low $|c_{\beta-\alpha}|$ values (right).

$h \to \gamma\gamma$ amplitude [259] (see also [352, 353]). Indeed, even for values of $|c_{\beta-\alpha}|$ as low as 10^{-4}, this signal strength does not converge to 1 until m_H (and thus $m_{H^\pm}$) is above about 1 TeV.

Putting everything together we find quite distinct correlations of signal strengths in both Type I and Type II that depend on whether the additional Higgs states are decoupled or not. This is illustrated in Fig. 5.13 for Type I and in Fig. 5.14 for Type II. In both figures, the panels on the left show the dependence on m_H while the panels on the right show the dependence on $|c_{\beta-\alpha}|$ for the non-decoupling regime with $m_H \leq 600$ GeV. We note that there are definite combinations of signal strengths that cannot be reached in the decoupling regime. A measurement of such values would be a very strong motivation to look for additional light Higgs states. In turn, when the masses of additional light Higgs states are measured, signal strength correlations as shown in Figs. 5.13 and 5.14 can help pin down the model. Furthermore, for $m_H \leq 600$ GeV even in the apparent alignment limit $|c_{\beta-\alpha}| \to 0$ there can be deviations in the signal strengths from unity that cannot be mimicked by decoupling.

Examples for Type I are the suppression of both $\mu_{gg}^h(\gamma\gamma)$ and $\mu_{gg}^h(ZZ^*)$, or the combination $\mu_{gg}^h(\gamma\gamma) > 1$ with $\mu_{gg}^h(ZZ^*) \approx 1$. The former case is also present in Type II for light m_H, while the latter does not occur at all in Type II. More concretely, in the decoupling regime
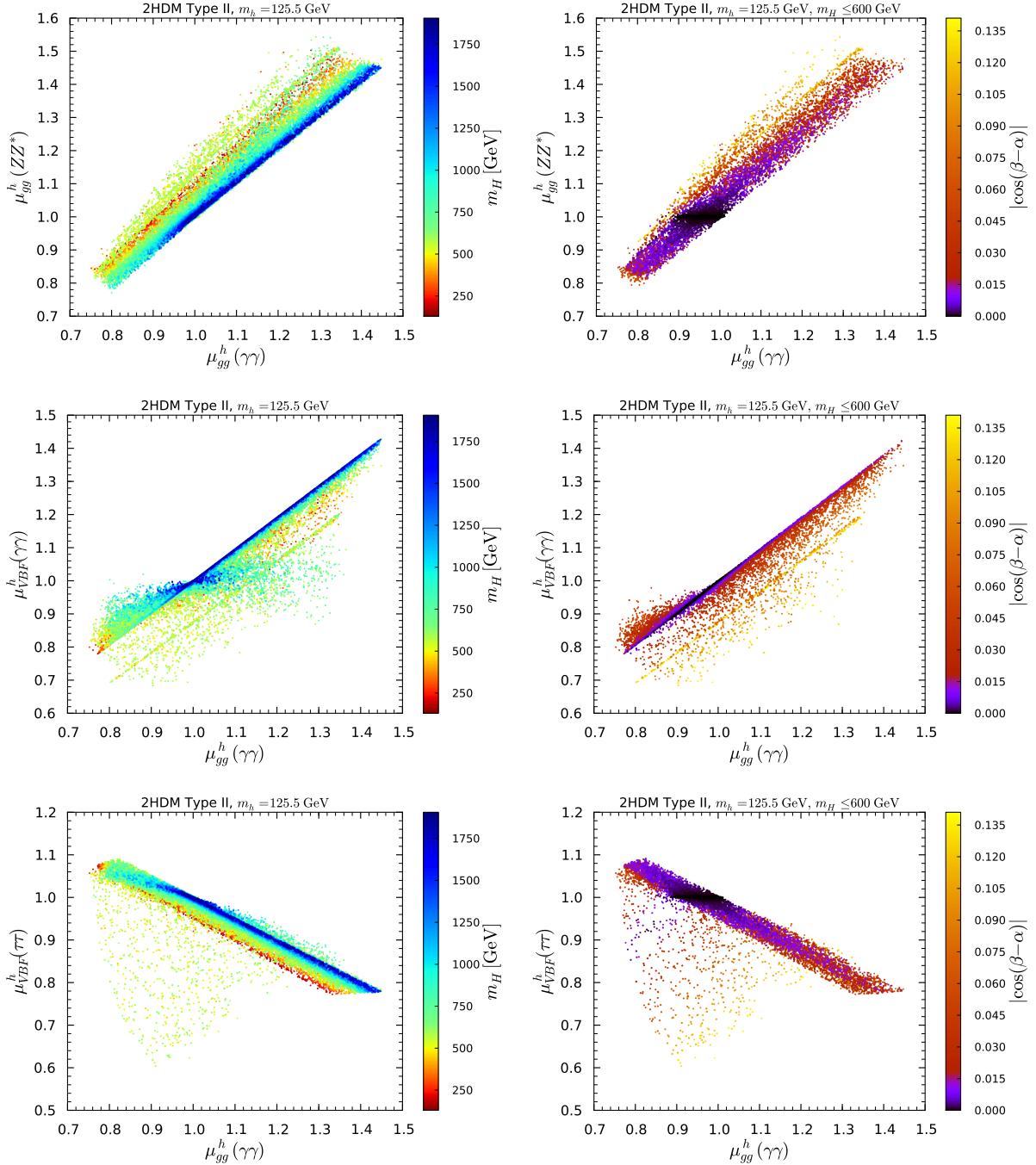
Figure 5.14: Correlations of signal strengths in Type II, on the left illustrating the dependence on m_H, on the right illustrating the dependence in $|c_{\beta-\alpha}|$. Points are ordered from low to high m_H values (left) and high to low $|c_{\beta-\alpha}|$ values (right).

of Type II, $\mu_{gg}^h(\gamma\gamma) \approx \mu_{gg}^h(ZZ^*)$, whereas for light m_H one can have $\mu_{gg}^h(\gamma\gamma) < \mu_{gg}^h(ZZ^*)$ even if $|c_{\beta-\alpha}|$ is very small (comparing Fig 5.14, top row, left vs. right). Another example is the simultaneous suppression or enhancement of $\mu_{gg}^h(\gamma\gamma)$ and $\mu_{\mathrm{VBF}}^h(\gamma\gamma)$ in Type I, that is not possible in the decoupling regime (cf. Fig 5.13, bottom left). In Type II, one can

have a simultaneous enhancement, up to 1.45 of $\mu^h_{gg}(\gamma\gamma)$ and $\mu^h_{\mathrm{VBF}}(\gamma\gamma)$ in the decoupling regime, but simultaneous suppression is limited to ~ 0.9–0.95 (cf. Fig 5.14, middle left); simultaneous suppression to a level of ~ 0.8 is however possible in the alignment limit for $m_H \lesssim 300$ GeV, i.e. well away from the decoupling regime. Precise enough signal strength measurements could therefore provide strong hints that we are in the alignment without decoupling regime of a 2HDM even if no additional Higgs states are discovered at that time.

5.2.4 *Probing H and A at the LHC*

Let us now turn to the prospects of discovering the additional neutral states. The two important production modes at the LHC are gluon fusion, $gg \to X$, and the associated production with a pair of b-quarks, $b\bar{b}X$, with $X = A, H$. The production modes involving electroweak gauge bosons are suppressed in the alignment limit for H, and non-existent at tree-level for A. The correlations of the $gg \to X$ and $b\bar{b}X$ cross sections at the 13 TeV LHC in the non-decoupling regime $m_H \leq 600$ GeV are shown in Fig. 5.15 for the Type I model and in Fig. 5.16 for the Type II model. We show the points that pass all present constraints (in beige) and highlight those that have a very SM-like Higgs state by constraining all the following signal strengths to be within 5% or 2% of their SM values, respectively, denoted as SM±5% (in red) and SM±2% (in dark red),

$$\mu^h_{gg}(\gamma\gamma),\ \mu^h_{gg}(ZZ^*),\ \mu^h_{gg}(\tau\tau),\ \mu^h_{VBF}(\gamma\gamma),\ \mu^h_{VBF}(ZZ^*),\ \mu^h_{VBF}(\tau\tau),\ \mu^h_{VH}(b\bar{b}),\ \mu^h_{t\bar{t}}(b\bar{b})\,. \quad (5.6)$$

We start the discussion with production of A in Type I, shown in the left panel of Fig. 5.15. There is a strong correlation between the two production modes, gluon fusion and $b\bar{b}$ associated production, which stems from the fact that the relevant couplings are the same up to a sign: $C^A_U = -C^A_D = \cot\beta$. The larger spread in $\sigma(b\bar{b}A)$ observed for $\sigma(gg \to A) > 10^{-2}$ pb comes from the fact that for $m_A \lesssim 2m_t$ the $b\bar{b}A$ cross section grows faster with decreasing m_A than that of $gg \to A$. Therefore, along a line of fixed $\sigma(gg \to A)$ in the plot, a point with higher $\sigma(b\bar{b}A)$ has a smaller m_A. Overall, however, $\sigma(gg \to A)$ is always at least about two orders of magnitude larger than $\sigma(b\bar{b}A)$. The points with largest cross sections, $\sigma(b\bar{b}A) \approx 10$ pb and $\sigma(gg \to A) \approx 1000$ pb, correspond to the case $m_A < m_h/2$ presented in more details in a next section. One feature of this region is that $\mu^h_{gg}(\gamma\gamma)$ and $\mu^h_{gg}(ZZ^*, WW^*)$ always differ from each other by about 10%. Constraining all h signal strengths of Eq. (5.6) within 5% of unity therefore eliminates these points. Other points with high cross sections, but not in the very light pseudoscalar region, would also be eliminated by the SM±5% or SM±2% requirements. However, in this non-decoupling regime of $m_H \leq 600$ GeV, points with sizeable cross sections up to 0.2 pb for $\sigma(b\bar{b}A)$ and up to about 40 pb for $\sigma(gg \to A)$ still remain even at the SM±2% level. At this same SM±2% level, the smallest $\sigma(gg \to A)$ is about 0.1 fb.

Regarding the production of the scalar H in Type I, shown in the right panel of Fig. 5.15, the correlation is even stronger between $\sigma(b\bar{b}H)$ and $\sigma(gg \to H)$ since both are driven by the same fermionic coupling $C^H_F = \sin\alpha/\sin\beta$. Note that, as in the A case, the gluon-fusion cross section is always larger than that for $b\bar{b}$ associated production. Sizable cross sections are still allowed under the SM±2% constraint, which implies that in the non-decoupling regime there is a strong possibility of detecting a second scalar state at the
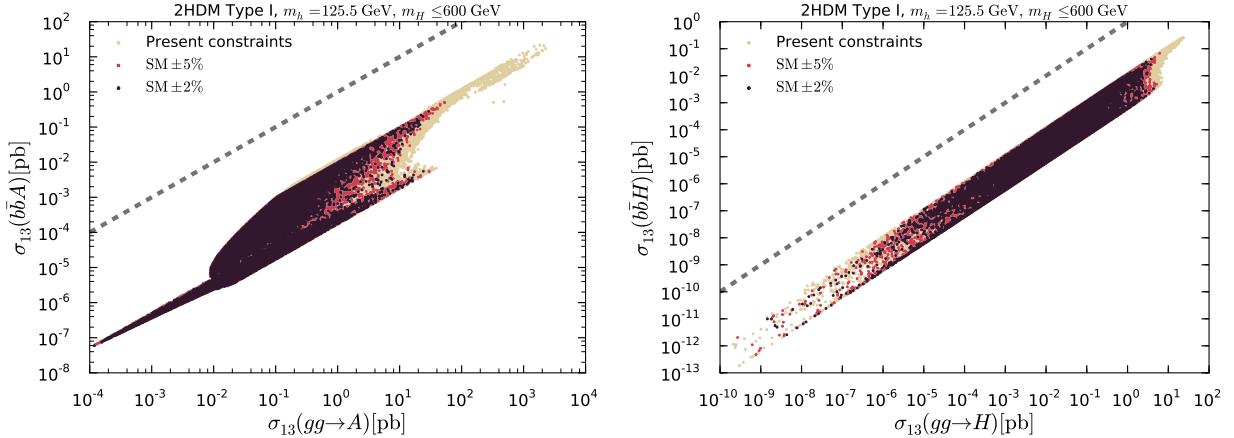
Figure 5.15: $\sigma(b\bar{b}X)$ versus $\sigma(gg \to X)$ for $X = A$ (left) and $X = H$ (right) in Type I at the 13 TeV LHC in the alignment without decoupling limit, $m_H \leq 600$ GeV, satisfying all present constraints (in beige) as well as points for which the signals strengths from Eq. (5.6) are within 5% and 2% of the SM predictions (in red and dark red, respectively). The dashed lines indicate $\sigma(b\bar{b}X) = \sigma(gg \to X)$.
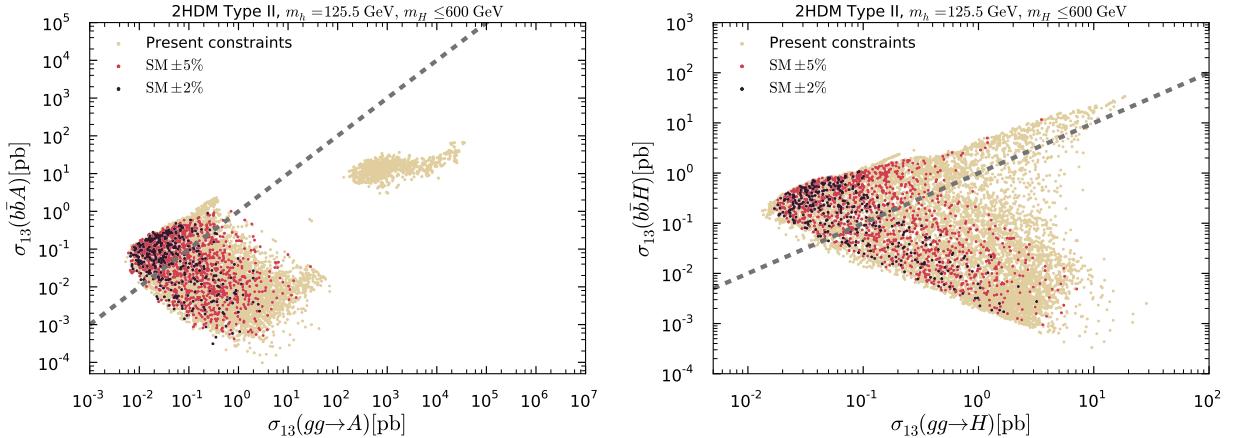

Figure 5.16: As Fig. 5.15 but for Type II.

LHC. The structure of C_F^H is however such that the coupling can equally well be very much suppressed, leading to extremely small cross sections. We will come back to this point below.

The corresponding results for Type II are presented in Fig. 5.16. In contrast to Type I, both $b\bar{b}$ associated production and gluon–gluon fusion modes for Type II are in principle important since either can be dominant in different regions of the parameter space. There is only modest correlation between the two production modes due to the more complex structure of the Type II fermionic couplings. For A production, one clearly sees the $m_A < m_h/2$ region as the detached scattered points with very large cross sections. As for Type I, these points disappear under the SM±5% constraint. Still, even for SM±2%, cross sections for $b\bar{b}A$ close to 1 pb and around 20 pb for $gg \to A$ can be achieved (although not simultaneously). For H production a similar picture emerges, with the maximal cross sections however being a factor of a few smaller than for A production. The minimal cross
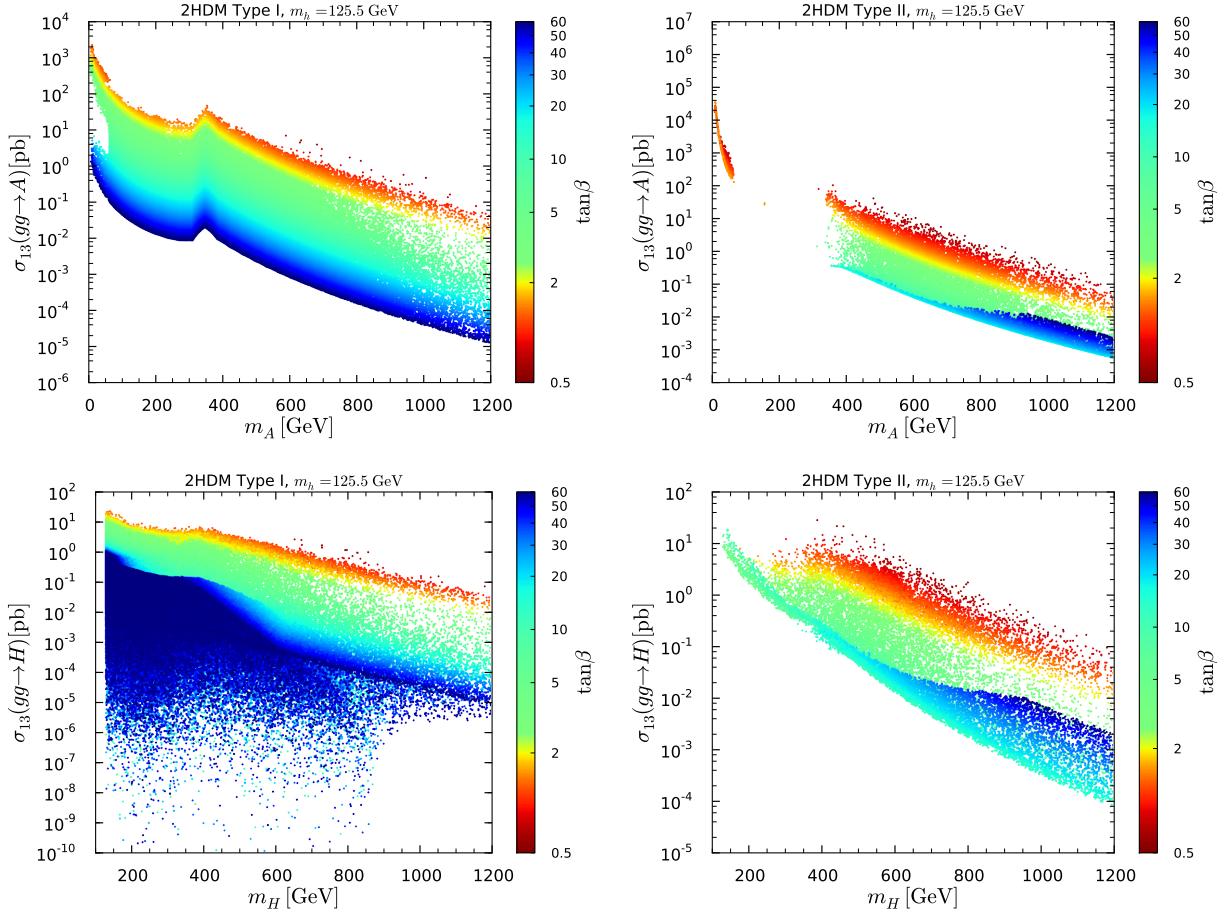
Figure 5.17: Cross sections in Type I (left) and Type II (right) for $gg \to X$ at the 13 TeV LHC as functions of m_X for $X = A$ (upper row) and $X = H$ (lower row) with $\tan\beta$ color code. In all four plots, points are ordered from low to high $\tan\beta$.

sections in this $m_H < 600$ GeV non-decoupling regime for the A and H are correlated in a way that is very favorable for discovery during Run 2 of the LHC. For example, if $\sigma(gg \to A)$ takes on its minimum SM±2% value of a few fb then $\sigma(b\bar{b}A) \gtrsim 80$ fb, whereas if $\sigma(b\bar{b}A)$ takes on its minimal value of few×10^{-1} fb then $\sigma(gg \to A) \approx 300$ fb. These cross section levels imply that the A should be discoverable in at least one of the two production modes even in the extreme alignment limit. Analogous arguments hold for H production.

Before considering specific decay channels of A and H, we present in Fig. 5.17 the gluon-fusion cross sections in Type I and Type II as functions of m_A and m_H at the 13 TeV LHC. Here, the color code shows the dependence on $\tan\beta$. In Type I, the $gg \to A$ cross section is proportional to $\cot^2\beta$. A cross section of 1 (0.1) fb is guaranteed for m_A as large as ≈ 600 (850) GeV. On the other hand, the $gg \to H$ cross section in Type I is proportional to $(C_F^H)^2$ and can take on extremely small values for $m_H \lesssim 850$ GeV. The reason is that, in this region, the reachable values of $c_{\beta-\alpha}$ are high enough such that a cancellation between the two terms of $C_F^H = s_{\beta-\alpha} - c_{\beta-\alpha}/t_\beta$ occurs and leads to an almost vanishing coupling. In contrast, for $m_H \gtrsim 850$ GeV, this cancellation is not possible as the values of $c_{\beta-\alpha}$ are forced to be smaller in the decoupling limit as can be seen in Fig. 5.1. In Type II, the A production cross section can be very large in the very low m_A region and more generally,

any mass smaller than 1.1 TeV gives a $gg \to A$ cross section larger than 1 fb. For $gg \to H$, a cross section > 1 (0.1) fb is guaranteed up to $m_H \approx 850$ GeV (1.2 TeV). From these considerations, the prospects for discovering the additional neutral states look promising should alignment be realized without decoupling.

Let us now turn to specific signatures. Figure 5.18 presents the cross sections for $gg \to A \to Y$ for $Y = \gamma\gamma, \tau\tau, t\bar{t}$ in Types I and II. Note that the y-axis is cut off at 10^{-7} pb. Although much lower values of the cross section are possible, we do not show these lower values since they will not be observable at the LHC. (With perfect efficiencies and acceptances, a 10^{-7} pb cross section would only lead to 0.3 event with 3 ab^{-1} of collected luminosity.) As expected, for the $\gamma\gamma$ and $\tau\tau$ final states, the cross sections fall sharply above the $t\bar{t}$ threshold, with the noticeable exception of the $A \to \tau\tau$ decay in Type II due to the strong constraints from LHC direct searches that exclude points with large corresponding cross section. For the $A \to \gamma\gamma$ decay, cross sections of 0.1 fb are reachable for $m_A \lesssim 470$ GeV ($m_A \lesssim 530$ GeV) in Type I (Type II) but not guaranteed. The maximal cross section is approximatively 30 fb in Type I and 100 fb in Type II (not considering the $m_A \leq m_h/2$ region). In both Types I and II, the $gg \to A \to \tau\tau$ cross section can be substantially larger. In Type I, 0.1 fb is reachable for $m_A \lesssim 600$ GeV, while in Type II $m_A \lesssim 550$ GeV *guarantees* a cross section larger than 0.1 fb. In both cases, very large cross sections are predicted at low m_A. The $gg \to A \to t\bar{t}$ cross section peaks around 100 pb in both Types I and II and is guaranteed to be larger than 0.1 fb in Type II for $350 \lesssim m_A \lesssim 600$ GeV. These sizable cross sections therefore provide interesting probes of the extended Higgs sector in the alignment limit.

In evaluating the potential for the discovery of A via the $t\bar{t}$ final state, it is noteworthy that $gg \to A \to t\bar{t}$ strongly interferes with the $pp \to t\bar{t}$ SM background, which yields a peak-dip structure in the $t\bar{t}$ invariant mass distribution [354–356]. One should also consider the set of complementary modes, $t\bar{t}A$ associated production in Types I and II, and $b\bar{b}A$ associated production in Type II, followed (in both cases) by $A \to t\bar{t}$, as recently explored in [327, 357, 358].

The corresponding results for the H cross sections are presented in Fig. 5.19. Sizable values of $\sigma \times$BR are possible in both Types I and II but heavily suppressed values are still possible for most of the cases. Only in Type II, for $H \to \tau\tau$ (as well as for $H \to t\bar{t}$), is the corresponding cross section guaranteed to be larger than 0.1 fb for $m_H \lesssim 460$ GeV ($m_A \approx 400$ GeV). Note that, for both Types I and II, the cross sections for A/H decays into a muon pair are related to the $A/H \to \tau\tau$ ones through the suppression factor $(m_\mu/m_\tau)^2 \approx 1/280$.

Non-standard production modes of the SM-like state, through $A \to Zh$ and $H \to hh$, are presented in Fig. 5.20. While these can be interesting discovery modes for the A and/or H, their cross sections can also be extremely suppressed. For $gg \to A \to Zh$, the $\tan\beta$ dependence, which follows the dependence of the $gg \to A$ cross section shown in Fig. 5.17, explains a part of this suppression. Moreover, the AZh coupling is proportional to $c^2_{\beta-\alpha}$ which is suppressed in the alignment region. Nevertheless, the $gg \to A \to Zh$ cross section can be larger than 100 fb for $m_A \lesssim 600$ GeV in both Types I and II. The $gg \to H \to hh$ cross section, as expected, attains its maximum below the $t\bar{t}$ threshold in both Types I and II and can reach about 10 pb at low $\tan\beta$. For any m_H, the cross section can however also be extremely suppressed.
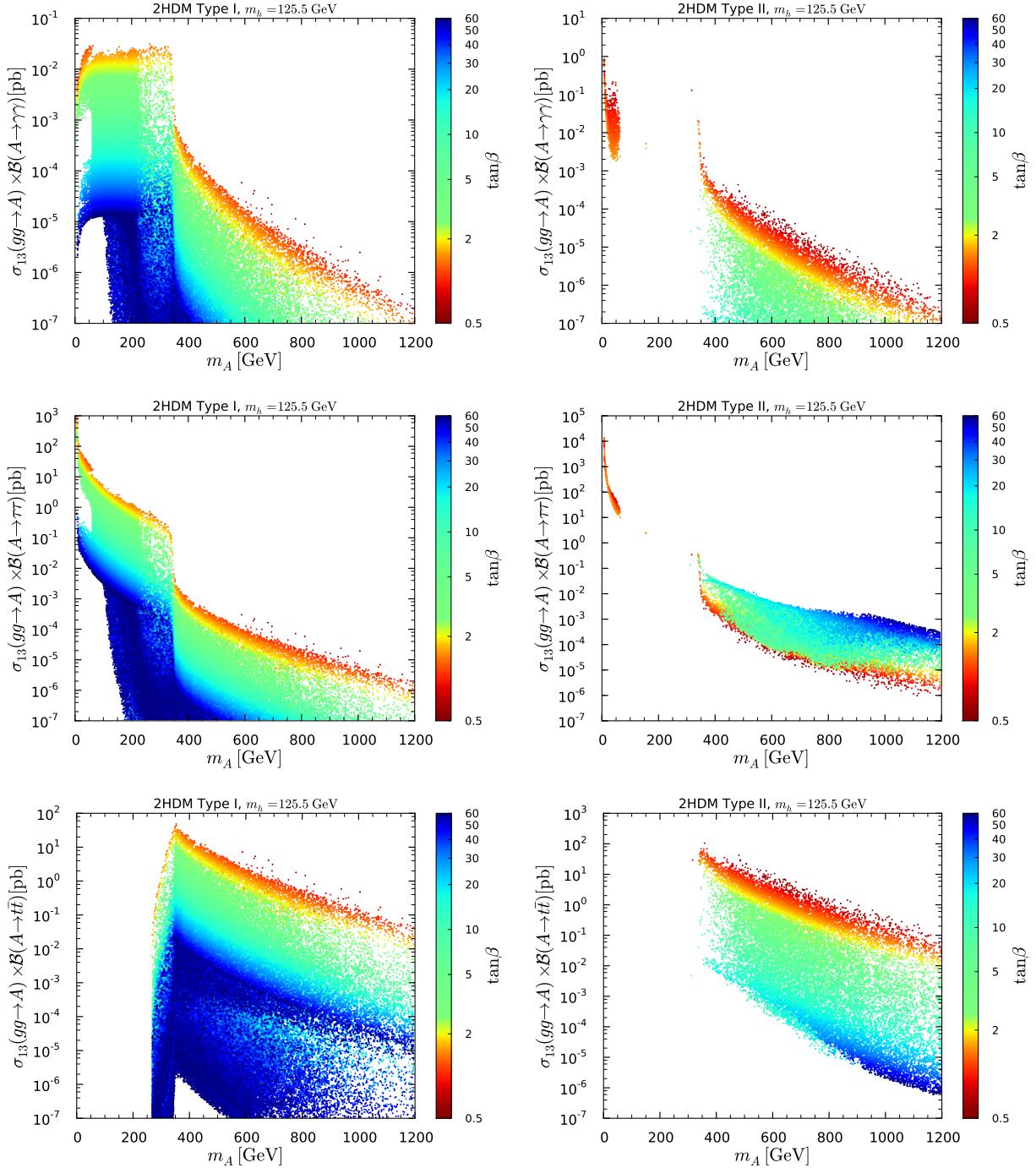
Figure 5.18: Cross sections times branching ratio in Type I (left) and in Type II (right) for $gg \to A \to Y$ at the 13 TeV LHC as functions of m_A for $Y = \gamma\gamma$ (upper panels), $Y = \tau\tau$ (middle panels) and $Y = t\bar{t}$ (lower panels) with $\tan\beta$ color code. Points are ordered from low to high $\tan\beta$.

A comment is in order here on the possible "feed down" (FD) [207, 359] to the production of the 125 GeV state through the decay of heavier Higgs states, which might modify the observed signal strengths. Given a specific channel, this issue was approximately addressed in [207] by imposing limits on the maximal amount of signal coming from the decay of heavier scalar states into h. For instance, the $A \to Zh$ decays contribute
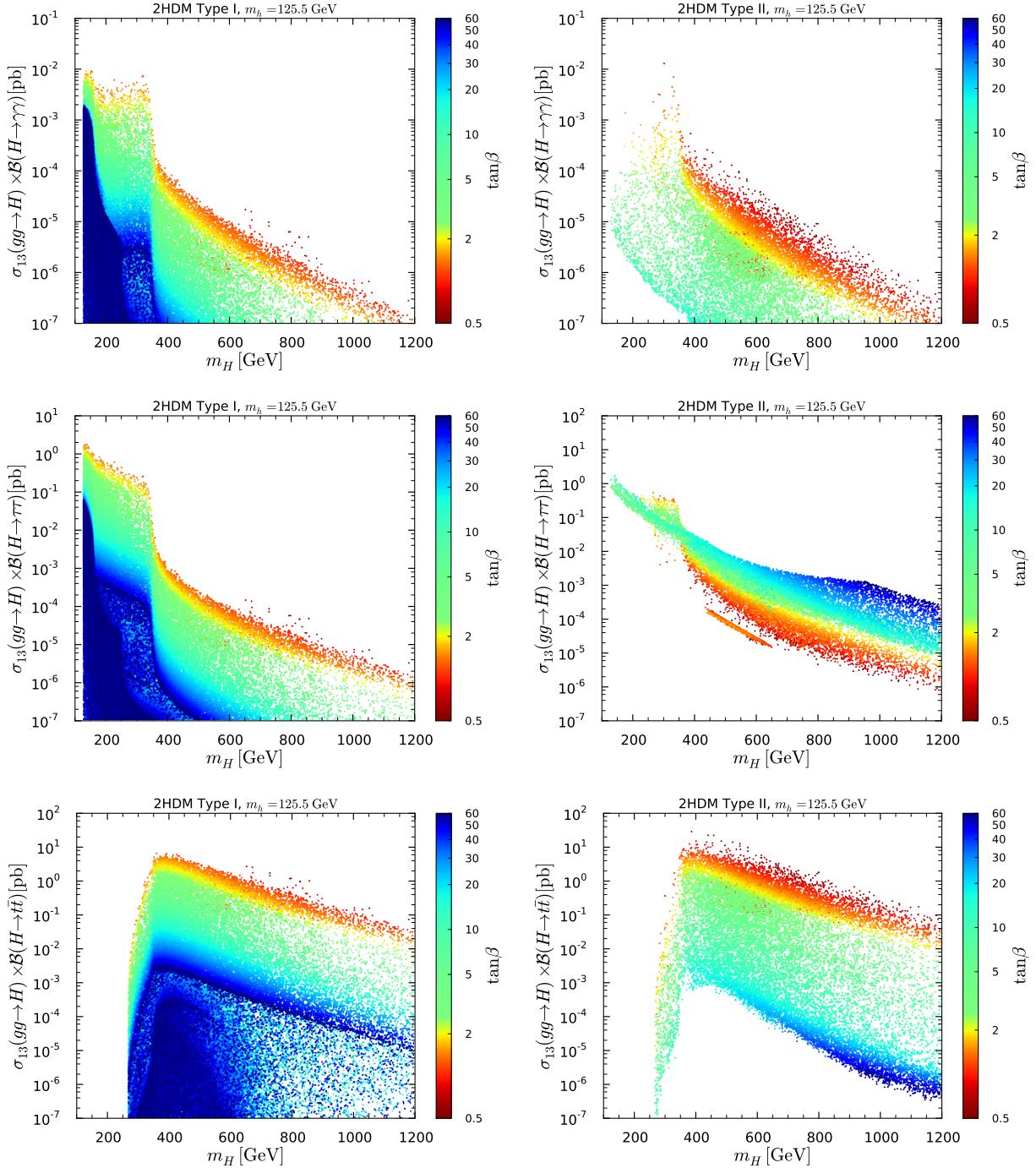
Figure 5.19: Cross section times branching ratio in Type I (left) and in Type II (right) for $gg \rightarrow H \rightarrow Y$ at the 13 TeV LHC as functions of m_H for $Y = \gamma\gamma$ (upper panels), $Y = \tau\tau$ (middle panels) and $Y = t\bar{t}$ (lower panels) with $\tan\beta$ color code. Points are ordered from low to high $\tan\beta$.

to the $\mu_{\mathrm{ZH}}(Y)$ signal strengths and a limit on $\sigma(gg \rightarrow A \rightarrow Zh)/\sigma(gg \rightarrow Z^* \rightarrow Zh)$ was then applied. Specifically the FD contamination to the Zh associated production and to $gg + b\bar{b}h$ production was restricted to 30% and to 10% respectively. Imposing these conditions here would remove the points with $\sigma_{13}(gg \rightarrow A) \times \mathrm{BR}(A \rightarrow Zh) \gtrsim 0.2$ pb and $\sigma_{13}(gg \rightarrow H) \times \mathrm{BR}(H \rightarrow hh) \gtrsim 2$ pb in Fig. 5.20. This is, however, a maximally
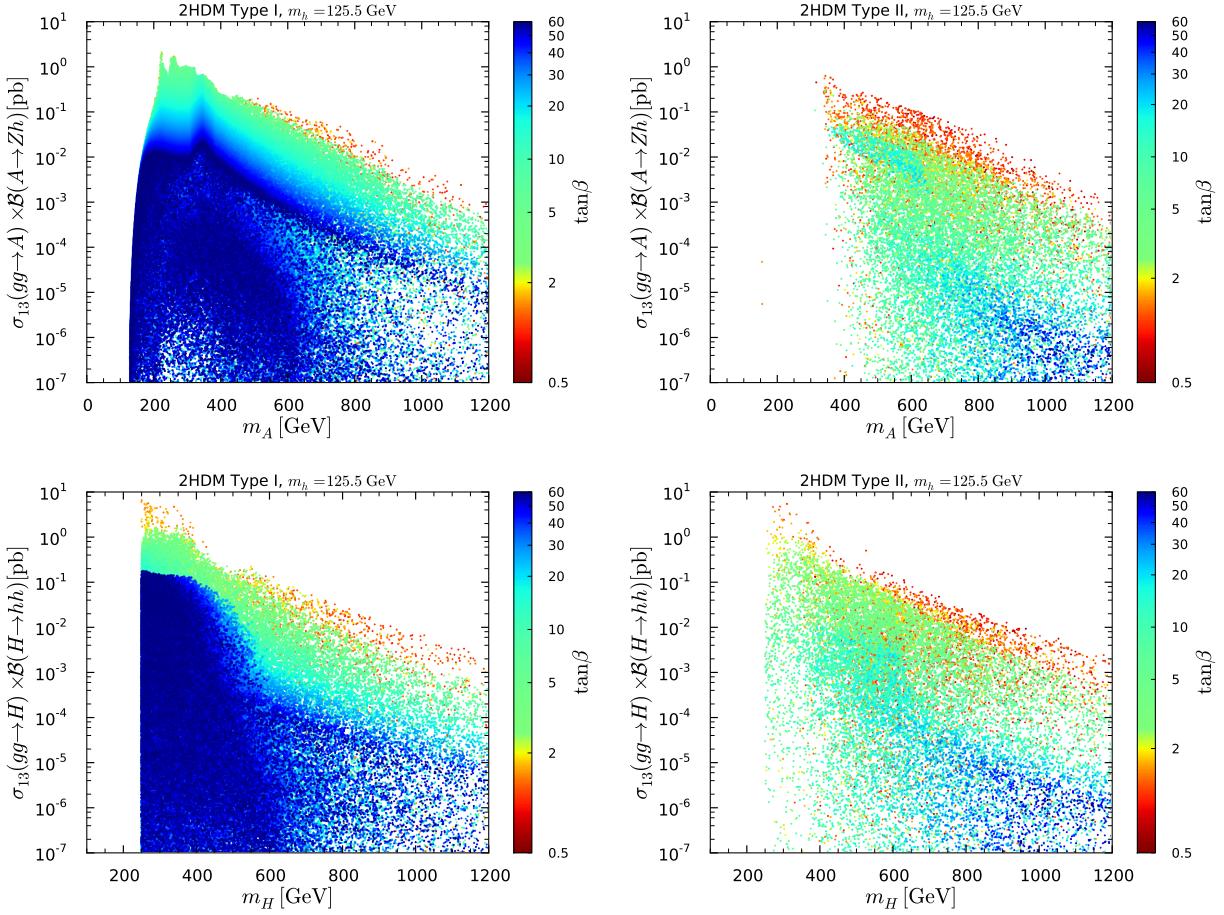
Figure 5.20: Cross sections times branching ratio in Type I (left) and in Type II (right) for $gg \rightarrow X \rightarrow Y$ at the 13 TeV LHC as functions of m_X for $X, Y = A, Zh$ (upper panel) and $X, Y = H, hh$ (lower panel) with $\tan\beta$ color code. Points are ordered from low to high $\tan\beta$.

conservative constraint for two reasons. Firstly, the amount of FD is computed without accounting for any reduced acceptance of such events into the 125 GeV signal as a result of the experimental cuts used to define the $gg \rightarrow h$, bbh or $Z^* \rightarrow Zh$ channels. Secondly, it puts individual limits on specific production×decay modes instead of including all signal strengths in a global fit, which is the approach followed in this paper. Indeed, when directly adding the contribution of $gg \rightarrow A \rightarrow Zh$ to the Zh signal strength in the global fit, it turns out that only cross sections of $\sigma_{13}(gg \rightarrow A) \times \text{BR}(A \rightarrow Zh) \gtrsim 1.6$ pb are definitely excluded. This still assumes that the signal acceptance of the experimental analysis is the same for $gg \rightarrow A \rightarrow Zh$ as for $gg \rightarrow Z^* \rightarrow Zh$, which should however be a reasonable approximation, as the main difference would be the Zh invariant-mass distribution, which is not used as a selection criterion in this case. The contribution of $H \rightarrow hh$ to the h signal strengths is a more difficult question, as here the acceptances (in each final state considered in the experimental analyses) will certainly be different from those of single h production. A detailed study based on event simulation would be necessary to better understand the impact of FD on the 125 GeV Higgs signal.

Finally, if the mass splitting is large enough, $A \to ZH$, $H \to ZA$, and $H \to AA$ decays offer intriguing possibilities for discovering the extra non-SM-like neutral Higgs states in the regime of approximate alignment without decoupling. In Fig. 5.21, the cross sections for $gg \to A \to ZH$, $gg \to H \to ZA$ and $gg \to H \to AA$ are exhibited. Large $gg \to A \to ZH$ cross sections are obtained for large $m_A - m_H$ splitting.[24] Looking back at Fig. 5.2 one sees that, in both Type I and Type II, the splitting can only be large for $m_A \lesssim 650$ GeV. This explains the preponderance of low m_H points with cross sections up to 20 pb (6 pb) in Type I (II) for $m_A \lesssim 650$ GeV. (In Type II the $m_{H^\pm} > 480$ GeV constraint allows a large enough $m_A - m_H$ mass splitting only for $m_A \gtrsim 350$ GeV.) However, $gg \to A \to ZH$ can also be heavily suppressed; since the AHZ coupling is proportional to $s_{\beta-\alpha}$, this suppression is a purely kinematical effect.

Turning to the $H \to ZA$ and $H \to AA$ signatures, in Type I we observe a depleted area for $m_H > 300$ GeV and cross sections of the order of 0.1 pb. In this region, $\tan\beta = 2$–10 and Z_5 is small or negative leading to H and A masses for which the $H \to ZA$, AA decays are kinematically forbidden [cf. Eq. (4.57)]. In the region below, $\tan\beta > 10$ and Z_5 can be large enough to achieve $m_H > m_A + m_Z$ and/or $m_H > 2m_A$, but nevertheless the cross section is small because of the $\tan\beta$ dependence of $\sigma(gg \to H)$, see Fig. 5.17. The distinct branch with $gg \to H \to ZA$ and $gg \to H \to AA$ cross sections larger than about 1 pb, on the other hand, has $\tan\beta \lesssim 2$ and $\lambda_5 \approx 0$. Here, the term proportional to $\sin 2\beta$ in Eq. (4.38) gives a large enough $Z_5 > 0$ so that the $H \to ZA$ and/or $H \to AA$ decay is kinematically allowed. The small $\tan\beta$ leads to a large $gg \to H$ production cross section, see again Fig. 5.17. In Type II, $gg \to H \to ZA$ and $gg \to H \to AA$ cross sections can also be large (even above 1 pb for $H \to ZA$) in the non-decoupling regime. However, due to the charged Higgs mass constraint these processes are allowed only for $m_H \gtrsim 430$ GeV. A detailed phenomenological analysis of the $A \to ZH$ and $H \to ZA$ decays at the LHC was performed in Ref. [361].

Last but not least, due to the kinematic constraint $m_H \geq 2m_A$ and the non-trivial correlation between m_H and m_A observed in Fig. 5.2, the $H \to AA$ channel is only open for $m_H \lesssim 700$ GeV. In Type I the branch of points with cross sections ranging from about 10^{-1} pb to 10 pb is mainly populated by $m_A \leq 100$ GeV points with relatively low $\tan\beta \lesssim 10$. In Type II, essentially only points with low $m_A \lesssim 60$ GeV and $\tan\beta \lesssim 2$ experience the $H \to AA$ decays. This channel thus offers an interesting probe to the low m_A region.

Finally, let us take a moment to consider the 750 GeV potential signal observed by both ATLAS and CMS in the di-photon channel in December 2015 [362, 363][25]. The experimental results suggest a cross section of about 5–10 fb. It is then clear from the upper panels of Figs. 5.18 and 5.19 that the simplest explanation in the context of 2HDMs, *i.e.*, a 750 GeV H or A decaying to $\gamma\gamma$, does not work. The predicted cross section in the 2HDM is simply too low to account for the observed signal by a few orders of magnitude. This can of course easily be solved by adding extra (vector-like) quarks that can enhance both the gluon-fusion production of H or A and their $\gamma\gamma$ branching ratio. However there may exist

---

24 A large splitting $m_A - m_H \simeq v$ can be motivated by the possibility of a strong first order phase transition in 2HDMs [360].

25 With increased luminosity, the ATLAS and CMS collaborations announced in August 2016 that this excess has significantly weakened [364, 365], hinting strongly for a statistical fluctuation interpretation.
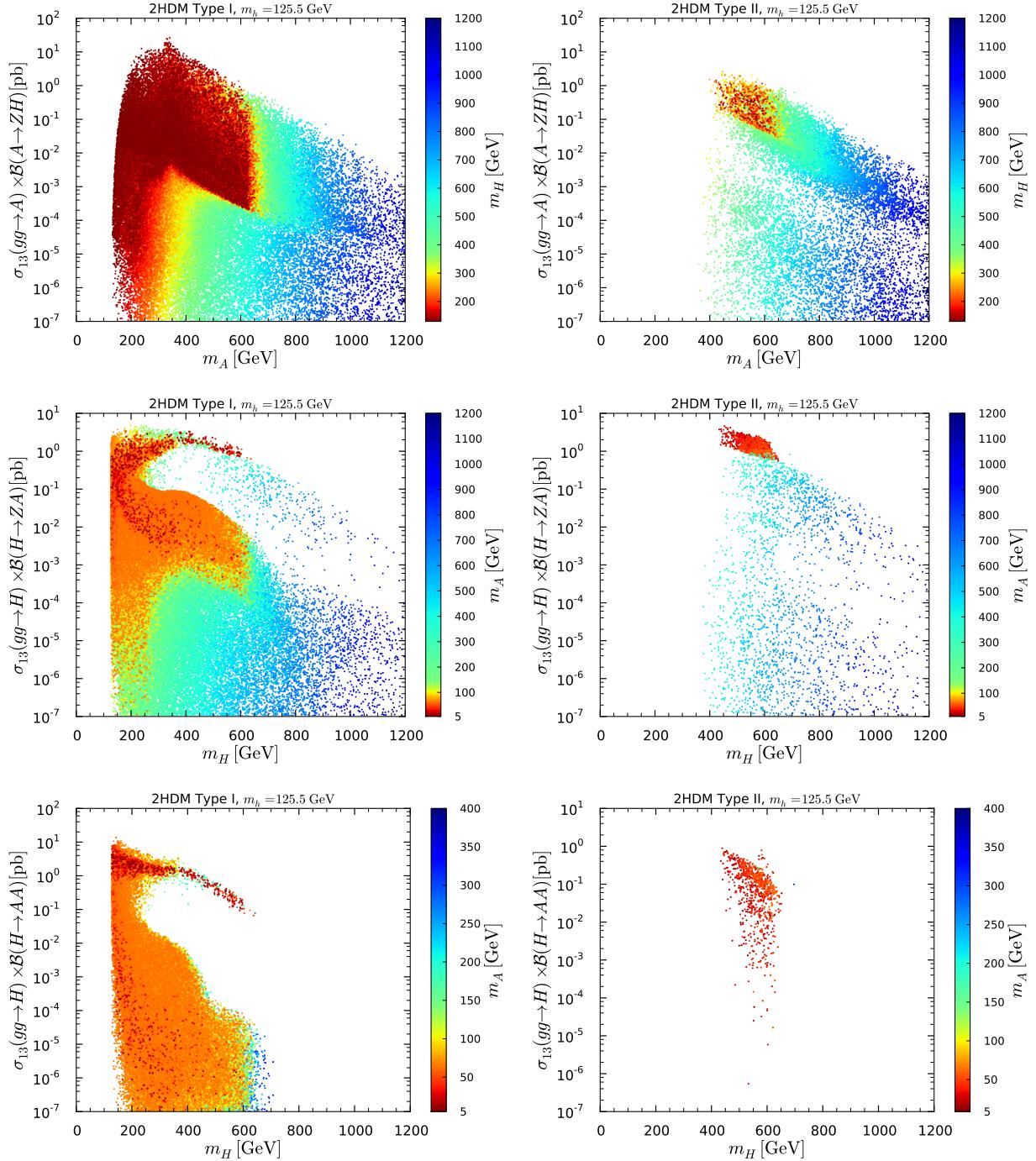
Figure 5.21: Cross sections times branching ratio in Type I (left) and in Type II (right) for Higgs-to-Higgs signatures at the 13 TeV LHC, in the upper panel $gg \rightarrow A \rightarrow ZH$ with m_H color code, and in the middle and lower panels for $gg \rightarrow H \rightarrow ZA$ and $gg \rightarrow H \rightarrow AA$, respectively, with m_A color code. Points are ordered from high to low m_A or m_H, with the exception of the $H \rightarrow ZA$, and $H \rightarrow AA$ plots in Type II, where points are ordered from low to high m_A.

a possibility in the minimal 2HDM to explain this signal. As we were just discussing, the $H \rightarrow AA$ cross section can be quite large in both Type I and Type II. A 750 GeV H state decaying into two very light and boosted pseudoscalars, which then each decay into two collimated photon could then perfectly well mimic the observed signal. This signature was

discussed in various analyses [366–372]. However in the 2HDM, as seen previously, this only happens for $m_H \lesssim 700$ GeV. This bound might be opened by slightly weakening the theoretical constraints imposed that partially control the non-trivial correlation between m_A and m_H presented in Fig. 5.2. The large $A \to \gamma\gamma$ branching ratio can then be achieved in various ways [369]. For instance m_A could be just below $2m_\mu$, the $\mu\mu$ threshold, so that the only open decay channels would be $A \to e^+e^-$ and $A \to \gamma\gamma$ while maximizing the size of the muon loop contribution to $\gamma\gamma$. Another way would be to make A mix with π^0 or η, which would insure sizable diphoton branching ratio. One should then make sure that such boosted pseudoscalars, with potential small total width, decay before or within the ATLAS and CMS electromagnetic calorimeters, their decay length might indeed be quite large. The viability of this explanation within the 2HDM should however be carefully assessed.

5.2.5 *Alignment in the h–125 scenario: summary*

We specifically investigated the phenomenological consequences of alignment without decoupling and contrasted them to the decoupling case. Two aspects are interesting in this respect: one being precision measurements of the couplings and signal strengths of the SM-like Higgs boson at 125 GeV, the other being the ways to discover the additional Higgs states of the 2HDM when they are light. Allowing for 1% deviation from unity in C_V^h, which corresponds to the ultimate expected LHC precision at high luminosity, the main results can be summarized as follows.

In the alignment limit without decoupling, despite C_V^h being very close to 1, the fermionic couplings of the 125 GeV Higgs can deviate substantially from the SM values. Concretely, C_U^h can deviate as much as about 10% (20%) from unity in Type I (Type II), and C_D^h as much as 30% in Type II. While C_U^h rather quickly approaches 1 with increasing m_H and/or $c_{\beta-\alpha} \to 0$, the approach of the bottom Yukawa coupling to its SM value in the alignment limit is delayed in Type II, with $C_D^h \approx 0.70$–1.15 even for $|c_{\beta-\alpha}| \sim 10^{-2}$. Large values of $C_D^h > 1$ are associated with light H, A. Moreover, for 330 GeV $\leq m_H \leq 660$ GeV and 350 GeV $\leq m_A \leq 660$ GeV, there is an allowed region with $C_D^h \approx -1 \pm 0.2$; this "wrong-sign" solution can be tested decisively at Run 2.

The trilinear hhh coupling can also exhibit large deviations. Large values of $C_{hhh} > 1$ (up to $C_{hhh} \approx 1.7$ in Type I and up to $C_{hhh} \approx 1.35$ in Type II) can be achieved in the non-decoupling regime $m_H \lesssim 600$ GeV, for $|c_{\beta-\alpha}|$ of the order of 0.1, whereas for heavier m_H, C_{hhh} is always suppressed as compared to its SM prediction. The suppression can be about 50% for m_H of ~ 1 TeV and much larger for lighter m_H.

For the ratios $\mu_X^h(Y)$ of the $X \to h \to Y$ signal rates relative to the SM prediction, we found distinct correlations of these signal strengths in both Type I and Type II that depend on whether the additional Higgs states are decoupled or not. In fact, in the regime of alignment without decoupling, there are characteristic combinations of the $\mu_X^h(Y)$ signal strengths that cannot be mimicked by the decoupling limit. However, it is of course also possible that all signal strengths converge to 1 even though the additional Higgs states are very light.

A decisive test of the alignment without decoupling scenario would of course be the observation of the additional Higgs states of the 2HDM in the mass range below about

600 GeV. We delineated the many possibilities for such observations. While there are no guarantees in the case of the Type I model, in the Type II model there is always a definite lower bound on the $gg \to A, H \to \tau\tau$ cross sections at the LHC at any given m_A. For low $\tan\beta \sim 1$, this lower bound is still of order 0.1 fb for $m_A \sim 500$ GeV, a level that we deem likely to be observable at the LHC during Run 2. For high $\tan\beta$, the lower bound is roughly two orders of magnitude higher and only falls below the 0.1 fb level for $m_{A,H} \gtrsim 1.2$ TeV, which is already in the decoupling region. Moreover, while in Type I gluon-gluon fusion is always dominant for H or A production, in Type II both $b\bar{b}$ associated production and gluon-gluon fusion modes are in principle important since either can be dominant in different regions of the parameter space.

Finally, Higgs-to-Higgs decays of the non-SM-like states ($A \to ZH$, $H \to ZA$, $H \to AA$) also open intriguing possibilities for testing the regime of alignment without decoupling, with cross sections often in the range of 1–10 pb (although they can also be quite suppressed). Particularly promising are $gg \to H \to ZA$ and $gg \to H \to AA$ in Type II for light pseudoscalars below about 100 GeV; for such a light A, m_H can be at most ~ 650 GeV, and $\sigma \times$ BR values for these channels typically range from 10 fb to 10 pb.

5.3 THE H–125 SCENARIO IN THE ALIGNMENT LIMIT

We now turn to the H–125 scenario. As a small reminder, we now suppose that H is the SM-like state with a mass of $m_H = 125.5$ GeV and a reduced coupling to gauge bosons $C_V^H = c_{\beta-\alpha} > 0.99$ in order to be close to the alignment limit. By convention $c_{\beta-\alpha}$ is here non-negative while $s_{\beta-\alpha}$ can have both signs. An important phenomenological difference as compared to the h–125 scenario is that there always exists a light scalar, h, with mass below m_H.

5.3.1 *Parameters*

We start by illustrating the parameter space of the analysis. Figure 5.22 shows the relation between m_h, $|s_{\beta-\alpha}|$ and $\log_{10}|Z_6|$. The expected correlation between the three parameters is clearly observed. In particular, larger values of m_h imply smaller $|Z_6|$ for the same value of $|s_{\beta-\alpha}|$, and for each m_h, $\log_{10}|Z_6|$ can be as small as desired if $|s_{\beta-\alpha}|$ is allowed to be correspondingly small. Here, as in the h–125 scenario, we only show results down to $|s_{\beta-\alpha}| = 10^{-5}$. Because of the absence of a decoupling limit, $|Z_6|$ does not exceed $\sim 10^{-1.5}$ in our scan. This illustrates that in the scenario under consideration, alignment is solely controlled by the smallness of $|Z_6|$. Note also that the region of $m_h \leq \frac{1}{2}m_H$ requires subtle correlations among the 2HDM parameters to ensure that BR($H \to hh$) is sufficiently small to be in agreement with the experimental constraints, as will be discussed in more details in the next section. This explains the relatively low density of points in this region. On the other hand, the higher density of points seen in Type II for $m_h \in [80\,\text{GeV}, 90\,\text{GeV}]$ arises because light neutral states $X = h, A$ with masses below 80 GeV are severely constrained by the CMS $b\bar{b}X$ with $X \to \tau\tau$ search [340],[26] while

---

26 The CMS analysis given in [340] considers only $pp \to b\bar{b}A$ production with $A \to \tau\tau$. However, the same limit should also apply to $pp \to b\bar{b}h$ with $h \to \tau\tau$; see *e.g.* [373].
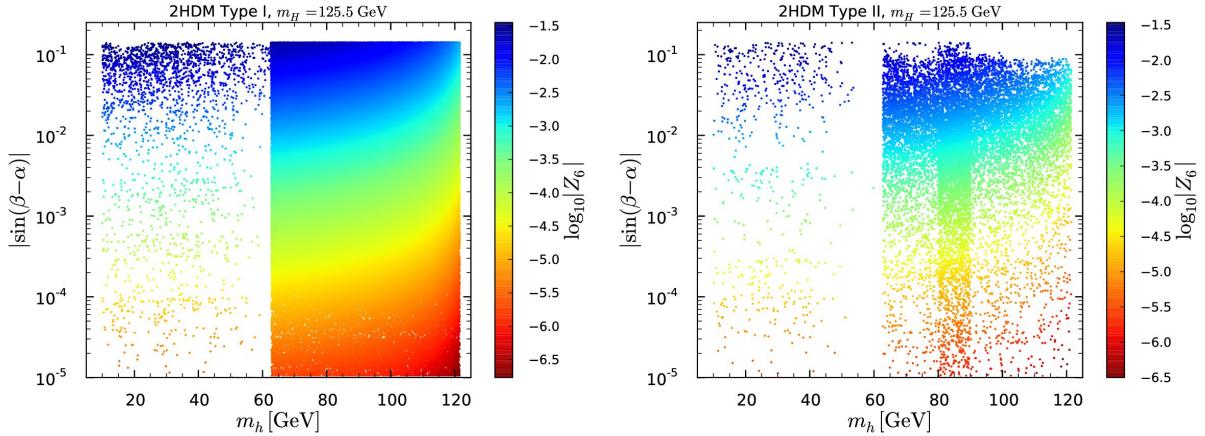
Figure 5.22: $|s_{\beta-\alpha}|$ versus m_h in Type I (left) and Type II (right) with $\log_{10}|Z_6|$ color code. Points are plotted in the order of high to low $\log_{10}|Z_6|$ values.
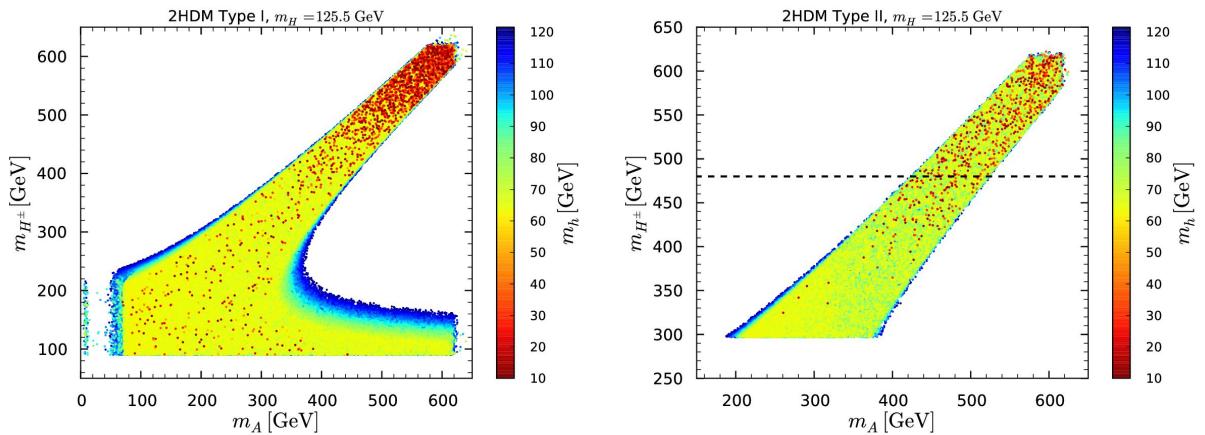

Figure 5.23: $m_{H^\pm}$ versus m_A in Type I (left) and Type II (right) with m_h color code. Points are ordered from high to low m_h values. The right plot shows the whole parameter space scanned over for Type II, with the horizontal line indicating the limit on the charged Higgs mass, $m_{H^\pm} > 480$ GeV. The points below this line are not considered in the rest of the analysis.

masses above 90 GeV are also constrained by the ATLAS [343] and CMS [344] searches for $X \to \tau\tau$ decays in both the $gg \to X$ and $b\bar{b}X$ production modes. No search has ever explored the 80–90 GeV region.

The relation between the three free Higgs masses, m_A, $m_{H^\pm}$ and m_h is shown in Fig. 5.23. The absence of a decoupling limit results in an upper bound on the CP-odd and charged Higgs masses, $m_A, m_{H^\pm} \lesssim 630$ GeV, which depends on the allowed values of $c_{\beta-\alpha}$. Indeed, without the $c_{\beta-\alpha} \geq 0.99$ constraint that we imposed to focus on the alignment scenario, one would find instead $m_A, m_{H^\pm} \lesssim 800$ GeV, where the bound is saturated for $s_{\beta-\alpha} \simeq 0.7$ [207]. Perturbativity and unitarity conditions, the fact that the Z_i cannot be too large, as well restrain the possible range of m_A and $m_{H^\pm}$ as can be seen from Eqs. (4.88) and (4.89). The characteristic correlation between m_A and $m_{H^\pm}$ is a consequence of the precision electroweak measurements, primarily the T parameter [334]. In Type II, a large part of the parameter space is excluded by weak radiative B meson decays for which agreement with observations sets a strong lower bound on the charged Higgs mass, $m_{H^\pm} > 480$ GeV at

95% CL [309]. The combination of this constraint and the EW precision observables then sets a bound on the CP-odd Higgs mass. We find that $m_A \gtrsim 420$ GeV, which of course rules out the region of $m_A \leq \frac{1}{2} m_H$ in Type II. We also note that this forces the CP-odd and charged Higgs states to be relatively close in mass.

In contrast to Type II, in Type I the charged Higgs mass is much less impacted from flavor physics constraints [265, 269]. For $m_{H^\pm} \lesssim 160$ GeV, the CP-odd state can have any mass below 630 GeV in Type I, as shown in the left panel in Fig. 5.23. Moreover, whereas $m_h \leq \frac{1}{2} m_H$ can only be found for $m_A, m_{H^\pm} \gtrsim 400$ GeV in Type II, such a light h is possible for most of the allowed combinations of m_A and $m_{H^\pm}$ in Type I—with the notable exception of the light $m_A \leq \frac{1}{2} m_H$ region, since LEP constraints imply that A and h cannot both have a mass below $\frac{1}{2} m_H$ simultaneously [322]. However, there are narrow bands at the border of the allowed m_A vs. $m_{H^\pm}$ region that unambiguously lead to values of $m_h \gtrsim 100$ GeV. One such region is the blue band in the left panel of Fig. 5.23 with $m_A \gtrsim 350$ GeV and $m_{H^\pm} \lesssim 200$ GeV. Such mass correlations may be used to predict or cross-check the validity of the scenario in the case that two or three extra Higgs states are discovered in the future. Finally, as discussed in Ref. [322] and presented in the next section, m_h values below about 60 GeV are only possible for $\tan\beta \lesssim 2$ in Type II. Hence, if such a low mass h is observed and its properties require a high value of $\tan\beta$, then the Type II model would be eliminated.

5.3.2 Impact of the CMS $A \to Zh$ search

Before going on with the results description, let us discuss a very important constraint on the H–125 scenario. Both ATLAS and CMS have performed searches at $\sqrt{s} = 8$ TeV for a new heavy resonance decaying to a Z boson and a light resonance, with the Z decaying to $\ell\ell = ee, \mu\mu$ and the light resonance decaying to $b\bar{b}$ or $\tau\tau$. While the ATLAS analysis [347] required that the light resonance be consistent with the observed 125 GeV Higgs boson, the CMS analysis [346] treated the masses of the two resonances as free parameters and published limits on cross section times branching ratios as functions of the two masses. We can therefore use this CMS result as a constraint on the $A \to Zh$ channel in our study.

For values of $m_A \simeq 200$–600 GeV, which is the mass range of particular interest for our analysis, the 95% CL limit on $\sigma(gg \to A \to Zh) \times \mathrm{BR}(Z \to \ell\ell) \times \mathrm{BR}(h \to b\bar{b})$ obtained by CMS is about 100 fb for $m_h \simeq 40$–45 GeV, corresponding to the lowest m_h considered in [346]. For heavier m_h, the limit is about 100 fb at $m_A \approx 200$ GeV going down to about 5 fb at $m_A \approx 600$ GeV. The limit on $\sigma(gg \to A \to Zh) \times \mathrm{BR}(Z \to \ell\ell) \times \mathrm{BR}(h \to \tau\tau)$ has a weaker impact; most of the points excluded by the $\ell\ell\tau\tau$ search channel are also excluded by the $\ell\ell b\bar{b}$ channel. Nonetheless, in Type I there is a small corner of parameter space at $\tan\beta \approx 2$ and $m_A \lesssim 400$ GeV that is mostly constrained by the $A \to Zh \to \ell\ell\tau\tau$ CMS limit. All in all, this leads to very severe constraints on the 2HDM in the alignment limit with $m_H \approx 125$ GeV, cutting out whole slices of parameter space, in particular at low $\tan\beta$ since the C_U^A coupling, which drives the gluon-fusion production of A, is proportional to $\cot\beta$. The reason for such a strong exclusion in this scenario is that, here, the h state is light and thus has a very large branching ratio to $b\bar{b}$, close to 90%, in the major parts of the parameter space. In Fig. 5.24, we show the projections of the scan points onto the $\tan\beta$ versus m_A plane for both Type I and Type II.
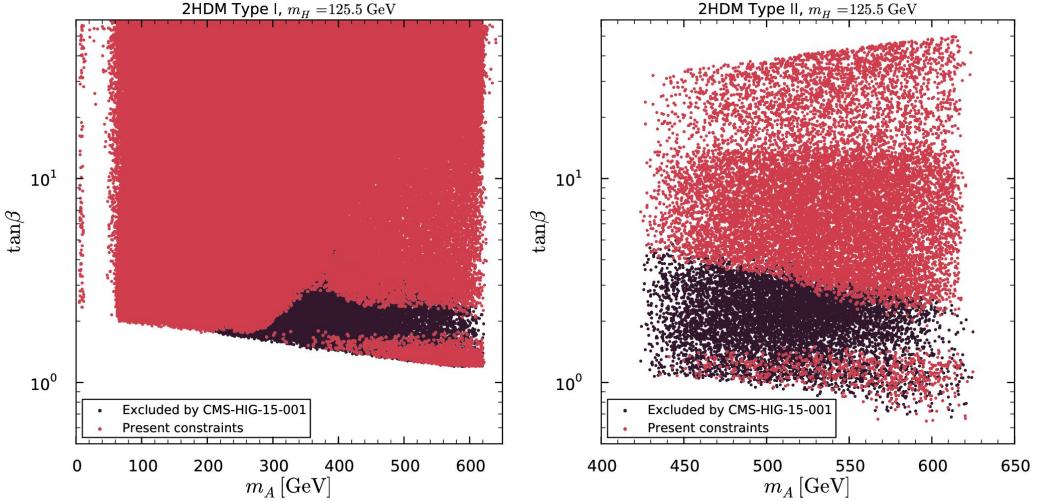
Figure 5.24: Projection of the scan points in the plane $\tan\beta$ vs. m_A, on the left for Type I, on the right for Type II. The red points are consistent with all constraints used in this analysis, while the underlying black points are those which are solely excluded by the CMS $A \to Zh$ ($Z \to \ell\ell$, $h \to b\bar{b}, \tau\tau$) search [346] after all other constraints have been applied.

The red points are consistent with all constraints used in this paper, while the underlying black points are those which are excluded by the CMS $A \to Zh$ ($Z \to \ell\ell$, $h \to b\bar{b}, \tau\tau$) limits [346] after all other constraints have been applied. We see that the $A \to Zh$ limit from Run 1 excludes a whole slice of parameter space at low $\tan\beta$ and m_A above about 300 GeV. The surviving red points with $m_A > 400$ GeV and $\tan\beta < 2$ have $m_h \lesssim 40$ GeV. As a result, some of the subsequent analysis plots will show disconnected islands of points. Had the CMS analysis been sensitive to light resonance masses below 40 GeV, the entire parameter space with $m_A > 400$ GeV and $\tan\beta \lesssim 2$ may have been ruled out.

5.3.3 Couplings of the SM-like state H

Regarding the properties of H, Fig. 5.25 shows the possible variation of the coupling to up-type fermions, $C_U^H = C_D^H \equiv C_F^H$ in Type I and C_U^H in Type II. Deviations from unity ranging from -12% to $+8\%$ are possible in Type I for $|s_{\beta-\alpha}| \approx 0.14$, while in Type II the deviations range from -7% to $+20\%$. As expected, in both types C_U^H quickly approaches unity as $|s_{\beta-\alpha}|$ decreases. It is interesting to note that, while $C_U^H = \sin\alpha/\sin\beta$ in both Type I and Type II, the actual values that can be reached are different in the two models because of constraints involving the down-type coupling. The largest deviations occur for large h–A mass splitting, when m_h is below 60 GeV, while m_A is close to its upper bound and $\tan\beta$ very close to 1. In Type I, there is also another region with $m_h < \frac{1}{2}m_H$ at larger values of $\tan\beta$, although this is only achieved when $|s_{\beta-\alpha}| \gtrsim 10^{-2}$. This is seen as the narrow banana-shaped red strip with $C_F \approx 1$–1.01 in the upper left panel of Fig. 5.25. Also noteworthy are the gaps between the regions filled with valid scan points, these are caused by the CMS limits [346] on $A \to Zh \to \ell\ell b\bar{b}$ (and $\ell\ell\tau\tau$) and will appear in many of the subsequent figures.
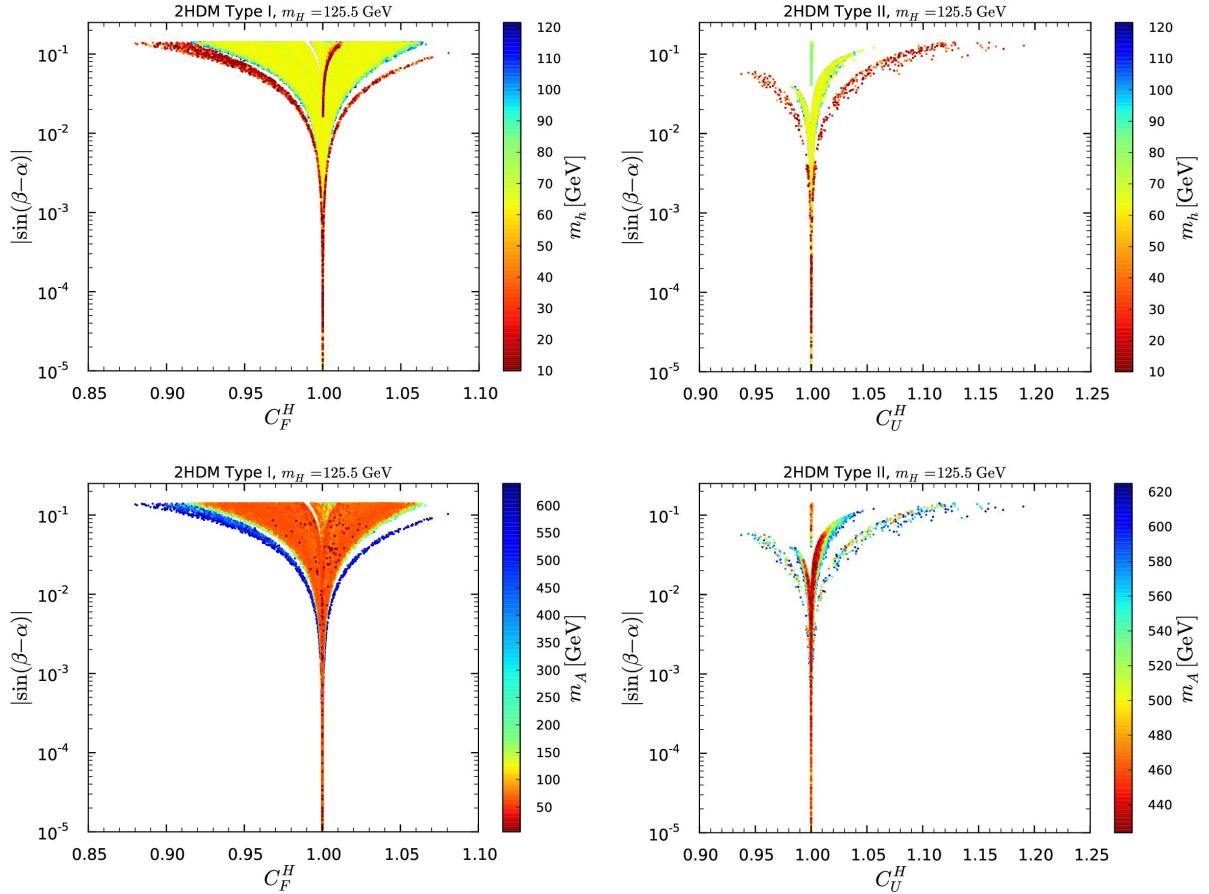
Figure 5.25: $|s_{\beta-\alpha}|$ versus reduced fermionic coupling C_F^H in Type I (left) and C_U^H in Type II (right). In the upper two panels, the color code shows the dependence on m_h; in the lower two panels the dependence on m_A, with points ordered from high to low m_h and m_A values, respectively. Note that the color scales for m_A are different for Type I and Type II because of the very different allowed ranges of m_A.

The possible variation of the coupling to down-type fermions, C_D^H, in Type II is shown in Fig. 5.26. Let us first consider the left panel. As in the h–125 scenario, there are two possibilities: one where C_V^H, C_U^H and C_D^H all have the same sign, and one where C_D^H has opposite sign relative to C_U^H and C_V^H [259]. In the normal (same) sign region, deviations from the predicted SM coupling in the range of roughly -30% to $+12\%$ are possible even for rather low $|s_{\beta-\alpha}| \approx 5 \times 10^{-3}$, as long as the $H \to hh$ decay mode is closed. If the $H \to hh$ decay contributes to the total width, then C_D^H is confined to the range $[0.83, 1.08]$ and quickly converges to unity as $|s_{\beta-\alpha}|$ decreases. The gap between the red and the yellow/green/blue points is again caused by the CMS limits on $A \to Zh$. On the other hand, the opposite-sign region, $C_D^H \in [-1.1, -0.7]$, requires $s_{\beta-\alpha} \lesssim -0.04$ due to the fact that $s_{\beta-\alpha}$ and $\tan\beta$ are correlated in Type II as illustrated in the right panel of Fig. 5.26. We see that $C_D^H = c_{\beta-\alpha} + s_{\beta-\alpha}t_\beta \gtrsim 1$ for $s_{\beta-\alpha} \gtrsim 0$ but decreases below 1 when $s_{\beta-\alpha}$ turns negative. Consequently, for moderately negative $s_{\beta-\alpha}$ and large enough $\tan\beta$, C_D^H flips sign. Values of $|C_D^H| \lesssim 0.7$ are excluded by the fit of the signal strengths, but the opposite-sign solution with $C_D^H \approx -1$ is still phenomenologically viable. The region of $\tan\beta \gtrsim 50$ is excluded because of the strong constraints on $A \to \tau\tau$ decays from ATLAS [343] and
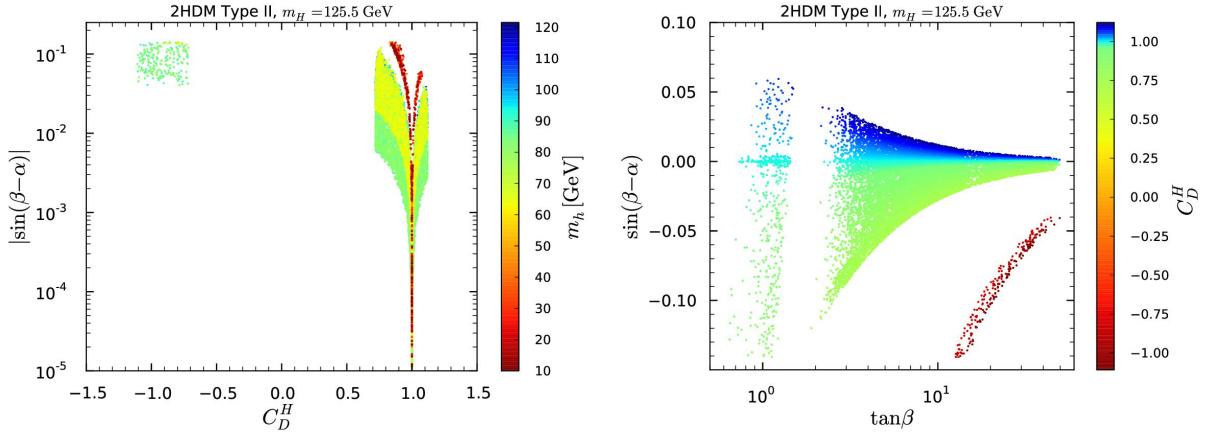
Figure 5.26: In the left panel, we exhibit $|s_{\beta-\alpha}|$ versus C_D^H in Type II. The color code shows the dependence on m_h, with points ordered from high to low m_h values. In the right panel, we exhibit $s_{\beta-\alpha}$ vs. $\tan\beta$ with the color code showing C_D^H ordered from high to low values.

CMS [344]; see also [207]. The CP-odd scalar mass m_A does not have much influence since it can only vary over the very limited range 420–630 GeV in Type II.

The $\tan\beta$ dependence of the fermionic couplings, shown in Fig. 5.27, is also noteworthy. In both Type I and Type II, sizable deviations from $C_U^H = c_{\beta-\alpha} - s_{\beta-\alpha}/t_\beta = 1$ are possible only for small $\tan\beta$. In Type II, C_U^H very quickly converges to 1 once $\tan\beta \gtrsim 7$–8 because the allowed range of $s_{\beta-\alpha}$ decreases with increasing $\tan\beta$, as can be seen in the right panel of Fig. 5.26. In Type I, the convergence of the fermionic couplings to their SM values is less pronounced due to the fact that, even for $\tan\beta = 60$, the full $|s_{\beta-\alpha}|$ range considered is allowed. For C_D^H in Type II, the situation is quite different, as this coupling is given by $\cos\alpha/\cos\beta$ instead of $\sin\alpha/\sin\beta$. For the normal-sign region, as soon as $\tan\beta$ is at least moderate in size, $\tan\beta \approx 10$, C_D^H saturates the full range allowed by the measured signal strengths, even for small values of $|s_{\beta-\alpha}|$ of a few times 10^{-3}. In contrast, as discussed in the previous paragraph, the opposite-sign solution is only possible for large enough negative $s_{\beta-\alpha}$, concretely $s_{\beta-\alpha} \lesssim -0.04$, cf. the right panel of Fig. 5.26. Overall, in these plots, the impact of the CMS limit on $A \to Zh$ is even more striking than in Fig. 5.25, as it excludes most points with $\tan\beta \approx 1.2$–1.8 in Type I and the entire range of $\tan\beta \approx 1.5$–2 in Type II. Note however that in both Types, points with smaller $\tan\beta$ are not excluded. Most of these points have $m_A \gtrsim 400$ GeV and $m_h \lesssim 40$ GeV; a region not probed by the current CMS analysis.

Turning to the loop-induced Higgs couplings to gluons and to photons, we first note that the H coupling to gluons, C_g^H, is dominated by the top-quark loop, and its behavior is thus practically the same as that of C_U^H in Figs. 5.25 and 5.27. We therefore do not show separate plots for C_g^H. However, as in the h–125 scenario, an exception occurs for the opposite-sign C_D^H solution, for which the b-loop contribution interferes constructively with the t-loop contribution, resulting in $C_g^H \approx 1.06$.

The structure of the coupling to photons, C_γ^H, is more complicated. Here, the main contributions come from $W^\pm$ and top-quark loops as in the SM, as well as from loops with charged Higgs bosons. The $W^\pm$ and top-quark loops contribute with opposite signs. The $H^\pm$ loop typically also has the opposite sign relative to the $W^\pm$ loop and can thus
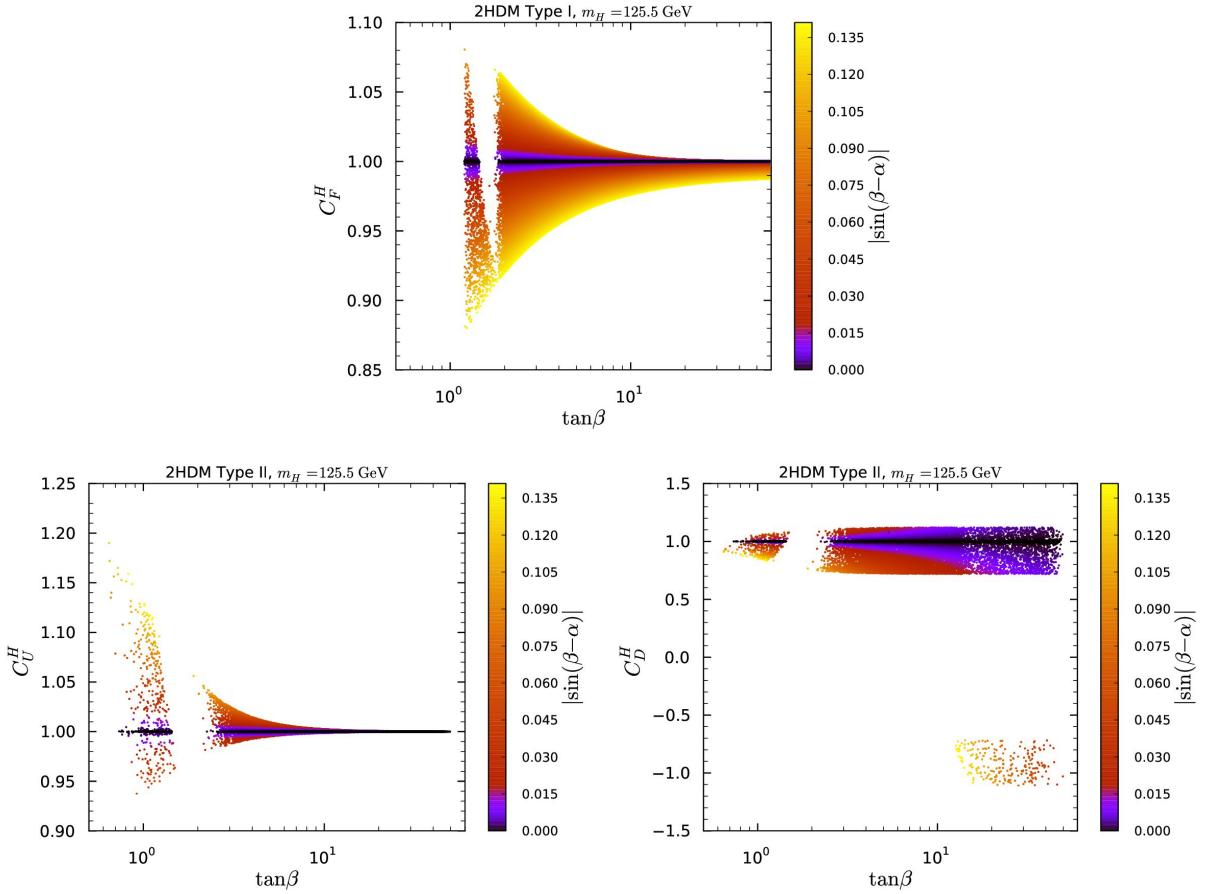
Figure 5.27: Fermionic couplings versus $\tan\beta$ in Type I (upper panel) and Type II (lower panels) with $|s_{\beta-\alpha}|$ color code. Points are ordered from high to low $|s_{\beta-\alpha}|$.

substantially suppress C_γ^H even at very small $s_{\beta-\alpha}$. (Positive interference of the $W^\pm$ and $H^\pm$ loops is however possible for low $m_{H^\pm}$, as noted at the end of Section 4.2.2.) The net effect on C_γ^H is shown in Fig. 5.28. In particular, we observe a large variation in C_γ^H in Type I, where the charged Higgs boson can be light. For $|s_{\beta-\alpha}| \lesssim 10^{-2}$ and $m_{H^\pm} \gtrsim 500$ GeV, we find $C_\gamma^H \approx 0.95$ in both Type I and Type II, in agreement with the expected 5–6% reduction of C_γ^H relative to the SM in the limit $|s_{\beta-\alpha}| \to 0$ with heavy $m_{H^\pm}$ [cf. Eq. (4.112)]. For $|s_{\beta-\alpha}| \gtrsim 10^{-2}$ (but still assuming that $m_{H^\pm}$ is large), this reduction can be more or less than 5% depending on the sign of $\overline{m}^2 \equiv m_{12}^2/(s_\beta c_\beta)$. The dependence on $\overline{m}^2$ is illustrated explicitly in Fig. 5.29. Note however, that while $\overline{m}^2 < 0$ can reach values as large as $-(350$ GeV$)^2$ $\left[-(200$ GeV$)^2\right]$ in Type I [Type II], respectively, $\overline{m}^2 > 0$ does not exceed $\sim (150$ GeV$)^2$. Therefore, in Type II where $m_{H^\pm} > 480$ GeV, C_γ^H is always below 1 (although one will need linear collider precision to pin this down with sufficient accuracy [374]). In contrast, in Type I, for $m_{H^\pm} \lesssim 160$ GeV a value of $\overline{m}^2$ between about $(60$ GeV$)^2$ and $(120$ GeV$)^2$ can lead to a switch in sign of $g_{HH^+H^-}$, giving $C_\gamma^H > 1$. Of course such a light charged Higgs boson can also (and in fact more easily) suppress C_γ^H, down to $C_\gamma^H \approx 0.8$, irrespective of the value of $|s_{\beta-\alpha}|$.

Finally, we consider the trilinear HHH coupling, which is useful for consistency checks of the model, provided it can be measured precisely enough. The dependence of $C_{HHH} \equiv$
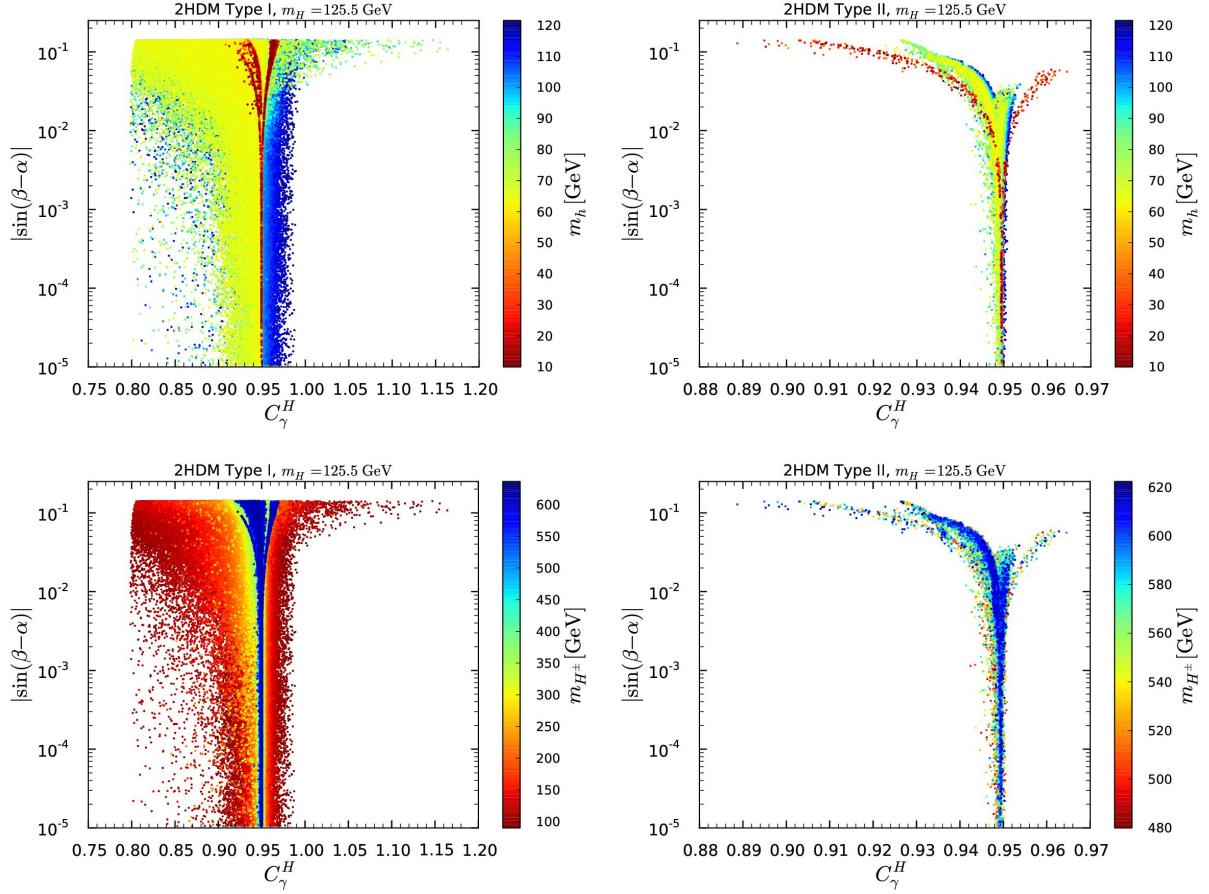
Figure 5.28: $|s_{\beta-\alpha}|$ versus C_γ^H in Type I (left) and Type II (right) with m_h color code (upper panels) and with $m_{H^\pm}$ color code (lower panels). Points are ordered from high to low m_h in the upper panels and from low to high $m_{H^\pm}$ in the lower panels.
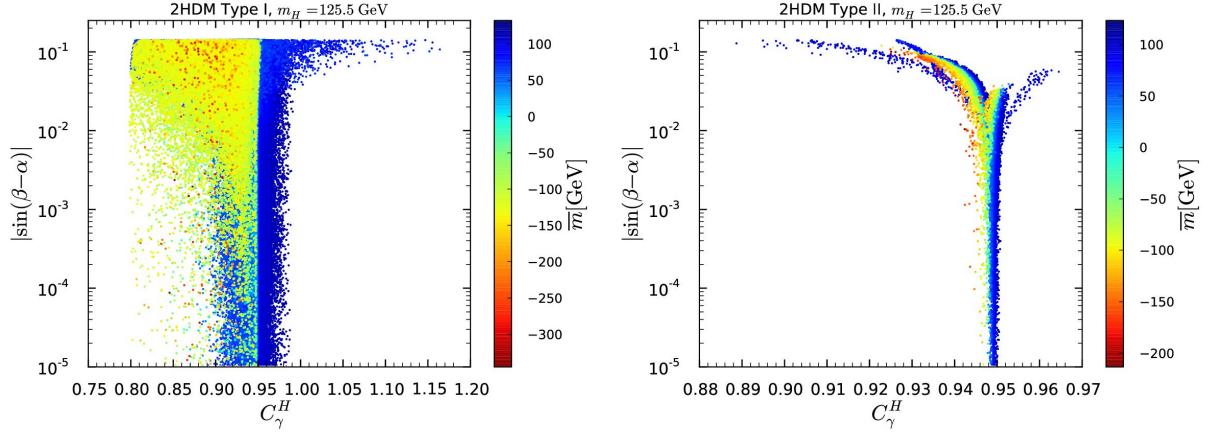
Figure 5.29: As for Fig. 5.28 but showing the dependence of C_γ^H on $\overline{m} \equiv \mathrm{sign}(\overline{m})\sqrt{|\overline{m}^2|}$. Points are ordered from high to low $\overline{m}$.

$g_{HHH}/g_{HHH}^{\mathrm{SM}}$ on $|s_{\beta-\alpha}|$ and m_h (top panels) as well as m_A (bottom panels) is shown in Fig. 5.30. In Type I, similarly to C_{hhh} in the non-decoupling regime of the h–125 scenario, large values of the triple Higgs coupling beyond 1 can be achieved for $|s_{\beta-\alpha}|$ values of the order of 0.1. However, there is no direct analog to the decoupling regime of the h–
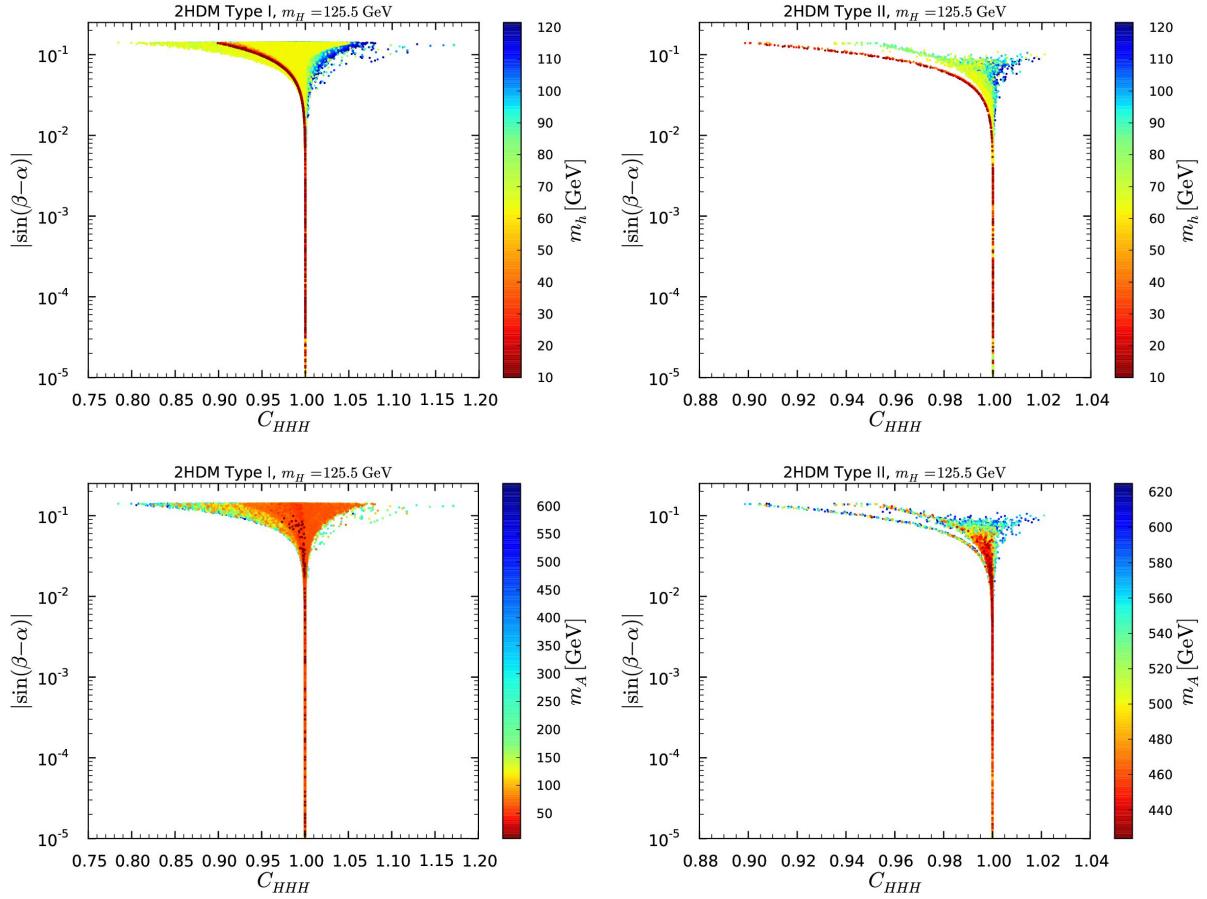
Figure 5.30: Reduced triple Higgs coupling C_{HHH} in Type I (left) and Type II (right), in the top panels with m_h and in the bottom panels with m_A color coding. Points are ordered from high to low $\overline{m}$, m_h or m_A values.
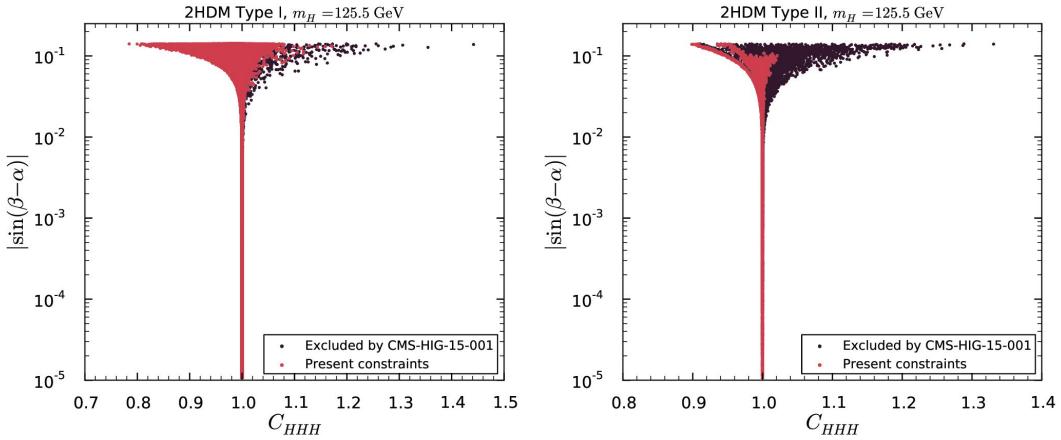
Figure 5.31: As in Fig. 5.24 but in the plane $|s_{\beta-\alpha}|$ vs. C_{HHH}.

125 scenario, where the triple Higgs coupling was always suppressed as compared to its SM prediction. Instead, here, C_{HHH} can be enhanced or suppressed for any value of m_A. However, most of the points which might have had $C_{HHH} \gg 1$ are associated with $\tan\beta \approx$ 1–2, which is precisely the range eliminated by the CMS limits on $gg \to A \to Zh$. In the end we are left with $C_{HHH} \approx 0.8$–1.2 in Type I and $C_{HHH} \approx 0.9$–1.02 in Type II. Without

the $gg \to A \to Zh$ limits, we find that values up to $C_{HHH} \approx 1.4$ would actually be allowed, see Fig. 5.31.

In Type I, the possible variation is less important for smaller m_A, in particular for m_A below about 100 GeV. Moreover, we note that $C_{HHH} \leq 1$ for $m_h \lesssim 60$ GeV in both Type I and Type II. Finally, the smallest values of $C_{HHH} < 1$ in Type I are found for large $\tan \beta$, while in Type II C_{HHH} converges to 1 with increasing $\tan \beta$.

5.3.4 *Signal strengths of the SM-like state H*

The variations in the couplings to fermions discussed above have direct consequences for the signal strengths of H. In Type I, the signal strengths in the $H \to \gamma\gamma$ decay mode are driven by the value of $m_{H^\pm}$, while for the $H \to VV^*$ ($VV^* = ZZ^*, WW^*$) and $H \to \tau\tau$ decay modes they depend mostly on C_F^H, as illustrated in Fig. 5.32. Notice that the C_F^H dependence in the ZZ^* mode is opposite for gg fusion and vector boson fusion production. In the case of VBF, a smaller value of C_F^H implies a smaller $b\bar{b}$ partial width and therefore a larger ZZ^* branching ratio, whereas in gg production C_F^H determines the size of the top-quark loop contribution which is enhanced for a larger value of C_F^H. In contrast, in Type II, the signal strengths are always dominantly driven by C_D^H, as it determines the $H \to b\bar{b}$ partial width. This is illustrated in Fig. 5.33. In this case, the dependence is always the same for gg and VBF production.
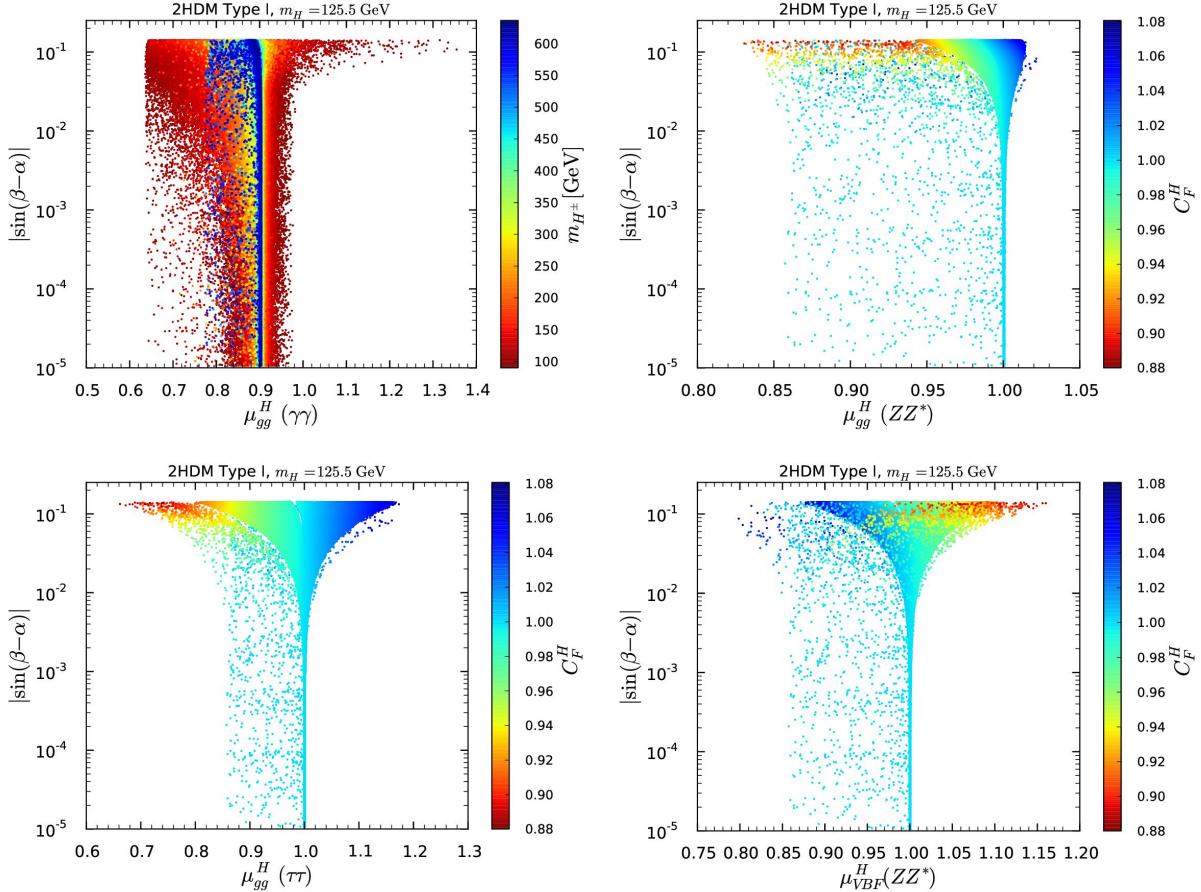

Figure 5.32: Signal strengths in Type I versus $|\sin(\beta - \alpha)|$ with $m_{H^\pm}$ and C_F^H color codes.
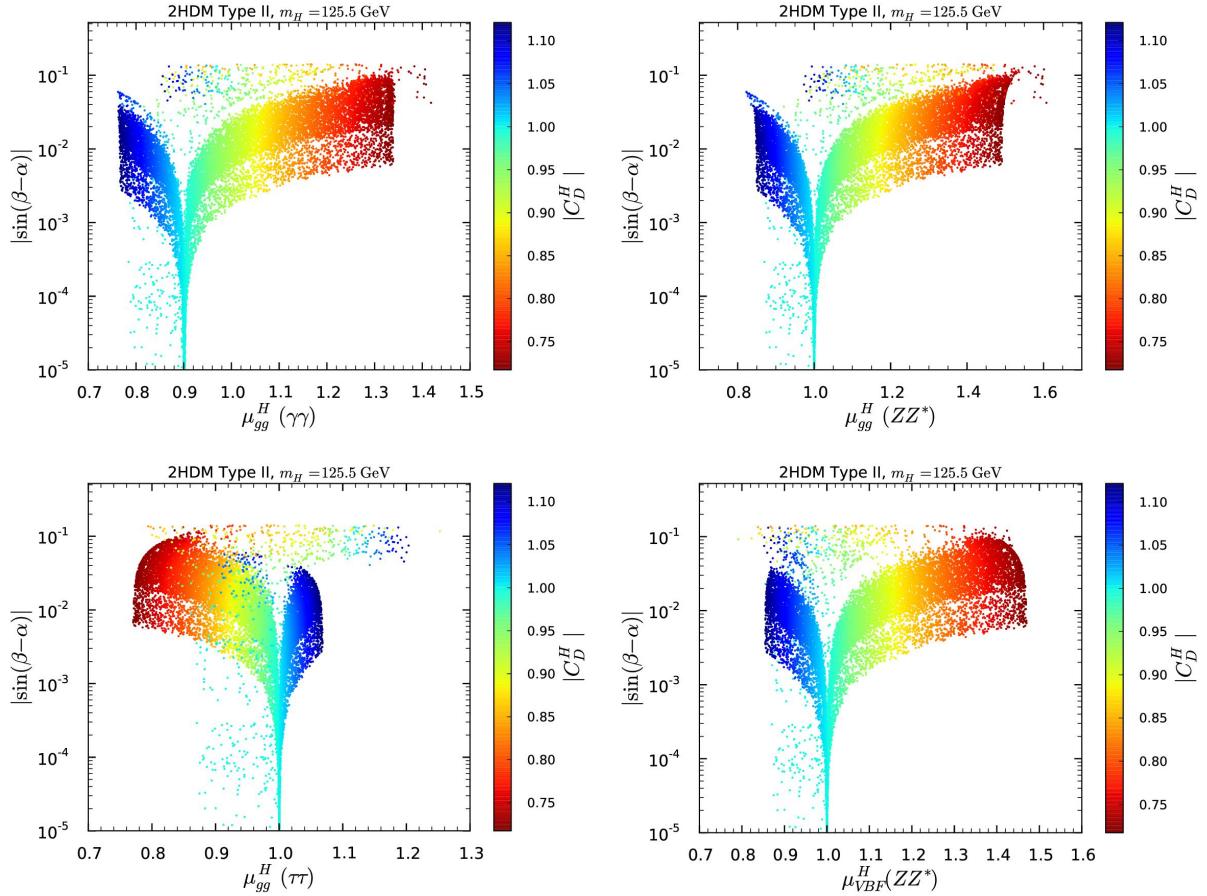
Figure 5.33: Signal strengths in Type II versus $|\sin(\beta - \alpha)|$ with $m_{H^\pm}$ and C_F^H color codes. The horizontal bars near $|s_{\beta - \alpha}| \approx 0.1$ arise from the opposite-sign C_D^H solution.

Putting everything together we find quite distinct correlations of signal strengths as shown in Fig. 5.34 for Type I and in Fig. 5.35 for Type II. It is especially noteworthy that even in the deep alignment limit, the signal strengths can significantly differ from the corresponding SM predictions. Moreover, certain combinations can only be reached for specific ranges of m_h and/or m_A values. For example, $\mu_{gg}^H(\gamma\gamma) \simeq \mu_{\mathrm{VBF}}^H(\gamma\gamma) \approx 0.7$ requires $m_h \gtrsim 60$ GeV in Type I while it is not reached at all in Type II. Likewise, a suppression of $\mu_{gg}^H(\gamma\gamma)$ while $\mu_{\mathrm{VBF}}^H(\gamma\gamma) \gtrsim 1$ would point towards a somewhat heavy A in Type I with a slight departure from strict alignment, while again this combination is not possible in Type II. Another example is the relation between $\mu_{gg}^H(\gamma\gamma)$ and $\mu_{gg}^H(ZZ^*)$. In the alignment limit in Type II we expect $\mu_{gg}^H(\gamma\gamma)/\mu_{gg}^H(ZZ^*) \simeq 0.9$, with both enhancement or suppression of the individual $\mu_{gg}^H(\gamma\gamma), \mu_{gg}^H(ZZ^*)$ with respect to the SM being possible. In Type I, there is a band in which this ratio also applies (for all m_h) and the signals are always suppressed. For values of $m_h \gtrsim 60$ GeV in Type I, in the deep (near) alignment limit we find $\mu_{gg}^H(ZZ^*) \approx 1$ ($\in [0.95, 1.02]$), while $\mu_{gg}^H(\gamma\gamma)$ can range from 0.64 to 0.98 (1.4). An analogous discussion is possible for $\mu_{gg}^H(\tau\tau)$ versus $\mu_{gg}^H(\gamma\gamma)$.

In general, when $H \to hh$ or $H \to AA$ decays are kinematically allowed, these (so far) unobserved decay modes suppress the H branching ratios into SM final states, thus leading to a simultaneous suppression of all the $\mu_X^H(Y)$ even in the deep alignment regime. This is apparent in all the correlations shown in Figs. 5.34 and 5.35, in particular it is most notably visible as the upward-sloping diagonal lines of points in the $\mu_{gg}^H(ZZ^*)$ vs. $\mu_{gg}^H(\gamma\gamma)$ and $\mu_{gg}^H(\tau\tau)$ vs. $\mu_{gg}^H(\gamma\gamma)$ plots for Type I. (However, note that in Type II due to the non-universal nature of the Yukawa couplings the signal strengths can also be larger than 1 when the $H \to hh$ decay mode is open.)

Comparing these results with the h–125 scenario case, it seems very difficult to distinguish the h–125 scenario from the H–125 one with signal strength measurements and coupling fits alone. One possibility for such a distinction might be that the measured values point towards Type I or Type II but are excluded by $A \to Zh$ in the case of $m_H \approx 125$ GeV for a particular model type. Such a result would obviously favor the $m_h \approx 125$ GeV scenario.
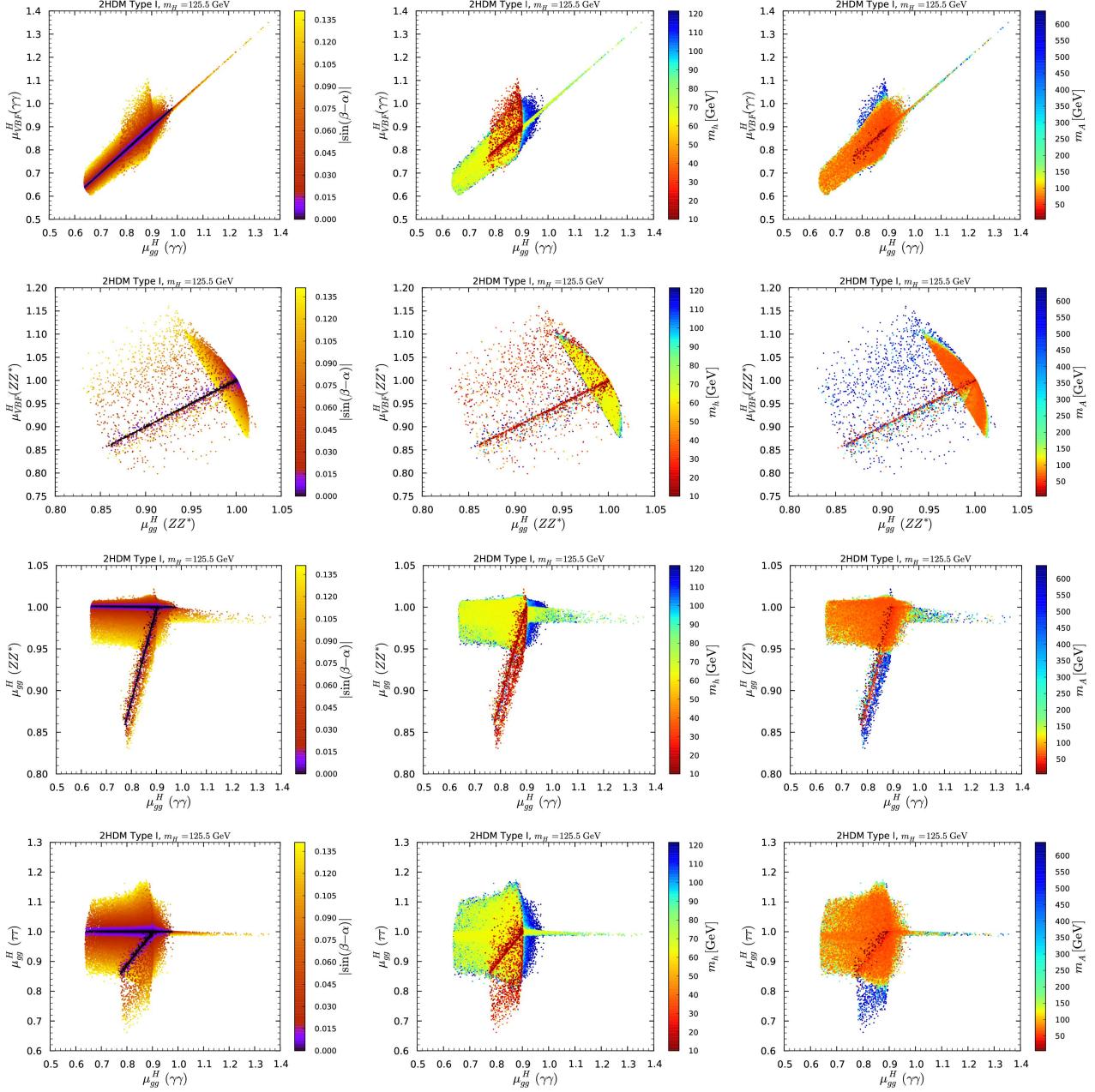
Figure 5.34: Examples of correlations between signal strengths in Type I. The top panels show $\mu_{\mathrm{VBF}}^H(\gamma\gamma)$ vs. $\mu_{gg}^H(\gamma\gamma)$, the upper middle panels show $\mu_{\mathrm{VBF}}^H(ZZ^*)$ vs. $\mu_{gg}^H(ZZ^*)$, the lower middle panels show $\mu_{gg}^H(ZZ^*)$ vs. $\mu_{gg}^H(\gamma\gamma)$ and the bottom panels show $\mu_{gg}^H(\tau\tau)$ vs. $\mu_{gg}^H(\gamma\gamma)$. The color code indicates, from left to right, the dependence on $|s_{\beta-\alpha}|$, m_h and m_A. Points are ordered from high to low $|s_{\beta-\alpha}|$, m_h and m_A values.
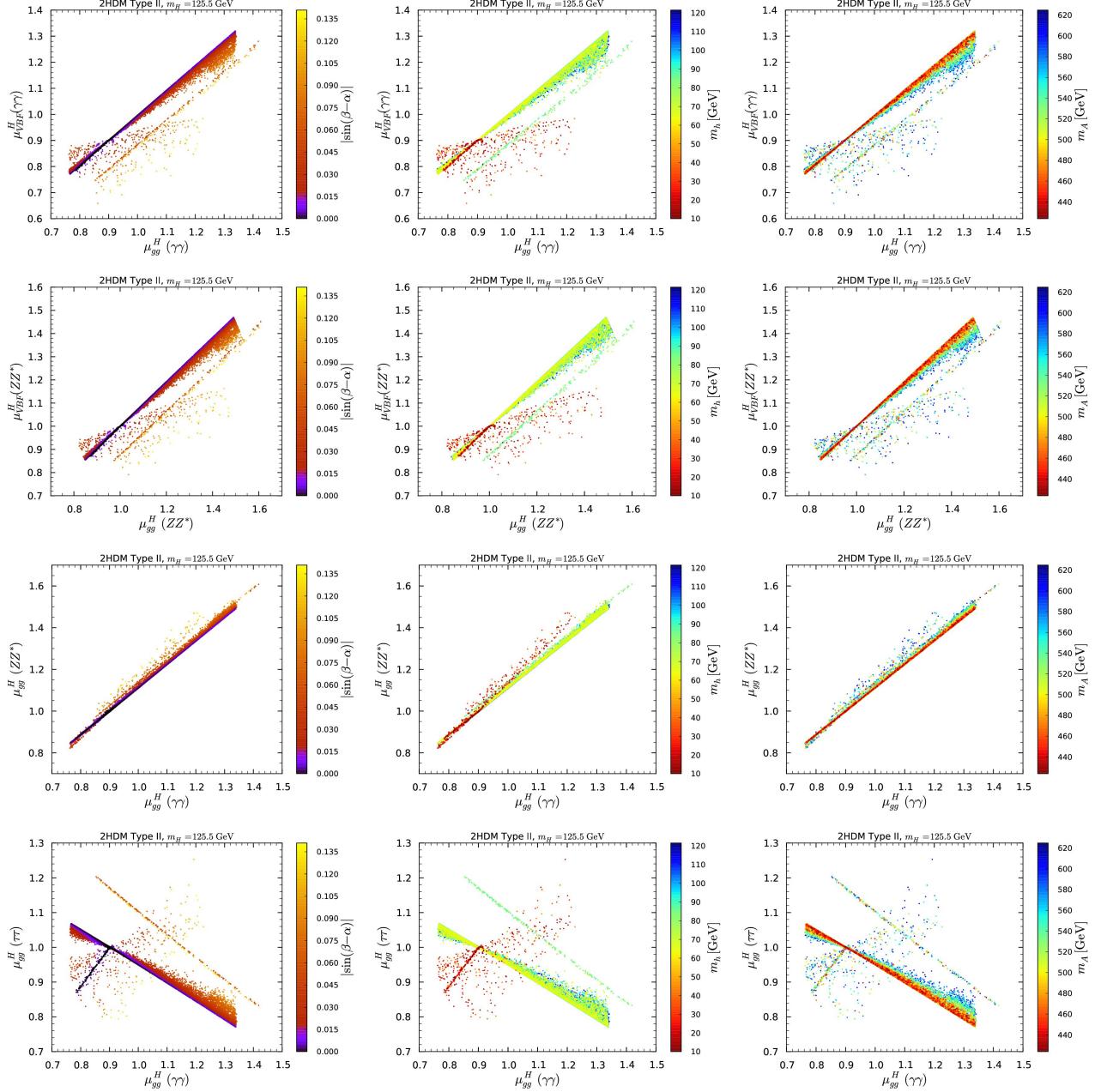
Figure 5.35: Examples of correlations between signal strengths in Type II. The top panels shows $\mu_{\text{VBF}}^H(\gamma\gamma)$ vs. $\mu_{gg}^H(\gamma\gamma)$, the upper middle panels show $\mu_{\text{VBF}}^H(ZZ^*)$ vs. $\mu_{gg}^H(ZZ^*)$, the lower middle panels show $\mu_{gg}^H(ZZ^*)$ vs. $\mu_{gg}^H(\gamma\gamma)$ and the bottom panels show $\mu_{gg}^H(\tau\tau)$ vs. $\mu_{gg}^H(\gamma\gamma)$. The color code indicates, from left to right, the dependence on $|s_{\beta-\alpha}|$, m_h and m_A. Points are ordered from high to low $|s_{\beta-\alpha}|$, m_h and m_A values. Note that the correlations look the same in the first two rows of plots (*i.e.*, for VBF vs. gg production in $\gamma\gamma$ or ZZ^* final state) but the actual μ values are different. The opposite-sign C_D^H solution is visible as a separate narrow line with: $|s_{\beta-\alpha}| \approx 0.1$ (left-hand panels), $m_h \gtrsim 65$ GeV (middle panels) and $m_A \in [420, 630]$ GeV (right-hand panels).

5.3.5 *Probing h and A at the LHC*

Direct detection of the extra scalar states would naturally be the most direct way to identify a 2HDM structure. Here, we discuss the prospects to observe either h or A at the 13 TeV LHC. The correlations of the $gg \to X$ and $b\bar{b}X$ cross sections with $X = h, A$ are shown in Fig. 5.36 for the Type I model and in Fig. 5.37 for the Type II model with the beige color code representing all points that satisfy the present constraints and the red and dark red ones, representing points that have a SM-like state H with signal strengths within 5% and 2% of their SM values respectively.

Figure 5.36: $\sigma(b\bar{b}X)$ versus $\sigma(gg \to X)$ for $X = h$ (left) and $X = A$ (right) in Type I at the 13 TeV LHC for points satisfying all present constraints (in beige) as well as points for which the signals strengths from Eq. (5.6) are within 5% and 2% of the SM predictions (in red and dark red, respectively). The dashed lines indicate $\sigma_{13}(b\bar{b}X) = \sigma_{13}(gg \to X)$.
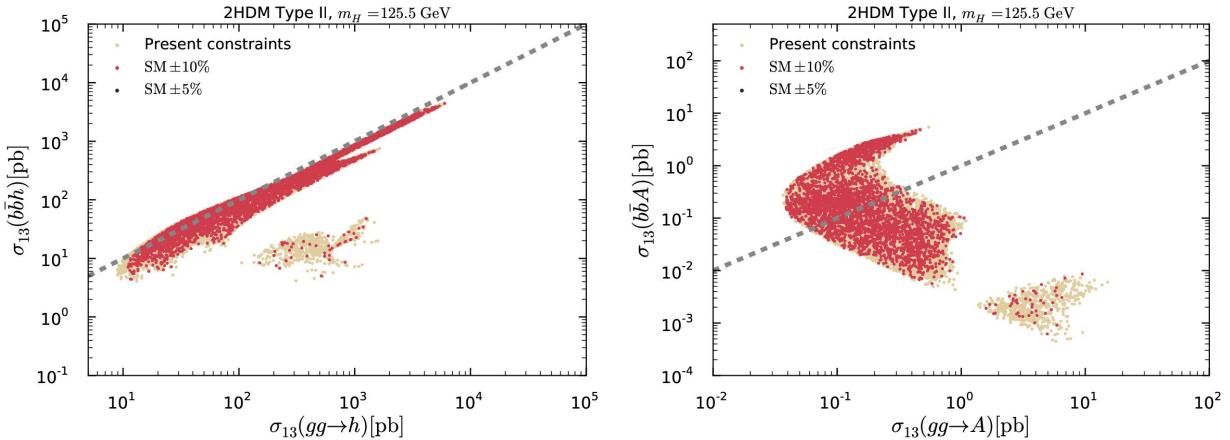
Figure 5.37: As in Fig. 5.36 but for Type II.

As expected for the production of h and A in Type I, shown in Fig. 5.36, there is a strong correlation between the gluon fusion and $b\bar{b}$ associated production cross sections since the couplings controlling their sizes are the same (up to a sign in the case of the A);

$C_U^h = C_D^h = \cos\alpha/\sin\beta$ and $C_U^A = -C_D^A = \cot\beta$, respectively. On the full parameter space, $\sigma(gg \to A)$ dominates over $\sigma(b\bar{b}A)$.

Turning to Type II, for the pseudoscalar production, either the $b\bar{b}A$ or the $gg \to A$ cross section can be dominant depending on the size $\tan\beta$ due to the fact that $C_D^A \propto 1/C_U^A \propto \tan\beta$. Also, as already noted in Ref. [207], the H−125 scenario can be either eliminated or confirmed when the LHC measurements of signal strengths reach a precision about 5%. This could also be observed in the $(\mu_{gg}(ZZ^*), \mu_{gg}(\gamma\gamma))$ correlation shown in Fig. (5.35).

Before considering specific decay channels, we present the gluon-fusion and $b\bar{b}A$ cross sections, as functions of m_h and m_A in Type I and Type II at the 13 TeV LHC in Fig. 5.38. A cross section of 1 fb is guaranteed for m_A up to the maximum possible mass of approximatively 600 GeV. At very small m_A and low $\tan\beta$ it can reach 100 pb (recall that the $gg \to A$ cross section is proportional to $\cot^2\beta$ in Type I). On the other hand, the $gg \to h$ cross section in Type I is proportional to $(C_F^h)^2$ and can take on extremely small values. The reason is that $s_{\beta-\alpha}$ can take either sign and its values are such that a perfect cancellation between the two terms of $C_F^h = s_{\beta-\alpha} + c_{\beta-\alpha}\cot\beta$ can occur at large $\tan\beta$. For $m_h < \frac{1}{2}m_H$, this cancellation is also possible, but for most points $\tan\beta$ is small and the cross section can be as large as 5×10^3 pb at $m_h \sim 10$ GeV. In Type II, any phenomenologically viable mass in the range 420–630 GeV gives a $gg \to A$ cross section larger than 30 fb with values as large as 10 pb possible for $\tan\beta \lesssim 1$. Moreover, note that the $\tan\beta$ dependence is opposite for $b\bar{b}A$ compared to $gg \to A$ so that one or the other cross section is always large, as illustrated in the right panel of Fig. 5.37. As for h in Type II, the smallest $gg \to h$ cross section is of order 8 pb at $m_h \approx 120$ GeV, with values as large as 4–6×10^3 pb for $m_h \sim 80$–90 GeV at very large $\tan\beta$. As previously mentioned, large values of $\tan\beta$ are excluded for $m_h < 80$ GeV and $m_h > 90$ GeV because of the severe constraints from $h \to \tau\tau$ decays. For values of $m_h < \frac{1}{2}m_H$, for which $\tan\beta$ must be small, the $gg \to h$ cross section takes a minimum value of approximatively 100 pb reaching 2×10^3 pb at $m_h \approx 10$ GeV. To summarize, the prospects for observing the h are good in Type II, while the prospects for discovering the A look promising in both Type I and Type II.

Turning now to specific to specific signatures, the cross sections for $gg \to h \to Y$ with $Y = \gamma\gamma$ and $\tau\tau$ in Types I and II are exhibited in Figure 5.39. In Type II, $gg \to h \to \gamma\gamma$ cross sections of at least 1 fb are guaranteed if $m_h < \frac{1}{2}m_H$. In this same region one finds that $\sigma(gg \to h \to \gamma\gamma) > 0.1$ fb in Type I if $\tan\beta < 2$. For $m_h \gtrsim \frac{1}{2}m_H$, cross sections in the $\gamma\gamma$ final state can reach 10 fb (3 fb) in Type I (Type II), though they can also be much lower, especially in Type I. The behavior of $\sigma(gg \to h \to \tau\tau)$ is similar with cross sections above 1 pb over the full m_h range in Type II, and also in Type I if $\tan\beta$ is small enough. Existing limits on $\sigma(gg \to h \to \gamma\gamma)$ at 8 TeV from CMS for $m_h = 80$–110 GeV are roughly 0.05–0.1 pb at 68% CL [375]. Thus, we expect that future Run 2 data will eventually provide a sensitive probe in this channel, which will be particularly interesting if the analyses can be extended to cover the whole m_h range down to about 10 GeV.

The cross sections for A production with decays into SM channels, $A \to \gamma\gamma$, $\tau\tau$, $t\bar{t}$, are presented in Fig. 5.40. In Type I, the $gg \to A \to \gamma\gamma$ ($\tau\tau$) cross section can be as large as roughly 15 fb (10 to 1 pb), respectively, for $m_A \in [60, 200]$ GeV, with minimum values that would still be potentially observable for $m_A \lesssim 100$ GeV for a very large integrated luminosity. We also note a narrow band of non-excluded points with m_A between 10 and 60 GeV, with very large $gg \to A \to \tau\tau$ cross sections for $m_A \approx 10$ GeV. For $m_A \in [200, 2m_t]$
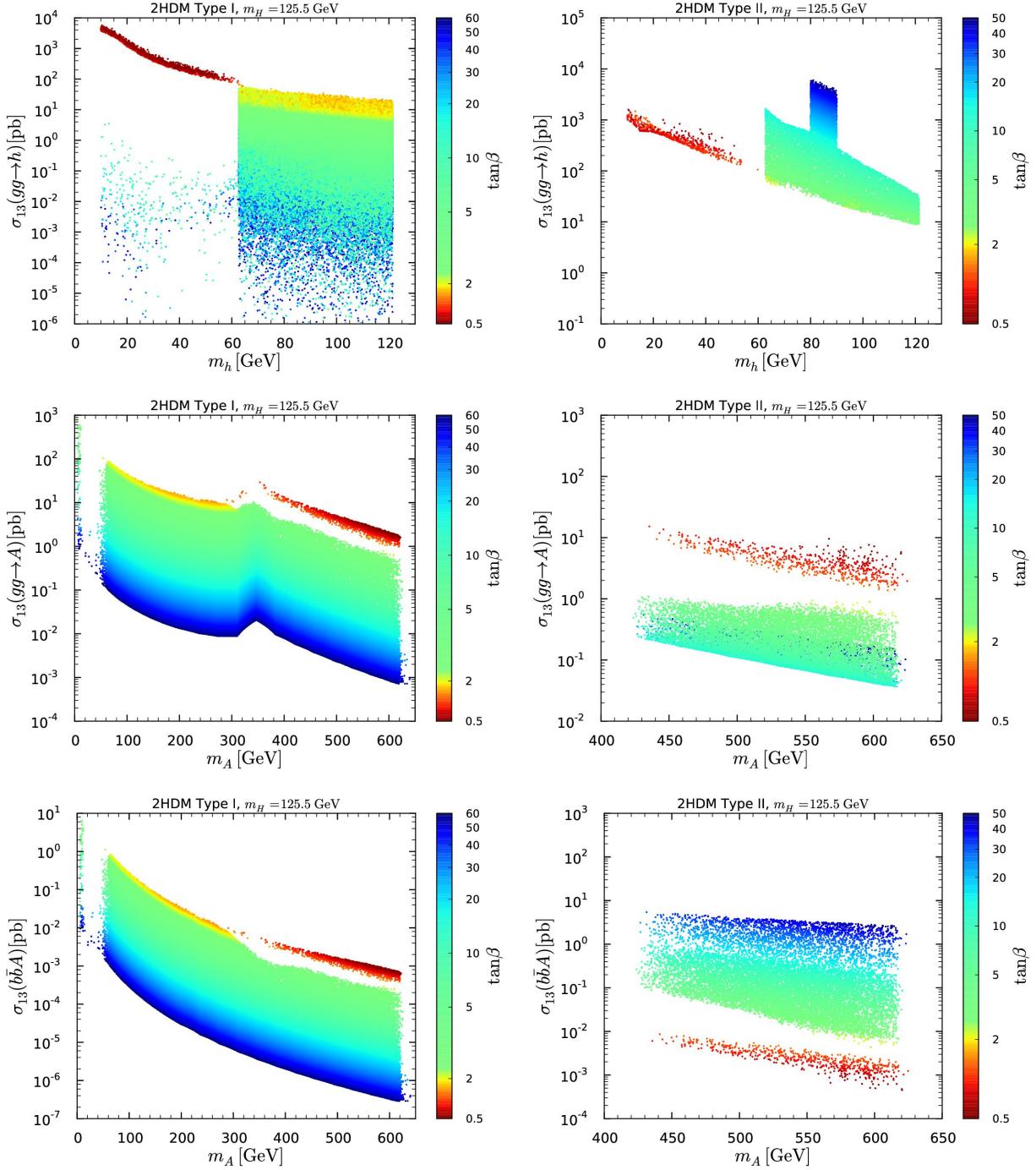
Figure 5.38: Cross sections in Type I (left) and Type II (right) for $gg \rightarrow X$ as functions of m_X for $X = h$ (upper panels) and $X = A$ (middle panels) with $\tan\beta$ color code. The bottom panels depict the cross sections for $b\bar{b}A$ production as function of m_A with $\tan\beta$ color code. In all six plots, points are ordered from high to low $\tan\beta$.

the A cross section is small in both the $\gamma\gamma$ and $\tau\tau$ channels, and the $t\bar{t}$ cross section is either zero or very tiny. Once $m_A > 2m_t$, a very substantial $gg \rightarrow A \rightarrow t\bar{t}$ cross section (up to about 0.3 pb for $\tan\beta > 2$ and roughly 0.1–6 pb for $\tan\beta < 2$) is possible for small $\tan\beta$, but as $\tan\beta$ increases this cross section declines rapidly. Turning to Type II, we see that observation of the A in the $\gamma\gamma$ final state will be, at best, extremely difficult. In contrast,
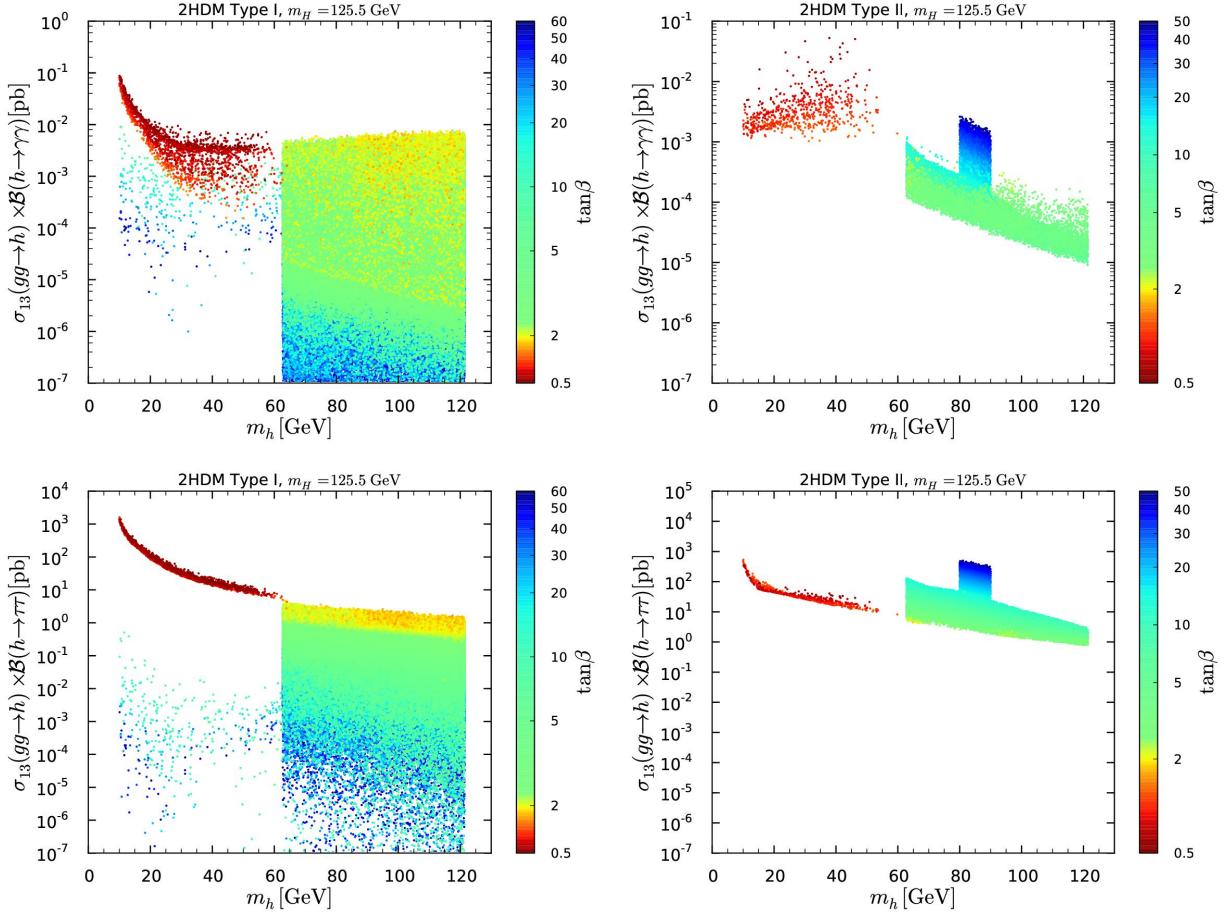
Figure 5.39: Cross sections times branching ratios in Type I (left) and in Type II (right) for $gg \to h \to Y$ at the 13 TeV LHC as functions of m_h for $Y = \gamma\gamma$ (upper panels) and $Y = \tau\tau$ (lower panels) with $\tan\beta$ color code. Points are ordered from high to low $\tan\beta$.

observation of $b\bar{b}A$ production with $A \to \tau\tau$ may be possible at large $\tan\beta$. Moreover, $b\bar{b}A$ production is useful for observing the $A \to t\bar{t}$ decay in Type II. The cross section (not shown) ranges from 60–0.2 fb for $m_A \simeq 420$–630 GeV, with only little dependence on $\tan\beta$. The cross section for $gg \to A \to t\bar{t}$ is sizeable (up to 8 pb) for very small $\tan\beta$, but below 0.1 pb for $\tan\beta \gtrsim 2$.

While the sizable cross sections discussed above provide interesting probes of the extended Higgs sector in the alignment limit, the non-standard signatures of $A \to Zh$ and/or $A \to ZH$ shown in Fig. 5.41 appear to be even more promising. In Type II, there is a strict lower bound on the $gg \to A \to Zh$ cross section, with values above 1 pb at small $\tan\beta$ and at least of order 25 fb at large $\tan\beta$ even at the maximal value of $m_A = 630$ GeV. In Type I, at low $\tan\beta$ the $gg \to A \to Zh$ cross sections fall in the range ~ 1 pb to 20 pb while at large $\tan\beta$ this cross section could be as small as ~ 0.1 fb (or even smaller for $m_A < 220$ GeV). Given that the Run 1 searches in this channel remove a significant portion of the low $\tan\beta$ 2HDM Type I and Type II points, it seems certain that Run 2 results would either be substantially more constraining or reveal a signal.
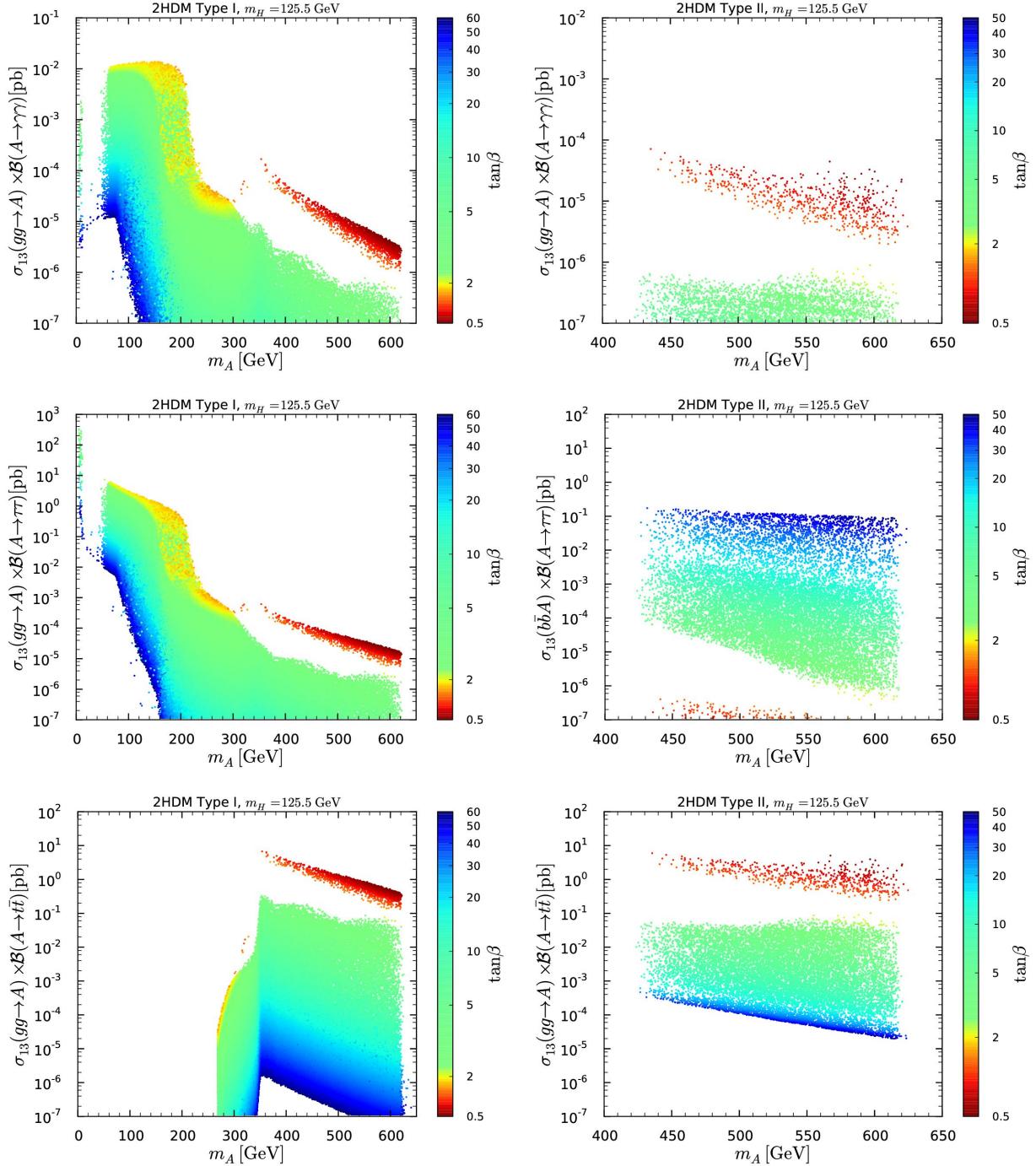
Figure 5.40: Cross sections times branching ratios in Type I (left) and in Type II (right) for $A \to Y$ signatures at the 13 TeV LHC as functions of m_A with $Y = \gamma\gamma$ (upper panels), $Y = \tau\tau$ (middle panels) and $Y = t\bar{t}$ (lower panels) with $\tan\beta$ color code. Points are ordered from high to low $\tan\beta$.

The cross sections for $gg \to A \to ZH$ are typically at least a factor of 100 smaller than those for the Zh final state. Nevertheless, the $A \to ZH$ decay could provide an additional probe of the small-to-intermediate $\tan\beta$ regime, but will likely be unobservable at large $\tan\beta$ in both Type I and Type II.
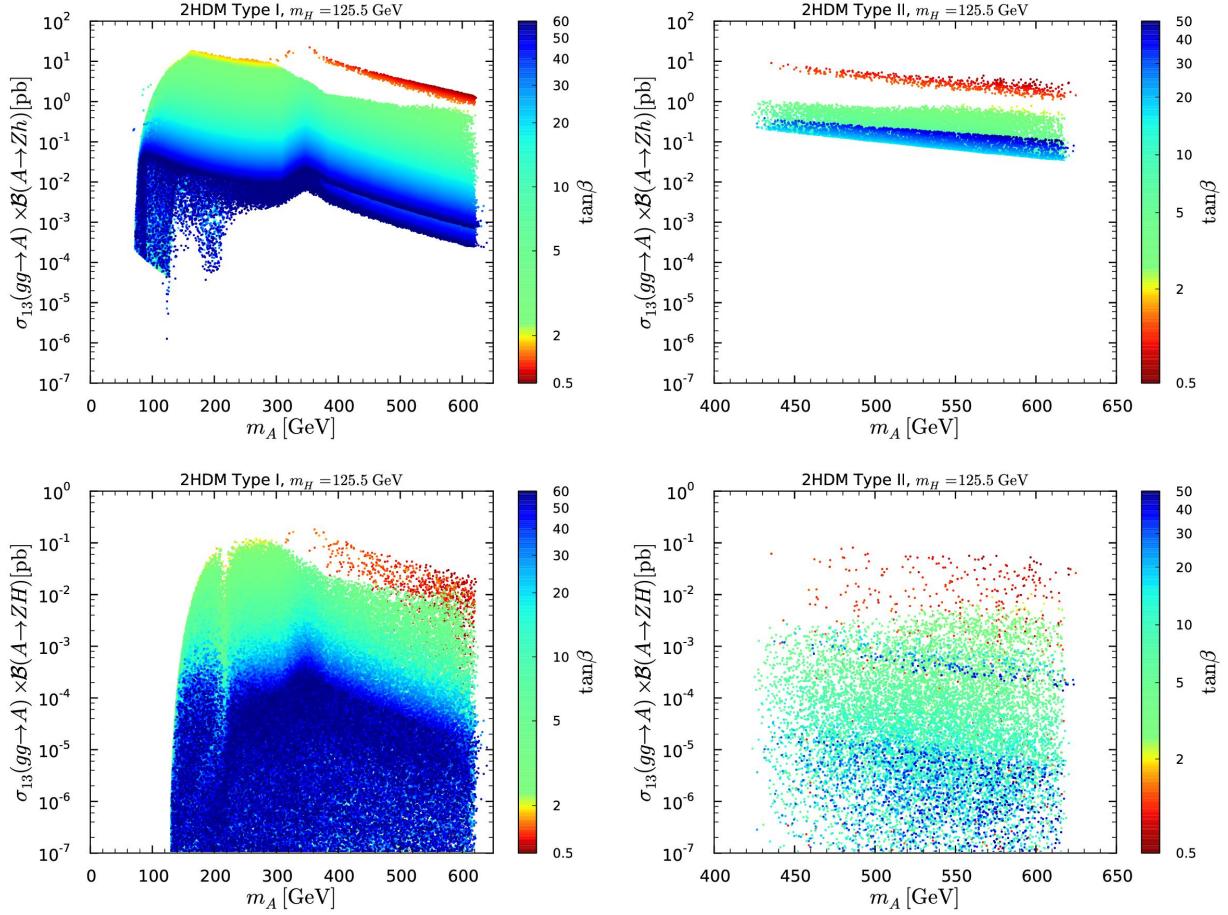
Figure 5.41: Cross sections times branching ratios in Type I (left) and in Type II (right) at the 13 TeV LHC as functions of m_A for $gg \to A \to Zh$ (upper panels) and for $gg \to A \to ZH$ (lower panels) with $\tan\beta$ color code. Points are ordered from low to high $\tan\beta$.

A large $gg \to A \to ZH$ cross section could potentially have a substantial impact on the $\mu_{ZH}^H(Y)$ signal strength through the so-called "feed-down" effects [207, 359], parametrized here by $\mu_{ZH}^{FD} \equiv \sigma_8(gg \to A \to ZH)/\sigma_8(q\bar{q} \to ZH)$. However, we observe that this effect is small in both Types I and II, where $\mu_{ZH}^{FD} < 0.16, 0.06$, respectively, for all points, implying that our global fit of the H properties is not affected by the feed-down.

5.3.6 *Alignment in the H–125 scenario: summary*

With the H mass eigenstate being approximately aligned with the direction of the scalar field vacuum expectation value in field space, its coupling to the W and Z bosons tends towards the SM value, $C_V^H \to 1$. Allowing for at most a 1% deviation from unity in C_V^H, we found that deviations in the couplings to fermions of 10–20% are possible while maintaining consistency at 95% CL with the LHC Run 1 Higgs measurements. While C_F^H in Type I and C_U^H in Type II rather quickly approach unity as $|s_{\beta-\alpha}| \to 0$, the approach of the bottom Yukawa coupling to its SM value in the alignment limit is delayed in Type II, with $C_D^H \simeq 0.72$–1.12 even for values of $|s_{\beta-\alpha}| \approx 10^{-2}$. Moreover, there can be significant deviations from 1 in the loop-induced coupling to photons: $C_\gamma \simeq 0.80$–1.17 (0.88–0.97) in Type I (II). In the case of Type I, the reason for the larger range of C_γ and for its extending also to values above 1 is that the charged Higgs can be light. All these variations in the couplings feed into distinctive behaviors of the signal strengths. Thus, even in the deep alignment regime, where one might naively expect everything to be very SM-like, precise measurements of the signal strengths at 125 GeV can help determine the existence of the extended Higgs sector. Furthermore, correlations between signal strengths are characteristic for the model and can point towards a 2HDM of Type I or Type II.

Distinguishing the h–125 scenario from the H–125 one with signal strength measurements and coupling fits alone however seems very difficult, unless one finds values that are excluded by the $A \to Zh$ search in the $m_H \approx 125$ GeV case. Preferably, and certainly more definitively, one would wish to observe the second CP-even scalar, h. We observed an upper limit on the masses of the CP-odd and the charged Higgs of $m_{A,H^\pm} \lesssim 630$ GeV, suggesting that all the extra Higgs states of the 2HDM are at least kinematically accessible at the LHC in this setup. While we did not study the potential for observing the $H^\pm$, direct detection of the h and/or A might be possible in a variety of production $\times$ decay channels. Most exciting and enticing is the channel $gg \to A \to Zh$ which would reveal the presence of both the h and A simultaneously. The associated cross section at $\sqrt{s} = 13$ TeV is at least 20 fb (and can be as large as 10 pb) in Type II. In Type I, $\sigma(gg \to A \to Zh)$ is also large, 10 fb to 30 pb, over most of the parameter space, although for very large $\tan\beta$ it can drop below 1 fb in the ranges $m_A \simeq 90$–250 GeV and $m_A \gtrsim 500$ GeV. The searches for $A \to Zh$ with $Z \to \ell\ell$ and $h \to b\bar{b}$ or $\tau\tau$ are therefore excellent probes for discovering or excluding the 2HDM scenarios with a SM-like H, provided that they are performed *without* requiring a SM-like h with $m_h = 125$ GeV. In fact, CMS has already performed such a search for $A \to Zh$ at $\sqrt{s} = 8$ TeV for general m_A and m_h values (down to 40 GeV), and the limits they obtained are among the most severe constraints for the scenario studied in this paper.

Other channels of high interest include $gg \to h \to \gamma\gamma$ (for $m_h \lesssim 90$ GeV) as well as $gg \to h \to \tau\tau$ (or $\mu\mu$) in Type II. The $\gamma\gamma$ channel may also reveal a light A in Type I if $\tan\beta$ is small. Moreover, $gg \to A \to \tau\tau$ (or $\mu\mu$) can be used to search for a light A in the 10–250 GeV mass range in Type I, while in Type II it would be preferable to exploit the $b\bar{b}A$ production mode to search for the same A decays (over the relevant mass range of $m_A \simeq 420$–630 GeV).

5.4 LIGHT HIGGS STATES

Going further in the possibility of light additional states, we address the seemingly extreme case in which the h (H) is the SM-like 125 GeV state and the A (A and/or h) are lighter than 125 GeV, in particular light enough that the SM-like state can decay into them. Such decays generically have a large branching ratio (early references are [376], [377] and [258]) and would conflict with the measured signal strengths unless the Higgs-to-Higgs-pair branching ratio is below about 0.1–0.3 as shown in the global fit performed in Section 3.4, depending on the model.[27] A large survey of exotic Higgs decays may be found in [378]. Only by tuning the model parameters so that the SM-like Higgs has very small coupling to a pair of lighter Higgs bosons can such a small branching ratio be achieved. Nonetheless, this is a parameter space window that is not yet totally excluded and that has many interesting special features, including rather large predicted cross sections for direct production of the light Higgs boson(s).

Let us note that these scenarios are not achievable in the MSSM because of the strong interrelations of the Higgs potential parameters required by supersymmetry; a light A is simply not consistent within the MSSM when the h has mass 125 GeV (unless the Higgs sector is CP-violating). MSSM scenarios in which the H has mass of 125 GeV and m_A, m_h are below m_H have been constructed [379], but those to date do not have $m_A, m_h < 125/2$ GeV. In the NMSSM, scenarios with a light a_1 and/or h_1 are possible in light of the current data [380–383] but they typically imply small cross sections for production of the light Higgs boson.[28]

The key consideration here is the magnitude of the coupling of the SM-like Higgs to a pair of the other Higgs bosons; g_{hAA}, g_{HAA} and g_{Hhh} given by

$$g_{hAA} = -v\left[(Z_3 + Z_4 - Z_5)s_{\beta-\alpha} + Z_7 c_{\beta-\alpha}\right], \tag{5.7}$$

$$g_{HAA} = -v\left[(Z_3 + Z_4 - Z_5)c_{\beta-\alpha} - Z_7 s_{\beta-\alpha}\right], \tag{5.8}$$

$$g_{Hhh} = -3v\left[Z_1 c_{\beta-\alpha} s_{\beta-\alpha}^2 + Z_{345} c_{\beta-\alpha}\left(\tfrac{1}{3} - s_{\beta-\alpha}^2\right) - Z_6 s_{\beta-\alpha}(1 - 3c_{\beta-\alpha}^2)\right.$$
$$\left. Z_7 c_{\beta-\alpha}^2 s_{\beta-\alpha}\right]. \tag{5.9}$$

A simple estimate of this magnitude required to satisfy the undetected branching ratio constraint can be obtained. In terms of g_{YXX}, where Y is the SM-like Higgs and X is the A for $Y = h$ and either the A or h for $Y = H$, one can define

$$R(XX) \equiv \frac{\Gamma(Y \to XX)}{\Gamma(Y \to bb)} \simeq \frac{1}{12K}\left(\frac{g_{YXX}v}{m_Y m_b}\right)^2 \frac{\beta(m_X)}{\beta^3(m_b)}, \tag{5.10}$$

where $\beta(m_X) = \sqrt{1 - 4m_X^2/m_Y^2}$ and the factor K accounts for QCD corrections and running quark mass. Taking $m_Y = 125$ GeV and assuming purely SM-like couplings for Y, the constraint $\mathrm{BR}(Y \to XX) = \Gamma(Y \to XX)/(\Gamma(Y \to XX) + \Gamma_{\mathrm{tot}}^{\mathrm{SM}}) \lesssim 0.3$ translates

---

27 Recall that in Section 3.4, the fit to the 2HDMs did not take into account the contribution of the charged Higgs bosons. Such additional freedom generally weakens the upper bound on BSM width contribution of the 125 GeV state.

28 NMSSM scenarios with a light a_1 and/or h_1 that appears in the decay of a SM-like Higgs (*e.g.* $h_2 \to a_1 a_1$, where h_2 is SM-like) have a large literature, the original study being [384].

into $R(XX) \lesssim 0.7$, where we have used $\Gamma(Y \to bb) \approx 0.6\,\Gamma_{\rm tot}^{\rm SM}$ as in the SM for simplicity. Using the SM-predicted value $K \approx 0.6$, we find that $|g_{YXX}| \lesssim 15$ GeV is required for $m_X = 62$ GeV, which goes down to $|g_{YXX}| \lesssim 5$ GeV for $m_X \simeq 10-40$ GeV. We will see that such a small g_{YXX} is a very strong constraint — without parameter tuning $|g_{YXX}|$ is most naturally of the order of a TeV.

Let us note that the results presented in this section have not been updated with the most recent ATLAS and CMS results, and correspond to the original analysis presented in Ref. [322]. We will however comment on a particularly important result from CMS for this analysis: the search for the pseudoscalar A in the $b\bar{b}A$, $A \to \tau\tau$ channel in the mass range $m_A = 25$–80 GeV [340].

5.4.1 *Light pseudoscalar in the h–125 scenario*

In this scenario, only A can be lighter than the SM-like state. Trading the Z_i for the physical masses, Eqs. (4.53)–(4.55) and (4.59)–(4.62), the hAA coupling is expressed as,

$$g_{hAA} = \frac{1}{2v}\left[\left(2m_A^2 - m_h^2\right)\frac{c_{\alpha-3\beta}}{s_{2\beta}} + \left[8m_{12}^2 - s_{2\beta}\left(2m_A^2 + 3m_h^2\right)\right]\frac{c_{\beta+\alpha}}{s_{2\beta}^2}\right] \quad (5.11)$$

where in the exact alignment limit, $s_{\beta-\alpha} = 1$,

$$g_{hAA} = \frac{2\overline{m}^2 - 2m_A^2 - m_h^2}{v}. \quad (5.12)$$

Given that $|g_{hAA}|$ must be very small to have small BR$(h \to AA)$, we see that in this limit $2\overline{m}^2 \simeq m_h^2 + 2m_A^2$ is required. While no symmetry motivates this particular choice, it can certainly be satisfied and we find many allowed points of this nature. In the SM limit, the interrelations of the parameters in this region are illustrated in Fig. 5.42. This shows the combined impact of perturbativity and the requirement of small BR$(h \to AA)$. The large solid filled regions are those allowed by perturbativity for various different values of m_H. The regions surrounded by dashed lines are those consistent with BR$(h \to AA) \le 0.3$, with the central solid line corresponding to BR$(h \to AA) = 0$ (or equivalently $g_{hAA}=0$ here), for the various m_A values coded as shown in the upper-right corner of the plot. We see that the higher the value of m_H, the smaller the $\tan\beta$ that is required by perturbativity. Imposing both perturbativity and BR$(h \to AA) \le 0.3$ strongly constrains $m_{12} \equiv {\rm sgn}(m_{12}^2)\sqrt{|m_{12}^2|}$ as well as $\tan\beta$. Roughly, $m_{12} \simeq 30$–100 GeV and $\tan\beta \lesssim 10$ are the phenomenologically viable ranges.

Going away from the strict SM limit, there is also another parameter region that gives small $|g_{hAA}|$ through a cancellation between the first and second terms in Eq. (5.11). This can be achieved when $\sin(\beta+\alpha)$ is close to one and allows also for larger m_{12}^2. As described at the end of Section 4.1.4, this requires that $\tan\beta$ is not too small. Indeed, in this limit,

$$C_V^h = s_{\beta-\alpha} \to \frac{\tan^2\beta - 1}{\tan^2\beta + 1}, \quad (5.13)$$

where $C_V^h \gtrsim 0.95$ is realized, as approximatively required by the LHC Higgs measurements, if $\tan\beta \gtrsim 6$. As discussed previously, the $\sin(\beta+\alpha) \approx 1$ region leads to a coupling of
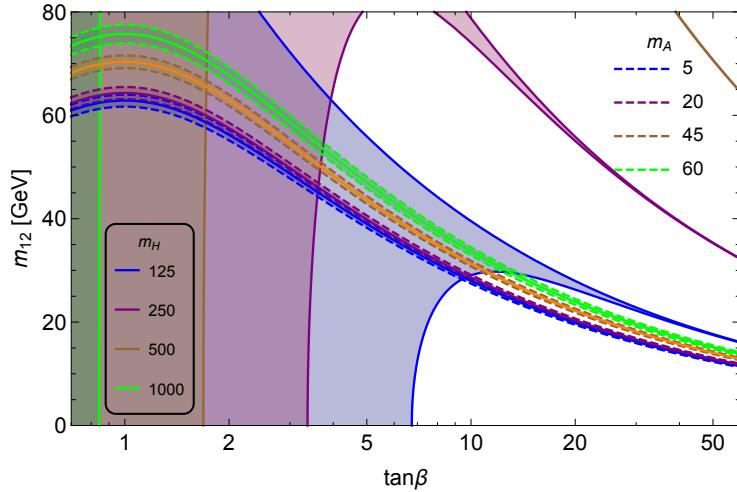
Figure 5.42: In the exact alignment limit, regions of the m_{12} vs. $\tan\beta$ parameter space consistent with perturbativity for various m_H values (see in-figure color code in lower-left corner) and with $BR(h \to AA) < 0.3$ for the indicated values of m_A shown in the upper-right corner. These results apply to both the Type I and Type II 2HDM. The perturbatively acceptable region also extends to $m_{12}^2 < 0$, but this region is not presented since Eq. (5.12) would give large $|g_{hAA}|$ and therefore large $BR(h \to AA)$.

the SM-like state to down-fermions of opposite sign as compared to the coupling to gauge bosons and up-type fermions. There is therefore an interesting link between the wrong-sign Yukawa regime and the presence of a light pseudoscalar state.

An overall view of the allowed low-m_A points in m_{12} vs. $\cos(\beta + \alpha)$ space for the Type I and Type II 2HDMs is provided by Fig. 5.43, and in the $\tan\beta$ vs. $\sin\alpha$ plane in Fig. 5.44.
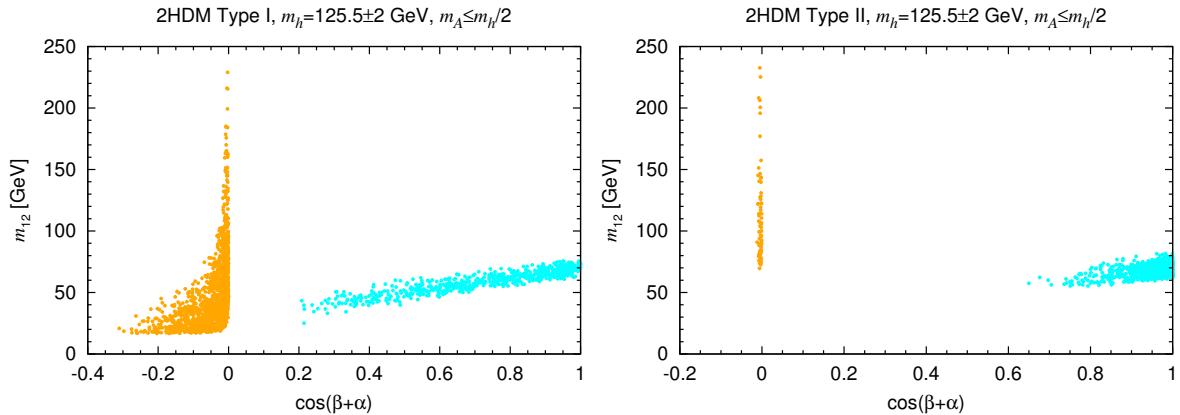
Figure 5.43: Phenomenologically viable points with $m_A \leq m_h/2$ in the m_{12} vs. $\cos(\beta + \alpha)$ plane, for 2HDM Type I (left) and Type II (right). The cyan points realize the small g_{hAA} condition close to the alignment limit, with $2\overline{m}^2 \simeq m_h^2 + 2m_A^2$ as shown in Fig. 5.42. The orange points have $\sin(\beta + \alpha) \sim 1$, small $\cos(\beta + \alpha) < 0$ and $\tan\beta \gtrsim 5$.

The cyan points have $s_{\beta-\alpha} \approx 1$, $\cos(\beta + \alpha) > 0$ and modest m_{12}, while the orange points are those with $\sin(\beta + \alpha) \sim 1$, small $\cos(\beta + \alpha) < 0$, $\tan\beta > 5$ and $m_{12} > 0$. (The opposite case with $m_{12} < 0$ and $\cos(\beta + \alpha) > 0$ could also lead to the necessary cancellations in Eq. (5.11) but turns out to be excluded by the 125 GeV Higgs signal constraints.)
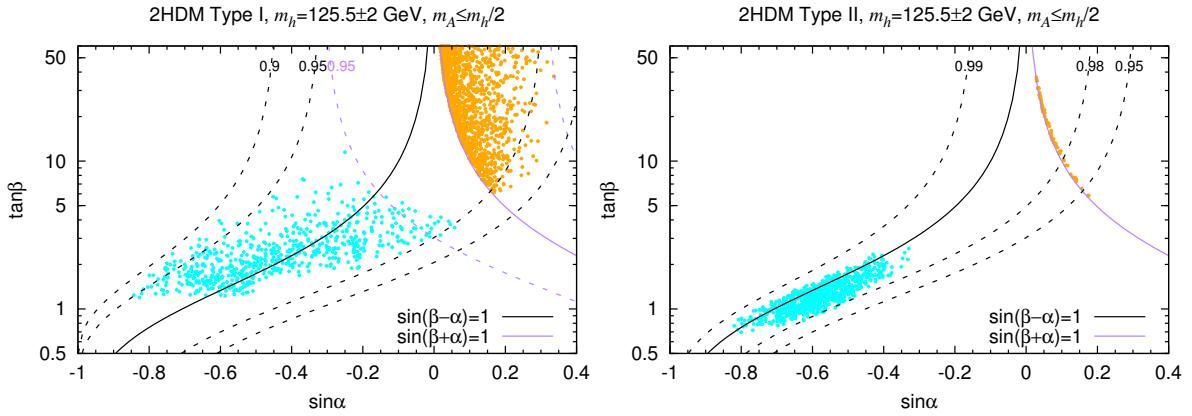
Figure 5.44: Same as Fig. 5.43 but in the $\tan\beta$ vs. $\sin\alpha$ plane. The solid black and purple lines indicate $s_{\beta-\alpha} = 1$ and $\sin(\beta + \alpha) = 1$, respectively. The dashed black (purple) lines are iso-contours of values of $s_{\beta-\alpha}$ ($\sin(\beta + \alpha)$) as indicated on the plots.
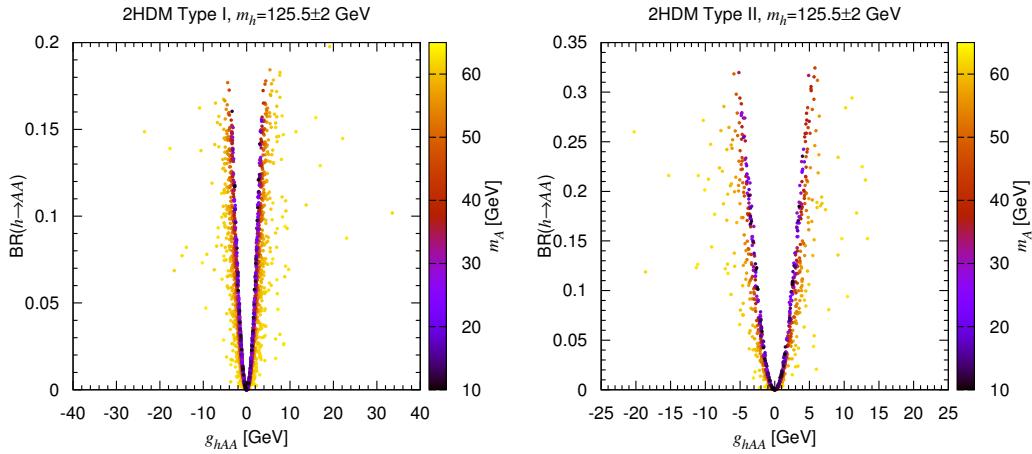
Figure 5.45: Allowed points in the $\mathrm{BR}(h \to AA)$ vs. g_{hAA} plane, on the left for Type I, on the right for Type II. The value of m_A is colour-coded as indicated by the scales on the right of the plots.

In Fig. 5.44, points to the right of the $\sin(\beta + \alpha) = 1$ curve have $\cos(\beta + \alpha) < 0$ and those to the left have $\cos(\beta + \alpha) > 0$. The requirement of small g_{hAA} (coupled with $m_{12} > 0$) thus creates a very sharp boundary between acceptable vs. non-acceptable parameter points. In the Type II model the orange points correspond to the wrong-sign Yukawa coupling $C_D^h \approx -1$, whereas the cyan points have $C_D^h > 0$.

For completeness, we show in Fig. 5.45 the explicit values of $\mathrm{BR}(h \to AA)$ vs. g_{hAA} for the allowed points. We see that g_{hAA} is indeed tightly constrained to small values of the order of 10 GeV. Note that the allowed range for $\mathrm{BR}(h \to AA)$ is different for Type I and Type II models because of the different structure of the h couplings to fermions.

Having understood the constraints on this scenario, we now pursue the implications for LHC phenomenology. In Fig. 5.46 we plot the reduced couplings of h to gluons and to photons, C_g^h vs. C_γ^h. The suppressed values of C_γ^h come from the negative contribution of the charged Higgs to the $h\gamma\gamma$ loop-induced coupling. In the exact alignment limit, $s_{\beta-\alpha} = 1$,

$$g_{hH^\pm H^\pm} = g_{hAA} - (\lambda_5 - \lambda_4)v = g_{hAA} - 2(m_{H^\pm}^2 - m_A^2)/v \,. \tag{5.14}$$
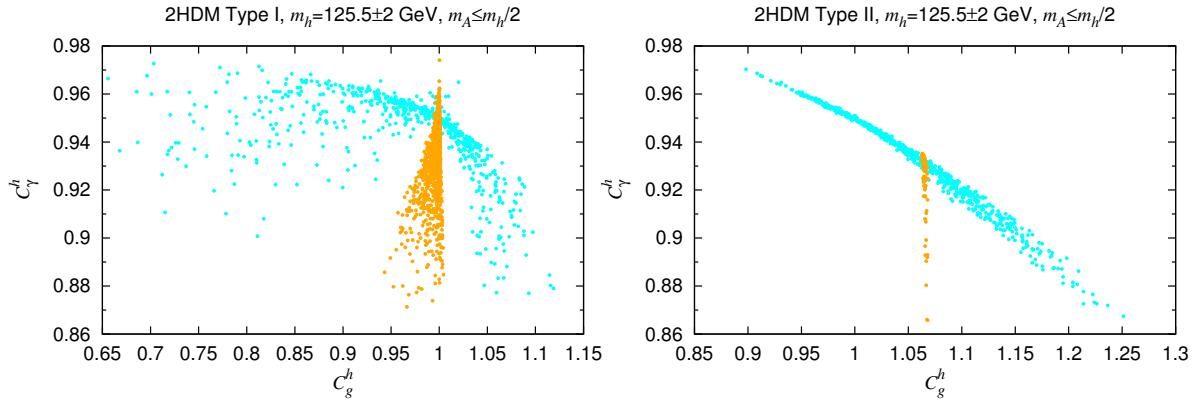
Figure 5.46: As Fig. 5.43 but for C_γ^h vs. C_g^h.
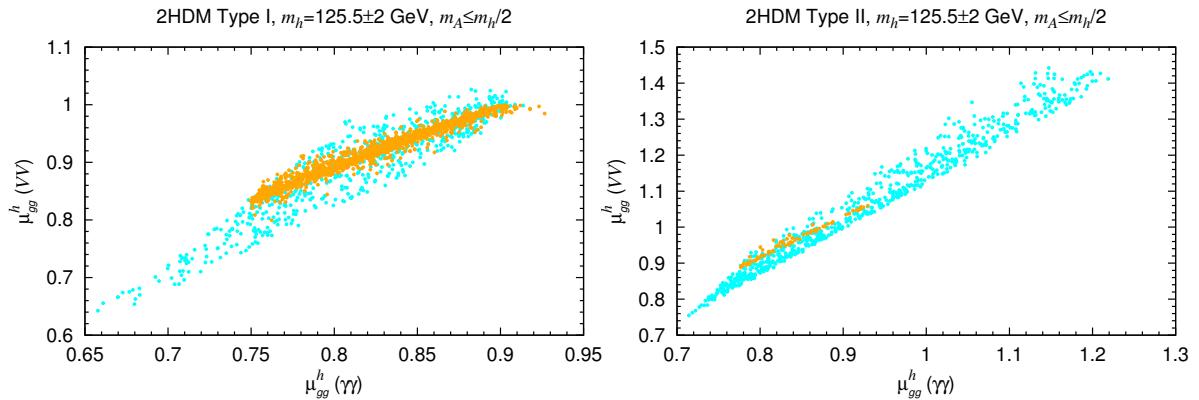
Figure 5.47: Signal strengths $\mu_{gg}^h(VV)$ vs. $\mu_{gg}^h(\gamma\gamma)$ for the Type I and Type II models. The orange points are, as for previous plots, the points with $\sin(\beta + \alpha) \sim 1$.

The first term, g_{hAA}, has to be small as discussed above and the second term is always negative because $m_{H^\pm}$ is necessarily larger than about 80 GeV due to direct LEP constraints.

To illustrate the impact on observables, we plot in Fig. 5.47 the signal strengths for $gg \to h \to VV$ versus $gg \to h \to \gamma\gamma$, i.e., $\mu_{gg}^h(VV)$ vs. $\mu_{gg}^h(\gamma\gamma)$. Our first observation is that $\mu_{gg}^h(\gamma\gamma)$ is suppressed for all points in Type I as well as for the orange points in Type II. The observed deviations from the SM predictions of unity are of course consistent with current data, since this was a requirement of the scan, but it is obvious that future higher precision measurements will strongly constrain these scenarios. Remarkably — and in contrast to the case when $m_A > m_h/2$ — it is impossible to simultaneously achieve $\mu_{gg}^h(\gamma\gamma) = 1$ and $\mu_{gg}^h(VV) = 1$ in either Type I or Type II when $m_A \leq m_h/2$ as contrary to the general 2HDM case (see Fig. 2 of [208] for comparison). Thus, this scenario will be excluded should the Higgs observations converge sufficiently close to the SM expectations.

Figure 5.48 shows $\mathrm{BR}(h \to AA)$ vs. the signal strength $\mu_{gg}^h(\gamma\gamma)$. From the left plot we can directly see that in Type I a precise measurement of this signal strength gives an upper bound on the allowed $h \to AA$ branching ratio. For instance, if $\mu_{gg}^h(\gamma\gamma)$ is measured to be within 10% of unity, this means $\mathrm{BR}(h \to AA) \lesssim 0.01$. Conversely, a measurement of $\mu_{gg}^h(\gamma\gamma) \simeq 1$ combined with detection of $h \to AA$ decays implies that the Type II model is strongly preferred and that the wrong-sign Yukawa solution (orange points) is excluded.
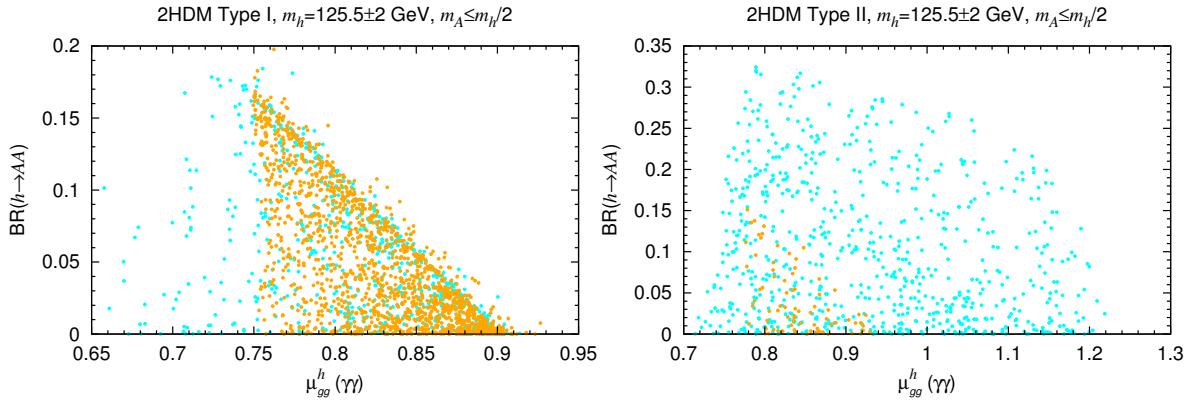
Figure 5.48: BR($h \to AA$) vs. $\mu^h_{gg}(\gamma\gamma)$ for the Type I and Type II models.

Let us now turn to the question of the size of the cross sections for A production with decays to the potentially observable $\tau\tau$ and $\mu\mu$ final states. Figure 5.49 shows the gluon fusion and $b\bar{b}$ associated production cross sections at $\sqrt{s} = 8$ TeV times BR($A \to \tau\tau$). As can be seen, the $A \to \tau\tau$ signal can have quite substantial cross sections over the whole mass range considered. The cross sections for the $A \to \mu\mu$ signal have exactly the same shape but are about a factor 280 lower. For reference, naive estimates suggest that, before cuts and efficiencies, for the existing 8 TeV data set with integrated luminosity of $L \simeq 20$ fb^{-1}, a cross section of order 10 pb (200,000 events) should be observable in the $\tau\tau$ final state while 0.1 pb (2000 events) should be observable in the $\mu\mu$ final state, especially in the case of $b\bar{b}$ associated production by using modest p_T b-tagging. From Fig. 5.49, we observe that these levels are reached in the case of Type II for essentially the entire $m_A \le m_h/2$ region in the case of gluon fusion and for the orange points in the case of $b\bar{b}$ associated production.[29] The cross sections for the orange points are very large and should produce readily observable peaks.

Based on this analysis, the CMS collaboration has initiated a dedicated search for $b\bar{b}A, A \to \tau\tau$ in the $m_A = 25\text{–}80$ GeV mass range [340], see Fig. (5.50). As expected, their sensitivity to the wrong-sign solution points is impressive and the majority of these points are actually excluded by the analysis. More than an order of magnitude in sensitivity should be gained in order to begin to probe they cyan points with low $\tan\beta$. In Type I many of the cyan points have a gluon fusion cross section at the probably observable 10 pb (0.1 pb) level in the $\tau\tau$ ($\mu\mu$) final states and the orange points have cross sections that are almost certainly too small for detection in the Run 1 data set. We also observe that the CMS search is not sensitive to the $b\bar{b}A$ channel in Type I, the predicted cross sections are at least an order of magnitude smaller than the current experimental exclusion.

Finally, we note that running at higher energies will not straightforwardly improve the sensitivity to the low m_A region, as the cross sections at 13–14 TeV are barely a factor 2 larger than those at 8 TeV. Therefore, one will need to accumulate more statistics via higher total integrated luminosity.

---

29 Recall from Fig. 5.44 that the orange points can have high $\tan\beta$ while the cyan points have quite modest $\tan\beta$ values. This implies that the $b\bar{b}$ coupling in the Type I (Type II) model is suppressed (enhanced). As a result, the orange points have the smallest (largest) cross sections in the case of Type I (Type II).
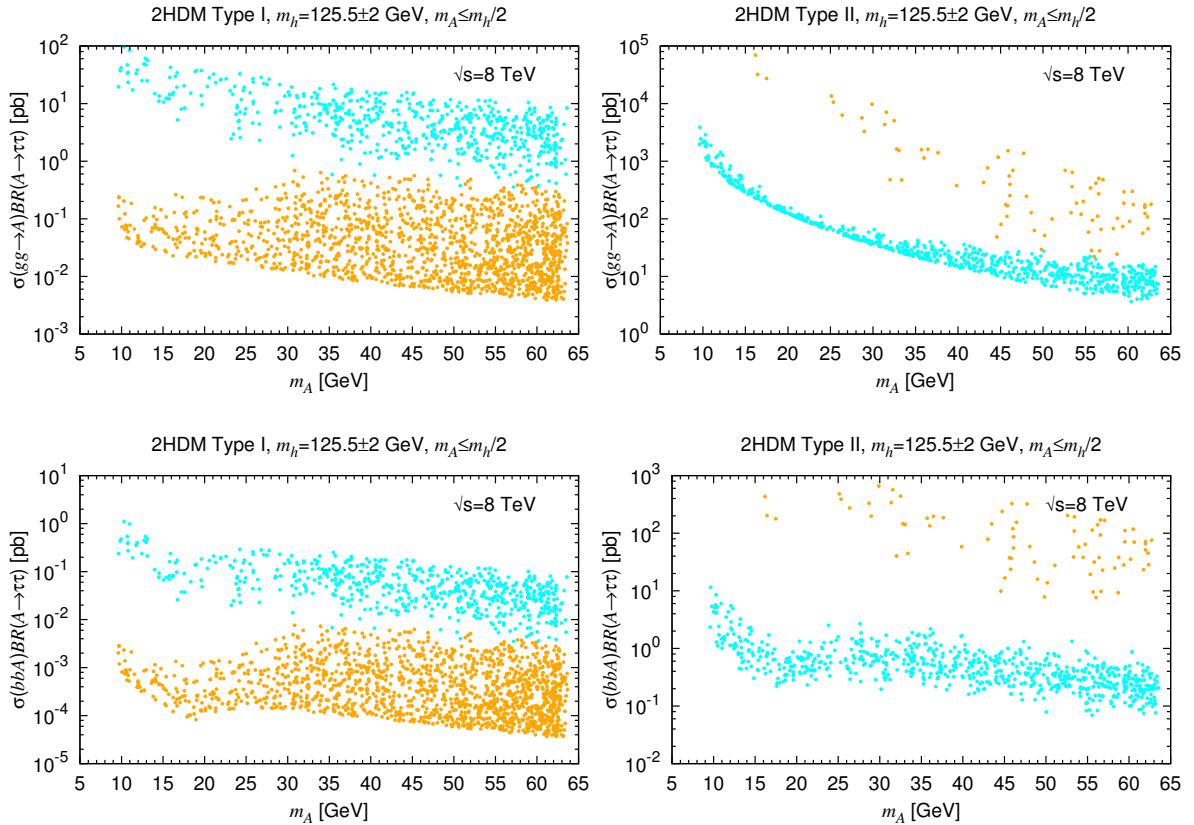
Figure 5.49: Cross sections at $\sqrt{s} = 8$ TeV for light A production from gluon fusion (top row) and $b\bar{b}$ associated production (bottom row) in the $\tau\tau$ final state. The cross sections for the $\mu\mu$ final state have exactly the same form but are a factor of $(m_\tau/m_\mu)^2 \approx 280$ smaller.
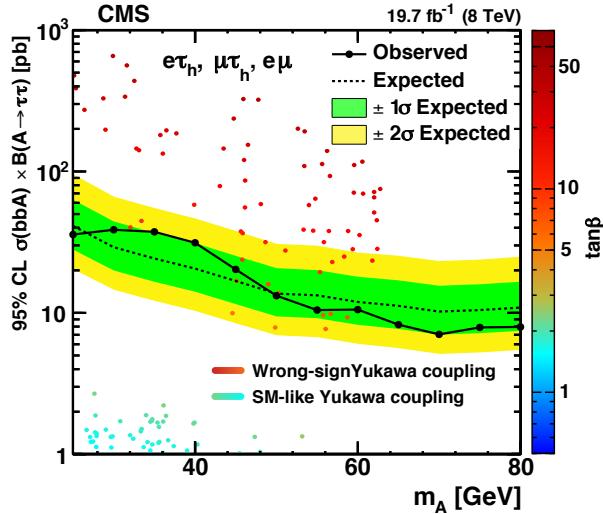
Figure 5.50: CMS exclusion for the $b\bar{b}A$, $A \to \tau\tau$ search in the $m_A = 25$–80 GeV mass range based on the Run 1 dataset [340]. The scattered points displayed are from the lower-right panel of Fig. 5.49, i.e. in the Type II model. Most of the points with a wrong-sign Yukawa coupling above $m_A = 25$ GeV are thus excluded.

5.4.2 *Light (pseudo-)scalars in the H–125 scenario*

We first note that in the H–125 scenario of Type II the combination of B-physics constraints and EW precision observables impose a strong lower bound on A, above ~ 400 GeV, as shown in Fig 5.23. Only h can thus have a mass below $m_H/2$ in Type II. In contrast, in the Type I model either m_A or m_h can be smaller than $m_H/2$, but LEP limits imply that they cannot be simultaneously light. This follows from the fact that the HVV coupling and the ZhA coupling are both proportional to $c_{\beta-\alpha}$. Thus, for a SM-like H, *i.e.*, $|c_{\beta-\alpha}| \approx 1$ as required by signal strengths measurements, the ZhA coupling is nearly maximal and the $Z^* \to hA$ cross section is too large, barring phase-space suppression, to be in agreement with the LEP measurements.

In practice we can therefore consider the $H \to AA$ and $H \to hh$ cases independently of one another. With this in mind, we turn to the conditions for achieving small trilinear couplings in order to evade too large $\mathrm{BR}(H \to AA)$ or $\mathrm{BR}(H \to hh)$. Analogous to Eq. (5.11) we find

$$g_{HAA} = \frac{1}{2v}\left[\left(2m_A^2 - m_H^2\right)\frac{s_{\alpha-3\beta}}{s_{2\beta}} + \left[8m_{12}^2 - s_{2\beta}\left(2m_A^2 + 3m_H^2\right)\right]\frac{s_{\beta+\alpha}}{s_{2\beta}^2} \right] \qquad (5.15)$$

and

$$g_{Hhh} = -\frac{1}{v}c_{\beta-\alpha}\left[\frac{2m_{12}^2}{s_{2\beta}} + \left(2m_h^2 + m_H^2 - \frac{6m_{12}^2}{s_{2\beta}}\right)\frac{s_{2\alpha}}{s_{2\beta}} \right]. \qquad (5.16)$$

One class of scenarios is easily understood by taking the strict limit of $c_{\beta-\alpha} = 1$, yielding

$$g_{HXX} = \frac{2\overline{m}^2 - 2m_X^2 - m_H^2}{v}, \qquad X = h, A. \qquad (5.17)$$

Analogous to the h–125 case, $\overline{m}^2$ should be small and positive to achieve small enough $|g_{HXX}|$. The interplay of the requirements of perturbativity and of small $|g_{HXX}|$ is illustrated in Fig. 5.51. We see that for $m_h \leq 60$ GeV, small $\tan\beta$ below about 2 is required. If A is below $m_H/2$ but not h however, there is a bit more freedom and $\tan\beta$ can go up to 10–15, tightly related, however, with m_{12} for any given value of m_A.

As in the h–125 scenario, sufficiently small $|g_{HXX}|$ can also be achieved by resorting to cancellations between the various terms in Eq. (5.15) and Eq. (5.16). Here, the $c_{\beta-\alpha} = 1$ term shown in Eq. (5.17) is positive for larger m_{12} values than those shown in Fig. 5.51 and can be canceled by the remaining term(s) for $\cos(\beta + \alpha) \approx 1$.

Putting everything together, including the experimental constraints, we end up with the situation shown in Fig. 5.52. The top row shows allowed points in the m_{12} vs. $\tan\beta$ plane (analogous to Fig. 5.51); the bottom row displays these same allowed points in the $\tan\beta$ vs. $\sin\alpha$ plane. As explained at the beginning of this section, in Type I either h or A can be light (but not both) while in Type II only h can be light. To distinguish these two cases, points with $m_A < m_H/2$ are shown in red and points with $m_h < m_H/2$ in blue. Considering first the top row of plots we see that, in agreement with Fig. 5.51, there is a small allowed region with $m_h < m_H/2$ at $m_{12} \simeq 60$–80 GeV and $\tan\beta \lesssim 2$. This region occurs for both Type I and Type II, although it is more constrained in Type I. In Type I there is moreover a diagonal strip of allowed points with $m_A < m_H/2$ at $\tan\beta \simeq 2 - 12$,
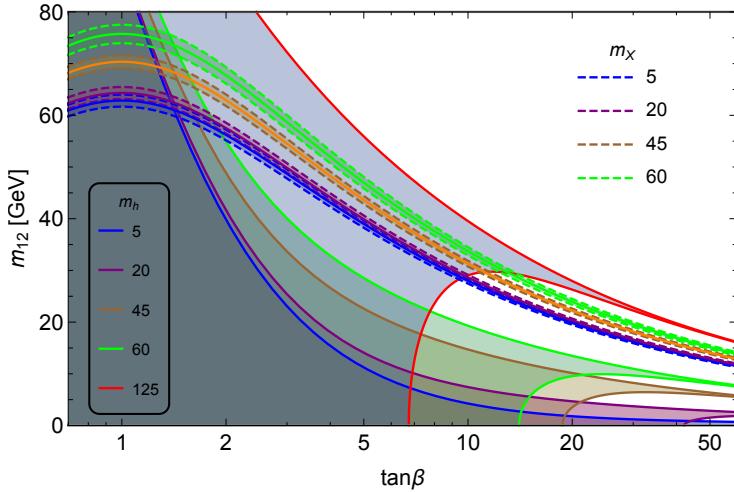
Figure 5.51: Constraints in the m_{12} vs. $\tan\beta$ plane for the H–125 case in the exact alignment limit. The shaded regions are those allowed by perturbativity for m_h values indicated in the lower-left corner of the plot. The narrow strips between the dashed lines have $\mathrm{BR}(H \to XX) < 0.3$ for $m_A < m_H/2$ or $m_h < m_H/2$ (the regions are the same for the two cases) with the color code for the $X = h$ or A masses given in the upper-right corner of the plot. The solid line in the middle of the dashed ones shows $\mathrm{BR}(H \to XX) = 0$ or equivalently here $g_{HXX} = 0$.

as expected from Fig. 5.51. The points below this strip are mostly $\cos(\beta + \alpha) \approx 1$ points for which cancellations occur and they can have both $m_A < m_H/2$ or $m_h < m_H/2$. Note that no such points survive in Type II.

In Fig. 5.53, we take a closer look at the allowed points in the m_h vs. m_A plane for Type I. We see that indeed no points survive in the region where both m_h and m_A are below $m_H/2$. As m_h increases, some low m_A points appear, but these correspond to either $m_A \lesssim 12$ GeV for which there are no published limits at large m_h on $e^+e^- \to Z^* \to hA$ or to $m_A \gtrsim 40 - 50$ GeV and $m_h \gtrsim 90$ GeV *i.e.*, sufficiently close to LEP threshold as to escape limits on the hA final state by virtue of suppressed cross section. Between 15 GeV and 40 GeV, LEP limits are strong enough to eliminate most of the points. It is also worth noting that the cyan points with $\sin\alpha > 0$ and the orange points with $\sin\alpha \approx -1$ occupy rather distinct parts of the m_h vs. m_A plane. In particular, if a light scalar with $m_h < 60$ GeV plus a pseudoscalar with $m_A < 400$ GeV were discovered, this would fix $\sin\alpha \approx -1$ in Type I.

Let us now explore the phenomenological consequences of the H–125 scenario for the LHC. To this end, we first show in Fig. 5.54 the relation between the signal strengths for the high-resolution channels $\mu_{gg}^H(VV)$ versus $\mu_{gg}^H(\gamma\gamma)$. As in the h–125 case, quite substantial deviations from the SM values of unity are possible. With the increased precision expected at Run 2, the Higgs measurements at the LHC should be sensitive to such deviations. Moreover, as in the h–125 scenario, the exact SM case $\mu_{gg}^H(\gamma\gamma) = \mu_{gg}^H(VV) = 1$ cannot be obtained in these scenarios with light h or A. Though not shown here, this tension with SM-like signal strengths is also apparent in the $\mu_{\mathrm{VBF}}^H(\gamma\gamma)$ vs. $\mu_{gg}^H(\gamma\gamma)$ plane. Should the signal strength measurements for either of these pairs converge to values that lie within
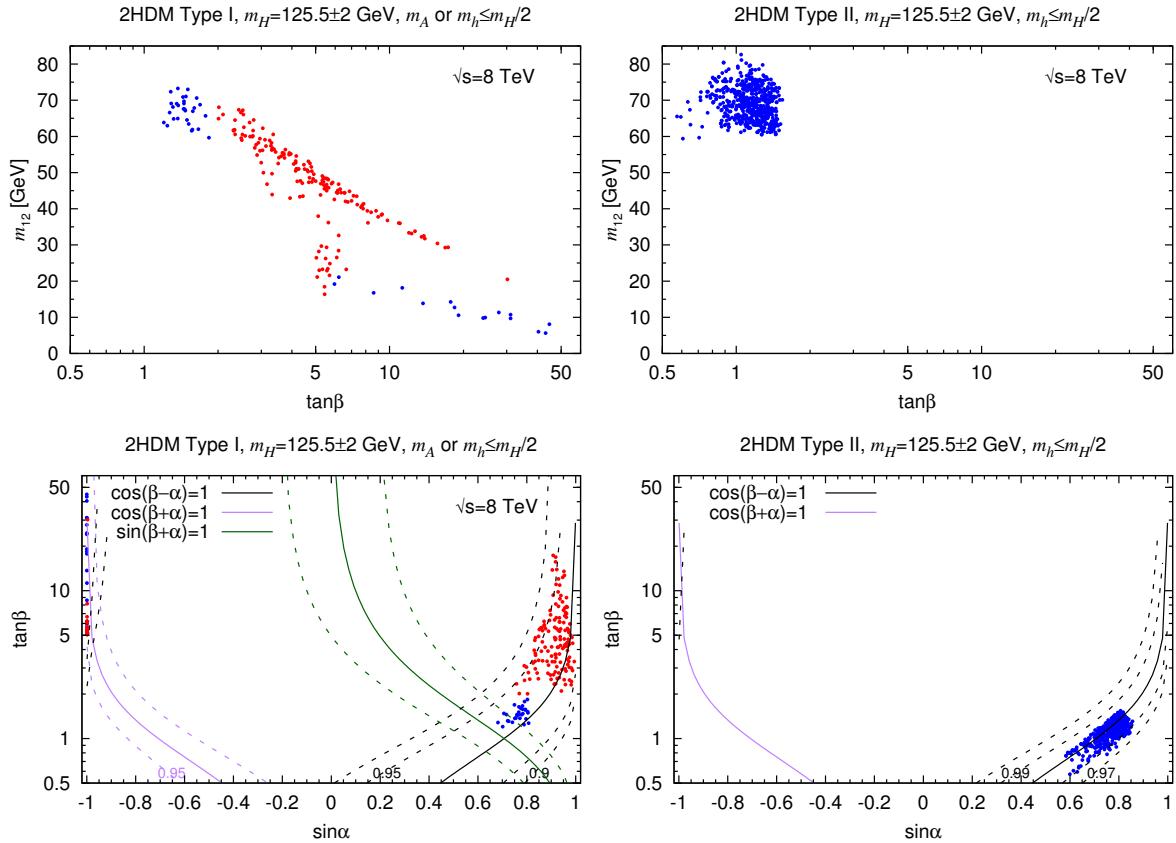
Figure 5.52: Phenomenologically viable points in the H–125 scenario with light (pseudo-)scalars in the Type I (left) and Type II (right) models. The upper row shows the projection onto the m_{12} vs. $\tan\beta$ plane for comparison with Fig. 5.51. The lower row shows the $\tan\beta$ vs. $\sin\alpha$ plane, including contours of constant $\cos(\beta\pm\alpha)$ and $\sin(\beta+\alpha)$. In all four plots, the red points have $m_A \leq m_H/2$ while the blue points have $m_h \leq m_H/2$.

10% of their SM values the H–125 scenarios with m_h or m_A below $m_H/2$ will be excluded.[30] For completeness we show in Fig. 5.55 the Higgs-to-Higgs-pair $\mathrm{BR}(H \to XX)$, $X = h$ or A, versus $\mu_{gg}^H(\gamma\gamma)$. Despite the existing Run 1 constraints, the branching ratios can be sizeable and it is thus interesting to look for these decays.

The most important issue is whether or not the existing 8 TeV, $L = 20$ fb^{-1} data set could be sensitive to this scenario by looking for the light h or A in the $\tau\tau$ or $\mu\mu$ final states. The relevant plots are given in Fig. 5.56. Since $\tan\beta$ cannot be large in the Type II model (see Fig. 5.52) and there is no $\tan\beta$ enhancement of the $b\bar{b}$ coupling in the Type I model, it is mostly gluon fusion that is relevant. $\sigma(gg \to X) \times \mathrm{BR}(X \to \tau\tau)$ exceeds the required 10 pb (or 0.1 pb for decays into $\mu\mu$) in particular for the light h case, $X = h$. Light pseudoscalars (possible only in Type I) have smaller cross sections and will be harder to detect. Concretely, only for gluon fusion with $A \to \tau\tau$ and $m_A \lesssim 12$ GeV does one obtain a cross section as large as 10 pb in the $\tau\tau$ channel, though for $m_A > 40$ GeV cross sections are still between 1 pb and 10 pb.

---

30 Comparing with Fig. 7 of [208] we see that this tension with SM-like signal strengths is much less in the general H–125 case with heavier h, A.
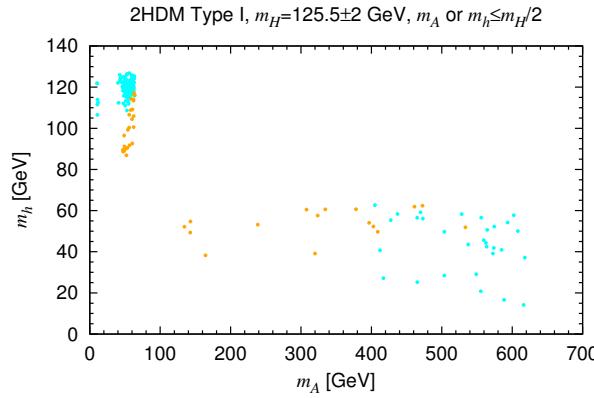
Figure 5.53: Allowed points for the Type I model in the m_h vs. m_A plane. The cyan points have $\sin\alpha > 0$, while the orange points have $\sin\alpha \approx -1$, cf. the bottom-left plot in Fig. 5.52.
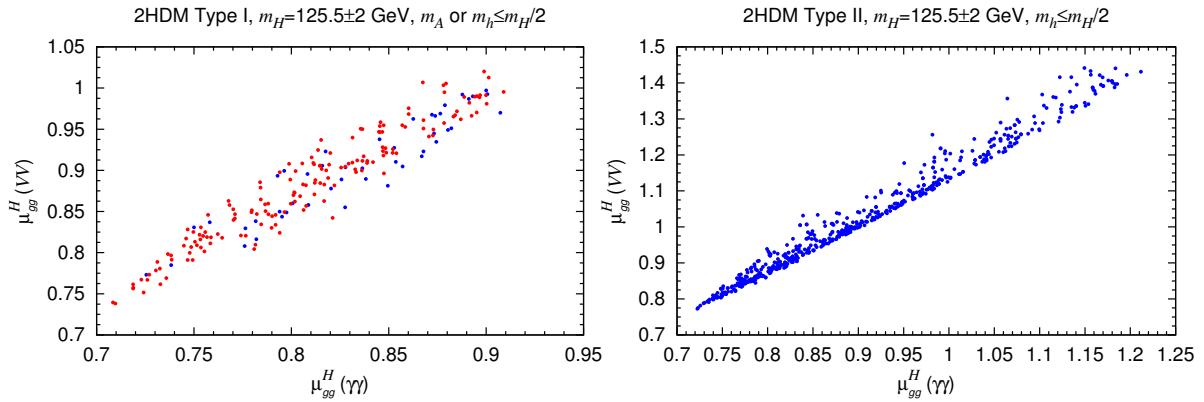
Figure 5.54: Signal strengths $\mu_{gg}^H(VV)$ vs. $\mu_{gg}^H(\gamma\gamma)$ for the Type I and Type II models. Points with $m_A \leq m_H/2$ are shown in red and points with $m_h \leq m_H/2$ in blue.
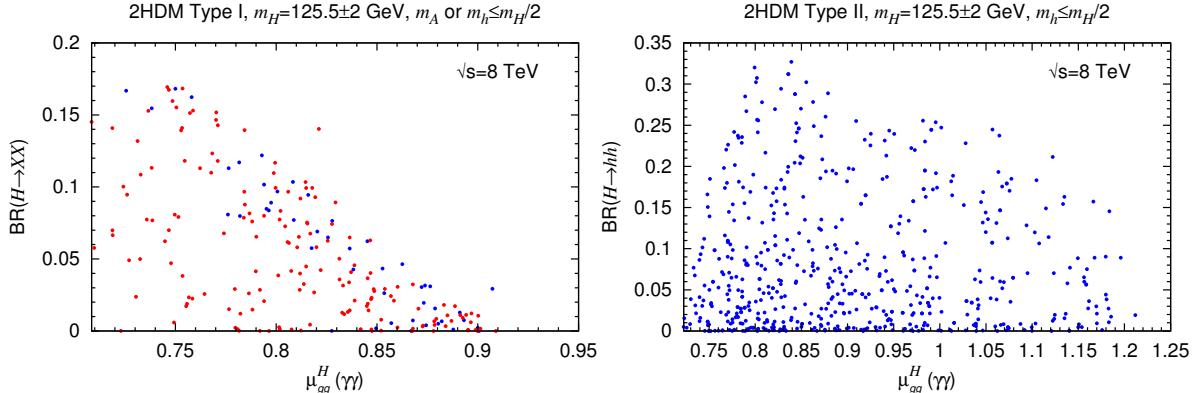
Figure 5.55: Branching ratios of $H \to XX$ ($X = h, A$) decays vs. $\mu_{gg}^H(\gamma\gamma)$ for the Type I and Type II models. Points with $m_A \leq m_H/2$ are shown in red and points with $m_h \leq m_H/2$ in blue.

A final comment concerns the issue of vacuum stability in these scenarios. As shown in [293] and already mentioned in Section 4.1.5, the 2HDM minimum is the global minimum only if $D \equiv m_{12}^2(m_{11}^2 - k^2 m_{22}^2)(\tan\beta - k) > 0$, where $k = (\lambda_1/\lambda_2)^{1/4}$. However, given that $D < 0$ may still correspond to a metastable vacuum, we have chosen not to require
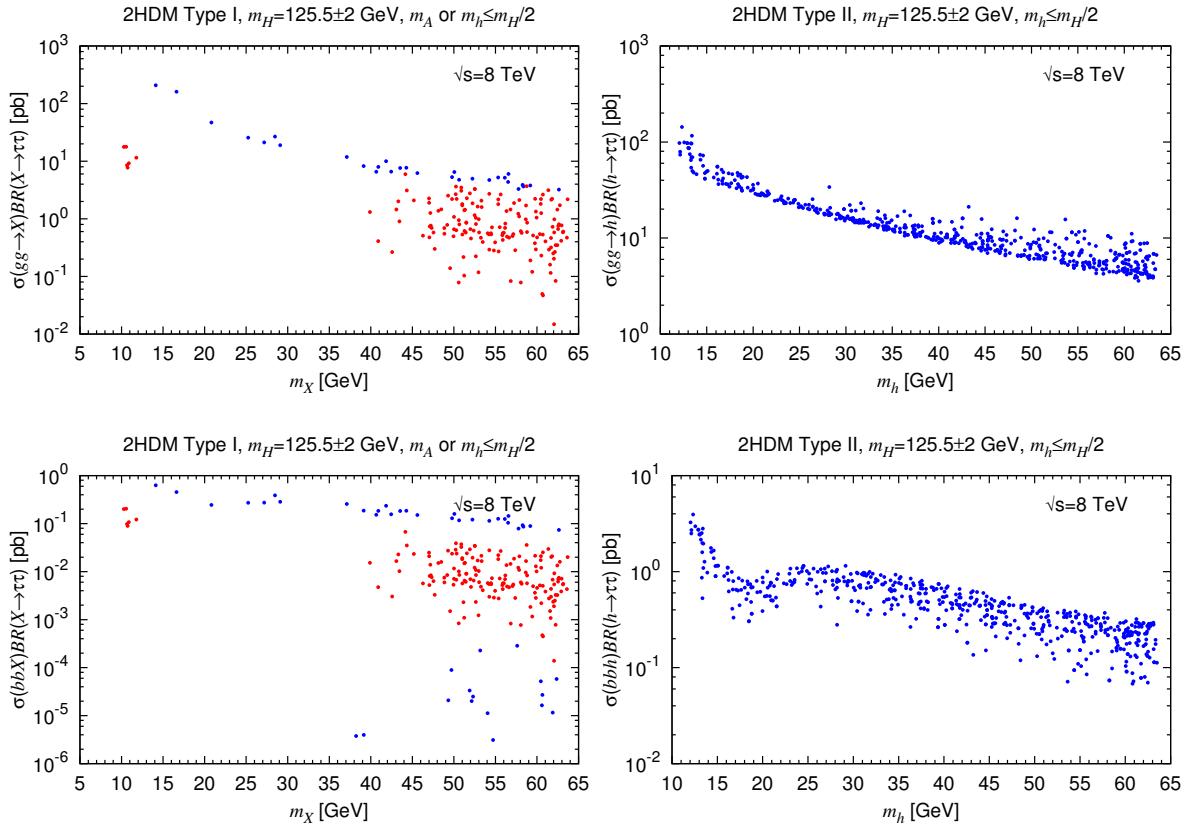
Figure 5.56: Cross sections at the 8 TeV LHC for light $X = h, A$ production from gluon fusion (upper row) and $b\bar{b}$ associated production (lower row) in the $\tau\tau$ final state. The blue points are for $X = h$, the red points for $X = A$.

$D > 0$; one would need to compute the corresponding vacuum lifetime, which was beyond the scope of this study. We note that were we to require $D > 0$ this would eliminate only a small percentage of the h–125 scenario points, but would exclude about 20% of the points in the H–125 scenario.

5.4.3 Conclusions: light states and the alignment limit

We have considered 2HDM scenarios of Type I and Type II in which the A or h has mass below one-half that of the observed 125 GeV SM-like Higgs state, when the latter is identified with either the lighter CP-even h or heavier CP-even H. Though signal strength measurements of the 125 GeV state lead to non-negligible tuning between the 2HDM parameters, this region is perfectly sound phenomenologically and we investigated its signatures at the LHC. In the scenarios under consideration, the signal strengths of the ~ 125 GeV Higgs boson can actually not all be SM-like. Should the signal strength measurements in the high-resolution $\gamma\gamma$ and VV channels converge to their SM values to within 10% or better, then these scenarios could be excluded. Moreover, in the h–125 case, surprisingly large gluon fusion and $b\bar{b}$ associated production cross sections are possible for a light pseudoscalar in the 10–60 GeV mass range. A recent CMS analysis investigated the $b\bar{b}A$, $A \to \tau\tau$ channel in the low-mass region and lead to the exclusion of a large portion of

the previously allowed parameter space. We eagerly await for new results from the second run of the LHC.

Overall, one finds ample motivation from these 2HDM scenarios for the experimental exploration of channels with Higgs particles with masses below about 60 GeV in the $\tau\tau$ and $\mu\mu$ final states. If sufficient sensitivity is reached and nothing is observed, then many of the 2HDM scenarios explored in this analysis will be eliminated. On the other hand, if such a light Higgs is detected then models such as the MSSM will be eliminated and a strong preference in favor of, *e.g.*, a general 2HDM or the NMSSM will arise.

More generally, it is possible that the observed 125 GeV Higgs boson appears SM-like due to the alignment limit of a multi-doublet Higgs sector. This does not necessarily imply that the additional Higgs states of the model are heavy, and they could in fact be lighter than 60 GeV. Such realization of the alignment limit, if realized in nature, would lead to exciting new effects to be probed at Run 2 of the LHC. The precision measurements of the 125 GeV state properties can be used to discriminate between the Yukawa structure of the 2HDM and more importantly, can act as indirect probes of the extra scalar states. We also identified several channels of interest for the near-future that could provide severe constraints on the 2HDM parameter space. For instance, in the H–125 scenario, the $A \rightarrow Zh$ channel has a lower bound on the cross section that is very favorable for a total exclusion, or possible discovery, during the next few years.

Part III

MINIMAL FLAVOR VIOLATION IN THE MINIMAL SUPERSYMMETRIC STANDARD MODEL

In this part, the idea of flavor alignment as a solution to the flavor puzzles present beyond the Standard Model is discussed. Going further, the Minimal Flavor Violation hypothesis is defined as a minimal and natural breaking of the flavor symmetry. We enforce it in the R-parity violating Minimal Supersymmetric Standard Model, which remarkably allows the model to pass all flavor bounds, including the tight constraints on the proton lifetime. Our focus here will be to analyze the evolution of the baryonic R-parity violating couplings under the renormalization group. If present, the flavor alignment might originate from a very high scale, where a fundamental flavor mechanism takes place. It is then crucial to understand whether such an alignment could hold down to the low-scales.

Dans cette partie, l'idée d'alignement de la saveur est discutée comme une solution aux problèmes de saveur au-delà du Modèle Standard. L'hypothèse de Violation Minimale de la Saveur est ensuite définie comme une brisure minimale et naturelle de la symétrie de saveur, et est implémentée dans le Modèle Standard Sypersymétrique Minimal avec violation de la parité R. Remarquablement, cela permet au modèle d'être en accord avec toutes les contraintes de saveur, en particulier celles particulièrement fortes sur la durée de vie du proton. Notre but principal ici est d'analyser l'évolution des couplages violant la parité R et le nombre baryonique sous le groupe de renormalisation. Une telle étude est en effet primordiale étant donné que l'alignement de saveur, si présent dans la nature, devrait émerger d'un mécanisme dynamique fondamental de la saveur à très haute énergie. Il est ainsi déterminant de savoir si un tel alignement de la saveur est conservé à basse énergie.

6

MINIMAL FLAVOR VIOLATION AND SUPERSYMMETRY

As discussed in Section 2.4, the SM Yukawa sector is highly non-generic and presents large hierarchies among its parameters. Moreover, there are wide classes of flavor violating processes that are highly suppressed for several accidental reasons. So far however, in the flavor sector, no persisting large deviation from the SM predictions has been observed. New sources of flavor violation should therefore either originate from new high scale phenomena, which would then require an immense fine tuning to live with the quantum instability of the electroweak scale and would raise the hierarchy problem, or it should be highly non-generic if the NP scale is relatively light. Decoupling of NP is certainly possible but not very satisfying theoretically or even for less pragmatic reasons; we sure would like to directly observe new phenomena at energy scales that we can currently probe. The latter possibility, on the contrary, is something that might be more acceptable. After all, the SM flavor sector is itself very tuned and we should accept the possibility that a similar amount of tuning is also present in the NP flavor structures. It is not difficult to realize that a kind of alignment of the NP structures with the SM Yukawa sector would automatically soften the flavor problem.

In this chapter we make use of the SM flavor symmetry in order to define a framework in which such alignment, or possibly misalignment, of the new sources of flavor violation with the SM flavor sector can easily be identified. Going further, this can be used to define a naturalness criterion for flavor structures and it even gives a well-defined way to enforce flavor naturalness in a given NP scenario: this is the Minimal Flavor Violation (MFV) hypothesis [385, 386]. We then describe how MFV is implemented in a specific model that suffers largely from flavor issues otherwise: the Minimal Supersymmetric Standard Model (MSSM). Our focus will be on the renormalization group properties of the minimally flavor violating MSSM. Clearly, if such a flavor alignment takes place it should be generated at a high scale, presumably at the scale where yet-unknown fundamental dynamics should generate all flavor structures. It is then important to check whether this alignment holds at low scales and thus, whether we could expect MFV to have any direct observable consequences. Specifically, we will present a study of the baryon number violating dimension-4 operator in the MSSM based on "*Baryonic R-Parity Violation and its Running*" [387], in collaboration with Christopher Smith and published in JHEP.

6.1 A FLAVOR ALIGNMENT

6.1.1 *Restoring the flavor symmetry*

Let us recall that the SM fermion kinetic terms have a large global symmetry under which, for a given quark representation, the different quark flavors can be mixed into one another. Specifically, the flavor symmetry group G_F consists of a $U(N_f = 3)$ factor for each fermion representation,

$$G_F = \left[U(3)_Q \times U(3)_U \times U(3)_D \right] \times \left[U(3)_L \times U(3)_E \right] \equiv G_F^q \times G_F^l \,, \qquad (6.1)$$

where G_F^q and G_F^l are defined as the subgroups acting on quarks and leptons respectively. In the SM the flavor symmetry is only broken, explicitly, in the Yukawa sector and this leads to the physical distinction between fermion flavors. The flavor group can also be schematically factorized as $G_F = SU(3)^5 \times U(1)^5$. The five independent $U(1)_{Q,U,D,L,E}$ factors can be linearly transformed into the equivalent set $U(1)_{\mathcal{B},\mathcal{L},Y,PQ,E}$, where PQ is the Peccei-Quinn charge while Y is the hypercharge (under which the Higgs doublet is not charged in contrast to the gauge hypercharge). The charges of the different fermion representations under these abelian groups are given in Table 13. Out of these five $U(1)$'s, only two are non-anomalous: Y and $\mathcal{B} - \mathcal{L}$. This will however have no consequence for our following considerations, a particularly clear discussion of these matters can be found in Ref. [106].

	$U(1)_{\mathcal{B}}$	$U(1)_{\mathcal{L}}$	$U(1)_{PQ}$	$U(1)_Y$	$U(1)_E$
Q	1/3	0	0	1/3	0
U	-1/3	0	1	-4/3	0
D	-1/3	0	1	2/3	0
L	0	1	0	1	0
E	0	-1	-1	2	1

Table 13: Charges of the different fermion representations under a specific linear combination of the five $U(1)$ flavor factors. Under the original $U(1)^5$, the charges are simply diagonal. The linear transformation between the two bases is then $\mathcal{B} = (Q - U - D)/3$, $\mathcal{L} = L - E$, $PQ = U + D + E$ and $Y = (Q - 4U + 2D)/3 - (L - 2E)$.

Under a G_F transformation, the Yukawa Lagrangian takes the following form [recall Eqs.(2.59) and (2.58)],

$$- \mathscr{L}_{\text{Yukawa}} \xrightarrow{G_F} U g_U^\dagger \mathbf{Y}_u g_Q Q H + D g_D^\dagger \mathbf{Y}_d g_Q Q \widetilde{H} + E g_E^\dagger \mathbf{Y}_e g_L L \widetilde{H} + \text{h.c.} \,, \qquad (6.2)$$

and is clearly not invariant. The flavor symmetry can however be formally recovered if the Yukawa couplings are given non-trivial transformations under G_F, *i.e.*, they are promoted to spurions; non dynamical fields that have a specific transformation under G_F. Even though it is an artificial construction, a better understanding of the effects of the G_F

breaking will be gained using this formalism.[31] Generally, promoting order parameters to spurions allows to write new operators in terms of the spurions while formally realizing the original symmetry. Freezing them to their physical values (*background values*) afterwards, captures the effects of the explicit symmetry breaking. Here, the Yukawa couplings should transform as

$$\mathbf{Y}_u \to g_U \mathbf{Y}_u g_Q^\dagger, \qquad \mathbf{Y}_d \to g_D \mathbf{Y}_d g_Q^\dagger, \qquad \mathbf{Y}_e \to g_E \mathbf{Y}_e g_L^\dagger, \qquad (6.3)$$

in order to recover flavor invariance of the SM. Defining $\mathbf{X}_{u,d} \equiv \mathbf{Y}_{u,d}^\dagger \mathbf{Y}_{u,d}$ for future convenience, we note that,

$$\mathbf{X}_{u,d} \to g_Q \mathbf{X}_{u,d} g_Q^\dagger, \quad \mathbf{Y}_{u,d} \mathbf{Y}_{u,d}^\dagger \to g_{U,D} (\mathbf{Y}_{u,d} \mathbf{Y}_{u,d}^\dagger) g_{U,D}^\dagger. \qquad (6.4)$$

Alternatively we can write,

$$\mathbf{Y}_u \sim (\bar{\mathbf{3}}, \mathbf{3}, \mathbf{1})_{G_F^q}, \qquad \mathbf{Y}_d \sim (\bar{\mathbf{3}}, \mathbf{1}, \mathbf{3})_{G_F^q}, \qquad \mathbf{Y}_e \sim (\bar{\mathbf{3}}, \mathbf{3})_{G_F^l}, \qquad (6.5)$$

where $\mathbf{3}$ and $\bar{\mathbf{3}}$ are the fundamental representation of the flavor SU(3)'s and its conjugate, respectively. This represents the directions of the G_F breaking by the Yukawa couplings. In this notation, we only keep track of the spurion behavior under the non-abelian group part. According to Eq. (6.4), $\mathbf{X}_u \sim \mathbf{X}_d$, *i.e.*, they have the same transformation under G_F. Once all terms formally invariant under G_F are written, spurions should be frozen to their physical values for numerical evaluation. Here we have two choices (see *e.g.* Eq. (2.64) and text around): either going to the basis in which the up-type quark mass eigenstates are aligned with the gauge eigenstates, the *up-basis*, or going to the basis in which the down-quark mass and gauge eigenstates are aligned, the *down-basis*:

$$\text{up-basis:} \quad \frac{v}{\sqrt{2}} \mathbf{Y}_u = \mathbf{m}_u, \quad \frac{v}{\sqrt{2}} \mathbf{Y}_d = \mathbf{m}_d . V_{CKM}^\dagger, \quad \frac{v}{\sqrt{2}} \mathbf{Y}_e = \mathbf{m}_e, \qquad (6.6)$$

$$\text{down-basis:} \quad \frac{v}{\sqrt{2}} \mathbf{Y}_u = \mathbf{m}_u . V_{CKM}, \quad \frac{v}{\sqrt{2}} \mathbf{Y}_d = \mathbf{m}_d, \quad \frac{v}{\sqrt{2}} \mathbf{Y}_e = \mathbf{m}_e. \qquad (6.7)$$

In both bases, the lepton Yukawa matrix is diagonal, $\mathbf{Y}_e = \text{Diag}(y_e, y_\mu, y_\tau)$, as we have not included flavor mixing in the lepton sector (absence of right-handed neutrinos).

6.1.2 *Using the flavor symmetry in the Standard Model*

Under the spurious transformation of the Yukawa couplings, the SM is formally invariant under G_F but what can we gain from that ? At the dimension-4 level, all operators inducing flavor violation are naturally all already present in the SM, these are the terms present in $\mathscr{L}_{\text{Yukawa}}$. Having recovered the flavor symmetry hence does not provide any more information about the structure of flavor violation at this level. It is however very useful to gain insights about higher-order operators.

---

31 This approach is widely used in the study of effective QCD models after the chiral symmetry SU(3)$_L \times$ SU(3)$_R$ is explicitly broken due to quark mass terms. The quark mass matrix is promoted to a spurion by allowing it to transform under the chiral group. Lagrangian terms formally invariant under the chiral symmetry are written in terms of the spurion and the explicit effects of chiral symmetry breaking are obtained by setting the mass matrix to its background value $\text{Diag}(m_u, m_d, m_s)$.

For instance, let us go back to the $b \to s\gamma$ transition. At dimension-6, the operator with the right structure is the following,

$$\mathcal{O}_7 = e \frac{c^{IJ}}{\Lambda^2} D^I \sigma_{\mu\nu} Q^J \widetilde{H} F^{\mu\nu} \tag{6.8}$$

where $\sigma_{\mu\nu} = \frac{1}{2} i [\sigma_\mu, \sigma_\nu]$, I, J are flavor indices, c is a Wilson coefficient and Λ the scale at which this effective operator is generated. Clearly, this operator is not G_F invariant since $DQ \to Dg_D^\dagger g_Q Q \neq DQ$. Let us use the spurion formalism introduced in the previous paragraph in order to formally recover G_F invariance. This can be achieved if the Wilson coefficient carries a non-trivial flavor structure, $c^{IJ} \not\propto \delta^{IJ}$, specifically it should transform as,

$$c \to g_D c g_Q^\dagger, \tag{6.9}$$

i.e., $c \sim \mathbf{Y}_D$ according to Eq. (6.3). There is actually an infinite number of terms that have the right transformation property,

$$c = \mathbf{Y}_d \mathbf{Q}_8, \tag{6.10}$$

where $\mathbf{Q}_8$ transforms as $\mathbf{Q}_8 \to g_Q \mathbf{Q}_8 g_Q^\dagger \sim (\mathbf{8}, \mathbf{1}, \mathbf{1})_{G_F^q}$, i.e., it is an octet under $\mathrm{SU}(3)_Q$. Following Eq. (6.4), $\mathbf{Q}_8$ has the general form,

$$\mathbf{Q}_8 = \sum_{n=0}^{+\infty} \sum_{i=1}^{2^n} x_{n,i} \, \mathbf{P}_n^{(i)}(\mathbf{X}_u, \mathbf{X}_d), \tag{6.11}$$

where $\mathbf{P}_n^{(i)}(\mathbf{X}_u, \mathbf{X}_d)$ is the i-th polynomial term with degree n and $x_{n,i}$ is a complex number. The polynomial degree is defined as the total number of $\mathbf{X}_u$ and $\mathbf{X}_d$ powers, there are indeed 2^n such terms for a given order n. For instance, $\mathbf{P}_0^{(i)} = \{\mathbb{1}\}$, $\mathbf{P}_1^{(i)} = \{\mathbf{X}_u, \mathbf{X}_d\}$, $\mathbf{P}_2^{(i)} = \{\mathbf{X}_u^2, \mathbf{X}_u \mathbf{X}_d, \mathbf{X}_d \mathbf{X}_u, \mathbf{X}_d^2\}$ and $\mathbf{P}_3^{(i)} = \{\mathbf{X}_u^3, \mathbf{X}_u^2 \mathbf{X}_d, \mathbf{X}_u \mathbf{X}_d \mathbf{X}_u, \mathbf{X}_d \mathbf{X}_u^2\} + \{\mathbf{X}_u \leftrightarrow \mathbf{X}_d\}$. All these terms transform as $\mathrm{SU}(3)_Q$ octets as desired. Of course terms with high powers of the fundamental octets $\mathbf{X}_u$ and $\mathbf{X}_d$ are numerically suppressed by the generally small Yukawa couplings and $\mathbf{X}_u$ can be considered dominant over $\mathbf{X}_d$ (if their respective coefficients are of the same order). Going back to $\mathcal{O}_7$, the dominant terms in the expansion of the Wilson coefficient can therefore be written as

$$c = \mathbf{Y}_d \left(c_1 \mathbb{1} + c_2 \mathbf{Y}_u^\dagger \mathbf{Y}_u + \ldots \right). \tag{6.12}$$

Such series are dubbed *flavor expansions*. Studying down-type quark transitions, it is more convenient to go in the down-basis, in which case c takes the form,

$$\frac{v}{\sqrt{2}} c = \mathbf{m}_d \left(c_1 \mathbb{1} + c_2 V_{CKM}^\dagger \frac{2\mathbf{m}_u^2}{v^2} V_{CKM} + \ldots \right). \tag{6.13}$$

After EWSB and picking the terms contributing to $b \to s\gamma$ yield (the first term is flavor-diagonal and thus does not contribute),

$$
\begin{aligned}
\mathcal{O}_7 \supset & \; e \frac{c_2}{\Lambda^2} \sum_{i=u,c,t} \left[\frac{2m_i^2}{v^2} \left(m_b V_{ib}^* V_{is} \right) \right] \times \bar{b}_R \sigma_{\mu\nu} s_L F^{\mu\nu} \\
\simeq & \; e \frac{c_2}{\Lambda^2} \left[\frac{2m_t^2}{v^2} \left(m_b V_{tb}^* V_{ts} \right) \right] \times \bar{b}_R \sigma_{\mu\nu} s_L F^{\mu\nu}.
\end{aligned} \tag{6.14}
$$

The m_b factor is the expected chirality-flip factor. The CKM structure that is found, $V_{tb}^* V_{ts}$, is exactly the one that would have been obtained by computing the amplitude of the corresponding Feynman diagram. This approach therefore predicts accurately the SM scaling of flavor violating processes. This should be no surprise. Since the Yukawa couplings are the only source of flavor breaking in the SM, this approach is actually exact in the SM. This example illustrates how the MFV hypothesis can generically reconcile flavor observables with TeV scale new physics. Due to the CKM scaling, the scale Λ is now allowed to take small values, whereas it should have been several orders of magnitude above the TeV scale were the Wilson coefficient c of order 1 [104, 106].

6.1.3 *Minimal Flavor Violation*

Beyond the SM, new sources of flavor breaking may be present. The program that we have previously performed in the SM can be extended to larger flavor sectors. First, the new flavor structures and their G_F breaking directions need to be identified, the appropriate spurious transformations of these new structures can then easily be determined. In this theory, expressing the non-renormalizable operators in terms of the new spurions and the Yukawa couplings accurately predicts the flavor scaling of the operators. Of course, in order to make definite predictions, the physical background values of the BSM flavor structures should be known, which is generally not the case. The MFV hypothesis will allow us to write these unknown flavor structures in terms of the Yukawa couplings.

An important guidance to keep in mind is the possible high scale dynamics behind the breaking of G_F. Above a certain scale M_{Flavor}, the flavor symmetry may be exact but is spontaneously broken by the dynamics of a finite set of fundamental flavor fields. Acquiring vevs, the low-energy flavor structures might arise in this way. A simple realization of this idea is the Froggatt-Nielsen mechanism [388] that can reproduce the large mass hierarchies of the Yukawa couplings. However in the presence of flavor structures beyond the Yukawa sector, a more complicated setup could be present. If such a mechanism is at work in nature, we could expect a possible redundancy in the low-energy flavor structures, as they all originate from the same fundamental flavor sector [106]. Let us consider for instance a fundamental flavor structure $\mathbf{F}$ that gives rise to two low-energy structures $\mathbf{L}_1$ and $\mathbf{L}_2$ that break G_F in the same directions, *i.e.*, $\mathbf{L}_1 \sim \mathbf{L}_2$. We can thus write,

$$\mathbf{L}_1 = a_1 \mathbb{1} + a_2 \mathbf{F} + a_3 \mathbf{F}^2 + a_3 \mathbf{F}^3 + \dots \ , \quad \mathbf{L}_2 = b_1 \mathbb{1} + b_2 \mathbf{F} + b_3 \mathbf{F}^2 + b_3 \mathbf{F}^3 + \dots \quad (6.15)$$

In that case, $\mathbf{L}_2$ can be expressed in terms of $\mathbf{L}_1$ (or the other way around),

$$\mathbf{L}_2 = c_1 \mathbb{1} + c_2 \mathbf{L}_1 + c_3 \mathbf{L}_1^2 + \dots \quad (6.16)$$

Due to the common flavor structure at high-scale, the low-energy structures can be expressed in terms of each other. Assuming that $\mathbf{L}_1$ is known experimentally but not $\mathbf{L}_2$, this can be used to predict the structure of the unknown flavor structures. In particular, the perturbative convergence of the expression above may be such that only the first terms are enough to fully capture the structure of $\mathbf{L}_2$, this would require $\text{Tr}(\mathbf{F}) \lesssim 1$ (when properly normalized). Of course the coefficients a_i and b_i are actually unknown (but could be presumably calculable in the high-energy theory). A naturality criterion can now be

defined. These expressions are deemed natural if the a_i and b_i coefficients are of order 1, which means that the low-energy hierarchies are directly determined by the fundamental structure of $\mathbf{F}$. In that case, the c_i coefficients will also be of order 1.

We can now use this to state the MFV hypothesis [385, 386]: the G_F symmetry is only broken by the Yukawa couplings, in a natural way. Technically, the flavor symmetry should be formally restored by promoting all flavor structures to spurions, the new BSM flavor couplings are then expressed as natural expansions of the Yukawa spurions. This means that if there exists a new structure $\mathbf{X}$ with a given spurious transformation, then,

$$\mathbf{X} = \sum_i x_i \mathcal{O}_i \,, \tag{6.17}$$

where the $\mathcal{O}_i$ are polynomials constructed out of the Yukawa couplings only (*minimality condition*) transforming as $\mathbf{X}$ ($\mathcal{O}_i \sim \mathbf{X} \, \forall i$) and all coefficients x_i are of order 1 (*naturalness condition*). The minimality condition can be motivated by the possible low-energy flavor redundancy between all flavor structure; it would then be possible to express the unknown BSM structures in terms of the known ones. Clearly, it is a minimal breaking of G_F in the sense that only the known and necessary flavor structures describing the observed fermions masses and mixings are used to break G_F. For instance, if $\mathbf{X} \to g_U \mathbf{X} g_U^\dagger$, then $\mathbf{X} = \mathbf{Y}_u \mathbf{Q}_8 \mathbf{Y}_u^\dagger$ where the octet coefficients should be of order 1. This does not mean that the Yukawa couplings are more important or more fundamental than the unknown flavor structures, but this solely reflects the possible redundancy. The MFV hypothesis leads to a direct transmission of the SM flavor hierarchies to the BSM sector, hence automatically suppress the contributions to flavor violating processes and soften the flavor puzzles [389–391].

Following Eq. (6.11), the octet term has actually an infinite number of terms. It has however been shown that this series can be partially resummed into 17 independent terms [392]. The Cayley-Hamilton theorem is used to prove this result: a generic $n \times n$ matrix $\mathbf{M}$ cancels its characteristic polynomial. In particular, for a 3×3 matrix,

$$\mathbf{M}^3 - \mathrm{Tr}(\mathbf{M})\mathbf{M}^2 + \frac{1}{2}\left[\mathrm{Tr}(\mathbf{M})^2 - \mathrm{Tr}(\mathbf{M}^2)\right]\mathbf{M} - \det(\mathbf{M})\mathbb{1} = 0 \,. \tag{6.18}$$

The third power of the matrix can therefore be expressed in terms of lower powers, with the expansion coefficients being related to the traces of powers of $\mathbf{M}$ which are all of order 1 if the trace of $\mathbf{M}$ also is [the determinant can be expressed as traces of powers of $\mathbf{M}$ by taking the trace of Eq. (6.18)]. Therefore, the reduction of flavor expansions using the Cayley-Hamilton theorem is compatible with MFV since no large coefficients can be generated in this process. The 17 terms are clearly too much to describe a generic octet $\mathbf{Q}_8$, only 9 complex terms are needed to build a generic basis of the 3×3 complex matrices. The octet can be redefined by taking the 9 leading terms, *i.e.* there terms that involve the least powers of Yukawa couplings,

$$\mathbf{Q}_8 = q_1 \mathbb{1} + q_2 \mathbf{X}_u + q_3 \mathbf{X}_d + q_4 \mathbf{X}_u^2 + q_5 \mathbf{X}_d^2 + q_6\{\mathbf{X}_u, \mathbf{X}_d\} + iq_7[\mathbf{X}_u, \mathbf{X}_d] + iq_8[\mathbf{X}_u^2, \mathbf{X}_d] + iq_9[\mathbf{X}_d^2, \mathbf{X}_u] \,. \tag{6.19}$$

By construction, the coefficients of the flavor expansions are basis-independent, *i.e.*, they have the same numerical values in all flavor bases (in the up-basis and down-basis for instance). They thus provide a very convenient and unambiguous way to parametrize flavor

structures. It should be realized that requiring natural expansion coefficients is a strong constraint. For instance, projecting a generic 3×3 matrix on Eq. (6.19) will generate very large coefficients q_i because of the very hierarchical structure of the 9 terms. For a given flavor expansion, if experimental constraints indicate the presence of very large expansion coefficients, this would signal the presence of a new type of flavor structure, not aligned with the Yukawa couplings and probably originating from a different fundamental flavor sector. On the contrary, very small coefficients would indicate that the MFV flavor suppression is not enough and that a stronger fine tuning in the new flavor structures is present. All in all, these flavor expansions provide a well-defined naturalness criterion for flavor structures, where BSM flavor structures are considered natural if they contain Yukawa-like hierarchies.

To summarize, let us recall the main properties and advantages of the flavor expansions:

1. As long as the coefficients are left free, any complex or hermitian matrix can be projected onto the flavor expansions. There are as many free coefficients as there are free parameters [393]. At this level, flavor expansions can thus be seen as a completely generic parametrization of flavor structures.

2. Once the flavor expansions are obtained, the MFV hypothesis is immediate to formulate: the naturality criterion simply requires all the coefficients to be of $\mathcal{O}(1)$ or smaller. By contrast, the coefficients are in general much larger than one whenever a new flavor structure not precisely aligned with the Yukawa couplings is present.

3. In practice, when none of the coefficients is large, many terms in these expansions can be dropped because $\mathbf{X}_{u,d}^2 \simeq \mathrm{Tr}(\mathbf{X}_{u,d})\mathbf{X}_{u,d}$ with the flavor trace $\mathrm{Tr}(\mathbf{X}_{u,d}) \lesssim 1$. In addition (when $\tan\beta$ is not large for supersymmetric models), terms involving $\mathbf{X}_d$ are negligible compared to those involving $\mathbf{X}_u$. In those cases, this procedure offers a simple phenomenological parametrization for a fully realistic flavor sector.

4. Because of the SM-like suppression of most of the flavored processes, the MFV hypothesis allows to reconcile the flavor sector with TeV scale new physics, making it phenomenologically very attractive.

6.2 THE MINIMAL SUPERSYMMETRIC STANDARD MODEL UNDER MFV

In the following, we implement the MFV hypothesis in the R-parity violating Minimal Supersymmetric Standard Model (MSSM). We start by briefly introducing the supersymmetry algebra and the construction of the MSSM. The general construction of the superspace formalism, the natural framework to build supersymmetric theories, and the technical construction of supersymmetric gauge theories are not reviewed here. A comprehensive presentation can be found in, *e.g.*, Ref. [394].

6.2.1 *The supersymmetry algebra*

The supersymmetric generators Q_α and $Q_{\dot{\alpha}}^\dagger$ are objects belonging in the $(\mathbf{1/2}, \mathbf{0})$ and $(\mathbf{0}, \mathbf{1/2})$ representations of the Lorentz algebra, respectively, *i.e.*, supersymmetry is ge-

nerated by spinorial (super)charges. Acting on a bosonic state, a supersymmetry transformation leads to a fermionic state and vice-versa. Here, we only consider one set of supersymmetric generators. In addition to the Poincaré algebra already discussed in Section 1, the $\mathcal{N} = 1$ supersymmetry algebra reads

$$
\begin{aligned}
\{Q_\alpha, Q_{\dot\alpha}^\dagger\} =& \ 2\sigma_{\alpha\dot\alpha}^\mu P_\mu \,, & (6.20) \\
\{Q_\alpha, Q_\beta\} =& \ \{Q_{\dot\alpha}^\dagger, Q_{\dot\beta}^\dagger\} = 0 \,, & (6.21) \\
[Q_\alpha, P^\mu] =& \ [Q_{\dot\alpha}^\dagger, P^\mu] = 0 \,, & (6.22)
\end{aligned}
$$

where $\sigma^\mu = (\mathbb{1}, \sigma^i)$. Irreducible representations of the supersymmetry algebra form *supermultiplets*, they contain both bosonic and fermionic states. The number of bosonic and fermionic degrees of freedom is the same within a given supermultiplet: $n_F = n_B$. Moreover, the generators of the (possible) internal symmetries of the theory commute with the supersymmetric ones, schematically $\left[Q_\alpha^{(\dagger)}, T^a\right] = 0$, such that all states in a given supermultiplet have the same gauge quantum numbers. In order to build the minimal realistic supersymmetric model, two kinds of supermultiplets are needed.

- The chiral supermultiplet: on-shell, it consists of one Weyl spinor ψ_α ($n_F = 2$) and two real scalars ($n_B = 2$). The two real scalars are naturally embedded into one complex scalar ϕ. Off-shell, an additional auxiliary complex scalar field F needs to be included in order to match the fermionic degrees of freedom $n_F = 4$. In other words, an auxiliary field is needed to close the supersymmetry algebra off-shell as well as on-shell.

- The vector supermultiplet: on-shell, it consists of one massless spin-1 vector boson A_μ ($n_B = 2$) and a Weyl spinor λ_α ($n_F = 2$) dubbed gaugino. Off-shell, an auxiliary real scalar field D is introduced. Vector multiplet will be used to embed gauge bosons in the MSSM. As such, the corresponding gaugino will transform under a self-conjugate representation of the gauge group and are Majorana fermions.

The field representation of a supermultiplet is called a superfield. Explicit expressions for the supercharges and the superfields can be found in [394].

One of the most important consequences of Eq. (6.22) is that $[Q^{(\dagger)}, P^2] = 0$. Since $P^2 = -m^2$, all particles within a given supermultiplet have actually the same mass. This is in striking contradiction with experimental observations if we were to embed each SM state into a supermultiplet since no copy of the known particle spectrum has ever been observed. Therefore if supersymmetry is present at all in nature, it must be a broken symmetry at low-energy, *i.e.*, $Q_\alpha|0\rangle \neq 0$ and $Q_{\dot\alpha}^\dagger|0\rangle \neq 0$. The vacuum expectation value of the trace of Eq. (6.20) then yields,

$$
\langle 0|(P^0 = H)|0\rangle = \frac{1}{4}\sum_{\alpha=1,2}\left(\||Q_\alpha|0\rangle\|^2 + \||Q_\alpha^\dagger|0\rangle\|^2\right) \geq 0 \,. \tag{6.23}
$$

In a supersymmetric theory, the vacuum energy is therefore exactly vanishing. The inequality shows that the vacuum energy of a theory that underwent spontaneous breaking of supersymmetry is strictly positive.

Superfields	Spin-0	Spin-1/2	$SU(3)_c$	$SU(2)_L$	$U(1)_Y$	$\mathcal{L}$	$\mathcal{B}$
Q	$(\widetilde{u}_L, \widetilde{d}_L)^T$	$(u_L, d_L)^T$	$\mathbf{3}$	$\mathbf{2}$	$+1/3$	0	1/3
U	$\widetilde{u}_R^*$	$(u_R)^c$	$\bar{\mathbf{3}}$	$\mathbf{1}$	$-4/3$	0	-1/3
D	$\widetilde{d}_R^*$	$(d_R)^c$	$\bar{\mathbf{3}}$	$\mathbf{1}$	$+2/3$	0	-1/3
L	$(\widetilde{\nu}, \widetilde{e}_L)^T$	$(\nu, e_L)^T$	$\mathbf{1}$	$\mathbf{2}$	-1	1	0
E	$\widetilde{e}_R^*$	$(e_R)^c$	$\mathbf{1}$	$\mathbf{1}$	$+2$	-1	0
H_u	$(H_u^+, H_u^0)^T$	$(\widetilde{H}_u^+, \widetilde{H}_u^0)^T$	$\mathbf{1}$	$\mathbf{2}$	$+1$	0	0
H_d	$(H_d^0, H_d^-)^T$	$(\widetilde{H}_d^0, \widetilde{H}_d^-)^T$	$\mathbf{1}$	$\mathbf{2}$	-1	0	0

Superfields	Spin-1/2	Spin-1	$SU(3)_c$	$SU(2)_L$	$U(1)_Y$	$\mathcal{L}$	$\mathcal{B}$
g	$\widetilde{g}$	g	$\mathbf{8}$	$\mathbf{1}$	0	0	0
W	$(\widetilde{W}^1, \widetilde{W}^2, \widetilde{W}^3)^T$	$(W^1, W^2, W^3)^T$	$\mathbf{1}$	$\mathbf{3}$	0	0	0
B	$\widetilde{B}$	B	$\mathbf{1}$	$\mathbf{1}$	0	0	0

Table 14: (Super)field content of the MSSM. The L and R subscripts of the scalar-fermions are simply a reminder of their superpartners, the SM fermions. Three copies of the fermionic supermultiplets Q, U, D, L, E should be considered.

6.2.2 *The particle content*

The MSSM is minimal in the sense that it is the supersymmetric gauge theory based on the SM gauge group and particle content that introduces the least number of supermultiplets. Its superfield content of the MSSM is summarized in Table 14.

Each SM particle should be embedded into a supermultiplet. To achieve that, one should remember that supersymmetry and gauge symmetry commute so that all states of a supermultiplet are in the same gauge representation. Since the SM is a chiral theory, the known fermions should be embedded in chiral supermultiplets. Vector multiplets indeed transform under self-conjugate representations of the gauge group and thus cannot provide chiral fermions. For each fermion generation, we therefore introduce five chiral supermultiplets Q, U, D, L, E that describe the SM fermions and their superpartners, the sfermions. The latter are scalar flavored particles. All gauge bosons belong to different (self-conjugate) vector supermultiplets, their superpartners are (self-conjugate) Majorana fermions dubbed gauginos.[32] Finally, in the Higgs sector, while in the SM the doublet H can couple to both up- and down-type fermions, using the self-conjugacy property of the $\mathbf{2}$ representation of SU(2), this is not possible in supersymmetric models. Indeed, imposing supersymmetry gives rise to strong constraints on the possible interactions of the various fields. Interactions terms are obtained from the derivatives of a (dimension-3) *holomorphic* function of

---

[32] Motivated by a continuous R-symmetry and $\mathcal{N} = 2$ supersymmetry, Dirac gauginos may also be considered [395–397], they require extra degrees of freedom, *i.e.*, extra supermultiplets in the adjoint representation of the gauge groups.

chiral superfields, the superpotential $\mathcal{W}$.[33] A non-holomorphic superpotential would explicitly break supersymmetry. This means that complex conjugate chiral superfields cannot appear in $\mathcal{W}$. Two different doublets with opposite hypercharge $Y = \pm 1$ are then needed, one coupling to up-type fermions and the other to down-type fermions. This gives rise to a Type II 2HDM structure. The phenomenology of the Higgs sector will however be very different from the one described in Section 4 since the particle content is extended and the λ_i parameters of the 2HDM potential are all fixed by supersymmetry: they are related to gauge couplings (see Ref. [398] for a recent study about 2HDMs with a supersymmetric ultraviolet completion and their phenomenological consequences). Alternatively, since a single Higgs superfield contains additional chiral fermions, the gauge anomaly coming from the triangle diagram with 3 hypercharge currents, that is absent in the SM, will arise. A second Higgs doublet with opposite hypercharge should is then needed in order to cancel the anomaly, it automatically couples to down-type fermions.

After EWSB, particles with the same quantum numbers will mix. The bino, neutral wino and neutral Higgsinos will form 3 weakly interacting mass eigenstates, the neutralinos. The charged winos and charged Higgsinos form charginos. The gluino do not mix since it is the only fermion being in a $SU(3)_c$ octet. Finally, squarks will also mix between themselves, in full generality three 6×6 mass matrices need to be considered. These are given in the bases $(\widetilde{u}_L^I, \widetilde{u}_R^I)_{I=1,2,3}$, $(\widetilde{d}_L^I, \widetilde{d}_R^I)_{I=1,2,3}$ and $(\widetilde{e}_L^I, \widetilde{e}_R^I)_{I=1,2,3}$ for instance.

6.2.3 *Flavor interactions*

Supersymmetric interactions

The most general renormalizable, Lorentz and gauge invariant superpotential that can be built from the MSSM particle content is

$$
\begin{aligned}
\mathcal{W} = {} & U^I \mathbf{Y}_u^{IJ} Q^J H_u + D^I \mathbf{Y}_d^{IJ} Q^J H_d + E^I \mathbf{Y}_e^{IJ} L^J H_d + \mu H_u H_d \\
& + \frac{1}{2} \mathbf{Y}_{lle}^{IJK} L_I L_J E_K + \mathbf{Y}_{lqd}^{IJK} L_I Q_J D_K + \mu'^I L_I H_u \\
& + \frac{1}{2} \mathbf{Y}_{udd}^{IJK} U_I D_J D_K
\end{aligned} \tag{6.25}
$$

where I, J, K are flavor indices and all gauge contractions are implicit. The first three terms are Yukawa-like terms, they in particular lead to the fermion mass matrices after EWSB when the two Higgs doublets develop their vevs $v_u \equiv v \sin\beta$ and $v_d \equiv v \cos\beta$.[34]

---

33 Specifically, terms derived from the superpotential are given by

$$
\mathscr{L}_{\text{susy}} \supset -\frac{1}{2} \frac{\partial^2 \mathcal{W}}{\partial \Phi_i \partial \Phi_j} \psi_i \psi_j + \text{h.c.} - \frac{\partial \mathcal{W}}{\partial \Phi^i} \frac{\partial \mathcal{W}^\dagger}{\partial \Phi_i^\dagger}, \tag{6.24}
$$

where Φ_i are the chiral superfields of the theory, ψ_i is the fermionic component of Φ_i and after derivation with respect to the superfields, the remaining superfields are understood to be replaced by their respective scalar component. The first term thus leads to scalar-fermion-fermion vertices while the second leads to quartic scalar vertices.

34 It should be noted that the supersymmetric scalar potential is non-negative, hence it does not break the EW symmetry. It is only through the addition of soft-breaking terms (next paragraph) that EWSB can be triggered, mostly through radiative corrections to the soft-breaking Higgs masses [394].

Therefore, the down-type Yukawa coupling has a $\tan\beta$ enhancement factor as compared to the up-type one. In the large $\tan\beta$ regime, the down-type Yukawa entries can therefore be of the same order as the up-type ones. The μ term is the only supersymmetric dimensionful parameter of the MSSM, as such it should naturally lie near the cut-off scale of the theory, presumably many orders of magnitude higher than the EW scale, near the GUT or Planck scale. However, considerations on the particle spectrum indicate that μ should actually be quite close to the EW scale. This is the μ-problem of the MSSM. All terms in the second line violate lepton number by one unit ($\Delta\mathcal{L} = 1$) and the term in the third line violates baryon number by one unit ($\Delta\mathcal{B} = 1$): lepton and baryon number violations are present at the renormalizable level in the MSSM. Due to the anti-commutativity of the SU(2) and SU(3) products, $\mathbf{Y}_{lle}^{IJK}$ is antisymmetric under $I \leftrightarrow J$ and $\mathbf{Y}_{udd}^{IJK}$ under $J \leftrightarrow K$.

Generic lepton and baryon number violating structures are worrisome. In particular the $\mathbf{Y}_{lqd}$ and $\mathbf{Y}_{udd}$ couplings can mediate fast proton decay. For instance, $p \to e^+\pi^0$ may occur through $\mathbf{Y}_{udd}^{11I}$ (controlling $ud \to \widetilde{d}_R^{*I}$) and $\mathbf{Y}_{lqd}^{11I}$ (controlling $\widetilde{d}_R^{*I} \to e^+\bar{u}$). Upper bounds on the proton lifetime in different channels then impose severe constraints on the product of these two couplings, $|\mathbf{Y}_{udd}^{11I}\mathbf{Y}_{lqd}^{11I}| \lesssim 10^{-26}$ for squark masses around 300 GeV [399]. Clearly, for light squarks, these flavor structures cannot be generic and they should involve very large hierarchies. Since proton decay necessarily violates both lepton and baryon numbers, it is sufficient that either one of the corresponding couplings is forbidden or very hierarchical in flavor space. Discrete symmetries can be imposed to forbid these operators [400, 401].

R-parity [400] is usually considered as a definitive part of the MSSM. It is a multiplicative quantum number defined as,

$$R = (-1)^{3(\mathcal{B}-\mathcal{L})+2s} \tag{6.26}$$

where s is the spin of the particle. The SM particles and the five Higgs bosons have $R = +1$ while all other particles have $R = -1$. If R is conserved, the second and third lines of the superpotential (6.25) are forbidden: these interactions are R-parity violating (RPV). R-parity can arise from the spontaneous breaking of a $\mathrm{U}(1)_{\mathcal{B}-\mathcal{L}}$ gauge theory for instance [402]. However in the MSSM, enforcing it is arbitrary and is just meant to ensure proton stability. R-parity has however other very strong consequences in the phenomenology of the MSSM. As is well-known, see *e.g.* [399] for a review, it forces superparticles to be present in pairs in all vertices, and thus renders the lightest superparticle (LSP) perfectly stable. In colliders, supersymmetric events are accompanied by a significant amount of missing energy carried away by the LSP. On the other hand, if R-parity is not exact, the LSP decays and these missing energy signatures are simply not there. Bounds on the superparticle masses crucially depend on the R-parity conservation hypothesis and can be significantly weakened if re-interpreted in the context of R-parity violating scenarios. Moreover, with R-parity, lepton and baryon number conservations are only realized at the dimension-4 level and there exists dimension-5 operators allowed by R-parity that still mediate proton decay: $\mathcal{W}_5 \supset QQQL + UUDE$ [401]. An additional discrete symmetry, the baryon triality [403], should be imposed in order to forbid these terms. Clearly, this is not very satisfactory. As we will understand in the following, the MFV hypothesis predicts a long proton lifetime in the presence of R-parity violating interactions [389] and therefore constitutes a perfectly viable alternative to R-parity in the MSSM.

Supersymmetry-breaking interactions

At low-energy, supersymmetry is a broken symmetry. Several dynamical breaking mechanisms have been proposed (gauge mediated [404–408], anomaly mediated [409, 410], gravity mediated supersymmetry breaking [411–414] etc.) but for phenomenological purposes, it is mostly sufficient to parametrize the effects of supersymmetry breaking by introducing all possible soft breaking terms [415]. Soft meaning that we do not want to spoil the supersymmetric solution to the Higgs mass hierarchy problem by introducing terms that will lead to genuine quadratic divergences. Instead, introducing solely dimensionful new parameters will not affect sizably the ultraviolet behavior of the theory. For the RPV-MSSM without $\Delta \mathcal{L} = 1$ couplings (this will be motivated later) the soft-breaking Lagrangian reads:

$$
\begin{aligned}
\mathscr{L}_{\text{soft}} = & -\frac{1}{2} \left(M_3 \tilde{g}\tilde{g} + M_2 \widetilde{W}\widetilde{W} + M_1 \widetilde{B}\widetilde{B} + \text{h.c.} \right) - m_{H_u}^2 H_u^* H_u - m_{H_d}^2 H_d^* H_d - (bH_u H_d + \text{h.c.}) \\
& - \widetilde{Q}^{\dagger I}(\mathbf{m_Q^2})^{IJ}\widetilde{Q}^J - \widetilde{L}^{\dagger I}(\mathbf{m_L^2})^{IJ}\widetilde{L}^J - \widetilde{U}^I(\mathbf{m_u^2})^{IJ}\widetilde{U}^{\dagger J} - \widetilde{D}^I(\mathbf{m_d^2})^{IJ}\widetilde{D}^{\dagger J} - \widetilde{E}^I(\mathbf{m_e^2})^{IJ}\widetilde{E}^{\dagger J} \\
& - \left(\widetilde{U}^I \mathbf{A}_u^{IJ} \widetilde{Q}^J H_u - \widetilde{D}^I \mathbf{A}_d^{IJ} \widetilde{Q}^J H_d - \widetilde{E}^I \mathbf{A}_e^{IJ} \widetilde{L}^J H_d + \mathbf{A}_{udd}^{IJK} \widetilde{U}_I \widetilde{D}_J \widetilde{D}_K + \text{h.c.} \right) .
\end{aligned}
$$
(6.27)

These terms explicitly introduce mass splittings between the SM particles and their superpartners. M_1, M_2 and M_3 are gaugino mass terms, $m_{H_u}^2$ and $m_{H_d}^2$ are the soft breaking Higgs mass terms and b is the soft-term associated to μ. In the second line $\mathbf{m_Q^2}, \mathbf{m_L^2}, \mathbf{m_u^2}, \mathbf{m_d^2}$ and $\mathbf{m_e^2}$ are the hermitian sfermion squared mass matrices. In the third line $\mathbf{A}_u, \mathbf{A}_d$ and $\mathbf{A}_e$ are trilinear couplings, they are 3×3 matrices in flavor space and are analog to the Yukawa couplings for the sfermions. $\mathbf{A}_{udd}$ is the soft-term associated to the $\mathbf{Y}_{udd}$ coupling.

While the general supersymmetric Lagrangian is very constrained and has a limited number of new parameters, the soft-breaking Lagrangian possesses $\mathcal{O}(100)$ new parameters. All flavor structures are a priori generic. At the same time, many of these parameters are constrained by the now precise data from flavor physics. Assuming that superparticles are not far heavier than about 1 TeV, squark mixing cannot be large and R-parity violation must be limited. In an attempt at systematically embedding these constraints, the MFV hypothesis is particularly well suited.

6.2.4 Enforcing Minimal Flavor Violation

As the MSSM does not contain any additional generational fermion, its kinetic terms are invariant under the same flavor symmetry group as in the SM, $G_F = \text{U}(3)^5$. Within a given chiral superfield, the fermion and scalar component should transform identically under G_F because of supersymmetry. The transformations given in Eq. (2.58) can therefore be interpreted here as the G_F transformations of the Q, U, D, L, E superfields. In order to promote the MSSM flavor couplings to spurions, only the flavor structure of the corresponding operators matter. Therefore, in order to find the spurious transformations of both the supersymmetric and non-supersymmetric couplings, we can look at the flavor structure of the superpotential Eq. (6.25) and of the softly supersymmetry breaking Lagrangian Eq. (6.27), disregarding the fact that the involve objects of very different nature (superfields and fields).

The baryonic R-parity conserving sector

When non-vanishing, all the flavor couplings break the $U(3)^5$ flavor symmetry, which means that they vary when (s)fermions undergo U(3) rotations in flavor space. Since quark mass terms originate from the Yukawa couplings $\mathbf{Y}_{u,d}$, this freedom is in general used to bring all but either the up- or the down-type left-handed quarks to their mass eigenstates as shown in Section 2.4. The lepton sector is trivial as long as neutrinos are considered massless, *i.e.*, $\mathbf{Y}_e$ can always be brought into a diagonal form. Obviously, performing the same unitary rotations on both quark and squark fields redefines the different (s)quark flavor structures. Denoting the singular value decompositions for the Yukawa couplings as $V_R^{u,d}\mathbf{Y}_{u,d\dagger}V_L^{u,d}$, see Eq. (2.61), the $V_R^{u,d}$ matrices find their way into the flavor structures when rotating $U \to UV_R^{u\dagger}$ and $D \to DV_R^{d\dagger}$. Except if a flavor model is prescribed, $V_{R,L}^{u,d}$ are unknown matrices so there is a numerical ambiguity in defining the whole flavor sector.

As described in Section 6.1, to ensure the independence on the flavor basis, the RPC soft-breaking terms are written as manifestly G_F symmetric polynomial expansions in the Yukawa spurions. As the MSSM Yukawa couplings present in the superpotential Eq. (6.25) have the same flavor structure as in the SM, their spurion transformations are the same as in the SM and are given in Eq. (6.5). Only then are we certain that performing G_F rotations of the (s)fermion fields leaves invariant the expansion coefficients. Specifically, because both $\mathbf{Y}_u$ and $\mathbf{Y}_d$ transform non-trivially under $SU(3)_Q$, the most generic expansions are constructed using the $SU(3)_Q$ octet $\mathbf{Q}_8$, see Eq. (6.19), where its nine independent terms are indeed sufficient to project an arbitrary complex matrix.

The G_F transformations of the soft-breaking flavor couplings are inferred from Eq. (6.27),

$$\mathbf{m_Q^2} \xrightarrow{G_F} g_Q \mathbf{m_Q^2} g_Q^\dagger, \qquad \mathbf{m_U^2} \xrightarrow{G_F} g_U \mathbf{m_U^2} g_U^\dagger, \qquad \mathbf{m_D^2} \xrightarrow{G_F} g_D \mathbf{m_D^2} g_D^\dagger,$$
$$\mathbf{A}_u \xrightarrow{G_F} g_U \mathbf{A}_u g_Q^\dagger, \qquad \mathbf{A}_d \xrightarrow{G_F} g_D \mathbf{A}_d g_Q^\dagger. \tag{6.28}$$

Their respective flavor expansions are therefore,

$$\mathbf{m}_Q^2/m_q^2 = a_1^q \, \mathbb{1} + a_2^q \, \mathbf{X}_u + a_3^q \, \mathbf{X}_d + a_4^q \, \mathbf{X}_u^2 + a_5^q \, \mathbf{X}_d^2 + a_6^q \, \{\mathbf{X}_u, \mathbf{X}_d\}$$
$$+ b_1^q \, i[\mathbf{X}_u, \mathbf{X}_d] + b_2^q \, i[\mathbf{X}_u^2, \mathbf{X}_d] + b_3^q \, i[\mathbf{X}_u, \mathbf{X}_d^2] \;, \tag{6.29a}$$

$$\mathbf{m}_{U,D}^2/m_{u,d}^2 = a_1^{u,d} \, \mathbb{1} + \mathbf{Y}_{u,d} \, (a_1^{u,d} \, \mathbb{1} + a_2^{u,d} \, \mathbf{X}_u + a_3^{u,d} \, \mathbf{X}_d + a_4^{u,d} \, \mathbf{X}_{d,u}^2 + a_5^q \, \{\mathbf{X}_u, \mathbf{X}_d\}) \, \mathbf{Y}_{u,d}^\dagger$$
$$+ \mathbf{Y}_{u,d} \, (b_1^{u,d} \, i[\mathbf{X}_u, \mathbf{X}_d] + b_2^{u,d} \, i[\mathbf{X}_u^2, \mathbf{X}_d] + b_3^{u,d} \, i[\mathbf{X}_u, \mathbf{X}_d^2]) \, \mathbf{Y}_{u,d}^\dagger \;, \tag{6.29b}$$

$$\mathbf{A}_{u,d}/A_{u,d} = \mathbf{Y}_{u,d} \, (c_1^{u,d} \, \mathbb{1} + c_2^{u,d} \, \mathbf{X}_u + c_3^{u,d} \, \mathbf{X}_d + c_4^{u,d} \, \mathbf{X}_u^2 + c_5^{u,d} \, \mathbf{X}_d^2 + c_6^{u,d} \, \{\mathbf{X}_u, \mathbf{X}_d\}$$
$$+ c_7^{u,d} \, i[\mathbf{X}_u, \mathbf{X}_d] + c_8^{u,d} \, i[\mathbf{X}_u^2, \mathbf{X}_d] + c_9^{u,d} \, i[\mathbf{X}_u, \mathbf{X}_d^2]) \;, \tag{6.29c}$$

where $A_{u,d}$ and $m_{q,u,d}$ set the soft-breaking scales. Note that the octet definition and the hermicity of $\mathbf{m}_{Q,U,D}^2$ force the $a_i^{q,u,d}$ and $b_i^{q,u,d}$ coefficients to be real. MFV is then easily enforced by requiring all expansion coefficients to be of order 1 or less. This allows the MSSM to pass all current flavor constraints [391], including electric dipole moments [390].

The leptonic R-parity conserving and violating sectors

We briefly discuss the leptonic sector, see Ref. [389] for a complete discussion. The construction of the flavor expansions for the baryonic-RPV coupling is more involved, and Section 6.3 is dedicated to their study.

The only Yukawa coupling charged under the leptonic flavor subgroup G_F^l is $\mathbf{Y}_e$ and transforms as $\mathbf{Y}_e \sim (\bar{\mathbf{3}}, \mathbf{3})_{G_F^l}$. The flavor expansions of $\mathbf{m}_{\mathbf{L},\mathbf{E}}^2$ and $\mathbf{A}_e$ can then be readily written, defining $\mathbf{X}_e \equiv \mathbf{Y}_e^\dagger \mathbf{Y}_e \xrightarrow{G_F^l} g_L \mathbf{X}_e g_L^\dagger$,

$$\mathbf{m}_{\mathbf{L}}^2/m_l^2 = a_1^l \, \mathbb{1} + a_2^l \, \mathbf{X}_e + a_3^l \, \mathbf{X}_e^2 \,, \tag{6.30a}$$

$$\mathbf{m}_{\mathbf{E}}^2/m_e^2 = a_1^e \, \mathbb{1} + \mathbf{Y}_e \, (a_2^e \, \mathbb{1} + a_3^e \, \mathbf{X}_e) \mathbf{Y}_e^\dagger \,, \tag{6.30b}$$

$$\mathbf{A}_e/A_e = \mathbf{Y}_e \, (c_1^e \, \mathbb{1} + c_2^e \, \mathbf{X}_e + c_3^e \, \mathbf{X}_e^2) \,. \tag{6.30c}$$

Since we only have $\mathbf{Y}_e$ at our disposal, the flavor expansions are more compact. Higher order terms can straightforwardly be recast into the first three terms using the Cayley-Hamilton theorem for 3×3 matrices Eq. (6.18). Since $\mathbf{Y}_e$ is diagonal, none of the structures can mediate flavor violation.

Looking back at the MSSM superpotential, there is a RPC flavor coupling that we have not discussed so far: $\mathcal{W} \supset \mu'^I L^I H_u$. However, since $L \sim (\mathbf{3}, \mathbf{1})_{G_F^l}$, μ' should transform as $(\bar{\mathbf{3}}, \mathbf{1})_{G_F^l}$ which simply cannot be expressed in terms of $\mathbf{Y}_e$. Therefore, under MFV, in the MSSM with a minimal neutrino sector, the μ' coupling is forbidden and the same applies for the leptonic-RPV couplings of Eq. (6.25). An additional spurion is needed to render the lepton sector non-trivial. For instance, a seesaw mechanism [108] can be implemented as follows. Heavy right-handed neutrinos superfields are introduced in the superpotential with a Majorana mass term:

$$\mathcal{W}_{seesaw} = \frac{1}{2} N^I \mathbf{M}_R^{IJ} N^J + N^I \mathbf{Y}_\nu^{IJ} L^J H_u \tag{6.31}$$

where, for simplicity, $\mathbf{M}_R = M_R \mathbb{1}$. The right-handed neutrino fields are integrated out, yielding

$$\mathcal{W}_{seesaw} \supset \frac{1}{2} v_u^2 \nu_L \mathbf{Y}_\nu^T (\mathbf{M})^{-1} \mathbf{Y}_\nu \nu_L \tag{6.32}$$

after EWSB. This is a neutrino mass term with $m_\nu \simeq v_u^2/M_R$. The neutrino mass spurion is defined as

$$\Upsilon_\nu \equiv v_u \mathbf{Y}_\nu^T (\mathbf{M})^{-1} \mathbf{Y}_\nu \xrightarrow{G_F} g_L^* \Upsilon_\nu g_L^\dagger \tag{6.33}$$

and along with $\mathbf{Y}_\nu^\dagger \mathbf{Y}_\nu$, all the $\Delta\mathcal{L} = 1$ terms can now be made G_F invariant. In the RPV sector, each term in the subsequent MFV expansions turns out to contain at least one Υ_ν and $\mathbf{Y}_e$ contracted with some ϵ^{IJK} tensors from the flavored SU(3)'s. Since $\Upsilon_\nu \sim \mathcal{O}(m_\nu/v_u)$ and the ϵ tensors necessarily involve the light fermion generations, MFV predicts a very large suppression of the $\Delta\mathcal{L} = 1$ couplings. This is why MFV is reconcilable with the extremely tight bounds on the proton lifetime and can be considered as an alternative to R-parity [389]. In the following, we stick to the minimal lepton sector and the $\Delta\mathcal{L} = 1$ couplings will therefore not be considered.

6.2.5 *Renormalization group evolution*

All parameters present in $\mathscr{L}_{\text{soft}}$ [Eq. (6.27)] fundamentally emerge from a dynamical break-
ing of supersymmetry at a very high scale M_X. Assuming that the mechanism behind MFV
takes also place at this scale, we should expect the RPC soft-breaking flavor structures
to be given by Eqs. (6.29) [and (6.30)] at M_X. Unless the flavor model is specified, the
coefficients at the scale M_X are unknown but requiring MFV leads to order 1 coefficients.
In the following, we will assume that only the most minimal flavor structures are generated,
i.e., only the first term of each expansion. There still remain several unknown soft-breaking
scales, $m_{q,u,d}$ and $A_{u,d}$, which are not fixed by the flavor-breaking mechanism or even the
supersymmetry-breaking one. However, the latter can actually lead to relations among
the different scales. In the following, we will inspire ourselves from the minimal super-
gravity (mSUGRA) parametrization, coming from minimal scenarios of gravity mediated
supersymmetry breaking, which predicts that all the $m_{q,u,d}$ are equal and the $A_{u,d}$ as well.
The non-flavored part of $\mathscr{L}_{\text{soft}}$, the Higgs and gaugino masses, are also subject to some
constraints. Specifically, at the scale M_X, the soft-breaking parameters are given by,

$$
\begin{aligned}
\mathbf{A}_u &= A_0 \mathbf{Y}_u, \qquad \mathbf{A}_d = A_0 \mathbf{Y}_d, \qquad \mathbf{A}_e = A_0 \mathbf{Y}_e, \qquad \mathbf{A}_{udd} = A_0 \mathbf{Y}_{udd}, \\
\mathbf{m}_\mathbf{Q}^2 &= \mathbf{m}_\mathbf{L}^2 = \mathbf{m}_\mathbf{u}^2 = \mathbf{m}_\mathbf{d}^2 = \mathbf{m}_\mathbf{e}^2 = m_0^2 \mathbb{1}, \quad m_{H_u}^2 = m_{H_d}^2 = m_1^2, \\
M_1 &= M_2 = M_3 = M_{1/2}\,,
\end{aligned}
\tag{6.34}
$$

where A_0 is a common trilinear mass, m_0 and m_1 scalar masses and $M_{1/2}$ a common
gaugino mass. Note that we chose here to split the squarks and Higgs masses at M_X by
introducing two mass scales m_0 and m_1. In the constrained-MSSM (based on mSUGRA),
the mass scales are actually equal $m_0 = m_1$. We moreover impose an extra condition on
the RPV sector: the soft-breaking coupling A_{udd} is proportional to the supersymmetric
$\mathbf{Y}_{udd}$ couplings at M_X. For the flavor structures, we will impose these relations in the
super-CKM basis, in which either the up-type or down-type quarks are brought to their
mass eigenstates, and the squarks fields are rotated as their respective quark fields.

The theory is now fixed at M_X, presumably near the GUT or Planck scale, but what we
would really like to know are its predictions close to the EW scale. All these parameters
should therefore be evolved down to these lower scales with their respective renormalization
group (RG) equations. Under the RG, supersymmetric parameters form a closed system
under the RG, *i.e.*, they do not feel the presence of the soft-breaking terms. On the con-
trary, the supersymmetric parameters do affect the running of the soft-breaking ones. The
two-loop MSSM RG equations, including the RPV and soft-breaking sectors, have been
obtained in Refs. [416, 417].

In the lepton sector, since the initial conditions at M_X are flavor diagonal and that
there is no PMNS matrix, the corresponding structures stay diagonal at every scales. On
the contrary, in the quark sector, even though some structures are diagonal at M_X, off-
diagonal contributions will be generated by the running and will be tuned by the CKM
matrix elements. In terms of the flavor expansions Eqs. (6.29), this means that even though
there might be only one non-vanishing coefficient at M_X, all the coefficients are expected
to be generated by the RG running. Since the flavor expansions can be defined at any
scale, the RG evolution of the corresponding flavor structures can be encoded into that
of their expansion coefficients. In Refs. [392, 418], it was shown that the RPC coefficients

exhibit infrared "quasi"-fixed points compatible with MFV (*i.e.,* no large coefficients are generated), meaning that the coefficient values at low-scale are mostly insensitive to the initial conditions at the M_X scale. Their specific low-scale values actually depend on the soft-breaking scales A_0, m_0, $M_{1/2}$ and on $\tan\beta$, hence the denomination "quasi"-fixed points as opposed to true fixed points. This means that the previously listed parameters are enough to determine the low-scale flavor sector, and that the specifics of the fundamental flavor model actually do not matter much. Moreover, since the low-scale values of the coefficients are natural, MFV could only be effective at the low-scale while the flavor sector at M_X could present large deviations from the Yukawa hierarchies. In this case, low-scale MFV would have been generated or reinforced by the RG running. Interestingly, the RPV coefficients also show a similar behavior, as we will now discuss.

6.3 BARYONIC R-PARITY VIOLATION AND ITS RUNNING

In the present analysis, our goal is to study the behavior of the minimally flavor violating RPV couplings in the quark sector under the RG evolution. Indeed, if valid, MFV is likely to derive from a new flavor dynamics taking place at a very high scale (see e.g. Refs. [419–423]), and it is crucial to check whether it survives down to the low scale. We will see that this survival severely constrains the formulation of MFV, and in particular the viable flavor symmetry group. At the same time, once these constraints are in place, MFV is not only stable, it is even radiatively reinforced through the evolution.

Before being able to delve into the numerics of the evolution, we must set up the formalism. The first task is to construct a flavor-symmetric reparametrization of the RPV couplings in terms of the Yukawa couplings. At that stage, the RPV couplings need not satisfy MFV. Actually, this reparametrization provides a unique way to specify fully generic RPV couplings independently of the flavor basis chosen for the (s)quark fields, and thus extends to the RPV sector the procedure proposed in Refs. [390, 424]. This is presented in Section 6.3.1. With this tool in hand, the second step is to impose MFV. In the RPC sector, this was very easy: the reparametrization had to be natural, hence must involve at most $\mathcal{O}(1)$ coefficients [392]. In the RPV sector, however, we find that this $\mathcal{O}(1)$ criterion is neither stable nor well-defined. The reasons for this and the conditions under which consistency is recovered are detailed in Section 6.3.2. Once these initial steps are completed, the numerical study of the RG evolution is undertaken in Section 6.3.3. Special emphasis is laid on the holomorphic implementation of MFV, as proposed in Ref. [425], for which we prove several unique features, most notably the RG invariance.

6.3.1 *Generic RPV couplings*

Let us now construct the expansions for the RPV couplings $\mathcal{W} \supset \frac{1}{2}\mathbf{Y}_{udd}^{IJK}U^I D^J D^K$. Considering the transformation of the UDD structure,

$$U^I D^J D^K \rightarrow (Ug_U^\dagger)^I (Dg_D^\dagger)^J (Dg_D^\dagger)^K \tag{6.35}$$

it is clear that the flavor expansion of $\mathbf{Y}_{udd}$ should involve SU(3) flavor epsilon tensors in order to render the overall term G_F^q invariant. Since there are three SU(3) factors in G_F^q,

we can consider the three simplest terms that can be constructed out of the corresponding epsilon tensors,

$$(\mathbf{Y}_{udd}^{Q})^{IJK} \ni \varepsilon_Q^{LMN} \mathbf{Y}_u^{IL} \mathbf{Y}_d^{JM} \mathbf{Y}_d^{KN} \,, \tag{6.36a}$$

$$(\mathbf{Y}_{udd}^{D})^{IJK} \ni \varepsilon_D^{LJK} (\mathbf{Y}_u \mathbf{Y}_d^{\dagger})^{IL} \,, \tag{6.36b}$$

$$(\mathbf{Y}_{udd}^{U})^{IJK} \ni \varepsilon_U^{IMN} (\mathbf{Y}_d \mathbf{Y}_u^{\dagger})^{JM} (\mathbf{Y}_d \mathbf{Y}_u^{\dagger})^{KN} \,, \tag{6.36c}$$

where either the epsilon tensor of $SU(3)_Q$, $SU(3)_D$, or $SU(3)_U$ is used, respectively noted ϵ_Q, ϵ_D or ϵ_U. Let us check explicitly the G_F invariance of the superpotential based on the flavor expansion with the ϵ_D term for instance,

$$\begin{aligned}
2\mathcal{W} \supset{}& \epsilon_D^{AJK} (\mathbf{Y}_u \mathbf{Y}_d^{\dagger})^{IA} U^I D^J D^K \\
\xrightarrow{G_F}{}& \epsilon_D^{AJK} (g_U)^{IB} (\mathbf{Y}_u \mathbf{Y}_d^{\dagger})^{BC} (g_D^{\dagger})^{CA} U^D (g_U^{\dagger})^{DI} D^E (g_D^{\dagger})^{EJ} D^F (g_D^{\dagger})^{FK} \\
={}& \mathrm{Det}(g_D^{\dagger}) \epsilon_D^{CEF} \delta^{DB} (\mathbf{Y}_u \mathbf{Y}_d^{\dagger})^{BC} U^D D^E D^F \\
={}& \mathrm{Det}(g_D^{\dagger}) \epsilon_D^{AJK} (\mathbf{Y}_u \mathbf{Y}_d^{\dagger})^{IA} U^I D^J D^K
\end{aligned} \tag{6.37}$$

this is invariant only if $\mathrm{Det}(g_D^{\dagger}) = 1$, *i.e.*, $g_D \in \mathrm{SU}(3)_D$ rather than the full $\mathrm{U}(3)_D$. The same applies for the other terms. Therefore, the flavor expansions can only be written if at least one of the quark U(1)'s is explicitly broken. We will come back to this point in the following.

Given that a generic $\mathbf{Y}_{udd}$ introduces nine arbitrary complex parameters, the simplest polynomial expansions require nine independent terms. From the three terms given in Eq. (6.36), the most general expansions are obtained by inserting in all possible ways the $SU(3)_Q$ octet $\mathbf{Q}_8$, Eq. (6.19). At this stage, because of the epsilon contractions, some redundant terms remain. The final step is to remove them and identify the minimal set of nine independent terms using the matrix identities derived from the Cayley-Hamilton theorem. Such identities permit to get rid of many terms. Taking for example the $\varepsilon_Q^{LMN} \mathbf{Y}_u^{IL} \mathbf{Y}_d^{JM} \mathbf{Y}_d^{KN}$ structure, any $SU(3)_Q$ octet insertion acting on $\mathbf{Y}_d$ can be moved to act on $\mathbf{Y}_u$ using either,

$$\begin{aligned}
& \varepsilon_Q^{LMN} \mathbf{Y}_u^{IL} [(\mathbf{Y}_d \mathbf{Q}_8)^{JM} \mathbf{Y}_d^{KN} + \mathbf{Y}_d^{JM} (\mathbf{Y}_d \mathbf{Q}_8)^{KN}] \\
&\qquad = \varepsilon_Q^{LMN} (\mathbf{Y}_u [\mathrm{Tr}(\mathbf{Q}_8) - \mathbf{Q}_8])^{IL} \mathbf{Y}_d^{JM} \mathbf{Y}_d^{KN} \,,
\end{aligned} \tag{6.38}$$

where the two terms on the left-hand side enforce $\mathbf{Y}_{udd}^{IJK} = -\mathbf{Y}_{udd}^{IKJ}$, or,

$$\begin{aligned}
& \varepsilon_Q^{LMN} \mathbf{Y}_u^{IL} (\mathbf{Y}_d \mathbf{Q}_8)^{JM} (\mathbf{Y}_d \mathbf{Q}_8)^{KN} \\
&\quad = \varepsilon_Q^{LMN} \left(\mathbf{Y}_u \left[\mathbf{Q}_8^2 - \mathrm{Tr}(\mathbf{Q}_8)\mathbf{Q}_8 + \tfrac{1}{2}\mathrm{Tr}(\mathbf{Q}_8)^2 - \tfrac{1}{2}\mathrm{Tr}(\mathbf{Q}_8^2)\right]\right)^{IL} \mathbf{Y}_d^{JM} \mathbf{Y}_d^{KN} \,.
\end{aligned} \tag{6.39}$$

The right-hand side retains a manifestly $SU(3)_Q$ invariant form since $\mathbf{Q}_8$ transforms as an octet. Therefore, octets need to act on the $\mathbf{Y}_u$ factor only, and the final set of nine terms can be chosen as (remember $\mathbf{X}_{u,d} \equiv \mathbf{Y}_{u,d}^{\dagger} \mathbf{Y}_{u,d}$)

$$\begin{aligned}
(\mathbf{Y}_{udd}^{Q})^{IJK} = \varepsilon_Q^{LMN} \Big(& \mathbf{Y}_u (\lambda_1^q \mathbf{1} + \lambda_2^q \mathbf{X}_u + \lambda_3^q \mathbf{X}_d + \lambda_4^q \mathbf{X}_u^2 + \lambda_5^q \mathbf{X}_d^2 + \lambda_6^q \{\mathbf{X}_u, \mathbf{X}_d\} \\
& + \lambda_7^q i[\mathbf{X}_u, \mathbf{X}_d] + \lambda_8^q\, i[\mathbf{X}_u^2, \mathbf{X}_d] + \lambda_9^q i[\mathbf{X}_u, \mathbf{X}_d^2])\Big)^{IL} \mathbf{Y}_d^{JM} \mathbf{Y}_d^{KN} \,,
\end{aligned} \tag{6.40}$$

where $\lambda_{1,\dots,9}^q$ are nine free complex parameters. A similar reduction can be done starting from Eq. (6.36b), leading to the alternative basis

$$(\mathbf{Y}_{udd}^D)^{IJK} = \varepsilon_D^{LJK} \left(\mathbf{Y}_u(\lambda_1^d\mathbf{1} + \lambda_2^d\mathbf{X}_u + \lambda_3^d\mathbf{X}_d + \lambda_4^d\mathbf{X}_u^2 + \lambda_5^d\mathbf{X}_d^2 + \lambda_6^d\{\mathbf{X}_u, \mathbf{X}_d\} \right.$$
$$\left. + \lambda_7^d i[\mathbf{X}_u, \mathbf{X}_d] + \lambda_8^d i[\mathbf{X}_u^2, \mathbf{X}_d] + \lambda_9^d i[\mathbf{X}_u, \mathbf{X}_d^2])\mathbf{Y}_d^\dagger \right)^{IL} . \qquad (6.41)$$

Finally, for the last structure, Eq. (6.36c), all octet insertions but those involving $\mathbf{Y}_d\mathbf{X}_d\mathbf{Y}_u^\dagger$ and $\mathbf{Y}_d\mathbf{X}_d^2\mathbf{Y}_u^\dagger$ can be moved to the first index, and we remain with 12 possible terms. This time, there seems to be some latitude in the identification of the basis. For reasons that will be detailed below, the best choice is to keep two such $\mathbf{X}_d$ insertions (which have to be antisymmetrized under $J \leftrightarrow K$):

$$(\mathbf{Y}_{udd}^U)^{IJK} = \varepsilon_U^{LMN} \left(\lambda_1^u\mathbf{1} + \mathbf{Y}_u(\lambda_2^u\mathbf{1} + \lambda_4^u\mathbf{X}_u + \lambda_5^u\mathbf{X}_d + \lambda_7^u\mathbf{X}_d^2)\mathbf{Y}_u^\dagger \right)^{IL} (\mathbf{Y}_d\mathbf{Y}_u^\dagger)^{JM} (\mathbf{Y}_d\mathbf{Y}_u^\dagger)^{KN}$$
$$+ \varepsilon_U^{LMN} \left(\mathbf{Y}_u(\lambda_8^u\{\mathbf{X}_u, \mathbf{X}_d\} + \lambda_9^u i[\mathbf{X}_u, \mathbf{X}_d])\mathbf{Y}_u^\dagger \right)^{IL} (\mathbf{Y}_d\mathbf{Y}_u^\dagger)^{JM} (\mathbf{Y}_d\mathbf{Y}_u^\dagger)^{KN}$$
$$+ \varepsilon_U^{IMN}\lambda_3^u \left((\mathbf{Y}_d\mathbf{X}_d\mathbf{Y}_u^\dagger)^{JM}(\mathbf{Y}_d\mathbf{Y}_u^\dagger)^{KN} + (\mathbf{Y}_d\mathbf{Y}_u^\dagger)^{JM}(\mathbf{Y}_d\mathbf{X}_d\mathbf{Y}_u^\dagger)^{KN} \right)$$
$$+ \varepsilon_U^{IMN}\lambda_6^u(\mathbf{Y}_d\mathbf{X}_d\mathbf{Y}_u^\dagger)^{JM}(\mathbf{Y}_d\mathbf{X}_d\mathbf{Y}_u^\dagger)^{KN} , \qquad (6.42)$$

where the coefficients are ordered according to the number of Yukawa spurions.

The RPV soft-breaking term $\mathbf{A}_{udd}$ transforms exactly like $\mathbf{Y}_{udd}$ under the $SU(3)^3$ symmetry, so admits the same expansions, up to a pre-factor A_0 setting the soft-breaking scale, and of course a priori different coefficients. Therefore,

$$(\mathbf{A}_{udd}^Q)^{IJK} = A_0\, \varepsilon_Q^{LMN} \left(\mathbf{Y}_u(\kappa_1^q\mathbf{1} + \kappa_2^q\mathbf{X}_u + \kappa_3^q\mathbf{X}_d + \kappa_4^q\mathbf{X}_u^2 + \kappa_5^q\mathbf{X}_d^2 + \kappa_6^q\{\mathbf{X}_u, \mathbf{X}_d\} \right.$$
$$\left. + \kappa_7^q i[\mathbf{X}_u, \mathbf{X}_d] + \kappa_8^q i[\mathbf{X}_u^2, \mathbf{X}_d] + \kappa_9^q i[\mathbf{X}_u, \mathbf{X}_d^2]) \right)^{IL} \mathbf{Y}_d^{JM}\mathbf{Y}_d^{KN} , \qquad (6.43)$$

and similarly for $\mathbf{A}_{udd}^{U,D}$.

6.3.2 *The MFV limit for the RPV couplings*

At this stage, one may wonder why three different bases, Eqs. (6.40), (6.41), and (6.42), are constructed to parametrize $\mathbf{Y}_{udd}$ while any one of them is sufficient to project a completely arbitrary set of $\mathbf{Y}_{udd}^{IJK}$ couplings. Generalizing, it is clear that there is an infinity of equally valid bases of nine terms, at least from a mathematical point of view.

Though this is indeed true when these bases are just meant to parametrize generic couplings, the situation changes when MFV is enforced. Indeed, we must make sure that the MFV limit is stable and well-defined. More precisely, if a flavor coupling is expressed as a combination of Yukawa spurions with the adequate symmetry properties and $\mathcal{O}(1)$ coefficients, then by definition it satisfies the MFV requirement. Thus, once projected on a specific choice of basis, it must give back $\mathcal{O}(1)$ coefficients only. This is trivial if that particular combination of Yukawa spurions is part of the basis, but not automatic otherwise, as we now explore.

Internal stability of the epsilon contractions

Within a given basis, *i.e.*, for a given epsilon structure, the stability is ensured by the systematic use of the Cayley-Hamilton theorem. For example, if MFV holds, then $\langle \mathbf{Q}_8 \rangle$ in Eq. (6.38) and (6.39) is at most of $\mathcal{O}(1)$, hence can be absorbed into the coefficients without upsetting their scaling [392]. Therefore, both the $\mathbf{Y}_{udd}^Q$ and $\mathbf{Y}_{udd}^D$ bases are internally

consistent. On the other hand, the $\mathbf{Y}^U_{udd}$ basis must contain the λ^u_3 and λ^u_6 terms instead of, for example, $\varepsilon^{LMN}(\mathbf{Y}_u[\mathbf{X}^2_{u,d}, \mathbf{X}_{d,u}]\mathbf{Y}^\dagger_u)^{IL}(\mathbf{Y}_d\mathbf{Y}^\dagger_u)^{JM}(\mathbf{Y}_d\mathbf{Y}^\dagger_u)^{KN}$. If λ^u_3 and λ^u_6 were not part of the $\mathbf{Y}^U_{udd}$ basis, the other terms could not reproduce them with only $\mathcal{O}(1)$ coefficients because there is no matrix identity relating them. The converse holds though: the $\varepsilon^{LMN}(\mathbf{Y}_u[\mathbf{X}^2_{u,d}, \mathbf{X}_{d,u}]\mathbf{Y}^\dagger_u)^{IL}(\mathbf{Y}_d\mathbf{Y}^\dagger_u)^{JM}(\mathbf{Y}_d\mathbf{Y}^\dagger_u)^{KN}$ structures are so suppressed numerically (12 powers of Yukawa couplings) that no large coefficients are generated when projected on the $\mathbf{Y}^U_{udd}$ basis of Eq. (6.42).

Incompatibility between epsilon contractions

The stability of MFV within a given basis can be ensured, but not that between the bases with different epsilon contractions. Consider for example the identity:

$$\varepsilon^{LMN}(\mathbf{Y}_u\mathbf{Y}^\dagger_d\mathbf{Y}_d)^{IL}\mathbf{Y}^{JM}_d\mathbf{Y}^{KN}_d = \det(\mathbf{Y}_d)\varepsilon^{LJK}(\mathbf{Y}_u\mathbf{Y}^\dagger_d)^{IL} . \tag{6.44}$$

It shows that projecting the λ^d_1 structure of the $\mathbf{Y}^D_{udd}$ basis on the $\mathbf{Y}^Q_{udd}$ basis just produces the λ^q_3 term, but that $\lambda^q_3 = \lambda^d_1/\det(\mathbf{Y}_d)$. With $\det(\mathbf{Y}_d) \approx 10^{-10}\tan^3\beta$, it is clear that both λ^d_1 and λ^q_3 cannot be simultaneously of $\mathcal{O}(1)$. Thus, what is MFV for one basis is not necessarily MFV for another basis.

At this stage, there are two possible ways to restore a well-defined MFV principle. Either we combine terms from the three bases to construct a fully general one, or we constrain the possible U(1) breakings. For example, if only U(1)$_Q$ is broken, then only the $\mathbf{Y}^Q_{udd}$ basis is allowed. Indeed, once U(1)$_D$ and U(1)$_U$ are enforced, all the terms of the $\mathbf{Y}^D_{udd}$ and $\mathbf{Y}^U_{udd}$ bases are forbidden, since they involve an epsilon tensor acting in either SU(3)$_D$ or SU(3)$_U$. This latter alternative will be followed here, because allowing for the simultaneous presence of different U(1)-breaking terms would cause also other difficulties, as detailed below.

Compatibility with the R-parity conserving MFV expansions

When constructing the expansions of the soft-breaking terms, Eq. (6.29), the invariance under $U(3)^3$ is enforced. In principle, if the invariance under $SU(3)^3$ is imposed instead, additional terms should occur in their expansions, like for example

$$(\mathbf{m}^2_D)^{IJ}/m^2_0 \ni \varepsilon^{LMN}_Q\mathbf{Y}^{AL}_u\mathbf{Y}^{IM}_d\mathbf{Y}^{KN}_d \times \varepsilon^{RJK}_D(\mathbf{Y}_d\mathbf{Y}^\dagger_u)^{RA} , \tag{6.45}$$

or

$$\begin{aligned}(\mathbf{m}^2_D)^{IJ}/m^2_0 &\ni \varepsilon^{LMN}_Q\mathbf{Y}^{AL}_u\mathbf{Y}^{IM}_d\mathbf{Y}^{KN}_d \times \varepsilon^{RST}_Q\mathbf{Y}^{\dagger RA}_u\mathbf{Y}^{\dagger SJ}_d\mathbf{Y}^{\dagger TK}_d \\ &= \varepsilon^{LMN}_Q\varepsilon^{RST}_Q\mathbf{Y}^{IL}_d\mathbf{X}^{RM}_u\mathbf{X}^{SN}_d\mathbf{Y}^{\dagger TJ}_d .\end{aligned} \tag{6.46}$$

In this latter case, having two epsilons simultaneously acting on SU(3)$_Q$ actually preserves the corresponding U(1)$_Q$ symmetry, so this term must be redundant with those already present in Eq. (6.29). This can be checked explicitly by simplifying the epsilon contractions while maintaining the flavor symmetry manifest as

$$\begin{aligned}&\varepsilon^{LMN}\varepsilon^{RST}\mathbf{Y}^{IL}_d\mathbf{X}^{RM}_u\mathbf{X}^{SN}_d\mathbf{Y}^{\dagger TJ}_d \\ &= (\mathbf{Y}_d[\{\mathbf{X}_u, \mathbf{X}_d\} - \text{Tr}(\mathbf{X}_d)\mathbf{X}_u - \text{Tr}(\mathbf{X}_u)\mathbf{X}_d + \text{Tr}(\mathbf{X}_d)\text{Tr}(\mathbf{X}_u) - \text{Tr}(\mathbf{X}_u\mathbf{X}_d)]\mathbf{Y}^\dagger_d)^{IJ} .\end{aligned} \tag{6.47}$$

On the contrary, the term of Eq. (6.45) does not match those already present in Eq. (6.29). Even worse, if projected onto the MFV basis of Eq. (6.29), it generates large non-MFV coefficients. So, if one insists on the pure $\text{SU}(3)^3$ invariance, with all the U(1) simultaneously broken, the usual MFV basis for the R-parity conserving soft-breaking terms has to be extended.

It should be stressed that this is not just a matter of principle. Through the RG evolution, the soft-breaking terms receive corrections from the RPV couplings. For example, the one-loop β function of $\mathbf{m}_D^2$ contains [416, 417]

$$(\beta_{\mathbf{m}_D^2})^{IJ} \ni \mathbf{Y}_{udd}^{\dagger AIB} \mathbf{Y}_{udd}^{ACB} (\mathbf{m}_D^2)^{CJ} . \tag{6.48}$$

Therefore, if $\mathbf{Y}_{udd}$ or $\mathbf{A}_{udd}$ contain epsilon tensors acting in different SU(3) spaces, terms similar to that in Eq. (6.45) will occur. In that case, MFV would only be maintained through the RG evolution provided additional terms are included in the expansions of Eq. (6.29). For the time being, we prefer not to follow that route. We thus stick to the terms in Eq. (6.29), but must allow for only a single flavored U(1) to be broken when constructing the expansions for the RPV couplings $\mathbf{Y}_{udd}$ and $\mathbf{A}_{udd}$.

U(1) phases and Yukawa background values

In Section 2.4, we stated that it is always possible to perform $\text{U}(3)^3$ rotations to reach a basis where, e.g., $v_u \mathbf{Y}_u = \sqrt{2}\mathbf{m}_u \cdot V_{CKM}$ and $v_d \mathbf{Y}_d = \sqrt{2}\mathbf{m}_d$.[35] However, only the invariance under $\text{SU}(3)^3$ can be used in the construction of the $\mathbf{Y}_{udd}$ expansion. Because of this mismatch, these expansions may not fully fulfill their role of rendering $\mathbf{Y}_{udd}$ independent of the flavor basis: the unknown phases corresponding to the broken U(1) may affect the coefficients.

Let us be more precise. The singular value decompositions of the Yukawa couplings are

$$V_R^{u,d\dagger} \mathbf{Y}_{u,d} V_L^{u,d} = \mathbf{m}_{u,d} \sqrt{2}/v_{u,d} , \quad V_{CKM} = V_L^{u\dagger} V_L^d , \tag{6.49}$$

where $\mathbf{m}_{u,d}$ are diagonal and positive-definite, $V_R^{u,d} \in \text{U}(3)_{U,D}$ and $V_L^{u,d} \in U(3)_Q$. Clearly, V_L^u and V_R^u are defined up to a diagonal matrix of phases $D_u = \text{diag}(\exp(i\alpha_1^u), \exp(i\alpha_2^u), \exp(i\alpha_3^u))$, since $\mathbf{m}_u = D^\dagger \mathbf{m}_u D$, and similarly for the down sector. Requiring that $\mathbf{m}_{u,d}$ have real and positive entries only and that V_{CKM} is conventionally phased remove five linear combinations of the six phases. At that stage, $\det(V_L^u) = \det(V_L^d) \neq \det(V_R^u) \neq \det(V_R^d)$ in general, and they all depend on the remaining sixth phase. Therefore, it is always possible to force either $V_L^{u,d} \in \text{SU}(3)_Q$, or $V_R^u \in \text{SU}(3)_U$, or $V_R^d \in \text{SU}(3)_D$, but not more than that. Said differently, we need at least an exact $\text{SU}(3)_Q \otimes \text{U}(3)_U \otimes \text{U}(3)_D$, $\text{U}(3)_Q \otimes \text{SU}(3)_U \otimes \text{U}(3)_D$, or $\text{U}(3)_Q \otimes \text{U}(3)_U \otimes \text{SU}(3)_D$ flavor symmetry to reach the up- or down-basis.

Since two out of the three U(1)'s of $\text{U}(3)^3$ have to remain exact, only the epsilon tensor of a single SU(3) can occur in the expansions of the RPV couplings. This constraint prevents the phases of the expansion coefficients from depending on the flavor basis. For example, if both $\mathbf{Y}_{udd}^Q$ and $\mathbf{Y}_{udd}^D$ are present, then the phases of the $\mathbf{Y}_{udd}^Q$ coefficients depend on $\arg(\det(V_L^{u,d}))$ and those of $\mathbf{Y}_{udd}^D$ on $\arg(\det(V_R^d))$, but both $\arg(\det(V_L^{u,d}))$ and $\arg(\det(V_R^d))$ cannot be set to zero in general. Therefore, for this and the other reasons discussed above, we will restrict our attention to scenarios where only a single U(1) is broken in the rest of the study.

---

35 The actual argument was developed in the framework of the SM, but it applies equivalently to the MSSM.

	Broken $U(1)_Q$			Broken $U(1)_D$			Broken $U(1)_U$		
	ds	sb	db	ds	sb	db	ds	sb	db
u	10^{-14}	10^{-9}	10^{-11}	10^{-9}	10^{-9}	10^{-9}	10^{-12}	10^{-6}	10^{-8}
c	10^{-12}	10^{-7}	10^{-7}	10^{-5}	10^{-7}	10^{-5}	10^{-13}	10^{-9}	10^{-10}
t	10^{-7}	10^{-6}	10^{-6}	0.1	10^{-6}	10^{-4}	10^{-14}	10^{-13}	10^{-14}

Table 15: Typical hierarchies for the modulus of the $\mathbf{Y}_{udd}$ couplings (in the super-CKM basis) at the low scale under MFV with either $U(1)_Q$, $U(1)_D$, or $U(1)_U$ broken, and when $\tan\beta = 10$. Because $\mathbf{Y}_{udd}^{IJK}$ is antisymmetric under $J \leftrightarrow K$, its entries can be put in a 3×3 matrix form with $I = u, c, t$ and $JK = ds, sb, db$. Hierarchies for the RPV trilinear coupling $\mathbf{A}_{udd}/A_0$ are similar.

6.3.3 *Renormalization group evolution*

In the previous section, we have seen that simply asking for MFV to have a chance to remain valid through the running brings a strong restriction on its formulation. Only one U(1) can be broken at a time. Consequently, there are only three possible patterns of hierarchies for the RPV couplings when MFV is valid, and those depend only on $\tan\beta$. For example, with $\tan\beta = 10$, both $\mathbf{Y}_{udd}$ and $\mathbf{A}_{udd}/A_0$ scale as in Table 15.

In the present section, we investigate in details the evolution of the coefficients. We start with the broken $U(1)_Q$ scenario, whose main interest is to cover the special case of holomorphic MFV [425]. As a result, we will see that this scenario has several unique properties, not shared by any other couplings under MFV. By contrast, the behavior of the broken $U(1)_D$ or $U(1)_U$ scenarios is more in line with that of the RPC soft-breaking terms [392, 418]. This will be illustrated for the broken $U(1)_D$ case only. A detailed analysis of the $U(1)_U$ case is not very useful since it is similar. In addition, looking at Table 15, this scenario is much less interesting phenomenologically. First, the (s)top couplings are the largest when $U(1)_D$ is broken, but never exceed $\mathcal{O}(10^{-13})$ for $U(1)_U$. Such a large $\mathbf{Y}_{udd}^{tds}$ coupling of order 0.1 in the broken $U(1)_D$ scenario leads to the very interesting same-sign top quark signature [426–434] at the LHC but would therefore essentially disappear in the $U(1)_U$ broken scenario, and be replaced by the more challenging two or three light-jet resonances. Second, the couplings involving the up quark are the largest when $U(1)_U$ is broken, hence the superparticles have to be heavier to pass the current bounds on the proton lifetime or neutron oscillation. Finally, note that in all three scenarios some RPV couplings are tiny. This can indirectly constrain the supersymmetric mass spectrum because the squark lifetimes have to be short enough to circumvent R-hadron signatures [425, 430].

The RG evolution of the $\mathbf{A}_{udd}$ couplings will also be discussed for the broken $U(1)_Q$ and broken $U(1)_D$ scenarios, though briefly. Indeed, the impact of $\mathbf{A}_{udd}$ is very limited phenomenologically. Whenever an $\mathbf{A}_{udd}$ coupling is large, the corresponding $\mathbf{Y}_{udd}$ coupling is also large. So, if a squark can decay into two other squarks through $\mathbf{A}_{udd}$, it can also decay to the corresponding quarks through $\mathbf{Y}_{udd}$ with a larger available phase-space. For this reason, except maybe for a slight reduction in the RPV branching ratios to quark final states, even a relatively large $\mathbf{A}_{udd}$ coupling does not significantly affect the RPV signatures at the LHC.

Throughout this section, to illustrate the evolution of the RPV expansion coefficients in a realistic setting, we use a mSUGRA-like parameter point described in the next paragraph. We select the boundary conditions at the GUT scale so that, in the RPC case, the Higgs boson mass is close to 125 GeV. The impact of the RPV couplings on the particle spectrum is in general limited since most RPV couplings are very suppressed, hence will be neglected here.

6.3.3.1 *Numerical procedure and mass spectrum*

Throughout this analysis, we illustrate the behavior of the RPV couplings using a mSUGRA-like scenario with $\tan \beta = 10$ at the low scale. At the GUT scale, the boundary conditions are set as $m_{1/2} = m_0 = -A_0/2 = 1$ TeV, $m_{H_u}^2 = m_{H_d}^2 = (1.2 m_0)^2$ and $\mathbf{m}_{Q,U,D,L,E}^2 = m_0^2 \mathbb{1}$, $\mathbf{A}_{u,d,e} = A_0 \mathbf{Y}_{u,d,e}$. We do not fully unify the scalar masses in order to reproduce more easily the observed Higgs boson mass. Specifically, in the RPC case, running these values through SPheno 3.2.4 [435, 436], the Higgs sector mass spectrum is $m_h \approx 123$ GeV together with $m_A \approx m_H \approx m_{H^\pm} \approx 2.0$ TeV, while the spectrum is

$$m_{\tilde{g}} = 2.2 \text{ TeV} , \quad m_{\tilde{\chi}^\pm} = (0.82, \ 1.5) \text{ TeV} , \quad m_{\tilde{\chi}^0} = (0.43, \ 0.82, \ 1.5, \ 1.5) \text{ TeV} , \quad (6.50)$$

$$m_{\tilde{u}} = (1.4, \ 1.9, \ 2.2, \ 2.2, \ 2.2, \ 2.2) \text{ TeV} , \ m_{\tilde{d}} = (1.9, \ 2.1, \ 2.1, \ 2.1, \ 2.2, \ 2.2) \text{ TeV} , \quad (6.51)$$

$$m_{\tilde{e}} = (1.0, \ 1.1, \ 1.1, \ 1.2, \ 1.2, \ 1.2) \text{ TeV} , \ m_{\tilde{\nu}} = (1.2, \ 1.2, \ 1.2) \text{ TeV} . \quad (6.52)$$

Let us stress that this benchmark is not tailored to induce an interesting phenomenology at the LHC but rather, to illustrate the behavior of the RPV structure under the RG. To find interesting benchmarks for the LHC is certainly interesting, but beyond our scope here.

Turning to our numerical analysis, the one-loop RG equations [416, 417] are solved with custom Mathematica programs between $M_{\text{SUSY}} \equiv 1$ TeV and $M_X \equiv M_{GUT}$. We check that they agree at the percent level with SPheno in the CP- and R-parity conserving case. In the RPC case, at the low scale, the expansion coefficients for the RPC soft-breaking terms are compatible with MFV, with for example [see Eq. (6.29)]

$$a_i^q = (4.8, \ -3.0, \ -2.4, \ 0.27, \ 0.87, \ 0.93, \ 0.003, \ -0.004, \ -0.004) , \quad (6.53)$$

This, combined with the heavy superparticle masses ensure that all the flavor observables are in check in this scenario.

The SM parameters are set at M_Z and run up to M_{SUSY} using the two-loop RG equations [437]. The RPV couplings $\mathbf{Y}_{udd}$ and $\mathbf{A}_{udd}$ are set at the GUT scale in a basis-independent way through their expansion coefficients. The multiscale boundary conditions $\mathbf{Y}_{u,d,e}[M_{\text{SUSY}}]$ and $\mathbf{Y}_{udd}[M_{\text{GUT}}]$, with in addition $\mathbf{Y}_{udd}[M_{\text{GUT}}] = F(\mathbf{Y}_{u,d,e}[M_{\text{GUT}}])$ for some expansion F, are imposed iteratively. Starting with $\mathbf{Y}_{udd}^0[M_{\text{SUSY}}] = F(\mathbf{Y}_{u,d,e}[M_{\text{SUSY}}])$, a few iterations permit to find the input value $\mathbf{Y}_{udd}[M_{\text{SUSY}}]$ that evolves up to the desired $F(\mathbf{Y}_{u,d,e}[M_{\text{GUT}}])$. This is rather fast since only the supersymmetric parameters are involved at that stage.

We do not derive the RG equations for the expansion coefficients of $\mathbf{Y}_{udd}$ (nor of $\mathbf{A}_{udd}$). Instead, their evolutions are obtained indirectly by projecting $\mathbf{Y}_{udd}[M_Q]$ on one of the bases written in terms of $\mathbf{Y}_{u,d}[M_Q]$ at various intermediate scales M_Q. This means each time solving a linear system of nine equations, one for each of the independent entries of $\mathbf{Y}_{udd}[M_Q]$.

In practice, this is trickier than it seems because of the very large hierarchies involved. For example, the largest and smallest couplings of $\varepsilon^{LMN}(\mathbf{Y}_u\mathbf{X}_u^2)^{IL}\mathbf{Y}_d^{JM}\mathbf{Y}_d^{KN}$ are 22 orders of magnitude apart (because of a factor m_u^4/m_t^4). Both the evolution and the matching at M_{GUT} are therefore performed with a high numerical precision within `Mathematica`.

6.3.3.2 *RG invariance of MFV holomorphy*

The holomorphic restriction of MFV proposed in Ref. [425] originates from the hypothesis that the flavor symmetry is dynamical at some scale M_{Flavor}. There, the Yukawa spurions would either be true dynamical fields, or they would be directly related to those of this unknown flavor dynamics. At the same time, supersymmetry requires the superpotential to be holomorphic, so $\mathbf{Y}_{udd}$ must be insensitive to $\mathbf{Y}_u^\dagger$ and $\mathbf{Y}_d^\dagger$ above the scale M_{Flavor}. The most general flavor-symmetric expansion is then very simple, since there is only one way to write $\mathbf{Y}_{udd}$ in terms of $\mathbf{Y}_u$ and $\mathbf{Y}_d$:

$$\mathbf{Y}_{udd}^{IJK} = \lambda\,\varepsilon_Q^{LMN}\mathbf{Y}_u^{IL}\mathbf{Y}_d^{JM}\mathbf{Y}_d^{KN}\ . \tag{6.54}$$

The holomorphic restriction thus respects MFV under the $\mathrm{SU}(3)_Q\otimes \mathrm{U}(3)_U\otimes \mathrm{U}(3)_D$ flavor group. With only $\mathrm{U}(1)_Q$ broken, it respects all the requirements discussed in the previous section and MFV is stable and well defined.

However, the scale M_{Flavor} at which holomorphy is imposed could be very high. Even if MFV is in itself stable, whether holomorphy is a reasonable approximation at the low scale is not obvious. Indeed, the RG equations of the Yukawa and $\mathbf{Y}_{udd}$ couplings are coupled:[36]

$$\frac{d}{dt}\mathbf{Y}_u^{IJ} = \mathbf{Y}_u^{KJ}\gamma_{U^K}^{U^I} + \mathbf{Y}_u^{IJ}\gamma_{H_2}^{H_2} + \mathbf{Y}_u^{IK}\gamma_{Q^K}^{Q^J}\ , \tag{6.55}$$

$$\frac{d}{dt}\mathbf{Y}_d^{IJ} = \mathbf{Y}_d^{KJ}\gamma_{D^K}^{D^I} + \mathbf{Y}_d^{IJ}\gamma_{H_1}^{H_1} + \mathbf{Y}_d^{IK}\gamma_{Q^K}^{Q^J}\ , \tag{6.56}$$

$$\frac{d}{dt}\mathbf{Y}_{udd}^{IJK} = \mathbf{Y}_{udd}^{IJL}\gamma_{D^L}^{D^K} + \mathbf{Y}_{udd}^{ILK}\gamma_{D^L}^{D^J} + \mathbf{Y}_{udd}^{LJK}\gamma_{U^L}^{U^I}\ , \tag{6.57}$$

where $t = \log Q^2$. At one loop, $\gamma_{U^J}^{U^I}$, $\gamma_{D^J}^{D^I}$, and $\gamma_{Q^J}^{Q^I}$ all involve "non-holomorphic" spurion insertions. For example, $\gamma_{Q^J}^{Q^I}$ contains $\mathbf{Y}_u^\dagger\mathbf{Y}_u$ and $\mathbf{Y}_d^\dagger\mathbf{Y}_d$ terms. The consequence for the soft-breaking terms is well-known: even starting from universal squark masses $\mathbf{m}_Q^2 = \mathbf{m}_U^2 = \mathbf{m}_D^2 = m_0^2\mathbb{1}$ at the unification scale, the whole series of coefficients in Eq. (6.29) end up non-zero at the low scale. One would expect the same to happen for the $\mathbf{Y}_{udd}$ coupling: the whole series of coefficients in Eq. (6.40) would appear at the low scale.

Remarkably, the holomorphy of $\mathbf{Y}_{udd}$ holds at all scale because all these non-holomorphic effects precisely cancel out. This can be checked analytically:

$$\frac{d}{dt}\mathbf{Y}_{udd}^{IJK} = \frac{d}{dt}(\lambda\varepsilon_Q^{LMN}\mathbf{Y}_u^{IL}\mathbf{Y}_d^{JM}\mathbf{Y}_d^{KN})$$

$$= \lambda\varepsilon_Q^{LMN}\left(\frac{d\ln\lambda}{dt}\mathbf{Y}_u^{IL}\mathbf{Y}_d^{JM}\mathbf{Y}_d^{KN} + \frac{d\mathbf{Y}_u^{IL}}{dt}\mathbf{Y}_d^{JM}\mathbf{Y}_d^{KN} + \mathbf{Y}_u^{IL}\frac{d\mathbf{Y}_d^{JM}}{dt}\mathbf{Y}_d^{KN} + \mathbf{Y}_u^{IL}\mathbf{Y}_d^{JM}\frac{d\mathbf{Y}_d^{KN}}{dt}\right)$$

$$= \mathbf{Y}_{udd}^{IJK}\left(\frac{d\ln\lambda}{dt} + \gamma_{Q^P}^{Q^P} + \gamma_{H_2}^{H_2} + 2\gamma_{H_1}^{H_1}\right) + \frac{d}{dt}\mathbf{Y}_{udd}^{IJK}\ . \tag{6.58}$$

---

36 We follow the notations of Ref. [416, 417], with a slight change of conventions in the indices.

To reach the last line, the following identity derived from the Cayley-Hamilton theorem was used,

$$\gamma_{Q^P}^{Q^P}\varepsilon^{LMN} = \varepsilon^{PMN}\gamma_{Q^L}^{Q^P} + \varepsilon^{LPN}\gamma_{Q^M}^{Q^P} + \varepsilon^{LMP}\gamma_{Q^N}^{Q^P} . \tag{6.59}$$

Then, the whole evolution of the holomorphic $\mathbf{Y}_{udd}$ can be encoded into a single coefficient:

$$\frac{d\lambda}{dt} = -\lambda\beta_\lambda , \quad \beta_\lambda = \gamma_{Q^P}^{Q^P} + \gamma_{H_2}^{H_2} + 2\gamma_{H_1}^{H_1} . \tag{6.60}$$

The linear dependence of $d\lambda/dt$ over λ ensures the RG invariance of $\lambda = 0$, when R-parity is unbroken. The beta function β_λ involves only purely left-handed anomalous terms: its sole role is to compensate for the left-handed evolutions of the Yukawa couplings, since $\mathbf{Y}_{udd}$ evolves according to right-handed anomalous terms only. It is important to realize that while MFV holomorphy is an RG invariant property of $\mathbf{Y}_{udd}$, these couplings are far from invariant numerically. Not only is the coefficient evolving, but the Yukawa couplings on which $\mathbf{Y}_{udd}$ is defined are themselves scale-dependent.

At the one-loop order, the beta function of the coefficient λ is [416, 417]

$$\beta_\lambda = \frac{1}{32\pi^2}(4\langle\mathbf{Y}_u^\dagger\mathbf{Y}_u\rangle + 7\langle\mathbf{Y}_d^\dagger\mathbf{Y}_d\rangle + 2\langle\mathbf{Y}_e^\dagger\mathbf{Y}_e\rangle - g_1^2 - 9g_2^2 - 8g_3^2) , \tag{6.61}$$

where g_1, g_2, and g_3 are the $U(1)_Y$, $SU(2)_L$, and $SU(3)_c$ gauge couplings (with the $SU(5)$ normalization for the hypercharge). The leading order RG equation of λ can easily be solved. Indeed, the evolution of the Yukawa couplings depends quadratically on $\mathbf{Y}_{udd}$, whose maximal entry in the holomorphic case is about $\lambda \times 10^{-4}$ when $\tan\beta \approx 50$. Except for very large non-MFV values of the coefficient, the impact of $\mathbf{Y}_{udd}$ on $\mathbf{Y}_{u,d}$ is completely negligible. So, the ratio between the coefficients at the GUT scale and M_{SUSY} is immediately found once the RPC evolution of the Yukawa and gauge couplings is known,

$$\frac{\lambda[M_{\mathrm{SUSY}}]}{\lambda[M_{\mathrm{GUT}}]} = \exp\left\{-\int_{\log M_{\mathrm{SUSY}}^2}^{\log M_{\mathrm{GUT}}^2}\beta_\lambda(t)dt\right\} \approx \exp\left\{-\frac{1}{32\pi^2}\int_{\log M_{\mathrm{SUSY}}^2}^{\log M_{\mathrm{GUT}}^2}(4y_t^2 - 9g_2^2 - 8g_3^2)dt\right\}_{\mathrm{RPC}} . \tag{6.62}$$

Numerically, the right-hand side has only a very weak dependence on the rest of the MSSM parameters. Though the sensitivity is a bit enhanced by the exponential, we find that with $M_{\mathrm{SUSY}} \approx 1$ TeV, the ratio is quite stable, varying within $1/5$ and $1/4$. For the point considered in this analysis, we get $\lambda[M_{\mathrm{SUSY}}]/\lambda[M_{\mathrm{GUT}}] \approx 0.22$. Note though that the $\mathbf{Y}_{udd}$ couplings are nevertheless larger at the low scale because the decrease of λ is more than compensated by the increase of the Yukawa couplings.

The other RPC parameters are also insensitive to $\mathbf{Y}_{udd}$ when λ is of $\mathcal{O}(1)$, as well as to the RPV soft-breaking term $\mathbf{A}_{udd}$ when its overall mass scale is of the same order as that of $\mathbf{A}_u$ and $\mathbf{A}_d$ (*i.e.*, all are tuned by the same A_0 parameter, see Eq. (6.34)). Indeed, under these assumptions and since holomorphy does not apply to soft breaking terms, $\mathbf{A}_{udd}$ admits an expansion of the form in Eq. (6.43) with the nine κ_i^q coefficients of $\mathcal{O}(1)$ or less. Numerically, all the $\mathbf{A}_{udd}$ couplings are then very suppressed compared to $\mathbf{A}_u$ and $\mathbf{A}_d$.

On the other hand, $\mathbf{Y}_{udd}$ does affect $\mathbf{A}_{udd}$ significantly. Even starting from $\mathbf{A}_{udd}^{IJK}[M_{\mathrm{GUT}}] = 0$, it is radiatively induced entirely through $\mathbf{Y}_{udd}$ and end up sizeable at the low scale. For instance, with $\lambda[M_{\mathrm{GUT}}] = 1$ and $\kappa_i^q[M_{\mathrm{GUT}}] = 0$, we find that the MFV coefficients at M_{SUSY} for $\mathbf{A}_{udd}$ are

$$\kappa_{1,2,3}^q[M_{\mathrm{SUSY}}] = (0.36, -0.12, 0.12) , \quad \kappa_{4,\ldots,9}^q \lesssim 10^{-3} . \tag{6.63}$$
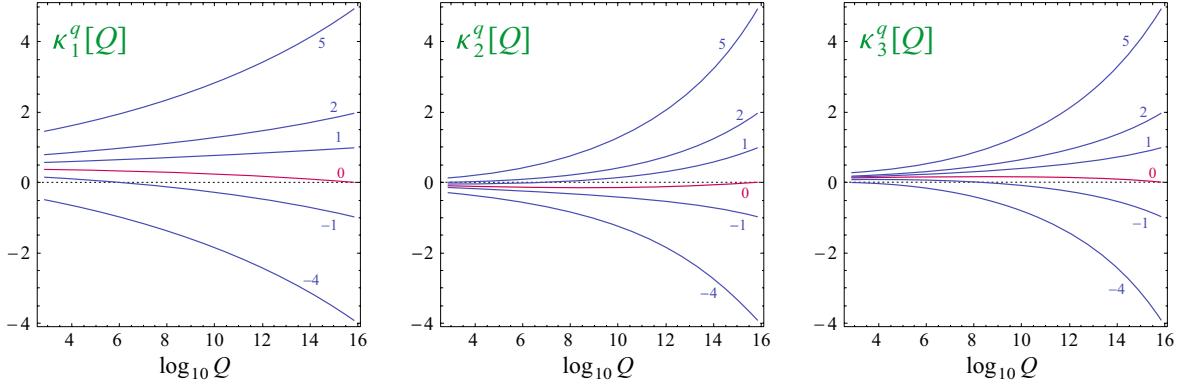
Figure 6.1: Evolution of the leading coefficients for the trilinear couplings $\mathbf{A}_{udd}$ in the holomorphic scenario, with $\lambda[M_{\mathrm{GUT}}] = 1$, together with $\kappa_i^q[M_{\mathrm{GUT}}] = \kappa\delta_{ia}$ where $\kappa = \{-4, -1, 0, 1, 2, 5\}$ and $a = 1$ (left), $a = 2$ (middle), and $a = 3$ (right). The central curves (in red) correspond to the purely radiative generation, with the values at $M_{\mathrm{SUSY}} = 1$ TeV given in Eq. (6.63).

The first three coefficients scale linearly with $\lambda[M_{\mathrm{GUT}}]$, so $\kappa_1^q[M_{\mathrm{SUSY}}]$ stays of the order of $\lambda[M_{\mathrm{SUSY}}]$. The radiative feeding of $\mathbf{A}_{udd}$ by $\mathbf{Y}_{udd}$ is thus quite intense; it is impossible to have $\mathbf{A}_{udd}^{IJK}[M_{\mathrm{SUSY}}] \approx 0$ once $\lambda[M_{\mathrm{GUT}}]$ is turned on. Also, note that even though the leading coefficient is the largest, even a radiatively-induced $\mathbf{A}_{udd}[M_{\mathrm{SUSY}}]$ is not holomorphic at the low scale. In addition, these values are rather stable. If one starts with a non-vanishing $\mathbf{A}_{udd}$ at the GUT scale, the RG evolution pushes the κ_i^q coefficients back to the same values as in Eq. (6.63). As shown in Fig. 6.1, this fixed-point behavior is impressively effective for the subleading coefficients. Thus, in the holomorphic case, not only $\mathbf{Y}_{udd}[M_{\mathrm{SUSY}}]$ depends on the single input parameter $\lambda[M_{\mathrm{GUT}}]$, but to a good approximation also $\mathbf{A}_{udd}[M_{\mathrm{SUSY}}]$ since $\lambda[M_{\mathrm{GUT}}]$ defines the fixed-point values of Eq. (6.63).

6.3.3.3 *Holomorphy as an attractor*

If $\mathbf{Y}_{udd}$ is not holomorphic at some scale, it will remain so at all scales since the subleading expansion coefficients λ_i^q of $\mathbf{Y}_{udd}^Q$ are non-zero. Looking back at Eq. (6.40), it is clear that these coefficients do not multiply RG invariant structures. Rather, through the evolution, all of these coefficients contribute a priori to all the others.

What is remarkable is that the holomorphic scenario of Ref. [425] emerges as an infrared (IR) fixed point. Specifically, starting from some non-zero $\lambda_{i\neq1}^q$ at the GUT scale, they all evolve towards much reduced values at the low scale. For example, starting with

$$\lambda_i^q[M_{\mathrm{GUT}}] = (1,\ 1,\ 1,\ 1,\ 1,\ 1,\ 1,\ 1,\ 1)\,, \tag{6.64}$$

the leading coefficient evolves by itself, while all the others are suppressed by more than an order of magnitude:

$$\begin{aligned}\lambda_i^q[M_{\mathrm{SUSY}}] = &(0.221,\ 0.049,\ 0.031,\ 0.079,\ 0.023,\ 0.025,\ 0.013,\ -0.005,\ 0.007)\\ &+ i(0.000,\ 0.000,\ 0.000,\ 0.000,\ -0.001,\ 0.001,\ 0.003,\ 0.008,\ 0.003)\,.\end{aligned} \tag{6.65}$$

This convergence towards zero is effective even when the starting values $\lambda_{i\neq1}^q[M_{\mathrm{GUT}}]$ are much larger than one, as illustrated in Fig. 6.2 for λ_2^q and λ_3^q. The scaling between the
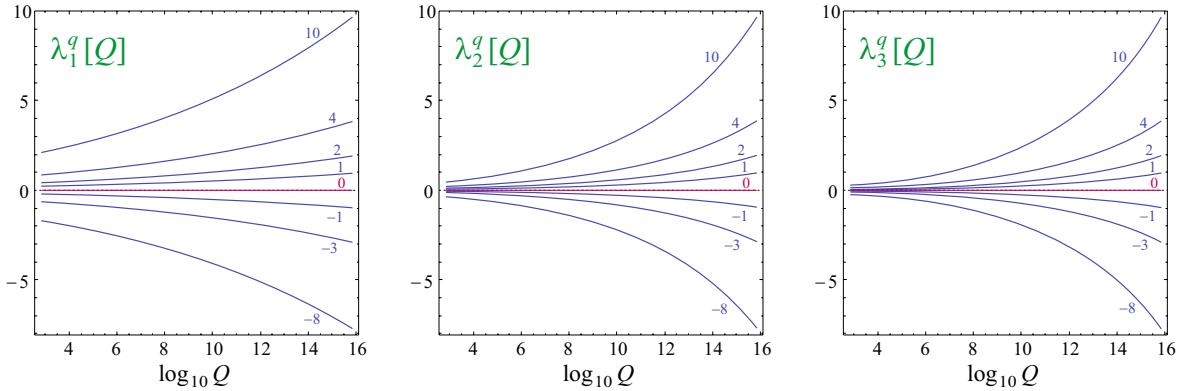
Figure 6.2: Evolution of the leading coefficients of $\mathbf{Y}_{udd}$ in the broken $U(1)_Q$ scenario. At the GUT scale, $\lambda_i^q[M_{\mathrm{GUT}}] = \lambda\delta_{i1}$ (left), $\lambda_i^q[M_{\mathrm{GUT}}] = \delta_{i1} + \lambda\delta_{i2}$ (middle), and $\lambda_i^q[M_{\mathrm{GUT}}] = \delta_{i1} + \lambda\delta_{i3}$ (right), with $\lambda = \{-8, -3, -1, 0, 1, 2, 4, 10\}$. The left-hand plot corresponds to the pure holomorphic case, and shows the factor ~ 5 reduction, see Eq. (6.62). The other two plots show that the sub-leading coefficients always converge towards zero, i.e., $\mathbf{Y}_{udd}$ runs towards a pure holomorphic form.

values at the GUT and SUSY scale is mostly linear, with for example $\lambda_{i\neq1}^q[M_{\mathrm{GUT}}] \sim \mathcal{O}(100)$ leading to $\lambda_{i\neq1}^q[M_{\mathrm{SUSY}}] \sim \mathcal{O}(1)$. This observation has an important corollary: if any of the $\lambda_{i\neq1}^q$ is $\mathcal{O}(1)$ or larger at the low-scale, then they necessarily evolve towards non-MFV values at the GUT scale.

This behavior is similar to that of the coefficients of the RPC soft-breaking terms discussed in Refs. [392, 418], but for two differences. First, it is much more pronounced in the present case. The IR values are very small, $\lambda_{i\neq1}^q[M_{\mathrm{SUSY}}] \ll 1$, while the RPC soft-breaking coefficients are $\mathcal{O}(1)$ at the low scale in general. Second, the values of the IR fixed points of all the $\lambda_{i\neq1}^q$ are trivially independent of the SUSY parameters since they are simply zero. On the contrary, for the RPC soft-breaking terms, the IR values depend on the MSSM parameters (gluino mass, scalar masses, etc), hence were dubbed "quasi" fixed points in Ref. [392].

The presence of this unique and true fixed point is of immediate phenomenological relevance. If MFV is active at some very high scale and if $U(1)_Q$ is broken, then to an excellent approximation, $\mathbf{Y}_{udd}[M_{\mathrm{SUSY}}]$ is holomorphic at the low scale since the subleading coefficients $\lambda_{i\neq1}^q[M_{\mathrm{SUSY}}]$ are tiny. The non-holomorphic corrections to $\mathbf{Y}_{udd}[M_{\mathrm{SUSY}}]$, which are in any case rather suppressed since they involve more Yukawa couplings, are thus entirely negligible and the whole baryonic RPV sector can be parametrized by a single parameter.

6.3.3.4 *Comparison with the broken $U(1)_D$ case*

To illustrate how peculiar is the behavior of $\mathbf{Y}_{udd}^Q$, we perform the same analysis with $\mathbf{Y}_{udd}^D$ instead. To start with, let us evolve down the leading $\mathbf{Y}_{udd}^D$ structure, i.e., $\lambda_i^d[M_{\mathrm{GUT}}] = \delta_{1i}$. At the low-scale, the whole series of nine coefficients is generated:

$$\begin{aligned}
\lambda_i^d[M_{\mathrm{SUSY}}] = &\ (0.54,\ 0.10,\ 0.25,\ 0.06,\ 0.09,\ 0.02,\ 0.03,\ 0.04,\ 0.00) \\
&+ i(0.00,\ 0.00,\ 0.00,\ 0.00,\ 0.00,\ 0.00,\ 0.03,\ -0.03,\ 0.03)\ .
\end{aligned} \tag{6.66}$$
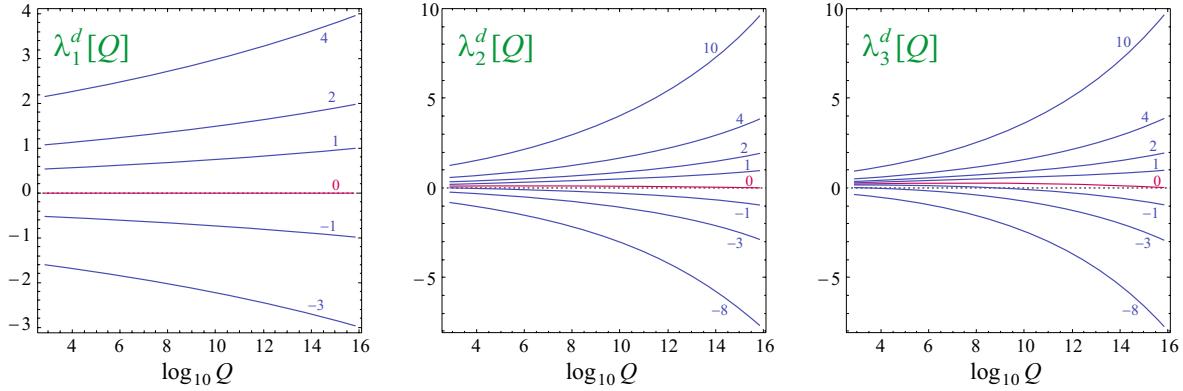
Figure 6.3: Evolution of the leading coefficients of $\mathbf{Y}_{udd}$ in the broken $U(1)_D$ scenario. At the GUT scale, $\lambda_i^d[M_{\mathrm{GUT}}] = \lambda\delta_{i1}$ (left), $\lambda_i^d[M_{\mathrm{GUT}}] = \delta_{i1} + \lambda\delta_{i2}$ (middle), and $\lambda_i^d[M_{\mathrm{GUT}}] = \delta_{i1} + \lambda\delta_{i3}$ (right), with $\lambda = \{-8, -3, -1, 0, 1, 2, 4, 10\}$. For the left-hand plot, $|\lambda|$ is limited to be less than about 5, otherwise the large $\mathbf{Y}_{tds}$ coupling renders the RGE numerically unstable. For the other two, the central curves (in red) correspond to the purely radiative generation, with the values at $M_{\mathrm{SUSY}} = 1$ TeV given in Eq. (6.66).

For comparison, if we now set all the $\mathbf{Y}_{udd}^D$ coefficients to one at the GUT scale,

$$\lambda_i^d[M_{\mathrm{GUT}}] = (1,\ 1,\ 1,\ 1,\ 1,\ 1,\ 1,\ 1,\ 1)\,, \tag{6.67}$$

we find the low-scale values,

$$\begin{aligned}\lambda_i^d[M_{\mathrm{SUSY}}] =\ & (0.54,\ 0.22,\ 0.32,\ 0.32,\ 0.16,\ 0.14,\ 0.11,\ 0.09,\ 0.03) \\ & + i(0.00,\ 0.00,\ 0.00,\ 0.00,\ 0.01,\ 0.00,\ 0.01,\ -0.16,\ 0.11)\,.\end{aligned} \tag{6.68}$$

These examples show that MFV is preserved through the running, but the subleading coefficients are not particularly reduced at the low scale. Compared to the broken $\mathrm{U}(1)_Q$ scenario, the leading coefficient λ_1^d still evolves essentially independently of the others but the $\lambda_{i\neq1}^d$ do not converge towards zero. This can be seen in Fig. 6.3, where the evolutions of λ_1^d, λ_2^d, and λ_3^d are shown for various boundary conditions. Though a strong convergence of λ_2^d and λ_3^d towards their purely radiative values of Eq. (6.66) is apparent, these are not true fixed points. Indeed, being finite, they must necessarily depend on the specific MSSM scenario. In other words, for a different choice of MSSM parameters, λ_2^d and λ_3^d would run towards different values.

The existence of these IR fixed points implies that MFV at the low scale does not necessarily transcribe into MFV at the high scale. In view of Fig. 6.3, it is clear that low scale values of a few units for λ_2^d or λ_3^d correspond to large non-MFV values at the GUT scale. So, imposing that MFV remains valid at all scales requires $\lambda_i^d[M_{\mathrm{SUSY}}] \lesssim 1$ when $\lambda_1^d[M_{\mathrm{GUT}}] = 1$. Note also that at the GUT scale, $\lambda_1^d[M_{\mathrm{GUT}}]$ cannot exceed a few units, because otherwise $\mathbf{Y}_{tds}^D[M_{\mathrm{GUT}}] > 1$ and perturbativity collapses. In this respect, it must be stressed that when $\lambda_1^d[M_{\mathrm{GUT}}] \approx 1$, the impact of $\mathbf{Y}_{udd}^D$ on the Yukawa couplings and on the soft-breaking terms is far from negligible. Given that the mSUGRA parameters used throughout this work are quite fine-tuned to get a viable mass spectrum in the R-parity conserving case, especially a Higgs boson mass of around 125 GeV, the above numerical evaluations should be understood as illustrations for the behavior of the coefficients.
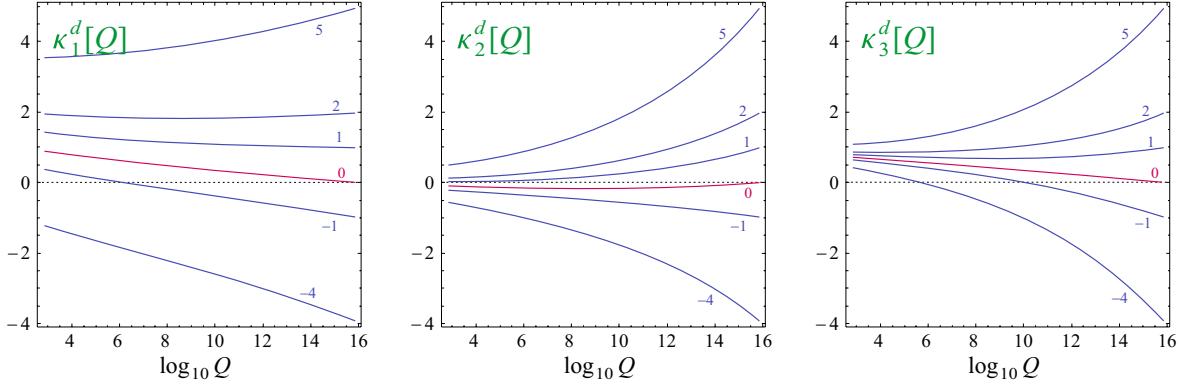
Figure 6.4: Evolution of the leading coefficients for the trilinear couplings $\mathbf{A}_{udd}$ in the broken $U(1)_D$ scenario. At the GUT scale, $\lambda_i^d[M_{\mathrm{GUT}}] = \delta_{i1}$ and $\kappa_i^d[M_{\mathrm{GUT}}] = \kappa\delta_{ia}$ where $\kappa = \{-4, -1, 0, 1, 2, 5\}$ and $a = 1$ (left), $a = 2$ (middle), and $a = 3$ (right). The central curves (in red) correspond to the purely radiative generation, with the values at $M_{\mathrm{SUSY}} = 1$ TeV given in Eq. (6.69).

Finally, in the soft-breaking sector, the radiative generation of $\mathbf{A}_{udd}^D$ from $\mathbf{Y}_{udd}^D$ is even stronger than in the holomorphic case, with for example

$$\kappa_i^d[M_{\mathrm{SUSY}}] = (0.89,\ -0.12,\ 0.69,\ 0.02,\ 0.23,\ -0.06,\ 0.04,\ 0.06,\ 0.01)$$
$$+ i(0.00,\ 0.00,\ 0.00,\ 0.00,\ 0.00,\ 0.00,\ 0.05,\ -0.05,\ 0.09)\,, \qquad (6.69)$$

when starting with $\kappa_i^d[M_{\mathrm{GUT}}] = 0$ and $\lambda_i^d[M_{\mathrm{GUT}}] = \delta_{i1}$. If we instead allow for non-zero values for the $\mathbf{A}_{udd}^D[M_{\mathrm{GUT}}]$ coefficients, their low-scale values all respect the MFV principle, and a quasi-fixed point behavior is again apparent, see Fig. 6.4.

All in all, the evolution of the scenario based on $U(3)_Q \otimes U(3)_U \otimes SU(3)_D$ is less simple than for the one based on $SU(3)_Q \otimes U(3)_U \otimes U(3)_D$, which is very peculiar because of the presence of the holomorphic true fixed point. Still, the behaviors of the coefficients of $\mathbf{Y}_{udd}^D$ and $\mathbf{A}_{udd}^D$ remain rather smooth, MFV is preserved down from the GUT scale, and quasi-fixed points in the IR are apparent (the same could be said for $\mathbf{Y}_{udd}^U$ and $\mathbf{A}_{udd}^U$ in the broken $U(1)_U$ scenario). Actually, this is perfectly in line with the behaviors of the coefficients of the RPC sector [392, 418].

6.3.4 *Summary*

We have analyzed the behavior of the R-parity violating couplings under the renormalization group evolution. Particular emphasis is laid on the MFV restriction since it permits to naturally pass all the bounds from proton decay or neutron oscillations even for relatively light superparticles [389]. To this end, the formulation of the MFV hypothesis in the RPV sector first had to be made more precise and robust.

A basis-independent parametrization of generic baryonic R-parity violating couplings was constructed, in a similar way to that for the R-parity conserving soft-breaking terms of the slepton sector in Ref. [390] and of the squark sector in Ref. [424]. It trades the 18 independent RPV couplings for 18 free expansion parameters, whose numerical values are independent of the flavor basis chosen for the (s)quark fields. As such, they thus fully

encode the RPV sector. In particular, they permit to describe the whole RG evolution of the RPV couplings.

We have shown that in order to impose MFV on the whole R-parity violating MSSM and at vastly different scales, it is necessary to restrict the flavor symmetry group. Out of the U(3)^3 symmetry of the (s)quark kinetic terms, only one U(1) can be broken at a time. If not the case, the $\mathcal{O}(1)$ naturality criterion for expansion coefficients becomes ambiguous and issues with the usual MFV expansions in the R-parity conserving sector arise. On the other hand, once properly set, the multi-scale MFV hypothesis is rather resilient. The RG evolution of the RPV expansion coefficients displays striking infrared fixed or quasi-fixed point behavior, ensuring that MFV at the low scale arises even from far from-MFV scenarios at the unification scale. The corollary also holds: if the expansion coefficients at the low scale are $\mathcal{O}(1)$ but far from their (quasi-) fixed points, then MFV is lost at the unification scale. In these respects, the RPV sector behaves very similarly to the R-parity conserving soft-breaking sector [392, 418].

Finally, we have explored the RG behavior of the holomorphic MFV scenario. First, we proved analytically that the holomorphic restriction is RG invariant. This has far-reaching consequences. In particular, it implies that holomorphy acts as a powerful infrared attractor for the RG evolution. If present at the high scale, all the non-holomorphic corrections evolve towards zero at the low scale. Whether exact or approximate, low-scale holomorphy thus systematically emerges as the phenomenological paradigm once the broken flavored U(1) is that of the quark doublet.

Part IV

CONCLUSIONS

7

CONCLUSIONS

As of May 2016, the LHC has just re-started to collect data at 13 TeV and the ATLAS and CMS experiments are expected to deliver new results in Summer 2016. The next few months, or years for sure, will shape the future of particle physics for the decades to come, and ultimately, of our comprehension of the electroweak symmetry breaking mechanism realized in nature. If a discovery near the TeV scale is made, and its link to the electroweak sector is confirmed, this may be the long-sighted hint for a natural solution to the SM hierarchy problem. Deviations of the SM predictions may also indirectly point out the presence of new physics, in particular in the Higgs couplings and in the flavor sector. Of course such discoveries are not guaranteed and null-results from future LHC analyses would dramatically affect the level of fine-tuning needed to interpret the hierarchy between the electroweak and Planck scales.

As of now, all eyes are on the tantalizing di-photon excess observed by both ATLAS [362] and CMS [363] in December 2015 at a common mass of around 750 GeV. With only a handful of observed events, little is actually currently known about the properties of this potential signal. Similar excesses in the ZZ or $Z\gamma$ channels in particular, though not observed so far, would strongly hint at a particle interpretation of this signal and would put aside the statistical fluctuation interpretation. The next release of analyses at 13 TeV will prove decisive for such an interpretation. The best case scenario would be an increase of the significance of the excess, associated with observations in the previously evoked channels. The announcement of this di-photon excess generated a tremendous reaction from the phenomenology side, with hundreds of (variations of) models explaining this excess proposed in a few weeks. An important conclusion derived from these studies is that the minimal versions of models solving the hierarchy problem are generally inconsistent with this signal, and more baroque versions are needed. Taking quite a different direction, together with Christopher Smith, we proposed a three-body interpretation of this excess without invoking a 750 GeV state, $A \to B\gamma\gamma$ where A and B could be either scalars, fermions or vectors, this was published in Physics Letters B under the title "*Could the width of the diphoton anomaly signal a three-body decay ?*" [438]. This special kinematic configuration, along with other ones, were later further characterized from a collider perspective with Andreas Goudelis, Sabine Kraml, Kentarou Mawatari and Dipan Sengupta in "*Characterising the 750 GeV diphoton excess*" [439], published in Journal of High Energy Physics. Despite their physical content, these studies were not presented in this manuscript as the signal they describe may very soon be considered as a mere statistical fluke. On the contrary, a confirmation of this signal may rule out the 2HDM scenarios described in Chapter 5. In August 2016, with increased luminosity, the ATLAS and CMS collaborations updated this

207

di-photon search [364, 365] and found an important decrease of the significance of this excess, hinting strongly to a statistical fluctuation interpretation of the December 2015 anomaly.

The observed Higgs boson is certainly a direct window to the hypothetical new physics present beyond the SM and the precision study of its properties is one of the main goal of the LHC program. In the first part of this thesis manuscript, we described how the measurements of the Higgs production and decay rates at colliders can provide crucial information on new physics models. To this end, the public tool `Lilith` was developed and presented. `Lilith` uses as primary experimental inputs signal strengths in physical categories, *i.e.*, in pure production and decay modes space. Modifications of the Higgs rates can then consistently be taken into account in this framework through the parametrization of the signal strengths by reduced couplings. Theoretically, this requires that the underlying interaction operators between the Higgs boson and other SM particles have the same Lorentz tensor structure as in the SM, or that operators with a different tensor structure have small effects. The latter operators would indeed imply distortions of the kinematic distributions of the Higgs boson and its decay products, which would consequently modify the acceptance and efficiency of the experimental selection cuts and thus invalidate the interpretation of the signals strengths. Using `Lilith`, we performed a global fit to the final results of the first run of the LHC in a variety of benchmark scenarios, taking into account the possibility of invisible or undetected new decay channels. No deviation from the SM expectations was observed. The current uncertainties on the reduced couplings range within 20 to 40% depending on their nature and on the benchmark model, thus still leaving sizable room for possible deviations to be probed in the second LHC run.

In the second part of the manuscript, we were interested in the possibility that the low-energy Higgs sector is comprised of two weak doublets. The two-Higgs-doublet model was used here as a possible effective model relevant for LHC physics. In multi-doublet Higgs sectors, there is a special limit in which one of the CP-even mass eigenstates aligns with the direction of the vacuum expectation values of the various doublets in field space. This alignment limit immediately confers SM-like properties to this state. The presence of extra scalar states, such as the charged Higgs bosons, can however lead to sizable modifications of these properties, yet to be observed. As the Higgs couplings are observed to be very close to the SM ones, the alignment limit of the 2HDM is a very well motivated parameter space region. Here, taking into account all relevant experiment constraints, we focused on the alignment limit of the Type I and Type II 2HDMs and explored their phenomenologies at the 13 TeV LHC. The two CP-even Higgs mass eigenstates of the 2HDM can in principle be identified with the 125 GeV observed state and both these cases were systematically analyzed in detail. The alignment limit does not require a decoupling of the extra Higgs states. Instead, they can be quite light and hence directly accessible at the LHC. We also considered the seemingly extreme case in which the 2HDM spectrum exhibits one or two scalar states light enough such that the 125 GeV state could decay into them. We identified a number of channels that could provide severe or even total exclusion of some of the scenarios investigated here, through the next few years of LHC measurements. Precision measurements of the observed Higgs properties were also shown to significantly probe these scenarios.

The SM flavor sector, through its Yukawa couplings and the CKM matrix, is impressively successful. So far, no deviation from its predictions was ever confirmed experimentally. On phenomenological grounds, flavor structures beyond the SM should therefore either be effectively harmless, which is the case if the new flavored particles are decoupled, or they should be highly hierarchical. We have argued that the Yukawa couplings are already highly non-generic in the SM and a similar amount of fine tuning could therefore also be acceptable for these new flavor structures. In particular, if they were somehow aligned with the Yukawa couplings, the flavor puzzles present beyond the SM would be significantly softened. In the last part of the manuscript, we have defined the Minimal Flavor Violation hypothesis, as a way to systematically enforce this flavor alignment in a well-defined manner, using a symmetry principle. An important motivation for it could be found in the hypothetical fundamental mechanism at the origin of the flavor structures. Since this mechanism presumably takes place at a very high scale, the stability of the flavor alignment down to low-scales should explicitly be checked. In principle, there is indeed no reason why it should hold under the renormalization group. Only if it does, could the flavor puzzles truly be softened. We performed this RG evolution study for the baryonic R-parity couplings of the MSSM. After constructing the required flavor expansions for these couplings, we showed that MFV was not only present at low-scales for reasonable high-scale initial conditions, it was even reinforced through the RG evolution. The holomorphic MFV scenario was in particular shown to enjoy remarkable properties under the RG. As a consequence, the broken $U(1)_Q$ scenarios at low energy were shown to be parametrizable with a single parameter to a very good precision, due to the powerful holomorphic infrared attractor. All in all, this gives a clear motivation for the possibility of low-scale baryon number violation.

With about fifteen orders of magnitude separating the TeV and Planck scales, new physics has a significant latitude to kick in. Present days are however crucial for fundamental physics, with the LHC probing unexplored territories with unprecedented energy reach and precision. At any time in the next few weeks, months or maybe years, a dramatic conceptual change of our vision of nature may arise if naturalness arguments are of any guide. Let us hope to see null-results turning to hints, hints turning to discoveries, and the Standard Model's title losing its meaning very soon.

Version française

En Mai 2016, le LHC vient de recommencer à acquérir des données à une énergie de centre de masse de 13 TeV. Les collaborations ATLAS et CMS devraient annoncer de nouveaux résultats durant l'été 2016. Les prochains mois, ou années pour sûr, vont être décisifs pour le futur de la physique des particules et, au final, pour notre niveau de compréhension du mécanisme à l'origine de la brisure de la symétrie électrofaible réalisé dans la nature. Si une découverte à l'échelle du TeV est réalisée, et que son lien avec le secteur électrofaible est avéré, cela pourrait être l'indice tant attendu d'une possible solution naturelle au problème de la hiérarchie du Modèle Standard (MS). Des déviations des prédictions du MS pourraient également indirectement signaler la présence de nouvelle physique, en particulier dans les couplages du boson de Higgs et dans le secteur de la saveur. Bien entendu, ces découvertes ne sont en aucun cas garanties et des résultats nuls des analyses futures du LHC pourraient dramatiquement affecter le niveau d'ajustement nécessaire pour interpréter la hiérarchie entre l'échelle électrofaible et celle de Planck.

Actuellement, tous les regards sont portés sur l'excès di-photon observé par ATLAS [362] et CMS [363] à une masse commune d'environ 750 GeV. Avec seulement un petit nombre d'évènements observés, les propriétés de ce signal potentiel sont peu connues. Des excès similaires dans les canaux de désintégration en ZZ, $Z\gamma$ ou jj en particulier, non observés jusqu'à présent, renforcerait la réalité de ce signal et pourrait balayer l'hypothèse d'une simple fluctuation statistique. Les prochaines analyses à 13 TeV vont être décisives et devraient définitivement confirmer ou infirmer la présence d'une telle particule. Dans le meilleur des cas, la significance du signal di-photon augmenterait avec l'ajout de nouvelles données et des excès similaires seraient observés dans les canaux évoqués précédemment. L'annonce de ces résultats a provoqué un engouement exceptionnel de la part des phénoménologistes, avec des centaines de (variations de) modèles proposés en quelques semaines afin d'expliquer ce signal. Une importante conclusion tirée des ces nombreuses études est que les version minimales des modèles résolvant le problème de hiérarchie ne parviennent généralement pas à expliquer ce signal potentiel, et des versions plus élaborées sont nécessaires. Prenant une direction assez différente, avec Christopher Smith, nous avons proposé une explication basée sur une désintégration à trois corps qui ne fait pas intervenir de particule à 750 GeV, $A \to B\gamma\gamma$ où A et B peuvent être des scalaires, fermions ou vecteurs. Cette étude a été publiée dans Physics Letters B sous le titre "*Could the width of the diphoton anomaly signal a three-body decay ?*" [438]. Cette configuration cinématique particulière, ainsi que plusieurs autres, ont été caractérisées plus en détails dans le cadre d'une étude avec Andreas Goudelis, Sabine Kraml, Kentarou Mawatari and Dipan Sengupta dans "*Characterising the 750 GeV diphoton excess*" [439], publiée dans Journal of High Energy Physics. Malgré le contenu physique des ces études, celles-ci n'ont néanmoins pas été présentées dans ce manuscrit puisque le signal qu'elle caractérisent pourrait se révéler n'être qu'une simple fluctuation statistique. Au contraire la confirmation de ce signal pourrait exclure les scénarios de modèles à deux doublets de Higgs présentés en Chapitre 5. En Août 2016, avec plus de luminosité, ATLAS et CMS n'ont pu confirmer la présence de cet excès dans le canal di-photon [364, 365], ce qui suggère fortement la présence d'une simple fluctuation statistique dans les analyses de Décembre 2015 .

Le boson de Higgs est une fenêtre directe sur la nouvelle physique attendue au-delà du MS et la mesure précise de ses propriétés est l'un des objectifs principaux du LHC. Dans la première partie de ce manuscrit de thèse, nous avons décrit comment les mesures de ses taux de production et désintégration pouvaient apporter des informations cruciales sur les modèles de nouvelle physique. A cet effet, l'outil public `Lilith` a été développé et décrit. `Lilith` utilise comme inputs expérimentaux les *signal strengths* dans l'espace des modes de production et de désintégration physiques. Les modifications de ces taux peuvent être décrites de manière consistante en paramétrant les *signal strengths* à l'aide de couplages réduits. Formellement, cela nécessite que les opérateurs à l'origine de ces modifications aient la même structure de Lorentz que les opérateurs du MS, ou que les opérateurs qui n'ont pas cette même structure aient des effets faibles. Ces derniers opérateurs mèneraient en effet à des modifications des distributions cinématiques du Higgs et de ses produits de désintégration, ce qui modifierait les efficacités et acceptances des analyses expérimentales et invaliderait l'interprétation des *signal strengths*. À l'aide de `Lilith`, nous avons effectué une étude globale des couplages du Higgs dans différents scénarios à l'aide des résultats finaux de la première période d'exploitation du LHC. Aucune déviation par rapport aux prédictions du MS n'a été observée. Les incertitudes actuelles sur les couplages réduits se situent dans la fourchette 20–40% suivant leurs natures et le scénario considéré, ce qui laisse toujours une place non négligeable à de possibles effets de nouvelle physique.

Dans la seconde partie de ce manuscrit, nous nous sommes intéressé à la possibilité que le secteur de Higgs à basse énergie comprenne deux doublets de Higgs. Le modèle à deux doublets de Higgs (M2DH) a été utilisé ici comme un modèle effectif pertinent pour la physique du LHC. Dans les modèles à plusieurs doublets de Higgs, il existe une limite particulière où l'un des états propres de masse est aligné dans la direction des valeurs moyennes dans le vide des différents doublets. Cette limite d'alignement confère automatiquement à cet état des propriétés proches de celles du boson de Higgs du MS. La présence de particules scalaires supplémentaires, telles que les bosons de Higgs chargés, peut néanmoins modifier ces propriétés de façon non négligeable. Etant donné que le boson de Higgs observé est compatible avec celui du MS, la limite d'alignement du M2DH est une région très motivée phénoménologiquement. En prenant en compte toutes les contraintes expérimentales pertinentes, nous nous sommes concentré sur cette limite dans le cadre du M2DH de Type I et Type II, et avons exploré leurs phénoménologies respectives. Dans le M2DH, les deux états propres de masse pairs sous CP peuvent être en principe identifiés avec le boson de Higgs observé au LHC, nous avons ainsi systématiquement analysé ces deux possibilités dans nos études. La limite d'alignement n'est pas équivalente à la limite de découplage, où les états scalaires supplémentaires sont découplés. Au contraire, ces états peuvent être légers et ainsi directement accessibles au LHC. Nous avons également étudié le cas où l'un ou deux de ces états ont une masse inférieure à environ 60 GeV, de façon à ce que le boson de Higgs observé puisse se désintégrer en une paire de ces particules. Nous avons identifié des canaux pouvant mener à l'exclusion (quasi-) totale de certains des scénarios étudiés dans les prochaines années au LHC. Les mesures de précision du Higgs sont également très sensibles à ces scénarios.

Le secteur de la saveur du MS, à travers ses couplages de Yukawa et de la matrice CKM, a un succès expérimental impressionnant. Jusqu'à présent, aucune déviation de ses prédictions n'a jamais été confirmée. Les structures de la saveur au-delà du MS doivent ainsi

soit ne pas avoir d'effets phénoménologiques considérables, ce qui est le cas si les nouvelles particules de saveur sont découplées, ou elles doivent être extrêmement hiérarchiques. Les couplages de Yukawa du MS étant eux même hautement non-génériques, un ajustement équivalent des nouvelles structures de saveurs devrait être considéré comme acceptable. En particulier, si elles étaient d'une certaine manière alignées avec les couplages de Yukawa, alors les problèmes de la saveur seraient grandement résolus. Dans la dernière partie de ce manuscrit de thèse, nous avons défini l'hypothèse de Violation Minimale de la Saveur (VMS), comme un moyen d'assurer systématiquement l'alignement de saveur, de façon bien définie, à l'aide d'un principe de symétrie. Une motivation importante pour cette hypothèse peut se trouver dans le mécanisme (hypothétique) fondamental à l'origine des structures de la saveur. Puisqu'un tel mécanisme prend certainement place à très haute énergie, la stabilité de l'alignement de saveur jusqu'à basse énergie doit être explicitement vérifiée afin de garantir la résolution des problèmes de saveur. En principe, cet alignement pourrait en effet être perdu lors de l'évolution des structures à basse énergie sous le groupe de renormalisation (GR). Nous avons effectué cette analyse pour les couplages violant la parité R et le nombre baryonique dans le Modèle Standard Supersymmetrique Minimal (MSSM). En premier lieu, nous avons construit le cadre théorique nécessaire pour imposer l'hypothèse VMS dans le MSSM et avons par la suite montré que l'hypothèse VMS était non seulement effective à basse énergie, en partant de conditions initiales assez génériques à haute énergie, mais qu'elle était même accentuée voire générée par l'évolution sous le GR. L'étude du scénario holomorphique a montré qu'il possédait des propriétés remarquables sous le GR. En conséquence, les scénarios avec $U(1)_Q$ brisé sont paramétrables à basse énergie à l'aide d'un unique paramètre à une très grande précision, cela est dû au scénario holomorphique agissant comme un attracteur puissant dans l'infrarouge. Au final, la possibilité de la violation du nombre baryonique à basse énergie est très motivée.

Avec près de quinze ordres de magnitude séparant l'échelle du TeV et l'échelle de Planck, la physique au-delà du MS dispose d'une très grande latitude pour entrer en action. La période actuelle est néanmoins cruciale pour la physique fondamentale puisque que le LHC est en train d'explorer des territoires inconnus avec une précision et des énergies jamais atteintes auparavant. A tout moment dans les quelques prochains mois, ou peut-être années, un changement conceptuel majeur de notre vision de la nature pourrait avoir lieu si les arguments de naturalité ont une quelconque signification. Espérons voir des résultats nuls devenir des excès, des excès devenir des découvertes, et voir le titre du Modèle Standard déchu de son sens.

BIBLIOGRAPHY

[1] E. Noether, *Invariant Variation Problems*, *Gott. Nachr.* **1918** (1918) 235–257, [`physics/0503066`]. [Transp. Theory Statist. Phys.1, 186(1971)].

[2] D. J. Gross and F. Wilczek, *Ultraviolet Behavior of Nonabelian Gauge Theories*, *Phys. Rev. Lett.* **30** (1973) 1343–1346.

[3] H. D. Politzer, *Reliable Perturbative Results for Strong Interactions?*, *Phys. Rev. Lett.* **30** (1973) 1346–1349.

[4] J. S. Schwinger, *A Theory of the Fundamental Interactions*, *Annals Phys.* **2** (1957) 407–434.

[5] S. L. Glashow, *Partial Symmetries of Weak Interactions*, *Nucl. Phys.* **22** (1961) 579–588.

[6] A. Salam and J. C. Ward, *Electromagnetic and weak interactions*, *Phys. Lett.* **13** (1964) 168–171.

[7] Y. Nambu, *Quasiparticles and Gauge Invariance in the Theory of Superconductivity*, *Phys. Rev.* **117** (1960) 648–663.

[8] J. Goldstone, *Field Theories with Superconductor Solutions*, *Nuovo Cim.* **19** (1961) 154–164.

[9] F. Englert and R. Brout, *Broken Symmetry and the Mass of Gauge Vector Mesons*, *Phys. Rev. Lett.* **13** (1964) 321–323.

[10] P. W. Higgs, *Broken Symmetries and the Masses of Gauge Bosons*, *Phys. Rev. Lett.* **13** (1964) 508–509.

[11] G. S. Guralnik, C. R. Hagen, and T. W. B. Kibble, *Global Conservation Laws and Massless Particles*, *Phys. Rev. Lett.* **13** (1964) 585–587.

[12] S. Weinberg, *A Model of Leptons*, *Phys. Rev. Lett.* **19** (1967) 1264–1266.

[13] A. Salam, *Weak and Electromagnetic Interactions*, *Conf. Proc.* **C680519** (1968) 367–377.

[14] **ATLAS** Collaboration, G. Aad et al., *Observation of a new particle in the search for the Standard Model Higgs boson with the ATLAS detector at the LHC*, *Phys.Lett.* **B716** (2012) 1–29, [`arXiv:1207.7214`].

[15] **CMS** Collaboration, S. Chatrchyan et al., *Observation of a new boson at a mass of 125 GeV with the CMS experiment at the LHC*, *Phys.Lett.* **B716** (2012) 30–61, [`arXiv:1207.7235`].

[16] **ATLAS and CMS** Collaborations, G. Aad et al., *Combined Measurement of the Higgs Boson Mass in pp Collisions at $\sqrt{s} = 7$ and 8 TeV with the ATLAS and CMS Experiments*, Phys. Rev. Lett. **114** (2015) 191803, [`arXiv:1503.07589`].

[17] **LEP Working Group for Higgs boson searches and the ALEPH, DELPHI, L3, OPAL** Collaborations, R. Barate et al., *Search for the standard model Higgs boson at LEP*, Phys. Lett. **B565** (2003) 61–75, [`hep-ex/0306033`].

[18] **Tevatron New Physics Higgs Working Group and the CDF, DO** Collaborations, *Updated Combination of CDF and DO Searches for Standard Model Higgs Boson Production with up to 10.0 fb^{-1} of Data*, 2012. `arXiv:1207.0449`.

[19] **The ALEPH, DELPHI, L3, OPAL, SLD Collaborations, the LEP Electroweak Working Group, the SLD Electroweak and Heavy Flavour Groups,** Schael, S. et al., *Precision electroweak measurements on the Z resonance*, Phys. Rept. **427** (2006) 257–454, [`hep-ex/0509008`].

[20] R. N. Cahn, *Semi-Simple Lie Algebras and Their Representations*. Benjamin Cummings, 1984.

[21] E. Cartan, *Sur la structure des groupes de transformations finis et continus*. PhD thesis, Faculté des sciences de Paris, 1894.

[22] S. Weinberg, *The Quantum Theory of Fields - Modern Applications*, vol. 2. Cambridge University Press, 1996.

[23] S. Weinberg, *The Quantum Theory of Fields - Foundations*, vol. 1. Cambridge University Press, 1995.

[24] M. Maggiore, *A Modern Introduction to Quantum Field Theory*. Oxford Master Series, 2005.

[25] S. R. Coleman and J. Mandula, *All Possible Symmetries of the S-Matrix*, Phys. Rev. **159** (1967) 1251–1256.

[26] R. Haag, J. T. Lopuszanski, and M. Sohnius, *All Possible Generators of Supersymmetries of the S-Matrix*, Nucl. Phys. **B88** (1975) 257.

[27] C.-N. Yang and R. L. Mills, *Conservation of Isotopic Spin and Isotopic Gauge Invariance*, Phys. Rev. **96** (1954) 191–195.

[28] L. D. Faddeev and V. N. Popov, *Feynman Diagrams for the Yang-Mills Field*, Phys. Lett. **B25** (1967) 29–30.

[29] C. Becchi, A. Rouet, and R. Stora, *Renormalization of Gauge Theories*, Annals Phys. **98** (1976) 287–321.

[30] I. V. Tyutin, *Gauge Invariance in Field Theory and Statistical Physics in Operator Formalism*, `arXiv:0812.0580`.

[31] R. A. Bertlmann, *Anomalies in Quantum Field Theory*. Oxford University Press, 1996.

[32] M. Nakahara, *Geometry, Topology and Physics*. Institute of Physics Publishing, 2003.

[33] W. Pauli, *Niels Bohrand the Development of Physics*. Pergamon Press, 1955.

[34] G. Luders, *On the Equivalence of Invariance under Time Reversal and under Particle-Antiparticle Conjugation for Relativistic Field Theories*, *Kong. Dan. Vid. Sel. Mat. Fys. Med.* **28N5** (1954) 1–17.

[35] R. Bjorklund, W. E. Crandall, B. J. Moyer, and H. F. York, *High Energy Photons from Proton-Nucleon Collisions*, *Phys. Rev.* **77** (1950) 213–218.

[36] J. Steinberger, W. K. H. Panofsky, and J. Steller, *Evidence for the Production of Neutral Mesons by Photons*, *Phys. Rev.* **78** (1950) 802–805.

[37] S. L. Adler, *Axial vector vertex in spinor electrodynamics*, *Phys. Rev.* **177** (1969) 2426–2438.

[38] J. S. Bell and R. Jackiw, *A PCAC puzzle: $\pi^0 \to \gamma\gamma$ in the sigma model*, *Nuovo Cim.* **A60** (1969) 47–61.

[39] G. 't Hooft, *Symmetry Breaking Through Bell-Jackiw Anomalies*, *Phys. Rev. Lett.* **37** (1976) 8–11.

[40] S. H. H. Tye and S. S. C. Wong, *Bloch Wave Function for the Periodic Sphaleron Potential and Unsuppressed Baryon and Lepton Number Violating Processes*, *Phys. Rev.* **D92** (2015), no. 4 045005, [`arXiv:1505.03690`].

[41] J. Ellis and K. Sakurai, *Search for Sphalerons in Proton-Proton Collisions*, *JHEP* **04** (2016) 086, [`arXiv:1601.03654`].

[42] J. Ellis, K. Sakurai, and M. Spannowsky, *Search for Sphalerons: IceCube vs. LHC*, *JHEP* **05** (2016) 085, [`arXiv:1603.06573`].

[43] V. A. Kuzmin, V. A. Rubakov, and M. E. Shaposhnikov, *On the Anomalous Electroweak Baryon Number Nonconservation in the Early Universe*, *Phys. Lett.* **B155** (1985) 36.

[44] M. Fukugita and T. Yanagida, *Baryogenesis Without Grand Unification*, *Phys. Lett.* **B174** (1986) 45.

[45] M. C. Gonzalez-Garcia and M. Maltoni, *Phenomenology with Massive Neutrinos*, *Phys. Rept.* **460** (2008) 1–129, [`arXiv:0704.1800`].

[46] C. S. Wu, E. Ambler, R. W. Hayward, D. D. Hoppes, and R. P. Hudson, *Experimental Test of Parity Conservation in Beta Decay*, *Phys. Rev.* **105** (1957) 1413–1414.

[47] M. Dine, *TASI lectures on the strong CP problem*, in *Flavor physics for the millennium. Proceedings, Theoretical Advanced Study Institute in elementary particle physics, TASI 2000, Boulder, USA, June 4-30, 2000*, pp. 349–369, 2000. `hep-ph/0011376`.

[48] R. D. Peccei, *The Strong CP problem and axions*, Lect. Notes Phys. **741** (2008) 3–17, [`hep-ph/0607268`].

[49] V. Baluni, *CP Violating Effects in QCD*, Phys. Rev. **D19** (1979) 2227–2230.

[50] R. J. Crewther, P. Di Vecchia, G. Veneziano, and E. Witten, *Chiral Estimate of the Electric Dipole Moment of the Neutron in Quantum Chromodynamics*, Phys. Lett. **B88** (1979) 123. [Erratum: Phys. Lett.B91, 487(1980)].

[51] M. Pospelov and A. Ritz, *Theta induced electric dipole moment of the neutron via QCD sum rules*, Phys. Rev. Lett. **83** (1999) 2526–2529, [`hep-ph/9904483`].

[52] R. D. Peccei and H. R. Quinn, *CP Conservation in the Presence of Instantons*, Phys. Rev. Lett. **38** (1977) 1440–1443.

[53] R. D. Peccei and H. R. Quinn, *Constraints Imposed by CP Conservation in the Presence of Instantons*, Phys. Rev. **D16** (1977) 1791–1797.

[54] S. Weinberg, *A New Light Boson?*, Phys. Rev. Lett. **40** (1978) 223–226.

[55] F. Wilczek, *Problem of Strong p and t Invariance in the Presence of Instantons*, Phys. Rev. Lett. **40** (1978) 279–282.

[56] P. W. Graham, I. G. Irastorza, S. K. Lamoreaux, A. Lindner, and K. A. van Bibber, *Experimental Searches for the Axion and Axion-Like Particles*, Ann. Rev. Nucl. Part. Sci. **65** (2015) 485–514, [`arXiv:1602.00039`].

[57] E. C. G. Stueckelberg, *Interaction energy in electrodynamics and in the field theory of nuclear forces*, Helv. Phys. Acta **11** (1938) 225–244.

[58] H. Ruegg and M. Ruiz-Altaba, *The Stueckelberg field*, Int. J. Mod. Phys. **A19** (2004) 3265–3348, [`hep-th/0304245`].

[59] D. A. Ross and M. J. G. Veltman, *Neutral Currents in Neutrino Experiments*, Nucl. Phys. **B95** (1975) 135.

[60] **Particle Data Group,** K. A. Olive et al., *Review of Particle Physics*, Chin. Phys. **C38** (2014) 090001.

[61] M. J. G. Veltman, *Limit on Mass Differences in the Weinberg Model*, Nucl. Phys. **B123** (1977) 89–99.

[62] P. Sikivie, L. Susskind, M. B. Voloshin, and V. I. Zakharov, *Isospin Breaking in Technicolor Models*, Nucl. Phys. **B173** (1980) 189.

[63] M. B. Einhorn, D. R. T. Jones, and M. J. G. Veltman, *Heavy Particles and the rho Parameter in the Standard Model*, Nucl. Phys. **B191** (1981) 146.

[64] J. M. Cornwall, D. N. Levin, and G. Tiktopoulos, *Derivation of Gauge Invariance from High-Energy Unitarity Bounds on the S-Matrix*, Phys. Rev. **D10** (1974) 1145. [Erratum: Phys. Rev.D11, 972(1975)].

[65] S. Mandelstam, *Determination of the pion - nucleon scattering amplitude from dispersion relations and unitarity. General theory*, Phys. Rev. **112** (1958) 1344–1360.

[66] J. C. Romao, *The need for the Higgs boson in the Standard Model*, 2016. `arXiv:1603.04251`.

[67] M. S. Chanowitz and M. K. Gaillard, *The TeV Physics of Strongly Interacting W's and Z's*, Nucl. Phys. **B261** (1985) 379.

[68] B. W. Lee, C. Quigg, and H. B. Thacker, *The Strength of Weak Interactions at Very High-Energies and the Higgs Boson Mass*, Phys. Rev. Lett. **38** (1977) 883–885.

[69] B. W. Lee, C. Quigg, and H. B. Thacker, *Weak Interactions at Very High-Energies: The Role of the Higgs Boson Mass*, Phys. Rev. **D16** (1977) 1519.

[70] N. Cabibbo, L. Maiani, G. Parisi, and R. Petronzio, *Bounds on the Fermions and Higgs Boson Masses in Grand Unified Theories*, Nucl. Phys. **B158** (1979) 295–305.

[71] M. Lindner, *Implications of Triviality for the Standard Model*, Z. Phys. **C31** (1986) 295.

[72] T. Hambye and K. Riesselmann, *Matching conditions and Higgs mass upper bounds revisited*, Phys. Rev. **D55** (1997) 7255–7262, [`hep-ph/9610272`].

[73] D. Buttazzo, G. Degrassi, P. P. Giardino, G. F. Giudice, F. Sala, A. Salvio, and A. Strumia, *Investigating the near-criticality of the Higgs boson*, JHEP **12** (2013) 089, [`arXiv:1307.3536`].

[74] V. Branchina, E. Messina, and M. Sher, *Lifetime of the electroweak vacuum and sensitivity to Planck scale physics*, Phys. Rev. **D91** (2015) 013003, [`arXiv:1408.5302`].

[75] **LHC Higgs Cross Section Working Group,** S. Dittmaier, C. Mariotti, G. Passarino, and R. Tanaka (Eds.), *Handbook of LHC Higgs Cross Sections: 1. Inclusive Observables*, CERN-2011-002 (CERN, Geneva, 2011) [`arXiv:1101.0593`].

[76] **LHC Higgs Cross Section Working Group,** S. Dittmaier, C. Mariotti, G. Passarino, and R. Tanaka (Eds.), *Handbook of LHC Higgs Cross Sections: 2. Differential Distributions*, CERN-2012-002 (CERN, Geneva, 2012) [`arXiv:1201.3084`].

[77] **LHC Higgs Cross Section Working Group,** S. Heinemeyer, C. Mariotti, G. Passarino, and R. Tanaka (Eds.), *Handbook of LHC Higgs Cross Sections: 3. Higgs Properties, CERN-2013-004* (CERN, Geneva, 2013) [`arXiv:1307.1347`].

[78] C. Delaunay, R. Ozeri, G. Perez, and Y. Soreq, *Probing The Atomic Higgs Force,* `arXiv:1601.05087`.

[79] G. T. Bodwin, F. Petriello, S. Stoynev, and M. Velasco, *Higgs boson decays to quarkonia and the H$\bar{c}c$ coupling, Phys. Rev.* **D88** (2013), no. 5 053003, [`arXiv:1306.5770`].

[80] S. G. Gorishnii, A. L. Kataev, S. A. Larin, and L. R. Surguladze, *Scheme dependence of the next to next-to-leading QCD corrections to Γ(tot) (H$_0$ → hadrons) and the spurious QCD infrared fixed point, Phys. Rev.* **D43** (1991) 1633–1640.

[81] K. G. Chetyrkin and M. Steinhauser, *Complete QCD corrections of order $\mathcal{O}(\alpha_s^3)$ to the hadronic Higgs decay, Phys. Lett.* **B408** (1997) 320–324, [`hep-ph/9706462`].

[82] A. Djouadi, *The Anatomy of electro-weak symmetry breaking. I: The Higgs boson in the standard model, Phys.Rept.* **457** (2008) 1–216, [`hep-ph/0503172`].

[83] M. Spira, A. Djouadi, D. Graudenz, and P. M. Zerwas, *Higgs boson production at the LHC, Nucl. Phys.* **B453** (1995) 17–82, [`hep-ph/9504378`].

[84] T. Plehn and M. Rauch, *The quartic higgs coupling at hadron colliders, Phys. Rev.* **D72** (2005) 053008, [`hep-ph/0507321`].

[85] U. Baur, T. Plehn, and D. L. Rainwater, *Determining the Higgs boson selfcoupling at hadron colliders, Phys. Rev.* **D67** (2003) 033003, [`hep-ph/0211224`].

[86] M. J. Dolan, C. Englert, and M. Spannowsky, *Higgs self-coupling measurements at the LHC, JHEP* **10** (2012) 112, [`arXiv:1206.5001`].

[87] R. S. Chivukula and H. Georgi, *Composite Technicolor Standard Model, Phys. Lett.* **B188** (1987) 99.

[88] N. Cabibbo, *Unitary Symmetry and Leptonic Decays, Phys. Rev. Lett.* **10** (1963) 531–533.

[89] M. Kobayashi and T. Maskawa, *CP Violation in the Renormalizable Theory of Weak Interaction, Prog. Theor. Phys.* **49** (1973) 652–657.

[90] B. Pontecorvo, *Mesonium and anti-mesonium, Sov. Phys. JETP* **6** (1957) 429.

[91] Z. Maki, M. Nakagawa, and S. Sakata, *Remarks on the unified model of elementary particles, Prog. Theor. Phys.* **28** (1962) 870–880.

[92] L. Wolfenstein, *Parametrization of the Kobayashi-Maskawa Matrix, Phys. Rev. Lett.* **51** (1983) 1945.

[93] **CKMfitter Group,** J. Charles et al. *Eur. Phys. J.* **C41** (2005) 1–131,
[`hep-ph/0406184`].

[94] J. Charles et al., *Current status of the Standard Model CKM fit and constraints on
$\Delta F = 2$ New Physics*, *Phys. Rev.* **D91** (2015), no. 7 073007, [`arXiv:1501.05013`].

[95] Y. Grossman, *Introduction to flavor physics*, in *Flavianet School on Flavour Physics
Karlsruhe, Germany, September 7-18, 2009*, pp. 111–144, 2014. `arXiv:1006.3534`.

[96] C. Jarlskog, *Commutator of the Quark Mass Matrices in the Standard Electroweak
Model and a Measure of Maximal CP Violation*, *Phys. Rev. Lett.* **55** (1985) 1039.

[97] T. Inami and C. S. Lim, *Effects of Superheavy Quarks and Leptons in Low-Energy
Weak Processes $K_L \to \mu\bar{\mu}$, $K^+ \to \pi^+ \nu\bar{\nu}$ and $K^0 \leftrightarrow \bar{K}^0$*, *Prog. Theor. Phys.* **65**
(1981) 297. [Erratum: Prog. Theor. Phys.65, 1772(1981)].

[98] S. L. Glashow, J. Iliopoulos, and L. Maiani, *Weak Interactions with Lepton-Hadron
Symmetry*, *Phys. Rev.* **D2** (1970) 1285–1292.

[99] C. Bobeth, M. Gorbahn, T. Hermann, M. Misiak, E. Stamou, and M. Steinhauser,
$B_{s,d} \to l^+ l^-$ in the Standard Model with Reduced Theoretical Uncertainty, *Phys.
Rev. Lett.* **112** (2014) 101801, [`arXiv:1311.0903`].

[100] K. S. Babu and C. F. Kolda, *Higgs mediated $B^0 \to \mu^+ \mu^-$ in minimal
supersymmetry*, *Phys. Rev. Lett.* **84** (2000) 228–231, [`hep-ph/9909476`].

[101] S. R. Choudhury and N. Gaur, *Dileptonic decay of B(s) meson in SUSY models
with large tan Beta*, *Phys. Lett.* **B451** (1999) 86–92, [`hep-ph/9810307`].

[102] C.-S. Huang, W. Liao, Q.-S. Yan, and S.-H. Zhu, *$B_s \to$ lepton + lepton - in a
general 2 HDM and MSSM*, *Phys. Rev.* **D63** (2001) 114021, [`hep-ph/0006250`].
[Erratum: Phys. Rev.D64, 059902(2001)].

[103] **LHCb and CMS** Collaborations, V. Khachatryan et al., *Observation of the rare
$B_s^0 \to \mu^+ \mu^-$ decay from the combined analysis of CMS and LHCb data*, *Nature* **522**
(2015) 68–72, [`arXiv:1411.4413`].

[104] G. Isidori, Y. Nir, and G. Perez, *Flavor Physics Constraints for Physics Beyond the
Standard Model*, *Ann. Rev. Nucl. Part. Sci.* **60** (2010) 355, [`arXiv:1002.0900`].

[105] G. Isidori, *Flavour Physics and Implication for New Phenomena*,
`arXiv:1507.00867`.

[106] C. Smith, *Minimal Flavor Violation*. Habilitation à diriger des recherches, 2015.

[107] P. Langacker, *Grand Unified Theories and Proton Decay*, *Phys. Rept.* **72** (1981) 185.

[108] P. Minkowski, *$\mu \to e\gamma$ at a Rate of One Out of 10^9 Muon Decays?*, *Phys. Lett.* **B67**
(1977) 421–428.

[109] **Planck** Collaboration, P. A. R. Ade et al., *Planck 2015 results. XIII. Cosmological parameters*, `arXiv:1502.01589`.

[110] A. D. Sakharov, *Violation of CP Invariance, c Asymmetry, and Baryon Asymmetry of the Universe*, *Pisma Zh. Eksp. Teor. Fiz.* **5** (1967) 32–35.

[111] K. Kajantie, M. Laine, K. Rummukainen, and M. E. Shaposhnikov, *The Electroweak phase transition: A Nonperturbative analysis*, *Nucl. Phys.* **B466** (1996) 189–258, [`hep-lat/9510020`].

[112] J. R. Ellis, M. K. Gaillard, and D. V. Nanopoulos, *A Phenomenological Profile of the Higgs Boson*, *Nucl. Phys.* **B106** (1976) 292.

[113] R. Barbieri and T. E. O. Ericson, *Evidence Against the Existence of a Low Mass Scalar Boson from Neutron-Nucleus Scattering*, *Phys. Lett.* **B57** (1975) 270.

[114] J. Bernon and B. Dumont, *Lilith: a tool for constraining new physics from Higgs measurements*, *Eur. Phys. J.* **C75** (2015) 440, [`arXiv:1502.04138`].

[115] J. Bernon, B. Dumont, and S. Kraml, *Status of Higgs couplings after run 1 of the LHC*, *Phys.Rev.* **D90** (2014), no. 7 071301, [`arXiv:1409.1588`].

[116] **L3** Collaboration, O. Adriani et al., *A Search for the neutral Higgs boson at LEP*, *Phys. Lett.* **B303** (1993) 391–399.

[117] **ALEPH** Collaboration, D. Buskulic et al., *Search for the Standard Model Higgs boson*, *Phys. Lett.* **B313** (1993) 299–311.

[118] **DELPHI** Collaboration, P. Abreu et al., *Search for the standard model Higgs boson in Z0 decays*, *Nucl. Phys.* **B421** (1994) 3–37.

[119] **OPAL** Collaboration, R. Akers et al., *Search for the minimal Standard Model Higgs boson*, *Phys. Lett.* **B327** (1994) 397–410.

[120] **ALEPH** Collaboration, R. Barate et al., *Observation of an excess in the search for the standard model Higgs boson at ALEPH*, *Phys. Lett.* **B495** (2000) 1–17, [`hep-ex/0011045`].

[121] **L3** Collaboration, M. Acciarri et al., *Higgs candidates in e^+e^- interactions at $\sqrt{s} = 206.6$-GeV*, *Phys. Lett.* **B495** (2000) 18–25, [`hep-ex/0011043`].

[122] M. J. G. Veltman, *Second Threshold in Weak Interactions*, *Acta Phys. Polon.* **B8** (1977) 475.

[123] **CDF** Collaboration, F. Abe et al., *Observation of top quark production in $\bar{p}p$ collisions*, *Phys. Rev. Lett.* **74** (1995) 2626–2631, [`hep-ex/9503002`].

[124] **The ALEPH, DELPHI, L3, OPAL Collaborations, The LEP Electroweak Working Group,** S. Schael et al., *Electroweak Measurements in Electron-Positron Collisions at W-Boson-Pair Energies at LEP*, *Phys. Rept.* **532** (2013) 119–244, [`arXiv:1302.3415`].

[125] M. Baak, M. Goebel, J. Haller, A. Hoecker, D. Ludwig, K. Moenig, M. Schott, and J. Stelzer, *Updated Status of the Global Electroweak Fit and Constraints on New Physics*, Eur. Phys. J. **C72** (2012) 2003, [`arXiv:1107.0975`].

[126] M. Baak, M. Goebel, J. Haller, A. Hoecker, D. Kennedy, R. Kogler, K. Moenig, M. Schott, and J. Stelzer, *The Electroweak Fit of the Standard Model after the Discovery of a New Boson at the LHC*, Eur. Phys. J. **C72** (2012) 2205, [`arXiv:1209.2716`].

[127] **ATLAS** Collaboration, G. Aad et al., *Combined search for the Standard Model Higgs boson using up to 4.9 fb^{-1} of pp collision data at $\sqrt{s} = 7$ TeV with the ATLAS detector at the LHC*, Phys. Lett. **B710** (2012) 49–66, [`arXiv:1202.1408`].

[128] **CMS** Collaboration, S. Chatrchyan et al., *Combined results of searches for the standard model Higgs boson in pp collisions at $\sqrt{s} = 7$ TeV*, Phys. Lett. **B710** (2012) 26–48, [`arXiv:1202.1488`].

[129] H. M. Georgi, S. L. Glashow, M. E. Machacek, and D. V. Nanopoulos, *Higgs Bosons from Two Gluon Annihilation in Proton Proton Collisions*, Phys. Rev. Lett. **40** (1978) 692.

[130] S. Dawson, *Radiative corrections to Higgs boson production*, Nucl. Phys. **B359** (1991) 283–300.

[131] A. Djouadi, M. Spira, and P. M. Zerwas, *Production of Higgs bosons in proton colliders: QCD corrections*, Phys. Lett. **B264** (1991) 440–446.

[132] C. Anastasiou and K. Melnikov, *Higgs boson production at hadron colliders in NNLO QCD*, Nucl. Phys. **B646** (2002) 220–256, [`hep-ph/0207004`].

[133] R. V. Harlander and W. B. Kilgore, *Next-to-next-to-leading order Higgs production at hadron colliders*, Phys. Rev. Lett. **88** (2002) 201801, [`hep-ph/0201206`].

[134] R. V. Harlander, H. Mantler, S. Marzani, and K. J. Ozeren, *Higgs production in gluon fusion at next-to-next-to-leading order QCD for finite top mass*, Eur. Phys. J. **C66** (2010) 359–372, [`arXiv:0912.2104`].

[135] S. Actis, G. Passarino, C. Sturm, and S. Uccirati, *NLO Electroweak Corrections to Higgs Boson Production at Hadron Colliders*, Phys. Lett. **B670** (2008) 12–17, [`arXiv:0809.1301`].

[136] C. Anastasiou, R. Boughezal, and F. Petriello, *Mixed QCD-electroweak corrections to Higgs boson production in gluon fusion*, JHEP **04** (2009) 003, [`arXiv:0811.3458`].

[137] C. Anastasiou, C. Duhr, F. Dulat, E. Furlan, T. Gehrmann, F. Herzog, A. Lazopoulos, and B. Mistlberger, *High precision determination of the gluon fusion Higgs boson cross-section at the LHC*, JHEP **05** (2016) 058, [`arXiv:1602.00695`].

[138] T. Figy, C. Oleari, and D. Zeppenfeld, *Next-to-leading order jet distributions for Higgs boson production via weak boson fusion*, Phys. Rev. **D68** (2003) 073005, [`hep-ph/0306109`].

[139] M. Ciccolini, A. Denner, and S. Dittmaier, *Electroweak and QCD corrections to Higgs production via vector-boson fusion at the LHC*, Phys. Rev. **D77** (2008) 013002, [arXiv:0710.4749].

[140] M. Ciccolini, A. Denner, and S. Dittmaier, *Strong and electroweak corrections to the production of Higgs + 2jets via weak interactions at the LHC*, Phys. Rev. Lett. **99** (2007) 161803, [arXiv:0707.0381].

[141] P. Bolzoni, F. Maltoni, S.-O. Moch, and M. Zaro, *Higgs production via vector-boson fusion at NNLO in QCD*, Phys. Rev. Lett. **105** (2010) 011801, [arXiv:1003.4451].

[142] S. L. Glashow, D. V. Nanopoulos, and A. Yildiz, *Associated Production of Higgs Bosons and Z Particles*, Phys. Rev. **D18** (1978) 1724–1727.

[143] T. Han and S. Willenbrock, *QCD correction to the $pp \rightarrow WH$ and ZH total cross-sections*, Phys. Lett. **B273** (1991) 167–172.

[144] O. Brein, A. Djouadi, and R. Harlander, *NNLO QCD corrections to the Higgs-strahlung processes at hadron colliders*, Phys. Lett. **B579** (2004) 149–156, [hep-ph/0307206].

[145] M. L. Ciccolini, S. Dittmaier, and M. Kramer, *Electroweak radiative corrections to associated WH and ZH production at hadron colliders*, Phys. Rev. **D68** (2003) 073003, [hep-ph/0306234].

[146] Z. Kunszt, *Associated Production of Heavy Higgs Boson with Top Quarks*, Nucl. Phys. **B247** (1984) 339.

[147] W. Beenakker, S. Dittmaier, M. Kramer, B. Plumper, M. Spira, and P. M. Zerwas, *Higgs radiation off top quarks at the Tevatron and the LHC*, Phys. Rev. Lett. **87** (2001) 201805, [hep-ph/0107081].

[148] W. Beenakker, S. Dittmaier, M. Kramer, B. Plumper, M. Spira, and P. M. Zerwas, *NLO QCD corrections to $t\bar{t}H$ production in hadron collisions*, Nucl. Phys. **B653** (2003) 151–203, [hep-ph/0211352].

[149] S. Dawson, L. H. Orr, L. Reina, and D. Wackeroth, *Associated top quark Higgs boson production at the LHC*, Phys. Rev. **D67** (2003) 071503, [hep-ph/0211438].

[150] S. Dawson, C. Jackson, L. H. Orr, L. Reina, and D. Wackeroth, *Associated Higgs production with top quarks at the large hadron collider: NLO QCD corrections*, Phys. Rev. **D68** (2003) 034022, [hep-ph/0305087].

[151] D. A. Dicus and S. Willenbrock, *Higgs Boson Production from Heavy Quark Fusion*, Phys. Rev. **D39** (1989) 751.

[152] D. Dicus, T. Stelzer, Z. Sullivan, and S. Willenbrock, *Higgs boson production in association with bottom quarks at next-to-leading order*, Phys. Rev. **D59** (1999) 094016, [hep-ph/9811492].

[153] S. Dittmaier, M. Kramer, 1, and M. Spira, *Higgs radiation off bottom quarks at the Tevatron and the CERN LHC*, Phys. Rev. **D70** (2004) 074010, [`hep-ph/0309204`].

[154] S. Dawson, C. B. Jackson, L. Reina, and D. Wackeroth, *Exclusive Higgs boson production with bottom quarks at hadron colliders*, Phys. Rev. **D69** (2004) 074027, [`hep-ph/0311067`].

[155] L. D. Landau, *On the angular momentum of a system of two photons*, Dokl. Akad. Nauk Ser. Fiz. **60** (1948), no. 2 207–209.

[156] C.-N. Yang, *Selection Rules for the Dematerialization of a Particle Into Two Photons*, Phys. Rev. **77** (1950) 242–245.

[157] R. Godbole, S. Kraml, M. Krawczyk, D. Miller, P. Niezurawski, et al., *CP studies of the Higgs sector: A Contribution to the LHC / LC Study Group document*, `hep-ph/0404024`.

[158] S. Kraml et al., *Workshop on CP Studies and Non-Standard Higgs Physics*, `hep-ph/0608079`.

[159] J. C. Collins and D. E. Soper, *Angular Distribution of Dileptons in High-Energy Hadron Collisions*, Phys. Rev. **D16** (1977) 2219.

[160] **ATLAS** Collaboration, G. Aad et al., *Study of the spin and parity of the Higgs boson in diboson decays with the ATLAS detector*, Eur. Phys. J. **C75** (2015), no. 10 476, [`arXiv:1506.05669`]. [Erratum: Eur. Phys. J.C76, no.3, 152(2016)].

[161] **CMS** Collaboration, V. Khachatryan et al., *Constraints on the spin-parity and anomalous HVV couplings of the Higgs boson in proton collisions at 7 and 8 TeV*, Phys. Rev. **D92** (2015), no. 1 012004, [`arXiv:1411.3441`].

[162] G. F. Giudice, C. Grojean, A. Pomarol, and R. Rattazzi, *The Strongly-Interacting Light Higgs*, JHEP **06** (2007) 045, [`hep-ph/0703164`].

[163] B. Grzadkowski, M. Iskrzynski, M. Misiak, and J. Rosiek, *Dimension-Six Terms in the Standard Model Lagrangian*, JHEP **10** (2010) 085, [`arXiv:1008.4884`].

[164] G. Isidori and M. Trott, *Higgs form factors in Associated Production*, JHEP **02** (2014) 082, [`arXiv:1307.4051`].

[165] M. Gonzalez-Alonso, A. Greljo, G. Isidori, and D. Marzocca, *Pseudo-observables in Higgs decays*, Eur. Phys. J. **C75** (2015) 128, [`arXiv:1412.6038`].

[166] **ATLAS** Collaboration, G. Aad et al., *Measurements of fiducial and differential cross sections for Higgs boson production in the diphoton decay channel at $\sqrt{s} = 8$ TeV with ATLAS*, JHEP **09** (2014) 112, [`arXiv:1407.4222`].

[167] **ATLAS** Collaboration, G. Aad et al., *Fiducial and differential cross sections of Higgs boson production measured in the four-lepton decay channel in pp collisions at $\sqrt{s}=8$ TeV with the ATLAS detector*, Phys. Lett. **B738** (2014) 234–253, [`arXiv:1408.3226`].

[168] **ATLAS** Collaboration, G. Aad et al., *Measurements of the Total and Differential Higgs Boson Production Cross Sections Combining the $H \to \gamma\gamma$ and $H \to ZZ^* \to 4\ell$ Decay Channels at $\sqrt{s}$=8TeV with the ATLAS Detector*, Phys. Rev. Lett. **115** (2015), no. 9 091801, [`arXiv:1504.05833`].

[169] **CMS** Collaboration, V. Khachatryan et al., *Measurement of differential cross sections for Higgs boson production in the diphoton decay channel in pp collisions at $\sqrt{s} = 8$ TeV*, Eur. Phys. J. **C76** (2016), no. 1 13, [`arXiv:1508.07819`].

[170] **CMS** Collaboration, V. Khachatryan et al., *Measurement of differential and integrated fiducial cross sections for Higgs boson production in the four-lepton decay channel in pp collisions at $\sqrt{s} = 7$ and 8 TeV*, JHEP **04** (2016) 005, [`arXiv:1512.08377`].

[171] **CMS** Collaboration, V. Khachatryan et al., *Precise determination of the mass of the Higgs boson and tests of compatibility of its couplings with the standard model predictions using proton collisions at 7 and 8 TeV*, Eur. Phys. J. **C75** (2015), no. 5 212, [`arXiv:1412.8662`].

[172] **ATLAS** Collaboration, G. Aad et al., *Measurements of the Higgs boson production and decay rates and coupling strengths using pp collision data at $\sqrt{s} = 7$ and 8 TeV in the ATLAS experiment*, Eur. Phys. J. **C76** (2016), no. 1 6, [`arXiv:1507.04548`].

[173] **ATLAS** Collaboration, G. Aad et al., *Measurement of Higgs boson production in the diphoton decay channel in pp collisions at center-of-mass energies of 7 and 8 TeV with the ATLAS detector*, Phys. Rev. **D90** (2014), no. 11 112015, [`arXiv:1408.7084`].

[174] **CMS** Collaboration, V. Khachatryan et al., *Observation of the diphoton decay of the Higgs boson and measurement of its properties*, Eur.Phys.J. **C74** (2014), no. 10 3076, [`arXiv:1407.0558`].

[175] **ATLAS** Collaboration, G. Aad et al., *Measurements of Higgs boson production and couplings in the four-lepton channel in pp collisions at center-of-mass energies of 7 and 8 TeV with the ATLAS detector*, Phys. Rev. **D91** (2015), no. 1 012006, [`arXiv:1408.5191`].

[176] **CMS** Collaboration, S. Chatrchyan et al., *Measurement of the properties of a Higgs boson in the four-lepton final state*, Phys. Rev. **D89** (2014) 092007, [`arXiv:1312.5353`].

[177] **ATLAS** Collaboration, G. Aad et al., *Observation and measurement of Higgs boson decays to WW^* with the ATLAS detector*, Phys. Rev. **D92** (2015), no. 1 012006, [`arXiv:1412.2641`].

[178] **ATLAS** Collaboration, G. Aad et al., *Study of (W/Z)H production and Higgs boson couplings using $H \to WW^*$ decays with the ATLAS detector*, JHEP **08** (2015) 137, [`arXiv:1506.06641`].

[179] **CMS** Collaboration, S. Chatrchyan et al., *Measurement of Higgs boson production and properties in the WW decay channel with leptonic final states*, JHEP **1401** (2014) 096, [arXiv:1312.1129].

[180] **ATLAS** Collaboration, G. Aad et al., *Evidence for the Higgs-boson Yukawa coupling to tau leptons with the ATLAS detector*, JHEP **1504** (2015) 117, [arXiv:1501.04943].

[181] **CMS** Collaboration, S. Chatrchyan et al., *Evidence for the 125 GeV Higgs boson decaying to a pair of τ leptons*, JHEP **05** (2014) 104, [arXiv:1401.5041].

[182] **ATLAS** Collaboration, G. Aad et al., *Search for the $b\bar{b}$ decay of the Standard Model Higgs boson in associated $(W/Z)H$ production with the ATLAS detector*, JHEP **1501** (2015) 069, [arXiv:1409.6212].

[183] **CMS** Collaboration, S. Chatrchyan et al., *Search for the standard model Higgs boson produced in association with a W or a Z boson and decaying to bottom quarks*, Phys. Rev. **D89** (2014) 012003, [arXiv:1310.3687].

[184] **ATLAS** Collaboration, G. Aad et al., *Search for the Standard Model Higgs boson decay to $\mu^+\mu^-$ with the ATLAS detector*, Phys. Lett. **B738** (2014) 68–86, [arXiv:1406.7663].

[185] **CMS** Collaboration, V. Khachatryan et al., *Search for a standard model-like Higgs boson in the $\mu^+\mu^-$ and e^+e^- decay channels at the LHC*, Phys. Lett. **B744** (2015) 184–207, [arXiv:1410.6679].

[186] **ATLAS** Collaboration, G. Aad et al., *Search for Higgs boson decays to a photon and a Z boson in pp collisions at $\sqrt{s}$=7 and 8 TeV with the ATLAS detector*, Phys. Lett. **B732** (2014) 8–27, [arXiv:1402.3051].

[187] **CMS** Collaboration, S. Chatrchyan et al., *Search for a Higgs boson decaying into a Z and a photon in pp collisions at sqrt(s) = 7 and 8 TeV*, Phys. Lett. **B726** (2013) 587–609, [arXiv:1307.5515].

[188] **ATLAS and CMS** Collaborations, *Measurements of the Higgs boson production and decay rates and constraints on its couplings from a combined ATLAS and CMS analysis of the LHC pp collision data at $\sqrt{s} = 7$ and 8 TeV*, Tech. Rep. ATLAS-CONF-2015-044 and CMS-PAS-HIG-15-002, CERN, Geneva, 2015.

[189] A. Falkowski, F. Riva, and A. Urbano, *Higgs at last*, JHEP **1311** (2013) 111, [arXiv:1303.1812].

[190] P. P. Giardino, K. Kannike, I. Masina, M. Raidal, and A. Strumia, *The universal Higgs fit*, JHEP **1405** (2014) 046, [arXiv:1303.3570].

[191] J. Ellis and T. You, *Updated Global Analysis of Higgs Couplings*, JHEP **1306** (2013) 103, [arXiv:1303.3879].

[192] A. Djouadi and G. Moreau, *The couplings of the Higgs boson and its CP properties from fits of the signal strengths and their ratios at the 7+8 TeV LHC*, *Eur.Phys.J.* **C73** (2013), no. 9 2512, [arXiv:1303.6591].

[193] B. Dumont, S. Fichet, and G. von Gersdorff, *A Bayesian view of the Higgs sector with higher dimensional operators*, *JHEP* **1307** (2013) 065, [arXiv:1304.3369].

[194] G. Belanger, B. Dumont, U. Ellwanger, J. Gunion, and S. Kraml, *Global fit to Higgs signal strengths and couplings and implications for extended Higgs sectors*, *Phys. Rev.* **D88** (2013) 075008, [arXiv:1306.2941].

[195] S. Choi, S. Jung, and P. Ko, *Implications of LHC data on 125 GeV Higgs-like boson for the Standard Model and its various extensions*, *JHEP* **1310** (2013) 225, [arXiv:1307.3948].

[196] D. López-Val, T. Plehn, and M. Rauch, *Measuring Extended Higgs Sectors as a Consistent Free Couplings Model*, *JHEP* **1310** (2013) 134, [arXiv:1308.1979].

[197] S. Banerjee, S. Mukhopadhyay, and B. Mukhopadhyaya, *Higher dimensional operators and the LHC Higgs data: The role of modified kinematics*, *Phys.Rev.* **D89** (2014), no. 5 053010, [arXiv:1308.4860].

[198] A. Belyaev, M. S. Brown, R. Foadi, and M. T. Frandsen, *The Technicolor Higgs in the Light of LHC Data*, *Phys.Rev.* **D90** (2014), no. 3 035012, [arXiv:1309.2097].

[199] K. Cheung, J. S. Lee, and P.-Y. Tseng, *Higgcision in the Two-Higgs Doublet Models*, *JHEP* **1401** (2014) 085, [arXiv:1310.3937].

[200] J. Cao, Y. He, P. Wu, M. Zhang, and J. Zhu, *Higgs Phenomenology in the Minimal Dilaton Model after Run I of the LHC*, *JHEP* **1401** (2014) 150, [arXiv:1311.6661].

[201] L. Wang and X.-F. Han, *Status of the aligned two-Higgs-doublet model confronted with the Higgs data*, *JHEP* **1404** (2014) 128, [arXiv:1312.4759].

[202] B. Dumont, J. F. Gunion, and S. Kraml, *Phenomenological MSSM in view of the 125 GeV Higgs data*, *Phys.Rev.* **D89** (2014), no. 5 055018, [arXiv:1312.7027].

[203] J. Fan and M. Reece, *A New Look at Higgs Constraints on Stops*, *JHEP* **1406** (2014) 031, [arXiv:1401.7671].

[204] G. Belanger, V. Bizouard, and G. Chalons, *Boosting Higgs boson decays into gamma and a Z in the NMSSM*, *Phys.Rev.* **D89** (2014), no. 9 095023, [arXiv:1402.3522].

[205] P. Bechtle, S. Heinemeyer, O. Stål, T. Stefaniak, and G. Weiglein, *Probing the Standard Model with Higgs signal rates from the Tevatron, the LHC and a future ILC*, *JHEP* **1411** (2014) 039, [arXiv:1403.1582].

[206] J. Ellis, V. Sanz, and T. You, *Complete Higgs Sector Constraints on Dimension-6 Operators*, *JHEP* **1407** (2014) 036, [arXiv:1404.3667].

[207] B. Dumont, J. F. Gunion, Y. Jiang, and S. Kraml, *Constraints on and future prospects for Two-Higgs-Doublet Models in light of the LHC Higgs signal*, Phys.Rev. **D90** (2014), no. 3 035021, [`arXiv:1405.3584`].

[208] B. Dumont, J. F. Gunion, Y. Jiang, and S. Kraml, *Addendum to "Constraints on and future prospects for Two-Higgs-Doublet Models in light of the LHC Higgs signal"*, `arXiv:1409.4088`.

[209] K. Cheung, J. S. Lee, and P.-Y. Tseng, *Higgs precision analysis updates 2014*, Phys.Rev. **D90** (2014), no. 9 095009, [`arXiv:1407.8236`].

[210] J. de Blas, M. Ciuchini, E. Franco, D. Ghosh, S. Mishima, M. Pierini, L. Reina, and L. Silvestrini, *Global Bayesian Analysis of the Higgs-boson Couplings*, `arXiv:1410.4204`.

[211] M. Ciuchini, E. Franco, S. Mishima, M. Pierini, L. Reina, and L. Silvestrini, *Update of the electroweak precision fit, interplay with Higgs-boson signal strengths and model-independent constraints on new physics*, in *International Conference on High Energy Physics 2014 (ICHEP 2014) Valencia, Spain, July 2-9, 2014*, 2014. `arXiv:1410.6940`.

[212] J. Bergstrom and S. Riad, *Bayesian Model comparison of Higgs couplings*, Phys. Rev. **D91** (2015), no. 7 075008, [`arXiv:1411.4876`].

[213] T. Robens and T. Stefaniak, *Status of the Higgs Singlet Extension of the Standard Model after LHC Run 1*, Eur. Phys. J. **C75** (2015) 104, [`arXiv:1501.02234`].

[214] K. Cheung, J. S. Lee, and P.-Y. Tseng, *Higgs data constraints on the minimal supersymmetric standard model*, Phys. Rev. **D92** (2015), no. 9 095004, [`arXiv:1501.03552`].

[215] P. Bechtle, S. Heinemeyer, O. Stal, T. Stefaniak, and G. Weiglein, *HiggsSignals: Confronting arbitrary Higgs sectors with measurements at the Tevatron and the LHC*, Eur.Phys.J. **C74** (2014) 2711, [`arXiv:1305.1933`].

[216] G. Cacciapaglia, A. Deandrea, G. D. La Rochelle, and J.-B. Flament, *Higgs couplings beyond the Standard Model*, JHEP **1303** (2013) 029, [`arXiv:1210.8120`].

[217] G. Belanger, B. Dumont, U. Ellwanger, J. Gunion, and S. Kraml, *Higgs Couplings at the End of 2012*, JHEP **1302** (2013) 053, [`arXiv:1212.5244`].

[218] **ATLAS** Collaboration, G. Aad et al., *Constraints on new phenomena via Higgs boson couplings and invisible decays with the ATLAS detector*, JHEP **11** (2015) 206, [`arXiv:1509.00672`].

[219] **CMS** Collaboration, V. Khachatryan et al., *Search for the associated production of the Higgs boson with a top-quark pair*, JHEP **1409** (2014) 087, [`arXiv:1408.1682`].

[220] **The ATLAS and CMS Collaborations, the LHC Higgs Combination Group**, *Procedure for the LHC Higgs boson search combination in Summer 2011*, Tech. Rep. CMS-NOTE-2011-005. ATL-PHYS-PUB-2011-11, CERN, Geneva, Aug, 2011.

[221] **CMS** Collaboration, S. Chatrchyan et al., *Evidence for the direct decay of the 125 GeV Higgs boson to fermions*, *Nature Phys.* **10** (2014) 557–560, [arXiv:1401.6527].

[222] **ATLAS** Collaboration, *Data from Figure 7 from: Measurements of Higgs boson production and couplings in diboson final states with the ATLAS detector at the LHC: $H \to \gamma\gamma$*, http://doi.org/10.7484/INSPIREHEP.DATA.A78C.HK44.

[223] **ATLAS** Collaboration, *Data from Figure 7 from: Measurements of Higgs boson production and couplings in diboson final states with the ATLAS detector at the LHC: $H \to ZZ^* \to 4l$*, http://doi.org/10.7484/INSPIREHEP.DATA.RF5P.6M3K.

[224] **ATLAS** Collaboration, *Data from Figure 7 from: Measurements of Higgs boson production and couplings in diboson final states with the ATLAS detector at the LHC: $H \to WW^* \to l\nu l\nu$*, http://doi.org/10.7484/INSPIREHEP.DATA.26B4.TY5F.

[225] F. Boudjema, G. Cacciapaglia, K. Cranmer, G. Dissertori, A. Deandrea, et al., *On the presentation of the LHC Higgs Results*, arXiv:1307.5865.

[226] **ATLAS** Collaboration, *Search for the Standard Model Higgs boson produced in association with top quarks and decaying to $b\bar{b}$ in pp collisions at $\sqrt{s} = 8$ TeV with the ATLAS detector at the LHC*, Tech. Rep. ATLAS-CONF-2014-011, CERN, Geneva, Mar, 2014.

[227] **ATLAS** Collaboration, G. Aad et al., *Search for Invisible Decays of a Higgs Boson Produced in Association with a Z Boson in ATLAS*, *Phys. Rev. Lett.* **112** (2014) 201802, [arXiv:1402.3244].

[228] **CMS** Collaboration, S. Chatrchyan et al., *Search for invisible decays of Higgs bosons in the vector boson fusion and associated ZH production modes*, *Eur. Phys. J.* **C74** (2014) 2980, [arXiv:1404.1344].

[229] **CDF and DO** Collaborations, T. Aaltonen et al., *Higgs Boson Studies at the Tevatron*, *Phys.Rev.* **D88** (2013), no. 5 052014, [arXiv:1303.6346].

[230] **LHC Higgs Cross Section Working Group,** A. David et al., *LHC HXSWG interim recommendations to explore the coupling structure of a Higgs-like particle*, arXiv:1209.0040.

[231] G. Brooijmans, R. Contino, B. Fuks, F. Moortgat, P. Richardson, et al., *Les Houches 2013: Physics at TeV Colliders: New Physics Working Group Report*, arXiv:1405.1617.

[232] R. Frederix, S. Frixione, V. Hirschi, F. Maltoni, R. Pittau, et al., *Scalar and pseudoscalar Higgs production in association with a top-antitop pair*, Phys.Lett. **B701** (2011) 427–433, [arXiv:1104.5613].

[233] F. Demartin, F. Maltoni, K. Mawatari, B. Page, and M. Zaro, *Higgs characterisation at NLO in QCD: CP properties of the top-quark Yukawa interaction*, Eur.Phys.J. **C74** (2014), no. 9 3065, [arXiv:1407.5089].

[234] S. Berge, W. Bernreuther, and S. Kirchner, *Determination of the Higgs CP-mixing angle in the tau decay channels at the LHC including the Drell-Yan background*, Eur.Phys.J. **C74** (2014), no. 11 3164, [arXiv:1408.0798].

[235] "Python." http://www.python.org.

[236] "SciPy." http://www.scipy.org.

[237] P. Z. Skands, B. Allanach, H. Baer, C. Balazs, G. Belanger, et al., *SUSY Les Houches accord: Interfacing SUSY spectrum calculators, decay packages, and event generators*, JHEP **0407** (2004) 036, [hep-ph/0311123].

[238] K. Arnold, M. Bahr, G. Bozzi, F. Campanario, C. Englert, et al., *VBFNLO: A Parton level Monte Carlo for processes with electroweak bosons*, Comput.Phys.Commun. **180** (2009) 1661–1670, [arXiv:0811.4559].

[239] A. Martin, W. Stirling, R. Thorne, and G. Watt, *Parton distributions for the LHC*, Eur.Phys.J. **C63** (2009) 189–285, [arXiv:0901.0002].

[240] M. Spira, *HIGLU: A program for the calculation of the total Higgs production cross-section at hadron colliders via gluon fusion including QCD corrections*, hep-ph/9510347.

[241] A. Djouadi, J. Kalinowski, and M. Spira, *HDECAY: A Program for Higgs boson decays in the standard model and its supersymmetric extension*, Comput. Phys. Commun. **108** (1998) 56–74, [hep-ph/9704448].

[242] **ATLAS** Collaboration, *Updated coupling measurements of the Higgs boson with the ATLAS detector using up to 25 fb^{-1} of proton-proton collision data*, Tech. Rep. ATLAS-CONF-2014-009, CERN, Geneva, Mar, 2014.

[243] "iminuit." https://pypi.python.org/pypi/iminuit.

[244] F. James and M. Roos, *Minuit: A System for Function Minimization and Analysis of the Parameter Errors and Correlations*, Comput.Phys.Commun. **10** (1975) 343–367.

[245] M. Carena, S. Gori, N. R. Shah, C. E. Wagner, and L.-T. Wang, *Light Stau Phenomenology and the Higgs $\gamma\gamma$ Rate*, JHEP **1207** (2012) 175, [arXiv:1205.5842].

[246] M. Endo, T. Kitahara, and T. Yoshinaga, *Future Prospects for Stau in Higgs Coupling to Di-photon*, JHEP **1404** (2014) 139, [arXiv:1401.3748].

[247] A. Djouadi, *The Anatomy of electro-weak symmetry breaking. II. The Higgs bosons in the minimal supersymmetric model*, Phys.Rept. **459** (2008) 1–241, [hep-ph/0503173].

[248] **The ALEPH, DELPHI, L3 and OPAL experiments, the LEP SUSY working group,** note LEPSUSYWG/04-01.1. http://lepsusy.web.cern.ch/lepsusy/Welcome.html.

[249] T. Kitahara and T. Yoshinaga, *Stau with Large Mass Difference and Enhancement of the Higgs to Diphoton Decay Rate in the MSSM*, JHEP **1305** (2013) 035, [arXiv:1303.0461].

[250] G. Bélanger, G. Drieu La Rochelle, B. Dumont, R. M. Godbole, S. Kraml, et al., *LHC constraints on light neutralino dark matter in the MSSM*, Phys.Lett. **B726** (2013) 773–780, [arXiv:1308.3735].

[251] K. Cranmer, S. Kreiss, D. Lopez-Val, and T. Plehn, *Decoupling Theoretical Uncertainties from Measurements of the Higgs Boson*, Phys. Rev. **D91** (2015), no. 5 054032, [arXiv:1401.0080].

[252] **ATLAS** Collaboration, *Search for an Invisibly Decaying Higgs Boson Produced via Vector Boson Fusion in pp Collisions at $\sqrt{s} = 8$ TeV using the ATLAS Detector at the LHC*, .

[253] **ATLAS** Collaboration, G. Aad et al., *Search for the associated production of the Higgs boson with a top quark pair in multilepton final states with the ATLAS detector*, Phys. Lett. **B749** (2015) 519–541, [arXiv:1506.05988].

[254] **ATLAS** Collaboration, G. Aad et al., *Search for the Standard Model Higgs boson produced in association with top quarks and decaying into $b\bar{b}$ in pp collisions at $\sqrt{s} = 8$ TeV with the ATLAS detector*, Eur. Phys. J. **C75** (2015), no. 7 349, [arXiv:1503.05066].

[255] **CMS** Collaboration, V. Khachatryan et al., *Search for the standard model Higgs boson produced through vector boson fusion and decaying to $b\bar{b}$*, Phys. Rev. **D92** (2015), no. 3 032008, [arXiv:1506.01010].

[256] **CMS** Collaboration, V. Khachatryan et al., *Search for a standard model Higgs boson produced in association with a top-quark pair and decaying to bottom quarks using a matrix element method*, Eur. Phys. J. **C75** (2015) 251, [arXiv:1502.02485].

[257] K. Arnold, J. Bellm, G. Bozzi, M. Brieg, F. Campanario, et al., *VBFNLO: A Parton Level Monte Carlo for Processes with Electroweak Bosons – Manual for Version 2.5.0*, arXiv:1107.4038.

[258] J. F. Gunion, H. E. Haber, G. L. Kane, and S. Dawson, *The Higgs Hunter's Guide*. Westview Press, Boulder, CO, 2000.

[259] P. Ferreira, J. F. Gunion, H. E. Haber, and R. Santos, *Probing wrong-sign Yukawa couplings at the LHC and a future linear collider*, Phys. Rev. **D89** (2014) 115003, [arXiv:1403.4736].

[260] T. D. Lee, *A Theory of Spontaneous T Violation*, Phys. Rev. **D8** (1973) 1226–1239.

[261] J. Bernon, J. F. Gunion, H. E. Haber, Y. Jiang, and S. Kraml, *Scrutinizing the alignment limit in two-Higgs-doublet models: m_h = 125 GeV*, Phys. Rev. **D92** (2015) 075004, [arXiv:1507.00933].

[262] J. Bernon, J. F. Gunion, H. E. Haber, Y. Jiang, and S. Kraml, *Scrutinizing the alignment limit in two-Higgs-doublet models. II. m_H=125 GeV*, Phys. Rev. **D93** (2016), no. 3 035027, [arXiv:1511.03682].

[263] D. M. Asner et al., *ILC Higgs White Paper*, in *Community Summer Study 2013: Snowmass on the Mississippi (CSS2013) Minneapolis, MN, USA, July 29-August 6, 2013*, 2013. arXiv:1310.0763.

[264] J. F. Gunion and H. E. Haber, *The CP conserving two Higgs doublet model: The Approach to the decoupling limit*, Phys. Rev. **D67** (2003) 075019, [hep-ph/0207010].

[265] G. Branco, P. Ferreira, L. Lavoura, M. Rebelo, M. Sher, et al., *Theory and phenomenology of two-Higgs-doublet models*, Phys. Rept. **516** (2012) 1–102, [arXiv:1106.0034].

[266] S. L. Glashow and S. Weinberg, *Natural Conservation Laws for Neutral Currents*, Phys. Rev. **D15** (1977) 1958.

[267] E. A. Paschos, *Diagonal Neutral Currents*, Phys. Rev. **D15** (1977) 1966.

[268] U. Haisch, $\bar{B} \rightarrow X_s\gamma$: *Standard Model and Beyond*, arXiv:0805.2141.

[269] F. Mahmoudi and O. Stal, *Flavor constraints on the two-Higgs-doublet model with general Yukawa couplings*, Phys. Rev. **D81** (2010) 035016, [arXiv:0907.1791].

[270] R. S. Gupta and J. D. Wells, *Next Generation Higgs Bosons: Theory, Constraints and Discovery Prospects at the Large Hadron Collider*, Phys. Rev. **D81** (2010) 055012, [arXiv:0912.0267].

[271] M. Jung, A. Pich, and P. Tuzon, *Charged-Higgs phenomenology in the Aligned two-Higgs-doublet model*, JHEP **1011** (2010) 003, [arXiv:1006.0470].

[272] A. Barroso, P. M. Ferreira, and R. Santos, *Charge and CP symmetry breaking in two Higgs doublet models*, Phys. Lett. **B632** (2006) 684–687, [hep-ph/0507224].

[273] I. Ivanov, *Minkowski space structure of the Higgs potential in 2HDM*, Phys. Rev. **D75** (2007) 035001, [hep-ph/0609018].

[274] S. Davidson and H. E. Haber, *Basis-independent methods for the two-Higgs-doublet model*, Phys. Rev. **D72** (2005) 035004, [hep-ph/0504050].

[275] H. E. Haber and D. O'Neil, *Basis-independent methods for the two-Higgs-doublet model. II. The Significance of* $\tan\beta$, *Phys. Rev.* **D74** (2006) 015018, [`hep-ph/0602242`].

[276] H. E. Haber and D. O'Neil, *Basis-independent methods for the two-Higgs-doublet model III: The CP-conserving limit, custodial symmetry, and the oblique parameters S, T, U, Phys. Rev.* **D83** (2011) 055017, [`arXiv:1011.6188`].

[277] L. Lavoura and J. P. Silva, *Fundamental CP violating quantities in a SU(2) x U(1) model with many Higgs doublets, Phys. Rev.* **D50** (1994) 4619–4624, [`hep-ph/9404276`].

[278] F. J. Botella and J. P. Silva, *Jarlskog - like invariants for theories with scalars and fermions, Phys. Rev.* **D51** (1995) 3870–3875, [`hep-ph/9411288`].

[279] G. C. Branco, L. Lavoura, and J. P. Silva, *CP Violation.* Oxford University Press, Oxford, UK, 1999.

[280] G. C. Branco, M. N. Rebelo, and J. I. Silva-Marcos, *CP-odd invariants in models with several Higgs doublets, Phys. Lett.* **B614** (2005) 187–194, [`hep-ph/0502118`].

[281] J. F. Gunion and H. E. Haber, *Conditions for CP-violation in the general two-Higgs-doublet model, Phys. Rev.* **D72** (2005) 095002, [`hep-ph/0506227`].

[282] L. Lavoura, *Signatures of discrete symmetries in the scalar sector, Phys. Rev.* **D50** (1994) 7089–7092, [`hep-ph/9405307`].

[283] I. F. Ginzburg and M. Krawczyk, *Symmetries of two Higgs doublet model and CP violation, Phys. Rev.* **D72** (2005) 115013, [`hep-ph/0408011`].

[284] I. P. Ivanov, *Two-Higgs-doublet model from the group-theoretic perspective, Phys. Lett.* **B632** (2006) 360–365, [`hep-ph/0507132`].

[285] C. C. Nishi, *CP violation conditions in N-Higgs-doublet potentials, Phys. Rev.* **D74** (2006) 036003, [`hep-ph/0605153`]. [Erratum: Phys. Rev.D76, 119901(2007)].

[286] M. Maniatis, A. von Manteuffel, and O. Nachtmann, *CP violation in the general two-Higgs-doublet model: A Geometric view, Eur. Phys. J.* **C57** (2008) 719–738, [`arXiv:0707.3344`].

[287] B. Grzadkowski, O. M. Ogreid, and P. Osland, *Diagnosing CP properties of the 2HDM, JHEP* **01** (2014) 105, [`arXiv:1309.6229`].

[288] H. E. Haber and O. Stål, *New LHC benchmarks for the* $\mathcal{CP}$ *-conserving two-Higgs-doublet model, Eur. Phys. J.* **C75** (2015) 491, [`arXiv:1507.04281`].

[289] T. P. Cheng and M. Sher, *Mass Matrix Ansatz and Flavor Nonconservation in Models with Multiple Higgs Doublets, Phys. Rev.* **D35** (1987) 3484.

[290] M. Aoki, S. Kanemura, K. Tsumura, and K. Yagyu, *Models of Yukawa interaction in the two Higgs doublet model, and their collider phenomenology*, *Phys. Rev.* **D80** (2009) 015017, [`arXiv:0902.4665`].

[291] N. G. Deshpande and E. Ma, *Pattern of Symmetry Breaking with Two Higgs Doublets*, *Phys. Rev.* **D18** (1978) 2574.

[292] P. M. Ferreira, R. Santos, and A. Barroso, *Stability of the tree-level vacuum in two Higgs doublet models against charge or CP spontaneous violation*, *Phys. Lett.* **B603** (2004) 219–229, [`hep-ph/0406231`]. [Erratum: Phys. Lett.B629, 114(2005)].

[293] A. Barroso, P. Ferreira, I. Ivanov, and R. Santos, *Metastability bounds on the two Higgs doublet model*, *JHEP* **1306** (2013) 045, [`arXiv:1303.5098`].

[294] H. Huffel and G. Pocsik, *Unitarity Bounds on Higgs Boson Masses in the Weinberg-Salam Model With Two Higgs Doublets*, *Z. Phys.* **C8** (1981) 13.

[295] J. Maalampi, J. Sirkka, and I. Vilja, *Tree level unitarity and triviality bounds for two Higgs models*, *Phys. Lett.* **B265** (1991) 371–376.

[296] S. Kanemura, T. Kubota, and E. Takasugi, *Lee-Quigg-Thacker bounds for Higgs boson masses in a two doublet model*, *Phys. Lett.* **B313** (1993) 155–160, [`hep-ph/9303263`].

[297] A. G. Akeroyd, A. Arhrib, and E.-M. Naimi, *Note on tree level unitarity in the general two Higgs doublet model*, *Phys. Lett.* **B490** (2000) 119–124, [`hep-ph/0006035`].

[298] I. F. Ginzburg and I. P. Ivanov, *Tree-level unitarity constraints in the most general 2HDM*, *Phys. Rev.* **D72** (2005) 115010, [`hep-ph/0508020`].

[299] S. Kanemura and K. Yagyu, *Unitarity bound in the most general two Higgs doublet model*, *Phys. Lett.* **B751** (2015) 289–296, [`arXiv:1509.06060`].

[300] N. Chakrabarty, U. K. Dey, and B. Mukhopadhyaya, *High-scale validity of a two-Higgs doublet scenario: a study including LHC data*, *JHEP* **12** (2014) 166, [`arXiv:1407.2145`].

[301] D. Das and I. Saha, *Search for a stable alignment limit in two-Higgs-doublet models*, *Phys. Rev.* **D91** (2015), no. 9 095024, [`arXiv:1503.02135`].

[302] P. Ferreira, H. E. Haber, and E. Santos, *Preserving the validity of the Two-Higgs Doublet Model up to the Planck scale*, *Phys. Rev.* **D92** (2015) 033003, [`arXiv:1505.04001`].

[303] D. Chowdhury and O. Eberhardt, *Global fits of the two-loop renormalized Two-Higgs-Doublet model with soft Z_2 breaking*, *JHEP* **11** (2015) 052, [`arXiv:1503.08216`].

[304] H. E. Haber, *The Higgs data and the Decoupling Limit*, in *1st Toyama International Workshop on Higgs as a Probe of New Physics 2013 (HPNP2013) Toyama, Japan, February 13-16, 2013*, 2013. `arXiv:1401.0152`.

[305] H. E. Haber, M. J. Herrero, H. E. Logan, S. Penaranda, S. Rigolin, et al., *SUSY QCD corrections to the MSSM h0 b̄b vertex in the decoupling limit*, Phys. Rev. **D63** (2001) 055004, [`hep-ph/0007006`].

[306] M. Carena, H. E. Haber, H. E. Logan, and S. Mrenna, *Distinguishing a MSSM Higgs boson from the SM Higgs boson at a linear collider*, Phys. Rev. **D65** (2002) 055005, [`hep-ph/0106116`].

[307] S. Kanemura, S. Kiyoura, Y. Okada, E. Senaha, and C. P. Yuan, *New physics effect on the Higgs selfcoupling*, Phys. Lett. **B558** (2003) 157–164, [`hep-ph/0211308`].

[308] S. Kanemura, Y. Okada, E. Senaha, and C. P. Yuan, *Higgs coupling constants as a probe of new physics*, Phys. Rev. **D70** (2004) 115002, [`hep-ph/0408364`].

[309] M. Misiak, H. Asatrian, R. Boughezal, M. Czakon, T. Ewerth, et al., *Updated NNLO QCD predictions for the weak radiative B-meson decays*, Phys. Rev. Lett. **114** (2015) 221801, [`arXiv:1503.01789`].

[310] V. Weisskopf, *On the Self-Energy and the Electromagnetic Field of the Electron*, Phys. Rev. **56** (1939) 72–85.

[311] G. Altarelli, *The Higgs: so simple yet so unnatural*, Phys. Scripta **T158** (2013) 014011, [`arXiv:1308.0545`].

[312] P. S. B. Dev and A. Pilaftsis, *Maximally Symmetric Two Higgs Doublet Model with Natural Standard Model Alignment*, JHEP **12** (2014) 024, [`arXiv:1408.3405`].

[313] P. Ferreira, H. E. Haber, and J. P. Silva, *Generalized CP symmetries and special regions of parameter space in the two-Higgs-doublet model*, Phys. Rev. **D79** (2009) 116004, [`arXiv:0902.1537`].

[314] G. 't Hooft, *Naturalness, chiral symmetry, and spontaneous chiral symmetry breaking*, NATO Sci.Ser.B **59** (1980) 135.

[315] R. Barbieri, L. J. Hall, and V. S. Rychkov, *Improved naturalness with a heavy Higgs: An Alternative road to LHC physics*, Phys. Rev. **D74** (2006) 015007, [`hep-ph/0603188`].

[316] L. Lopez Honorez, E. Nezri, J. F. Oliver, and M. H. G. Tytgat, *The Inert Doublet Model: An Archetype for Dark Matter*, JCAP **0702** (2007) 028, [`hep-ph/0612275`].

[317] A. Goudelis, B. Herrmann, and O. Stål, *Dark matter in the Inert Doublet Model after the discovery of a Higgs-like boson at the LHC*, JHEP **09** (2013) 106, [`arXiv:1303.3010`].

[318] G. Belanger, B. Dumont, A. Goudelis, B. Herrmann, S. Kraml, and D. Sengupta, *Dilepton constraints in the Inert Doublet Model from Run 1 of the LHC*, Phys. Rev. **D91** (2015) 115011, [`arXiv:1503.07367`].

[319] A. Ilnicka, M. Krawczyk, and T. Robens, *Inert Doublet Model in light of LHC Run I and astrophysical data*, Phys. Rev. **D93** (2016), no. 5 055026, [`arXiv:1508.01671`].

[320] P. Ferreira and J. P. Silva, *A Two-Higgs Doublet Model With Remarkable CP Properties*, Eur. Phys. J. **C69** (2010) 45–52, [`arXiv:1001.0574`].

[321] A. Pilaftsis and P. S. B. Dev, *Looking for New Naturally Aligned Higgs Doublets at the LHC*, PoS **PLANCK2015** (2015) 105, [`arXiv:1510.08790`].

[322] J. Bernon, J. F. Gunion, Y. Jiang, and S. Kraml, *Light Higgs bosons in Two-Higgs-Doublet Models*, Phys. Rev. **D91** (2015), no. 7 075019, [`arXiv:1412.3385`].

[323] B. Coleppa, F. Kling, and S. Su, *Constraining Type II 2HDM in Light of LHC Higgs Searches*, JHEP **01** (2014) 161, [`arXiv:1305.0002`].

[324] O. Eberhardt, U. Nierste, and M. Wiebusch, *Status of the two-Higgs-doublet model of type II*, JHEP **07** (2013) 118, [`arXiv:1305.1649`].

[325] S. Chang, S. K. Kang, J.-P. Lee, K. Y. Lee, S. C. Park, and J. Song, *Two Higgs doublet models for the LHC Higgs boson data at $\sqrt{s} = 7$ and 8 TeV*, JHEP **09** (2014) 101, [`arXiv:1310.3374`].

[326] J. Baglio, O. Eberhardt, U. Nierste, and M. Wiebusch, *Benchmarks for Higgs Pair Production and Heavy Higgs boson Searches in the Two-Higgs-Doublet Model of Type II*, Phys. Rev. **D90** (2014), no. 1 015008, [`arXiv:1403.1264`].

[327] N. Craig, F. D'Eramo, P. Draper, S. Thomas, and H. Zhang, *The Hunt for the Rest of the Higgs Bosons*, JHEP **06** (2015) 137, [`arXiv:1504.04630`].

[328] N. Craig, J. Galloway, and S. Thomas, *Searching for Signs of the Second Higgs Doublet*, `arXiv:1305.2424`.

[329] M. Carena, I. Low, N. R. Shah, and C. E. Wagner, *Impersonating the Standard Model Higgs Boson: Alignment without Decoupling*, JHEP **1404** (2014) 015, [`arXiv:1310.2248`].

[330] M. Carena, H. E. Haber, I. Low, N. R. Shah, and C. E. M. Wagner, *Complementarity between nonstandard Higgs boson searches and precision Higgs boson measurements in the MSSM*, Phys. Rev. **D91** (2015) 035003, [`arXiv:1410.4969`].

[331] S. Dawson et al., *Working Group Report: Higgs Boson*, in *Community Summer Study 2013: Snowmass on the Mississippi (CSS2013) Minneapolis, MN, USA, July 29-August 6, 2013*, 2013. `arXiv:1310.8361`.

[332] **ALEPH, DELPHI, L3, OPAL Collaborations, the LEP working group for Higgs boson searches,** G. Abbiendi et al., *Search for Charged Higgs bosons: Combined Results Using LEP Data*, Eur. Phys. J. **C73** (2013) 2463, [`arXiv:1301.6065`].

[333] D. Eriksson, J. Rathsman, and O. Stål, *2HDMC: Two-Higgs-Doublet Model Calculator Physics and Manual*, Comput. Phys. Commun. **181** (2010) 189–205, [`arXiv:0902.0851`].

[334] M. E. Peskin and T. Takeuchi, *Estimation of oblique electroweak corrections*, Phys. Rev. **D46** (1992) 381–409.

[335] **Gfitter Group,** M. Baak et al., *The global electroweak fit at NNLO and prospects for the LHC and ILC*, Eur. Phys. J. **C74** (2014) 3046, [`arXiv:1407.3792`].

[336] **OPAL** Collaboration, G. Abbiendi et al., *Flavor independent h0A0 search and two Higgs doublet model interpretation of neutral Higgs boson searches at LEP*, Eur. Phys. J. **C40** (2005) 317–332, [`hep-ex/0408097`].

[337] F. Domingo, U. Ellwanger, E. Fullana, C. Hugonie, and M.-A. Sanchis-Lozano, *Radiative Upsilon decays and a light pseudoscalar Higgs in the NMSSM*, JHEP **0901** (2009) 061, [`arXiv:0810.4736`].

[338] U. Ellwanger and C. Hugonie, "`NMSSMTools_4.6.0`." `http://www.th.u-psud.fr/NMHDECAY/nmssmtools.html`.

[339] **CMS** Collaboration, S. Chatrchyan et al., *Search for a light pseudoscalar Higgs boson in the dimuon decay channel in pp collisions at $\sqrt{s} = 7$ TeV*, Phys. Rev. Lett. **109** (2012) 121801, [`arXiv:1206.6326`].

[340] **CMS** Collaboration, V. Khachatryan et al., *Search for a low-mass pseudoscalar Higgs boson produced in association with a $b\bar{b}$ pair in pp collisions at $\sqrt{s} = 8$ TeV*, Phys. Lett. **B758** (2016) 296–320, [`arXiv:1511.03610`].

[341] **ATLAS** Collaboration, *Measurements of the properties of the Higgs-like boson in the four lepton decay channel with the ATLAS detector using 25 fb^{-1} of proton-proton collision data*, Tech. Rep. ATLAS-CONF-2013-013, CERN, Geneva, Mar, 2013.

[342] **CMS** Collaboration, *Search for a heavy Higgs boson in the H to ZZ to 2l2nu channel in pp collisions at sqrt(s)= 7 and 8 TeV*, Tech. Rep. CMS-PAS-HIG-13-014, CERN, Geneva, 2013.

[343] **ATLAS** Collaboration, G. Aad et al., *Search for neutral Higgs bosons of the minimal supersymmetric standard model in pp collisions at $\sqrt{s} = 8$ TeV with the ATLAS detector*, JHEP **1411** (2014) 056, [`arXiv:1409.6064`].

[344] **CMS** Collaboration, V. Khachatryan et al., *Search for neutral MSSM Higgs bosons decaying to a pair of tau leptons in pp collisions*, JHEP **1410** (2014) 160, [`arXiv:1408.3316`].

[345] **CMS** Collaboration, *Search for a pseudoscalar boson A decaying into a Z and an h boson in the llbb final state*, Tech. Rep. CMS-PAS-HIG-14-011, CERN, Geneva, 2014.

[346] **CMS** Collaboration, V. Khachatryan et al., *Search for Neutral Resonances Decaying into a Z Boson and a Pair of b Jets or Tau Leptons*, `arXiv:1603.02991`.

[347] **ATLAS** Collaboration, G. Aad et al., *Search for a CP-odd Higgs boson decaying to Zh in pp collisions at $\sqrt{s} = 8$ TeV with the ATLAS detector*, *Phys. Lett.* **B744** (2015) 163–183, [`arXiv:1502.04478`].

[348] R. V. Harlander, S. Liebler, and H. Mantler, *SusHi: A program for the calculation of Higgs production in gluon fusion and bottom-quark annihilation in the Standard Model and the MSSM*, *Comput.Phys.Commun.* **184** (2013) 1605–1617, [`arXiv:1212.3249`].

[349] **ATLAS** Collaboration, *Measurements of the Higgs boson production and decay rates and coupling strengths using pp collision data at $\sqrt{s} = 7$ and 8 TeV in the ATLAS experiment*, Tech. Rep. ATLAS-CONF-2015-007, CERN, Geneva, Mars, 2015.

[350] **ATLAS** Collaboration, *Search for the associated production of the Higgs boson with a top quark pair in multi-lepton final states with the ATLAS detector*, Tech. Rep. ATLAS-CONF-2015-006, CERN, Geneva, Mar, 2015.

[351] **CDF and DO** Collaborations, T. Aaltonen et al., *Higgs Boson Studies at the Tevatron*, *Phys. Rev.* **D88** (2013) 052014, [`arXiv:1303.6346`].

[352] G. Bhattacharyya, D. Das, P. B. Pal, and M. N. Rebelo, *Scalar sector properties of two-Higgs-doublet models with a global U(1) symmetry*, *JHEP* **10** (2013) 081, [`arXiv:1308.4297`].

[353] G. Bhattacharyya and D. Das, *Nondecoupling of charged scalars in Higgs decay to two photons and symmetries of the scalar potential*, *Phys. Rev.* **D91** (2015) 015005, [`arXiv:1408.6133`].

[354] D. Dicus, A. Stange, and S. Willenbrock, *Higgs decay to top quarks at hadron colliders*, *Phys. Lett.* **B333** (1994) 126–131, [`hep-ph/9404359`].

[355] R. Frederix and F. Maltoni, *Top pair invariant mass distribution: A Window on new physics*, *JHEP* **01** (2009) 047, [`arXiv:0712.2355`].

[356] S. Jung, J. Song, and Y. W. Yoon, *Dip or nothingness of a Higgs resonance from the interference with a complex phase*, *Phys. Rev.* **D92** (2015) 055009, [`arXiv:1505.00291`].

[357] J. Hajer, Y.-Y. Li, T. Liu, and J. F. H. Shiu, *Heavy Higgs Bosons at 14 TeV and 100 TeV*, *JHEP* **11** (2015) 124, [`arXiv:1504.07617`].

[358] N. Chen, J. Li, and Y. Liu, *LHC searches for heavy neutral Higgs bosons with a top jet substructure analysis*, Phys. Rev. **D93** (2016), no. 9 095013, [arXiv:1509.03848].

[359] A. Arhrib, P. M. Ferreira, and R. Santos, *Are There Hidden Scalars in LHC Higgs Results?*, JHEP **03** (2014) 053, [arXiv:1311.1520].

[360] G. Dorsch, S. Huber, K. Mimasu, and J. No, *Echoes of the Electroweak Phase Transition: Discovering a second Higgs doublet through $A_0 \to ZH_0$*, Phys. Rev. Lett. **113** (2014) 211802, [arXiv:1405.5537].

[361] B. Coleppa, F. Kling, and S. Su, *Exotic Decays Of A Heavy Neutral Higgs Through HZ/AZ Channel*, JHEP **09** (2014) 161, [arXiv:1404.1922].

[362] **ATLAS** Collaboration, *Search for resonances decaying to photon pairs in 3.2 fb^{-1} of pp collisions at $\sqrt{s}$ = 13 TeV with the ATLAS detector*, ATLAS-CONF-2015-081 (2015).

[363] **CMS** Collaboration, *Search for new physics in high mass diphoton events in proton-proton collisions at 13TeV*, CMS-PAS-EXO-15-004 (2015).

[364] **ATLAS** Collaboration, *Search for scalar diphoton resonances with 15.4 fb^{-1} of data collected at $\sqrt{s}$=13 TeV in 2015 and 2016 with the ATLAS detector*, Tech. Rep. ATLAS-CONF-2016-059, CERN, Geneva, Aug, 2016.

[365] **CMS** Collaboration, V. Khachatryan et al., *Search for high-mass diphoton resonances in proton-proton collisions at 13 TeV and combination with 8 TeV search*, arXiv:1609.02507.

[366] J. Chang, K. Cheung, and C.-T. Lu, *Interpreting the 750 GeV diphoton resonance using photon jets in hidden-valley-like models*, Phys. Rev. **D93** (2016), no. 7 075013, [arXiv:1512.06671].

[367] X.-J. Bi, R. Ding, Y. Fan, L. Huang, C. Li, T. Li, S. Raza, X.-C. Wang, and B. Zhu, *A Promising Interpretation of Diphoton Resonance at 750 GeV*, arXiv:1512.08497.

[368] L. Aparicio, A. Azatov, E. Hardy, and A. Romanino, *Diphotons from Diaxions*, JHEP **05** (2016) 077, [arXiv:1602.00949].

[369] U. Ellwanger and C. Hugonie, *A 750 GeV Diphoton Signal from a Very Light Pseudoscalar in the NMSSM*, JHEP **05** (2016) 114, [arXiv:1602.03344].

[370] B. Dasgupta, J. Kopp, and P. Schwaller, *Photons, Photon Jets and Dark Photons at 750 GeV and Beyond*, arXiv:1602.04692.

[371] C.-W. Chiang, H. Fukuda, M. Ibe, and T. T. Yanagida, *750 GeV diphoton resonance in a visible heavy QCD axion model*, Phys. Rev. **D93** (2016), no. 9 095016, [arXiv:1602.07909].

[372] G. Arcadi, P. Ghosh, Y. Mambrini, and M. Pierre, *Re-opening dark matter windows compatible with a diphoton excess*, `arXiv:1603.05601`.

[373] J. F. Gunion and X.-G. He, *Determining the CP nature of a neutral Higgs boson at the LHC*, Phys. Rev. Lett. **76** (1996) 4468–4471, [`hep-ph/9602226`].

[374] M. E. Peskin, *Estimation of LHC and ILC Capabilities for Precision Higgs Boson Coupling Measurements*, in *Community Summer Study 2013: Snowmass on the Mississippi (CSS2013) Minneapolis, MN, USA, July 29-August 6, 2013*, 2013. `arXiv:1312.4974`.

[375] **CMS** Collaboration, *Search for new resonances in the diphoton final state in the mass range between 80 and 115 GeV in pp collisions at $\sqrt{s} = 8$ TeV*, Tech. Rep. CMS-PAS-HIG-14-037, CERN, Geneva, 2015.

[376] J. Gunion and H. E. Haber, *Higgs Bosons in Supersymmetric Models. 1.*, Nucl.Phys. **B272** (1986) 1.

[377] L.-F. Li, Y. Liu, and L. Wolfenstein, *Hidden Higgs Particles*, Phys.Lett. **B159** (1985) 45.

[378] D. Curtin, R. Essig, S. Gori, P. Jaiswal, A. Katz, et al., *Exotic decays of the 125 GeV Higgs boson*, Phys.Rev. **D90** (2014), no. 7 075004, [`arXiv:1312.4992`].

[379] M. Carena, S. Heinemeyer, O. Stål, C. Wagner, and G. Weiglein, *MSSM Higgs Boson Searches at the LHC: Benchmark Scenarios after the Discovery of a Higgs-like Particle*, Eur.Phys.J. **C73** (2013) 2552, [`arXiv:1302.7033`].

[380] D. G. Cerdeno, P. Ghosh, and C. B. Park, *Probing the two light Higgs scenario in the NMSSM with a low-mass pseudoscalar*, JHEP **1306** (2013) 031, [`arXiv:1301.1325`].

[381] J. Cao, F. Ding, C. Han, J. M. Yang, and J. Zhu, *A light Higgs scalar in the NMSSM confronted with the latest LHC Higgs data*, JHEP **1311** (2013) 018, [`arXiv:1309.4939`].

[382] N.-E. Bomark, S. Moretti, S. Munir, and L. Roszkowski, *A light NMSSM pseudoscalar Higgs boson at the LHC redux*, JHEP **02** (2015) 044, [`arXiv:1409.8393`].

[383] J. Huang, T. Liu, L.-T. Wang, and F. Yu, *Supersymmetric Exotic Decays of the 125 GeV Higgs Boson*, Phys.Rev.Lett. **112** (2014), no. 22 221803, [`arXiv:1309.6633`].

[384] J. F. Gunion, H. E. Haber, and T. Moroi, *Will at least one of the Higgs bosons of the next-to-minimal supersymmetric extension of the standard model be observable at LEP-2 or the LHC?*, eConf **C960625** (1996) LTH095, [`hep-ph/9610337`].

[385] L. Hall and L. Randall, *Weak scale effective supersymmetry*, Phys.Rev.Lett. **65** (1990) 2939–2942.

[386] G. D'Ambrosio, G. Giudice, G. Isidori, and A. Strumia, *Minimal flavor violation: An Effective field theory approach*, *Nucl.Phys.* **B645** (2002) 155–187, [`hep-ph/0207036`].

[387] J. Bernon and C. Smith, *Baryonic R-parity violation and its running*, *JHEP* **07** (2014) 038, [`arXiv:1404.5496`].

[388] C. D. Froggatt and H. B. Nielsen, *Hierarchy of Quark Masses, Cabibbo Angles and CP Violation*, *Nucl. Phys.* **B147** (1979) 277–298.

[389] E. Nikolidakis and C. Smith, *Minimal Flavor Violation, Seesaw, and R-parity*, *Phys. Rev.* **D77** (2008) 015021, [`arXiv:0710.3129`].

[390] L. Mercolli and C. Smith, *EDM constraints on flavored CP-violating phases*, *Nucl.Phys.* **B817** (2009) 1–24, [`arXiv:0902.1949`].

[391] G. Isidori, Y. Nir, and G. Perez, *Flavor Physics Constraints for Physics Beyond the Standard Model*, *Ann.Rev.Nucl.Part.Sci.* **60** (2010) 355, [`arXiv:1002.0900`].

[392] G. Colangelo, E. Nikolidakis, and C. Smith, *Supersymmetric models with minimal flavour violation and their running*, *Eur.Phys.J.* **C59** (2009) 75–98, [`arXiv:0807.0801`].

[393] E. Nikolidakis, *Renormalization group equations in the MSSM with Minimal Flavour Violation*. PhD thesis, University of Bern, 2008.

[394] S. P. Martin, *A Supersymmetry primer*, `hep-ph/9709356`. [Adv. Ser. Direct. High Energy Phys.18, 1(1998)].

[395] P. Fayet, *Massive gluinos*, *Phys. Lett.* **B78** (1978) 417–420.

[396] J. Polchinski and L. Susskind, *Breaking of Supersymmetry at Intermediate-Energy*, *Phys. Rev.* **D26** (1982) 3661.

[397] L. J. Hall and L. Randall, *U(1)-R symmetric supersymmetry*, *Nucl. Phys.* **B352** (1991) 289–308.

[398] E. Bagnaschi, F. Brummer, W. Buchmuller, A. Voigt, and G. Weiglein, *Vacuum stability and supersymmetry at high scales with two Higgs doublets*, *JHEP* **03** (2016) 158, [`arXiv:1512.07761`].

[399] R. Barbier, C. Berat, M. Besancon, M. Chemtob, A. Deandrea, et al., *R-parity violating supersymmetry*, *Phys.Rept.* **420** (2005) 1–202, [`hep-ph/0406039`].

[400] G. R. Farrar and P. Fayet, *Phenomenology of the Production, Decay, and Detection of New Hadronic States Associated with Supersymmetry*, *Phys. Lett.* **B76** (1978) 575–579.

[401] L. E. Ibanez and G. G. Ross, *Discrete gauge symmetries and the origin of baryon and lepton number conservation in supersymmetric versions of the standard model*, *Nucl. Phys.* **B368** (1992) 3–37.

[402] R. N. Mohapatra, *New Contributions to Neutrinoless Double beta Decay in Supersymmetric Theories*, Phys. Rev. **D34** (1986) 3457–3461.

[403] S. Dimopoulos, S. Raby, and F. Wilczek, *Proton Decay in Supersymmetric Models*, Phys. Lett. **B112** (1982) 133.

[404] M. Dine, W. Fischler, and M. Srednicki, *Supersymmetric Technicolor*, Nucl. Phys. **B189** (1981) 575–593.

[405] S. Dimopoulos and S. Raby, *Supercolor*, Nucl. Phys. **B192** (1981) 353–368.

[406] C. R. Nappi and B. A. Ovrut, *Supersymmetric Extension of the SU(3) x SU(2) x U(1) Model*, Phys. Lett. **B113** (1982) 175–179.

[407] L. Alvarez-Gaume, M. Claudson, and M. B. Wise, *Low-Energy Supersymmetry*, Nucl. Phys. **B207** (1982) 96.

[408] G. F. Giudice and R. Rattazzi, *Theories with gauge mediated supersymmetry breaking*, Phys. Rept. **322** (1999) 419–499, [`hep-ph/9801271`].

[409] L. Randall and R. Sundrum, *Out of this world supersymmetry breaking*, Nucl. Phys. **B557** (1999) 79–118, [`hep-th/9810155`].

[410] G. F. Giudice, M. A. Luty, H. Murayama, and R. Rattazzi, *Gaugino mass without singlets*, JHEP **12** (1998) 027, [`hep-ph/9810442`].

[411] A. H. Chamseddine, R. L. Arnowitt, and P. Nath, *Locally Supersymmetric Grand Unification*, Phys. Rev. Lett. **49** (1982) 970.

[412] R. Barbieri, S. Ferrara, and C. A. Savoy, *Gauge Models with Spontaneously Broken Local Supersymmetry*, Phys. Lett. **B119** (1982) 343.

[413] N. Ohta, *Grand unified theories based on local supersymmetry*, Prog. Theor. Phys. **70** (1983) 542.

[414] L. J. Hall, J. D. Lykken, and S. Weinberg, *Supergravity as the Messenger of Supersymmetry Breaking*, Phys. Rev. **D27** (1983) 2359–2378.

[415] L. Girardello and M. T. Grisaru, *Soft Breaking of Supersymmetry*, Nucl. Phys. **B194** (1982) 65.

[416] B. Allanach, A. Dedes, and H. K. Dreiner, *Two loop supersymmetric renormalization group equations including R-parity violation and aspects of unification*, Phys.Rev. **D60** (1999) 056002, [`hep-ph/9902251`].

[417] B. Allanach, A. Dedes, and H. Dreiner, *R parity violating minimal supergravity model*, Phys.Rev. **D69** (2004) 115002, [`hep-ph/0309196`].

[418] P. Paradisi, M. Ratz, R. Schieren, and C. Simonetto, *Running minimal flavor violation*, Phys.Lett. **B668** (2008) 202–209, [`arXiv:0805.3989`].

[419] G. Krnjaic and D. Stolarski, *Gauging the Way to MFV*, *JHEP* **1304** (2013) 064, [arXiv:1212.4860].

[420] R. Franceschini and R. Mohapatra, *New Patterns of Natural R-Parity Violation with Supersymmetric Gauged Flavor*, *JHEP* **1304** (2013) 098, [arXiv:1301.3637].

[421] C. Csaki and B. Heidenreich, *A Complete Model for R-parity Violation*, *Phys.Rev.* **D88** (2013) 055023, [arXiv:1302.0004].

[422] A. Florez, D. Restrepo, M. Velasquez, and O. Zapata, *Baryonic violation of R-parity from anomalous* $U(1)_H$, *Phys.Rev.* **D87** (2013), no. 9 095010, [arXiv:1303.0278].

[423] A. Monteux, *Natural, R-parity violating supersymmetry and horizontal flavor symmetries*, *Phys. Rev. D 88,* **045029** (2013) 045029, [arXiv:1305.2921].

[424] F. Brummer, S. Kraml, S. Kulkarni, and C. Smith, *The Flavour of Natural SUSY*, *Eur. Phys. J.* **C74** (2014), no. 9 3059, [arXiv:1402.4024].

[425] C. Csaki, Y. Grossman, and B. Heidenreich, *MFV SUSY: A Natural Theory for R-Parity Violation*, *Phys.Rev.* **D85** (2012) 095009, [arXiv:1111.1239].

[426] B. Allanach and B. Gripaios, *Hide and Seek With Natural Supersymmetry at the LHC*, *JHEP* **1205** (2012) 062, [arXiv:1202.6616].

[427] M. Asano, K. Rolbiecki, and K. Sakurai, *Can R-parity violation hide vanilla supersymmetry at the LHC?*, *JHEP* **1301** (2013) 128, [arXiv:1209.5778].

[428] G. Durieux, J.-M. Gerard, F. Maltoni, and C. Smith, *Three-generation baryon and lepton number violation at the LHC*, *Phys.Lett.* **B721** (2013) 82–85, [arXiv:1210.6598].

[429] J. Berger, M. Perelstein, M. Saelim, and P. Tanedo, *The Same-Sign Dilepton Signature of RPV/MFV SUSY*, *JHEP* **1304** (2013) 077, [arXiv:1302.2146].

[430] G. Durieux and C. Smith, *The same-sign top signature of R-parity violation*, *JHEP* **1310** (2013) 068, [arXiv:1307.1355].

[431] B. Batell, T. Lin, and L.-T. Wang, *Flavored Dark Matter and R-Parity Violation*, *JHEP* **1401** (2014) 075, [arXiv:1309.4462].

[432] M. Saelim and M. Perelstein, *RPV SUSY with Same-Sign Dileptons at LHC-14*, in *Community Summer Study 2013: Snowmass on the Mississippi (CSS2013) Minneapolis, MN, USA, July 29-August 6, 2013*, 2013. arXiv:1309.7707.

[433] B. Allanach and S. Renner, *Large Hadron Collider constraints on a light baryon number violating sbottom coupling to a top and a light quark*, *Eur.Phys.J.* **C74** (2014) 2707, [arXiv:1310.6016].

[434] B. Bhattacherjee and A. Chakraborty, *Study of the baryonic R-parity violating MSSM using the jet substructure technique at the 14 TeV LHC*, Phys. Rev. **D89** (2014), no. 11 115016, [`arXiv:1311.5785`].

[435] W. Porod, *SPheno, a program for calculating supersymmetric spectra, SUSY particle decays and SUSY particle production at e+ e- colliders*, Comput.Phys.Commun. **153** (2003) 275–315, [`hep-ph/0301101`].

[436] W. Porod and F. Staub, *SPheno 3.1: Extensions including flavour, CP-phases and models beyond the MSSM*, Comput.Phys.Commun. **183** (2012) 2458–2469, [`arXiv:1104.1573`].

[437] M.-x. Luo and Y. Xiao, *Two loop renormalization group equations in the standard model*, Phys. Rev. Lett. **90** (2003) 011601, [`hep-ph/0207271`].

[438] J. Bernon and C. Smith, *Could the width of the diphoton anomaly signal a three-body decay?*, Phys. Lett. **B757** (2016) 148–153, [`arXiv:1512.06113`].

[439] J. Bernon, A. Goudelis, S. Kraml, K. Mawatari, and D. Sengupta, *Characterising the 750 GeV diphoton excess*, JHEP **05** (2016) 128, [`arXiv:1603.03421`].

Higgs sector characterization and aspects of the flavor puzzle

Abstract: The Standard Model (SM) of particle physics stands as the most successful description of the fundamental interactions between elementary particles. The discovery of a Higgs boson, at a mass of 125 GeV, in July 2012 at the Large Hadron Collider (LHC), marked its ultimate confirmation. However, various observational and theoretical problems lie in the heart of the SM, with the majority of them linked to the Higgs sector. Being a scalar, the Higgs boson is subject to very large radiative corrections and this ultimately leads to the electroweak hierarchy problem. One of the main goals of the LHC program is to precisely probe the Higgs sector, in order to characterize the mechanism at the origin of the breaking of the electroweak symmetry and test possible solutions to the hierarchy problem. The Higgs sector is also responsible for the generation of the fermion masses, as it induces the Yukawa couplings. The SM flavor sector is highly hierarchical and this leads to flavor puzzles in theories beyond the SM.

The first part of this thesis is dedicated to the precise characterization of the Higgs sector. In particular, the public tool `Lilith` is presented, which allows to derive constraints on new physics models based on the Higgs measurements at colliders. It is then used to perform global fits of the Higgs couplings in the context of various scenarios. In the second part, the phenomenology of two-Higgs-doublet models is studied in the light of the results from the first run of the LHC. The so-called alignment limit is explored in detail, as well as the possible presence of light scalar states. Finally, in the last part of this thesis, the Minimal Flavor Violation hypothesis is introduced as a possible solution to the flavor puzzles beyond the SM. Enforcing it in the Minimal Supersymmetric Standard Model, the renormalisation group evolution of the baryonic R-parity violating couplings is then studied in detail.

Caractérisation du secteur de Higgs et aspects du problème de la saveur

Résumé: Le Modèle Standard (MS) de la physique des particules s'est imposé comme étant la description la plus précise des interactions fondamentales entre les particules élémentaires. La découverte d'un boson de Higgs, avec une masse de 125 GeV, en Juillet 2012 au Large Hadron Collider (LHC), en a marqué sa confirmation définitive. Cependant, de nombreux problèmes observationnels et théoriques sont au coeur du MS, la plupart liés au secteur de Higgs. Etant une particule scalaire, le boson de Higgs souffre de très grandes corrections radiatives, ce qui déstabilise l'échelle électro-faible et mène au problème de hiérarchie. L'un des buts principaux du LHC est d'explorer précisément le secteur de Higgs, afin de caractériser le mécanisme à l'origine de la brisure de la symétrie électro-faible et de tester de possibles solutions au problème de hiérarchie. Le secteur de Higgs est également responsable de la génération des masses des fermions dans le MS, par le biais des couplages de Yukawa. Ces couplages sont extrêmement non génériques et cela mène aux problèmes de la saveur au delà du MS.

La première partie de cette thèse se concentre sur la caractérisation précise du secteur de Higgs. En particulier, le code public `Lilith` est présenté, il permet de dériver des contraintes sur des scénarios de nouvelle physique à l'aide des mesures des propriétés du boson de Higgs en collisionneurs. Une analyse des couplages du boson de Higgs dans le contexte de plusieurs scénarios est ensuite effectuée. Dans la seconde partie, la phénoménologie des modèles à deux doublets de Higgs est étudiée à la lumière des résultats de la première période d'exploitation du LHC. La limite d'alignement, ainsi que la possible présence de bosons de Higgs légers, sont étudiées en détail. Finalement, dans la dernière partie de cette thèse, l'hypothèse de Violation Minimale de la Saveur est introduite comme une solution potentielle aux problèmes de la saveur au delà du MS. Appliquée au Modèle Standard Supersymétrique Minimal, l'évolution des couplages baryoniques violant la parité R sous le groupe de renormalisation est analysée en détail.